EFFECTS OF EXTREME WEATHER EVENTS ON COASTAL CARBON AND NUTRIENT CYCLING

EDITED BY: Christopher Osburn, Eero Asmala and Hans Paerl
PUBLISHED IN: Frontiers in Marine Science

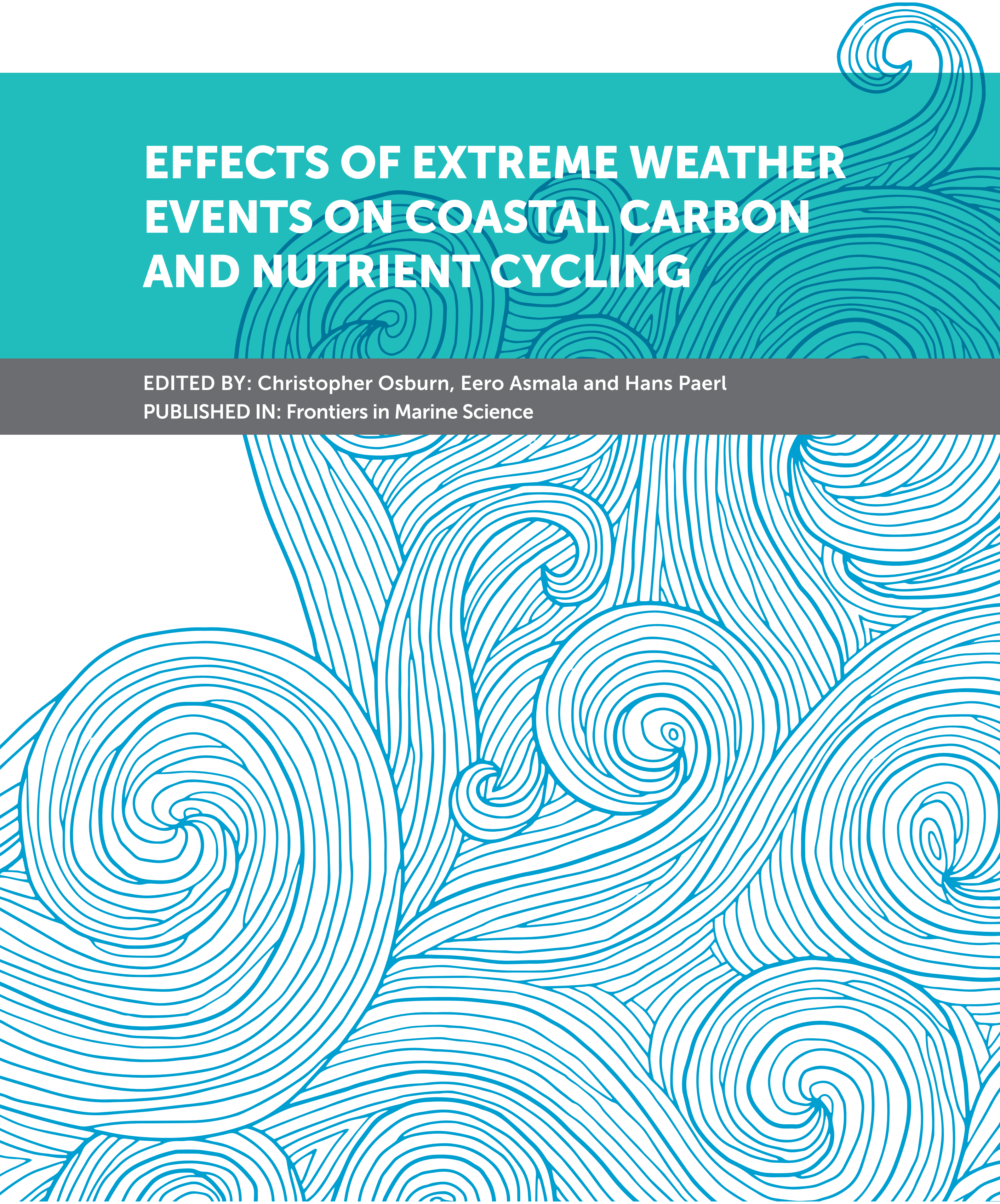

frontiers Research Topics

ISSN 1664-8714
ISBN 978-2-83250-492-5
DOI 10.3389/978-2-83250-492-5

About Frontiers

Frontiers is more than just an open-access publisher of scholarly articles: it is a pioneering approach to the world of academia, radically improving the way scholarly research is managed. The grand vision of Frontiers is a world where all people have an equal opportunity to seek, share and generate knowledge. Frontiers provides immediate and permanent online open access to all its publications, but this alone is not enough to realize our grand goals.

Frontiers Journal Series

The Frontiers Journal Series is a multi-tier and interdisciplinary set of open-access, online journals, promising a paradigm shift from the current review, selection and dissemination processes in academic publishing. All Frontiers journals are driven by researchers for researchers; therefore, they constitute a service to the scholarly community. At the same time, the Frontiers Journal Series operates on a revolutionary invention, the tiered publishing system, initially addressing specific communities of scholars, and gradually climbing up to broader public understanding, thus serving the interests of the lay society, too.

Dedication to Quality

Each Frontiers article is a landmark of the highest quality, thanks to genuinely collaborative interactions between authors and review editors, who include some of the world's best academicians. Research must be certified by peers before entering a stream of knowledge that may eventually reach the public - and shape society; therefore, Frontiers only applies the most rigorous and unbiased reviews.
Frontiers revolutionizes research publishing by freely delivering the most outstanding research, evaluated with no bias from both the academic and social point of view. By applying the most advanced information technologies, Frontiers is catapulting scholarly publishing into a new generation.

What are Frontiers Research Topics?

Frontiers Research Topics are very popular trademarks of the Frontiers Journals Series: they are collections of at least ten articles, all centered on a particular subject. With their unique mix of varied contributions from Original Research to Review Articles, Frontiers Research Topics unify the most influential researchers, the latest key findings and historical advances in a hot research area! Find out more on how to host your own Frontiers Research Topic or contribute to one as an author by contacting the Frontiers Editorial Office: frontiersin.org/about/contact

EFFECTS OF EXTREME WEATHER EVENTS ON COASTAL CARBON AND NUTRIENT CYCLING

Topic Editors:
Christopher Osburn, North Carolina State University, United States
Eero Asmala, University of Helsinki, Finland
Hans Paerl, University of North Carolina at Chapel Hill, United States

Citation: Osburn, C., Asmala, E., Paerl, H., eds. (2022). Effects of Extreme Weather Events on Coastal Carbon and Nutrient Cycling. Lausanne: Frontiers Media SA. doi: 10.3389/978-2-83250-492-5

Table of Contents

frontiers
in Marine Science

ORIGINAL RESEARCH
published: 07 August 2019
doi: 10.3389/fmars.2019.00493

High Emissions of Carbon Dioxide and Methane From the Coastal Baltic Sea at the End of a Summer Heat Wave

Christoph Humborg[1,2], Marc. C. Geibel[1], Xiaole Sun[1], Michelle McCrackin[1], Carl-Magnus Mörth[3], Christian Stranne[3], Martin Jakobsson[3], Bo Gustafsson[1,2], Alexander Sokolov[1], Alf Norkko[1,2] and Joanna Norkko[2]*

[1] Baltic Sea Centre, Stockholm University, Stockholm, Sweden, [2] Faculty of Biological and Environmental Sciences, Tvärminne Zoological Station, University of Helsinki, Helsinki, Finland, [3] Department of Geological Sciences, Stockholm University, Stockholm, Sweden

Edited by:
Hans Paerl,
University of North Carolina at Chapel Hill, United States

Reviewed by:
Warwick F. Vincent,
Laval University, Canada
Jeffrey Chanton,
Florida State University, United States

***Correspondence:**
Christoph Humborg
christoph.humborg@su.se

Specialty section:
This article was submitted to Marine Biogeochemistry, a section of the journal Frontiers in Marine Science

Received: *06 May 2019*
Accepted: *22 July 2019*
Published: *07 August 2019*

Citation:
Humborg C, Geibel MC, Sun X, McCrackin M, Mörth C-M, Stranne C, Jakobsson M, Gustafsson B, Sokolov A, Norkko A and Norkko J (2019) High Emissions of Carbon Dioxide and Methane From the Coastal Baltic Sea at the End of a Summer Heat Wave. Front. Mar. Sci. 6:493. doi: 10.3389/fmars.2019.00493

The summer heat wave in 2018 led to the highest recorded water temperatures since 1926 – up to 21°C – in bottom coastal waters of the Baltic Sea, with implications for the respiration patterns in these shallow coastal systems. We applied cavity ring-down spectrometer measurements to continuously monitor carbon dioxide (CO_2) and methane (CH_4) surface-water concentrations, covering the coastal archipelagos of Sweden and Finland and the open and deeper parts of the Northern Baltic Proper. This allowed us to (i) follow an upwelling event near the Swedish coast leading to elevated CO_2 and moderate CH_4 outgassing, and (ii) to estimate CH_4 sources and fluxes along the coast by investigating water column inventories and air-sea fluxes during a storm and an associated downwelling event. At the end of the heat wave, before the storm event, we found elevated CO_2 (1583 μatm) and CH_4 (70 nmol/L) concentrations. During the storm, a massive CO_2 sea-air flux of up to 274 mmol m^{-2} d^{-1} was observed. While water-column CO_2 concentrations were depleted during several hours of the storm, CH_4 concentrations remained elevated. Overall, we found a positive relationship between CO_2 and CH_4 wind-driven sea-air fluxes, however, the highest CH_4 fluxes were observed at low winds whereas highest CO_2 fluxes were during peak winds, suggesting different sources and processes controlling their fluxes besides wind. We applied a box-model approach to estimate the CH_4 supply needed to sustain these elevated CH_4 concentrations and the results suggest a large source flux of CH_4 to the water column of 2.5 mmol m^{-2} d^{-1}. These results are qualitatively supported by acoustic observations of vigorous and widespread outgassing from the sediments, with flares that could be traced throughout the water column penetrating the pycnocline and reaching the sea surface. The results suggest that the heat wave triggered CO_2 and CH_4 fluxes in the coastal zones that are comparable with maximum emission rates found in other hot spots, such as boreal and arctic lakes and wetlands. Further, the results suggest that heat waves are as important for CO_2 and CH_4 sea-air fluxes as the ice break up in spring.

Keywords: heat wave, sea-air fluxes, carbon dioxide, methane, shallow coastal areas

INTRODUCTION

The sheltered coastal waters and estuaries are often oversaturated with CO_2 and CH_4 as a result of high supply of autochthonous and allochthonous riverine organic matter that is partly respired in the sediments and water column (Borges and Abril, 2012). Polar amplification of global warming may lead to more frequent extreme warming events (Mann et al., 2018) in high latitude coastal systems such as the northern Baltic Sea. This, in combination with the observed redistribution of land-derived carbon from land to sea, i.e., increased riverine total organic carbon (TOC) loads (Humborg et al., 2007; Andersson et al., 2015), potentially increases respiration patterns and sea-air fluxes of CO_2 and CH_4.

The two barriers constraining CO_2 and CH_4 outgassing from marine water bodies are anaerobic and aerobic oxidation of CH_4 in the sediments and water column (Reeburgh, 2007, 2013) and limited vertical mixing across density gradients that often lead to an accumulation of CO_2 and CH_4 in deeper parts of the water column (Gentz et al., 2014). The latter barrier is particular important in the strongly stratified Baltic Sea (Jakobs et al., 2014). A portion of the CO_2 can be exported laterally with increasing salinity and pH as dissolved inorganic carbon (DIC) from the inland coastal waters to larger depths, as seen in the shallow East Siberian Sea and the central deep Arctic Ocean (Anderson et al., 2017).

Ebullition of CH_4 is often discussed as a significant source to sea-air CH_4 fluxes, but the detection and spatiotemporal analysis are poorly constrained (Leifer and Patro, 2002; McGinnis et al., 2006; Rehder et al., 2009; Weber et al., 2014; Lindgren et al., 2016). However, recent studies suggest that the deeper, vertically stratified outer parts of high latitude coastal seas, such as the East Siberian Sea or the Baltic Sea, are moderate sinks for CO_2 (Gustafsson et al., 2014, 2015; Omstedt et al., 2014; Humborg et al., 2017; Schneider et al., 2017) and that net sea-air CH_4 fluxes from the Siberian Shelf have been heavily overestimated (Parmentier et al., 2017). For example, only moderate CH_4 fluxes to the atmosphere have been reported for the open East Siberian Sea (Thornton et al., 2016) and the open Baltic Sea (Jakobs et al., 2014). In contrast, the inner parts of coastal waters and estuaries are potential hotspots of CH_4 and CO_2 outgassing (Bange et al., 1994) due to (i) the high organic matter content in coastal sediments, (ii) short residence time of gaseous compounds in the shallow water column, (iii) sediment gas release that is transported directly, as gas bubbles, to the atmosphere (meaning significantly less CH_4 oxidation within the water column), and (iv) the often high turbidity that potentially lowers primary production and CO_2 uptake.

Even if extreme weather events in coastal waters become more frequent, as predicted for the future for the Baltic Sea (Meier et al., 2012), their sampling remain difficult to schedule due to the randomness of their occurrence. However, modern instrumentation provides new opportunities; the online monitoring coastal observatory MONICOAST, near the Tvärminne Zoological Station (TZS) in southern Finland, has been recently launched to understand and visualize the impacts of long-term climate and environmental change[1]. This high-resolution monitoring station is the site of almost 100 years of weekly observations at the same station. Thus, this monitoring station constitutes one of the longest temperature records available for a coastal site in the Baltic Sea. Temperature records at 32 m water depth indicated record high temperatures of $>20°C$ at the end of the heat wave during the summer of 2018.

Previous studies have shown that the combination of high temperatures and high organic matter contents in sediments and the water column along the Belgian coast in the North Sea led to high concentrations of CO_2 and CH_4 in the water column (Borges et al., 2016). Based on these previous results and the records from TZS, revealing the exceptionally high water temperatures, we conducted our cruise at the end of the extended heat wave in the summer of 2018. The main objective of this study was to quantify emission patterns of CO_2 and CH_4 under these extreme conditions, which can be regarded as a snap-shot of future emission regimes in coastal areas. Further, we wanted to investigate whether a sharp vertical water column stratification as established mainly by a halocline in the Baltic Sea and in the East Siberian Sea but not in other areas as the North Sea act as an efficient barrier for CO_2 and especially CH_4 fluxes also in shallow coastal parts. We followed a west-east transect across the Baltic Sea starting in the Swedish Archipelago and ending in the Finnish Archipelago, crossing the deeper open parts of the Northern Baltic Proper. We investigated CO_2 and CH_4 water column inventories and sea-air exchange patterns in contrasting environments where wind mixing and upwelling/downwelling are physical drivers that may trigger outgassing events of CO_2 and CH_4. Additionally, we were able follow the break-up of the heat wave and summer stagnation that came after the first autumn storms (in this case, gale force winds) that deepened the surface water layer. By collecting continuous measurements by means of a seawater intake system, an equilibrator set-up and CO_2 and CH_4 analyzers and combing these measurements with acoustic mapping of the water column, we were able to map and follow outgassing patterns in the Finnish coastal waters over several days before, during, and after the storm. This spatially integrated and non-invasive approach allowed us to detect a high flux event across an entire bay related to extreme weather, something that needs to be considered in order to deepen our knowledge of coastal biogeochemistry and carbon processing in a warmer and potentially stormier world.

MATERIALS AND METHODS

Study Area and Cruise Track

The Baltic Sea is a semi-enclosed brackish water body consisting of a set of major relatively deep basins, shallower bays, gulfs, and archipelagoes. The most recent digital bathymetric model by the European Marine Observation and Data Network (EMODnet Bathymetry Consortium, 2018) delineates the various sub basins of the Baltic Sea that are used throughout this study and indicate the average depth of the Baltic Sea with 53 m

---

[1] https://www.helsinki.fi/monicoast

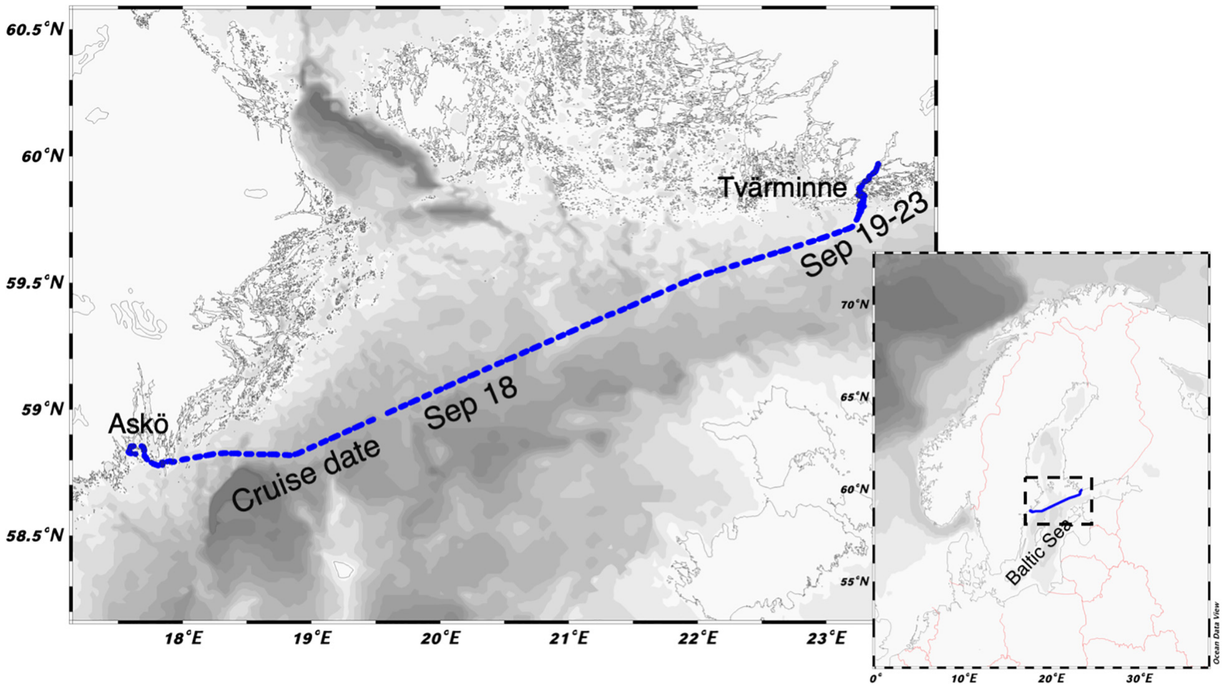

FIGURE 1 | Cruise track.

(Jakobsson et al., 2019). After the Black Sea, the central Baltic Sea is the second largest anoxic coastal water body in the world. This is due to water residence time of ~30 years, a strong vertical salinity gradient (halocline) at 60–90 m water depth, and ongoing eutrophication (Wulff et al., 2007).

The cruise was conducted with Stockholm University's Research Vessel (RV) Electra with the aim of obtaining a comprehensive and representative picture of the distribution of CO_2 and CH_4 concentrations in surface water across the Baltic Sea, covering a broad depth range, at the end of the heat wave during the summer of 2018. We covered archipelago-type coastal seascapes of Sweden and Finland, the Northern Baltic Proper, the Åland Sea, and the Gulf Finland (**Figure 1**). In fact, these shallower coastal seascapes consisting of hundreds to thousands of semi-enclosed bays and basins make up a huge proportion of the Baltic Sea, i.e., 25% of the Northern Baltic Proper, 70% of the Åland Sea, and 60% of the Gulf of Finland are shallower than 40 m depth (Jakobsson et al., 2019). The 40 m boundary used in this study to discriminate shallower from deeper sites is chosen because it separates two concentration regimes in the Baltic Sea and the shallower parts show much more elevated concentration of CO_2 and CH_4. In general, very little is known about sea-air gas exchange in these shallow areas of the Baltic Sea, and hardly any data are available with only a few exceptions for the Gulf of Finland, i.e., the harbor areas of St. Petersburg and Helsinki (Schneider et al., 2014). For the northern boreal part of the Baltic Sea consisting of the Bothnian Bay, the Quark, the Bothnian Sea, the Gulf of Finland, and the Northern, Western and Eastern Baltic Proper the total area shallower than 40 m is some 71,000 km^2 (Jakobsson et al., 2019). For perspective, impressive data sets on water-air CO_2 and CH_4 exchange are available (Juutinen et al., 2009; Humborg et al., 2010) for Sweden and Finland, where total lake area is about 33,000 km^2 and 30,000 km^2, respectively (the Swedish lake area was estimated excepting the largest deep lakes Vättern and Vänern where no CH_4 and CO_2 exchange estimate exists).

Statistical Evaluation of Long-Term Temperature Records

The long-term temperature record from the TZS coastal monitoring site (lat: 59.85548N, lon: 23.26033E) covers August 1926 to December 2018. A moving average was adopted to smooth the short-term fluctuations in the temperature data by taking the average value of a 1-year length and shifting forward, i.e., for each average annual value calculation, the first number of the 1-year data series was excluded and the next value was included. Note that the time interval of each temperature record varied slightly, from 10 days in the years before 1997 down to 4–7 days after 1998 and finally daily records in 2018. Thus, the 1-year length used in this study is fixed from a day in a year to the same day in the year after regardless of the time interval between two specific temperature records.

Continuous CO_2 and CH_4 Measurements in Surface Water and Atmosphere

The partial pressures of atmospheric and dissolved CO_2 and CH_4 were measured using the Water Equilibration Gas Analyzer System (WEGAS) coupled to cavity ring-down spectrometer (CRDS). This system consists of three major components: (i) a water handling system comprised of a showerhead equilibrator (1 L headspace volume) fed by the seawater intake, an E&H electrode probe and a thermosalinograph (Seabird TSG 45); (ii) a gas handling system with circulation pumps for the showerhead and ambient air from the bow of the ship; and (iii) CRDS gas analyzers for CO_2 and CH_4 concentrations (model G2131-i, Picarro Inc.); and A detailed description of the WEGAS systems and its performance can be found in the **Supplementary Material**.

Measurements of surface water CO_2 and CH_4 concentrations were performed using the seawater intake located just below the sea surface. Water was pumped through spray nozzles into the open headspace equilibrator at ∼4.5 L min^{-1}. By creating a fine spray of droplets, the exchange surface between showerhead and water was maximized and an optimal equilibration is achieved. The ambient pressure was maintained through a ambient air-fed vent flow that was monitored continuously during the measurements. The gas equilibrated in the showerhead was measured using the CRDS analyzer. For the standard CO_2 and CH_4 analysis routine, ambient air is measured for 8 min followed by the gas measurements in the showerhead of the equilibrator for 12 min, i.e., one complete analysis cycle is 20 min. Cycles are performed continuously during the cruise including the station time when RV Electra is not steaming.

Continuous CO_2 and CH_4 measurements in both ambient air and surface water were conducted during September 18–23, 2018; in total, 80,393 data points for both CO_2 and CH_4 in air and water were recorded. The recorded data were filtered by removing data taken during the transition period between ambient air and water measurements (see detailed description in **Supplementary Material**) and collected during improper functioning of WEGAS (e.g., low water flow, exceptional values due to air contamination by the ship) and thereafter the data were also corrected for the vent flow to the equilibrator that was induced while WEGAS was running. Any remaining data with CO_2 concentrations above 450 ppm were also removed. After filtering, atmospheric CO_2 averaged 401.3 ± 2.08 ppm (2σ). As a result of spatial normalization and excluding data that could have been contaminated by the ship, here we present 15,733 data points for both air and water concentrations.

For reporting the CO_2 content in water, the ppm value obtained by the cavity ring down spectrometer (CRDS) were converted to pressure units (pCO2 in μatm). We assumed ambient atmospheric pressure because water was taken at depth of around half a meter below the surface and the pressure in the showerhead is equal to ambient air as achieved by the vent flow taken at the bow of the ship.

For reporting the CH_4 concentrations in water, the ppm value obtained by CRDS were converted to molar units (i.e., nmol/L) by Henry's law (Equation 1), because the achieved equilibration means that the gas content in the showerhead is equivalent to that in the water phase, i.e., CH_4 measured by CRDS is considered as the real-time concentration of CH_4 in water. This makes Henry's law applicable for dealing with gas/liquid equilibria and the Henry's constant for molar concentration and partial pressure conversion is chosen in this case. As the showerhead in the equilibrator is maintained at ambient pressure and the water temperature is measured by thermosalinograph right before the water reaches the equilibrator, Henry's law constant is corrected for each calculation by the measured temperature at atmospheric pressure.

$$C = p \times K_{\mathrm{H}} \tag{1}$$

where C is the concentration of CH_4 (mol/L), p is the partial pressure in unit of atm (1 atm = 10^6 ppm) of CH_4. K_{H} is the Henry's law constant that is dependent on temperature and is corrected in this study following the van 't Hoff equation (Sander, 2015):

$$K_{\mathrm{H}} = K_{\mathrm{H}}^{*} \times \exp[\frac{-\Delta_{\mathrm{sol}}H}{R} \times (\frac{1}{T} - \frac{1}{T^{*}})] \tag{2}$$

Where K_{H}^{*} is the Henry's law constant at the reference temperature, 298 K, T* is the reference temperature, 298 K and T is the measured temperature in water (K). The temperature dependence of the equilibrium constant, $\frac{-\Delta_{\mathrm{sol}}H}{R}$ does not change much with temperature and is tabulated (Sander, 2015). K_{H} also varies with pressure, but in this study, pressure was assumed to be atmospheric pressure because water was taken at depth of around half a meter.

In the Baltic Sea both CO_2 and CH_4 concentrations span an order of magnitude and the highest concentrations reported are >2500 μatm of CO_2 (Fransner et al., 2019) and >1200 nM of CH_4 (Jakobs et al., 2014).

Calculations of Sea-Air Gas Fluxes

The sea-air flux (F) of CO_2 and CH_4 is commonly expressed by the following equation (Liss and Slater, 1974):

$$F = k \times (C_{\mathrm{sea}} - C_{\mathrm{air}}) \tag{3}$$

where k is the gas transfer velocity and C_{sea} and C_{air} are concentrations of gases in the sea and the overlying air, respectively. This is also frequently written as Equation 4

$$F = k \times K_0 \times \left(p_{\mathrm{sea}} - p_{\mathrm{air}}\right) \tag{4}$$

where K_0 is the solubility of CO_2 or CH_4, p_{sea} and p_{air} are the measured partial pressures of the gases in equilibrium with surface water and in the air, respectively. k is the gas transfer velocity that has been optimized as Equation 5 (Wanninkhof, 2014):

$$k = 0.251 \times U^2 \times \left(\frac{Sc}{660}\right)^{-0.5} \tag{5}$$

where U is wind speed (m/s) and Sc is the Schmidt number, which is highly dependent on temperature and gas. Sc in our calculations was corrected for the corresponding temperature that was measured simultaneously with partial pressures of CH_4 and CO_2 (pCH_4 and pCO_2).

Combining Equations 3, 4 and 5, the flux of CO_2 and CH_4 in this study is finally calculated as Equation 6:

$$F = 0.251 \times U^2 \times \left(\frac{Sc}{660}\right)^{-0.5} \times K_0 \times (p_{\mathrm{sea}} - p_{\mathrm{air}}) \quad (6)$$

Regional Meteorological and Oceanographic Data

Surface water temperature data observation in the open Northern Baltic Proper from the automatic buoy Huvudskär (lat: 58.9333 N, lon: 19.1667 E; 100 m water depth) were retrieved from the Swedish Hydrological and Meteorological Service[2]. Wind data observation from the Raasepori Jussarö (lat: 59.82076N, lon: 23.57309E) weather station and wave height observations from the buoy Raassepori Hästö Busö (lat: 59.82583N, lon: 23.30783E), which are located some 15 km and 5 km from the TZS, respectively, were retrieved from Finnish Meteorological Institute[3].

Box Model Approach to Address Sources and Sinks of CO_2 and CH_4

Using the surface CO_2 and CH_4 concentration in inshore and offshore surface waters and sea-air flux data and the information about the deepening of the upper mixed surface layer after the storm event, we can construct a budget evaluating the sources and sinks of CO_2 and CH_4 (**Figure 2**). The conservation of mass for the surface layer under the assumptions mentioned is:

$$\begin{aligned} &\mathrm{h}_{\mathrm{after}} CO_{2after} - \mathrm{h}_{\mathrm{before}} CO_{2before} = \\ &\quad CO_{2offshore}(h_{\mathrm{after}} - h_{\mathrm{before}}) - F_{\mathrm{CO_2}}\Delta t + I_{\mathrm{CO_2}}\Delta t \end{aligned} \quad (7)$$

$$\begin{aligned} &\mathrm{h}_{\mathrm{after}} CH_{4after} - \mathrm{h}_{\mathrm{before}} CH_{4before} = \\ &\quad CH_{4offshore}(h_{\mathrm{after}} - h_{\mathrm{before}}) - F_{\mathrm{CH_4}}\Delta t + I_{\mathrm{CH_4}}\Delta t \end{aligned} \quad (8)$$

Where h is the mixed layer depth before and after the storm, respectively, F atmospheric flux and I an internal source term. The source water for the advection term, i.e., $CO_{2offshore}$ *and* $CH_{4offshore}$ are assumed to have properties close to what was observed offshore on September 19 and 20.

Continuous Measurements of Gas Flares and Bubbles

The acoustic water column data presented here were continuously collected with a Simrad EK80 wideband split-beam scientific echo sounder with a center frequency at 70 kHz that was installed on RV Electra. The vertical range resolution is approximately 2 cm and the ping rate was about 2.5 Hz. The sonar produces a linear frequency modulated acoustic signal which provides improved signal-to-noise ratio and a higher vertical range resolution compared to similar narrow-band systems (Stanton and Chu, 2008). The dataset collected with the EK80 was match filtered with an ideal replica signal using a MATLAB software package version R2017a provided by the system manufacturer, Kongsberg Maritime (Lars Anderson, personal communication). Position and altitude information

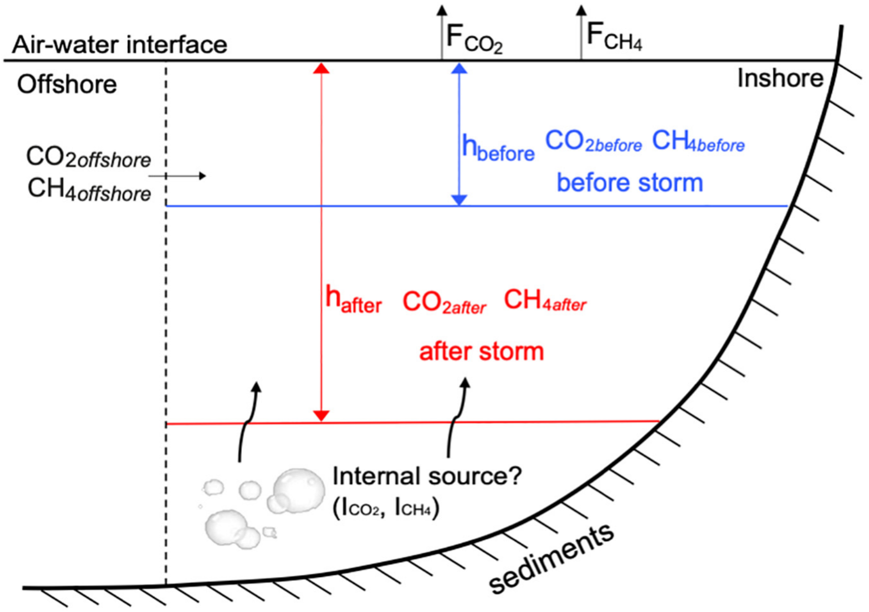

FIGURE 2 | Scheme over the budget approach evaluating the internal sources and sinks of CO_2 and CH_4 in TZS coastal waters.

---

[2] http://www.smhi.se/kunskapsbanken?query=huvudsk%C3%A4r+ost&doSearch=

[3] https://en.ilmatieteenlaitos.fi/download-observations

were provided to the sonar by a Seapath 330 + motion sensor. Ranges from the transducer were calculated using the cumulative travel times through sound speed profile layers based on the nearest (in time) CTD profile (SEA-Bird SBE 911 plus), following the approach by Stranne et al. (2017).

RESULTS

Temperature Records in the Open Northern Baltic Proper and in the Finnish Coastal Waters Near Tvärminne

Temperatures of up to 23.04°C (daily mean) were recorded in the upper surface layer in the open Northern Baltic Proper on 6 August at the autonomous measuring stations (**Figure 3A**). A similar picture appears when evaluating the coastal monitoring stations near TZS. Since 2017, water temperatures have been continuously recorded using *in situ* instrumentation, allowing us to follow the effects of the summer 2018 heat wave in even greater detail. The highest bottom-water temperatures (32 m depth) of 20.53°C were recorded on 30 July at this coastal monitoring station (**Figure 3B**) and these are the highest temperatures ever recorded at this depth over the past 93 years. A second warming event in bottom waters above the sediments was recorded in early September 2018 just before our sampling campaign with temperatures reaching nearly 17°C (**Figure 2B**). The record-high bottom temperatures measured in the TZS area in 2018 follow an increasing trend observed over the past century until today. In **Figure 3C**, the long-term temperature record (moving average) between 1926 and 2018 is presented showing a mean water temperature of 4°C above the sediments between the 1920s and the 1980s. Thereafter, we see a dramatic increase in bottom-water temperatures starting in the 1990s to about 6°C in the 2010s.

Spatial CO_2 and CH_4 Patterns in Open vs. Coastal Areas of the Baltic Sea

Surface-water temperatures were between 14 and 18°C throughout the transect (**Figure 4A**) which is somewhat cooler than at the peak of the heat wave during July/August, when temperatures of up to 23°C were recorded in the surface layer (**Figure 3A**). Both pCO_2 and CH_4 concentrations were closer to equilibrium with the atmosphere in the central basin of the Northern Baltic Proper, but they were elevated in coastal areas (**Figures 4C,D**). However, off the Swedish coast at 70–100 m water depth, we encountered an upwelling event indicated by low temperatures and high salinity at the water surface (**Figures 4A,B**) and with elevated pCO_2 of up to >800 μatm (**Figure 4C**). CH_4 showed only moderately elevated concentrations of 12 nmol/L (**Figure 4D**). Toward the Finnish coast, both CO_2 and CH_4 gradually increased to concentrations of ∼700 μatm for CO_2 and over 30 nmol/L for CH_4. Partial pressure and concentration vs. seafloor depth plots reveal that in coastal areas, with water depths <40 m, both CO_2 and CH_4 (**Figures 5A,B**) show more elevated pCO_2 and CH_4 concentrations in the upper mixed layer compared to the open Northern Baltic Proper.

At the easternmost end of the transect, we investigated parts of Finnish Archipelago Sea near the TZS in more detail between September 19–23, 2018. pCO_2 and CH_4 concentrations followed a salinity gradient with higher values toward the freshwater end-member (**Figure 6**) that is formed by the small river Karjaanjoki (runoff 0.59 km^3 y^{-1}, Räike et al., 2012) that runs into the Pojo Bay and further into the Storfjärden Bay (black dashed box in **Figure 8A**). The highest pCO_2 (1583 μatm) was measured at the northernmost part of the Storfjärden where salinities were <5 psu. A similar pattern was recorded for CH_4, which reached its highest concentration of 70 nmol/L a bit south from the position where CO_2 peak concentrations were found. An interesting pattern appeared when plotting pCO_2 and CH_4 concentrations against seafloor depth (**Figure 7**). pCO_2 in surface water were lowest at the shallowest seafloor depth and continuously increased from 751 μatm at <5 m seafloor depth to 1020 μatm at 20–25 m seafloor depth (**Figure 7A**). In contrast, the high CH_4 concentration of 44 nmol/L (median) was recorded at the lowest seafloor depth, while concentrations ranged between 24 and 40 nmol/L at deeper depths between 5 and 25 m (**Figure 7B**). Note, that all median pCO_2 values and CH_4 concentrations were calculated before the wind event described in the next section.

Wind-Induced Changes in CO_2 and CH_4 Water Column Inventories and Inferred CO_2 and CH_4 Source and Sink Terms in Coastal Waters

Figures 8B,D show the temporal development of pCO_2 and CH_4 concentrations inshore and offshore the TZS coastal area. Elevated pCO_2 of some 800 μatm were recorded by the WEGAS system on September 19 and 20 within the inshore waters (indicated with the black dashed box in **Figure 8A**) and the offshore pCO_2 (indicated with the red dashed box in **Figure 8A**) were also at the same elevated range as the inshore concentrations (median of 740–856 μatm; **Figure 8B**). During sampling on September 21, the wind gradually increased from 5 m sec^{-1} to some 10 m sec^{-1} and pCO_2 in the inshore waters increased to 1,015 μatm, although this increase is not significant when taking the variability of the measurements in the inshore waters that day (between 700 and 1 300 μatm; **Figure 8B**) into account. Wave height increased simultaneously from 0.6 to 1.6 m. Wind speeds peaked at 20 m sec^{-1} during September 22 and decreased again down to 3 m sec^{-1} during the evening hours of September 23 (**Figure 8C**). During the same time peak wave height of 1.9 m was recorded at the monitoring buoy near TZS, which decreased to 0.5 m. Thus, during the entire period between September 19–23 the average wind was between 8 and 10 m sec^{-1} (0.5–0.8 m wave height), disrupted by the peak wind event on September 22 with wave heights of up to 1.9 m. CO_2 sea-air fluxes were greatest during this peak wind event with 274 mmol m^{-2} d^{-1} (**Figure 8C**), whereas at the end of the wind event, CO_2 was undersaturated in the upper surface layer and even negative sea-air fluxes were calculated. However, during the entire wind event, the pCO_2 decreased sharply from a 2–3 times oversaturation (median of 1015 μatm) to a slight undersaturation (median of

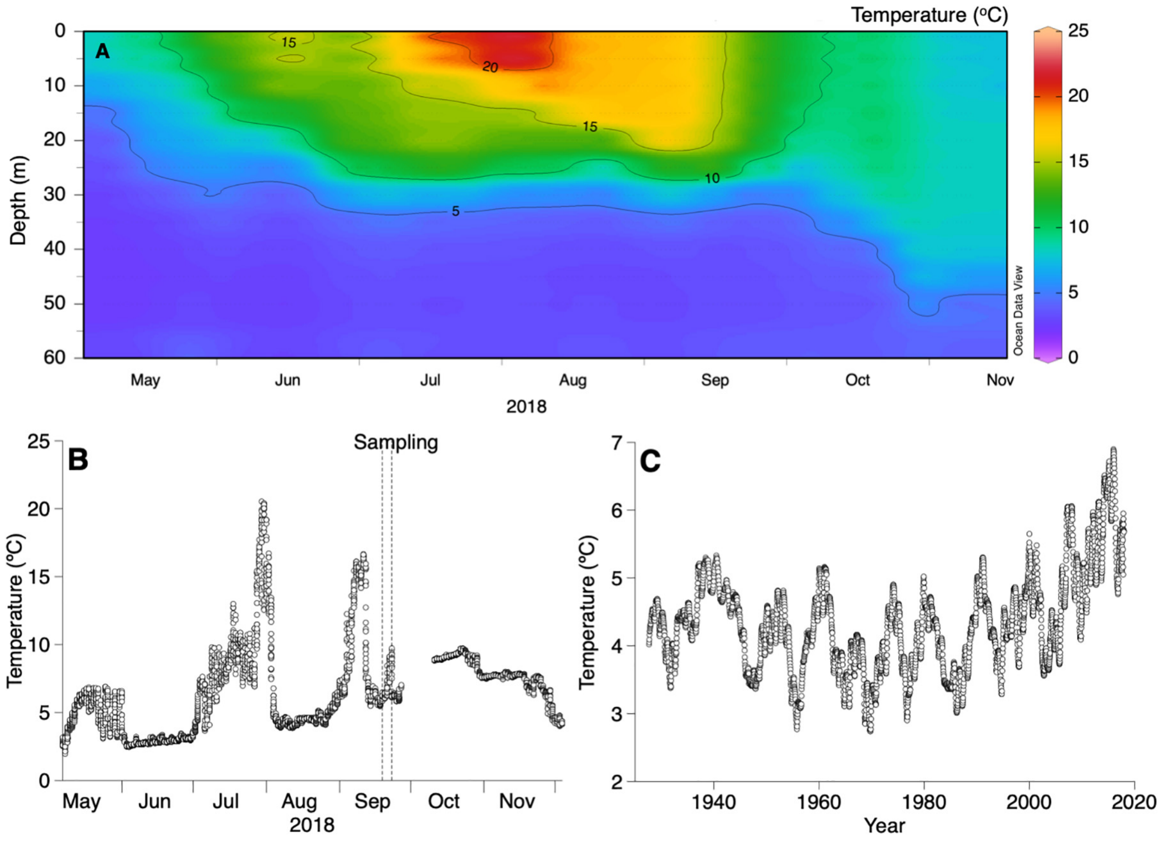

FIGURE 3 | Temperature records from **(A)** open Baltic Sea (vertical water column profile) during the heat wave in 2018 (May–November; Huvudskär, lat: 58.9333, lon: 19.1667; 100 m water depth; daily average), **(B)** bottom waters (31 m water depth) at the TZS coastal monitoring site during the heat wave in 2018 (May–November; Storfjärden, lat: 59.85548, lon: 23.26033; hourly measurements) and **(C)** bottom waters (31 m water depth) at the TZS coastal monitoring site (long-term temperature data 1926–2018; 1-year moving average).

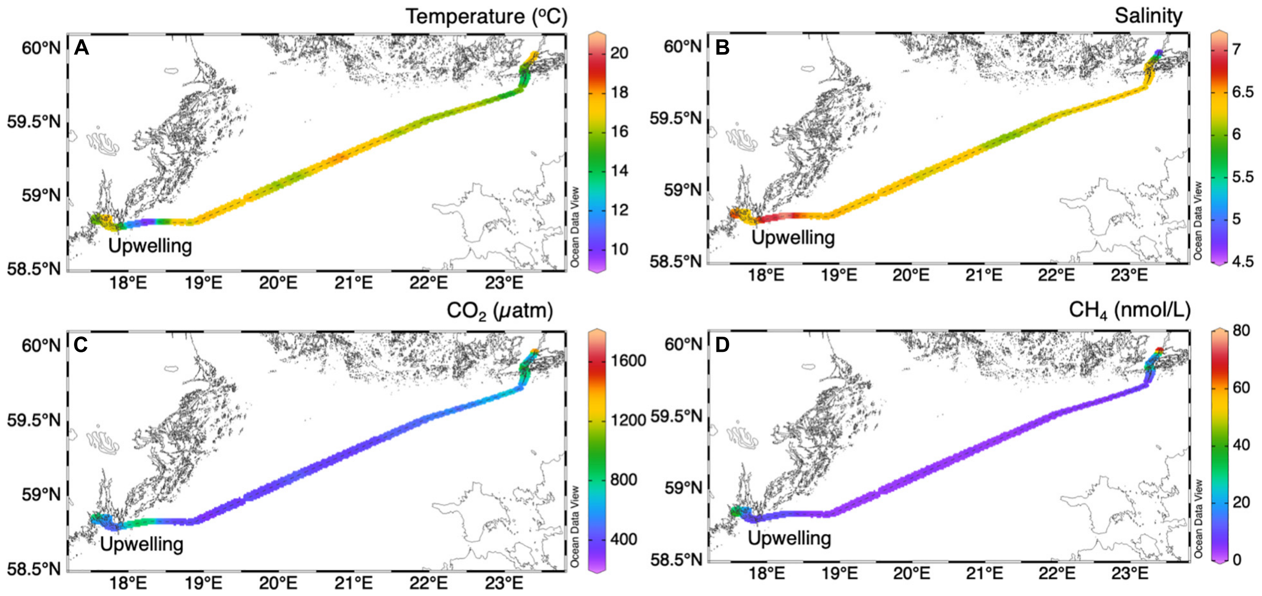

FIGURE 4 | Cross section from Askö to Tvärminne of **(A)** temperature, **(B)** salinity, **(C)** pCO_2 (μatm) and **(D)** CH_4 concentrations (nmol/L) in surface waters.

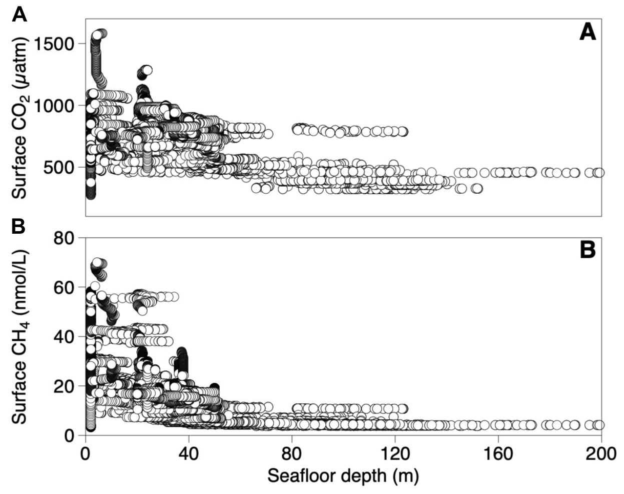

FIGURE 5 | (A) pCO$_2$ (μatm) and **(B)** CH$_4$ concentration (nmol/L) in the surface waters vs. seafloor depth along the cross section from Askö to Tvärminne.

321 μatm recorded at September 23). Thus, the wind event rather effectively depleted the water column with respect to pCO$_2$.

In contrast to the expected depletion of CO$_2$ from oversaturation caused by the wind event, CH$_4$ remained oversaturated before, during, and also after the wind event. Elevated CH$_4$ concentrations of 46 – 47 nmol/L (median; **Figure 8D**) were recorded by the WEGAS system on September 19 and 20 within the inshore waters, whereas for the offshore waters CH$_4$ concentrations were also supersaturated, but less so, with median concentrations between 13 and 15 nmol/L. During and after the wind event during September 22, CH$_4$ concentrations decreased in the inshore waters to a median value of 20–24 nmol/L, however, remained oversaturated by 5–8 times. Accordingly, the CH$_4$ sea-air flux calculations (**Figure 8E**) revealed the highest CH$_4$ average fluxes between 2.8 – 3.3 mmol m^{-2} d^{-1} before the wind event and lower, but still elevated, fluxes between 1.0 – 2.4 mmol m^{-2} d^{-1} during and after the wind event.

Although wind is directly related to the gas transfer velocity (k) in Equation 3, wind speed could only partly explain the variation in both CO$_2$ and CH$_4$ fluxes. However, the highest CH$_4$ fluxes were observed at relatively low winds (12 m sec^{-1}), whereas the highest CO$_2$ fluxes were observed at peak wind speeds (**Figures 8C,E**). Accordingly, the CO$_2$ and CH$_4$ fluxes show positive relationship (not shown), however, the highest CH$_4$ fluxes were recorded at very low CO$_2$ flux regimes, which indicates that CH$_4$ flux events are decoupled from CO$_2$ flux events during low wind regimes (9–12 m sec^{-1}).

As indicated in **Figures 8C,E**, the wind increased significantly after September 21 from less than 10 to nearly 20 m sec^{-1}. Simultaneously, CTD data collected between September 21 (10:25 UTC) and September 23 (14:00 UTC) show a deepening of the surface mixed layer after the wind event (**Figure 9**). Note that the temperature (**Figure 9B**) before and after the wind event (September 22) remained more or less constant at 11°C and that salinity (**Figure 9C**) decreased only slightly from 6.5 to 6.4 psu, whereas the upper mixed layer depth increased from roughly 10–25 m water depth. Thus, the surface mixed layer increased over these 2 days in depth from about 10 m to nearly 25 m and this was mainly caused by a downwelling event triggered by south-southeasterly winds pressing water masses into the Finnish inner coastal waters rather than by vertical mixing. Thereafter, the mixed layer depth remained at the same depth for the remainder of the cruise.

The concentrations, mixed layer depths, and atmospheric fluxes used to estimate the internal sink/source terms are given in **Table 1**. We assume that the transition occurs during 24 h corresponding to approximately the time of the storm event and the interval between the two CTD profiles mentioned above. The results of the budget calculation indicate a net sink of CO$_2$

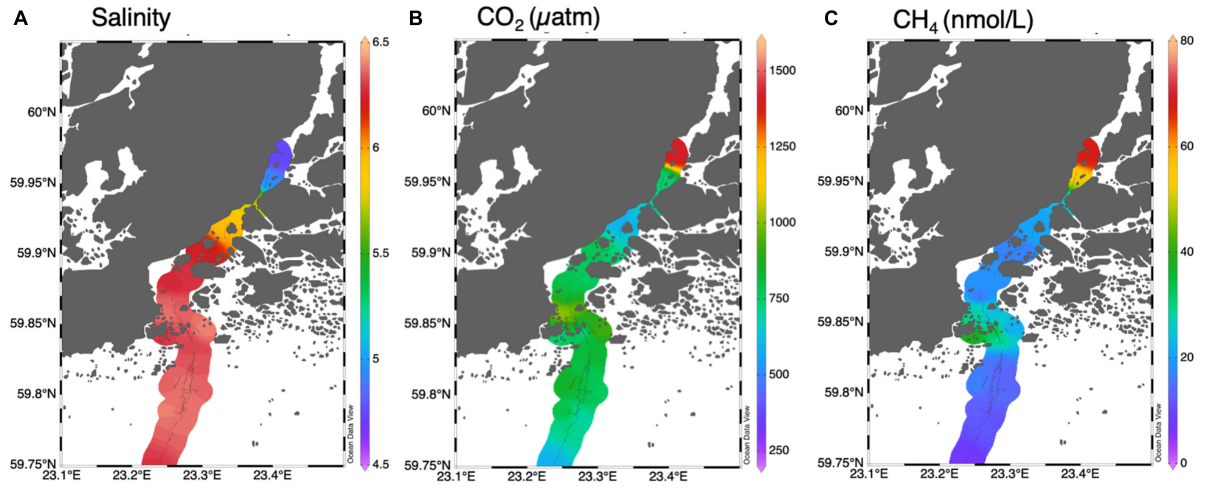

FIGURE 6 | Surface distribution of **(A)** salinity, **(B)** pCO$_2$ (μatm), and **(C)** CH$_4$ concentrations (nmol/L) within the TZS coastal waters; the black dots indicate daily cruise tracks within the area.

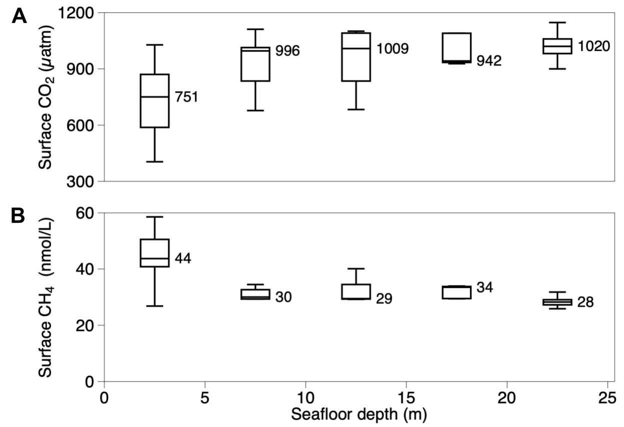

FIGURE 7 | (A) pCO$_2$ (µatm) and **(B)** CH$_4$ concentrations (nmol/L) as grouped by seafloor depth within TZS coastal waters before the storm event.

in the water column, however, the sink could be somewhat overestimated because the offshore concentrations decreased due to the massive outgassing. Further, the budget indicates a CH$_4$ source of about 2.5 mmol m^{-2} d^{-1} from below the mixed surface layer.

A possible explanation for the deviating patterns of CO$_2$ vs. CH$_4$ fluxes can be found in the geophysical variables investigated and continuously recorded during the cruise. The acoustic mid-water mapping revealed vigorous and widespread gas flares from the sediments in the Finnish coastal waters as exemplified in **Figure 10** where some 10–15 major flares and numerous trains of individual bubbles are visible along a 3 km transect, indicating intense bubble formation and ebullition at the sea floor. Further, gas bubbles are visible throughout the entire water column up to the water surface, penetrating into the mixed surface layer that was situated at around 10–15 m water depth (based on CTD data, **Figure 9**). The mixed layer is also discernable in the echogram, although vaguer than observations made in Arctic Ocean coastal waters (Stranne et al., 2017).

DISCUSSION

On a global scale, lakes and rivers are significant sources for CO$_2$ and CH$_4$, and their fluxes are relatively well constrained compared to the evaluation of sinks and sources in the global coastal ocean. CO$_2$ emissions from lakes and reservoirs are estimated to be 0.32 Pg C yr^{-1} and from rivers and streams to be 1.8 Pg C yr^{-1} (Raymond et al., 2013), whereas CH$_4$ emissions from inland waters are estimated to be 77 Tg C yr^{-1} (Bastviken et al., 2011). Upscaling exercises using a typology approach including four estuarine types and different types of continental shelves along three climatic zones estimates global CO$_2$ emissions to be 0.27 Pg C yr^{-1}, whereas global CH$_4$ emissions from estuaries to be 5.0 Tg C yr^{-1} (Laruelle et al., 2010; Borges and Abril, 2012). However, Laruelle et al. (2010) conclude that "the largest uncertainty of scaling approaches remains in the variability of CO$_2$ data to describe the spatial variability, and to capture relevant scales of variability." Note that the global estimates of coastal gas emissions are biased toward the many investigations focusing on estuaries, lagoons, salt marches, and tidal flats (Borges and Abril, 2012), whereas studies capturing shorelines that are less affected by river inputs are less studied. Further, CH$_4$ emissions in coastal areas are clearly coupled to temperature (Borges et al., 2016; Sawicka and Brüchert, 2017) and the highest rates of change are to be expected in organic-rich shallower parts affected by warming water bodies overlaying marine sediments. In fact, experimental studies show that a temperature increase of only 2°C can increase anaerobic organic matter degradation by 40% in marine sediments (Roussel et al., 2015). We clearly demonstrate in this study that the temperature increases in Finnish coastal waters correspond to such a 2°C rise during the last 3 decades. Bottom waters and surface sediments in this sub-arctic setting experience peak temperatures of over 20°C coinciding with elevated CO$_2$ and CH$_4$ concentrations and fluxes that are comparable to the more frequently investigated terrestrial hot spots for CO$_2$ and CH$_4$ emissions, such as arctic lakes, wetlands and thawing permafrost areas.

We suggest that the sea-air CH$_4$ flux is likely dominated by frequent bubbling from sediments, which we observed even during low winds, when CO$_2$ fluxes were at their minimum, high CH$_4$ fluxes occurred, knowing that this notion lacks a quantitative approach that has to be developed in the future by new ways of interpreting geophysical data of the water column. However, we have shown that surface CH$_4$ concentrations were highest at the shallowest seafloor depth (**Figure 7**) indicating that the proximity to the sediments and gas flares as well as the short residence times that prevent full CH$_4$-oxidation in the water column as observed in the deep open ocean (Reeburgh, 2007). In contrast, CO$_2$ in surface water shows a positive relationship with seafloor depths, indicating that respiration of autochthonous and allochthonous organic carbon in the water column is the predominant source for CO$_2$ even in shallow coastal systems. This has bearing for the understanding and future model parametrizations especially of CH$_4$ fluxes in arctic and subarctic shelf systems, i.e., a comprehensive understanding of spatial and seasonal CH$_4$ accumulation and flare distribution in sediments as stimulated by heat waves is needed to quantify CH$_4$ fluxes from shallow coastal waters. Acoustic methods directly addressing bubble-mediated methane flux are becoming more available (Weidner et al., 2019) and similar studies using mid-water sonar systems near Spitzbergen have shown that CH$_4$ partly originating from ebullition and transformed into the dissolved pool during upward transport is efficiently trapped below the halocline at some 200 m water depth for at least part of the year, which prevents outgassing to the atmosphere (Gentz et al., 2014). This is corroborated by our findings in the deeper stratified Northern Baltic Proper where even a strong upwelling event led to strong outgassing of CO$_2$ (**Figure 4C**), but only moderate increased CH$_4$ concentrations were observed (**Figure 4D**). Recent findings suggest that methanogenic Archaea in zooplankton guts significantly contributes to the CH$_4$ supersaturation in the upper surface layer of the Baltic Sea (Schmale et al., 2018), i.e., the role of bubble-mediated CH$_4$ transport in the central parts of Baltic appear less likely. In

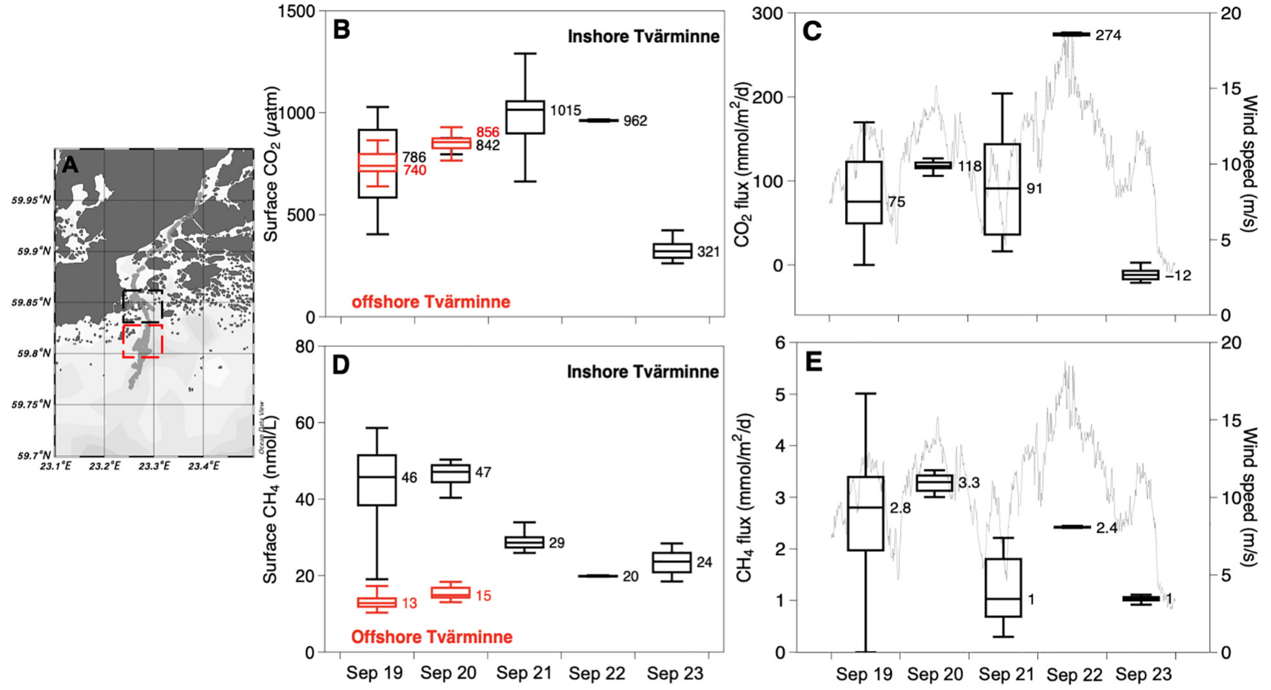

FIGURE 8 | Temporal variations in the surface waters in the inshore (black dashed square in **A**) and offshore (red dashed square in **A**) TZS coastal area **(A)** of **(B)** pCO$_2$ (μatm), **(C)** CO$_2$ flux (mmol/m^2/d), **(D)** CH$_4$ concentration (nmol/L) and **(E)** CH$_4$ flux (mmol/m^2/d) including wind speed between September 19 and 23.

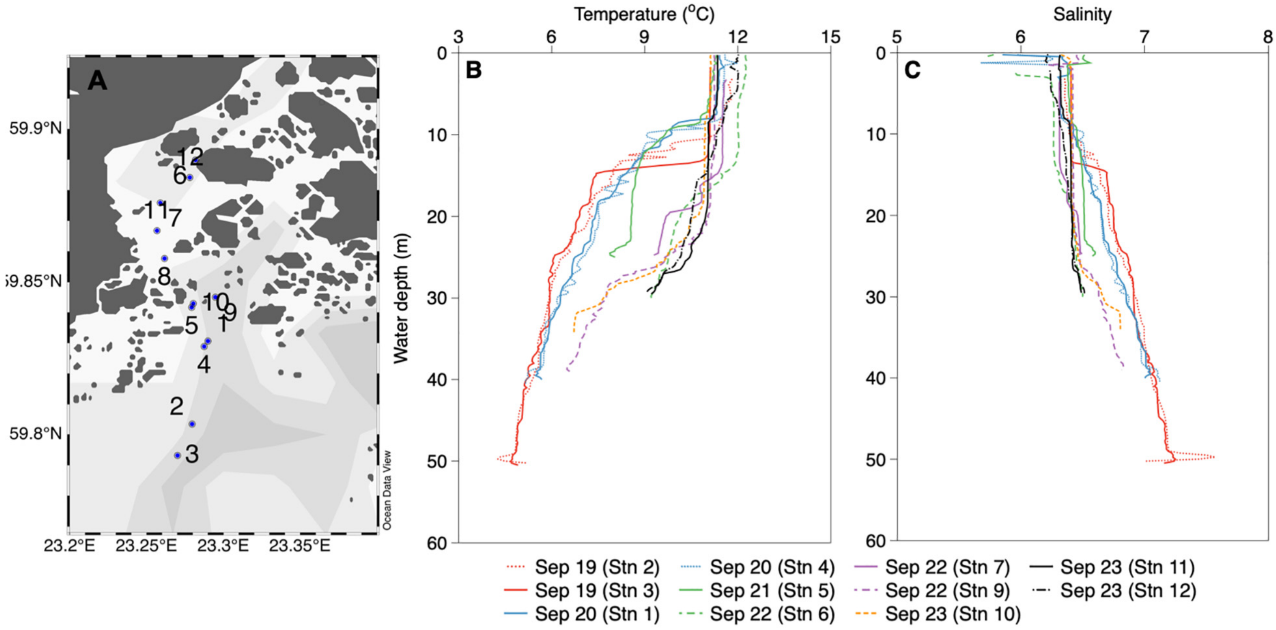

FIGURE 9 | Ventilation of the upper mixed layer in TZS coastal waters **(A)** by the storm event as demonstrated by vertical temperature **(B)** and salinity **(C)** profiles taken between 19 and 23 September 2018; position of individual CTD casts are indicated by station numbers in **(A)**.

shallow coastal areas the role of such pelagic sources may presumably be less important, because the zooplankton biomass is simply limited by the lower volume of water, but this cannot be ruled out.

We observed a pronounced pycnocline also in the coastal waters around TZS (**Figure 9**), but in this shallow coastal setting we could observe bubbles rising from the seafloor and throughout the entire water column and penetrating the

TABLE 1 | Concentrations, fluxes and mixed layer depths used in the box model calculations of CO_2 and CH_4 sources and sinks in TZS coastal waters during the storm event 21–23 September 2018.

Variables	Description	Values			
		Offshore	Before storm	After storm	During storm
CO_2	CO_2 concentration (μmol/L)	39	44	13	
CH_4	CH_4 concentration (nmol/L)	15	29	24	
h	Mixed layer depth (m)	-	10	25	
F_{CO2}	Sea-air flux of CO_2 (mmol m^{-2} d^{-1})				274
F_{CH4}	Sea-air flux of CH_4 (mmol m^{-2} d^{-1})				2.4

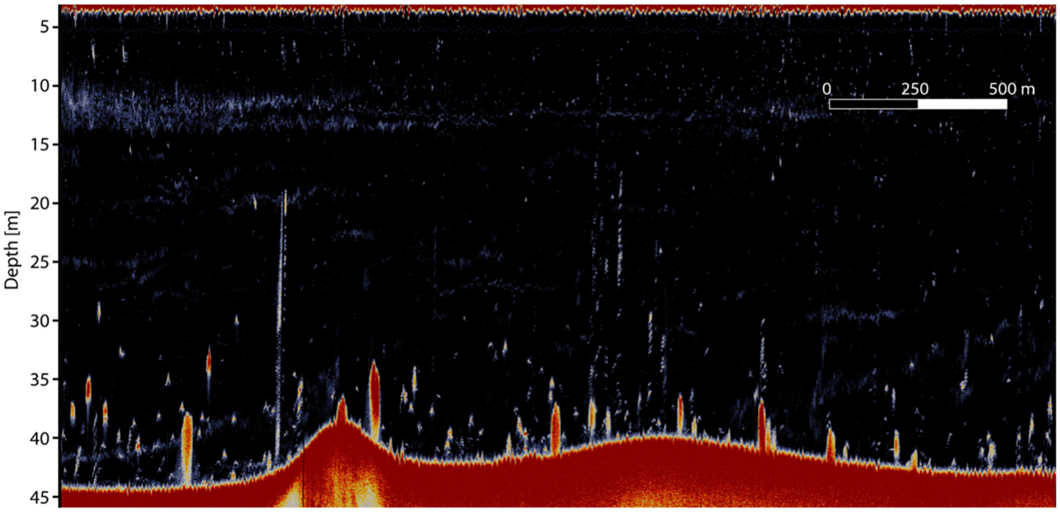

FIGURE 10 | EK80 echogram showing acoustic anomalies associated with gas seeps from the bottom sediments in TZS coastal area (black dashed square in **Figure 8A**), following the cruise track from left to right and with color indicating the acoustic target strength (black is <–80 dB and red is >–60 dB). Compass coordinates for the beginning/end of the echogram (23° 17.4′ E, 59° 49.8′ N)/(23° 16.4′ E, 59° 49.0′ N).

pycnocline (**Figure 10**). Note that the WEGAS system is capturing both diffusive and bubble flux collected by the sea water intake. We do not know whether a CH_4 reservoir has accumulated below the pycnocline in the Finnish coastal waters and thereby contributing to the elevated CH_4 concentration in the water column and significant sea-air fluxes. However, gas bubbles can only survive a certain rise height of some 100 m in the water column before they are depleted in CH_4 (McGinnis et al., 2006). Once CH_4 is dissolved, it is prone to oxidation before reaching the atmosphere and here vertical density gradients such as pycnoclines form a barrier for dissolved CH_4. This barrier to CH_4 transport from the seafloor to the atmosphere does not work in shallow coastal systems where ebullition from the seafloor can reach the atmosphere directly and our investigations show intensive bubble mediated transport between the sediments and the atmosphere down to 45 m water depth (**Figure 10**). Future investigations will show whether CH_4 concentrations in the bubbles do decrease with increasing water column travel time, i.e., whether these bubbles still contain significant amounts of CH_4 when reaching the sea-air interface. Further, it appears highly likely that the gas bubbles are of biogenic origin, because we found an inverse pattern, though not statistically significant, between CH_4 concentrations and seafloor depth and/or proximity to the shore (**Figures 6**, **7**) – a coastal effect. Eutrophication, high productivity and organic matter from runoff leads to accumulation of sediments with thick sequences of organic mud nearshore the TZS coastal area (Kauppi et al., 2018), which in turn leads to methane production and seepage. These patterns wouldn't appear when the bubbles were of thermogenic origin, i.e., from petrogenic deposits that may occur in folds that should be more randomly distributed.

A striking result of this study is that CH_4, which has a lower solubility compared to CO_2, never equilibrated with the atmosphere, whereas simultaneously the slower reacting gas (CO_2) with a higher solubility was depleted within a few hours after the wind event. Our box model approach inferred a source term for CH_4 – that might originate directly from sediment flares, or a diffusive flux from the sediments and a theoretical water column reservoir – that is significant (2.5 mmol m^{-2} d^{-1} or 30 mg C m^{-2} d^{-1}). A comparable benthic study from the nearshore shallow coastal areas along the Swedish coast (Sawicka and Brüchert,

2017) reported nearshore sediment-water fluxes between 0.1 and 2.6 mmolm^{-2}d^{-1}. Our reported rate is at the high end, indicating that the heat wave played an important role in a massive flux event of CH_4, although we have to bear in mind that the benthic sediment fluxes and fluxes from a potential reservoir in the water column cannot be disentangled from our CH_4 supply estimates. Although we do not have any quantitative measurements, the observed extensive occurrence of gas flares and bubbles point toward a significant contribution from the sediments. A comparable study addressing sea-air fluxes in the North Sea (Borges et al., 2018) report elevated fluxes between 28 and 126 mmol m^{-2} per year. Our observed accumulated flux for the 5-day period at the end of the heat wave was 11 mmol m^{-2} (averagely 2.2 mmol m^{-2} d^{-1}), which is similar to CH_4 emissions observed in thermokarst lakes in subarctic areas (Matveev et al., 2016). This result supplies further evidence that heat waves trigger massive CH_4 fluxes to the atmosphere from nearshore sites.

The sea-air CO_2 exchange of 75–274 mmol m^{-2} d^{-1} or 0.9–3.3 g C m^{-2} d^{-1} also indicates extreme outgassing during the end of the heat wave and can be compared with recent model studies indicating outgassing of up to 60 g C m^{-2} yr^{-1} in the nearshore areas of the northern Baltic Sea (Fransner et al., 2019). It is of course difficult to compare simulated annual rates with our measurements that were taken over a few days but it is, nevertheless, striking that the daily sea-air exchange rates of CO_2 presented here are one order of magnitude higher than the simulated ones. It could be that the effects of heat waves followed by increasing autumn winds for the outgassing of CO_2 haven't been considered, i.e., our 5-day estimated sea-air exchange of 6.5 g C m^{-2} is already 10% of the highest simulated annual values reproducing the spatial hot spots near the coast. The model has been calibrated/validated with ferry-box observations and clearly indicates the classical CO_2 accumulation of up to 2500 μatm under the ice and values close to equilibrium in ice-out situations. However, this study demonstrates that heat waves produce similar accumulations of CO_2 in the water column and the outgassing events can be as significant as ice-out situations that have been described also for other high latitude coastal systems, such as the East Siberia Sea (Thornton et al., 2016; Humborg et al., 2017).

CONCLUSION

In the past decade, continuously recording CO_2 and CH_4 instruments have become state-of-the-art equipment on large research vessels and on commercial ships which run ferry-box solutions. Thus, we have a fairly good understanding of CO_2 and CH_4 exchange processes in open waters of the Baltic Sea, the open Atlantic, or even in remote areas as the Siberian Sea (Körtzinger et al., 1996; Gülzow et al., 2011; Schneider et al., 2014; Thornton et al., 2016; Humborg et al., 2017). Even sediment-water exchange of CH_4 is investigated by automated lander techniques, and many of these studies focus on deeper sites (Boetius and Wenzhöfer, 2013). For the Baltic Sea and the North Sea, there are only a few datasets on nearshore shallow area emissions available and this situation may be representative for many shallow coastal systems that make up half of the Baltic Sea or a third of the global continental shelfs. In this study we show that these nearshore coastal systems are CO_2 and CH_4 emission hotspots and fluxes are comparable to terrestrial hot spot in Arctic lakes (Huttunen et al., 2006; Repo et al., 2007; Juutinen et al., 2009; Wik et al., 2013) and that shallow coastal systems are highly responsive to ongoing changes in temperature. Coastal seascapes constitute a mosaic of heterogeneous environments and habitats, and sediment-water interactions become more pertinent compared to the well-studied open coastal and ocean waters. For shallow coastal waters, the non-invasive and continuous instruments that record sediment and water column gas inventories and fluxes are still not sufficiently used and must be deployed on small research vessels that can reach the shallowest sites, which often host complex habitats such as algal belts, mussel beds, or seaweeds. The combination of the automated continuous CO_2- and CH_4-measurement devices and lander techniques, together with modern geophysics as mid-water sonar, multibeam or sub-bottom profilers, will allow identifying gas accumulations, pock marks, as well as flares and bubbles. As a result, we hypothesize that the sediment accumulation and event driven high gas emissions from nearshore shallow sediments is a major carbon capacitor in coastal areas that is not accounted for by the classical invasive core-incubation methods (Reeburgh, 1968) or by lander techniques (Boetius and Wenzhöfer, 2013) that still govern our view and process understanding of sediment-water CH_4 fluxes, and that these event-driven massive fluxes will increase with rising temperatures.

DATA AVAILABILITY

All data necessary to evaluate and build upon the work in this manuscript can be requested from the corresponding author. Atmospheric and surface water CO_2 and CH_4 data as well as CTD water profile data presented in this manuscript will be archived and freely available from the Bolin Centre Database, http://bolin.su.se/data.

AUTHOR CONTRIBUTIONS

CH wrote the manuscript and performed the measurements. MG developed the WEGAS system. XS, MM, and CM-M performed the carbon dioxide and methane measurements and did the statistical data analyses. CS and MJ did the geophysical measurements. BG did the budget calculations. AS performed the CTD measurements and analyses of wind data. AN and JN responsible for the long-term temperature measurements.

FUNDING

AN, CH, and BG acknowledge funding from the Academy of Finland (project ID 294853).

ACKNOWLEDGMENTS

This research is part of the Baltic Bridge strategic partnership between the Stockholm University and the University of Helsinki. We thank the crew and captain of RV Electra, and the staff at Stockholm Universities' field station Askö and Helsinki Universities' field station Tvärminne Zooological Station for their support. Maps were produced using Ocean Data View by R. Schlitzer, https://odv.awi.de, 2019.

SUPPLEMENTARY MATERIAL

The Supplementary Material for this article can be found online at: https://www.frontiersin.org/articles/10.3389/fmars.2019.00493/full#supplementary-material

REFERENCES

Anderson, L. G., Ek, J., Ericson, Y., Humborg, C., Semiletov, I., Sundbom, M., et al. (2017). Export of calcium carbonate corrosive waters from the East Siberian Sea. *Biogeosciences* 14, 1811–1823. doi: 10.5194/bg-14-1811-2017

Andersson, A., Meier, H. E. M., Ripszam, M., Rowe, O., Wikner, J., Haglund, P., et al. (2015). Projected future climate change and Baltic Sea ecosystem management. *Ambio* 44, 345–356. doi: 10.1007/s13280-015-0654-8

Bange, H. W., Bartell, U. H., Rapsomanikis, S., and Andreae, M. O. (1994). Methane in the Baltic and North Seas and a reassessment of the marine emissions of methane. *Glob. Biogeochem. Cycles* 8, 465–480. doi: 10.1029/94GB02181

Bastviken, D., Tranvik, L. J., Downing, J. A., Crill, P. M., and Enrich-Prast, A. (2011). Freshwater methane emissions offset the continental carbon sink. *Science* 331:50. doi: 10.1126/science.1196808

Boetius, A., and Wenzhöfer, F. (2013). Seafloor oxygen consumption fuelled by methane from cold seeps. *Nat. Geosci.* 6, 725–734. doi: 10.1038/ngeo1926

Borges, A. V., and Abril, G. (2012). "Carbon Dioxide and Methane Dynamics in Estuaries," in *Treatise on Estuarine and Coastal Science*, eds E. Wolanski, and D. S. McLusky, (Waltham, MA: Academic Press), 119–161. doi: 10.1016/b978-0-12-374711-2.00504-0

Borges, A. V., Champenois, W., Gypens, N., Delille, B., and Harlay, J. (2016). Massive marine methane emissions from near-shore shallow coastal areas. *Sci. Rep.* 6:27908. doi: 10.1038/srep27908

Borges, A. V., Speeckaert, G., Champenois, W., Scranton, M. I., and Gypens, N. (2018). Productivity and temperature as drivers of seasonal and spatial variations of dissolved methane in the southern bight of the North Sea. *Ecosystems* 21, 583–599. doi: 10.1007/s10021-017-0171-7

EMODnet Bathymetry Consortium (2018). "EMODnet digital bathymetry (DTM)," in *European Marine Observation and Data Network*, ed. E. B. Consortium. doi: 10.12770/18ff0d48-b203-4a65-94a9-5fd8b0ec35f6

Fransner, F., Fransson, A., Humborg, C., Gustafsson, E., Tedesco, L., Hordoir, R., et al. (2019). Remineralization rate of terrestrial DOC as inferred from CO2 supersaturated coastal waters. *Biogeosciences* 16, 863–879. doi: 10.5194/bg-16-863-2019

Gentz, T., Damm, E., Schneider von Deimling, J., Mau, S., McGinnis, D. F., and Schlüter, M. (2014). A water column study of methane around gas flares located at the West Spitsbergen continental margin. *Cont. Shelf Res.* 72, 107–118. doi: 10.1016/j.csr.2013.07.013

Gülzow, W., Rehder, G., Schneider, B., Schneider von Deimling, J., and Sadkowiak, B. (2011). A new method for continuous measurement of methane and carbon dioxide in surface waters using off-axis integrated cavity output spectroscopy (ICOS): an example from the Baltic Sea. *Limnol. Oceanogr. Methods* 9, 176–184. doi: 10.4319/lom.2011.9.176

Gustafsson, E., Deutsch, B., Gustafsson, B. G., Humborg, C., and Mörth, C.-M. (2014). Carbon cycling in the Baltic Sea - The fate of allochthonous organic carbon and its impact on air-sea CO2 exchange. *J. Mar. Syst.* 129, 289–302. doi: 10.1016/j.jmarsys.2013.07.005

Gustafsson, E., Omstedt, A., and Gustafsson, B. G. (2015). The air-water CO2 exchange of a coastal sea - A sensitivity study on factors that influence the absorption and outgassing of CO2 in the Baltic Sea. *J. Geophys. Res. Oceans* 120, 5342–5357. doi: 10.1002/2015JC010832

Humborg, C., Geibel, M. C., Anderson, L. G., Björk, G., Mörth, C.-M., Sundbom, M., et al. (2017). Sea-air exchange patterns along the central and outer East Siberian Arctic Shelf as inferred from continuous CO2, stable isotope, and bulk chemistry measurements. *Glob. Biogeochem. Cycles* 31, 1173–1191. doi: 10.1002/2017GB005656

Humborg, C., Mörth, C.-M., Sundbom, M., Borg, H., Blenckner, T., Giesler, R., et al. (2010). CO2 supersaturation along the aquatic conduit in Swedish watersheds as constrained by terrestrial respiration, aquatic respiration and weathering. *Glob. Change Biol.* 16, 1966–1978. doi: 10.1111/j.1365-2486.2009.02092.x

Humborg, C., Mörth, C.-M., Sundbom, M., and Wulff, F. (2007). Riverine transport of biogenic elements to the Baltic Sea - Past and possible future perspectives. *Hydrol. Earth Syst. Sci.* 11, 1593–1607. doi: 10.5194/hess-11-1593-2007

Huttunen, J. T., Väisänen, T. S., Hellsten, S. K., and Martikainen, P. J. (2006). Methane fluxes at the sediment-water interface in some boreal lakes and reservoirs. *Boreal Environ. Res.* 11, 27–34.

Jakobs, G., Holtermann, P., Berndmeyer, C., Rehder, G., Blumenberg, M., Jost, G., et al. (2014). Seasonal and spatial methane dynamics in the water column of the central Baltic Sea (Gotland Sea). *Cont. Shelf Res.* 91, 12–25. doi: 10.1016/j.csr.2014.07.005

Jakobsson, M., Stranne, C., O'Regan, M., Greenwood, S. L., Gustafsson, B., Humborg, C., et al. (2019). Bathymetric Properties of the Baltic Sea. *Ocean Sci Discuss* 2019, 1–33. doi: 10.5194/os-2019-18

Juutinen, S., Rantakari, M., Kortelainen, P., Huttunen, J. T., Larmola, T., Alm, J., et al. (2009). Methane dynamics in different boreal lake types. *Biogeosciences* 6, 209–223. doi: 10.5194/bg-6-209-2009

Kauppi, L., Norkko, A., and Norkko, J. (2018). Seasonal population dynamics of invasive polychaete genus *Marenzelleria* spp. in contrasting soft-sediment habitats. *J. Sea Res.* 131, 46–60. doi: 10.1016/j.seares.2017.10.005

Körtzinger, A., Thomas, H., Schneider, B., Gronau, N., Mintrop, L., and Duinker, J. C. (1996). At-sea intercomparison of two newly designed underway pCO2 systems - encouraging results. *Mar. Chem.* 52, 133–145. doi: 10.1016/0304-4203(95)00083-6

Laruelle, G. G., Dürr, H. H., Slomp, C. P., and Borges, A. V. (2010). Evaluation of sinks and sources of CO2 in the global coastal ocean using a spatially-explicit typology of estuaries and continental shelves. *Geophys. Res. Lett.* 37:L15607. doi: 10.1029/2010GL043691

Leifer, I., and Patro, R. K. (2002). The bubble mechanism for methane transport from the shallow sea bed to the surface: a review and sensitivity study. *Cont. Shelf Res.* 22, 2409–2428. doi: 10.1016/S0278-4343(02)00065-1

Lindgren, P. R., Grosse, G., Walter Anthony, K. M., and Meyer, F. J. (2016). Detection and spatiotemporal analysis of methane ebullition on thermokarst lake ice using high-resolution optical aerial imagery. *Biogeosciences* 13, 27–44. doi: 10.5194/bg-13-27-2016

Liss, P. S., and Slater, P. G. (1974). Flux of gases across the Air-Sea interface. *Nature* 247, 181–184. doi: 10.1038/247181a0

Mann, M. E., Rahmstorf, S., Kornhuber, K., Steinman, B. A., Miller, S. K., Petri, S., et al. (2018). Projected changes in persistent extreme summer weather events: the role of quasi-resonant amplification. *Sci. Adv.* 4:eaat3272. doi: 10.1126/sciadv.aat3272

Matveev, A., Laurion, I., Desphande, B. N., Bhiry, N., and Vincent, W. F. (2016). High methane emissions from thermocast lakes in subarctic peatlands. *Limnol. Oceanogr.* 61, 150–164. doi: 10.1002/lno.10311

McGinnis, D. F., Greinert, J., Artemov, Y., Beaubien, S. E., and Wüest, A. (2006). Fate of rising methane bubbles in stratified waters: how much methane reaches the atmosphere? *J. Geophys. Res. Oceans* 111:C09007. doi: 10.1029/2005JC003183

Meier, H. E. M., Hordoir, R., Andersson, H. C., Dieterich, C., Eilola, K., Gustafsson, B. G., et al. (2012). Modeling the combined impact of changing climate and changing nutrient loads on the Baltic Sea environment in an ensemble of transient simulations for 1961-2099. *Clim. Dyn.* 39, 2421–2441. doi: 10.1007/s00382-012-1339-7

Omstedt, A., Humborg, C., Pempkowiak, J., Perttilä, M., Rutgersson, A., Schneider, B., et al. (2014). Biogeochemical control of the coupled CO2-O2 system of the Baltic Sea: a review of the results of Baltic-C. *Ambio* 43, 49–59. doi: 10.1007/s13280-013-0485-4

Parmentier, F.-J. W., Christensen, T. R., Rysgaard, S., Bendtsen, J., Glud, R. N., Else, B., et al. (2017). A synthesis of the arctic terrestrial and marine carbon cycles under pressure from a dwindling cryosphere. *Ambio* 46, 53–69. doi: 10.1007/s13280-016-0872-8

Räike, A., Kortelainen, P., Mattsson, T., and Thomas, D. N. (2012). 36year trends in dissolved organic carbon export from Finnish rivers to the Baltic Sea. *Sci. Total Environ.* 435–436, 188–201. doi: 10.1016/j.scitotenv.2012.06.111

Raymond, P. A., Hartmann, J., Lauerwald, R., Sobek, S., McDonald, C., Hoover, M., et al. (2013). Global carbon dioxide emissions from inland waters. *Nature* 503, 355–359. doi: 10.1038/nature12760

Reeburgh, W. S. (1968). Determination of Gases in Sediments. *Environ. Sci. Technol.* 2, 140–141. doi: 10.1021/es60014a004

Reeburgh, W. S. (2007). Oceanic methane biogeochemistry. *Chem. Rev.* 107, 486–513. doi: 10.1021/cr050362v

Reeburgh, W. S. (2013). "Global Methane Biogeochemistry," in *Treatise on Geochemistry*, 2nd Edn, eds H. D. Holland, and K. K. Turekian, (Boston, MA: Elsevier), 71–94. doi: 10.1016/b978-0-08-095975-7.00403-4

Rehder, G., Leifer, I., Brewer, P. G., Friederich, G., and Peltzer, E. T. (2009). Controls on methane bubble dissolution inside and outside the hydrate stability field from open ocean field experiments and numerical modeling. *Mar. Chem.* 114, 19–30. doi: 10.1016/j.marchem.2009.03.004

Repo, M. E., Huttunen, J. T., Naumov, A. V., Chichulin, A. V., Lapshina, E. D., Bleuten, W., et al. (2007). Release of CO2 and CH4 from small wetland lakes in western Siberia. *Tellus Ser. B Chem. Phys. Meteorol.* 59, 788–796. doi: 10.1111/j.1600-0889.2007.00301.x

Roussel, E. G., Cragg, B. A., Webster, G., Sass, H., Tang, X., Williams, A. S., et al. (2015). Complex coupled metabolic and prokaryotic community responses to increasing temperatures in anaerobic marine sediments: critical temperatures and substrate changes. *FEMS Microbiol. Ecol.* 91:fiv084. doi: 10.1093/femsec/fiv084

Sander, R. (2015). Compilation of Henry's law constants (version 4.0) for water as solvent. *Atmos. Chem. Phys.* 15, 4399–4981. doi: 10.5194/acp-15-4399-2015

Sawicka, J. E., and Brüchert, V. (2017). Annual variability and regulation of methane and sulfate fluxes in Baltic Sea estuarine sediments. *Biogeosciences* 14, 325–339. doi: 10.5194/bg-14-325-2017

Schmale, O., Wäge, J., Mohrholz, V., Wasmund, N., Gräwe, U., Rehder, G., et al. (2018). The contribution of zooplankton to methane supersaturation in the oxygenated upper waters of the central Baltic Sea. *Limnol. Oceanogr.* 63, 412–430. doi: 10.1002/lno.10640

Schneider, B., Dellwig, O., Kuliński, K., Omstedt, A., Pollehne, F., Rehder, G., et al. (2017). "Biogeochemical cycles," in *Biological Oceanography of the Baltic Sea*, eds P. Snoeijs-Leijonmalm, H. Schubert, and T. Radziejewska, (Dordrecht: Springer), 87–122.

Schneider, B., Gülzow, W., Sadkowiak, B., and Rehder, G. (2014). Detecting sinks and sources of CO2 and CH4 by ferrybox-based measurements in the Baltic Sea: three case studies. *J. Mar. Syst.* 140, 13–25. doi: 10.1016/j.jmarsys.2014.03.014

Stanton, T. K., and Chu, D. (2008). Calibration of broadband active acoustic systems using a single standard spherical target. *J. Acoust. Soc. Am.* 124, 128–136. doi: 10.1121/1.2917387

Stranne, C., Mayer, L., Weber, T. C., Ruddick, B. R., Jakobsson, M., Jerram, K., et al. (2017). Acoustic mapping of thermohaline staircases in the arctic ocean. *Sci. Rep.* 7:15192. doi: 10.1038/s41598-017-15486-3

Thornton, B. F., Geibel, M. C., Crill, P. M., Humborg, C., and Mörth, C.-M. (2016). Methane fluxes from the sea to the atmosphere across the Siberian shelf seas. *Geophys. Res. Lett.* 43, 5869–5877. doi: 10.1002/2016GL068977

Wanninkhof, R. (2014). Relationship between wind speed and gas exchange over the ocean revisited. *Limnol. Oceanogr. Methods* 12, 351–362. doi: 10.4319/lom.2014.12.351

Weber, T. C., Mayer, L., Jerram, K., Beaudoin, J., Rzhanov, Y., and Lovalvo, D. (2014). Acoustic estimates of methane gas flux from the seabed in a 6000 km 2 region in the Northern Gulf of Mexico. *Geochem. Geophys. Geosystems* 15, 1911–1925. doi: 10.1002/2014GC005271

Weidner, E., Weber, T. C., Mayer, L., Jakobsson, M., Chernykh, D., and Semiletov, I. (2019). A wideband acoustic method for direct assessment of bubble-mediated methane flux. *Cont. Shelf Res.* 173, 104–115. doi: 10.1016/j.csr.2018.12.005

Wik, M., Crill, P. M., Varner, R. K., and Bastviken, D. (2013). Multiyear measurements of ebullitive methane flux from three subarctic lakes. *J. Geophys. Res. Biogeosciences* 118, 1307–1321. doi: 10.1002/jgrg.20103

Wulff, F., Savchuk, O. P., Sokolov, A., Humborg, C., and Mörth, C.-M. (2007). Management options and effects on a marine ecosystem: assessing the future of the baltic. *Ambio* 36, 243–249. doi: 10.1579/0044-7447(2007)36%5B243:moaeoa%5D2.0.co;2

Conflict of Interest Statement: The authors declare that the research was conducted in the absence of any commercial or financial relationships that could be construed as a potential conflict of interest.

frontiers
in Marine Science

ORIGINAL RESEARCH
published: 28 August 2019
doi: 10.3389/fmars.2019.00523

Biogeochemical Response of Apalachicola Bay and the Shelf Waters to Hurricane Michael Using Ocean Color Semi-Analytic/Inversion and Hydrodynamic Models

Eurico J. D'Sa[1], Ishan D. Joshi[1,2], Bingqing Liu[1], Dong S. Ko[3], Christopher L. Osburn[4] and Thomas S. Bianchi[5]*

[1] Department of Oceanography and Coastal Sciences, Louisiana State University, Baton Rouge, LA, United States, [2] Marine Physical Laboratory, Scripps Institution of Oceanography, University of California, San Diego, San Diego, CA, United States, [3] Oceanography Division, Naval Research Laboratory, Stennis Space Center, Bay Saint Louis, MS, United States, [4] Department of Marine Earth and Atmospheric Sciences, North Carolina State University, Raleigh, NC, United States, [5] Department of Geological Sciences, University of Florida, Gainesville, FL, United States

OPEN ACCESS

Edited by:
Toshi Nagata,
The University of Tokyo, Japan

Reviewed by:
Qian P. Li,
Chinese Academy of Sciences, China
Youhei Yamashita,
Hokkaido University, Japan

***Correspondence:**
Eurico J. D'Sa
ejdsa@lsu.edu

Specialty section:
This article was submitted to Marine Biogeochemistry, a section of the journal Frontiers in Marine Science

Received: 29 May 2019
Accepted: 12 August 2019
Published: 28 August 2019

Citation:
D'Sa EJ, Joshi ID, Liu B, Ko DS, Osburn CL and Bianchi TS (2019) Biogeochemical Response of Apalachicola Bay and the Shelf Waters to Hurricane Michael Using Ocean Color Semi-Analytic/Inversion and Hydrodynamic Models. Front. Mar. Sci. 6:523. doi: 10.3389/fmars.2019.00523

Hurricanes are increasingly being recognized as important episodic drivers in ocean biogeochemical cycling; however, spatiotemporal response of their impacts on coastal and estuarine ecosystems are limited. Hurricane Michael, which made landfall just west of Apalachicola Bay (ApB) on October 10, 2018 as a Category 5 hurricane with sustained winds of 250 km h^{-1}, caused widespread damage to the northwest Florida coast, and adverse effects on oyster reefs and water quality in ApB due to winds and coastal flooding associated with a strong storm surge. The impact of wind forcing and retreating storm surges on coastal and shelf biogeochemical properties remains, however, largely unknown. In this study, we use a combination of pre-hurricane field observations, ocean-color satellite imagery and the outputs (salinity, currents, sea surface height, and temperature) of a nested high-resolution three-dimensional hydrodynamic model (NCOM) to examine the biogeochemical response of ApB and the surrounding shelf waters to Hurricane Michael. MODIS-derived optical proxies (e.g., absorption of colored dissolved organic matter or CDOM and particle backscattering coefficients) of dissolved and particulate organic carbon (DOC and POC) were derived for a series of clear-sky imagery (prior to and following the hurricane) using a combination of estuarine-tuned semi-analytic and empirical algorithms. Following the hurricane, spatiotemporal distribution of both DOC and POC in ApB and the nearshore coastal waters showed a strong response to storm surge, increasing river discharge, currents, and wind field. Average flux estimates of organic carbon exported from ApB between October 5–21, 2018 to the coastal ocean were much greater for DOC (0.86×10^6 kg C d^{-1}) than POC (0.21×10^6 kg C d^{-1}) and increased with increasing river discharge and the wind field. A bio-optical inversion algorithm applied to Sentinel-3A OLCI imagery of 13 October, 2018 immediately following the hurricane's passage, showed a strong, week-long biological response with spatially distinct phytoplankton blooms of *Karenia brevis* and *Emiliania Huxleyi,* as detected by satellite imagery of pigments, an approach that could revolutionize our understanding of environmental impacts on phytoplankton. This study revealed spatiotemporal changes in estuarine and coastal ocean biogeochemistry reflective of a systematic regional ecosystem response to Hurricane Michael.

Keywords: hurricane, MODIS, OLCI, CDOM, DOC, POC, phytoplankton, NCOM

INTRODUCTION

Projections of increased intensity of hurricanes in a warming climate remains a major concern in terms of threats to human lives in expanding coastal communities and its economic consequences (Emanuel, 2005). Hurricanes also impact the natural cycles of local waters such as increases in primary production (Lin et al., 2003; McKinnon et al., 2003; Babin et al., 2004). This enhanced primary production has been attributed to increases in the mixed-layer depth, decreases in sea-surface temperature (SST), breakdown in water column stratification, and upwelling (Williams et al., 2001; Davis and Yan, 2004; Black and Dickey, 2008). Consequently, an increase in the intensity and frequency of hurricanes could potentially have dramatic regional effects on coastal biogeochemical cycles. Moreover, enhanced hurricane activity, coupled with higher precipitation events (Emanuel, 2013, 2017), could result in greater storm surge flooding, higher discharge from rivers and coastal watersheds, and increased nutrient, particulate and dissolved organic carbon (POC and DOC) loading, potentially driving large-scale changes in coastal ecosystems (Paerl et al., 1998; McKinnon et al., 2003; Liu et al., 2019a). For example, in 2001, Hurricane Irene caused major increases in freshwater discharges and DOC concentrations in the Neuse River which resulted in roughly 19 times more export of DOC to the Neuse River Estuary than pre-storm conditions (Brown et al., 2014). To date, the extents of these impacts are not well understood since access to these impacted regions are relatively restricted in conditions immediately following a hurricane. As such, remote sensing and hydrodynamic modeling have provided greater insights on the impact of hurricanes on oceanic and shelf waters (Babin et al., 2004; Davis and Yan, 2004; Walker et al., 2005; Lohrenz et al., 2008; Zamudio and Hogan, 2008; D'Sa et al., 2011; Farfan et al., 2014).

Ocean-color satellite remote sensing offers the capability for synoptic monitoring of the marine environment over large spatial scales, at frequent intervals, and during severe weather conditions. Most ocean-color studies have shown greater chlorophyll *a* concentrations (Chl *a*, an indicator of phytoplankton biomass) in oceanic, shelf and coastal waters following hurricane events (Babin et al., 2004; Yuan et al., 2004; Miller et al., 2006; Hanshaw et al., 2008). The passage of numerous hurricanes on both east and west coasts of Mexico and the US east coast resulted in distinct increases surface Chl *a* (Davis and Yan, 2004; Farfan et al., 2014). Satellite studies in the northern Gulf of Mexico (nGoM) have reported changes in Chl *a* that have been linked to a decrease in SST (Walker et al., 2005). While phytoplankton community responses to hurricane passage are important to estuarine food web dynamics (Paerl et al., 2001), their effects on phytoplankton composition using satellite ocean color have been limited. However, taxonomic changes in the phytoplankton community were recently observed in Galveston Bay (using satellite ocean color) after the passage of Hurricane Harvey (Liu et al., 2019a).

Hurricanes can enhance the delivery of DOC and POC to estuaries and coastal waters (Avery et al., 2004; Brown et al., 2014; Paerl et al., 2018). Ocean color estimates of DOC, based on robust relationships observed between DOC and CDOM (colored dissolved organic matter; an optically active constituent and proxy for DOC) have been largely made in river-dominated coastal waters (Fichot and Benner, 2011; Mannino et al., 2015; Le et al., 2016; Osburn et al., 2016; Joshi et al., 2017). Thus, numerous estimates of CDOM concentrations in coastal and shelf waters have been made with satellite ocean color using empirical algorithms that relate CDOM absorption coefficients to remote sensing reflectance band ratios (D'Sa and Miller, 2003; D'Sa et al., 2006; D'Sa, 2008; Mannino et al., 2008, 2014; Tehrani et al., 2013; Joshi and D'Sa, 2015; Joshi et al., 2017; Liu et al., 2019b). Similar approaches have been developed for POC, that include a direct empirical relationship between POC and a reflectance band ratio or two-step algorithms relating reflectance to backscattering coefficient and then to POC (Stramski et al., 1999; Gardner et al., 2006; Stramski et al., 2008). More recently, a multiple regression algorithm, relating POC to multiple reflectance bands of the MODIS-Aqua satellite sensor, was reported for Louisiana shelf/slope waters (Le et al., 2016). However, there are limitations with empirical band ratio algorithms because they are generally optimized for specific regions or seasons. In contrast, semi-analytic algorithms, based on radiative transfer theory (Gordon et al., 1988; Lee et al., 2002), allow for the estimation of inherent optical properties (IOPs), such as absorption and backscattering coefficients in oceanic and shelf waters directly from ocean-color data. The applicability of these semi-analytic approaches to optically complex coastal and estuarine waters would facilitate the estimation of IOPs, such as CDOM absorption and particle backscattering coefficients, the two optical proxies for DOC and POC, respectively.

Semi-analytic approaches such as the quasi-analytic algorithm or QAA (Lee et al., 2002) are based on the radiative transfer theory that relate spectral remote sensing reflectance R_{rs} (obtained just above sea water) to optical properties such as the total spectral absorption a (due to water itself, CDOM and non-algal particles), and backscattering b_{b} coefficients (m^{-1}) of the medium. More recently, a semi-analytical approach, based on the QAA, namely QAA-V, was tuned for the turbid coastal waters, and performed more effectively in estuarine waters (Joshi and D'Sa, 2018). The application of QAA-V to atmospherically corrected R_{rs} from ocean color sensors such as VIIRS-NPP or MODIS-Aqua allows the determination of total absorption and backscattering coefficients in estuarine waters - directly from satellite data. Additional information from field (e.g., slope of CDOM spectra) and satellite observations is often used to retrieve absorption by CDOM and non-algal particles (D'Sa et al., 2018). The QAA-V in conjunction with field derived relationships between absorption/backscattering coefficients and DOC/POC concentrations have been used to derive DOC and POC maps of Galveston Bay (D'Sa et al., 2018). Optical inversion algorithms such as the non-negative linear square (NNLS) algorithm have been developed to estimate phytoplankton pigment composition from satellite ocean color data (Moisan et al., 2017). The NNLS algorithm for example uses information on the *in vivo* spectral absorption coefficients of phytoplankton and pigments in combination with standard MODIS Chl *a* product to obtain phytoplankton pigment maps of northeastern US shelf waters (Moisan et al., 2017). A similar technique based on *in vitro* absorption properties of algal pigments and satellite-estimated Chl *a*, from a Red to NIR band ratio empirical algorithm, has also generated pigment composition maps in Galveston Bay, using the Sentinel-3A OLCI data with higher spectral and spatial resolution (Liu et al., 2019a). Ocean color remote sensing is however, often limited by cloud cover especially during and after hurricanes and numerical modeling approaches, in combination with ocean color, have allowed for a better understanding of the physical-biogeochemical interactions associated with hurricane passages in the coastal ocean (Chen et al., 2009; D'Sa et al., 2011).

The nGoM has been impacted by hurricanes with increasing frequency and intensity that have affected many coastal ecosystems in the region (Turner et al., 2006; Keim et al., 2007). Most recently, Hurricane Michael made its track along the northeastern Gulf of Mexico (neGoM), before making landfall as a Category 5 hurricane on October 10, 2018, just west of Apalachicola Bay (ApB), a shallow, sub-tropical, bar-built, and river-dominated estuary on the Florida Panhandle. It then moved rapidly inland depositing large amounts of precipitation before weakening to a tropical storm over Georgia. A storm surge of ~2.5 m was recorded in ApB which sustained severe damage due to the storm surge and intense winds. In this study, we used a combination of field observations collected prior to the hurricane, the outputs of a high-resolution numerical ocean model and satellite ocean color data, to examine the physical and biogeochemical response in ApB and the surrounding northwest Florida shelf waters to this event. An ocean color semi-analytic algorithm (QAA-V) was used to obtain absorption and backscattering coefficients from MODIS-Aqua imagery and then combined with empirical relationships based on pre-hurricane field data to estimate DOC and POC concentrations throughout ApB and surrounding coastal waters. The outputs of a numerical hydrodynamic model (NCOM) were then used in combination with satellite estimates of DOC and POC to calculate estuarine organic carbon fluxes to the coastal ocean. Finally, an inversion approach was applied to cloud free Sentinel-3A OLCI imagery to assess the phytoplankton response in northwest Florida shelf waters following the hurricane passage.

MATERIALS AND METHODS

Study Area

The path of Hurricane Michael through the nGoM and its landfall as a strong Category 5 hurricane strongly impacted the north Florida shelf and coastal waters including ApB, an elongated shallow estuary with an average depth ~ 3 m and area of ~540 km^2 (**Figure 1**). ApB, a highly productive estuary is designated as a National Estuarine Research Reserve, is well known for its oyster harvest that in the past accounted for ~10% of the nation's oyster production (Wilber, 1992; Havens et al., 2013). A major source of freshwater to the bay, Apalachicola River (AR) is the third largest river in the northern GOM with the greatest discharge of any Florida river, and a drainage basin of ca. 48,500 km^2 that extends into Georgia (Livingston, 2014). Another source of freshwater to the bay, albeit considerably smaller, is from the blackwater Carrabelle River (**Figure 1**). Water exchange between the relatively fresh bay and saline Gulf waters occur through a few passes (Indian Pass, West Pass, East Pass, and Sikes Cut) located between several barrier islands that separate the bay from the Gulf waters (**Figure 1**). The neGoM region impacted by the hurricane considered in this study includes the northwest Florida shelf, which is broadly sloping south of Big Bend and tapers narrower northwest of Cape San Blas (**Figure 1**). Shelf waters are generally stratified from April to November due to seasonally weaker winds and surface heat gain (He and Weisberg, 2002); eddies associated with the Loop Current, located adjacent to the shelf edge (Walker et al., 2011), can also impact the hydrodynamics of this region.

Optical and Hydrological Measurements

Surface water samples were collected in ApB during three field surveys in March 2015, November 2015, and July 2016 and processed for spectral CDOM and particulate absorption measurements (Joshi et al., 2017). Briefly, for CDOM spectral absorption measurements, water samples were filtered through 0.2-μm pre-rinsed Nuclepore filters on the same day and stored in acid cleaned, pre-combusted amber bottles with Teflon-lined caps at 4°C in the dark, and processed within a week for CDOM spectral absorption on a dual beam Perkin-Elmer Lambda 850 spectrophotometer. CDOM absorption coefficients were measured at 412 nm ($a_{\mathrm{g}}412$), as methods described in Joshi and D'Sa (2015). For determinations of light absorption by suspended particulate matter, particles were collected on a 25 mm diameter Whatman GF/F filter and stored in liquid nitrogen until measurement. Particulate (total – a_{p} and non-algal – a_{NAP}) absorption were measured on a Perkin-Elmer Lambda 850 spectrophotometer fitted with a 15-cm diameter integrating sphere (Naik and D'Sa, 2012). Sub-surface water particulate backscattering coefficients at 532 nm ($b_{\mathrm{bp}}532$) were measured with a Wetlabs Eco triplet sensor (D'Sa et al., 2006). Above-water remote sensing reflectance (Rrs^{0+}, sr^{-1}) were derived from above-water measurements of water-surface, sky, and reference

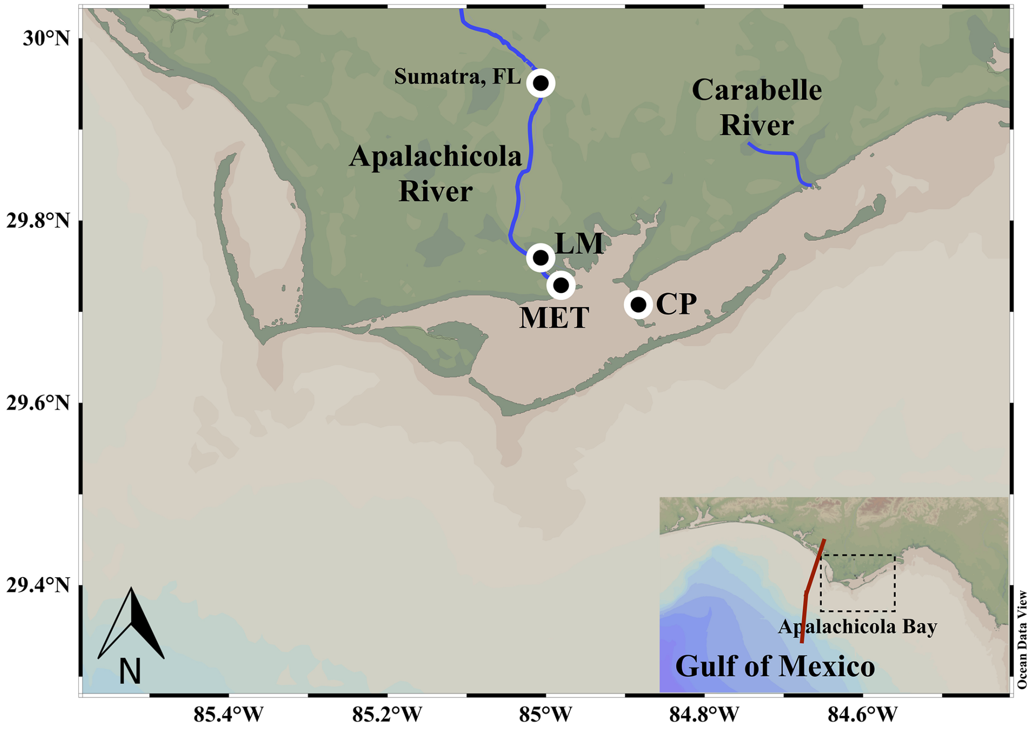

FIGURE 1 | Study area. Apalachicola Bay (ApB) and the surrounding shelf waters with the main Apalachicola River and the smaller Carabelle River flowing into the bay. Circles denote the location of the river stage station (Sumatra, FL, United States), meteorological station (LM) and the water quality monitoring station at Cat Point (CP) in ApB. Inset shows the northeast Gulf of Mexico region comprising ApB showing track of hurricane Michael (red line).

plate radiances, using a GER 1500 512iHR spectroradiometer under clear sky conditions (Mobley, 1999; additional details in Joshi et al., 2017). A total of 425 measurements of in-situ phytoplankton absorption spectra $a_{phy}(\lambda)$ and Chl *a* concentrations between 2006 to 2016 were also obtained from the NASA SeaBASS archive. Daily AR discharge data were obtained from USGS station near Sumatra, while the wind and pressure data were obtained from the Apalachicola National Estuarine Research reserve at the East Bay station (**Figures 1**, **2**).

Chemical Measurements

Samples for DOC were filtered through pre-combusted (450°C for 6 h), pre-rinsed Whatman GF/F filters and stored in acid cleaned, pre-combusted amber bottles with Teflon-lined caps. DOC was measured on an OI Analytical 1030D TOC analyzer using wet chemical oxidation (sodium persulfate) - modified for seawater analyses (Osburn and St-Jean, 2007). Milli-Q laboratory water (18.2 MΩ; <10 μg C L^{-1} TOC) was used to prepare standards and reagents and as a blank. Calibration of the instrument was achieved daily using solutions of caffeine (0–20 mg C L^{-1}); reproducibility was $<5\%$ RSD (relative standard deviation). Routine measurement of Hansell Certified Reference Material (CRM) DOC standards with each analytical run resulted in DOC values of 0.54 ± 0.07 mg C L^{-1}.

Particulate organic carbon concentration was measured on particles retained on the GF/F filters used to filter DOC. Each filter was packed into a solvent-rinsed air-dried tin capsule and combusted in a Thermo Flash 1112 elemental analyzer. The resulting CO_2 was quantified based on standards of acetanilide; reproducibility was $<5\%$ RSD.

NCOM Ocean Circulation Model and Flux Calculations

The Navy Coastal Ocean Model (NCOM), based on the Princeton Ocean Model (POM) uses a nested modeling approach (Ko et al., 2008) with a high-resolution (∼250 m) estuarine model for ApB (**Figure 3c**). This model is nested within a lower 1.5 km resolution neGoM regional model (**Figure 3b**) that connects the deep Gulf to the coast - and then to ApB (Joshi et al., 2017). The estuarine model is driven by realistic tides and real-time river flows and to a lesser extent by winds, evaporation and rainfall which are from a high-resolution regional weather forecast model, the coupled ocean/atmosphere mesoscale prediction system (COAMPS). In this study, we examined the ApB and neGoM model results of sea level, surface currents, salinity, and temperature for the month of October 2018. Specifically, we used cloud-free ocean color satellite imagery obtained on 4, 6, 12, 13, 17, and 21 October to estimate DOC and POC concentrations (**Figures 4**, **5**) and corresponding model outputs to examine physical linkages to DOC and POC distributions (**Figures 6**, **7**) and calculate their fluxes (**Figure 8**) in the study area. Volume fluxes of water in-or-out of the bay were obtained from the NCOM ocean model by integrating hourly flows (current, in m s^{-1}, times vertical cross-section, in m^2) around all the bay passes

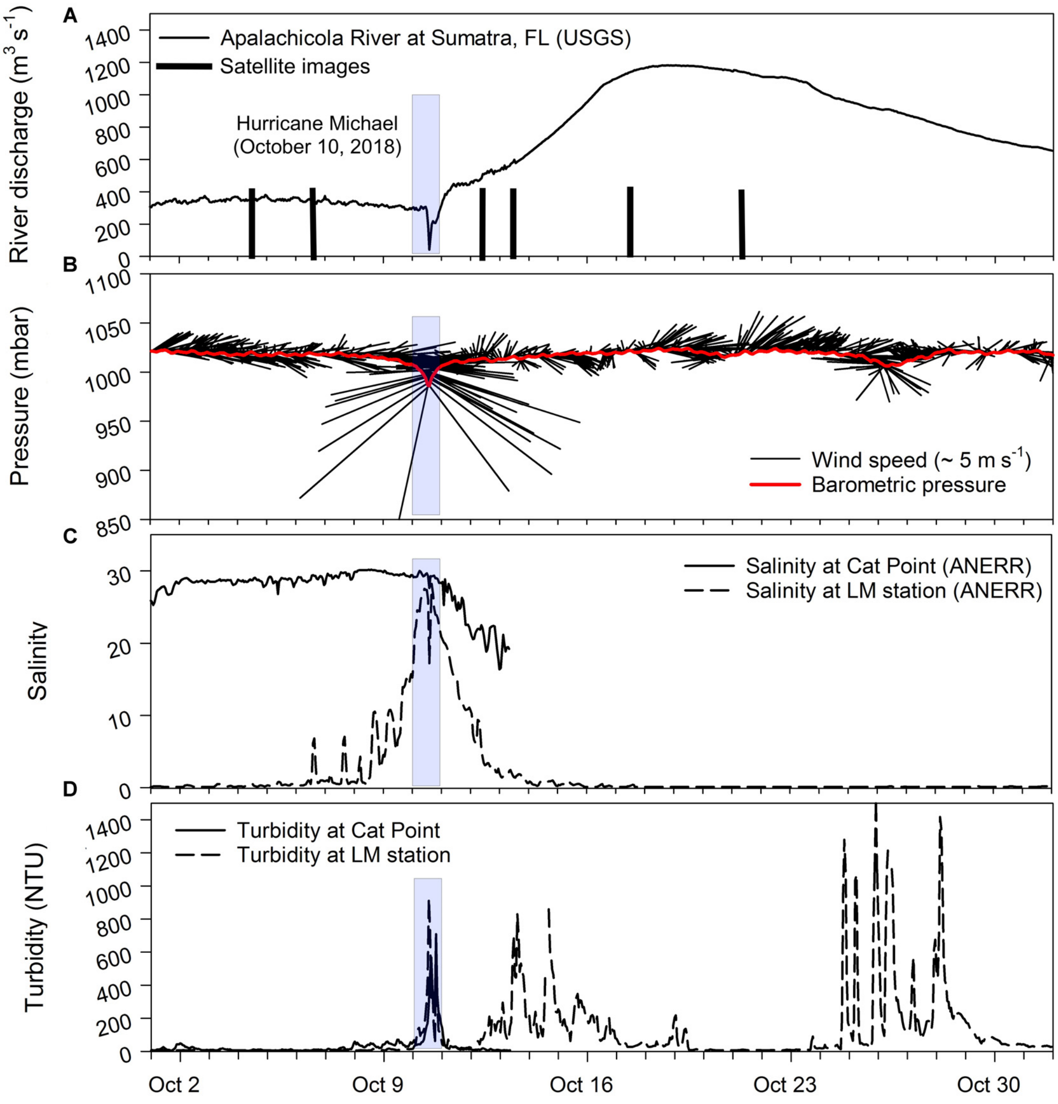

FIGURE 2 | Time-series measurements during October 2018. **(A)** Apalachicola River discharge (m^3s^{-1}) with vertical black bars denoting availability of mostly cloud free MODIS imagery on 4, 6, 12, 13, 17, and 21, October 2018. **(B)** air pressure and wind vectors (wind speed and direction from true north) with light blue bar on 10 October 2018 representing the Hurricane Michael landfall, **(C)** salinity at Cat Point (CP; solid line) and LM station (LM; dashed line), and **(D)** turbidity at CP and LM stations for the period 1–31 October 2018.

(Joshi et al., 2017). Hourly DOC and POC flux rates over multiple tidal cycles were then computed by multiplying the satellite-derived DOC and POC concentrations by the volume of water transported through the passes. Similarly, the neGOM regional NCOM model (**Figure 9a**) was used along with satellite imagery (**Figures 9b**, **10a**) to examine larger scale linkages in the shelf waters.

Ocean Color Satellite Data and Processing

MODIS-Aqua ocean color satellite data were downloaded from the NASA Ocean Biology Processing Group (OBPG) website before and after Hurricane Michael for low cloud cover or clear-sky days on 4, 6, 12, 13, 17, and 21 October, 2018. Data were processed to remove atmospheric effects using an adaptive atmospheric correction scheme that optimizes the selection of one of the three standard atmospheric correction methods (NIR, MUMM and SWIR; Joshi et al., 2017 and references there in; Joshi and D'Sa, in review) in optically complex coastal waters to obtain remote sensing reflectance (R_{rs_MODIS}, sr^{-1}). R_{rs_MODIS} were then processed using the QAA-V semi-analytic algorithm (Joshi and D'Sa, 2018) to obtain estimates of a and b_b; where, a is the additive sum of contributions by pure water (a_w), phytoplankton (a_{phy}), detrital or non-algal particles (a_{NAP}) and CDOM a_g absorption ($a = a_w + a_g + a_{NAP} + a_{phy}$); and total spectral backscattering coefficient (b_b) is the sum due to contributions by pure water and particle backscattering ($b_b = b_{bw} + b_{bp}$), respectively. Additional information on

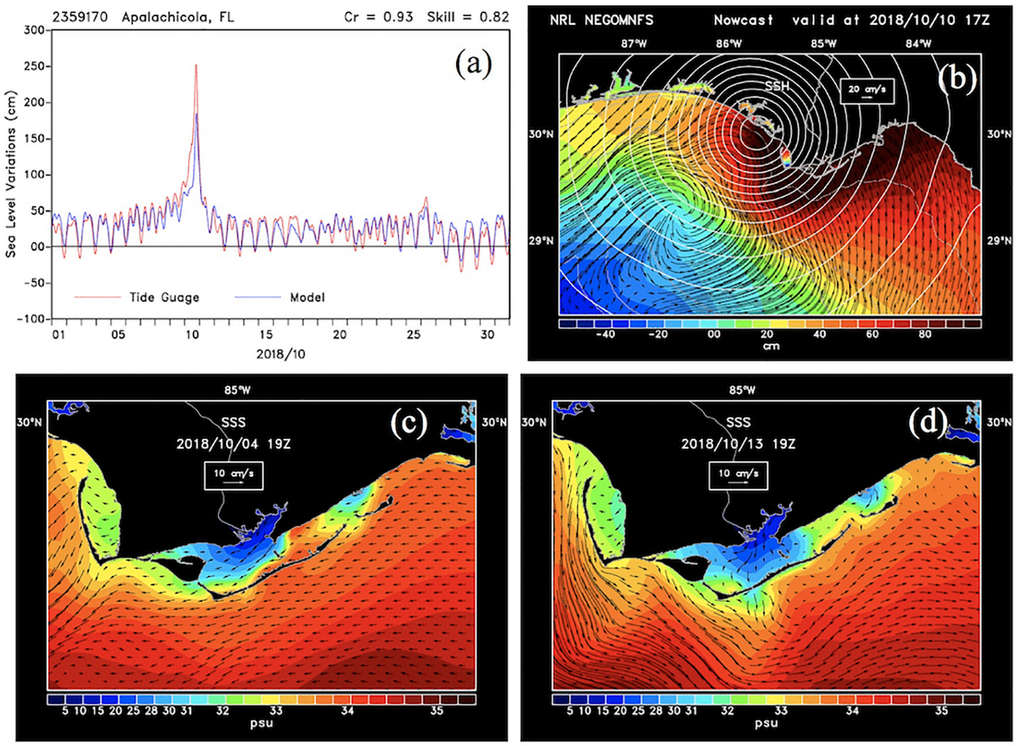

FIGURE 3 | NCOM model outputs. **(a)** Sea level variations from model simulations and the NOAA National Ocean Service (NOS) tide gauge station located in Apalachicola, Florida; **(b)** model simulation of surface elevation superimposed by surface currents and air pressure for October 10, 2018 during Hurricane Michael landfall just east of ApB. **(c,d)** Sea surface salinity (SSS) and superimposed by de-tided surface currents on October 4 and 13, 2018.

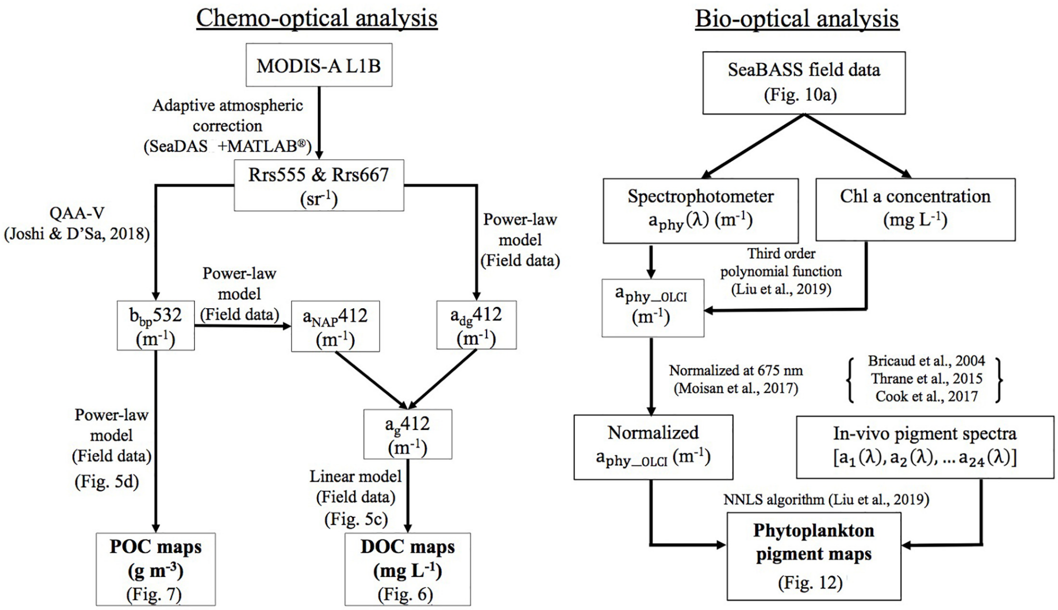

FIGURE 4 | Schematic diagrams. Processing pathways (**left panel:** chemo-optical analysis) for generation of DOC and POC maps of ApB from MODIS imagery and (**right panel:** bio-optical analysis) for generation of Chl *a* and phytoplankton pigment maps of the northwest Florida shelf waters from Sentinel-3 OLCI imagery.

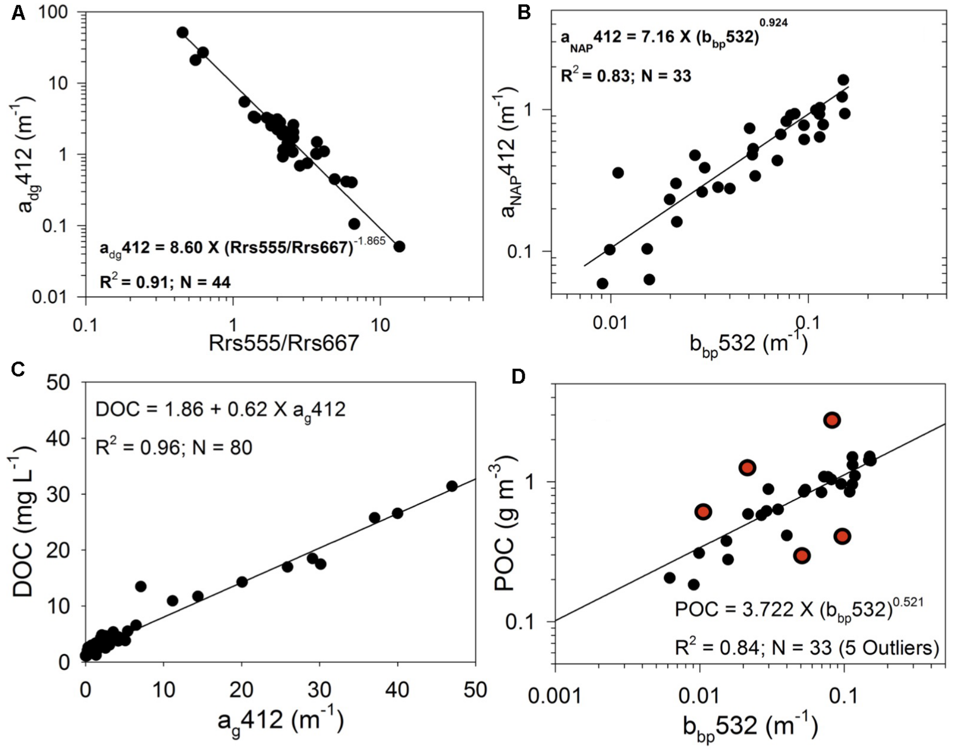

FIGURE 5 | *in situ* chemo-optical relationships. **(A)** MODIS-Aqua remote sensing reflectance band ratio ($R_{rs}555/R_{rs}667$) vs. $a_{dg}412$ nm; **(B)** particle backscattering at 532 nm ($b_{bp}532$) vs. $a_{NAP}412$ nm; **(C)** a_g412 vs. DOC; and **(D)** $b_{bp}532$ vs. POC.

spectral shapes of the absorption and scattering coefficients allowed for estimates of the relative contributions by constituents such as phytoplankton and CDOM plus non-algal particles (NAP) ($a_{dg} = a_g + a_{NAP}$) to total absorption and scattering coefficients. A combination of empirical relationships using field measurements and R_{rs_MODIS} band ratios were then used obtain estimates of DOC and POC in ApB (**Figure 4**; chemo-optical analysis).

Sentinel-3 OLCI full resolution mode (300 m) cloud-free images for October 13 and 17, 2018 over neGoM were obtained from the European Organization for Meteorological Satellites (EUMETSAT) and pre-processed using the Sentinel-3 Toolbox Kit Module (S3TBX) version 5.0.1 in Sentinel Application Platform (SNAP). The OLCI data were then atmospherically corrected using the Case-2 Regional Coast Color (C2RCC) module to obtain remote sensing reflectance (R_{rs_OLCI}, sr^{-1}). The Sentinel-3 OLCI data were then used to estimate Chl *a* (**Figure 11**) and phytoplankton pigment compositions (**Figure 12**) using the OLCI Case2R neural net standard algorithm and the NNLS inversion algorithm.

Phytoplankton Pigment Composition From Sentinel-3A OLCI

Phytoplankton pigment compositions were estimated using the NNLS inversion algorithm (Liu et al., 2019a) with a focus on the neGoM shelf waters (**Figure 4**; bio-optical analysis). Our goal was to obtain spatiotemporal distributions of some pigment ratios specific to algal-bloom species using a previously developed technique to study a hurricane-induced phytoplankton bloom event which appeared to be comprised of mixed algal blooms dominated by different species as indicated by the contrasting colors observed in post-hurricane enhanced high spatial resolution true color Sentinel-3A OLCI imagery (ERGB; band 6 – 560 nm, band 4 – 490 nm and band 3 – 442.5 nm) of the shelf waters (**Figure 10a**). Thus, Sentinel-3A OLCI pigment maps for October 13, 2018 were generated using the bio-optical analysis processing pathway (**Figure 4**) in a series of steps. Firstly, a total of 425 in-situ measurements including phytoplankton absorption spectra $a_{phy}(\lambda)$ and Chl *a* concentrations acquired from SeaBASS during 2006–2012 (**Figure 10a**; location shown by pins) were interpolated at 1 nm interval from 400 to 700 nm (**Figure 10e**), and modeled as a third order function of in-situ Chl *a* concentrations (Liu et al., 2019a) to obtain the wavelength-dependent coefficients. We then further applied these coefficients to Sentinel-3A OLCI Chl *a* to generate satellite-derived phytoplankton absorption spectrum (a_{phy_OLCI}) at each pixel (1851 × 1038). Since ~80% variations in the shape and magnitude of *in vivo* $a_{phy}(\lambda)$ by phytoplankton cells are attributed to the pigment composition (Ciotti et al., 2002), their concentrations were estimated by reconstructing a_{phy_OLCI} spectra using mass-specific absorption spectra

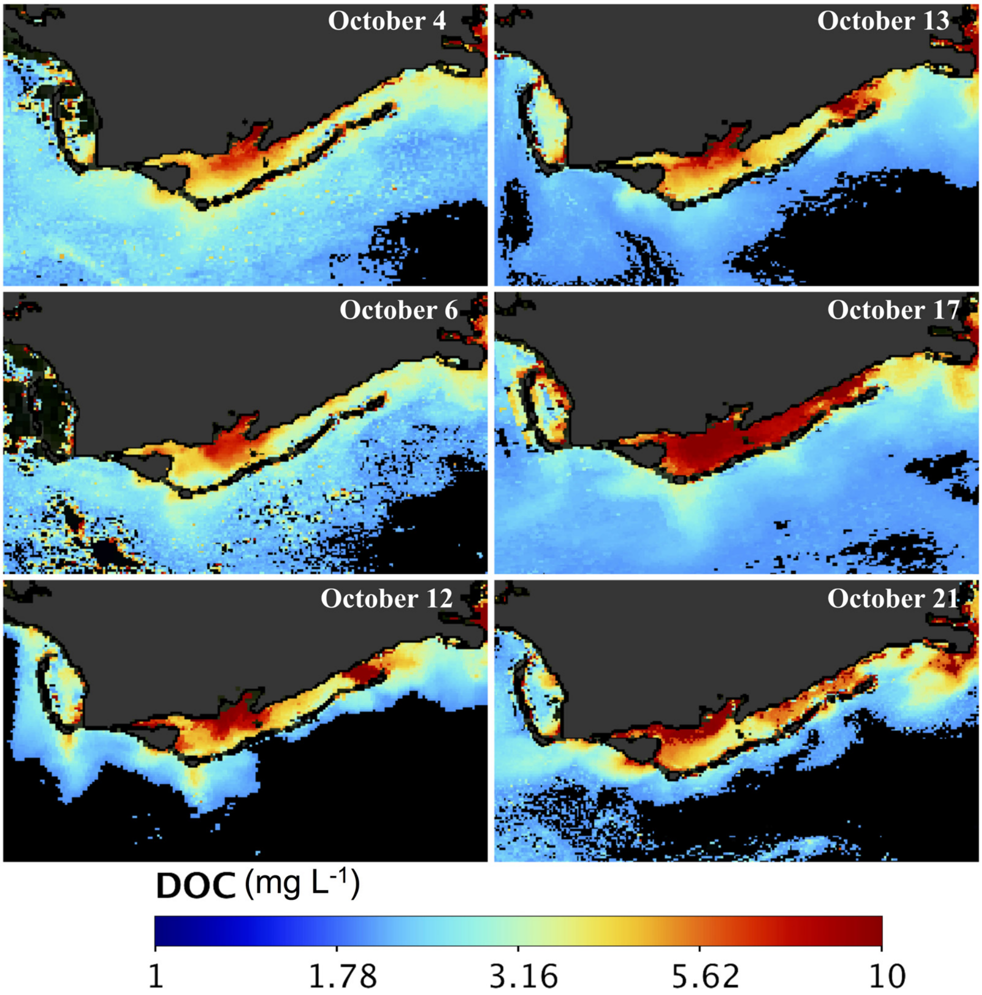

FIGURE 6 | DOC maps of Apalachicola Bay. MODIS-derived DOC maps (mg L^{-1}) for October 4, 6, 12, 13, 17, and 21, 2018.

of different pigments based on non-negative least square (NNLS) inversion algorithm (Liu et al., 2019a). In addition, pigment packaging effect is another import factor influencing the absorption spectra of phytoplankton; thus, $a_{phy}(\lambda)$ was normalized at 675 to minimize pigment packaging effects (Moisan et al., 2017) before spectrum reconstruction. A total of 22 mass-specific pigment spectra obtained from different published sources were included in this study. *In vivo* mass-specific absorption spectra of 14 pigments including Chl *a*, Chl *b*, divinyl (DV)-Chl *a*, DV-Chl *b*, Chl *c*, peridinin (peri), fucoxanthin (fuco), 19′hexanoyloxyfucoxanthin (19′hexa-fuco), 19′butanoyloxyfucoxanthin (19′buta-fuco), alloxanthin, diadinoxanthin (diadino), zeaxanthin, and α-carotenoid and β-carotenoid (β-caro) were obtained from Bricaud et al. (2004). Furthermore, total Chl *a* consists of active intact Chl *a* plus breakdown products called "pheopigments," mostly pheophytin, which modify $a_{phy}(\lambda)$ between 400 and 435 nm – due to a shift in the maximal absorption of pheophytin-*a* toward shorter wavelengths (Kiefer and SooHoo, 1982). Generally, healthy phytoplankton have mostly active Chl *a*, but a fraction of pheopigments increases with increasing senescence of algal cells (Mitchell and Kiefer, 1988; Bianchi and Canuel, 2011). Thus, spectra of pheophytins-*a* and -*b* were also included in the NNLS inversion algorithm (Thrane et al., 2015) due to the algal blooms detected in the enhanced RGB image (**Figure 10a**). Further, the *in vitro* (ethanol extracted) absorption spectra of 5 other chloroplast carotenoids including violaxanthin, lutein, neoxanthin, diatoxanthin, and dinoxanthin were obtained from Thrane et al. (2015). However, since the absorption peaks of these *in vitro* spectra have a slight shift (Bidigare et al., 1990) in comparison to those measured using the filter pad technique (Roesler et al., 2018), the absorption spectra from pure pigments *in vitro* are not the best illustration of the pigment absorption spectra contained in phytoplankton cellular complexes *in vivo* (Lutz et al., 2001). Therefore, the absorption maxima of these 5 *in vitro* absorption spectra were shifted to longer wavelength by +10 nm to *in vivo* positions (Bidigare et al., 1990; Kirk, 1994). The mass-specific absorption spectra of phycoerythrin and phycocyanin (Cook et al., 2017), were also included in the

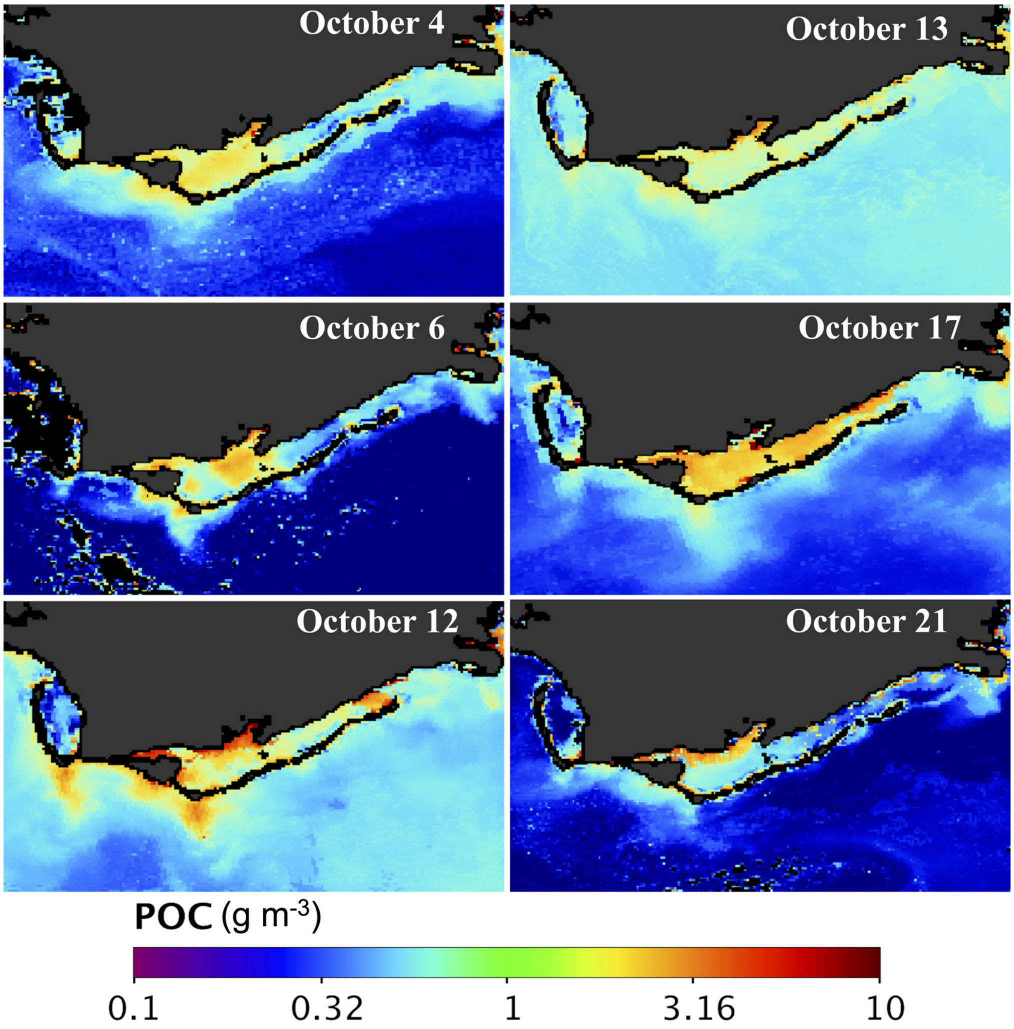

FIGURE 7 | POC maps of Apalachicola Bay. MODIS-derived POC maps (g m^{-3}) for October 4, 6, 12, 13, 17, and 21, 2018.

NNLS inversion algorithm to generate phytoplankton pigments maps (**Figure 12**).

RESULTS

Hydrodynamic Conditions in ApB

Apalachicola River discharge was slightly elevated in late summer and fall in comparison to typical flows before the Hurricane Michael made landfall on October 10, 2018 (**Figure 2A**). The hurricane storm surge (**Figure 3a**) appeared to have temporarily backed-up the flow from the AR up to about 30 km upstream – as indicated by the sharp drop recorded at the gage station at Sumatra, Florida. Precipitation associated with Hurricane Michael as it made landfall rapidly spread inland into Florida and Georgia, which resulted in increased discharge from the AR. After peaking around October 19, discharge gradually decreased but was still elevated by the end of October. Fall 2018 was an active season along the US southeast coast, with tropical storm Gordon (September 5), Hurricane Florence (September 14), in addition to Hurricane Michael impacting the region (NOAA National Ocean Service); so other precipitation events likely contributed to the more elevated levels in AR discharge later in October.

Prior to the hurricane, winds were light and from the east (**Figure 2B**). As the hurricane approached and made landfall, winds increased in intensity, with stronger northerly winds associated with a low pressure reading of ∼990 mbar - recorded at the ApB station. For the rest of the month, winds were variable with periods of strong wind patterns associated with frontal passages. Salinity at Cat Point before and during the hurricane passage remained stable (∼30), but decreased to low values of ∼20 before the sensor stopped recording on October 13. However, the salinity sensor at the river mouth (LM) station, which indicated the presence of freshwater (∼0) before the hurricane, started showing pulses of higher salinity as early as October 6, with salinity increasing as the hurricane approached the Florida coast. The highest salinity (∼30) was recorded on October 10 as

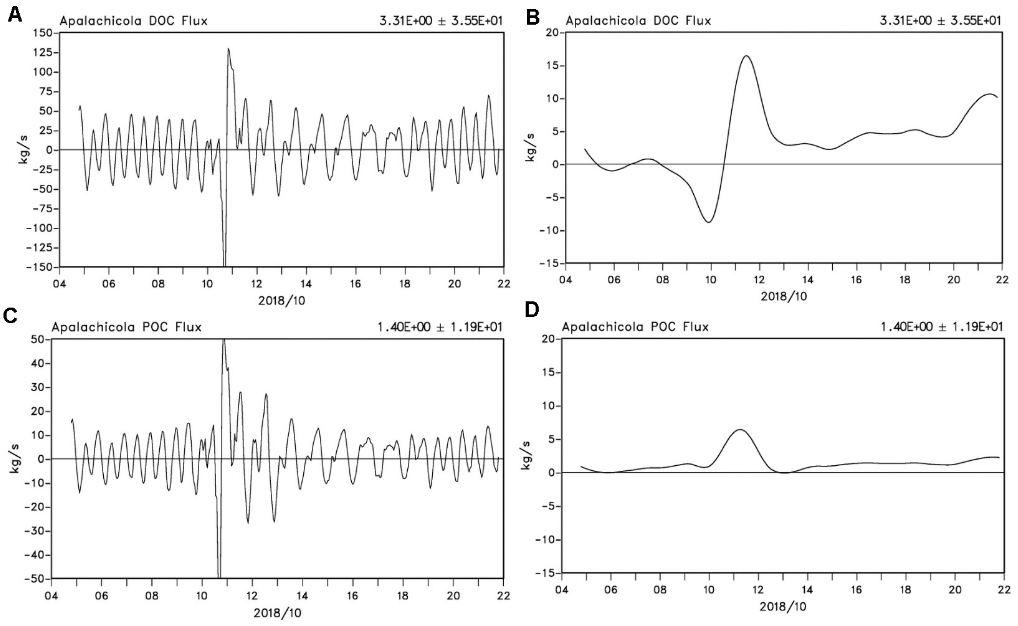

FIGURE 8 | Fluxes of DOC and POC from Apalachicola Bay. Hourly and de-tided fluxes (kg s^{-1}) of DOC **(A,B)** and POC **(C,D)** integrated through the all bay passes (positive – out of the bay and negative into the bay) between October 5 and 21, 2018.

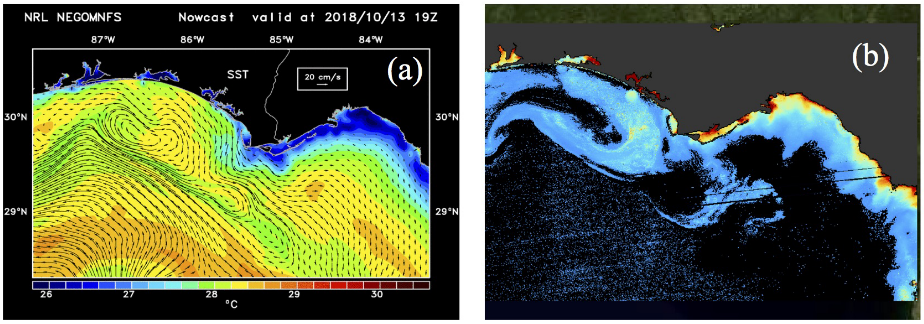

FIGURE 9 | Shelf SST, currents and DOC for 13 October 2018. **(a)** NCOM model derived sea surface temperature (SST) superimposed with de-tided currents; **(b)** MODIS-derived DOC map.

Hurricane Michael made landfall and was associated with a strong storm surge recorded at the tide station in ApB (**Figure 3a**). Salinity decreased gradually as the storm surge water flowed out of bay and returned to pre-hurricane levels by October 14 (**Figure 2C**). Turbidity in both the bay (Cat Point) and river mouth (LM) showed similar levels before the hurricane (**Figure 2D**). However, with approaching hurricane, turbidity levels started increasing in ApB likely due to increasing wave and wind mixing. Turbidity at both locations recorded highest levels (~900 NTU) on October 10 during landfall under extreme high wind conditions; levels decreased rapidly by October 11 at both locations. Thereafter, with only the LM sensor operational, turbidity at the river mouth showed pulses of highly turbid waters associated with increasing river discharge which peaked by October 19. Turbidity decreased to almost background levels at the river mouth by October 21. Large turbidity pulses late into October were likely associated with a frontal passage with strong winds (**Figures 2B,D**).

A comparison between model and tide-gage sea level at NOAA NOS Apalachicola station (id 2359170) for the month of October 2018 showed the model to simulate realistic sea levels (**Figure 3a**) with diurnal patterns of sea level variations and westerly surface currents before the hurricane (**Figure 3c**). Both model simulation and tide gage showed increasing sea levels by October 6 and storm surge at landfall. The model, however, underestimated the peak storm surge (~2.5 m) measured by the tide gauge likely due to coarser and therefore weaker hurricane winds predicted by COAMPS -used to drive the model. The coastal response to the hurricane was the generation of a storm surge, which appeared to peak on October 10, close to landfall and just west of ApB (**Figures 3a,b**). The

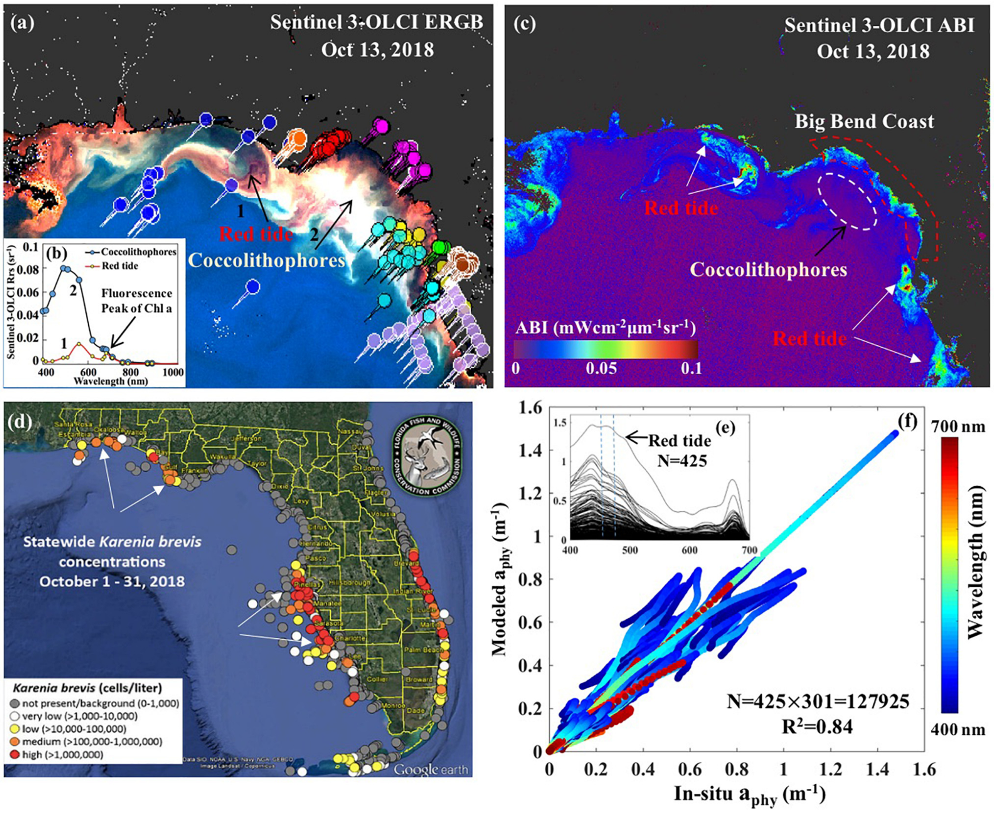

FIGURE 10 | Sentinel-3A OLCI imagery and field absorption spectra. **(a)** OLCI enhanced RGB imagery (ERGB) of 13 Oct 2018 with arrows indicating dark features associated with high absorption due to red tide and bright features related to coccolithophore bloom. (**b**-inset) OLCI-derived R_{rs} spectra corresponding to red tide and coccolithophore bloom locations in the imagery. **(c)** OLCI algal bloom index (ABI) of 13 Oct 2018 with white arrows indicating waters in bloom status. **(d)** Statewide map of archived status of red tide *Karenia brevis* in October, 2018 acquired from Florida Fish and Wildlife Conservation Commission (FWC) with colors circles representing the cell concentrations of *K. brevis*. **(e)** 425 $a_{phy}(\lambda)$ spectra acquired from NASA SeaBASS archive with locations shown as colored pins in **(a)**; blue dotted lines drawn to show spectra in the range 450–470 nm. **(f)** Comparison between modeled and in-situ measured $a_{phy}(\lambda)$ for all data across all wavelength with color representing wavelength.

storm surge was greatest to the right (east) of the hurricane track including ApB region with strong wind-driven coastally directed currents; both winds and currents showed decreasing trends eastward along the Florida coast into the Big Bend area. Coastal water levels, however, decreased to low or negative levels to the left (west) of the storm track with southward-directed currents appearing to deliver low salinity waters from the various bays (e.g., St Andrews Bay, Choctawhatchee Bay) - likely delivering large amounts of freshwater, nutrients, and organic matter to the coast. Coastal currents, which were predominantly westward and mild before the hurricane (**Figure 3c**), were highly variable in both intensity and direction just before, during, and following the hurricane (**Figures 3b–d**). Three days following the hurricane's landfall, currents were directed mostly southeastward in the coastal waters around ApB, likely due to relaxation of storm surge and prevailing easterly winds (**Figure 2B**) that pushed water out of ApB. Model simulation of salinity within the bay showed a strong influence of freshwater discharge from the AR and Carrabelle Rivers before the hurricane (October 4; **Figure 3c**). Salinity increased substantially during the hurricane due to a storm surge that brought high salinity water into ApB. After the hurricane on October 13 low salinity waters extended well beyond the bay's barrier islands and into more open Gulf waters (**Figure 3d**).

Satellite Estimates of DOC and POC From MODIS

The MODIS-derived atmospherically corrected R_{rs_MODIS} data were used to derive DOC and POC maps of ApB for October 4, 6, 12, 13, 17, and 21, 2018, using the approach described in **Figure 4** (chemo-optical analysis). Green and red MODIS bands ($R_{rs}555$ and $R_{rs}667$) were used as inputs to the QAA-V estuarine-tuned semi-analytic algorithm (Joshi and D'Sa, 2018) to derive satellite estimates of backscattering $b_{bp}532$. A power-law relationship between $b_{bp}532$ and POC (**Figure 5D**):

$$POC = 725.60 \times bbp532^{0.521} \quad (R^2 = 0.84; N = 33) \qquad (1)$$

was derived from field observations. The relationship was then applied to MODIS-derived $b_{bp}532$ to obtain POC maps of ApB (**Figure 7**).

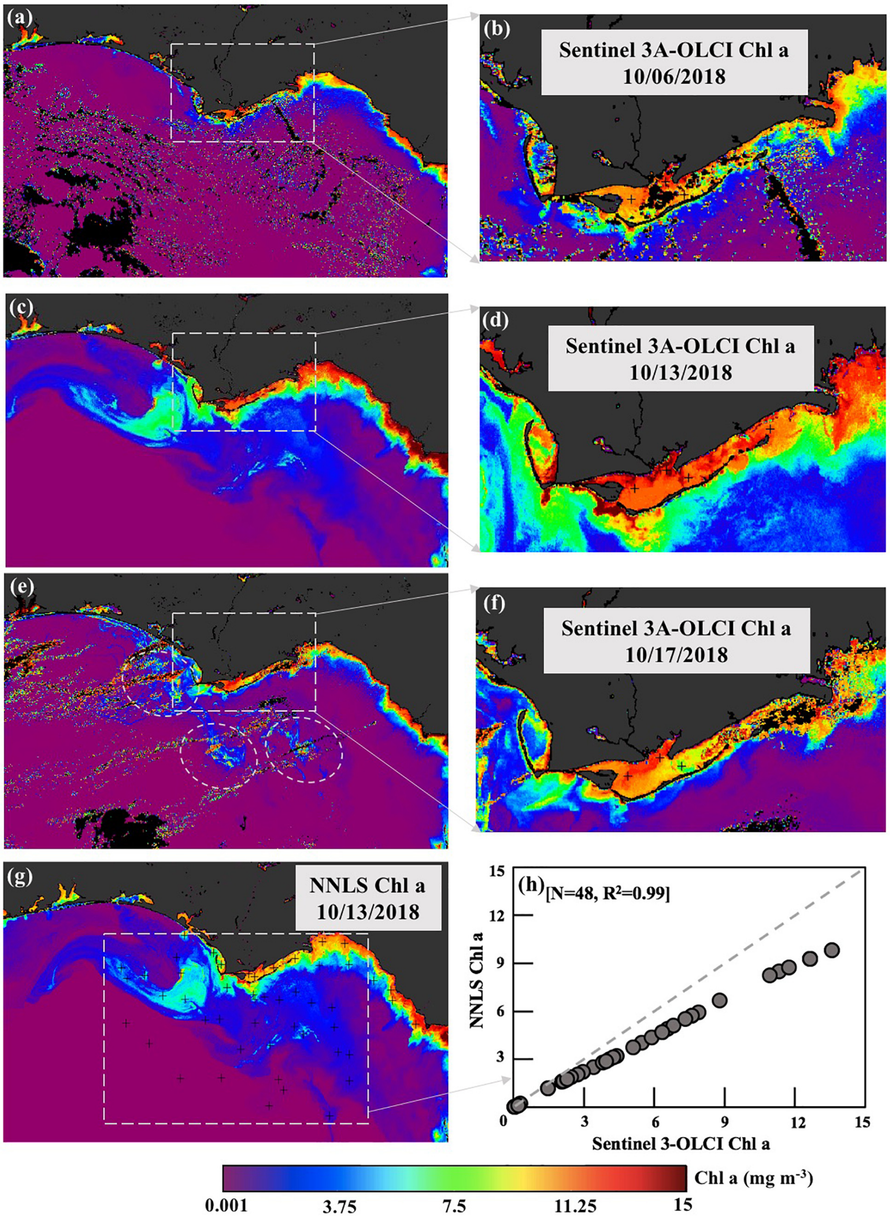

FIGURE 11 | Sentinel-3A OLCI-derived Chl *a* maps. **(a,c,e)** Chl *a* standard product of shelf waters for 06, 13, and 17 October 2018 with corresponding maps **(b,d,f)** of ApB and nearshore coastal waters. **(g)** Total Chl derived from the NNLS inversion algorithm for October 13, 2018; **(h)** comparison of OLCI-derived Chl *a* standard product vs. NNLS-derived Chl *a* for October 13, 2018.

Power law relationships between $R_{rs}555/R_{rs}667$ and $a_{dg}412$ (**Figure 5A**) given by:

$$a_{dg}412 = 8.60 \times \left(\frac{Rrs555}{Rrs667}\right)^{-1.865} \quad (R^2 = 0.91; N = 44) \quad (2)$$

and between $b_{bp}532$ and $a_{NAP}412$ (**Figure 5B**) given by:

$$a_{NAP}412 = 7.16 \times (b_{bp}532)^{0.924} \quad (R^2 = 0.83; N = 33) \quad (3)$$

obtained from *in situ* measurements in ApB, allowed the determination of a_g412 from the relationship:

$$a_g412 = a_{dg}412 - a_{NAP}412 \quad (4)$$

These relationships were applied to MODIS-derived ratios ($R_{rs}555/R_{rs}667$) and $b_{bp}532$ to derive satellite maps of a_g412. DOC was significantly correlated with CDOM (**Figure 5C**) as:

$$DOC = 1.86 + 0.62 \times a_g412 \quad (R^2 = 0.96, N = 80) \quad (5)$$

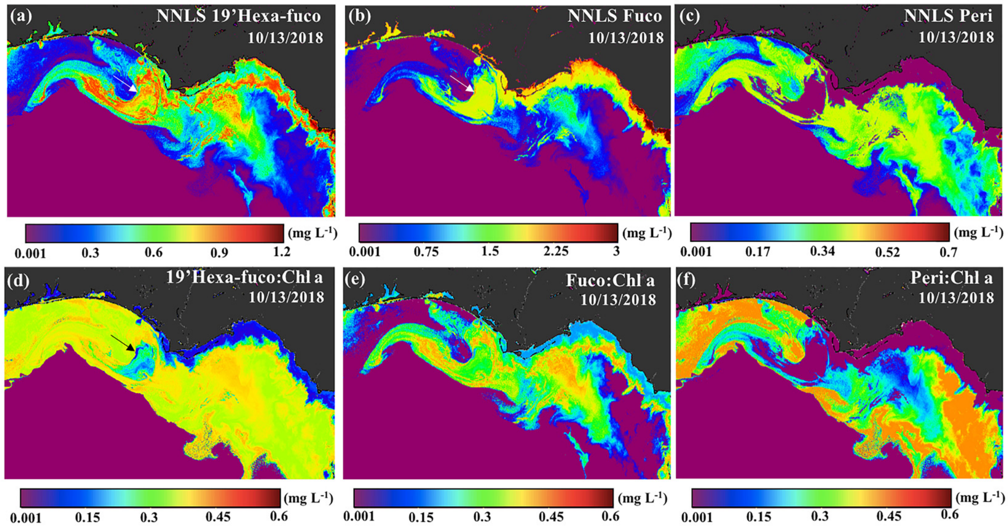

FIGURE 12 | Sentinel-3A OLCI-derived maps of diagnostic pigments and ratios for October 13, 2018. Pigment maps of **(a)** 19′hexa-fuco, **(b)** fuco, **(c)** peri, **(d)** 19′hexa-fuco:Chl *a*, **(e)** fuco:Chl *a*, **(f)** peri:Chl *a*.

Equation 5 was then applied to MODIS-derived a_g412 to generate DOC maps of ApB (**Figure 6**).

With particle backscattering strongly correlated to concentration of suspended particle matter (SPM) in various estuarine and coastal waters (Joshi and D'Sa, 2018), the power law relationships observed in ApB between $b_{bp}532$ and POC and $a_{NAP}412$ (Equations. 1, 3) could be attributed to factors such as, mineralization, residence of particles in the estuarine zone as well as the organic matter content of the suspended particle matter being discharged by the river (Bianchi et al., 1997; Abril et al., 2002; Warnken and Santschi, 2004). In contrast, a linear regression between a_g412 and DOC reflects the generally conservative mixing observed between the riverine and marine end members for both CDOM and DOC in ApB and other estuaries (Joshi et al., 2017; D'Sa et al., 2018). However, a limitation of these empirical relationships used to derive DOC and POC from ocean color following Hurricane Michael is that the field data used were acquired under non-hurricane conditions. In spite of potential for greater uncertainties in the relationships (e.g., due to wind induced resuspension), it appears reasonable to apply these relationships to hurricane impacted conditions in ApB since these relationships also included riverine-end members where the observed DOC and POC were several orders higher than other stations in the bay during normal conditions (Joshi et al., 2017) (**Figures 5C,D**).

DOC and POC Distributions and Fluxes From ApB

Maps of DOC and POC, derived from MODIS using a combination of semi-analytic and empirical algorithms (**Figures 4**, **5**), indicated strong geochemical responses to Hurricane Michael (**Figures 6**, **7**). Surface distribution of both DOC and POC prior to the hurricane (October 4, 6; **Figures 6**, **7**) indicated elevated levels in eastern ApB mainly due to the AR discharge with higher levels near the river mouth and decreasing seaward with elevated levels outside West Pass. The central and eastern bays showed low levels of DOC and POC concentrations. Two and three days following the hurricane passage (October 12, 13), elevated levels of DOC were observed throughout ApB with southward oriented plumes of DOC extending outside ApB. POC distribution patterns were similar to DOC, with some spatial differences and comparatively lower concentrations. A substantial increase in both DOC and POC concentrations was observed throughout ApB on October 17. By October 21, DOC concentrations were still high throughout the bay, while POC concentrations were elevated only close to the AR (**Figures 6**, **7**).

DOC and POC fluxes which were calculated from water volume fluxes through all the passes and satellite-derived DOC and POC concentrations between October 4 to 21 (with daily values interpolated from the satellite data) show large variations dominated by tidal cycles (**Figures 8A,C**) with DOC fluxes almost a factor of three greater than the POC fluxes. However, a large pulse (positive denotes out of and negative into the bay) was observed on October 10 as hurricane Michael made landfall just west of ApB. The de-tided DOC flux was low before the hurricane's passage with a strong pulse of DOC into ApB just before making landfall and quickly reversing, resulting in a peak seaward flux of ∼16 kg s^{-1} out of the bay as the hurricane moved inland by October 11. Seaward DOC fluxes decreased to ∼5 kg s^{-1} by October 13 and thereafter showed a generally increasing trend, with a second strong pulse on October 21 associated with a cold front (**Figure 8B**). POC fluxes in contrast were relatively lower than DOC and exhibited a positive flux out of the bay with a peak flux coinciding with that of DOC fluxes on October 11. Thereafter, with a minimum on October 13, POC fluxes showed a generally increasing trend with a small jump on October 21, similar to the DOC flux. The storm surge related landward DOC flux pulse into ApB (**Figure 8C**) in contrast to that of POC (no landward flux; **Figure 8D**) was likely due to the reversal of pre-hurricane coastal DOC plumes into ApB, further illustrating the DOM-rich nature of ApB in comparison to POC. Michael's winds and waves induced strong mixing, which also increased the concentration of DOC and POC inside ApB. Together with the large runoff from the AR and surrounding wetlands, both DOC and POC fluxes increased after hurricane (**Figures 8B,D**).

Bio-Physical Response of Shelf Waters to Hurricane Michael

Northward and southward currents to the right and left of the hurricane track at landfall (**Figure 3b**; NCOM model outputs) transitioned over a period of 3 days to a more complex current pattern that indicated easterly/southeasterly transport of cooler coastal waters. A component of this southeasterly flow veered to the west, likely influenced by a Loop Current eddy at the shelf edge (**Figure 9a**) as reflected in cyclonic currents – along with the presence of warmer and higher salinity waters (not shown) aligned along the shelf edge. The transport of the coastal waters into the mid-shelf region of the neGoM was clearly apparent in the extended DOC map on October 13, 2018 (**Figure 9b**). The region in the image east of ApB was due to very high reflectance that appeared to be associated with a coccolithophore bloom (Joshi and D'Sa, in review) with pixels set to black along with oligotrophic waters with low DOC (as the algorithm was optimized for ApB). In addition, the POC levels in the outer shelf were consistently higher on October 12 and 13 compared with October 4, 6, 17 and 21 (**Figure 7**); this increase in POC values were due to higher $b_{\mathrm{bp}}532$ estimated from the QAA-V that also appeared linked to an extensive algae bloom, possibly Coccolithophore.

Factors that could contribute to the distinct colors observed in the OLCI ERGB imagery in shelf waters, especially southwest and east of ApB after passage of the storm (**Figure 10a**) include sediment resuspension, CDOM-rich or bloom waters. Thus, an algal bloom index (ABI, $\mathrm{mWcm^{-2}\mu m^{-1}sr^{-1}}$) which has been used by Florida Fish and Wildlife Conservation Commission (FWC) for routine monitoring of red tide along the Florida Coast is adapted in this study for the Sentinel-3A OLCI atmospheric-corrected normalized water leaving radiance (Lwn at band 8–665 nm, band 10–681 nm and band 12–754 nm); the ABI which is based on the MODIS normalized fluorescence line height (nFLH) product, was further modified to reduce the contaminations from CDOM-rich waters and suspended sediments according to Hu and Feng (2016) as:

$$\mathrm{ABI} = \frac{Lwn\_681 - 1.005 \times \left(Lwn\_665 + (Lwn\_754 - Lwn\_665) \times \dfrac{(681-665)}{754-665} \right)}{1 + (Rrs_{560} - 0.0015) * 80} \tag{6}$$

The Sentinel-3 OLCI-derived ABI imagery indicated that most areas along the Florida Coast with high ABI ~0.08–0.09 (white arrows; **Figure 10c**) coincided with medium (~10,0000–100,0000 cells $\mathrm{L^{-1}}$) to high (>100,0000 cells $\mathrm{L^{-1}}$) concentrations of *Karenia brevis* reported in the statewide red tide status map from FWC for the month of October 2018 (white arrows; **Figure 10d**). For example, dark-reddish color in ERGB image (arrow 1; **Figure 10a**) with Chl *a* concentrations reaching ~10.5 mg $\mathrm{L^{-1}}$ (**Figure 11a**) in the areas southwest of ApB was likely due to the presence of a red tide bloom (*K. brevis)*; these type of waters have been associated with strong light absorption by *K. brevis* cells (Hu and Feng, 2016). Corresponding reflectance spectral profiles in the red tide area (arrow 1; **Figure 10a**) showed overall low reflectance but a strong fluorescence signal (red line; **Figure 10b**). However, along the Big Bend Coast of Florida stretching from Apalachee Bay (Wakulla County) to Anclote Key (Pasco County), ABI showed moderate levels ~0.055 (red circle; **Figure 10c**) while *K. brevis* cell concentrations were very low (0–1000 cells $\mathrm{L^{-1}}$) or not present (**Figure 10d**). It likely indicates that other species dominated the phytoplankton community along the Big Bend Coast, such as nitrate-assimilating diatom, which generally show dominance in the nutrient-rich river plume waters or during strong upwelling events (Qian et al., 2003; Chakraborty and Lohrenz, 2015); such events associated with Hurricane Michael (**Figure 9a**) likely contributed to elevated phytoplankton biomass along the coast and shelf waters (**Figures 11a,c**). However, the extremely bright milky-white color (arrow 2, **Figure 10a**) could be attributed to the coccolithophore *Emiliania huxleyi,* with its high reflectance across the visible spectrum induced by their detached coccoliths (Brown and Yoder, 1994). The *E. huxleyi* bloom area displayed relatively lower Chl *a* (~3.5 mg $\mathrm{L^{-1}}$; **Figure 11c**) but much higher reflectance compared to the *K. brevis* bloom (**Figure 10b**). This coccolithophore bloom area (white circle; **Figure 10c**) which was completely masked in the modified ABI due to its high reflectance at 560 nm as well as the reflectance threshold method (**Figure 9b**; Joshi and D'Sa, in review) suggests the potential of these techniques to differentiate between highly reflective and absorbing bloom waters.

A sequence of cloud-free Sentinel-3 OLCI derived Chl *a* imagery obtained before (October 06), and immediately following the hurricane (October 13) indicated a relatively large increase in Chl *a* in the shelf waters (~3.1 to ~7.5 mg $\mathrm{m^{-3}}$) before decreasing to lower values (~0.5 to ~4.1 mg $\mathrm{m^{-3}}$) by October 17, 2018 (**Figures 11a,c,e**). This increase was mainly associated with large scale algae blooms (**Figure 11c**) which nearly dissipated within a week (**Figure 11e**). Within ApB, Chl *a* values which were elevated before the hurricane (~9.5 mg $\mathrm{m^{-3}}$ on October 06) increased to ~14.2 mg $\mathrm{m^{-3}}$ on October 13 before decreasing to ~11.1 mg $\mathrm{m^{-3}}$ by October 17, 2018 (**Figures 11b,d,f**); these satellite estimates, however, have not been previously validated for these estuarine waters.

The Pigment Inversion Algorithm Performance

The inversion model used an extensive set of field bio-optical data [$a_{\mathrm{phy}}(\lambda)$ spectra and Chl *a*, *N* = 425; **Figure 10e**] obtained in the neGoM ranging from coastal ocean to estuaries including CDOM, sediment-rich and red-tide waters (**Figure 10a**-pin locations) to optimize regional tuning and obtain robust parameterization of Chl a-$a_{\text{phy}}(\lambda)$ relationship for the neGoM waters. The $a_{\text{phy}}(\lambda)$ showed large variations in magnitude (0.01 – 1.497 m^{-1} at 440 nm and 0.008 – 1.253 m^{-1} at 675 nm) while Chl a varied from ~0.12 mg m^{-3} in offshore waters to an average of ~12.67 mg m^{-3} in the various neGOM estuaries across different seasons; however, extremely high values reaching ~77 mg m^{-3} were observed in red tide bloom waters. The $a_{\text{phy}}(\lambda)$ spectra obtained in red-tide area displayed a small peak in the range of 450–470 nm (blue dotted lines; **Figure 10e**), likely attributed to the presence of fucoxanthin; in contrast, at lower Chl a levels corresponding to pico-phytoplankton dominated groups, $a_{\text{phy}}(\lambda)$ were steep were 450–470 nm range but lifted ~ 490 nm, probably due to the absorption of zeaxanthin. The modeled $a_{\text{phy}}(\lambda)$ agreed well with the spectrophotometrically measured $a_{\text{phy}}(\lambda)$ for all data across the whole spectra (R^2 = 0.84, **Figure 10f**). The vector coefficients were further applied to Sentinel-3A OLCI Chl a maps to generate 301 sentinel-3A OLCI a_{phy} images ($a_{\text{phy\_OLCI}}$), representing a_{phy} values at each wavelength (400–700 nm at 1 nm interval). However, since the parameterization for Chl a-a_{phy} correlation is optimized for the neGOM, it could show limitations when applied to other areas wherein phytoplankton communities show large seasonal and taxonomic differences, or where the algal blooms are not associated with red tide species, *K. brevis*; thus uncertainties could be introduced in satellite-derived a_{phy}. The $a_{\text{phy\_OLCI}}(\lambda)$ was then spectrally decomposed into 22 mass-specific pigment spectra at each pixel using NNLS technique to obtain the concentrations of 22 pigments. The NNLS-inversed Chl a (**Figure 11g**) exhibited exactly the same spatial patterns with Sentinel-3A OLCI Chl a product but showing slightly lower values (R^2 = 0.99; **Figure 11h**). In this study, the limitation is the lack of HPLC measurements during the study period, and thus, parameters associated with uncertainties (e.g., MAE, RMSE, and R^2) for the estimated pigments cannot be calculated at this time. However, the modeled $a_{\text{phy}}(\lambda)$ (**Figure 10f**) and NNLS-inversed Chl a (**Figure 11g**) showed acceptable range for predicting pigment compositions compared to Moisan et al. (2017) and Liu et al. (2019a), in which a similar NNLS-algorithm has been used and validated for estimation of phytoplankton pigments.

Satellite-Derived Pigment Distributions in Shelf Waters Following Hurricane Michael

Most photosynthetic type-1 dinoflagellates contain a chloroplast with peridinin as the major carotenoid; however, fucoxanthin and/or fucoxanthin derivatives such as 19′hexanoyloxyfucoxanthin (19′hexa-fuco) can also replace peridinin as the major carotenoid in the genus *Karenia* (5 species, 8 strains) - type-2 dinoflagellates (Jeffrey and Vesk, 1997). Fucoxanthin, a carotenoid largely used to trace diatoms (Bianchi and Canuel, 2011), was found to be the major carotenoid in *K. brevis*, *K. mikimotoi,* and *K. selliformis* (Zapata et al., 2012). HPLC analysis of a *K. brevis* culture, obtained in Galveston Bay and Florida Coast (Örnólfsdóttir et al., 2003), showed Chl a, Chl c_3, Chl c_1c_2, fuco, 19'buta-fuco, 19'hexa-fuco, diadino, gyro, and β-carotenoid (β-caro) – with no peridinin detected. Further HPLC analyses are clearly needed to examine for regional differences in pigment composition of *Karenia* spp.

In this study, the NNLS-inversed 19′hexa-fuco, fuco, and peri (**Figures 12a–c**) showed differences in distribution patterns and magnitude from estuarine to coastal waters and bloom areas. Values of 19′hexa-fuco (range of 0.001–0.9 mg L^{-1}) were obviously higher in the bloom areas in the midshelf waters than estuarine waters, which is consistent with Chakraborty and Lohrenz (2015) that haptophytes (coccolithophores) were more prevalent at midshelf resulting in an order of magnitude higher ratio of 19′hexa-fuco to total accessory pigment than inner shelf waters. In contrast, fucoxanthin displayed the same pattern as the Chl a map, decreasing from estuarine to shelf waters (**Figures 11a**, **12b**), which is likely attributed to the presence of diatoms. Diatoms are more abundant prevalent in the N and Si-rich estuarine/shelf waters of the NGoM compared to offshore waters (Qian et al., 2003). In contrast, dinoflagellates, which tend to have higher P demands, will generally increase in abundance with decreasing ratios of N:P and Si:P, resulting in a compositional shift from a diatom-to dinoflagellate-dominated community (Paerl, 1997; Heisler et al., 2008). Along these lines, the carotenoid peridinin, found in Type-I dinoflagellates, exhibited substantially different patterns compared to the distributions of Chl a and fuco (**Figure 12c**); peri displayed extremely low concentrations in estuarine waters (~0.001 mg L^{-1}), but elevated in shelf waters. consistent with more P-limited estuarine environments vs. more N-limited oceanic waters (Paerl, 1997). Moreover, extremely low concentration of peri (~ 0.001 mg L^{-1}) observed in bloom areas, indicated algal blooms were not associated with Type 1 dinoflagellates. Furthermore, the fringing area of the red tide, dark in color (black arrow 1; **Figure 10a**) with extremely high ABI (**Figure 10c**) and Chl a (**Figure 11a**), showed relatively lower values of 19′hexa-fuco (~0.6 mg L^{-1}, white arrow; **Figure 12a**), compared to the adjacent coccolithophore-dominated area (~0.85 mg L^{-1}; **Figure 12a**). In contrast, values of fuco (~2.3 mg L^{-1}) at the edge of red tide (white arrow; **Figure 12b**), were as high, as found in estuarine waters, with the mean value of the red tide dominated area (~2.0 mg L^{-1}) higher than the coccolithophore dominated area (~1.5 mg L^{-1}). Although fuco is a common biomarker for diatoms, the absence of 19'hexa-fuco suggests that *K. brevis* accounted for a major proportion of the phytoplankton community - with minor only contributions from diatoms (black arrow 1; **Figure 10a**). This supports previous work which showed that *K. brevis* have higher phosphorus demands than diatoms and are generally found in waters with very low DIN:PO_4 (~4) (Walsh et al., 2006). Some bloom-forming dinoflagellates (e.g., *K. brevis*) share several of the same pigment markers as bloom-forming haptophytes (e.g., *E. huxleyi*) (Zapata et al., 2004); thus, specific pigment to Chl a ratios including 19'hexa-fuco (**Figure 12d**), fuco (**Figure 12e**), and peri (**Figure 12f**) could help in discriminating *Karenia species* from 19′hexa-fuco-containing haptophytes. In the red tide area, fuco:Chl a varied from 0.24 to 0.30 and was lower than in coccolithophore bloom (~ 0.45). These ratios are within the range of previously reported fuco:Chl a values for *K. brevis* (0.31) and haptophytes

(0.58) (Örnólfsdóttir et al., 2003). Furthermore, 19′hexa-fuco:Chl *a* ratios had a higher mean value (∼0.4) in coccolithophore bloom (∼0.4) than the red tide area (∼0.15) (**Figure 12d**), consistent with previous studies (Örnólfsdóttir et al., 2003; Zapata et al., 2004, 2012). More specifically, higher 19'hexa-fuco:Chl *a* ratios are found in strains of type-6 haptophytes (*E. huxleyi*) than type-2 dinoflagellate (*Karenia* species).

DISCUSSION

Effects of Hurricane Michael's Storm System on DOC and POC Distributions in ApB and Fluxes to the Coastal Ocean

The semi-analytic approach (QAA-V) to estimate the absorption and backscattering coefficients in various coastal and estuarine waters from ocean color satellite data were found to be robust (Joshi and D'Sa, 2018). The use of empirical relationships (D'Sa et al., 2018; Equations 1–5, this study) to further estimate DOC and POC concentrations provides an alternative to solely using empirical algorithms which are more susceptible to regional and seasonal variabilities (Le et al., 2016; Joshi et al., 2017). Thus, a sequence of DOC and POC maps generated using the semi-analytic approach from clear sky MODIS-Aqua imagery of ApB from before and after Hurricane Michael passage just west of ApB allowed us to examine the biogeochemical response of this estuary to an extreme disturbance. The imagery revealed similarities and subtle differences in the distribution patterns of DOC and POC (**Figures 6**, **7**) that appeared to be strongly influenced by the hydrodynamics (river discharge, currents, salinity) associated with the hurricane's passage. Moderate easterly winds before the hurricane along with westward currents within ApB and the shelf waters (**Figures 2C**, **3c**; October 4) combined with slightly elevated fall river discharge conditions (**Figure 2A**) resulted in patterns of low DOC and POC distributions in east ApB (due to inflow of marine waters into ApB through the east passes). Higher levels were found in the west bay due to discharge from the AR which produced a strong DOC river plume. In addition, plumes of high DOC and POC outside the West and Indian Passes demonstrate this lateral C transport from the ApB into the adjacent coastal waters (**Figures 6**, **7**).

Although moderate, easterly wind conditions continued on October 6, increasing sea levels (**Figure 3a**) with pulses of high salinity waters at LM station and increasing turbidity in the water column (**Figures 2C,D**) indicated the effects of the approaching storm within the bay. Further, areas of low DOC and POC distributions at various locations within the bay were evident due to the intrusion of coastal seawater and indicated the storm's influence even 4 days before the hurricane made landfall. Two days after Michael's passage (October 12), strong southerly/southeasterly currents prevailed both inside and outside the bay (not shown). Along with increasing river discharge, this resulted in high levels of both DOC and POC and large plumes emanating from the bay. Hence, net DOC and POC fluxes following the hurricane's passage increased substantially (**Figure 8**). Moderate easterly winds on October 13 however, appeared to have dispersed these C plumes outside the bay (**Figure 8**). Peak river discharge occurred by October 17 (**Figure 2A**) which, combined with low wind conditions (**Figure 2B**), resulted in highest DOC and POC concentrations observed throughout the bay, along with elevated fluxes of DOC (∼5 kg s^{-1}) and POC (∼1 kg s^{-1}). Although river discharge levels were still at near peak on October 21, surface distributions of both DOC and POC increased dramatically likely triggered by moderately strong northeasterly winds (**Figure 2B**) indicating the rapid response of surface distributions of DOC and POC in the bay to the wind field (**Figures 6**, **7**). Nonetheless, fluxes of both DOC and POC from bay to the surrounding coastal waters were similar to those of October 17, with increased fluxes through the Indian and West Passes.

Although the DOC and POC fluxes were diurnal and tidally dominated in and out of all the passes, the de-tided fluxes showed increasing net fluxes out of the bay consistent with the increasing volume of the AR discharge. However, later in the month these fluxes were attributable to increasing wind fields which likely mobilized greater amounts of DOC and POC in the water column (**Figures 2A,B**, **8**). Average DOC flux exported during the 16-day period from October 5–21 was about 11,916 kg C h^{-1}, which was approximately twice that estimated during the fall of 2015 in ApB or 8.73% of the annual DOC flux from ApB using the same ocean color and modeling approach (Joshi et al., 2017). Since POC fluxes have not been previously reported for ApB, similar flux comparisons cannot be made for POC. The integrated export from ApB to the coastal ocean of total organic flux (DOC plus POC) over a 16-day period (between October 5 to 21) was 6.511×10^6 kg C ($4.576 \times 10^6 + 1.935 \times 10^6$ kg C). This flux was about a quarter of that exported from Galveston Bay to the shelf waters over a 10-day period during/following Hurricane Harvey over the Texas coast in August 2017 (D'Sa et al., 2018). In contrast to Hurricane Michael, which was a fast moving hurricane, Harvey was a slow moving hurricane that caused $>$500 mm of rainfall in the Houston metropolitan area further demonstrating that each hurricane can have unique characteristics and impacts on the coastal ecosystems.

Hurricane Impact on Phytoplankton Composition in Shelf Waters

The wind field and precipitation associated with Hurricane Michael caused a complex response in the coastal and shelf waters that led to reduced salinity and surface temperatures (as indicated by model outputs–not shown). This was likely due to enhanced water column mixing, upwelling and transport of coastal waters over a large area of the northwest Florida shelf, and elevated levels of organic matter in the shelf waters. Surface currents appeared to transport cooler coastal waters (with elevated DOC; **Figure 9b**) eastward alongshore and then steered westward by the presence of an eddy at the shelf edge (**Figure 9a**) that led to a strong biological response with spatially distinct distribution patterns in the shelf waters (**Figures 10**, **11**).

Observations of pigment ratios from the bio-optical inversion algorithm, ERGB image and the reflectance spectra in algal boom areas from Sentinel-3A OLCI and in-situ measured *K. brevis* cell concentration from FWC jointly suggest that shelf waters southwest of ApB was a mixed algal bloom of *K. brevis* and *E. huxleyi,* with fringing area more dominated by *K. brevis*. The coccolithophore *E. huxleyi* flourished in shelf waters east side of ApB, broadly extending to *K. brevis* bloom area. It is widely agreed that red tide of *K. brevis* near shore in the eastern GOM originate ∼15–65 km offshore in deep shelf waters due to the initial phosphorus-rich nutrients at low DIN/PO_4 ratios supplied by benthic sediments and recycled estuarine/ground water (Waters et al., 2015). Accumulated *K. brevis* seeds at the bottom of the Florida shelf which then upwell inshore by wind and tidal currents, often bloom in the estuarine-coastal surface waters (Hu et al., 2006); these are further enhanced by high dissolved organic nitrate (DON) from a variety of sources including land-based nutrients carried by estuarine waters, decomposing dead fish and nutrient inputs from N_2-fixation from *Trichodesmium* blooms, which generally co-occur with *K. brevis* blooms on the West Florida shelf (Walsh et al., 2006). In this study, the areas southwest of ApB were strongly influenced by hurricane-induced flux of organic matter out of bays which likely favor those species capable of assimilating organic forms of nutrients (e.g., *K. brevis*) rather than species more reliant on inorganic nutrients (e.g., diatoms) (Anderson et al., 2008; Heisler et al., 2008). To our knowledge, this is first time synchronous blooms of *K. brevis* and *E. huxleyi* were found in mid-shelf waters following Hurricane Michael. *E. huxleyi* is well-known as one of the more cosmopolitan coccolithophore species, forming extensive blooms from polar to tropical regions, in both open ocean and coastal shelf waters (Holligan et al., 1993). The particularly competitive ability of *E. huxleyi* at high N:P ratios, observed in cultures (Riegman et al., 2000) and eutrophic coastal waters with high N and P, but low silica (Si) concentrations (Yunev et al., 2007) may in part, explain for its rapid appearance after the passage of Hurricane Michael. Thus, low ratios of Si:N and Si:P could be a possible reason that coccolithophores outcompeted other phytoplankton species, such as diatoms, in this hurricane-impacted nutrient-rich environments.

More interestingly, MODIS ERGB imagery of October 11and 12, 2018 (**Supplementary Figure S1**) indicated that the *K. brevis* bloom expanded rapidly into areas dominated by the *E. huxleyi* bloom especially west of ApB and the area closer to where Hurricane Michael made landfall. Also notable was a small area south of ApB on October 11 (light pink, **Supplementary Figure S1**) that expanded eastward by October 12 (dark pink/red due to greater absorption) revealing the rapid and intense growth of *K. Brevis* bloom following the hurricane passage. Previous studies using MODIS images acquired in the western English Channel also observed similar phenomenon of *K. mikimotoi* development along coccolithophore blooms, which captured both dinoflagellate and coccolithophores blooms spanning across different seasons during 2002–2006 (Garcia-Soto et al., 1995; Garcia-Soto and Pingree, 2009). However, the statewide red tide status map acquired one week before Hurricane Michael (October 1–6, 2018) from FWC detected low concentrations of *K. brevis* (∼10,000-100,000 cells L^{-1}) adjacent to Dune Lakes in Walton, Panama City Beach and Apalachicola. With NCOM model results indicating plumes of these coastal waters with elevated DOM being transported into the mid-shelf region where satellite imagery detected algal blooms suggest that *K. brevis* did not initiate from coccolithophore bloom, but were likely transported into the bloom regions where hydrographic and nutrient conditions appears to create ecological preferences for *K. brevis* on the northwest Florida Coast. In fact, a previous study in this same area (McCulloch et al., 2013) documented the presence of gyroxanthin dinoflagellates (*K. brevis)* in near-surface and near-bottom shelf waters in this area and further suggested that under light and nutrient conditions typical of summer, *K. brevis* coastal blooms could originate from concentrated near-bottom populations during upwelling conditions (McCulloch et al., 2013). Upwelling conditions and strong offshore currents during hurricane landfall (**Figure 3b**) and subsequent transport of these coastal waters to the shelf (**Figures 9a,b**) strongly suggest that these coastal and estuarine waters with elevated organic nutrients and entrained seed populations of *K. brevis* conjointly led to a phytoplankton bloom including that of *K. brevis* (**Figures 10a**, **11**, **12**). Previous field measurements of the Florida shelf waters acquired in 2004 and 2005 hurricane season also showed that nutrient loading was an order of magnitude greater than pre-hurricane (Neely et al., 2006); following Hurricane Michael, the coastal plume likely contained high nutrients transported from the estuaries and bays along the northwest Florida coast that likely contributed to the intensive phytoplankton bloom. Further, estuarine CDOM additions in the shelf waters associated with the hurricane (e.g., **Figure 9b**) could have provided more favorable light-shield environment (Walsh et al., 2003) for the shade-adapted *K. brevis*. The identification of algal bloom pigment composition from the high spectral and spatial resolution Sentinel-3A OLCI imagery using inversion techniques (e.g., Moisan et al., 2017; Liu et al., 2019a) could revolutionize our understanding of phytoplankton spatiotemporal response to environmental variabilities.

CONCLUSION

In this study, the biogeochemical responses of ApB and northwest Florida shelf waters were examined following the passage of Hurricane Michael through the neGoM in October 2018. A combination of pre-hurricane field observations, ocean color data from two satellite sensors (MODIS-Aqua and Sentinel-3A OLCI) and the outputs of a high-resolution ocean model (NCOM) provided a robust assessment of the hurricane's impact on the coastal C cycle. A combination of an estuarine-tuned semi-analytic algorithm (QAA-V) and an empirical algorithm were applied using field and atmospherically corrected ocean color reflectance data to obtain estimates of DOC and POC distributions in ApB before and after the hurricane's landfall on the Florida coast. Spatial distribution of DOC and POC in ApB and their fluxes to the coastal ocean indicated strong hydrologic and hydrodynamic controls on the dynamics and export of organic matter to the coastal ocean associated with the hurricane such as wind forcing due to frontal passages and increasing river discharge. The integrated export from ApB to the coastal ocean of total organic flux (DOC plus POC) over a 16-day period (between October 5 and 21) was about a quarter of that exported from Galveston Bay to the shelf waters over a 10-day period during/following hurricane Harvey over the Texas coast in August 2017. This difference reflected the different characteristics of the two hurricanes, the two estuaries and the drainage basin impacted by the hurricanes. The implication is that slow-moving storms such as Harvey may saturate coastal watersheds inland mobilize more DOC and POC than fast-moving storms such as Michael.

In the shelf waters, water discoloration in a true color imagery obtained 3 days following the hurricane landfall (October 13) along with high surface Chl *a* concentrations indicated the presence of distinct algal blooms in the normally oligotrophic offshore waters. Observations of Sentinel-3A OLCI derived pigment ratios from the bio-optical inversion algorithm, and the shape of reflectance spectra in the algal boom areas suggested that shelf waters southwest of ApB was a mixed algal bloom of *K. brevis* and *E. huxleyi,* with fringing area mainly dominated by *K. brevis*; the area east/southeast of ApB, in contrast appeared to be dominated by coccolithophore *E. huxleyi*. The presence of a cyclonic loop current eddy along the shelf edge likely limited the response of deep waters to the hurricane passage. This study revealed a varied but shorter-term impact on the biogeochemistry and the ecosystem of ApB and surrounding shelf waters during Hurricane Michael. Additional longer-term studies of the hurricane impacts are warranted due to the socio-economic importance of the northwest Florida coast and shelf waters.

DATA AVAILABILITY

The datasets generated for this study are available on request to the corresponding author.

AUTHOR CONTRIBUTIONS

ED'S, IJ, BL, and DK designed the study and analyzed the data. ED'S, IJ, CO, and TB acquired and processed the pre-hurricane field data. DK developed the ocean model, performed the simulation, and estimated the DOC/POC fluxes. ED'S and BL wrote the manuscript with contribution of all authors.

FUNDING

Funding for this work was provided by NASA grants 80NSSC18K0177 and NNX14A043G.

ACKNOWLEDGMENTS

The authors would like to thank NASA Ocean Biology Processing Group (OBPG) for providing access to MODIS data, maintaining SeaDAS software package, and the SeaBASS public repository of *in situ* oceanographic data. The authors would also like to thank the European Space Agency (ESA) and the European Organization for Meteorological Satellites (EUMETSAT) for providing access to the Sentinel-3 OLCI ocean color data and the Sentinel-3 Toolbox Kit Module (S3TBX) version 5.0.1 in Sentinel Application Platform (SNAP).

SUPPLEMENTARY MATERIAL

The Supplementary Material for this article can be found online at: https://www.frontiersin.org/articles/10.3389/fmars.2019.00523/full#supplementary-material

REFERENCES

Abril, G., Nogueira, M., Etcheber, H., Cabecadas, G., Lemaire, E., and Brogueira, M. J. (2002). Behaviour of organic carbon in ninie contrasting European estuaries. *Estuar. Coast. Shelf Sci.* 54, 241–262. doi: 10.1006/ecss.2001.0844

Anderson, D. M., Burkholder, J. M., Cochlan, W. P., Glibert, P. M., Gobler, C. J., Heil, C. A., et al. (2008). Harmful algal blooms and eutrophication: examining linkages from selected coastal regions of the United States. *Harmful Algae* 8, 39–53. doi: 10.1016/j.hal.2008.08.017

Avery, G. B. Jr., Kieber, R. J., and Willey, J. D. (2004). Impact of hurricanes on the flux of rainwater and Cape Fear River water dissolved organic carbon to Long Bay, southeastern United States. *Glob. Biogeochem. Cycles* 18, 3015–3021.

Babin, S. M., Carton, J. A., Dickey, T. D., and Wiggert, J. D. (2004). Satellite evidence of hurricane-induced phytoplankton blooms in an oceanic desert. *J. Geophys. Res. Oceans* 109:C03043.

Bianchi, T. S., Baskaran, M., DeLord, J., and Ravichandran, M. (1997). Carbon cycling in a shallow turbid estuary of southeast Texas: the use of plant pigment biomarkers and water quality parameters. *Estuaries* 20, 404–415.

Bianchi, T. S., and Canuel, E. A. (2011). *Chemical Biomarkers in Aquatic Ecosystems*. Princeton, NJ: Princeton University Press. 396.

Bidigare, R. R., Ondrusek, M. E., Morrow, J. H., and Kiefer, D. A. (1990). "In-vivo absorption properties of algal pigments," in *Proceedings of SPIE Ocean Optical X. SPIE*, Orlando, FL, 290–303.

Black, W. J., and Dickey, T. D. (2008). Observations and analysis of upper ocean responses to tropical storms and hurricanes in the vicinity of Bermuda. *J. Geophys. Res.* 113:C08009.

Bricaud, A., Claustre, H., Ras, J., and Oubelkheir, K. (2004). Natural variability of phytoplanktonic absorption in oceanic waters: influence of the size structure of algal populations. *J. Geophys. Res. Oceans* 109:C11010.

Brown, C. W., and Yoder, J. A. (1994). Coccolithophorid blooms in the global ocean. *J. Geophys. Res. Oceans* 99, 7467–7482.

Brown, M. M., Mulligan, R. P., and Miller, R. L. (2014). Modeling the transport of freshwater and dissolved organic carbon in the Neuse River Estuary, NC, USA following Hurricane Irene (2011). *Estuar. Coast. Shelf Sci.* 139, 148–158. doi: 10.1016/j.ecss.2014.01.005

Chakraborty, S., and Lohrenz, S. E. (2015). Phytoplankton community structure in the river-influenced continental margin of the northern Gulf of Mexico. *Mar. Ecol. Progr. Ser.* 521, 31–47. doi: 10.3354/meps11107

Chen, S., Huang, W., Wang, H., and Li, D. (2009). Remote sensing assessment of sediment re-suspension during Hurricane Frances in Apalachicola Bay, USA. *Remote Sens. Environ.* 113, 2670–2681. doi: 10.1016/j.rse.2009.08.005

Ciotti, A. M., Lewis, M. R., and Cullen, J. J. (2002). Assessment of the relationships between dominant cell size in natural phytoplankton communities and the spectral shape of the absorption coefficient. *Limnol. Oceanogr.* 47, 404–417. doi: 10.4319/lo.2002.47.2.0404

Cook, J., Hodson, A. J., Taggart, A., Mernild, S. H., and Tranter, M. (2017). A predictive model for the spectral "bioalbedo" of snow. *J. Geophys. Res. Oceans* 122, 434–454. doi: 10.1002/2016jf003932

Davis, A., and Yan, X.-H. (2004). Hurricane forcing on chlorophyll-a concentration off the northeast coast of the U.S. *Geophys. Res. Lett.* 31:L17304.

D'Sa, E. J. (2008). Colored dissolved organic matter in coastal waters influenced by the Atchafalaya River, USA: effects of an algal bloom. *J. Appl. Remote Sens.* 2:023502. doi: 10.1117/1.2838253

D'Sa, E. J., Joshi, I., and Liu, B. (2018). Galveston Bay and coastal ocean optical-geochemical response to Hurricane Harvey from VIIRS ocean color. *Geophys. Res. Lett.* 45, 10579–10589. doi: 10.1029/2018GL079954

D'Sa, E. J., Korobkin, M., and Ko, D. S. (2011). Effects of Hurricane Ike on the Louisiana–Texas coast from satellite and model data. *Remote Sens. Lett.* 2, 11–19. doi: 10.1080/01431161.2010.489057

D'Sa, E. J., and Miller, R. L. (2003). Bio-optical properties in waters influenced by the Mississippi River during low flow conditions. *Remote Sens. Environ.* 84, 538–549. doi: 10.1016/s0034-4257(02)00163-3

D'Sa, E. J., Miller, R. L., and Del Castillo, C. (2006). Bio-optical properties and ocean color algorithms for coastal waters influenced by the Mississippi River during a cold front. *Appl. Opt.* 45, 7410–7428.

Emanuel, K. (2005). Increasing destructiveness of tropical cyclones over the past 30 years. *Nature* 436, 686–688. doi: 10.1038/nature03906

Emanuel, K. (2013). Downscaling CMIP5 climate models shows increased tropical cyclone activity over the 21st century. *Proc. Natl. Acad. Sci. U.S.A.* 110, 12219–12224. doi: 10.1073/pnas.1301293110

Emanuel, K. (2017). Assessing the present and future probability of Hurricane Harvey's rainfall. *Proc. Natl. Acad. Sci. U.S.A.* 114, 12681–12684. doi: 10.1073/pnas.1716222114

Farfan, L. M., D'Sa, E. J., and Liu, K. (2014). Tropical cyclone impacts on coastal regions: the case of the Yucatan and the Baja California Peninsulas. Mexico. *Estuar. Coast.* 37, 1388–1402. doi: 10.1007/s12237-014-9797-2

Fichot, C. G., and Benner, R. (2011). A novel method to estimate DOC concentrations from CDOM absorption coefficients in coastal waters. *Geophys. Res. Lett.* 38:L03610.

Garcia-Soto, C., Fernandez, E., Pingree, R., and Harbour, D. (1995). Evolution and structure of a shelf coccolithophore bloom in the Western english channel. *J. Plankton Res.* 17, 2011–2036. doi: 10.1093/plankt/17.11.2011

Garcia-Soto, C., and Pingree, R. D. (2009). Spring and summer blooms of phytoplankton (SeaWiFS/MODIS) along a ferry line in the Bay of Biscay and western English Channel. *Contl. Shelf Res.* 29, 1111–1122. doi: 10.1016/j.csr.2008.12.012

Gardner, W. D., Mishonov, A. V., and Richardson, M. J. (2006). Global POC concentrations from in-situ and satellite data. *Deep Sea Res. II* 53, 718–740. doi: 10.1016/j.dsr2.2006.01.029

Gordon, H. R., Brown, O. B., Evans, R. H., Brown, J. W., Smith, R. C., Baker, K. S., et al. (1988). A semianalytic radiance model of ocean color. *J. Geophys. Res. Atmos.* 93, 10909–10924.

Hanshaw, M. N., Lozier, M. S., and Palter, J. B. (2008). Integrated impact of tropical cyclones on sea surface chlorophyll in the North Atlantic. *Geophys. Res. Lett.* 35:L01601.

Havens, K., Allen, M., Camp, E., Irani, T., Lindsey, A., Morris, J., et al. (2013). *Apalachicola Bay Oyster Situation Report*. Gainesville, FL: University of Florida.

He, R. Y., and Weisberg, R. H. (2002). West Florida shelf circulation and temperature budget for the 1999 spring transiton. *Cont. Shelf Res.* 22, 719–748. doi: 10.1016/s0278-4343(01)00085-1

Heisler, J., Glibert, P. M., Burkholder, J. M., Anderson, D. M., Cochlan, W., Dennison, W. C., et al. (2008). Eutrophication and harmful algal blooms: a scientific consensus. *Harmful Algae* 8, 3–13. doi: 10.1016/j.hal.2008.08.006

Holligan, P. M., Fernández, E., Aiken, J., Balch, W. M., Boyd, P., Burkill, P. H., et al. (1993). A biogeochemical study of the coccolithophore, Emiliania huxleyi, in the North Atlantic. *Glob. Biogeochem. Cycles* 7, 879–900.

Hu, C., and Feng, L. (2016). Modified MODIS fluorescence line height data product to improve image interpretation for red tide monitoring in the eastern Gulf of Mexico. *J. Appl. Remote Sens.* 11:012003. doi: 10.1117/1.jrs.11.012003

Hu, C., Muller-Karger, F. E., and Swarzenski, P. W. (2006). Hurricanes, submarine groundwater discharge, and Florida's red tides. *Geophys. Res. Lett.* 33, 1–5.

Jeffrey, S., and Vesk, M. (1997). *Introduction to Marine Phytoplankton and their Pigment Signature, Phytoplankton Pigments in Oceanography*. Paris: UNESCO Publication, 3784.

Joshi, I. D., and D'Sa, E. J. (2015). Seasonal variation of colored dissolved organic matter in Barataria Bay, Louisiana, using combined Landsat and field data. *Remote Sens.* 7, 12478–12502. doi: 10.3390/rs70912478

Joshi, I. D., and D'Sa, E. J. (2018). An estuarine tuned Quasi-Analytical Algorithm for VIIRS (QAA-V): assessment and application to satellite estimates of SPM in Galveston Bay following Hurricane Harvey. *Biogeosciences* 15, 4065–4086. doi: 10.5194/bg-15-4065-2018

Joshi, I. D., D'Sa, E. J., Osburn, C. L., Bianchi, T. S., Ko, D. S., Oviedo-Vargas, D., et al. (2017). Assessing chromophoric dissolved organic matter (CDOM) distribution, stocks, and fluxes in Apalachicola Bay using combined field, VIIRS ocean color, and model observations. *Remote Sens. Environ.* 191, 359–372. doi: 10.1016/j.rse.2017.01.039

Keim, B. D., Muller, R. A., and Stone, G. E. (2007). Spatiotemporal patterns and return periods of tropical storm and hurricane strikes from Texas to Maine. *J. Clim.* 20, 3498–3509. doi: 10.1175/jcli4187.1

Kiefer, D. A., and SooHoo, J. B. (1982). Spectral absorption by marine particles of coastal waters of Baja California. *Limnol. Oceanogr.* 27, 492–499. doi: 10.4319/lo.1982.27.3.0492

Kirk, J. T. (1994). *Light and Photosynthesis in Aquatic Ecosystems*. Cambridge: Cambridge University Press.

Ko, D. S., Martin, P. J., Rowley, C. D., and Preller, R. H. (2008). A real-time coastal ocean prediction experiment for MREA04. *J. Mar. Syst.* 69, 17–28. doi: 10.1016/j.jmarsys.2007.02.022

Le, C., Lehrter, J. C., Hu, C., MacIntyre, H., and Beck, M. W. (2016). Satellite observation of particulate organic carbon dynamics on the Louisiana continental shelf. *J. Geophys. Res. Oceans* 122, 555–569. doi: 10.1002/2016JC012275

Lee, Z., Carder, K. L., and Arnone, R. A. (2002). Deriving inherent optical properties from water color: a multiband quasi-analytical algorithm for optically deep waters. *Appl. Opt.* 41, 5755–5772.

Lin, I., Liu, W. T., Wu, C.-C., Wong, G. T. F., Hu, C., Chen, Z., et al. (2003). New evidence for enhanced ocean primary production triggered by tropical cyclone. *Geophys. Res. Lett.* 30:1718. doi: 10.1029/2003GL017141

Liu, B., D'Sa, E. J., and Joshi, I. D. (2019a). Floodwater Impact on Galveston Bay phytoplankton taxonomy, pigment composition and photo-physiological state following Hurricane Harvey from field and ocean color (Sentinel-3A OLCI) observations. *Biogeosciences* 16, 1975–2001. doi: 10.5194/bg-16-1-2018

Liu, B., D'Sa, E. J., and Joshi, I. D. (2019b). Multi-decadal trends and influences on dissolved organic carbon distribution in the Barataria Basin, Louisiana from in-situ and Landsat/MODIS observations. *Rem. Sens. Environ.* 228, 183–202. doi: 10.1016/j.rse.2019.04.023

Livingston, R. J. (2014). *Climate Change and Coastal Ecosystems: Long-Term Effects of Climate and Nutrient Loading on Trophic Organization*, Boca Raton, FL: CRC Press, 572.

Lohrenz, S. E., Cai, W.-J., Chen, X., and Tuel, M. (2008). Satellite assessment of bio-optical properties of northern Gulf of Mexico coastal waters following Hurricanes Katrina and Rita. *Sensors* 8, 4135–4150. doi: 10.3390/s8074135

Lutz, V. A., Sathyendaranath, S., Head, E. J. H., and Li, W. K. W. (2001). Changes in the *in vivo* absorption and fluorescence excitation spectra with growth irradiance in three species of phytoplankton. *J. Plankton Res.* 23, 555–569. doi: 10.1093/plankt/23.6.555

Mannino, A., Novak, M. G., Hooker, S. B., Hyde, K., and Aurin, D. (2014). Algorithm development and validation of CDOM properties for estuarine and continental shelf waters along the northeastern U.S. coast. *Remote Sens. Environ.* 152, 576–602. doi: 10.1016/j.rse.2014.06.027

Mannino, A., Russ, M. E., and Hooker, S. B. (2008). Algorithm development and validation for satellite-derived distributions of DOC and CDOM in the US Middle Atlantic Bight. *J. Geophys. Res. Oceans* 113,

Mannino, A., Signorini, S. R., Novak, M. G., Wilkin, J., Friedrichs, M. A. M., and Najjar, R. G. (2015). Dissolved organic carbon fluxes in the Middle Atlantic Bight: an integrated approach based on satellite data and ocean model products. *J. Geophys. Res. Biogeosci.* 121, 312–336. doi: 10.1002/2015JG003031

McCulloch, A. A., Kamykowski, D., Morrison, J. M., Thomas, C. J., and Pridgen, K. G. (2013). A physical and biological context for karenia brevis seed populations on the northwest Florida shelf during July 2009. *Cont. Shelf Res.* 63, 94–111. doi: 10.1016/j.csr.2013.05.001

McKinnon, A. D., Meekan, M. G., Carleton, J. H., Furnas, M. J., Duggan, S., and Skirving, W. (2003). Rapid changes in shelf waters and pelagic communities on the southern Northwest Shelf, Australia, following a tropical cyclone. *Cont. Shelf Res.* 23, 93–111. doi: 10.1016/s0278-4343(02)00148-6

Miller, W. D., Harding, L. W., and Adolf, J. E. (2006). Hurricane Isabel generated an unusual fall bloom in Chesapeake Bay. *Geophys. Res. Lett.* 33:L06612.

Mitchell, B. G., and Kiefer, D. A. (1988). Chlorophyll α specific absorption and fluorescence excitation spectra for light-limited phytoplankton. *Deep Sea Res. Part A Oceanogr. Res. Pap.* 35, 639–663. doi: 10.1016/0198-0149(88)90024-6

Mobley, C. D. (1999). Estimation of the remote-sensing reflectance from above-surface measurements. *Appl. Opt.* 38, 7442–7455. doi: 10.1364/ao.38.007442

Moisan, T. A., Rufty, K. M., Moisan, J. R., and Linkswiler, M. A. (2017). Satellite observations of phytoplankton functional type spatial distributions, phenology, diversity, and ecotones. *Front. Mar. Sci.* 4:189. doi: 10.3389/fmars.2017.00189

Naik, P., and D'Sa, E. J. (2012). Phytoplankton light absorption of cultures and natural samples: comparisons using two spectrophotometers. *Opt. Express* 20, 4871–4886. doi: 10.1364/OE.20.004871

Neely, M., Heil, C., Murasko, S., Dziemiela, K., Faltin, E., Garrett, M., et al. (2006). "HAB's and Hurricanes in Florida," in *Proceedings of the 2006 AGU Fall Meeting Abstracts*, San Francisco, CA.

Örnólfsdóttir, E. B., Pinckney, J. L., and Tester, P. A. (2003). Quantification of the relative abundance of the toxic dinoflagellate, *Karenia brevis* (dinophyta), using unique photopigments 1. *J. Phycol.* 39, 449–457. doi: 10.1046/j.1529-8817.2003.01219.x

Osburn, C. L., Boyd, T. J., Montgomery, M. T., Bianchi, T. S., Coffin, R. B., and Paerl, H. W. (2016). Optical proxies for terrestrial dissolved organic matter in Estuaries and Coastal waters. *Front. Mar. Sci.* 2:127. doi: 10.3389/fmars.2015.00127

Osburn, C. L., and St-Jean, G. (2007). The use of wet chemical oxidation with high-amplification isotope ratio mass spectrometry (WCO-IRMS) to measure stable isotope values of dissolved organic carbon in seawater. *Limnol. Oceanogr. Methods* 5, 296–308. doi: 10.4319/lom.2007.5.296

Paerl, H. W. (1997). Coastal eutrophication and harmful algal blooms: importance of atmospheric deposition and groundwater as "new" nitrogen and other nutrient sources. *Limnol. Oceanogr.* 42, 1154–1165. doi: 10.4319/lo.1997.42.5_part_2.1154

Paerl, H. W., Bales, J. D., Ausley, L. W., Buzzelli, C. P., Crowder, L. B., Eby, L. A., et al. (2001). Ecosystem impacts of three sequential hurricanes (Dennis, Floyd, and Irene) on the United States' largest lagoonal estuary, Pamlico Sound, NC. *Proc. Natl. Acad. Sci. U.S.A.* 98, 5655–5660. doi: 10.1073/pnas.101097398

Paerl, H. W., Crosswell, J. R., Van Dam, B., Hall, N. S., Rossignol, K. L., Osburn, C. L., et al. (2018). Two decades of tropical cyclone impacts on North Carolina's estuarine carbon, nutrient and phytoplankton dynamics: implications for biogeochemical cycling and water quality in a stormier world. *Biogeochemistry* 141, 307–332. doi: 10.1007/s10533-018-0438-x

Paerl, H. W., Pinckney, J. L., Fear, J. M., and Peierls, B. L. (1998). Ecosystem responses to internal and watershed organic matter loading: consequences for hypoxia in the eutrophying Neuse River Estuary, North Carolina, USA. *Mar. Ecol. Progr. Ser.* 166, 17–25. doi: 10.3354/meps166017

Qian, Y., Jochens, A. E., Kennicutt, M. C. II, and Biggs, D. C. (2003). Spatial and temporal variability of phytoplankton biomass and community structure over the continental margin of the northeast Gulf of Mexico based on pigment analysis. *Cont. Shelf Res.* 23, 1–17. doi: 10.1016/s0278-4343(02)00173-5

Riegman, R., Stolte, W., Noordeloos, A. A., and Slezak, D. (2000). Nutrient uptake and alkaline phosphatase (EC 3: 1: 3: 1) activity of Emiliania huxleyi (Prymnesiophyceae) during growth under N and P limitation in continuous cultures. *J. Phycol.* 36, 87–96. doi: 10.1046/j.1529-8817.2000.99023.x

Roesler, C., Stramski, D., D'Sa, E. J., Rottgers, R., and Reynolds, R. A. (2018). "Spectrophotometric measurements of particulate absorption using filter pads," in *IOCCG Protocol Series - Ocean Optics and Biogeochemistry Protocols for Satellite Ocean Colour Sensor Validation*, eds A. R. Neeleycpesnm, and A. Manninocpesnm, (Dartmouth, NS: IOCCG).

Stramski, D., Reynolds, R. A., Babin, M., Kaczmarek, S., Lewis, M. R., Ruttgers, R., et al. (2008). Relationships between the surface concentration of particulate organic carbon and optical properties in the eastern South Pacific and eastern Atlantic Oceans. *Biogeosciences* 5, 171–201. doi: 10.5194/bg-5-171-2008

Stramski, D., Reynolds, R. A., Kahru, M., and Mitchell, G. (1999). Estimation of particulate organic carbon in the ocean from satellite remote sensing. *Science* 285, 239–242. doi: 10.1126/science.285.5425.239

Tehrani, N. C., D'Sa, E. J., Osburn, C. L., Bianchi, T. S., and Schaeffer, B. A. (2013). Chromophoric dissolved organic matter and dissolved organic carbon from sea-viewing wide field-of-view sensor (SeaWiFS), moderate resolution imaging spectroradiometer (MODIS) and MERIS sensors: case study for the northern Gulf of Mexico. *Remote Sens.* 5, 1439–1464. doi: 10.3390/rs5031439

Thrane, J.-E., Kyle, M., Striebel, M., Haande, S., Grung, M., Rohrlack, T., et al. (2015). Spectrophotometric analysis of pigments: a critical assessment of a high-throughput method for analysis of algal pigment mixtures by spectral deconvolution. *PLoS One* 10:e0137645. doi: 10.1371/journal.pone.0137645

Turner, R. E., Baustian, J. J., Swenson, E. M., and Spicer, J. S. (2006). Wetland sedimentation from Hurricanes Katrina and Rita. *Science* 314, 449–452. doi: 10.1126/science.1129116

Walker, N. D., Leben, R. B., and Balasubramanian, S. (2005). Hurricane forced upwelling and chlorophyll a enhancement within cold-core cyclones in the Gulf of Mexico. *Geophys. Res. Lett.* 32:L18610.

Walker, N. D., Pilley, C. T., Raghunathan, V. V., D'Sa, E. J., Leben, R. R., Hoffmann, N. G., et al. (2011). Impacts of loop current frontal cyclonic eddies and wind forcing on the 2010 Gulf of Mexio spill. *Geophys. Monog. Ser.* 195, 103–116. doi: 10.1029/2011gm001120

Walsh, J. J., Jolliff, J., Darrow, B., Lenes, J., Milroy, S., Remsen, A., et al. (2006). Red tides in the Gulf of Mexico: where, when, and why? *J. Geophys. Res. Oceans* 111, 1–46.

Walsh, J. J., Weisberg, R. H., Dieterle, D. A., He, R., Darrow, B. P., Jolliff, J. K., et al. (2003). Phytoplankton response to intrusions of slope water on the West Florida Shelf: models and observations. *J. Geophys. Res. Oceans* 108:3190.

Warnken, K. W., and Santschi, P. H. (2004). Biogeochemical behavior of organic carbon in the Trinity River downstream of a large reservoir lake in Texas, USA. *Sci. Total Environ.* 329, 131–144. doi: 10.1016/j.scitotenv.2004.02.017

Waters, L. G., Wolcott, T. G., Kamykowski, D., and Sinclair, G. (2015). Deep-water seed populations for red tide blooms in the Gulf of Mexico. *Mar. Ecol. Progr. Ser.* 529, 1–16. doi: 10.3354/meps11272

Wilber, D. H. (1992). Associations between freshwater inflows and oyster productivity in Apalachicola Bay, Florida. *Estuar. Coast. Shelf Sci.* 35, 179–190. doi: 10.1016/s0272-7714(05)80112-x

Williams, W., Beardsley, R., Irish, J., Smith, P., and Limeburner, R. (2001). The response of georges bank to the passage of Hurricane Edouard. *Deep Sea Res. Part II* 48, 179–197. doi: 10.1016/s0967-0645(00)00118-1

Yuan, J., Miller, R. L., Powell, R. T., and Dagg, M. J. (2004). Storm-induced injection of the Mississippi River plume into the open Gulf of Mexico. *Geophys. Res. Lett.* 31:L09312.

Yunev, O. A., Carstensen, J., Moncheva, S., Khaliulin, A., Ærtebjerg, G., and Nixon, S. (2007). Nutrient and phytoplankton trends on the western Black Sea shelf in response to cultural eutrophication and climate changes. *Estuar. Coast. Shelf Sci.* 74, 63–76. doi: 10.1016/j.ecss.2007.03.030

Zamudio, L., and Hogan, P. J. (2008). Nesting the Gulf of Mexico in Atlantic HYCOM: oceanographic processes generated by Hurricane Ivan. *Ocean Modell.* 21, 106–125. doi: 10.1016/j.ocemod.2007.12.002

Zapata, M., Fraga, S., Rodríguez, F., and Garrido, J. L. (2012). Pigment-based chloroplast types in dinoflagellates. *Mar. Ecol. Progr. Ser.* 465, 33–52. doi: 10.3354/meps09879

Zapata, M., Jeffrey, S., Wright, S. W., Rodríguez, F., Garrido, J. L., and Clementson, L. (2004). Photosynthetic pigments in 37 species (65 strains) of Haptophyta: implications for oceanography and chemotaxonomy. *Mar. Ecol. Progr. Ser.* 270, 83–102. doi: 10.3354/meps270083

Conflict of Interest Statement: The authors declare that the research was conducted in the absence of any commercial or financial relationships that could be construed as a potential conflict of interest.

frontiers in Marine Science

ORIGINAL RESEARCH
published: 16 October 2019
doi: 10.3389/fmars.2019.00640

Short Term Effects of Hurricane Irma and Cyanobacterial Blooms on Ammonium Cycling Along a Freshwater–Estuarine Continuum in South Florida

Justyna J. Hampel[1,2]*, Mark J. McCarthy[2], Megan H. Reed[2] and Silvia E. Newell[2]

[1] *School of Ocean Science and Engineering, The University of Southern Mississippi, Ocean Springs, MS, United States,*
[2] *Department of Earth and Environmental Sciences, Wright State University, Dayton, OH, United States*

Lacustrine and coastal systems are vulnerable to the increasing number and intensity of tropical storms driven by climate change. Strong winds associated with tropical storms can mobilize nutrients in sediments and alter nitrogen and phosphorus cycling, leading to amplification of preexisting conditions, such as eutrophication and cyanobacterial blooms (cyanoHABs). In 2016, Florida declared a State of Emergency within and downstream of Lake Okeechobee (LO) due to toxic cyanobacterial blooms (primarily *Microcystis*). The blooms originated in LO, but flood control measures released water from LO to the brackish St. Lucie Estuary (SLE). In September 2017, Hurricane Irma traversed the Florida peninsula with sustained winds exceeding 160 km h^{-1}, generating torrential rains over the watershed. We quantified ammonium (NH_4^+) regeneration and potential uptake rates, and *Microcystis* toxin gene (*mcyD*) abundance in LO and SLE during the massive bloom in July 2016, the bloom in August 2017 (2 weeks before Irma), and 10 days after Hurricane Irma landfall. In 2016, cyanoHABs were present in both LO and SLE, and potential NH_4^+ uptake rates were high in both systems. In 2017, the bloom was constrained to LO, potential NH_4^+ uptake rates in LO exceeded those in SLE, and *mcyD* gene abundance was greater in LO than SLE. Post Hurricane Irma, potential NH_4^+ uptake rates decreased significantly in LO and SLE, while *mcyD* gene abundance decreased in LO and increased slightly in SLE. Average NH_4^+ regeneration rates could support 25–40% of water column potential NH_4^+ demand in the lake and, when extrapolated to the entire LO water column, exceeded external nitrogen loading. These results emphasize the importance of internal NH_4^+ recycling for bloom expansion and toxicity in the lake and downstream estuaries. In 2018, the cyanobacterial bloom in the Okeechobee region was one of the largest recorded and is presumed to be driven by the aftermath of Hurricane Irma. Large-scale blooms have also been observed in SLE, likely due to LO flushing and decreased salinity post-hurricane. Thus, results from this study support predictions that increased frequency and strength of tropical storms will lead to more intense blooms in aquatic systems.

Keywords: hurricane, nitrogen, cyanobacteria, Florida, Okeechobee, St. Lucie Estuary

Edited by:
Christopher Osburn,
North Carolina State University,
United States

Reviewed by:
Richard Thomas James,
South Florida Water Management
District, United States
Corianne Tatariw,
The University of Alabama,
United States

***Correspondence:**
Justyna J. Hampel
justyna.hampel@usm.edu

Specialty section:
This article was submitted to
Marine Biogeochemistry,
a section of the journal
Frontiers in Marine Science

Received: *07 February 2019*
Accepted: *30 September 2019*
Published: *16 October 2019*

Citation:
Hampel JJ, McCarthy MJ,
Reed MH and Newell SE (2019) Short
Term Effects of Hurricane Irma
and Cyanobacterial Blooms on
Ammonium Cycling Along
a Freshwater–Estuarine Continuum
in South Florida.
Front. Mar. Sci. 6:640.
doi: 10.3389/fmars.2019.00640

INTRODUCTION

Anthropogenically-driven climate change has major effects on aquatic systems globally. Additionally, anthropogenic alterations to the nitrogen (N) cycle via synthetic fertilizer production (Haber–Bosch process) have quadrupled the amounts of chemically reduced N in the last 60 years (Erisman et al., 2015). Together, increased N runoff and climate change contribute to eutrophication and cyanobacterial harmful algal blooms (cyanoHABs; Paerl et al., 2016; Glibert, 2017) in freshwater and coastal systems. Internal loading of N and phosphorus (P) from sediments and recycling processes within the water column can enhance cyanoHABs (Havens et al., 2001a; McCarthy et al., 2007, 2016), especially in shallow lakes (Havens et al., 2001a; Moss et al., 2003; Jeppesen et al., 2007; James et al., 2009). However, external nutrient loading from non-point agricultural runoff and point sources is the major driver of internal nutrient loading/recycling and cyanoHABs in eutrophic lakes (Huisman et al., 2018).

Lake Okeechobee in southern Florida is a large (1800 km^2), shallow lake (mean depth = 2.7 m) and has experienced cyanoHABs for decades (Havens et al., 1994). Lake water levels are closely monitored and managed by the US Army Corps of Engineers. These activities allow the lake to fill in the winter dry season, supplying water for agricultural and urban uses, and lake water is released in spring to increase storage capacity for the summer wet season (Julian and Osborne, 2018). The St. Lucie Estuary (SLE) is subjected to high freshwater and nutrient inputs from Lake Okeechobee through the South Fork of the estuary and Indian River Lagoon. Lake Okeechobee and the SLE receive high external N and P loads from agricultural runoff and anthropogenic activities (James et al., 2011; Phlips et al., 2012), and recent toxic cyanoHABs have been well-documented in both systems (e.g., Phlips et al., 2012; Kramer et al., 2018). In 2016, a large, toxic cyanobacterial bloom occurred in Lake Okeechobee and SLE, leading to a State of Emergency declaration in Florida (Kramer et al., 2018). Increased rainfall in 2016, corresponding with an El Niño event, led to increased N concentrations in the water column and decreased salinity in the estuary, conditions ideal for development of a *Microcystis* bloom (Kramer et al., 2018). Environmental degradation in SLE (e.g., cyanoHABs, fecal bacteria, degradation of nearshore reefs) has also been attributed to on-site sewage disposal systems (septic tanks; Lapointe et al., 2012, 2017), which have led to nutrient enrichment and microbial contamination (Lapointe et al., 2017).

Cyanobacteria community structure in Lake Okeechobee has shifted from N-fixing to non-N fixing taxa (*Microcystis*) in recent decades (Havens et al., 2003). Eutrophication management efforts in Lake Okeechobee included 40% reductions of P loading and reducing back-pumping from the Everglades Agricultural Area (EAA; James et al., 2011). The Okeechobee Basin Management Action Plan (BMAP) was also implemented in 2014 to reduce daily loads for total P (Zhang et al., 2016), and these approaches will likely also reduce N loads. However, non-point source pollution remains a problem in the Lake Okeechobee watershed, and concerns about water-level and flood control management activities persist (Kramer et al., 2018).

Microcystis is a potential toxin-producing cyanobacterial genus and strong competitor for chemically reduced forms of N (Blomqvist et al., 1994; Yang et al., 2017; Hampel et al., 2018), such as ammonium (NH_4^+) and urea. Microcystin (MC), synthesized by *Microcystis* and other cyanobacteria, is a potent hepatotoxin and is N-rich (10 N atoms per molecule; Gobler et al., 2016). In fact, reduced forms of N can yield higher production of MC (Monchamp et al., 2014; Davis et al., 2015; Harke and Gobler, 2015). Ammonium is the preferred source of N for most primary producers, including non-N-fixing cyanobacteria (Blomqvist et al., 1994; Beversdorf et al., 2015). Thus, internal cycling of NH_4^+ is of particular importance in lakes affected by non-diazotrophic cyanoHABs, and internal NH_4^+ regeneration often sustains late summer blooms (Paerl et al., 2011; McCarthy et al., 2013; Hampel et al., 2019). NH_4^+ turnover rates in Lake Okeechobee are rapid, while ambient NH_4^+ concentrations are generally low, suggesting that NH_4^+ is in high demand (McCarthy et al., 2009; James et al., 2011). Large discrepancies have been observed between inflow and outflow N in previous mass balance studies for Lake Okeechobee (Havens et al., 2001a), suggesting that internal N cycling processes play a critical role in supporting primary productivity and cyanoHABs (James et al., 2011).

Current climate change models forecast increased severity of extreme weather events, including hurricanes and typhoons (Bender et al., 2010; Knutson et al., 2010; Paerl et al., 2018). Hurricane events increase rainfall in affected areas, leading to higher runoff and nutrient concentrations (Havens et al., 2001b; James et al., 2008). Strong winds associated with tropical storms also enhance eutrophication by mobilizing nutrients in sediments via resuspension (Havens et al., 2001b; James et al., 2008; Ding et al., 2012). Previous studies in Lake Okeechobee reported doubled to quadrupled concentrations of total N (TN) and total phosphorus (TP), along with major increases in soluble reactive phosphorus (SRP), NH_4^+, and other forms of N, after hurricanes (James et al., 2008; Ding et al., 2012). Increased nutrient availability after these events leads to amplified productivity, biomass, and chlorophyll levels (Fogel et al., 1999; Paerl et al., 2001).

The objectives of this study were to (1) quantify water column NH_4^+ dynamics during a severe cyanoHAB in 2016 that affected both Lake Okeechobee and the SLE and (2) compare those rates to those from 2017, when the cyanoHAB was restricted to Lake Okeechobee. We also aimed to (3) quantify these rates within 2 weeks after a major hurricane in September 2017 to examine post-hurricane NH_4^+ cycling rates in both the lake and estuary. Finally, we (4) quantified MC synthetase gene (*mcyD*) abundance before and after the hurricane to investigate the effects of hurricane passage on MC producing cyanobacteria. We hypothesized that NH_4^+ cycling rates in Lake Okeechobee would be higher during the large bloom in 2016 than in 2017 during the smaller bloom. We also hypothesized that NH_4^+ uptake and regeneration rates in the estuary in 2016 would decrease along the salinity gradient and be higher than in 2017. Lastly, we anticipated that the hurricane would have a major effect on NH_4^+ cycling and *Microcystis* in both systems, and that regeneration rates would increase post-disturbance, while uptake rates and abundance of MC synthetase would decrease.

MATERIALS AND METHODS

Sample Collection

Lake Okeechobee (LO) and SLE water samples were collected on three occasions: July 25–27, 2016; August 22–24, 2017; and September 20–21, 2017. Sampling in July 2016 followed a major cyanobacterial bloom in LO that extended into SLE and reached the Atlantic Ocean (Kramer et al., 2018). The August 2017 sampling occurred shortly before Hurricane Irma passed over the lake as a Category 3 hurricane (sustained winds 178–208 km h^{-1} at landfall near Marco Island) on September 10. The September 2017 sampling occurred 10 days after Hurricane Irma passed through central Florida and the Okeechobee region (sustained winds ~40 mph on September 10, DBHydro, SFWMD).

In July 2016, sampling was conducted at two stations in LO and four stations in SLE: L004 at surface and bottom (~3 m) water depths; LZ40 at surface and bottom (~4 m) water depths; and SLE80, SLE2, SLE4, and SLE8 (all SLE sampling was surface water; **Figure 1**). Bottom water samples were collected about 0.5 m above the sediment-water interface. L004 is located in eastern LO, ~8.5 km from the St. Lucie Canal, and LZ40 is in the center of the lake. Stations in SLE followed a salinity gradient (**Table 2**), with SLE80 closest to the canal discharge lock (S308; **Figure 1**), and SLE8 closest to the Atlantic Ocean. In August 2017, due to poor weather, only L004 (surface and bottom) and a northern LO station (SAV 165, surface water only) were sampled. Similarly, SLE stations (SLE7, SLE5, and SLE80) could only be sampled from land due to poor weather conditions. In September 2017, stations SLE5 and SLE7 were sampled in SLE, and stations L004 (surface), LZ40 (surface), and LOBG in southeastern LO were sampled (**Figure 1**).

Water for *in situ* nutrient analyses was filtered in the field using 0.2 μm syringe filters into 15 ml polypropylene tubes and frozen upon return to the laboratory. Geophysical parameters (temperature, dissolved oxygen, pH, salinity, and conductivity) were measured using a YSI multi-parameter sonde in July 2016 and August 2017 and a Manta 2 sonde (Eureka Waterprobes) in September 2017. Water for NH_4^+ dynamics experiments was collected into pre-washed and sample-rinsed 6 L cubitainers and returned to the lab within 3 h for incubations.

Samples for chlorophyll *a* (Chl *a*), TN, and TP analyses were collected and analyzed by South Florida Water Management District (SFWMD) according to standard USEPA methods (as described in SFWMD, 2002). Dissolved nutrient analyses included NH_4^+, NO_2^-, NO_3^-, orthophosphate (OP), and urea and were analyzed using a Lachat Quikchem 8500 FIA nutrient analyzer according to the manufacturer's instructions.

NH_4^+ Regeneration and Potential Uptake

Water column NH_4^+ regeneration and potential uptake experiments followed the protocol described in Hampel et al. (2018) with modifications for ^{15}N analysis. Briefly, 1 L of water collected at each station was amended with 98% $^{15}NH_4Cl$ (Isotec; final concentration added: 16 μM for all stations except SAV165 = 32 μM). Amended water was mixed thoroughly and decanted into six, 125 ml clear polystyrene Nalgene bottles (triplicates for light and dark incubations). Initial samples were filtered (0.2 μm syringe filter) immediately after spiking (T0) into 15 ml clear, polypropylene tubes (for total NH_4^+) and 12 ml gas-tight exetainers (for ^{15}N analysis). Dark incubation bottles were wrapped in aluminum foil, and all samples were placed in a standard lab incubator (also used for algal cultures), at near-ambient temperature (29°C) and set to the appropriate diurnal light cycle, for 20 h. After incubation, final samples (Tf) were processed as described for the T0 samples and stored frozen until analysis. Total NH_4^+ ($^{14+15}N$) concentrations were determined using the Lachat Quikchem 8500 FIA nutrient analyzer, and $^{15}NH_4^+$ concentrations were determined using the OX-MIMS method, combining membrane inlet mass spectrometry (MIMS; Kana et al., 1994) with NH_4^+ reduction to N_2 gas (Yin et al., 2014). Samples for OX-MIMS were treated with 200 μl of hypobromite iodine solution and immediately measured on the MIMS. $^{15}NH_4^+$ concentrations were determined using the line equation from the standard curve (0.1–100 μM $^{15}NH_4^+$) and total $^{15}N_2$ production (Yin et al., 2014). Potential uptake and actual regeneration rates were calculated using the Blackburn/Caperon model (Blackburn, 1979; Caperon et al., 1979). Volumetric NH_4^+ uptake rates (light and dark), but not regeneration rates (actual rates; Gardner et al., 2017), reported in this study are qualified as potential rates due to saturating additions of substrate, which can alter steady-state conditions (Glibert, 1988). However, in eutrophic systems, results from saturating- and tracer-level isotope additions tend to converge (Glibert, 1988).

DNA Collection and Extraction

Environmental DNA for gene abundance analysis was collected in August and September 2017 using 0.2 μm Sterivex filters (EMD Millipore, Burlington, MA, United States) and preserved with Ambion RNAlater (Invitrogen, Carlsbad, CA, United States). In August, approximately 120–240 ml of water was pushed through a Sterivex filter. However, due to highly turbid waters after the hurricane in September, only 45–60 ml of water were filtered for stations L004, LZ40, and SLE, and 300 ml for station LOBG. Preserved filters were frozen at −80°C. DNA was extracted using the Gentra PureGene kit (Qiagen, Inc., United States). Residual RNAlater in the Sterivex filters was removed by pushing 10 ml of Phosphate Buffer Saline 1X Solution (Fisher BioReagents, United States) through the filter. Lysis buffer (0.9 ml) and Proteinase K (10 μl) were added to the filters, followed by 1 h incubation at 55°C and 1 h incubation at 65°C (Newell et al., 2011). Concentration and purity of extracted DNA were measured spectrophotometrically (Nanodrop 2000, Thermo Scientific).

qPCR Analysis

The MC synthetase gene was amplified using the mcyD-F2 and mcyD-R2 primers, targeting a 298 bp region of the *mcy* operon (Kaebernick et al., 2000). qPCR standards were prepared by

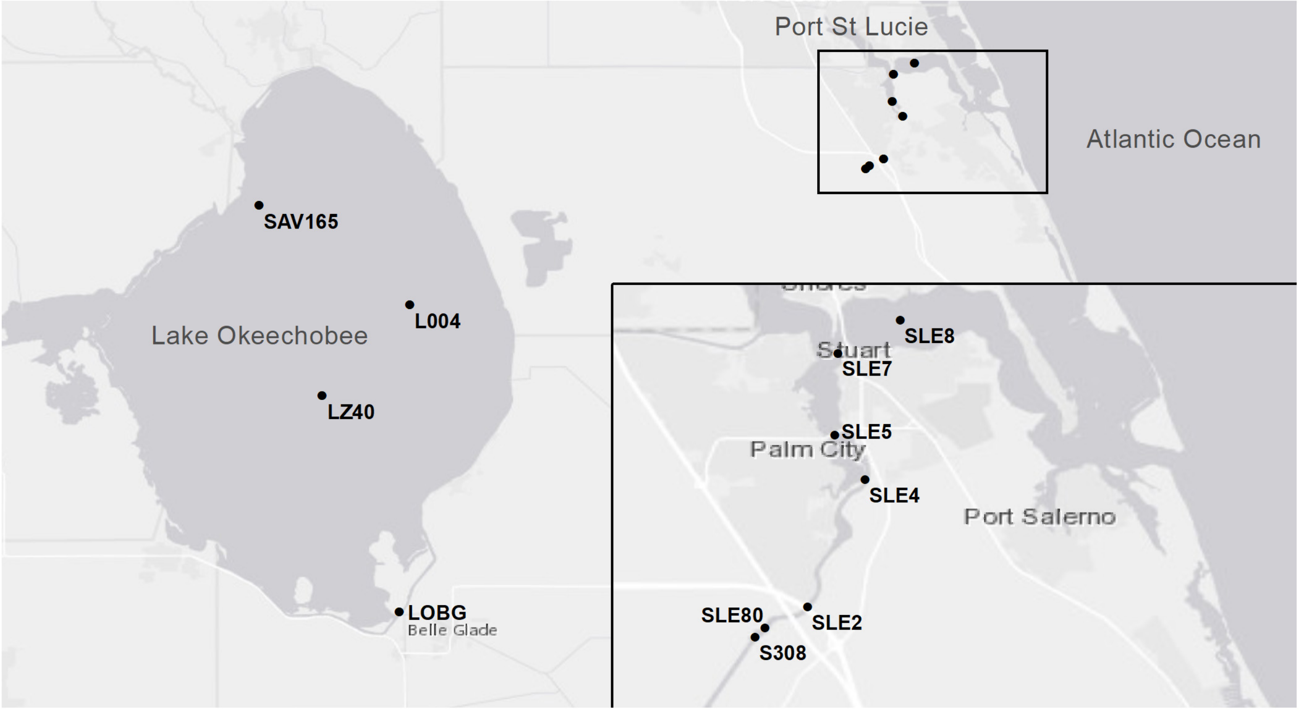

FIGURE 1 | Map of sampling locations in Lake Okeechobee and St. Lucie Estuary during 2016 and 2017 sampling events. The inset shows the South Fork of St. Lucie Estuary.

TABLE 1 | Environmental data and ambient nutrient concentrations in Lake Okeechobee.

Sampling date	Station	Temperature °C	Dissolved oxygen mg L^{-1}	pH	Chl *a* $\mu g\ L^{-1}$	Conductivity $\mu s\ cm^{-1}$	NH_4^+ μM	NO_2^- μM	NO_3^- μM	OP μM	Urea μM	TN μM	TP μM
27 July, 2016	L004 S	30.9	11.9	8.09	27.1	360	6.70	0.09	0.11	1.10	2.46	68.4	3.36
	L004 D						7.75	0.29	1.20	0.96	2.56	ND	ND
	LZ40 S	31.5	9.81	7.94	25.3	383	0.11	0.21	1.18	0.98	1.28	131	4.90
	LZ40 D						0.82	0.21	1.56	1.02	3.70	ND	ND
22 August, 2017	L004 S	29.6	8.24	8.17	33.5	372	0.19	0.07	2.06	0.94	2.44	103	4.39
	L004 D						0.11	0.07	1.74	0.96	0.93	ND	ND
	SAV 165	29.8	10.2	8.95	77.8	368	0.59	0.03	0.00	0.07	1.10	114	1.74
22 September, 2017	L004	28.4	6.47	7.91	11.3	391	0.11	0.08	53.6	1.05	1.90	164	7.42
	LZ40	28.1	7.63	8.16	8.16	405	0.58	0.10	24.4	0.75	3.41	117	5.19
	LOBG	29.8	2.47	7.36	22.0	556	19.1	3.28	18.7	4.93	4.34	ND	ND

Temperature, dissolved oxygen, pH, Chl a, and conductivity were only measured at surface stations. Nutrient concentrations were measured in triplicate within ± 10% error margin. ND, no data; S = surface water; D = bottom water.

cloning the fragment of interest with the TOPO TA Cloning Kit (Invitrogen, United States) and inserting it into a competent cell (One Shot *E. coli* cells, Invitrogen, United States). The plasmid containing the *mcyD* gene was isolated using the UltraClean Standard Mini Plasmid Prep Kit (Mo Bio Laboratories, Inc., Carlsbad, CA, United States). The qPCR run included three negative controls (no template), triplicates of five standards generated from serial dilution, and the environmental DNA samples in triplicate. Each sample and standard received 10 μl of Luna qPCR Master Mix (New England Biolabs, United States), 1 μl of each 10 μM primer, and 20–30 ng of template DNA.

qPCR protocol followed a method modified from Davis et al. (2009) for *mcyD* (95°C initial denaturation for 2 min, 95°C denaturation for 15 s, 50°C annealing for 1 min, and 60°C extension for 1 min; 45 cycles) followed by the melting curve. Automatic settings for the thermocycler (Realplex, Eppendorf) were used to determine the threshold cycle (Ct values), efficiency (98%), and a standard curve with R^2 values of 0.99. *mcyD* gene

TABLE 2 | Environmental data and ambient nutrient concentrations in St. Lucie Estuary.

Sampling date	Station	Temperature °C	Dissolved oxygen mg L^{-1}	pH	Chl *a* µg L^{-1}	Salinity	Conductivity µs cm^{-1}	NH_4^+ µM	NO_2^- µM	NO_3^- µM	OP µM	Urea µM	TN µM	TP µM
25 July, 2016	SLE80	31.1	7.1	7.4	12.1	0.19	0.395	3.19	0.82	6.67	2.03	3.22	80.0	3.97
	SLE2	30.2	7.4	7.5	19.3	0.19	0.399	1.87	0.77	7.09	1.46	1.05	ND	ND
	SLE4	29.6	7.6	7.6	8.9	0.2	0.42	3.61	1.06	7.59	1.30	1.86	82.9	5.29
	SLE8	29.8	6	7.6	10.2	8.9	15.5	2.95	0.42	3.00	3.28	1.37	58.2	5.00
24 August, 2017	SLE80	29.6	5.9	7.9	21.1	0.33	0.686	7.83	0.81	10.4	4.46	5.47	78.6	5.03
	SLE5	29.7	4.2	7.4	16.1	4.64	8.38	12.2	2.90	9.17	6.43	4.00	91.4	8.97
	SLE7	29.4	5.6	7.7	16.8	6.75	11.7	7.39	5.68	7.49	6.66	3.31	81.4	8.07
21 September, 2017	SLE5	29.4	6.9	7.5	13.6	0.19	405	0.25	0.34	34.6	2.48	2.04	124	6.74
	SLE7	29.4	3.9	7.5	12.8	0.22	466	2.22	1.09	35.3	4.45	5.13	127	6.84

Nutrient concentrations were measured in triplicate within ± 10% error margin. ND, no data.

copies were calculated as (ng * number mol^{-1})/(bp * ng g^{-1} * g mol^{-1} of bp) and is reported in gene copies ml^{-1} of sample water.

Statistical Analysis

All statistical analyses were performed using RStudio software (version 1.1.383). Environmental data were checked for normality using the Shapiro–Wilk normality test. After ensuring that the data were not normally distributed, the Kruskal–Wallis test for non-parametric data was used to determine significant differences between sites and time points. The Kendall correlation method for non-parametric data was used between environmental variables and geochemical rates and *mcyD* gene abundance. Kendall's *p*-values are usually more accurate for datasets with small sample sizes than Spearman's (Croux and Dehon, 2010). The correlation matrix presented below was constructed showing the Kendall's tau correlation coefficient and *p*-values ($p < 0.05$ was considered statistically significant).

RESULTS

Environmental Data

Lake Okeechobee

Environmental variables in LO varied between sampling events, with only temperature remaining stable (**Table 1**). DO was highest in July 2016 (10.9 ± 1.05 mg L^{-1}; mean ± standard error) and lowest following the hurricane in September 2017 (5.5 ± 1.5 mg L^{-1}). Similarly, pH was highest before the hurricane and decreased afterward. Chl *a* was also higher during the August 2017 bloom (55.6 ± 22.2 µg L^{-1}) than during the July 2016 bloom (26.2 ± 0.9 µg L^{-1}), and lowest values were observed post-Irma in September 2017 (13.8 ± 5.13 µg L^{-1}). Conductivity was similar in July 2016 and August 2017 (372 ± 11.5 and 370 ± 2.00 µs cm^{-1}, respectively) and increased in September 2017 (451 ± 64.7 µs cm^{-1}).

In July 2016, ambient NH_4^+ concentrations in the east–central lake (L004; 7.22 ± 0.53 µM) were significantly greater than in the lake center (LZ40; 0.47 ± 0.36 µM; $p < 0.05$). In September 2017, NH_4^+ concentrations were also significantly greater at the shore station (LOBG; 19.1 µM) than at L004 (0.1 µM; $p < 0.05$). NO_2^- concentrations were not statistically different between sampling events and ranged from 0.06 to 1.15 µM. Ambient NO_3^- concentrations were similar in July 2016 (1.01 ± 0.31 µM) and August 2017 (1.9 ± 0.16 µM) and significantly increased after the hurricane (32.2 ± 10.8 µM). Similarly, OP and urea concentrations both increased after the hurricane (2.24 ± 1.34 and 3.22 ± 0.71 µM, respectively).

St. Lucie Estuary

Water temperatures in SLE also were consistent between sampling events (29.4–31.1°C; **Table 2**). Salinity in July 2016 increased from SLE80 (closest to the canal; 0.19) to SLE8 (closest to the Atlantic Ocean; 8.9), and the same general pattern was observed in August 2017, with lower salinity at SLE5 (4.6) than SLE7 (6.75). However, after the hurricane, salinity decreased significantly to 0.19 (SLE5) and 0.22 (SLE7; $p < 0.05$). Similar to LO, highest conductivity was observed in September 2017 and was significantly different from other sampling events (436 ± 30.5 μs cm^{-1}; $p < 0.001$). Highest mean Chl *a* values were recorded in August 2017 (18 ± 1.9 μg L^{-1}).

Ambient NH_4^+ concentrations were highest in August 2017 (9.13 ± 1.52 μM) and decreased after the hurricane (1.23 ± 0.98 μM; **Table 2**). Similarly, NO_2^- concentrations were higher before the hurricane (August 2017: 3.15 ± 1.40 μM) and decreased afterward (September 2017: 0.71 ± 0.37 μM). In contrast, NO_3^- concentrations in SLE increased post-Irma (September: 34.9 ± 0.35 μM). OP and urea showed an opposite pattern than in LO and decreased after the hurricane (**Table 2**).

Potential Ammonium Uptake

Lake Okeechobee

As mentioned previously, light and dark uptake rates are qualified as potential rates because of added substrate. However, regeneration rates are considered actual rates because they represent $^{14}NH_4^+$ turnover (Gardner et al., 2017). In July 2016, potential NH_4^+ uptake rates in the light ranged from 0.54 to 2.24 μM h^{-1}, and peak light NH_4^+ uptake rates were observed at L004 in surface water (**Figure 2A**). Light NH_4^+ uptake rates in August 2017 (mean = 2.88 ± 0.72 μM h^{-1}; **Figure 2B**) were greater than in July 2016, with peak rates in the central–eastern part of the lake (L004; **Figure 2B**). After the hurricane (**Figure 2C**), light uptake rates significantly decreased (mean = 0.66 ± 0.27 μM h^{-1}; $p < 0.05$) and showed spatial variability; highest light uptake was observed at the shore station (LOBG) and lowest in the central lake (LZ40).

Dark NH_4^+ uptake rates were significantly lower than light rates on all occasions ($p < 0.001$). In July 2016, dark NH_4^+ uptake rates were comparable between stations and depths (mean = 0.30 ± 0.05 μM h^{-1}; **Figure 2A**). Dark rates in August 2017 were not statistically different from the July 2016 rates. However, dark uptake rates in September 2017 were significantly lower than in July 2016 (mean = 0.12 ± 0.02 μM h^{-1}; **Figure 2C**), with highest dark uptake in the central–eastern lake (L004; **Figure 2C**) and lowest at the shore station (LOBG).

St. Lucie Estuary

Light NH_4^+ uptake rates in the estuary were significantly different between sampling events and years ($p < 0.05$). Mean light uptake rates in the estuary were highest in July 2016 (mean = 1.76 ± 0.25 μM h^{-1}), with highest rates close to the canal (SLE80 and SLE2) and decreasing toward the ocean (**Figure 2A**). In August 2017, light uptake rates were significantly lower (mean 0.89 ± 0.22 μM h^{-1}; $p < 0.05$) but followed the same pattern, with peak uptake rates at the lock (SLE80) and decreasing at SLE5 and SLE7 (**Figure 2B**). After the hurricane, light uptake in the estuary decreased even further and was similar between stations SLE5 and SLE7 (mean = 0.22 ± 0.03 μM h^{-1}; **Figure 2C**).

Dark NH_4^+ uptake rates in the estuary were not statistically different between sampling events but were significantly lower than the light NH_4^+ uptake rates ($p < 0.001$). In July 2016, dark rates in the estuary ranged from 0.12 to 1.31 μM h^{-1},

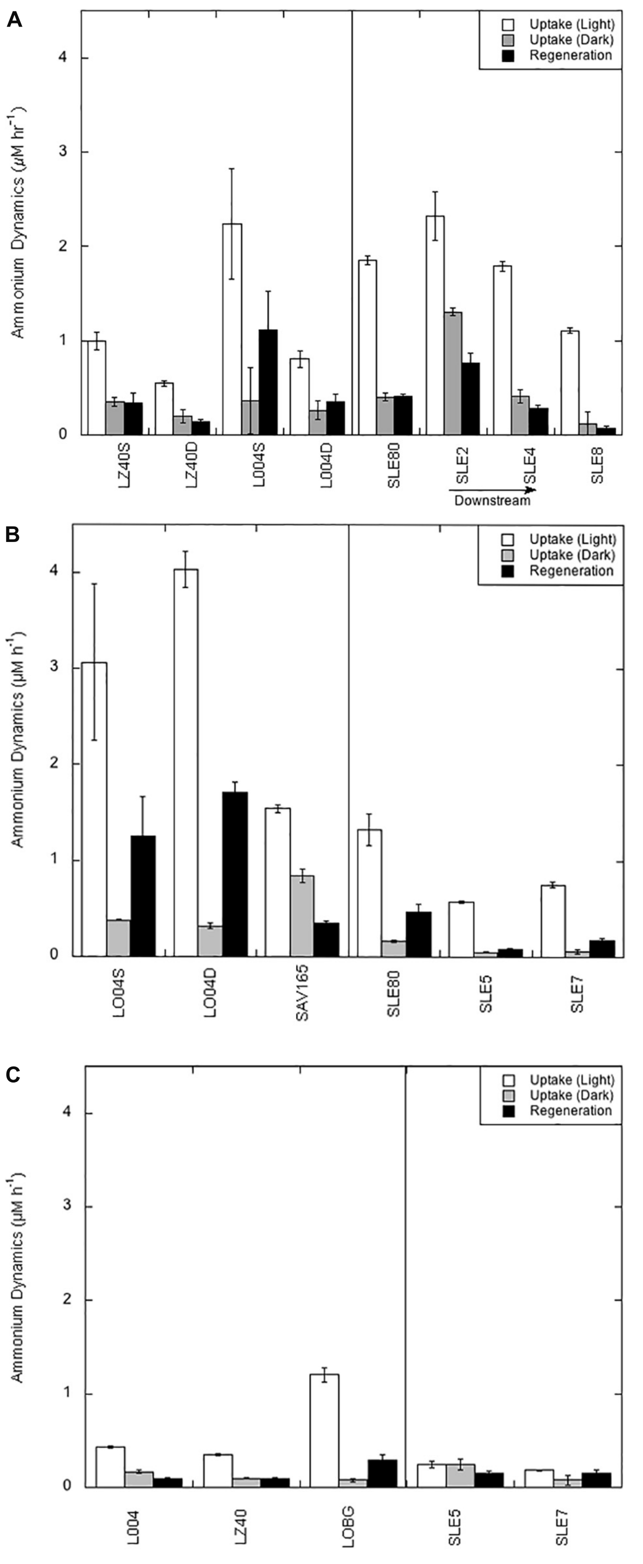

FIGURE 2 | Ammonium regeneration and potential uptake rates in Lake Okeechobee and St. Lucie Estuary in July 2016 **(A)**, August 2017 **(B)**, and September 2017 **(C)**. Values are averaged (three replicates) with error bars showing ± one standard error. Vertical line divides stations in the lake from stations in the estuary. S = surface water; D = bottom water.

with highest dark uptake near the lock at SLE2 and lowest further down the salinity gradient (SLE8; **Figure 2A**). In August 2017, dark uptake rates were lower than in 2016 (mean = 0.09 ± 0.03 μM h^{-1}) but followed a similar pattern, with peak rates observed at SLE80 (**Figure 2B**). In contrast to light uptake rates, dark uptake rates in the estuary in September 2017 were slightly greater than before the hurricane, but not statistically different (0.16 ± 0.08 μM h^{-1}; **Figure 2C**).

Light NH_4^+ uptake rates in LO and SLE were positively correlated with ambient temperature and negatively correlated with NO_3^-, TN, and TP concentrations (**Table 3**). Dark NH_4^+ uptake rates were positively correlated with DO concentration and *mcyD* abundance and negatively correlated with NO_2^-, OP, urea, and TP concentrations (**Table 3**).

Ammonium Regeneration

Lake Okeechobee

NH_4^+ regeneration rates in LO (averaged light and dark rates) were not statistically different between July 2016 and August 2017 sampling events. Mean NH_4^+ regeneration in July 2016 was 0.49 ± 0.22 μM h^{-1}, and highest regeneration rates were observed in the east-central part of the lake (L004; **Figure 2A**). In August 2017, NH_4^+ regeneration rates were higher than in July 2016 (mean = 1.10 ± 0.39 μM h^{-1}), with highest rates at L004 (surface: 1.25 ± 0.40 μM h^{-1}; deep: 1.70 ± 0.11 μM h^{-1}) and lowest at SAV165 in surface water (0.35 ± 0.03 μM h^{-1}). Following the hurricane, NH_4^+ regeneration rates decreased significantly (mean = 0.16 ± 0.06 μM h^{-1}; $p < 0.05$; **Figure 2C**), with very low values in the central and east-central lake (L004 and LZ40) and slightly higher rates nearshore (LOBG).

St. Lucie Estuary

NH_4^+ regeneration rates in the estuary were not statistically different between sampling events, and peak regeneration rates were observed in July 2016 (mean = 0.38 ± 0.15 μM h^{-1}; **Figure 2A**). NH_4^+ regeneration rates followed the same pattern as uptake rates in July 2016, with highest values observed at sites closest to the canal (SLE2 and SLE80) and decreasing toward the Atlantic Ocean (SLE8). In August 2017, regeneration rates at the lock (SLE80; 0.46 ± 0.08 μM h^{-1}) were similar to 2016 regeneration rates and decreased slightly along the salinity gradient (SLE5 and SLE7; **Figure 2B**). After the hurricane, NH_4^+ regeneration rates at SLE5 and SLE7 (mean = 0.16 ± 0.01 μM h^{-1}) remained similar to rates in August 2017. Ammonium regeneration rates in LO and SLE were positively correlated with temperature and Chl *a* and negatively correlated with salinity, NO_3^-, and TP concentrations (**Table 3**).

mcyD Abundance

Lake Okeechobee

Average abundance of the *mcyD* gene in August 2017 was 5.08 ± 1.45 × 10^6 copies ml^{-1} (**Figure 3A**), with highest *mcyD* gene abundance at L004 in bottom water (7.88 × 10^6 copies ml^{-1}) and lowest at L004 in surface water (3.02 × 10^6 copies ml^{-1}). *mcyD* abundance decreased after the hurricane (**Figure 3B**) and was significantly lower than in August (mean = 8.17 ± 6.36 × 10^4 copies ml^{-1}; $p < 0.05$). After the

TABLE 3 | Kendall correlation for non-parametric data.

		Temperature	Dissolved oxygen	pH	Salinity	Chl *a*	NH_4^+	NO_2^-	NO_3^-	OP	Urea	TN	TP	*mcyD*
Uptake L	Kendall T	**0.42**	0.33	0.11	−0.45	0.23	0.07	−0.15	**−0.53**	−0.20	−0.25	**−0.43**	**−0.47**	0.28
	p-value	**0.03**	0.07	0.52	0.09	0.21	0.72	0.42	**0.004**	0.28	0.18	**0.03**	**0.02**	0.24
Uptake D	Kendall T	0.30	**0.55**	0.27	−0.40	0.05	−0.25	**−0.40**	−0.31	**−0.48**	**−0.50**	−0.01	**−0.62**	**0.60**
	p-value	0.11	**0.003**	0.15	0.14	0.79	0.18	**0.03**	0.08	**0.01**	**0.01**	0.95	**0.00**	**0.01**
Regeneration	Kendall T	**0.38**	0.33	0.18	**−0.63**	**0.37**	0.03	−0.21	**−0.37**	−0.20	−0.11	−0.18	**−0.45**	0.47
	p-value	**0.04**	0.07	0.32	**0.02**	**0.05**	0.86	0.24	**0.05**	0.28	0.52	0.35	**0.02**	0.06
mcyD	Kendall T	0.28	0.46	0.38	−0.33	0.42	−0.20	−0.46	−0.29	−0.47	−0.24	0	**−0.83**	
	p-value	0.27	0.06	0.12	0.60	0.09	0.42	0.06	0.24	0.06	0.33	1	**0.00**	

Statistically significant ($p < 0.05$) Kendall's Tau coefficients are bold.

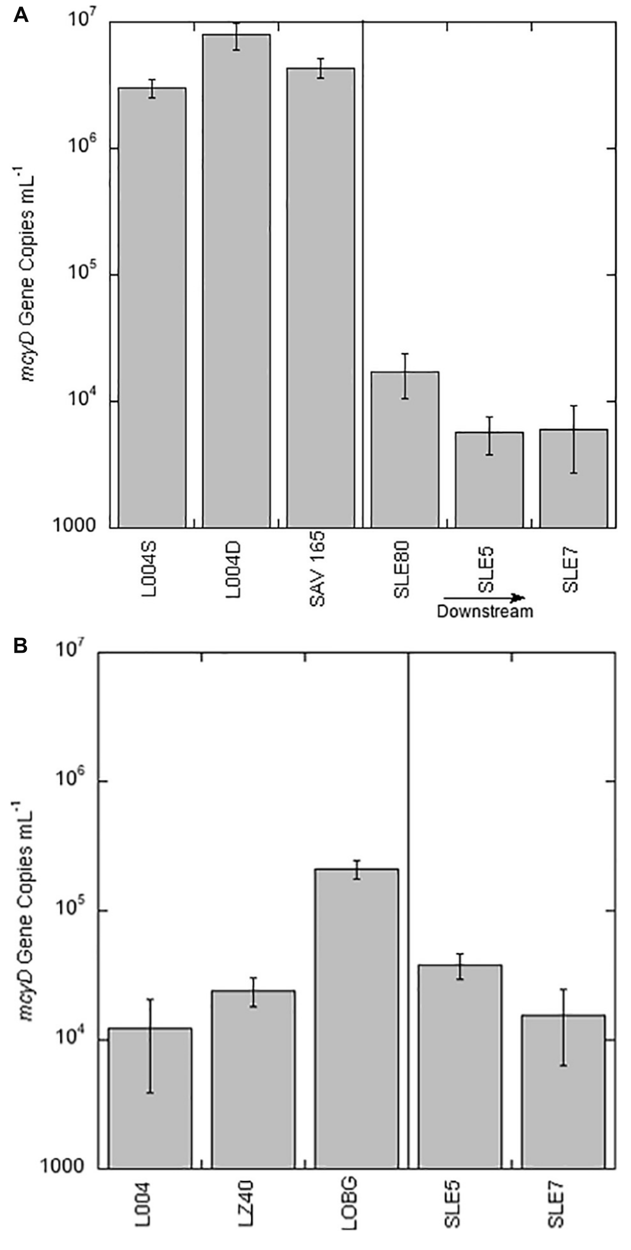

FIGURE 3 | *mcyD* gene abundance ± one standard deviation in Lake Okeechobee and St. Lucie Estuary in August 2017 **(A)** and September 2017 **(B)**. Vertical line divides stations in the lake from stations in the estuary. S = surface water; D = bottom water.

hurricane, highest and lowest abundances of the *mcyD* gene were observed near shore at LOBG and in the east-central region (L004; **Figure 3B**), respectively. *mcyD* gene abundance was negatively correlated with NO_3^- and TP concentrations (**Table 3**; $p < 0.05$).

St. Lucie Estuary

Abundance of *mcyD* in SLE in August 2017 (mean = $9.67 \pm 3.82 \times 10^3$ copies ml^{-1}) was significantly lower than in LO (**Figure 3A**; $p < 0.05$). Highest abundance of *mcyD* in August in SLE was observed at SLE80 near the canal, while lowest abundance was observed further along the salinity gradient at SLE5 (**Figure 3A**). After the hurricane, *mcyD* abundance in SLE (mean = $2.69 \pm 1.14 \times 10^4$ copies ml^{-1}; **Figure 3B**) was slightly greater than in August, but not statistically different ($p > 0.05$).

DISCUSSION

NH_4^+ Uptake During 2016 and 2017 Microcystis Blooms

Increased rainfall in 2016, an El Niño year, led to increased water levels in LO, requiring the release of billions of gallons of lake water through the St. Lucie Canal into SLE (**Figure 4A**; Kramer et al., 2018). Release of high nutrient freshwater into the brackish estuary created ideal conditions for a *Microcystis* bloom to develop (Kramer et al., 2018). In 2017, the net flow of water from LO and SLE was lower until Hurricane Irma made landfall in September (**Figure 4B**). We compared NH_4^+ cycling rates in LO and SLE during two summer blooms and 10 days after Hurricane Irma disturbance.

Potential NH_4^+ uptake rates measured in LO and SLE were on par with rates reported in other eutrophic and hypereutrophic ecosystems (McCarthy et al., 2007; Paerl et al., 2011; Gardner et al., 2017; Hampel et al., 2018), but higher than those previously reported in LO (0.58 ± 0.01 μM h^{-1}, James et al., 2011; 0.67 ± 0.15 μM h^{-1}, Gu et al., 1997). NH_4^+ uptake values in this study varied significantly based on bloom intensity and water flow (**Figure 2**). Peak bloom uptake rates in LO (August 2017, mean = 2.88 ± 1.25 μM h^{-1}) were similar to rates reported during the annual *Planktothrix* bloom in Sandusky Bay, Lake Erie (Hampel et al., 2019), *Microcystis* blooms in hypereutrophic Lake Taihu (Paerl et al., 2011; Hampel et al., 2018), and in hypereutrophic Lake Maracaibo, Venezuela (Gardner et al., 1998).

In July 2016 (El Niño year), potential NH_4^+ uptake rates were comparable between the lake and the estuary (**Figure 2A**). Bloom conditions were present in both systems, with high abundances of *Microcystis* (95% of algal biomass) and high MC and Chl *a* concentrations (Kramer et al., 2018). In the estuary, potential NH_4^+ uptake decreased following a gradient from the lock (SLE80, SLE2) into the saline part of the estuary (SLE8; **Figure 3A**). This eastward decrease in NH_4^+ dynamics corresponded with decreasing Chl *a* values in this study (**Table 1**), as well as decreased Chl *a* and MC concentrations and *mcyE* abundance reported previously (Kramer et al., 2018). Light NH_4^+ uptake rates exceeded dark uptake rates in both systems, suggesting that NH_4^+ demand was dominated by photoautotrophs.

In contrast, without water releases from LO in 2017 (**Figure 4B**), potential NH_4^+ uptake rates in the lake were significantly higher than in the estuary (**Figure 2B**). However, NH_4^+ uptake rates, Chl *a* concentrations, and *mcyD* abundances (**Figure 3A**) in SLE followed a similar pattern as in 2016, with highest values upstream (SLE80) and decreasing toward the coast. These results reflect the influence of water releases for flood

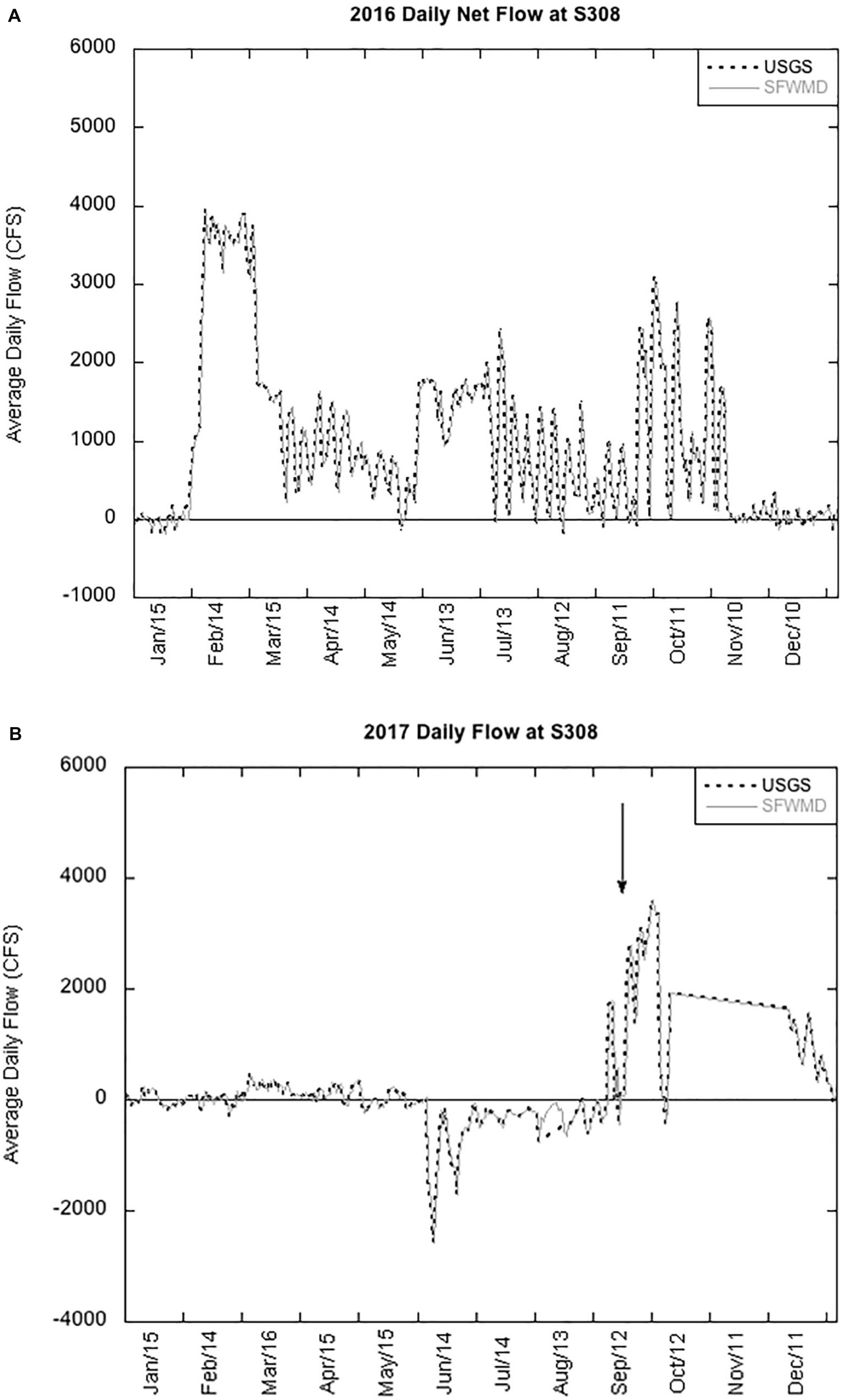

FIGURE 4 | Daily flow rates at the S308 lock between Lake Okeechobee and St. Lucie Estuary in 2016 **(A)** and 2017 **(B)** measured by U.S. Geological Survey (USGS) and South Florida Management District (SFWMD). The arrow points to increased flow during the Hurricane Irma disturbance.

control and support previous work showing that flood prevention practices in the Okeechobee region drive cyanoHABs in the downstream estuary, even when it may be beneficial for the trophic status of the lake (Lapointe et al., 2012; Phlips et al., 2012; Julian and Osborne, 2018).

Interestingly, *mcyD* abundance showed a strong, positive correlation with dark NH_4^+ uptake rates. *Microcystis* has been shown to synthesize MC at night (Penn et al., 2014; Davenport et al., 2019), suggesting that MC has a role in *Microcystis* diurnal metabolism. Dark NH_4^+ uptake rates observed here may be involved in MC production, but night time MC synthesis has not been extensively studied and merits future research, including diurnal transcriptomics and gene expression experiments.

Hurricane Irma

After Hurricane Irma, potential NH_4^+ uptake rates in both systems significantly decreased (**Figure 2C**). Uptake rates at pelagic stations (L004 and LZ40) were the lowest measured in LO in this study ($<0.5\ \mu M\ h^{-1}$) and suggest decreased algal biomass and activity. In contrast, uptake rates close to the shore (LOBG) were significantly higher than in the central lake ($1.2 \pm 0.07\ \mu M\ h^{-1}$), despite high ambient NH_4^+ concentrations (**Table 1**). Algal biomass may have accumulated along shorelines, driven by winds and seiches. Post-hurricane abundance of *mcyD* in LO also decreased significantly, and *mcyD* was most abundant at the shoreline station (LOBG, **Figure 3B**), where peak NH_4^+ uptake rates were also recorded (**Figure 2C**).

NH_4^+ uptake rates and Chl *a* concentrations in SLE after the hurricane were significantly lower, but *mcyD* abundance remained unchanged (**Figure 3B**). Following Hurricane Wilma in 2005, the phytoplankton community in LO shifted toward diatoms (James et al., 2008). Under poor light conditions, such as high turbidity and low water column stability, diatoms may have outcompeted cyanobacteria (James et al., 2008). Indeed, turbidity and total suspended solids (TSSs) increased significantly after the hurricane in both LO and SLE (**Supplementary Table 1**). Cyanobacteria are also susceptible to flushing events (Paerl et al., 2018), and rapid flushing can also explain the lower Chl *a* concentrations in SLE (**Table 2**; Paerl et al., 2018). Net water flow at S308 increased after Hurricane Irma and remained high for the rest of the year (**Figure 4B**).

These results represent the short-term (10 days) response of a HAB to a major storm disturbance. Numerous other studies have reported long-term responses of cyanobacteria and phytoplankton to hurricanes/typhoons in other systems (Yannarell et al., 2007; Zhu et al., 2014; Paerl et al., 2018). These studies have reported that increased pulses of nutrient loading, along with wind-induced nutrient resuspension from the sediments, may ultimately stimulate HABs and amplify preexisting eutrophication (James et al., 2008; Zhu et al., 2014). The HAB in the LO and SLE region in 2018 was one of the largest recorded and may have been related to rainfall and high winds from Hurricane Irma and heavy rainfall in spring 2018 (Paerl et al., 2019). Our short-term lake and estuary responses to Hurricane Irma emphasize that studies focusing on both short and long-term effects are necessary for understanding hurricane impacts on shallow, eutrophic ecosystems and cyanoHAB dynamics.

Ammonium Regeneration

Actual NH_4^+ regeneration rates in the lake and estuary followed the same general pattern as NH_4^+ uptake rates. During the 2016 bloom, internal NH_4^+ regeneration rates in the lake were similar to regeneration rates in SLE. In July 2016, actual regeneration could support 43% of the potential light uptake in LO. Similarly, during the 2017 bloom, 38% of light uptake could be supported by regeneration, despite higher uptake rates. Previous NH_4^+ dynamics experiments in LO showed that ~35% of light uptake could be supported by regeneration (James et al., 2011). Following the hurricane, water column regeneration decreased significantly in LO and SLE, and only 24% of NH_4^+ uptake in LO could be supported by regeneration, likely due to flushing and decreased biomass post-disturbance.

Total nitrogen (TN) from external loading into LO is estimated at $\sim 6.36 \times 10^3$ tons yr^{-1} (James et al., 2009). LO can be divided into three distinct regions: littoral zone, nearshore (1–2 m depth), and pelagic zone (offshore; James et al., 2008). Acknowledging the temporal and spatial limitations of the data generated in this study, we extrapolated the measured regeneration rates in the pelagic zone of the lake (stations L004 and LZ40) and nearshore (stations SAV165 and LOBG from this study and L005 from James et al., 2011) to estimate how much NH_4^+ may be regenerated in LO annually relative to external N loads. Extrapolating summer bloom values in the pelagic zone of LO (estimated volume = 2.85 km^3), 2.86×10^5 tons of N yr^{-1} could be regenerated internally. This value is 45 times greater than the estimated external loading of TN (6.36×10^3 tons yr^{-1}; James et al., 2009). Nearshore, regeneration could supply 7.94×10^3 tons of N yr^{-1}. These extrapolations of rates measured in summer months are almost certainly an overestimate due to higher productivity and algal biomass. However, the same calculations, using significantly lower regeneration rates from September 2017, showed that 3.37×10^4 tons of N yr^{-1} can be regenerated in the pelagic water column after a major disturbance. While this value is much lower than those reported based on July and August rates, it is still five times greater than annual external TN loading. These results suggest that internal NH_4^+ regeneration supplements external TN loading in LO to a large degree, even following a major disturbance, which led to significantly lower regeneration rates. This exercise also illustrates the importance of characterizing internal nutrient dynamics on more extensive temporal and spatial scales to more explicitly constrain annual nutrient budgets.

Results from this study, showing that internal N recycling in the pelagic zone of LO supports a large proportion of primary producer NH_4^+ demand, are supported by other studies in hypereutrophic lakes experiencing cyanoHABs, including: Lake Balaton, Hungary (Présing et al., 2001); Lake Biwa, Japan (Haga et al., 1995; Takahashi et al., 1995); Missisquoi Bay, Lake Champlain, United States/Canada (McCarthy et al., 2013); Lake Taihu, China (Paerl et al., 2011; Hampel et al., 2018), and Lake

Erie, United States/Canada (Hampel et al., 2019). This study contributes to the growing literature showing that rapid NH_4^+ turnover rates can fuel and sustain HABs, despite low NH_4^+ concentrations (McCarthy et al., 2007; Hampel et al., 2019). In hypereutrophic Lake Taihu, about 60% of potential light uptake was supported by regeneration during a mid-summer bloom (June), and all potential NH_4^+ demand could be supported internally in late summer (August; Hampel et al., 2018). In Sandusky Bay (Lake Erie), summer NH_4^+ regeneration in the water column provided bioavailable N equivalent to ∼77% of the annual N load and could support most of the primary producer NH_4^+ demand during the HAB season (Hampel et al., 2019).

CONCLUSION

Results from this study provided insight into NH_4^+ and HAB dynamics in Lake Okeechobee and St. Lucie Estuary during summer HABs and after Hurricane Irma. We emphasize the importance of NH_4^+ cycling on HAB expansion in LO and downstream nutrient pollution in SLE. Results from this study support those from previous studies (Lapointe et al., 2012; Phlips et al., 2012; Kramer et al., 2018), which call for water management strategies that balance flood control and health of downstream estuaries. Previous management strategies (40% P reductions and reduced nutrient inflow from Everglades Agricultural Area; James et al., 2011) have not prevented cyanoHABs in the Okeechobee–St. Lucie system. We show that NH_4^+ regeneration plays an important role in Lake Okeechobee in sustaining cyanoHABs, even after a major disturbance. High nutrient loading, combined with internal recycling and climate change, will likely continue to exacerbate cyanoHABs in the Okeechobee-St. Lucie and other freshwater-estuarine systems if further N and P reductions are not implemented. Lastly, short-term lake and estuary responses to Hurricane Irma emphasize that studies focusing on both short and long-term effects are necessary for understanding hurricane impacts on shallow, eutrophic ecosystems and cyanoHAB dynamics.

AUTHOR CONTRIBUTIONS

SN, MM, and JH designed the study and analyzed and interpreted the data. JH and MR collected and analyzed the samples. JH primarily wrote the manuscript. All authors contributed to text and revised the manuscript.

FUNDING

Funding for this work was provided by Florida Sea Grant (Project No. PD-16-10 to MM and SN).

ACKNOWLEDGMENTS

We thank the South Florida Water Management District for providing lab space, boat access, and assistance with incubations. We especially thank Therese L. East for her extensive assistance with all aspects of the project. We also thank Captain David Lauer for boat access on Lake Okeechobee after Hurricane Irma, Daniel Hoffman, Justin Myers, and Ashlynn Boedecker for help with sample analysis, and Donnie Peterson for help with field sampling.

SUPPLEMENTARY MATERIAL

The Supplementary Material for this article can be found online at: https://www.frontiersin.org/articles/10.3389/fmars.2019.00640/full#supplementary-material

REFERENCES

Bender, M. A., Knutson, T. R., Tuleya, R. E., Sirutis, J. J., Vecchi, G. A., Garner, S. T., et al. (2010). Modeled impact of anthropogenic warming on the frequency of intense Atlantic hurricanes. *Science* 327, 454–458. doi: 10.1126/science.1180568

Beversdorf, L. J., Miller, T. R., and McMahon, K. D. (2015). Long-term monitoring reveals carbon and nitrogen metabolism key to microcystin production in eutrophic lakes. *Front. Microbiol.* 6:456. doi: 10.3389/fmicb.2015.00456

Blackburn, T. H. (1979). Method for measuring rates of nh(4) turnover in anoxic marine sediments, using a N-NH(4) Dilution technique. *Appl. Environ. Microb.* 37, 760–765.

Blomqvist, P., Petterson, A., and Hyenstrand, P. (1994). Ammonium-nitrogen: a key regulatory factor causing dominance of non-nitrogen-fixing cyanobacteria in aquatic systems. *Arch. Hydrobiol.* 132, 141–164.

Caperon, J., Schell, D., Hirota, J., and Laws, E. (1979). Ammonium excretion rates in Kaneohe Bay, Hawaii, measured by a 15N isotope dilution technique. *Mar. Biol.* 54, 33–40. doi: 10.1007/BF00387049

Croux, C., and Dehon, C. (2010). Influence functions of the Spearman and Kendall correlation measures. *Stat. Method. Appl.* 19, 497–515. doi: 10.1007/s10260-010-0142-z

Davenport, E. J., Neudeck, M. J., Matson, P. G., Bullerjahn, G. S., Davis, T. W., Wilhelm, S. W., et al. (2019). Metatranscriptomic analyses of diel metabolic functions during a Microcystis bloom in western Lake Erie (USA). *Front. Microbiol.* 10:2081. doi: 10.3389/fmicb.2019.02081

Davis, T. W., Berry, D. L., Boyer, G. L., and Gobler, C. J. (2009). The effects of temperature and nutrients on the growth and dynamics of toxic and non-toxic strains of Microcystis during cyanobacteria blooms. *Harmful Algae* 8, 715–725. doi: 10.1016/j.hal.2009.02.004

Davis, T. W., Bullerjahn, G. S., Tuttle, T., McKay, R. M., and Watson, S. B. (2015). Effects of increasing nitrogen and phosphorus concentrations on phytoplankton community growth and toxicity during *Planktothrix* blooms in Sandusky Bay. Lake Erie. *Environ. Sci. Technol.* 49, 7197–7207. doi: 10.1021/acs.est.5b00799

Ding, Y., Qin, B., Zhu, G., Wu, T., Wang, Y., and Luo, L. (2012). Effects of typhoon Morakot on a large shallow lake ecosystem, Lake Taihu, China: effects of typhoon morakot on a large shallow lake ecosystem. *Ecohydrology* 5, 798–807. doi: 10.1002/eco.270

Erisman, J. W., Galloway, J. N., Dise, N. B., Sutton, M. A., Bleeker, A., Grizzetti, B., et al. (2015). *Nitrogen: too Much of a Vital Resource*. Available at: http://www.louisbolk.org/downloads/3005.pdf (accessed October 3, 2018).

Fogel, M. L., Aguilar, C., Cuhel, R., Hollander, D. J., Willey, J. D., and Paerl, H. W. (1999). Biological and isotopic changes in coastal waters induced by Hurricane Gordon. *Limnol. Oceanogr.* 44, 1359–1369. doi: 10.4319/lo.1999.44.6.1359

Gardner, W. S., Cavaletto, J. F., Bootsma, H. A., Lavrentyev, P. J., and Troncone, F. (1998). Nitrogen cycling rates and light effects in tropical Lake Maracaibo, Venezuela. *Limnol. Oceanogr.* 43, 1814–1825. doi: 10.4319/lo.1998.43.8.1814

Gardner, W. S., Newell, S. E., McCarthy, M. J., Hoffman, D. K., Lu, K., Lavrentyev, P. J., et al. (2017). community biological ammonium demand: a conceptual model for cyanobacteria blooms in eutrophic lakes. *Environ. Sci. Technol.* 51, 7785–7793. doi: 10.1021/acs.est.6b06296

Glibert, P. M. (1988). "Primary productivity and pelagic nitrogen cycling," in *Nitrogen Cycling in Coastal Marine Environments*, eds T. H. Blackburn, and J. Sorensen (Chichester: John Wiley & Sons), 3–31.

Glibert, P. M. (2017). Eutrophication, harmful algae and biodiversity — Challenging paradigms in a world of complex nutrient changes. *Mar. Pollut. Bull.* 124, 591–606. doi: 10.1016/j.marpolbul.2017.04.027

Gobler, C. J., Burkholder, J. M., Davis, T. W., Harke, M. J., Johengen, T., Stow, C. A., et al. (2016). The dual role of nitrogen supply in controlling the growth and toxicity of cyanobacterial blooms. *Harmful Algae* 54, 87–97. doi: 10.1016/j.hal.2016.01.010

Gu, B., Havens, K. E., Schelske, C. L., and Rosen, B. H. (1997). Uptake of dissolved nitrogen by phytoplankton in a eutrophic subtropical lake. *J. Plankton Res.* 19, 759–770. doi: 10.1093/plankt/19.6.759

Haga, H., Nagata, T., and Sakamoto, M. (1995). Size-fractionated NH4+ regeneration in the pelagic environments of two mesotrophic lakes. *Limnol. Oceanogr.* 40, 1091–1099. doi: 10.4319/lo.1995.40.6.1091

Hampel, J. J., McCarthy, M. J., Gardner, W. S., Zhang, L., Xu, H., Zhu, G., et al. (2018). Nitrification and ammonium dynamics in Taihu Lake, China: seasonal competition for ammonium between nitrifiers and cyanobacteria. *Biogeosciences* 15, 733–748. doi: 10.5194/bg-15-733-2018

Hampel, J. J., McCarthy, M. J., Neudeck, M., Bullerjahn, G. S., McKay, R. M. L., and Newell, S. E. (2019). Ammonium recycling supports toxic Planktothrix blooms in Sandusky Bay, Lake Erie: evidence from stable isotope and metatranscriptome data. *Harmful Algae* 81, 42–52. doi: 10.1016/j.hal.2018.11.011

Harke, M. J., and Gobler, C. J. (2015). Daily transcriptome changes reveal the role of nitrogen in controlling microcystin synthesis and nutrient transport in the toxic cyanobacterium, Microcystis aeruginosa. *BMC Genomics* 16:1068. doi: 10.1186/s12864-015-2275-9

Havens, K. E., Fukushima, T., Xie, P., Iwakuma, T., James, R., Takamura, N., et al. (2001a). Nutrient dynamics and the eutrophication of shallow lakes Kasumigaura (Japan), Donghu (PR China), and Okeechobee (USA). *Environ. Pollut.* 111, 263–272. doi: 10.1016/S0269-7491(00)00074-9

Havens, K. E., Jin, K.-R., Rodusky, A. J., Sharfstein, B., Brady, M. A., East, T. L., et al. (2001b). Hurricane effects on a shallow lake ecosystem and its response to a controlled manipulation of water level. *Sci. World J.* 1, 44–70. doi: 10.1100/tsw.2001.14

Havens, K. E., Hanlon, C., and James, R. T. (1994). Seasonal and spatial variation in algal bloom frequencies in lake okeechobee, Florida, U.S.A. *Lake Reserv. Manage.* 10, 139–148. doi: 10.1080/07438149409354185

Havens, K. E., James, R. T., East, T. L., and Smith, V. H. (2003). N:P ratios, light limitation, and cyanobacterial dominance in a subtropical lake impacted by non-point source nutrient pollution. *Environ. Pollut.* 122, 379–390. doi: 10.1016/S0269-7491(02)00304-4

Huisman, J., Codd, G. A., Paerl, H. W., Ibelings, B. W., Verspagen, J. M. H., and Visser, P. M. (2018). Cyanobacterial blooms. *Nat. Rev. Microbiol.* 16, 471–483. doi: 10.1038/s41579-018-0040-1

James, R. T., Gardner, W. S., McCarthy, M. J., and Carini, S. A. (2011). Nitrogen dynamics in Lake Okeechobee: forms, functions, and changes. *Hydrobiologia* 669, 199–212. doi: 10.1007/s10750-011-0683-7

James, R. T., Havens, K., Zhu, G., and Qin, B. (2009). Comparative analysis of nutrients, chlorophyll and transparency in two large shallow lakes (Lake Taihu, P.R. China and Lake Okeechobee, USA). *Hydrobiologia* 627, 211–231. doi: 10.1007/s10750-009-9729-5

James, T. R., Chimney, M. J., Sharfstein, B., Engstrom, D. R., Schottler, S. P., East, T., et al. (2008). Hurricane effects on a shallow lake ecosystem, Lake Okeechobee, Florida (USA). *Fund. Appl. Limnol.* 172, 273–287. doi: 10.1127/1863-9135/2008/0172-0273

Jeppesen, E., Søndergaard, M., Meerhoff, M., Lauridsen, T. L., and Jensen, J. P. (2007). Shallow lake restoration by nutrient loading reduction—some recent findings and challenges ahead. *Hydrobiologia* 584, 239–252. doi: 10.1007/s10750-007-0596-7

Julian, P., and Osborne, T. Z. (2018). From lake to estuary, the tale of two waters: a study of aquatic continuum biogeochemistry. *Environ. Monit. Assess.* 190:90. doi: 10.1007/s10661-017-6455-8

Kaebernick, M., Neilan, B. A., Borner, T., and Dittmann, E. (2000). Light and the transcriptional response of the microcystin biosynthesis gene cluster. *Appl. Environ. Microb.* 66, 3387–3392. doi: 10.1128/AEM.66.8.3387-3392.2000

Kana, T. M., Darkangelo, C., Hunt, M. D., Oldham, J. B., Bennett, G. E., and Cornwell, J. C. (1994). Membrane inlet mass spectrometer for rapid high-precision determination of N2, O2, and ar in environmental water samples. *Anal. Chem.* 66, 4166–4170. doi: 10.1021/ac00095a009

Knutson, T. R., McBride, J. L., Chan, J., Emanuel, K., Holland, G., Landsea, C., et al. (2010). Tropical cyclones and climate change. *Nat. Geosci.* 3:157.

Kramer, B. J., Davis, T. W., Meyer, K. A., Rosen, B. H., Goleski, J. A., Dick, G. J., et al. (2018). Nitrogen limitation, toxin synthesis potential, and toxicity of cyanobacterial populations in Lake Okeechobee and the St. Lucie River Estuary, Florida, during the 2016 state of emergency event. *PLoS One* 13:e0196278. doi: 10.1371/journal.pone.0196278

Lapointe, B. E., Herren, L. W., and Bedford, B. J. (2012). Effects of hurricanes, land use, and water management on nutrient and microbial pollution: St. Lucie Estuary, Southeast Florida. *J. Coastal Res.* 285, 1345–1361. doi: 10.2112/JCOASTRES-D-12-00070.1

Lapointe, B. E., Herren, L. W., and Paule, A. L. (2017). Septic systems contribute to nutrient pollution and harmful algal blooms in the St. Lucie Estuary, Southeast Florida, USA. *Harmful algae* 70, 1–22. doi: 10.1016/j.hal.2017.09.005

McCarthy, M. J., Gardner, W. S., Lavrentyev, P. J., Moats, K. M., Jochem, F. J., and Klarer, D. M. (2007). Effects of hydrological flow regime on sediment-water interface and water column nitrogen dynamics in a great lakes coastal wetland (Old Woman Creek, Lake Erie). *J. Great Lakes Res.* 33, 219–231. doi: 10.3394/0380-1330(2007)33%5B219:eohfro%5D2.0.co;2

McCarthy, M. J., Gardner, W. S., Lehmann, M. F., and Bird, D. F. (2013). Implications of water column ammonium uptake and regeneration for the nitrogen budget in temperate, eutrophic Missisquoi Bay, Lake Champlain (Canada/USA). *Hydrobiologia* 718, 173–188. doi: 10.1007/s10750-013-1614-6

McCarthy, M. J., Gardner, W. S., Lehmann, M. F., Guindon, A., and Bird, D. F. (2016). Benthic nitrogen regeneration, fixation, and denitrification in a temperate, eutrophic lake: effects on the nitrogen budget and cyanobacteria blooms: sediment N cycling in Missisquoi Bay. *Limnol. Oceanogr.* 61, 1406–1423. doi: 10.1002/lno.10306

McCarthy, M. J., James, R. T., Chen, Y., East, T. L., and Gardner, W. S. (2009). Nutrient ratios and phytoplankton community structure in the large, shallow, eutrophic, subtropical Lakes Okeechobee (Florida, USA) and Taihu (China). *Limnology* 10, 215–227. doi: 10.1007/s10201-009-0277-5

Monchamp, M. E., Pick, F. R., Beisner, B. E., and Maranger, R. (2014). Nitrogen forms influence microcystin concentration and composition via changes in cyanobacterial community structure. *PLoS One* 9:e85573. doi: 10.1371/journal.pone.0085573

Moss, B., Mckee, D., Atkinson, D., Collings, S. E., Eaton, J. W., Gill, A. B., et al. (2003). How important is climate? Effects of warming, nutrient addition and fish on phytoplankton in shallow lake microcosms: climate change and phytoplankton. *J. Appl. Ecol.* 40, 782–792. doi: 10.1046/j.1365-2664.2003.00839.x

Newell, S. E., Babbin, A. R., Jayakumar, A., and Ward, B. B. (2011). Ammonia oxidation rates and nitrification in the Arabian Sea: arabian sea ammonia oxidation and nitrification. *Glob. Biogeochem. Cycles* 25:4016. doi: 10.1029/2010GB003940

Paerl, H. W., Bales, J. D., Ausley, L. W., Buzzelli, C. P., Crowder, L. B., Eby, L. A., et al. (2001). Ecosystem impacts of three sequential hurricanes (Dennis, Floyd, and Irene) on the United States' largest lagoonal estuary, Pamlico Sound, NC. *Proc. Natl. Acad. Sci. U.S.A.* 98, 5655–5660. doi: 10.1073/pnas.101097398

Paerl, H. W., Crosswell, J. R., Van Dam, B., Hall, N. S., Rossignol, K. L., Osburn, C. L., et al. (2018). Two decades of tropical cyclone impacts on North Carolina's estuarine carbon, nutrient and phytoplankton dynamics: implications for biogeochemical cycling and water quality in a stormier world. *Biogeochemistry* 141, 307–322. doi: 10.1007/s10533-018-0438-x

Paerl, H. W., Gardner, W. S., Havens, K. E., Joyner, A. R., McCarthy, M. J., Newell, S. E., et al. (2016). Mitigating cyanobacterial harmful algal blooms in aquatic ecosystems impacted by climate change and anthropogenic nutrients. *Harmful Algae* 54, 213–222. doi: 10.1016/j.hal.2015.09.009

Paerl, H. W., Havens, K. E., Hall, N. S., Otten, T. G., Zhu, M., Xu, H., et al. (2019). Mitigating a global expansion of toxic cyanobacterial blooms: confounding effects and challenges posed by climate change. *Mar. Freshw. Res.* doi: 10.1071/mf18392

Paerl, H. W., Xu, H., McCarthy, M. J., Zhu, G., Qin, B., Li, Y., et al. (2011). Controlling harmful cyanobacterial blooms in a hyper-eutrophic lake (Lake Taihu, China): the need for a dual nutrient (N & P) management strategy. *Water Res.* 45, 1973–1983. doi: 10.1016/j.watres.2010.09.018

Penn, K., Wang, J., Fernando, S. C., and Thompson, J. R. (2014). Secondary metabolite gene expression and interplay of bacterial functions in a tropical freshwater cyanobacterial bloom. *ISME J.* 8, 1866–1878. doi: 10.1038/ismej.2014.27

Phlips, E. J., Badylak, S., Hart, J., Haunert, D., Lockwood, J., O'Donnell, K., et al. (2012). Climatic influences on autochthonous and allochthonous phytoplankton blooms in a subtropical estuary, St. Lucie Estuary, Florida, USA. *Estuar. Coast.* 35, 335–352. doi: 10.1007/s12237-011-9442-2

Présing, M., Herodek, S., Preston, T., and Vörös, L. (2001). Nitrogen uptake and the importance of internal nitrogen loading in Lake Balaton. *Freshw. Biol.* 46, 125–139. doi: 10.1046/j.1365-2427.2001.00622.x

Takahashi, M., Hama, T., Matsunaga, K., and Handa, N. (1995). Nitrogenous nutrient uptake by phytoplankton and ammonium regeneration by microbial assemblage in Lake Biwa. *J. Plank. Res.* 17, 1027–1037. doi: 10.1093/plankt/17.5.1027

Yang, J., Gao, H., Glibert, P. M., Wang, Y., and Tong, M. (2017). Rates of nitrogen uptake by cyanobacterially-dominated assemblages in Lake Taihu, China, during late summer. *Harmful Algae* 65, 71–84. doi: 10.1016/j.hal.2017.04.001

Yannarell, A. C., Steppe, T. F., and Paerl, H. W. (2007). Disturbance and recovery of microbial community structure and function following Hurricane Frances. *Environ. Microbiol.* 9, 576–583. doi: 10.1111/j.1462-2920.2006.01173.x

Yin, G., Hou, L., Liu, M., Liu, Z., and Gardner, W. S. (2014). A novel membrane inlet mass spectrometer method to measure 15 NH 4 + for isotope-enrichment experiments in aquatic ecosystems. *Environ. Sci. Technol.* 48, 9555–9562. doi: 10.1021/es501261s

Zhang, J., Burke, P., Baldwin, L., Mo, C., and Hill, S. (2016). *Lake Okeechobee Watershed Tributary Nutrient Loading Trends WY2006-WY2015*. West Palm Beach, FL: South Florida Water Management District.

Zhu, M., Paerl, H. W., Zhu, G., Wu, T., Li, W., Shi, K., et al. (2014). The role of tropical cyclones in stimulating cyanobacterial (*Microcystis* spp.) blooms in hypertrophic Lake Taihu. *China. Harmful Algae* 39, 310–321. doi: 10.1016/j.hal.2014.09.003

Conflict of Interest: The authors declare that the research was conducted in the absence of any commercial or financial relationships that could be construed as a potential conflict of interest.

frontiers
in Marine Science

ORIGINAL RESEARCH
published: 05 November 2019
doi: 10.3389/fmars.2019.00671

Tropical Coastal Wetlands Ameliorate Nitrogen Export During Floods

***Maria Fernanda Adame*[1]*, *Melanie E. Roberts*[1], *David P. Hamilton*[1], *Christopher E. Ndehedehe*[1], *Vanessa Reis*[1], *Jing Lu*[1], *Matthew Griffiths*[2], *Graeme Curwen*[1] and *Mike Ronan*[2]**

[1] Australian Rivers Institute, Griffith University, Nathan, QLD, Australia, [2] Department of Environment and Science, Wetlands Team, Queensland Government, Brisbane, QLD, Australia

Wetlands can increase resilience to extreme climatic events and have a key role in protection and water quality improvement in coastal ecosystems. Studies in tropical coastal wetlands at a catchment scale are scarce, and most work has been undertaken on small, temperate wetlands. In this study, we tested whether natural coastal wetlands in a tropical catchment (Tully-Murray, Queensland, Australia) could ameliorate nitrogen (N) exported to the Great Barrier Reef during a flood event. We measured denitrification rates in different types of coastal wetlands (mangroves, saltmarshes, waterbodies with macrophytes, and floodplain wetlands dominated by *Melaleuca* spp.) to assess their potential contribution to N losses during the 6-day duration of a flood in March 2018. Denitrification potential was variable across the landscape, and we identified "hotspots" in sub-catchments with high NO_3^--N concentrations (0.4–0.6 mg L^{-1}) and large areas of wetlands (>800 ha, >40% of the sub-catchment). These hotspots can denitrify up to 10 t of NO_3^--N per day during a flood. We used our measured denitrification rates to provide input parameters for a model that includes the main biogeochemical processes affecting N transformations within wetlands (nitrification, denitrification, plant uptake, sedimentation, anammox, and mineralization), and accounts for transport via the duration, depth, and flow of water. Model simulations of a sub-catchment of the Tully-Murray indicate that flood inundation of large areas of natural wetlands (>40% of the sub-catchment area) could potentially remove 70% of the incoming NO_3^--N load in the first 24 h of the flood. The management and restoration of coastal tropical wetlands could play a critical role in sustaining the health of coastal ecosystems through water quality improvement.

Keywords: denitrification, dissolved inorganic nitrogen, Great Barrier Reef, nitrate, mangroves, *Melaleuca*, Wet Tropics

Edited by:
Eero Asmala,
University of Helsinki, Finland

Reviewed by:
Sanni Leea Aalto,
University of Eastern Finland, Finland
Naomi Susan Wells,
Southern Cross University, Australia

****Correspondence:***
Maria Fernanda Adame
f.adame@griffith.edu.au

Specialty section:
This article was submitted to
Marine Biogeochemistry,
a section of the journal
Frontiers in Marine Science

Received: *17 June 2019*
Accepted: *16 October 2019*
Published: *05 November 2019*

Citation:
Adame MF, Roberts ME, Hamilton DP, Ndehedehe CE, Reis V, Lu J, Griffiths M, Curwen G and Ronan M (2019) Tropical Coastal Wetlands Ameliorate Nitrogen Export During Floods. Front. Mar. Sci. 6:671. doi: 10.3389/fmars.2019.00671

INTRODUCTION

Coastal wetlands are one of the most valuable ecosystems on Earth, considered essential for climate change adaptation and mitigation (Duarte et al., 2013). They provide key ecosystem services, including food provisioning, carbon sequestration, flood protection, and improvements in water quality (Barbier et al., 2011). Coastal wetlands are effective at improving water quality through three processes that remove nitrogen (N): plant uptake, soil accretion, and denitrification, with the latter accounting for most of the removal (>90%, Adame et al., 2019b,c, **Figure 1**). Denitrification

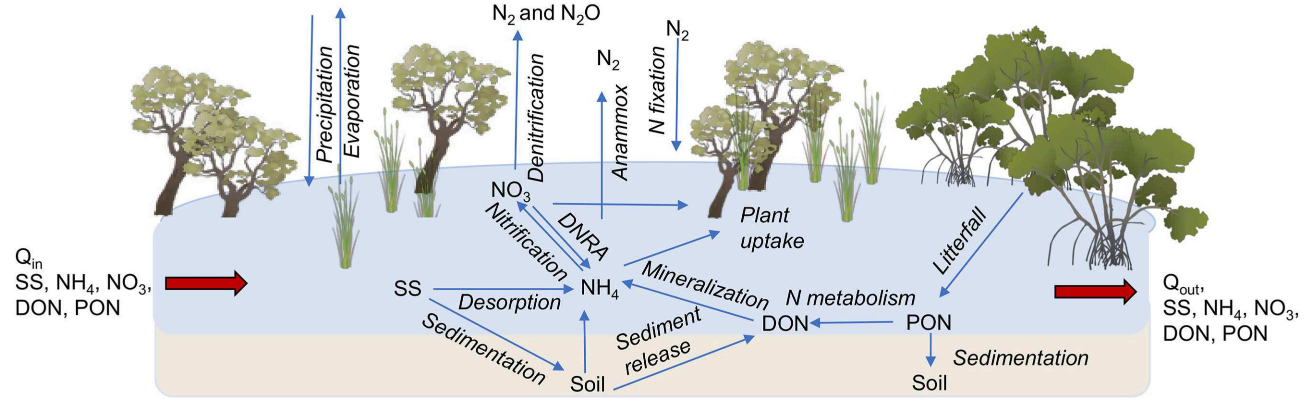

FIGURE 1 | Conceptual model of N fluxes during a flood in estuarine and palustrine wetlands in tropical Australia, which was used for the derivation of the numerical model.

is the conversion of nitrate (NO_3^-) to nitrous oxide (N_2O) and finally to nitrogen gas (N_2) and is the major pathway for permanent N removal from an ecosystem (Kulkarni et al., 2008). More recently, anaerobic ammonium oxidation (anammox) has been highlighted as an additional pathway for N removal through the conversion of nitrite (NO_2) and ammonium (NH_4^+) to N_2. Anammox is usually restricted to estuarine wetlands with low oxygen concentrations and accounts for 3–10% of N removal (Burgin and Hamilton, 2007; Zhou et al., 2014). Overall, denitrification is likely to be the most important pathway for N removal in coastal wetlands (Oliveira-Fernandes et al., 2012; Xiao et al., 2018), and thus a key process for the improvement of water quality by wetlands.

The potential to remove N through denitrification is closely associated with soil carbon and water NO_3^- concentration in many temperate (Piña-Ochoa and Álvarez-Cobelas, 2006; Zhou et al., 2014) and tropical wetlands (Adame et al., 2019b). Wetlands have carbon-rich soils due to high primary productivity (Mitsch and Gosselink, 2015), but NO_3^- concentrations can vary widely. The amount of NO_3^- a wetland receives is usually dependent on anthropogenic inputs (e.g., sewage, fertilizer) from the catchment (Wells et al., 2016). Additionally, wetlands obtain NO_3^- *in-situ* from nitrification, the conversion of NH_4^+ to NO_3^-, which, in some tropical wetlands, accounts for 30% of the NO_3^- that is denitrified (Adame et al., 2019b).

Wetlands can only improve water quality if they are hydrologically connected, i.e., if they are in contact with water long enough for denitrification to occur. Thus, hydrological connectivity is critical for the provision of ecosystem services through improvement of water quality. Many tropical regions have high hydrological variability, with frequent storms and intense rainfall events that connect large areas through flooding. The inundation of tropical catchments causes the delivery of large quantities of water and nutrients into the coastal zone (Junk et al., 1989; Junk and Furch, 1993; Wallace et al., 2008). In many tropical catchments, particularly during the dry season, fertilizers can accumulate as N in the soil; after a rainfall event, the highly mobile NO_3^- is flushed into coastal wetlands (Davis et al., 2016). The inundation of coastal wetlands by floodwaters can create biogeochemical "hot spots," which may contribute disproportionately to nutrient transformations, altering annual carbon, and N fluxes in the coastal zone (McClain et al., 2003). Denitrification fluxes occurring during floods are not easily accounted for but could be highly important.

In the Great Barrier Reef region, in the Wet Tropics of Australia, increased N loading from the catchment to the coastal zone due to intensification of agricultural activity has been highlighted as a significant stressor to the health of the reef (Hughes et al., 2015). Intense rainfall events are increasing in this region and are predicted to continue to increase as a result of climate change (ABM, 2019: 1970–2017, http://www.bom.gov.au/, Eccles et al., 2019). After intense rainfall, large areas of coastal wetlands are inundated, creating denitrification hotspots (Tomasek et al., 2019). Thus, coastal wetlands in tropical catchments could play a significant role in ameliorating the export of N into the coastal zone during flooding events.

In this study, we hypothesized that coastal wetlands could strongly influence N exports to the coastal zone. We tested the hypothesis in a catchment in north-east Australia that has intensive agricultural land use but also has large areas of coastal wetlands (**Figures 2A,C**). Rates of denitrification were measured in different types of coastal wetlands (mangroves, saltmarshes, waterbodies with macrophytes, and floodplain wetlands dominated by *Melaleuca* spp.) to assess their potential contribution to N losses during the 6-day duration of a flood in March 2018. We used the measured denitrification rates in a model to assess N losses during the flood. The model includes the main biogeochemical processes affecting N transformations within wetlands (nitrification, denitrification, anammox, plant uptake, sedimentation, and mineralisation) and accounts for transport via the duration, depth, and flow of water. We also tested for the presence of denitrification "hotspots" where large areas of wetland are flooded by water with relatively high NO_3^- concentrations.

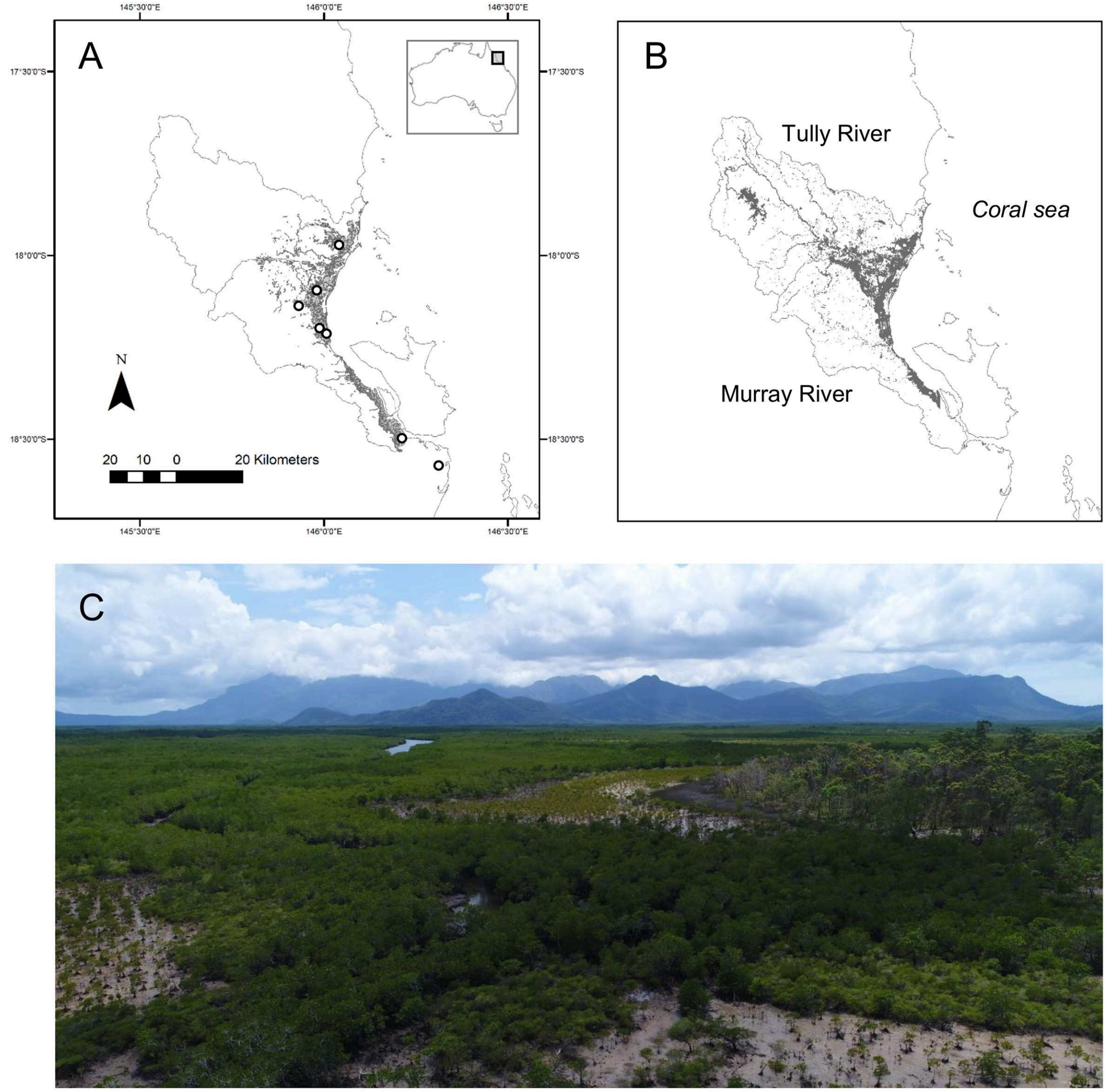

FIGURE 2 | (A) Wetland area within the catchments of the Tully-Murray River in tropical north-east Australia, and sampling locations from south to north: saltmarsh and mangroves at Hinchinbrook Channel, *Melaleuca quinquenervia* forest and freshwater marsh at Girramay National Park, lagoon with macrophytes (Nymphae spp. and grass at Barrett's Lagoon), *Melaleuca viridiflora* forest at Hull Heads National Park, and *Melaleuca-Eucalyptus* spp forest at Djiru National Park, **(B)** flood extent after intense rainfall (863 mm in 11 days) in March 30, 2018, and **(C)** composition of coastal wetlands with a mixture of *Melaleuca* forest, marshes and mangroves. Photo by MF Adame.

MATERIALS AND METHODS

Study Site

The Tully-Murray Rivers are located within the Wet Tropics region of north-east Australia. They drain a catchment of 279,200 ha and discharge into the Coral Sea and into the Great Barrier Reef (**Figure 2**). The climate is tropical with monthly mean temperatures ranging from 22 to 34°C (ABM, 2019: 1907–2018) and a mean annual rainfall of 2,700 mm (ABM, 2019: 1871–2018). The rivers in this region are characterized by dry periods during winter months and sporadic overbank floods in summer (between January and May) that inundate the adjacent wetlands from one to 12 days at a time (Karim et al., 2012). Contributions to flow from groundwater are also important, mainly after rainfall events, but also during the dry season (Rasiah et al., 2003). Tides in the region are classified as mesotidal with maximum amplitudes of 4 m (Lucinda Station, ABM, 2019).

The catchments of the Tully-Murray Rivers are characterized by alluvial fans in the lower slopes and an alluvial plain with swamps in wet areas close to the coast (Wilson and Baker, 1990). The soil types are typically Rudosol, Kandosol, and Sodosol on the alluvial fans, Dermosol, Kurosol, Vertosol, and Sodosol on the alluvial plain, Tenosol on the beach ridges, and Organosol in swamp areas (Isbell, 2002). The catchments have a total area of wetlands of 24,500 ha, defined according to the Ramsar convention as: "Areas of permanent or periodic/intermittent inundation with water that is static or flowing, fresh, brackish or salt." To be considered wetlands, they should support plants or animals adapted and dependent on wet conditions for at least part of their life cycle and have anaerobic, undrained soils that are saturated, flooded or ponded (WetlandInfo, 2019, https://wetlandinfo.des.qld.gov.au). Of the total wetland area of the catchments, 10,910 ha are estuarine, 9,390 ha are palustrine, and 200 ha are non-riverine waterbodies. Estuarine wetlands are influenced by tidal inundation and include mangroves, salt flats, and saltmarshes. Palustrine wetlands are vegetated swamps that are non-riverine or non-channel systems with more than 30% cover of emergent vegetation of grass, sedges, herbs, palms, or trees (*Melaleuca* and *Eucalyptus* spp., WetlandInfo, 2019).

The catchments of the Tully-Murray Rivers are characterized by steep mountains covered with tropical rainforests and a floodplain dominated by intensive cultivation of sugarcane and banana, as well as cattle grazing and pine plantations. As a result of intensive agricultural land use, mean annual N loads from rivers draining the catchments have increased significantly since European settlement. Dissolved inorganic N (DIN = NO_3^--N + NO_2-N + NH_4^+-N) has increased by a factor of five (from 170 to 840 t yr^{-1}) and particulate N by a factor of 27, from 14 to 380 t yr^{-1} in the Tully River and from 4 to 250 t yr^{-1} in the Murray River (Kroon et al., 2012). Current annual total nitrogen (TN) exports from the catchments are estimated at 2,320 t yr^{-1}, of which 1,310 t yr^{-1} are DIN (Kroon et al., 2012).

We measured denitrification rates at eight sites representative of coastal wetlands of these catchments. Previous studies have shown no significant differences in denitrification potential between the dry and wet seasons (Adame et al., 2019b). Thus, all measurements were conducted once at each site at the end of the wet season (May to June) in either 2017 or 2018. We measured two *Melaleuca* spp. palustrine wetlands (Girramay and Hull Heads National park), an ephemeral *Melaleuca–Eucalyptus* spp. palustrine wetland (Djiru National Park), two marshes (saltmarsh in the southern of Hinchinbrook Channel and a freshwater marsh), dominated by *Eleocharis* spp. in Girramay National Park), a mangrove forest dominated by *Brugueira guimnorriza,* and a coastal lagoon (Barrett's lagoon) with water lilies (*Nymphaea* spp.) and emergent grasses (**Figure 2A**). Denitrification rates for the two *Melaleuca* sites have previously been published in Adame et al. (2019b). The denitrification rates were used in conjunction with a map and hydrological characteristics of a flood that occurred on March 2018 to identify hotspots of denitrification. Finally, a numerical model was developed to estimate fluxes of different forms of N (NO_3^--N, NH_4^+-N), dissolved organic nitrogen (DON), and particulate organic nitrogen (PON) within a sub-catchment that was identified as a "denitrification hotspot." Detailed information on the methodology is given below.

Wetland Characteristics

At each site, we measured physicochemical characteristics of water and soil, including water temperature, electrical conductivity (EC), and pH with a calibrated water quality meter (ProPlus, YSI meter, OH, USA). Soil samples were analyzed for bulk density (BD) by weighing a dry sample of soil of known volume. Soils were also analyzed for N (%) and organic carbon (OC%) (EA-IRMS, Serco System at Griffith University). Water samples were collected in triplicate, filtered through a 0.45 μm membrane filter, and stored frozen before being analyzed for nutrients within the next week (colorimetric analyses; Chemistry Center, Department of Industry, Innovation and Science, Brisbane, Australia). Detection limits (mg L^{-1}) were: 0.002 for NH_4^+-N, and 0.001 for NO_x^--N and PO_4^--P.

Denitrification Rates

To measure denitrification rates, we used the isotope pairing technique (Nielsen, 1992; Steingruber et al., 2001), which consists of adding enriched NO_3^--^{15}N to water overlying sediments at a saturating concentration and estimating denitrification rates from ^{15}N-N_2 gas production. At each site, we collected intact sediment cores of ∼8 cm-depth inside Perspex tubes (4.8 cm internal diameter × 30 cm long) that were capped at the bottom with a rubber bung, filled with water collected from each site, and left to equilibrate overnight. The cores were sampled within each wetland in a location that had soil and vegetation representative of the site. The cores were taken 50 cm apart from each other and included small roots and leaf litter. For each experiment, we collected 12 sediment cores to allow three cores to be sampled at time 0, 2, and 5 h. For each experiment, we ran a blank sample of distilled water.

Nutrients were measured in three cores per treatment after flooding them with water and left overnight to equilibrate. The day after collection, the experiments were run at a nearby town (Ingham, Queensland) with similar ambient light and air temperature as in the field. The sediment cores were set in large plastic rectangular containers (1030 × 510 × 495 mm) filled with water maintained at a relatively constant temperature, which was recorded throughout the experiment (ProPlus, YSI meter, OH, USA; 29–31°C). At the beginning of the experiment, NO_3^--^{15}N was added to each core, and water samples were taken to measure NO_3^--N concentrations before and after ^{15}N- NO_3^- additions. The experiments were run with final concentrations between 0.02 and 0.56 mg L^{-1}, all within the range of natural background conditions (Water Monitoring Information Portal, Queensland Government, https://water-monitoring.information.qld.gov.au/). Cores were topped up with water and capped to minimize headspace. Natural water movement was simulated by a stirrer bar suspended ∼3 cm above the sediment of each core driven by a magnet (rotating at ∼60–70 rpm Adame et al., 2019a. After ∼20 min, one core from each batch was sacrificed as a time zero measurement by adding 1 ml of 50% w/v of zinc chloride ($ZnCl_2$) that was mixed throughout the sediment and overlying water to halt bacterial activity. Triplicate 10 mL-water samples from each core were collected using a syringe and placed in a 12.5-ml Exetainer vial (Labco, High Wycombe, UK) with 250 μL of 50% w/v $ZnCl_2$. At each time interval, a new set of cores was sacrificed. The headspace gas was analyzed by continuous-flow mass spectrometry for $^{28}N_2$, $^{29}N_2$, and $^{30}N_2$-gas (EA-IRMS, Serco System at Griffith University).

Denitrification rates were estimated from equations of Steingruber et al. (2001), from which we calculated the following:

D_{15}: denitrification from labeled^{15} NO_3^- as from the production rate of $^{29}N_2$ and $^{30}N_2$:

$$D_{15} = r_{29} + 2r_{30} \tag{1}$$

where r_{29} and r_{30} are the production rates of $^{29}N_2$ and $^{30}N_2$, respectively,

D_{14}: denitrification from unlabeled ^{14} NO_3^-:

$$D_{14} = D_{15} \cdot \frac{r_{29}}{2r_{30}}, \tag{2}$$

D_t = total denitrification or potential denitrification:

$$D_t = D_{15} + D_{14}, \tag{3}$$

$D_w$tot: total denitrification of NO_3^- derived from the water column:

$$D_w{}^{tot} = \frac{D_{15}}{\varepsilon} \tag{4}$$

where ε is NO_3^- enrichment during incubation from $^{15}NO_3$ additions:

$$\varepsilon = \frac{[NO_3{}^-]a - [NO_3{}^-]b}{[NO_3{}^-]_a}, \tag{5}$$

where a and b are NO_3 concentrations after and before $^{15}NO_3^-$ addition,

D_w: denitrification from NO_3^- derived from the water column and corrected for tracer addition:

$$D_w = D_w{}^{tot}(1 - \varepsilon), \tag{6}$$

D_n: Coupled nitrification-denitrification:

$$D_n = D^{tot} - D_w{}^{tot}. \tag{7}$$

Denitrification rates are reported for ambient light conditions, and detection limits were 0.01 mg N m^{-2} h^{-1}.

Inundation Mapping

Between 18 and 29 March 2018, a major rainfall event occurred in the area (863 mm in 11 days; Tully Sugar Mill Station 32042, ABM, 2019) causing daily discharges in the Tully River to peak at 86,000 ML day^{-1} (**Figure 2B**, **Supplementary Figure 1**). During this event, the floodplain started to inundate, which usually occurs at river flows >37,000 ML day^{-1} (Wallace et al., 2009). This level of flooding is representative of an event with a return period of about 4 years (Wallace et al., 2009). River discharges into the coastal flooding zone are between 700,000 and 1,500,000 ML throughout an event of this magnitude (Wallace et al., 2009).

Three tiles of level 1C Sentinel-2 data were acquired for 30 March 2018 and combined to generate a mosaic for the Tully-Murray catchment. The image scenes were retrieved from the European Space Agency open access data portal (https://scihub.copernicus.eu/dhus/#/home). The data were calibrated to standard surface reflectance values using the QUick Atmospheric Correction Code (QUAC, Bernstein et al., 2005) module in ENVI 5.5 (Exelis Visual Information Solutions). The flood inundation extent was quantified from the mosaic by applying an automated water extraction metric, the Modified Normalized Difference Water Index (MNDWI, Xu, 2006), which combines the green (G) and mid-infrared (MIR) bands (B) as MNDWI = $B_G - B_{MIR}/B_G + B_{MIR.}$

Daily stream water level and river discharge data from the Tully River (2017–2018) observed at Euramo (ID: 113006A; −17.99 S,145.94 E) were used to assess flood characteristics. Discharge and water level were integrated based on a non-parametric approach that relies on the empirical joint probability of any two hydrological units to estimate multivariate standardized indicators (MSIs) (Farahmand and AghaKouchak, 2015; Ndehedehe et al., 2016). Daily steps (493) from four different time series (i.e., mean and maximum values each of discharge and water level) were used to estimate two sets of MSIs (i.e., mean discharge/water level and maximum discharge/water level). The MSIs are interpreted similarly to the range of variability approach in which the value of one standard deviation is used to set the thresholds in the characterization of hydrological conditions (e.g., values > 1.5 are very wet and < -1.5 are very dry).

Wetland Area and Flooded Area

We used the sub-catchment areas of the Tully-Murray Rivers obtained by the stream network and a digital elevation model (DEM) as defined by the Paddock to Reef Integrated Monitoring, Modeling, and Reporting Program (P2R, Paddock to Reef program, Queensland Government, https://www.reefplan.qld.gov.au/tracking-progress/paddock-to-reef). We selected 28 sub-catchments within 25 km of the coastal zone (**Figure 4**) and obtained their wetland area, including palustrine, estuarine, and water bodies (WetlandInfo, 2019). The area of wetlands within each sub-catchment that was flooded during the rainfall event was determined by subtracting total wetland area minus flooding area.

We estimated the volume of water overlying wetlands for one sub-catchment (SC187) located within the coastal floodplain of the lower Murray River (**Figure 4C**, the mouth of the Murray River). Wetlands represented repeated information 46% of the selected sub-catchment area (**Supplementary Figure 2**). A Lidar image of 1-m resolution (Queensland LiDar Data, Cassowary Coast Project 2016, www.qldspatial.information.qld.gov.au/) with a vertical accuracy of 30 cm and horizontal accuracy of 80 cm was used in conjunction with the Sentinel imagery to calculate the height threshold above the main channel of the lower Murray River. In the wetland areas that were flooded, water depth was calculated by subtracting the DEM land values from the water surface elevation. Data analyses were conducted with ArcMap (v10.3 and 10.6, Esri ArcGIS, CA, USA).

Nitrogen Fate and Transport

Daily water flows ($m^3\ s^{-1}$), and dissolved inorganic N (DIN), dissolved organic N (DON) and particulate N (PN) loads ($kg\ d^{-1}$) were obtained from the P2R Program for each of the sub-catchment units. The model uses the eWater CRC Source Catchments modeling framework (eWater Limited, ACT, Australia, www.ewater.org.au) to simulate sediment, nutrients and pesticide runoff within the Great Barrier Reef catchments. Simulated N outputs are obtained at the sub-catchment scale by dividing each sub-catchment into land-use types and estimating runoff from rainfall, constituent generation and a filter model (For further information, see www.reefplan.qld.gov.au/tracking-progress/paddock-to-reef). For this exercise, we obtained the daily flow of water, loads ($kg\ d^{-1}$) and concentrations ($mg\ L^{-1}$) of DIN, DON, and PN from 22 March to 1 April 2018.

We identified "denitrification hotspots" within sub-catchments during 1 day of flooding (March 30, 2018, see inundation map **Figure 2B**). The hotspots were identified by multiplying the denitrification potential for wetlands within each sub-catchment (D_t; $mg\ m^{-2}\ h^{-1}$), by the area of wetlands that were flooded during the day. Total denitrification was predicted from the NO_3^- concentration of the floodwater, which is a major driver of denitrification for similar wetlands in the region (Adame et al., 2019b, this study, **Figure 3**) and other tropical and temperate wetlands (Piña-Ochoa and Álvarez-Cobelas, 2006). The NO_3^- concentrations were obtained from the Source Catchment model and corroborated by direct measurements obtained by the Water Quality Monitoring Program of the Great Barrier Reef (Euramo station at Tully River; Orr et al., 2014). The N concentrations during flooding are usually between 0.046 and 0.24 $mg\ L^{-1}$ for PN, 0.14 and 0.26 $mg\ L^{-1}$ for NO_3^--N, 0.004 and 0.012 $mg\ L^{-1}$ for NH_4^+-N and 0.08 and 0.19 $mg\ L^{-1}$ for DON (Orr et al., 2014). Most of the DIN during floods is in the form of NO_x -N (>95%, Orr et al., 2014).

Nitrogen Transformation Modeling

The fate of different forms of N (NO_3^--N, NH_4^+-N, DON, and PON) was modeled for water flooding the sub-catchment SC187, our identified "denitrification hotspot." The sub-catchment **Supplementary Table 1** has a total wetland area of 2,574 ha, of which 62% is estuarine wetland, 36% palustrine wetland, and the remainder (2%) riverine and lacustrine wetlands. The model describes the variation in the quantity of each form of N together with fine suspended sediment in the wetland (Equations 8–13). The wetland within this sub-catchment was simulated as a single box model considering the most important N processes in wetlands (**Figure 1**). During a flood, N enters the wetlands as rainfall and runoff. Internal releases to water within the wetland are from leaf litter and bottom-sediment release of DON and NH_4^+. Water column ammonium is converted to NO_3^- by nitrification, NO_3^- can be denitrified to N gases (N_2, N_2O) according to our measured rates (see above) or through anammox (NO_2^- and NH_4^+ converted to N_2), removing N permanently from the system. Both NH_4^+ and NO_3^- can be taken up by plants and algae, and water column PON (estimated as 98% of PN, Garzon-Garcia et al., 2018) can be deposited to the wetland sediment. The equations representing these processes for each nitrogen constituent in the model are given below, first for NO_3^--N mass in the wetland as a function of time:

$$\begin{aligned}\frac{d\,NO_3}{dt} &= Q_{in}\,C_{NO_3}^{flow\ in} - Q_{out}\,\frac{NO_3}{V} + A\,R\,C_{NO_3}^{rain}\\ &+ k_1\,\theta^{T-20}\,NH_4\left[\frac{NH_4\,/\,V}{NH_4/V\ +\ K_1}\right] - a_1\,\theta^{T-20}\,A\ (1\\ &- f(N)\big) - a_2\,\theta^{T-20}\,A\left[\frac{NO_3\,/\,V}{NO_3/V\ +\ K_{a2}}\right]\\ &-\frac{a_3}{2}\,\theta^{T-20}\,A\,\frac{\mathit{min}\ (NH_4, NO_3)/V}{K_{a3} + \mathit{min}\ (NH_4, NO_3)/V}\end{aligned} \tag{8}$$

where NO_3 is the total mass of NO_3^--N in the wetland, $C_{NO_3}^{flow\ in}$ is the concentration of NO_3^--N in the inflow, Q_{in} and Q_{out} are the inflow to and outflow from the wetland, respectively, A and V are the wetland area and volume, respectively, R is rainfall, $C_{NO_3}^{rain}$ is the concentration of NO_3^--N in rainfall, k_1 is the nitrification rate, K_1 is the half-saturation constant for effect the ammonium concentration on nitrification, a_1, a_2, and a_3 are the areal rates of plant uptake of nitrogen, denitrification, and anammox respectively, and K_{a2} and K_{a3} are the half-saturation constants for effect of nitrate concentration on denitrification and anammox. The nitrogen conversion rates are given for a reference temperature of 20°C with the influence of temperature (T) represented by a non-dimensional multiplier term θ^{T-20}. The value of the temperature multiplier was set at 1.073 (equivalent to doubling of the biogeochemical rate for each 10°C increase in temperature) for all processes as there was not enough information to vary it among all biogeochemical processes. f(N) is a preference factor for ammonium vs. nitrate uptake: where K_N is the half saturation for plant uptake

$$\begin{aligned}f(N) &= \frac{NH_4\ NO_3}{(NH_4\ +\ V\,K_N)\,(NO_3\ +\ V\,K_N)}\\ &+ \frac{NH_4\ V\,K_N}{(NH_4\ +\ NO_3)\,(NO_3\ +\ V\,K_N)}\end{aligned} \tag{9}$$

Ammonium mass in the wetland is given as:

$$\begin{aligned}\frac{d\,NH_4}{dt} &= Q_{in}C_{NH_4}^{flow\ in} - Q_{out}\frac{NH_4}{V} + ARC_{NH_4}^{rain}\\ &- k_1\theta^{T-20}NH_4\left[\frac{NH_4\,/\,V}{NH_4/V\ +\ K_1}\right] - a_1\theta^{T-20}Af\,(N)\\ &+ k_2\theta^{T-20}DON\left[\frac{DON\,/\,V}{DON/V\ +\ K_2}\right] + a_4\theta^{T-20}A\\ &+ k_3\theta^{T-20}SS_{16}\left[\frac{SS_{16}\,/\,V}{SS_{16}/V\ +\ K_3}\right] - \frac{a_3}{2}\,\theta^{T-20}\\ &A\,\frac{\mathit{min}\,(NH_4,\ NO_3)/V}{K_{a3} + \mathit{min}\,(NH_4,\ NO_3)/V}\end{aligned} \tag{10}$$

where $C_{NH_4}^{flow\ in}$ is the concentration of NH_4^+-N in the inflow, $C_{NH_4}^{rain}$ is the concentration of NH_4^+-N in rainfall, k_2 is the ammonification rate, K_2 is the half-saturation constant for effects the DON on ammonification, a_4 is the areal rate of release of NH_4^+-N from bottom sediments, k_3 is the rate of ammonium desorption from fine suspended material <16 μm in diameter (SS_{16}), and K_3 is the half saturation constant for the ammonium desorption process.

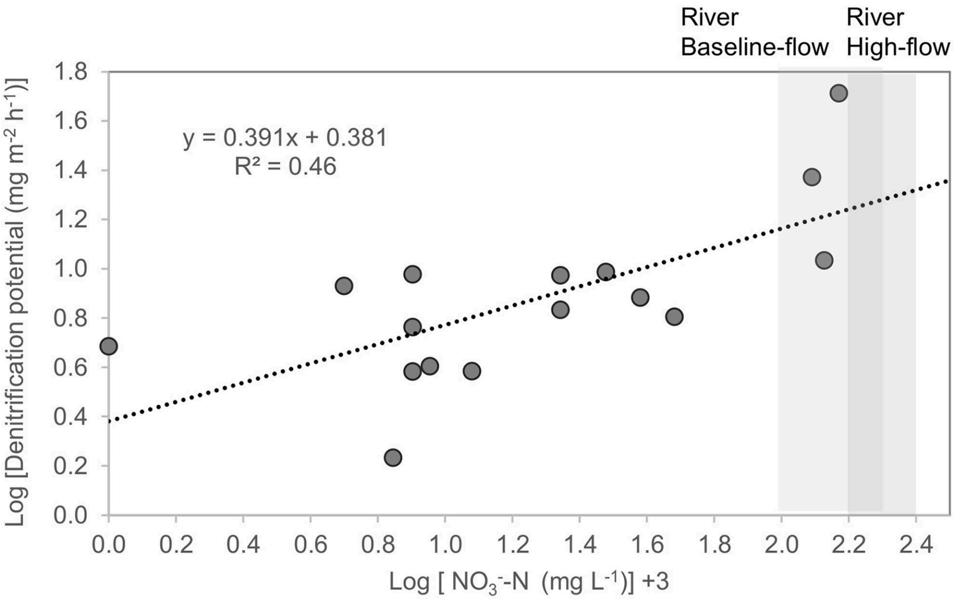

FIGURE 3 | Denitrification potential [log] (mg m^{-2} h^{-1}) of coastal wetlands (mangroves, *Melaleuca* spp. wetlands, saltmarsh, waterbodies with macrophytes) vs. NO_3^--N concentration in the floodwater [log + 3] (mg L^{-1}). Data from *Melaleuc*a spp. wetlands has been previously been published in Adame et al. (2019b). Ranges of NO_3^--N concentrations during baseline and high flows for the Tully River are shown as shaded areas (Orr et al., 2014).

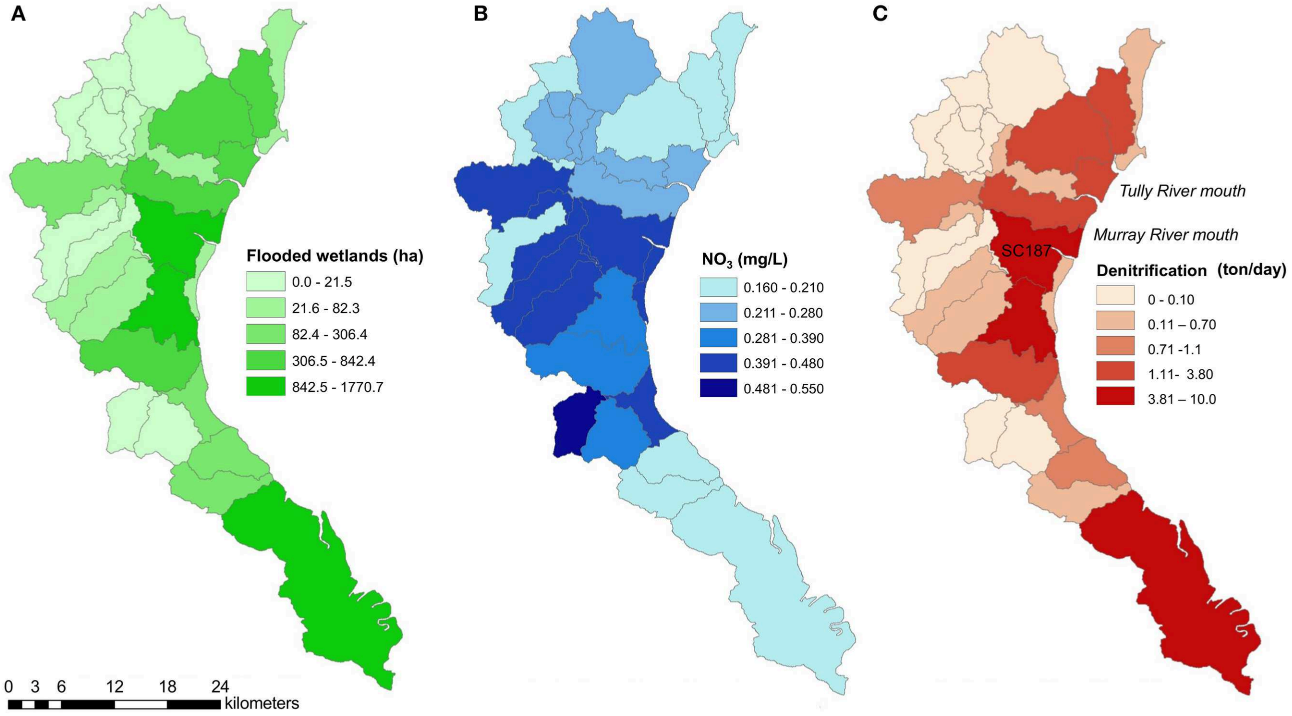

FIGURE 4 | (A) Area of flooded wetlands (ha); **(B)** mean NO_3^--N concentrations (mg L^{-1}); and **(C)** denitrification potential (t NO_3^--N d^{-1}) for sub-catchments of the Tully-Murray Rivers in tropical Australia during a flood event (March 30, 2018).

The DON mass in the wetland is given as:

$$\begin{aligned}\frac{d\,\mathrm{DON}}{dt} &= Q_{in}\, C_{\mathrm{DON}}^{\mathrm{flow\ in}} - Q_{out}\,\frac{\mathrm{DON}}{V}\\ &\quad - k_2\,\theta^{T-20}\,\mathrm{DON}\left[\frac{\mathrm{DON}\,/\,V}{\mathrm{DON}/V + K_2}\right] + a_5\,\theta^{T-20}\,A\\ &\quad + k_4\theta^{T-20}\,\mathrm{PON}\left[\frac{\mathrm{PON}/\,V}{\mathrm{PON}/V + K_4}\right] \qquad (11)\end{aligned}$$

where $C_{\mathrm{DON}}^{\mathrm{flow\ in}}$ is the concentration of DON in the inflow, a_5 is the areal rate of release of DON from bottom sediments, k_4 is conversion of PON to DON and K_4 is the half-saturation constant for the conversion of PON to DON. For PON mass, the equation is:

$$\begin{aligned}\frac{d\,\mathrm{PON}}{dt} &= Q_{in}\, C_{\mathrm{PON}}^{\mathrm{flow\ in}} - Q_{out}\,\frac{\mathrm{PON}}{V} + a_6\,\theta^{T-20}\,A\\ &\quad - k_4\theta^{T-20}\,\mathrm{PON}\left[\frac{\mathrm{PON}/\,V}{\mathrm{PON}/V + K_4}\right]\\ &\quad - \exp\left(\frac{-w_{s\mathrm{PON}}\,t}{z_{av}}\right)\mathrm{PON} \qquad (12)\end{aligned}$$

where $C_{\mathrm{PON}}^{\mathrm{flow\ in}}$ is the concentration of PON in the inflow, a_6 is the areal rate of release of PON from leaf litter, $w_{s\mathrm{PON}}$ is the settling rate of PON, and z_{av} is the average depth of the wetland. Finally, for SS_{16}, the equation is:

$$\frac{d\,SS_{16}}{dt} = Q_{in}\, C_{SS_{16}}^{\mathrm{flow\ in}} - Q_{out}\,\frac{SS_{16}}{V} - \exp\left(\frac{-w_s\,t}{z_{av}}\right)SS_{16} \qquad (13)$$

where w_s is the settling rate of sediment.

Table 1 provides a summary of the variables and parameters in the model. The mathematical model was solved with MATLAB routine *ode45,* with the initial conditions given by the mass of the four N constituents and SS_{16} in the wetland. The volume of water in the wetland was determined through a water balance equating the change in volume to the net flux in and out of the wetland each day. Hourly rainfall data and mean water temperature for the flooding event were obtained from the Tully River at Euramo (Station 113006A, Queensland Water Monitoring Information Portal), with hourly evaporation rates obtained for Innisfail Aerodrome (Bureau of Meteorology Product Code IDCKWCDEA0). Time-dependent parameters (indicated by an asterisk in **Table 1**) were linearly interpolated with routine *interp1* within the *ode45* routine. The sensitivity of the model to the selected parameters was explored with a Monte Carlo simulation with 500 replicates, varying the parameters by ± 20% of the values set in the model (**Table 1**). Random sampling was obtained from uniform distributions for the N conversion rates, half-saturation constants and settling rates. The proportion of TN removed by wetlands was compared among replicate results (**Supplementary Figure 3**).

RESULTS

Wetland Characteristics

Water flooding the wetlands had nutrient concentrations of (mean) 0.06 ± (standard error) 0.03 (range, 0.004–0.20) mg L^{-1} of NO_3^--N and 0.13 ± 0.061 (0.02–0.53) mg L^{-1} of NH_4^+-N. Concentrations of PO_4^--P were in general too low to be detected (<0.001 mg L^{-1}). The water pH ranged from neutral to acidic (3.2–7.4) across the wetlands, with values close to neutral pH in estuarine wetlands (mangroves and saltmarsh). EC varied from freshwater to marine, with ranges between 5 and >25,000 μS cm^{-1}. The OC in the soil across the wetlands was on average 9.7 ± 4.0 (1.1–35)%, and N was 0.48 ± 0.13 (0.1–1.5)%, with highest values in the water bodies with macrophytes and lowest in estuarine wetlands (**Table 2**).

Denitrification Rates Among Different Wetlands

Mean D_t (total or potential denitrification) was 14 ± 5.8 mg m^{-2} h^{-1} and ranged from 3.8 to 52 mg m^{-2} h^{-1} with highest values in waterbodies with macrophytes and lowest in mangroves (**Table 3**, **Supplementary Table 1**). Mean D_{wtot} (denitrification corrected for N additions) was 4.5 ± 0.87 mg m^{-2} h^{-1}, D_n (coupled denitrification-nitrification) was 3.0 ± 0.9 mg m^{-2} h^{-1}, and D_w (denitrification of NO_3^--N derived from the water column) was 9.1 ± 5.9 mg m^{-2} h^{-1}, or 64% of total denitrification. Total denitrification was highest at elevated NO_3^--N concentrations (**Figure 3**; $\log\,[Dt] = 0.391x + 0.381$; $R^2 = 0.46$, $p = 0.004$).

Flood Characteristics

The flooding lasted ∼6 days from March 27 to April 1, 2018. In March 30, 2018, the total flooded area of the sub-catchment was 15,000 ha, of which 9,421 ha were coastal wetlands (**Figures 2A,B**, **Supplementary Figure 1**). At this time, all sub-catchments had some level of flooding from 0.2 to 45% of the total area inundated. This corresponds to the flooding of 43% of the total wetland area of the Tully-Murray catchment.

Denitrification Hotspots

The NO_3^--N concentrations predicted from the Source Catchment model were highest at the sub-catchments at the mouth of the Murray River (**Figure 4B**). The denitrification potential calculated from NO_3^--N concentrations and flooded wetland area for March 30 was highest (10 t day^{-1}) in sub-catchments close to the mouth of the Tully and Murray-River (**Figure 4C**). However, some sub-catchments with low NO_3^--N concentrations were also denitrification hotspots due to extensive wetland areas (southernmost coastal area, **Figure 4C**). There were also sub-catchments with a denitrification potential close to zero, highlighting the patchiness of denitrification at the landscape scale. We estimate that for a given day during a flood, wetlands in the Tully-Murray catchment can potentially remove 48.5 t of NO_3^--N through denitrification. If considering lower rates of denitrification (5.3 mg m^{-2} h^{-1}; denitrification of *Melaleuca* spp. and mangroves, which are the dominant vegetation types), the denitrification potential is 12.0 t d^{-1}.

N Flows and Transformation Model

The model was run for one sub-catchment (SC187) with an area of flooded wetlands of 2,213 ha and a peak volume of water of 51,000 ML during the flood that lasted 6 days. Total N inputs

TABLE 1 | Notation for the mathematical model of nitrogen dynamics in wetlands.

Parameter	Unit	Value	Description	References
Q*	$m^3\ d^{-1}$		Wetland inflows (subscript: in) and outflows (subscript: out)	
R*	$m\ d^{-1}$		Precipitation	
A*	m^2		Surface area of the wetland	
V*	m^3		Volume of water in the wetland	
Z_{av}	m		Average depth of water in the wetland	
C_x^{flow}	$g\ m^{-3}$		Concentration in inflow (subscript denotes constituent)	
$C^{rain}{}_x$	$g\ m^{-3}$		Concentration in rainfall (subscript denotes constituent)	
T	°C		Water temperature	
t	d		Time	
f(N)	–		Preference factor (0–1) for ammonium vs. nitrate plant uptake	
θ	–		Non dimensional temperature multiplier	
Variables				
NO_3^-	g		Mass of nitrate-N	
NH_4^+	g		Mass of ammonium-N	
DON	g		Mass of dissolved organic nitrogen	
PON	g		Mass of particulate organic nitrogen	
SS_{16}	g		Mass of fine suspended material $< 16\,\mu m$ in diameter	
Rate constants				
k_1	d^{-1}	0.2	Nitrification rate (NH_4^+-N to NO_3^--N)	Kemp and Dodds, 2002; Hipsey et al., 2013
k_2	d^{-1}	0.01	Ammonification rate (DON to NH_4^+-N)	Hipsey et al., 2013
k_3	d^{-1}	0.0003	Pedotransfer function for NH_4^+-N release from SS_{16}	Garzon-Garcia et al., 2018
k_4	d^{-1}	0.1	PON to DON conversion rate	Hipsey et al., 2013
a_1	$g\ m^{-2}\ d^{-1}$	0.025	Plant uptake	Adame et al., 2019c
a_2	$g\ m^{-2}\ d^{-1}$	1.24	Denitrification rate	Adame et al., 2019b, and this study
a_3	$g\ m^{-2}\ d^{-1}$	0.0336	Areal rate of anammox	Oliveira-Fernandes et al., 2012
a_4	$g\ m^{-2}\ d^{-1}$	0.0075	Areal rate of ammonium release from bottom sediments	Lu et al., 2017, 2018
a_5	$g\ m^{-2}\ d^{-1}$	0.03	Areal rate of DON release from bottom sediments	Lu et al., 2017, 2018
a_6	$g\ m^{-2}\ d^{-1}$	0.00005	Areal rate of leaf litter decomposition	Lu et al., 2017, 2018
Half-saturation constants				
K_1	$g\ m^{-3}$	0.01	Half-saturation for nitrification	AED
K_N	$g\ m^{-3}$	0.01	Half-saturation for plant uptake	AED
K_2	$g\ m^{-3}$	0.01	Half saturation for ammonification	AED
K_3	$g\ m^{-3}$	2	Half saturation for pedotransfer, NH_4^+-N release from SS_{16}	AED
K_4	$g\ m^{-3}$	0.05	Half saturation for PON to DON conversion	AED
K_{a2}	$g\ m^{-3}$	0.1	Half saturation for denitrification	AED
K_{a3}	$g\ m^{-3}$	0.1	Half saturation for anammox	AED

**The parameter is time-dependent.*

to this sub-catchment during the flood were 62.2 t DIN (NO_3^--N + NH_4^+-N), 42.4 t DON, 24.5 t PN, and 5,183 t of suspended sediment. The model simulations showed a loss of 70.4% of the NO_3^--N that entered the wetland during the flood on the day of flooding (**Figure 5**). By the end of the 6 days of flooding, 85.9% of the NO_3^--N had been removed from the wetland through denitrification and anammox processes. For NH_4^+-N, despite the internal release as water flooded the wetland, the model simulations produced a reduction of 17.6% of the load 1 day after flooding; and 19.2% after 6 days of flooding. The PON load was also reduced by 34.9% by the end of the first day of flooding and 43.6% by the end of the 6 days of flooding. After 3 days of flooding DON load increased by 7%, and after 6 days, the DON load increased by 38.8%. Predictions from the model simulation indicated that the wetlands within this sub-catchment retained 29.3% of the TN load during this flooding event.

To assess the sensitivity of the model parameters, we ran the model varying the value for each parameter by ±20%. The

TABLE 2 | Nutrient concentrations in water, pH, electrical conductivity (EC), soil organic carbon (OC), nitrogen (N), and bulk density (BD), from eight coastal wetlands in tropical Australia.

Wetland type	N-NH_4^+ (mg L^{-1})	N-NO_3^- (mg L^{-1})	pH	EC (μS cm^{-1})	Soil OC (%)	Soil N (%)	BD (g cm^{-3})
Mangroves	0.02 ± 0.01	0.01 ± 0.003	6.7	38,000 ± 9,000	1.7 ± 0.22	0.1 ± 0.02	1.1 ± 0.10
Freshwater marsh	0.04 ± 0.01	0.004 ± 0.002	3.2	2,000	–	–	–
Saltmarsh	0.53 ± 0.08	0.04 ± 0.01	7.4	2,800	1.9 ± 0.87	0.3 ± 0.1	1.0 ± 0.19
M. quinquenervia	0.05 ± 0.01	0.003 ± 0.001	4.1	490	4.1 ± 0.44	0.3 ± 0.02	0.59 ± 0.02
M. viridiflora	0.05 ± 0.04	0.01 ± 0.004	5.5	4,400 ± 1,100	14 ± 1.4	0.8 ± 0.04	0.34 ± 0.05
Melaleuca-Eucalyptus	0.03 ± 0.01	0.02 ± 0.01	5.6	54	1.1 ± 0.04	0.09 ± 0.02	1.2 ± 0.02
Lagoon with *Nymphae* spp.	0.2 ± 0.02	0.2 ± 0.02	5.8	30–60	13 ± 23	0.8 ± 0.1	0.1 ± 0.001
Lagoon with emergent grasses	0.1 ± 0.02	0.2 ± 0.02	5.8	30–60	32 ± 1.6	1 ± 0.1	0.1 ± 0.02

Values are mean ± standard error of three samples per site for nutrients, soil OC, soil N and BD.

TABLE 3 | Denitrification rates (D_t, total denitrification; D_{wtot}, denitrification corrected for N additions; D_n coupled denitrification-nitrification, D_w, denitrification of NO_3^--N from the water column; mg m^{-2} h^{-1}).

Wetland type	D_{tot}	D_{wtot}	D_n	D_w
Mangroves	3.8 ± 1.1	1.5 ± 0.45	2.3 ± 0.7	0.9 ± 0.3
Freshwater marsh	7.3 ± 3.7	7.1 ± 3.6	0.18 ± 0.1	0.1 ± 0.03
Saltmarsh	7.6 ± 1.1	3.3 ± 0.5	4.3 ± 0.7	1.9 ± 0.3
M. quinquenervia	4.8 ± 1.0	3.2 ± 0.6	1.1 ± 0.2	1.6 ± 0.3
M. viridiflora	5.8 ± 0.7	3.5 ± 0.4	1.4 ± 0.2	2.3 ± 0.3
Melaleuca-Eucalyptus spp.	9.5 ± 1.3	5.7 ± 0.8	3.8 ± 0.5	2.3 ± 0.3
Waterbody *Nymphae* spp.	24 ± 4.5	8.8 ± 1.7	8.3 ± 1.6	15 ± 2.8
Waterbody with grasses	52 ± 4.4	3.0 ± 0.3	2.8 ± 0.2	49 ± 4.1

Denitrification rates for the Melaleuca forests were obtained from Adame et al. (2019b). Values are mean ± standard error of three replicate experiments per wetland type.

change in parameter values did not have a great effect on the model output, with a range in TN retention of 26.0–32.0% (**Supplementary Figure 3**). Increasing internal release of DON by 20.0% resulted in a reduction of TN retention from 29.3 to 21.0%. For the range of parameter values tested through the sensitivity analysis, the model consistently showed TN retention when wetlands were flooded.

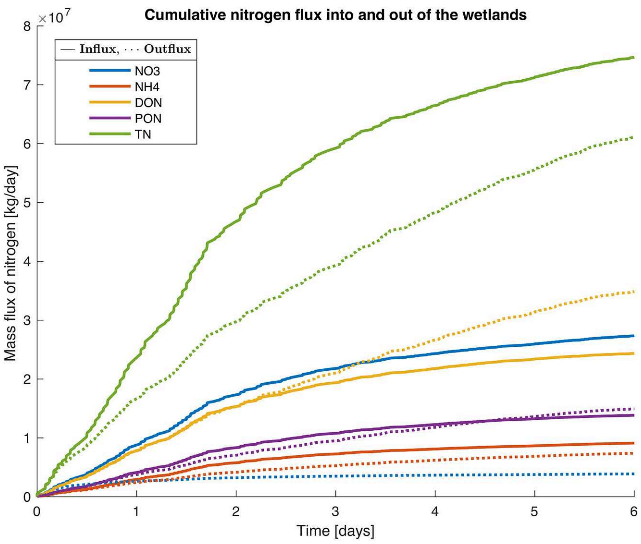

FIGURE 5 | Simulation of N conversion (NO_3^-, NH_4^+, DON, PON, and TN) within a wetland during a flooding event for 6 days on 28 March 2018. The model was run for a sub-catchment in the mouth of the Murray River (SC 187, see **Figure 4C**), with an area of flooded wetlands of 2,213 ha, a peak volume of water of 51,000 ML. Total N inputs during the flooding event for the sub-catchment were 62.2 t DIN, 42.4 t DON, 24.5 t PON and 5,183 t of suspended sediment.

DISCUSSION

During a flood with a recurrence time of ~4-years, coastal wetlands in the tropical catchment of the Tully-Murray River remove a large portion of the incoming NO_3^--N through denitrification. The nutrient removal was variable across the landscape, but our model simulations indicated the existence of "denitrification hotspots" corresponding to sub-catchments with high NO_3^--N concentrations (>0.20 mg L^{-1}), and large areas of wetlands (>24%) that became inundated during the flood. These "hotspots" had the potential to remove up to 10 t of NO_3^--N d^{-1} through denitrification. Hotspots were located at the mouth of rivers close to National Parks, which had large areas of protected and well-managed wetlands that effectively contributed an ecosystem service of protecting the coastal ecosystem from eutrophication through N removal. In other sub-catchments, the denitrification potential was close to zero due to very small areas of flooded wetlands. Our approach provided a comprehensive spatial and temporal distribution of "denitrification hotspots," validating that the patchiness of denitrification extends to tropical catchments and is indeed a global scale process (Groffman et al., 2009).

The importance of coastal wetlands for removing NO_3^--N can be interpreted at different spatial and temporal scales. From a spatial perspective, at the sub-catchment scale, large areas of frequently inundated wetlands can remove most of the NO_3^--N during a flooding event (**Figure 5**). At the catchment scale, they could also contribute substantially to the removal of NO_3^--N before it reaches the coast. For instance, a flooding event of similar magnitude as the one in March 2018, i.e., a 4-year return period, was associated with a load of 423 t of DIN (Wallace et al., 2009). Based on the range of denitrification rates measured in our study, we estimate that denitrification would remove between 17 and 68% of the NO_3^--N that would otherwise be flushed into the coastal zone (lower and higher end of the denitrification rates measured).

From a temporal perspective, this study shows that periods of high flows and flooding will increase denitrification in regions with large areas of wetlands, creating "denitrification hot times" (McClain et al., 2003). Similar results have been shown in subtropical Australia, where mangroves reduced 71% of the NO_3^--N after a rainfall event (Wadnerkar et al., 2019). Most of the removal was suggested to be due to high denitrification rates (12 mg m^2 d^{-1}); rates well within those derived from our denitrification measurements at similar NO_3^--N concentrations (**Figure 3**). In riverine systems, NO_3^--N uptake has been found to be highest after rainfall events (Wells et al., 2016) but removal rates from denitrification will also depend on the residence time and wetland area. Additionally, N loads after flooding events vary throughout the year, with highest concentrations during the first floods (Wallace et al., 2009). Thus, even though wetlands could remove large amounts of NO_3^--N during major floods, proportionally, they will remove more NO_3^--N per unit area during the first floods of the year, especially if they are of moderate intensity (Hansen et al., 2018).

During the dry season, much of the river flow is associated with baseflow from groundwater, and only sporadic rainfall events that generate some additional flow (Rasiah et al., 2010). Concentrations of NO_3^--N in rivers are generally relatively low at the beginning of the dry season but increase as the season progresses with nutrient inputs accumulation in catchment soils (Davis et al., 2016). Thus, wetlands with groundwater flows or those receiving surface discharge via rivers might receive continuous inputs of water that is rich in NO_3^--N (Karim et al., 2013). For these cases, there would be expected to be high denitrification rates throughout the year. Another major difference between the flooding season and the rest of the year is the tidal influence. During dry periods, mangroves, especially those in tidal channels, are flooded mainly by tidal water (Sadat-Noori et al., 2016), which is generally more diluted in nutrients than freshwater. Thus, removal rates could be lower during the dry compared to the wet season (Adame et al., 2010). The processes influencing nitrogen transformations are also likely to vary with rainfall; in wet periods, mangroves tend to be sinks of DIN, mostly due to microbial denitrification, but during dry periods, they can be sources of DIN associated with NH_4^+-N outputs (Adame et al., 2010), possibly due to dissimilatory NO_3^--N reduction to NH_4^+-N (DNRA) which is common in coastal wetlands (Giblin et al., 2013). Overall, the value of these coastal wetlands for improvement of water quality at the catchment scale during dry periods is yet to be determined.

The model used to quantify N dynamics within a wetland provided insights into the main processes dominating N transformations during a flood. Denitrification was a key process which resulted in loss of a large portion of incoming NO_3^--N loads within the first 24 h after flooding; sensitivity analysis based on the range of measured denitrification rates, revealed the same outcome. Anammox was also shown in model simulations to contribute to NO_3^--N loss, but at a much lower rate (<10% of denitrification, Oliveira-Fernandes et al., 2012) than denitrification, resulting in TN removal of around 1% of the incoming load. Changes in NH_4^+-N and DON fluxes were even more uncertain, due to the scarcity of studies in similar wetlands and large variability in the reported rates of mineralisation and sediment releases (Fagherazzi et al., 2013). Nevertheless, it appeared that the model was not particularly sensitive to the range selected (±20% of calibrated values) for NH_4^+-N and DON fluxes, with TN removal by the wetlands varying only between 26 and 32% and concentrations in the outflow being continuously low. Physical and hydrological factors such as the surface area of the wetland and the volume of the flood are likely to be more critical compared to the variability of these parameters when assessing the role of wetlands for N removal.

There were some factors that were not included in the model that could be important and should be considered for future studies. For instance, in estuarine wetlands, dissimilatory NO_3^--N reduction to NH_4^+-N (DNRA), is an important process in N removal (Giblin et al., 2013). The availability of NO_3^--N and organic carbon could shift the dominance of DNRA over denitrification or vs. (Christensen et al., 2000; Hardison et al., 2015). Rates of denitrification and mineralisation in tropical wetlands could also vary greatly with oxygen availability and organic matter inputs (Chapman et al., 2019). Thus, direct field measurements of DNRA and organic N mineralisation in wetlands with different conditions will greatly improve the predictions of the fate of all forms of N during flooding. It would also be useful to differentiate N_2 and N_2O emissions in measurements of denitrification as the latter is a potent greenhouse gas that could affect evaluations of the role of coastal wetlands in greenhouse gas emissions (Murray et al., 2018).

Extreme flooding events are increasing in tropical and temperate regions (Eccles et al., 2019), resulting in large flushes of water and nutrients into the coastal zone, which may cause algal blooms and the development of anoxic zones (e.g., Voynova et al., 2017). At a process level, increasing flood magnitude could alleviate nutrient limitation in mangroves (Lovelock et al., 2011) and increase fish production (Burford et al., 2008). Including flooding episodes will significantly improve the accuracy of estimates of fluxes of nutrients into the coastal zone, especially as flooding risk may increase in the future (Wallace et al., 2009; Abril and Borges, 2019). For instance, global models of nutrient exports to the coastal zone are still limited to the quantification of the nutrient outputs from river networks, and have not yet considered the role of coastal wetlands in ameliorating nutrient exports (Kroeze et al., 2012; Vilmin et al., 2018).

The improved understanding of the role of coastal wetlands to ameliorate N exports into the coastal zone has major management implications. The Reef 2050 Water Quality

Improvement Plan (Reef 2050 WQIP, www.reefplan.qld.gov.au/) has set targets for improving water quality in the catchments that flow into the Great Barrier Reef. The desired target for reduction for DIN is 60% by 2025. Significant investment has been made to achieve this target by encouraging the adoption of improved land management practices, such as optimizing fertilizer use and application. However, in 2014, the potential for improved management practice to meet the desired end-of-catchment reductions was modeled, and the conclusion was that even the adoption of best land management practices by all landholders would not be enough to meet the desired reductions. Thus, alternative nutrient management strategies need to be considered if current, and future targets are to be achieved (Waters et al., 2014). Restoration of existing wetlands or creation of new wetlands for the purpose of N mitigation have so far received relatively little attention as part of the Reef 2050 WQIP, partly because of uncertainty in the capacity of wetlands to achieve adequate levels of N removal. Our study provides an improved quantitative basis for wetlands to be assessed alongside other possible management actions to improve water quality of runoff entering the reef coastal zone.

Many waterways and floodplains in the Great Barrier Reef catchment have been drained and developed for agriculture and urban use. The regulation of river flows with dams and weirs has occurred to provide water storage for irrigation and levees to prevent floodwaters from entering agricultural lands (Dawson et al., 2017; Waltham et al., 2019). Restoration and rehabilitation of floodplain wetlands will require increased inundation frequency, depth and duration, and restoring peak flood events will be key to achieving this goal (Dawson et al., 2017). Management actions can include reconnecting waterways and their floodplains (Dawson et al., 2017; Waltham et al., 2019). Coastal wetlands within the catchments of the Great Barrier Reef are still abundant and are relatively well protected (Adame et al., 2019a), with opportunities to enhance their functionality with management actions. These wetlands provide a range of ecosystem services that are just now being incorporated into local management strategies (Adame et al., 2019a). Improved management and restoration of wetlands within tropical catchments can provide a complementary and cost-effective solution for improving water quality and the overall health of coastal and marine ecosystems.

DATA AVAILABILITY STATEMENT

The datasets generated and analyzed for this study can be found as **Supplementary Data**.

AUTHOR CONTRIBUTIONS

MA, MR, and MG designed the study. DH, MER, and JL designed, created, and solved the model. CN analyzed the flood hydrology. VR and GC did the geospatial analyses. MA did the field and laboratory experiments and wrote the manuscript with the help and input of all coauthors.

FUNDING

The study was funded by Griffith University and the Office of the Great Barrier Reef and Wetlands Team from the Department of Environment and Science. This work was also partially funded by the Australian Government's National Environmental Science Program, Tropical Water Quality Hub (Project 3.3.2).

ACKNOWLEDGMENTS

We acknowledge the Traditional Owners of the land in which the field study was conducted, especially the Girramay and Gulnay people. We thank Santo Silvestro from Barrett's lagoon for allowing us to work in his property and for sharing his knowledge on wetlands. We are also grateful to S. Rodriguez, E. Kavehei, M. Turschwell, and S. Balcombe for field support. We thank David Waters and Maria Askildsen for providing the data from the Source Catchment model.

SUPPLEMENTARY MATERIAL

The Supplementary Material for this article can be found online at: https://www.frontiersin.org/articles/10.3389/fmars.2019.00671/full#supplementary-material

REFERENCES

Abril, G., and Borges, A. V. (2019). Ideas and perspectives: carbon leaks from flooded land: do we need to replumb the inland water active pipe? *Biogeosciences* 16, 769–784. doi: 10.5194/bg-16-769-2019

Adame, M. F., Arthington, A. H., Waltham, N., Hasan, S., Selles, A., and Ronan, M. (2019a). Managing threats and restoring wetlands within catchments of the Great Barrier Reef, Australia. *Aquat. Conserv. Mar. Freshw. Ecosyst.* 29, 829–839. doi: 10.1002/aqc.3096

Adame, M. F., Franklin, H., Waltham, N. J., Rodriguez, S., Kavehei, E., Turschwell, M. P., et al. (2019b). Nitrogen removal by tropical floodplain wetlands through denitrification. *Mar. Freshw. Res.* 70, 1513–1521. doi: 10.1071/MF18490

Adame, M. F., Reef, R., Wong, V. N. L., Balcombe, S. R., Turschwell, M. P., Kavehei, E., et al. (2019c). Carbon and nitrogen sequestration of Melaleuca floodplain wetlands in tropical Australia. *Ecosystems.* doi: 10.1007/s10021-019-00414-5. [Epub ahead of print].

Adame, M. F., Virdis, B., and Lovelock, C. E. (2010). Effect of geomorphological setting and rainfall on nutrient exchange in mangroves during tidal inundation. *Mar. Freshw. Res.* 61, 1197–1206. doi: 10.1071/MF10013

Australian Bureau of Meteorology (ABM) (2019). Available online at: http://www.bom.gov.au/

Barbier, E. B., Hacker, S., Kennedy, C., Kock, E., Stier, A., and Silliman, B. (2011). The value of estuarine and coastal ecosystem services. *Ecol. Monogr.* 81, 169–193. doi: 10.1890/10-1510.1

Bernstein, L. S., Adler-Golden, S. M., Sundberg, R. L., Levine, R. Y., Perkins, T. C., Berk, A., et al. (2005). "A new method for atmospheric correction and aerosol optical property retrieval for VIS-SWIR multi- and hyperspectral imaging sensors: QUAC (QUick atmospheric correction)," in *Proceedings 2005 IEEE*

International Geoscience and Remote Sensing Symposium (Burlington, MA), 3549–3552.

Burford, M. A., Cook, A. J., Fellows, C. S., Balcombe, S. R., and Bunn, S. E. (2008). Sources of carbon fuelling production in an arid floodplain river. *Mar. Freshw. Res.* 59, 224–234. doi: 10.1071/MF07159

Burgin, A. J., and Hamilton, S. K. (2007). Have we overemphasized the role of denitrification in aquatic ecosystems? A review of nitrate removal pathways. *Front. Ecol. Environ.* 5, 89–96. doi: 10.1890/1540-9295(2007)5[89:HWOTRO]2.0.CO;2

Chapman, S., Hayes, M., Kelly, B., and Langley, J. (2019). Exploring the oxygen sensitivity of wetland soil carbon mineralization. *Biol. Lett.* 15:20180407. doi: 10.1098/rsbl.2018.0407

Christensen, P. B., Rysgaard, S., Sloth, N. P., Dalsgaard, T., and Schwærter, S. (2000). Sediment mineralization, nutrient fluxes, denitrification and dissimilatory nitrate reduction to ammonium in an estuarine fjord with sea cage trout farms. *Aquat. Microb. Ecol.* 21, 73–84. doi: 10.3354/ame021073

Davis, A., Pearson, R., Brodie, J., and Butler, B. (2016). Review and conceptual models of agricultural impacts and water quality in waterways of the Great Barrier Reef catchment area. *Mar. Freshw. Res.* 68, 1–19. doi: 10.1071/MF15301

Dawson, S. K., Kingsford, R. T., Berney, P., Catford, J. A., Keith, D. A., Stoklosa, J., et al. (2017). Contrasting influences of inundation and land use on the rate of floodplain restoration. *Aquat. Conserv. Mar. Freshw. Ecosyst.* 27, 663–674. doi: 10.1002/aqc.2749

Duarte, C. M., Losada, I. J., Hendriks, I. E., Mazarrasa, I., and Marba, N. (2013). The role of coastal plant communities for climate change mitigation and adaptation. *Nat. Clim. Chang.* 3, 961–968. doi: 10.1038/nclimate1970

Eccles, R., Zhang, H., and Hamilton, D. (2019). A review of the effects of climate change on riverine flooding in subtropical and tropical regions. *J. Water Clim. Chang*. doi: 10.2166/wcc.2019.175. [Epub ahead of print].

Fagherazzi, S., Wiberg, P. L., Temmerman, S., Struyf, E., Zhao, Y., and Raymond, P. A. (2013). Fluxes of water, sediments, and biogeochemical compounds in salt marshes. *Ecol Proc.* 2:3. doi: 10.1186/2192-1709-2-3

Farahmand, A., and AghaKouchak, A. (2015). A generalized framework for deriving nonparametric standardized drought indicators. *Adv. Water Resour.* 76, 140–145. doi: 10.1016/j.advwatres.2014.11.012

Garzon-Garcia, A., Burton, J., Franklin, H. M., Moody, P. W., Hayr, R. W., and De Burford, M. A. (2018). Indicators of phytoplankton response to particulate nutrient bioavailability in fresh and marine waters of the Great Barrier Reef. *Sci. Total Environ*. 636, 1416–1427. doi: 10.1016/j.scitotenv.2018.04.334

Giblin, A. E., Tobias, C. R., Song, B., Weston, N., Banta, G. T., and Rivera-Monroy, V. H. (2013). The importance of dissimilatory nitrate reduction to ammonium (DNRA) in the nitrogen cycle of coastal ecosystems. *Oceanography* 26, 124–131. doi: 10.5670/oceanog.2013.54

Groffman, P. M., Butterbach-Bahl, K., Fulweiler, R. W., Gold, A. J., Morse, J. L., Stander, E. K., et al. (2009). Challenges to incorporating spatially and temporally explicit phenomena (hotspots and hot moments) in denitrification models. *Biogeochemistry* 93, 49–77. doi: 10.1007/s10533-008-9277-5

Hansen, A. T., Dolph, C. L., Foufoula-Georgiou, E., and Finlay, J. C. (2018). Contribution of wetlands to nitrate removal at the watershed scale. *Nat. Geosci.* 11, 127–132. doi: 10.1038/s41561-017-0056-6

Hardison, A. K., Algar, C. K., Giblin, A. E., and Rich, J. J. (2015). Influence of organic carbon and nitrate loading on partitioning between dissimilatory nitrate reduction to ammonium (DNRA) and N_2 production. *Geochim. Cosmochim. Acta* 164, 146–160. doi: 10.1016/j.gca.2015.04.049

Hipsey, M. F., Bruce, L. C., and Hamilton, D. P. (2013). *Aquatic Ecodynamics (AED) Model Library*. Science manual. Perth, WA: University of Western Australia.

Hughes, T. P., Day, J. C., and Brodie, J. (2015). Securing the future of the Great Barrier Reef. *Nat. Clim. Chang.* 5, 4–6. doi: 10.1038/nclimate2604

Isbell, R. (2002). *The Australian Soil Classification*. Melbourne, VIC: C Publishing.

Junk, W. F., Bayley, P. B., and Sparks, R. E. (1989). "The flood pulse concept in river-floodplain systems," in *Proceedings of the International Large River Symposium,* ed. D. P. Dodge (Honey Harbour, ON: Canadian Journal of Fisheries and Aquatic Sciences), 110–127.

Junk, W. J., and Furch, K. (1993). A general review of tropical South American floodplains. *Wetl. Ecol. Manag.* 2, 231–238. doi: 10.1007/BF00188157

Karim, F., Kinsey-henderson, A., Wallace, J., Arthington, A. H., and Pearson, R. G. (2012). Modelling wetland connectivity during overbank flooding in a tropical floodplain in north Queensland, Australia. *Hydrol. Proces.* 2723, 2710–2723. doi: 10.1002/hyp.8364

Karim, F., Kinsey-henderson, A., Wallace, J., Godfrey, P., Arthington, A. H., and Pearson, R. G. (2013). Modelling hydrological connectivity of tropical floodplain wetlands via a combined natural and artificial stream network. *Hydrol. Proces.* 28, 5696–5710. doi: 10.1002/hyp.10065

Kemp, M., and Dodds, W. (2002). The influence of ammonium, nitrate, and dissolved oxygen concentrations on uptake, nitrification, and denitrification rates associated with prairie stream substrata *Limnol. Oceanogr*. 47, 1380–1393. doi: 10.4319/lo.2002.47.5.1380

Kroeze, C., Bowman, L., and Seitzinger, S. (2012). Modeling global nutrient export from watersheds. *Curr. Opin. Env. Sust*. 4, 195–202. doi: 10.1016/j.cosust.2012.01.009

Kroon, F. J., Kuhnert, P. M., Henderson, B. L., Wilkinson, S. N., Kinsey-henderson, A., Abbott, B., et al. (2012). River loads of suspended solids, nitrogen, phosphorus and herbicides delivered to the Great Barrier Reef lagoon. *Mar. Pollut. Bull.* 65, 167–181. doi: 10.1016/j.marpolbul.2011.10.018

Kulkarni, M. V., Groffman, P. M., and Yavitt, J. B. (2008). Solving the global nitrogen problem: It's a gas! *Front. Ecol. Environ.* 6, 199–206. doi: 10.1890/060163

Lovelock, C. E., Feller, I. C., Adame, M. F., Reef, R., Penrose, H. M., Wei, L., et al. (2011). Intense storms and the delivery of materials that relieve nutrient limitations in mangroves of an arid zone estuary. *Funct. Plant Biol.* 38, 514–522. doi: 10.1071/FP11027

Lu, J., Bunn, S. E., and Burford, M. A. (2018). Nutrient release and uptake by littoral macrophytes during water level fluctuations. *Sci. Total Environ*. 623, 29–40. doi: 10.1016/j.scitotenv.2017.11.199

Lu, J., Faggotter, S. J., Bunn, S. E., and Burford, M. A. (2017). Macrophyte beds in a subtropical reservoir shifted from a nutrient sink to a source after drying then rewetting. *Freshw. Biol.* 62, 854–867. doi: 10.1111/fwb.12904

McClain, M. E., Boyer, E. W., Dent, C. L., Gergel, S. E., Grimm, N. B., Groffman, P. M., et al. (2003). Biogeochemical hot spots and hot moments at the interface of terrestrial and aquatic ecosystems. *Ecosystems* 6, 301–312. doi: 10.1007/s10021-003-0161-9

Mitsch, W. J., and Gosselink, J. (2015). *Wetlands*, *5th Edn*. East Orange, NJ: Wiley.

Murray, R., Erler, D., Rosentreter, J., Maher, D., and Eyre, B. (2018). A seasonal source and sink of nitrous oxide in mangroves: insights from concentration, isotope, and isotopomer measurements. *Geochim. Cosmochim. Acta* 238, 169–192. doi: 10.1016/j.gca.2018.07.003

Ndehedehe, C., Agutu, N., Okwuashi, O., and Ferreira, V. G. (2016). Spatio-temporal variability of droughts and terrestrial water storage over Lake Chad Basin using independent component analysis. *J. Hydrol.* 540, 106–128. doi: 10.1016/j.jhydrol.2016.05.068

Nielsen, L. (1992). Denitrification in sediment determined from nitrogen isotope pairing. *FEMS Microbiol. Ecol.* 86, 357–362. doi: 10.1016/0378-1097(92)90800-4

Oliveira-Fernandes, S. O., Bonin, P. C., Michotey, V. D., Garcia, N., and LokaBharathi, P. A. (2012). Nitrogen-limited mangrove ecosystems conserve N through dissimilatory nitrate reduction to ammonium. *Sci Rep*. 2:419. doi: 10.1038/srep00419

Orr, D., Turner, R. D. R., Huggins, R., Vardy, S., and Warne, M. S. J. (2014). "Wet Tropics water quality statistics for high and base flow conditions," in *Great Barrier Reef Catchment Loads Monitoring Program, Water Quality and Investigations* (Brisbane, QLA: Department of Science, Information, Technology, innovation and the Arts, Environmental Monitoring and Assessment Sciences, Science Division Brisbane), 73.

Piña-Ochoa, E., and Álvarez-Cobelas, M. (2006). Denitrification in aquatic environments: a cross-system analysis. *Biogeochemistry* 81, 111–130. doi: 10.1007/s10533-006-9033-7

Rasiah, V., Armour, J. D., Cogle, A. L., and Florentine, S. K. (2010). Nitrate import-export dynamics in groundwater interacting with surface-water in a wet-tropical environment. *Aus. J. Soil Res.* 48, 361–370. doi: 10.1071/SR09120

Rasiah, V., Armour, J. D., Yamamoto, T., Mahendrarajah, S., and Heiner, D. H. (2003). Nitrate dynamics in shallow groundwater and the potential for transport to off-site water bodies. *Water. Air. Soil Pollut.* 147, 183–202. doi: 10.1023/A:1024529017142

Sadat-Noori, M., Santos, I. R., Tait, D. R., and Maher, D. T. (2016). Fresh meteoric versus recirculated saline groundwater nutrient inputs into a subtropical estuary. *Sci. Tot. Environ.* 566–567, 1440–1453. doi: 10.1016/j.scitotenv.2016.06.008

Steingruber, S., Friedrich, J., Gachter, R., and Wehrli, B. (2001). Measurement of denitrification in sediments with the ^{15}N isotope pairing technique. *Appl. Environ. Microbiol.* 67, 3771–3778. doi: 10.1128/AEM.67.9.3771-3778.2001

Tomasek, A. A., Hondzo, M., Kozarek, J. L., Staley, C., Wang, P., Lurndahl, N., et al. (2019). Intermittent flooding of organic-rich soil promotes the formation of denitrification hot moments and hot spots. *Ecosphere* 10:e02549. doi: 10.1002/ecs2.2549

Vilmin, L., Mogollón, J. M., Beusen, A. H. W., and Bowmana, A. F. (2018). Forms and subannual variability of nitrogen and phosphorus loading to global river networks over the 20th century. *Glob. Planet Change* 163, 67–85. doi: 10.1016/j.gloplacha.2018.02.007

Voynova, Y. G., Brix, H., Petersen, W., Weigelt-Krenz, S., and Scharfe, M. (2017). Extreme flood impact on estuarine and coastal biogeochemistry: the 2013 Elbe flood. *Biogeosciences* 14, 541–557. doi: 10.5194/bg-14-541-2017

Wadnerkar, P. D., Santos, I. R., Looman, A., Sanders, C. J., White, S., Tucker, J. P., et al. (2019). Significant nitrate attenuation in a mangrove-fringed estuary during a flood-chase experiment. *Environ. Pollut.* 253, 1000–1008. doi: 10.1016/j.envpol.2019.06.060

Wallace, J., Stewart, L., Hawdon, A., and Keen, R. (2008). The role of coastal floodplains in generating sediment and nutrient fluxes to the Great Barrier Reef lagoon in Australia. *Ecohydrol. Hydrobiol.* 8, 183–194. doi: 10.2478/v10104-009-0014-z

Wallace, J., Stewart, L., Hawdon, A., Keen, R., Karim, F., and Kemei, J. (2009). Flood water quality and marine sediment and nutrient loads from the Tully and Murray catchments in north Queensland, Australia. *Mar. Freshw. Res.* 60, 1123–1131. doi: 10.1071/MF08356

Waltham, N. J., Burrows, D., Wegscheidl, C., Buelow, C., Ronan, M., Connolly, N., et al. (2019). Lost floodplain wetland environments and efforts to restore connectivity, habitat, and water quality settings on the Great Barrier Reef. *Front. Mar. Sci.* 6:71. doi: 10.3389/fmars.2019.00071

Waters, D. K., Carroll, C., Ellis, R., Hateley, L., McCloskey, J., Packett, R., et al. (2014). *Modelling Reductions of Pollutant Loads due to Improved Management Practices in the Great Barrier Reef Catchments – Whole of GBR, Technical Report*. Department of Natural Resources and Mines, Toowoomba, Queensland.

Wells, N., Baisden, W., Horton, T., and Clough, T. (2016). Spatial and temporal variations in nitrogen export from a New Zealand pastoral catchment revealed by stream nitrate isotopic composition. *Water Resour. Res.* 52, 2840–2854. doi: 10.1002/2015WR017642

WetlandInfo, Department for Environment and Science, Queensland Government (2019). Available online at: https://wetlandinfo.des.qld.gov.au/wetlands/

Wilson, P., and Baker, D. (1990). *Soils and Agricultural Land Suitability of the Wet Tropical Coast of North Queensland: Ingham area*. Brisbane, QLA: Queensland Department of Primary Industries. Land Resources Bulletin. QV90001.

Xiao, K., Wu, J., Li, H., Hong, Y., Wilson, A. M., Jiao, J. J., et al. (2018). Nitrogen fate in a subtropical mangrove swamp: Potential association with seawater-groundwater exchange. *Sci. Total Environ.* 635, 586–597. doi: 10.1016/j.scitotenv.2018.04.143

Xu, H. (2006). Modification of normalised difference water index (NDWI) to enhance open water features in remotely sensed imagery. *Int. J. Remote Sens.* 27, 3025–3033. doi: 10.1080/01431160600589179

Zhou, S., Borjigin, S., Riya, S., Terada, A., and Hosomi, M. (2014). The relationship between anammox and denitrification in the sediment of an inland river. *Sci. Total Environ.* 490, 1029–1036. doi: 10.1016/j.scitotenv.2014.05.096

Conflict of Interest: The authors declare that the research was conducted in the absence of any commercial or financial relationships that could be construed as a potential conflict of interest.

frontiers in Marine Science

ORIGINAL RESEARCH
published: 07 November 2019
doi: 10.3389/fmars.2019.00673

Molecular Level Analysis Reveals Changes in Chemical Composition of Dissolved Organic Matter From South Texas Rivers After High Flow Events

*Kaijun Lu and Zhanfei Liu**

Marine Science Institute, The University of Texas at Austin, Port Aransas, TX, United States

Riverine dissolved organic matter (DOM) is a major source of reduced carbon exported from land to marine environments, and the inflow of riverine organic matter greatly affects biogeochemical cycling in estuaries and bays. Thus, any change in DOM composition, such as changes caused by flood waters as a result of storms and hurricanes, can subsequently affect estuarine environments. To investigate the impact of high flow events on riverine DOM, multidimensional molecular level information on DOM from four South Texas Rivers (Aransas, Lavaca, Mission, and Nueces Rivers) was acquired using high-resolution Ion Mobility Quadrupole Time of Flight Liquid Chromatography Mass Spectrometry (IM Q-TOF LCMS). Base-flow samples were collected in May, July, and October of 2016, June of 2017, and March of 2018, while high-flow samples were collected in September of 2017, as well as June and September of 2018. Based on the molecular formulas assigned from IM Q-TOF LCMS, the H/C ratio decreased during high-flow events (1.52 to 1.51 in ESI+ and 1.19 to 1.07 in ESI−), while the O/C ratio increased (0.31 to 0.33 in ESI−). Furthermore, DOM shifted from a protein-like and lipid-like dominated community at base flow conditions, to a lignin, tannin and condensed aromatic structure dominated community during high flow events, based on MS and tandem MS data. These changes in high-flow riverine DOM indicate an increase of terrestrial signal, which is likely a result of mobilization of terrestrial organic matter from the watersheds by flooding. The mobilized DOM, though refractory at high-flow conditions in rivers, could be reactive in coastal regions when conditions change, and thus could potentially fuel microbial activities downstream. In addition, about 3.76–21.8% of DOM molecules contain structural isomers among different flow conditions. This low number of isomer percentages suggests that DOM, as the products of various enzymatic biochemical reactions, is constrained in the number of isomers. Taken together, results from our study provide insights into structural changes of riverine DOM in response to extreme climate events in subtropical regions and have implications in understanding biogeochemical changes in estuaries under a changing climate.

Keywords: riverine dissolved organic matter, hurricane harvey, high flow, liquid chromatography mass spectrometry, South Texas, structural isomers

Edited by:
Christopher Osburn,
North Carolina State University,
United States

Reviewed by:
Sasha Wagner,
Rensselaer Polytechnic Institute,
United States
Elizabeth Minor,
University of Minnesota Duluth,
United States

***Correspondence:**
Zhanfei Liu
zhanfei.liu@utexas.edu

Specialty section:
This article was submitted to
Marine Biogeochemistry,
a section of the journal
Frontiers in Marine Science

Received: *31 July 2019*
Accepted: *16 October 2019*
Published: *07 November 2019*

Citation:
Lu K and Liu Z (2019) Molecular Level Analysis Reveals Changes in Chemical Composition of Dissolved Organic Matter From South Texas Rivers After High Flow Events.
Front. Mar. Sci. 6:673.
doi: 10.3389/fmars.2019.00673

INTRODUCTION

Dissolved organic matter (DOM) represents a major pool of reduced carbon (C) and nitrogen (N) in aquatic systems. With ca. 6.6×10^{17} g of C, oceanic dissolved organic carbon (DOC) is the second largest bioreactive pool of C (Carlson and Hansell, 2015), and plays an important role in global carbon cycling (Hedges, 2002; Jiao et al., 2011; Ridgwell and Arndt, 2015). The steady state in age and concentration of oceanic DOM is dependent on riverine input (Raymond and Spencer, 2015). Even though the origin of oceanic DOM is still under debate, the flux of riverine DOM from land to ocean is nevertheless a major source of reduced carbon to marine environments (Meybeck, 1993; Hedges et al., 1997; Raymond and Bauer, 2001). Globally, rivers transport a total amount of roughly 0.2×10^{17} g of C to the ocean annually (Meybeck, 1993; Ludwig et al., 1996; Cauwet, 2002; Seitzinger et al., 2005; Dai et al., 2012), with the top 30 largest rivers in terms of discharge contributing to over 51% of the total global flux (Raymond and Spencer, 2015).

The quantity and composition of DOM exported to coastal and oceanic waters are affected by hydrologic events, as river discharge could increase several hundred folds during storm events. The strong positive correlation between DOC export and river discharge has been well documented (e.g., Buffam et al., 2001; McGlynn and McDonnell, 2003; Inamdar et al., 2004; Hood et al., 2006; Dalzell et al., 2007; Vidon et al., 2008). For example, during an extreme flooding event caused by Hurricane Matthew in 2016, the Yadkin-Pee Dee River basin alone could export over 474 million kg of DOC (Majidzadeh et al., 2017); and a single two-to-three-day storm event could account for ca. 31% of the DOC flux in an Ontario headwater stream in Canada (Hinton et al., 1997). A meta-analysis of 30 small eastern United States forested watersheds showed a power-law relationship between DOC concentration and discharges, with 86% of DOC exported during hydrologic events (Raymond and Saiers, 2010). Also acknowledged is that the increase in stream water DOM concentration during high-flow events is generally concurrent with a change in the DOM composition (Gremm and Kaplan, 1998; Hood et al., 2006; Zhang et al., 2007; Spencer et al., 2008). This shift is a result of mobilization of a different terrestrial DOM pool, which is not available under base flow scenarios (Vidon et al., 2008; Fellman et al., 2009). However, a quick search on Web of Science[1] with the key words of ("dissolved organic matter" OR "DOM") AND ("composition") AND ("flood" OR "storm") returns a total number of 77 publications, suggesting that data are still scarce in evaluating how the chemical composition of riverine DOM changes during high-flow events.

A better understanding of how the riverine DOM community changes during high-flow events is needed under a changing global climate, as increasing frequency of strong tropical cyclones was predicted based on high resolution models, along with an increase of 20% in the precipitation rate within 100 km of the storm center (Knutson et al., 2010). Particularly, the frequency of category 4 and 5 storms in Atlantic Ocean was projected to double by the end of 21st century (Knutson et al., 2008; Bender et al., 2010). In 2017 alone, a total of six major hurricanes (category >3) were formed in Atlantic Ocean, marking the highest number since 2005 and twice of the averaged major hurricane number in the past decade (2006–2016). Besides the direct impact on the landfall area (e.g., Han et al., 2018), high-flow events after hurricane could subsequently change the hydrology and water quality in subtropical regions (e.g., Nesbit and Mitsch, 2018). Characterized by a semiarid climate and sporadic rainfalls, South Texas is known for very intense precipitation events cropping up within relatively short period of time (Bomar, 1983, 2017; Mooney and McClelland, 2012; Bruesewitz et al., 2013; Reyna et al., 2017). For instance, Hurricane Harvey, a category four major hurricane that made landfall near University of Texas Marine Science Institute (UTMSI) on August 25, 2017, caused unprecedented flooding in nearby areas. The USGS monitor station at Mission River (28°17′30′′N, 97°16′44′′W; 0.31 m above sea level) showed that the discharge experienced an over-4000-fold increase within 72 h of the landfall. Similarly, the storm event in June of 2018 caused an over-7000-fold increase in river discharge within a week. These episodic flood events make the region of South Texas an ideal study area to investigate how riverine DOM community reacts to high-flow events in tropical and subtropical regions.

The chemical composition of DOM in riverine systems, represented by its molecular formula composition, functional groups, geometric configuration of DOM molecules, as well as its isomeric composition, strongly affects its fate, and role in aquatic environments. Due to the inherent complexity of DOM composition, previous studies were mostly focused on measuring the bulk concentration and fluxes of DOM (e.g., Raymond and Saiers, 2010), with only a few paying attention to how the chemical composition of DOM changes during the storm (Fellman et al., 2009). The riverine DOM can be characterized by parameters, including bulk C:N ratio, stable (δ^{13}C, δ^{15}N; Cai et al., 2013) and radioactive isotopes (Δ^{14}C; Evans et al., 2007), optical properties (e.g., specific UV absorbance, $SUVA_{254}$; Fellman et al., 2009; Majidzadeh et al., 2017; Osburn et al., 2019), as well as specific compounds and biomarkers (e.g., amino acids, carbohydrates, and lignins; Ward et al., 2012). High-resolution and multi-dimension molecular level analytical techniques of riverine DOM have only recently become available (Cauwet, 2002; Raymond and Spencer, 2015), and have not been widely applied to study how DOM composition reacts to high-flow events. Previous work has implied that isomeric information on DOM is crucial in understanding its chemical composition diversity (Zark et al., 2017; Wagner et al., 2019) and its reactivity. However, even with ultra-high-resolution mass spectrometry, isomeric information is often not accessible easily (Zark et al., 2017; Zark and Dittmar, 2018). To the best of our knowledge, a direct measurement of the isomers on riverine DOM across a temporal range has not yet been conducted.

The objective of this work is to investigate the impact of high-flow events on the composition of riverine DOM via molecular level analysis. Specifically, we aim to elucidate the change of DOM composition, including its molecular formulas, geometric configurations (i.e., the 3D structure), as well as isomeric information (i.e., the number of isomers), in response to

---

[1] https://www.webofknowledge.com/

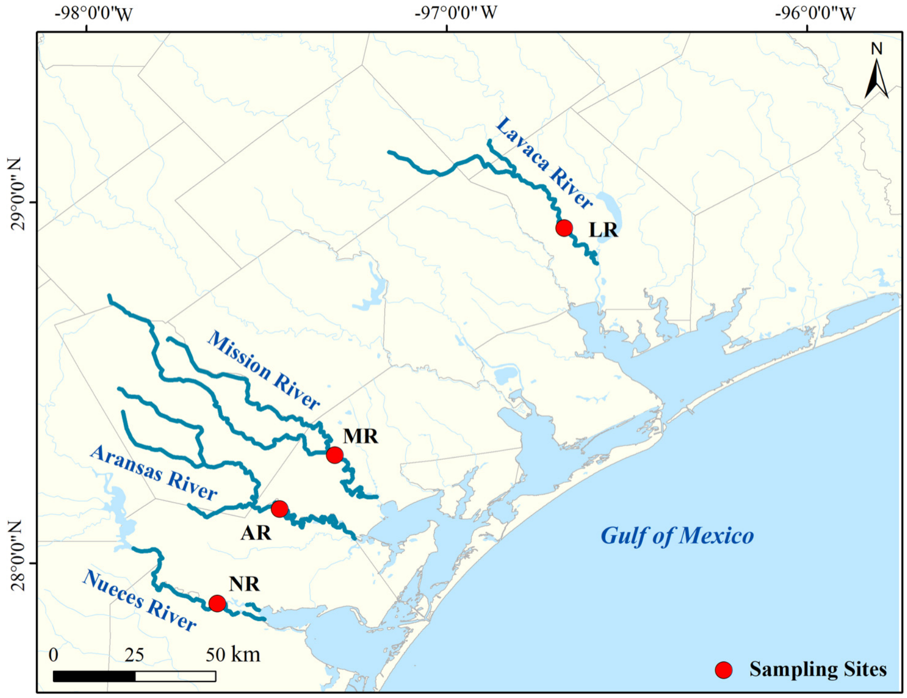

FIGURE 1 | Sampling sites in South Texas. Sampling sites are indicated by red dots.

high-flow events using a combination of liquid chromatography, ion mobility, and high-resolution quadrupole time-of-flight mass spectrometry (IM Q-TOF LCMS).

MATERIALS AND METHODS

Sample Collection

Water samples were collected from four South Texas rivers in the lower-river region but without saltwater influence (Aransas River, AR: N 28.13°, W 97.43°; Lavaca River, LR: N 28.83°, W 96.58°; Mission River, MR: N 28.29°, W 97.28°; and Nueces River, NR: N 27.88°, W 97.63°; **Figure 1**). Gage and discharge data from the nearest USGS stations were used as a proxy to indicate the flow condition of each river. From 2016 to 2018, the median discharge rate of four rivers ranged from 0.06 to 43.25 feet^3 s^{-1}. In this study a high-flow event was defined as at least 10 times of the median discharge. The exception is NR, where the discharge is mainly affected by the water dam. Therefore, the flow condition in NR was determined based on weather and flow conditions of other rivers, given the rivers in this work share a very close drainage area. Base-flow samples were collected on May 27th, July 19th and October 7th of 2016, June 19th of 2017, and March 21st of 2018, and high-flow samples were collected on September 28th of 2017, and June 21st and September 19th of 2018 (**Supplementary Figure S1**). High-flow samples were all collected, either during a flooding event or within 2 days after the peak discharge/gage height.

Water samples were collected with a Van Dorn sampler and transferred to acid-washed 1-L polycarbonate bottles in a cooler with ice. Salinity, pH, dissolved oxygen (concentration and saturation level), and temperature were measured *in situ* at each site using a YSI Sonde. Upon returning to lab the same day, 1 L samples were filtered through 0.2 μm pore size Nylon membrane filters (Whatman^{TM} 47 mm 0.2 μm membrane filter; Catalog No 7402-004) or filter cartridges (Whatman^{TM} Polycap AS 75 Capsule filter, 0.2 μm; Catalog No 2706T) to remove suspended particles. Ca. 30 mL of the filtered water was preserved at −20°C until further DOC and amino acids analysis. DOM was isolated from the filtered water and prepared for LC/MS analysis by solid-phase extraction (SPE) using a PPL cartridge (Agilent Bond Elut PPL cartridge, P/N 12105006), following the established protocol (Dittmar et al., 2008). DOM extracts were eluted with four-cartridge volume of methanol and were re-concentrated to a final volume of 1 mL and stored at −20°C until further analysis. The extracts were diluted 10-fold with methanol prior to analysis. The carbon-based recovery rate of DOM extraction, calculated as DOC of extract/DOC of filtered water × 100%, ranged from 31 to 44% on a carbon basis. All solvents and chemicals were LC/MS grade (acquired from Fisher or Sigma-Aldrich).

DOC and Amino Acids Analysis

Bulk DOC concentration was measured with a total organic carbon/total dissolved nitrogen analyzer (Shimadzu TOC-V/TDM-1). The precision of DOC measurement between duplicate samples agreed within 6%, and the accuracy ranged from 102 to 111% compared with a 10 ppm DOC standard. Total dissolved amino acids (TDAA) were analyzed using high performance liquid chromatography (HPLC) with fluorescence detection. Briefly, the filtered water was hydrolyzed using 6 M HCl under nitrogen gas at 110°C for 20 h (Kuznetsova and Lee, 2002). Then, TDAA, including dissolved free and combined amino acids, in the water were measured using HPLC after pre-column *o*-phthaldialdehyde derivatization (Lee et al., 2000; Liu et al., 2013). The relative standard deviations of TDAA in replicate samples were within 10%.

Molecular Level Characterization of Riverine DOM

Molecular level characterization of riverine DOM was performed on an Agilent 6560 Ion Mobility Quadrupole Time of Flight Liquid Chromatography Mass Spectrometer (IM Q-TOF LC/MS). Electrospray ionization negative (ESI−) mode has been commonly applied in the molecular characterization of complex DOM mixtures (e.g., Kujawinski, 2002; Kim et al., 2003; Wagner et al., 2019), which primarily contain molecules with carboxyl groups that can be ionized efficiently in negative mode. However, the presence of high carboxyl-content aromatic compounds, especially in terrestrial DOM (Kramer et al., 2012), can lead to the suppressed ionization of aliphatic, and carbohydrate-like DOM (Ohno et al., 2016). Therefore, both ESI− and ESI+ modes were applied in this work, aiming at providing a more comprehensive picture of riverine DOM.

The instrument and data acquisition methods followed our previous study (Lu et al., 2018). Briefly, for ESI+ mode, mobile phase A was H_2O with 0.1% (v/v) formic acid, and B was acetonitrile. One-μL of each sample was eluted through a StableBond C_{18} column (Poroshell 120 SB-C18; 2.7 μm, 2.1 × 100 mm; Agilent P/N 685775-902) at a flow rate of 0.5 $mL{\cdot}min^{-1}$. During the 21-min run, mobile phase B was increased from 3 to 90% during the first 15 min, and held at 90% from 15 to 20 min, and then dropped to 3% from 20 to 21 min. A post-run time of 4 min allowed the column to reach equilibrium. For ESI− mode, mobile phase A was H_2O with 10 mM ammonium acetate, and mobile phase B was acetonitrile. One-μL of samples was eluted through a HILIC column (2.7 μm, 15 cm × 4.6 mm SUPELCO, P/N 53981-U) at a flow rate of 0.5 $mL{\cdot}min^{-1}$. During the 10-min run, mobile phase B was held at 98% during the first 1 min, and dropped to 95% from 1 to 10 min. A post-run period of 15 min allowed the column to reach equilibrium before the injection of next sample.

Mass spectrum (MS) data, non-targeted tandem MS (MS/MS) and ion mobility-mass spectrum (IM-MS) data were acquired with software MassHunter LC/MS Data Acquisition (Version B.07.00) in both ESI− and ESI+ modes. The estimated resolving power (calculated as $t/\Delta t$, in which t is drift time and Δt is the peak width measured in milliseconds at half height) of ion mobility exceeds 60 at drift time of 30 ms. The TOF MS alone has resolving power greater than 40 000 at m/z of 1200, while the whole instrument IM Q-TOF LC/MS can resolve up to 2 000 000 at m/z of 300. Samples were run in duplication. The acquisition parameters followed the published protocol (Lu et al., 2018). Briefly, the MS acquisition rate was 4 spectra/s. The collision gas for MS/MS was He. The MS/MS acquisition rate was 2 spectra/s, and acquisition time was 500 ms/spectrum. The resolution for the precursor ion was maintained at 40 000 at m/z of 1200, with a precursor window of ±2 *m/z*. The number of precursor ions in the precursor window was constrained by a preferred ID list created based on the MS results. Collision energy for ESI+ mode was 30 V, with a threshold to trigger MS/MS of at least 2000 counts for the precursor ion. Collision energy for ESI− mode was 40 V, with a threshold to trigger MS/MS of at least 6000 counts for the precursor ion.

Data analysis also followed the published protocol (Lu et al., 2018). Briefly, MS data and MS/MS data were analyzed with MassHunter Qualitative Analysis (Version B.07.00, Service Pack 2), and IM-MS data was analyzed with MassHunter IM-MS Browser (Version B.07.01). Detected peaks were filtered based on signal-to-noise (S/N) ratios of ≥8 for ESI+ mode and of ≥5 for ESI− mode. The elements allowed in formulas in this work were C, H, N, O, and S. +H and +Na were allowed in positive data, while −H, +HCOO, and $+CH_3COO$ were allowed in negative data. A neutral loss of H_2O was enabled in both modes. The mass inaccuracy tolerance was set at ≤1.5 ppm. Formulas of DOM were then calculated and assigned with the following rules (Kujawinski and Behn, 2006; Stubbins et al., 2010; Liu et al., 2011; Hertkorn et al., 2013; Lu et al., 2018): (1) Double Bond Equivalent (DBE) = $1 + 1/2(2C\text{-}H + N) \geq 0$; (2) $O{:}C \leq 1$; (3) $N \leq 4$ and $N{:}C \leq 1$; (4) $0.333 \leq H/C \leq 2.25$; (5) Nitrogen Rule; (6) $S \leq 2$; and (7) Correct isotopic spacing and abundance. On average, 1818 peaks per sample were detected, and 1006 peaks were assigned with a formula under ESI+. Under ESI−, 748 peaks per sample were detected, and 488 were assigned with a formula. Riverine DOM was further divided into eight sub-classes based on its element stoichiometries (Kim et al., 2003; Ohno and Ohno, 2013; Mangal et al., 2016, 2017): (1) Lipid-like structures with elements ratios of: $0.01 \leq O/C \leq 0.1$; $1.5 \leq H/C \leq 2.0$; (2) Unsaturated hydrocarbon-like structures: $0.01 \leq O/C \leq 0.1$; $0.75 \leq H/C < 1.5$; (3) Condensed aromatic structures: $0.01 \leq O/C \leq 0.65$; $0.25 \leq H/C < 0.75$; (4) Protein-like structures: $0.1 < O/C \leq 0.65$; $1.5 \leq H/C \leq 2.3$; $N \geq 1$; (5) Lignin-like structures: $0.1 < O/C \leq 0.65$; $0.75 \leq H/C < 1.5$; (6) Tannin-like structures: $0.65 < O/C \leq 0.85$; $0.75 \leq H/C \leq 1.5$; (7) Carbohydrate-like structures: $0.65 < O/C \leq 1.0$; $1.5 < H/C \leq 2.5$; and (8) Others: those do not fall into any other category. Based on the Aromaticity Index (AI; Koch and Dittmar, 2006, 2016), which can be calculated from the number of C, H, O, N, and S in the molecular formula, the DOM can also be categorized into non-aromatic ($AI < 0.5$), aromatic ($0.5 \leq AI < 0.67$), and condensed aromatic structures ($AI \geq 0.67$). It has been demonstrated that ionization efficiencies among different molecules and compound classes are not equal (Oss et al., 2010), which means that the peak area of a specific molecular formula obtained from IM Q-TOF LCMS does not accurately represent its actual molecular concentration (the same is applied to all other ESI-MS). Therefore, in this work, the percentage of each compound group was calculated using the number of formulas, rather than peak area, following a previous study (e.g., Mangal et al., 2016).

Features obtained through non-targeted MS/MS were assigned with possible structures by comparing the product ion spectra with a standalone version of METLIN Metabolites database (Smith et al., 2005). MS/MS data were further examined in detail using Molecular Structure Correlator, which provided fragmentation information by comparing results with ChemSpider and METLIN Metabolites databases. Note that this assignment can only be used as a guide, not an identification, as there is no database for natural DOM and further evidence (e.g., direct comparison with a standard) is required for true identification. However, the product ion spectra of a DOM molecule can provide information on its fragmentation pathway and functional groups during the collision induced dissociation (CID) process.

IM-MS provides insights into structural isomers of DOM molecules and thus structural diversity (Lu et al., 2018; Leyva et al., 2019), which adds another level of information on the top of accurate molecular formulas. The IM-MS spectra were calibrated for mass and ion mobility measurements using the Agilent Tuning Mix mass calibration standard (Tune Mix, G2421A, Agilent Technologies, Santa Clara, CA, United States). Features with same *m/z* but different LC retention time (RT) and/or different collision cross section (CCS) are characterized as isomers following our previous study (Lu et al., 2018). Given the current resolving power (ca. 60; Lu et al., 2018), this drift time ion mobility instrument is able to differentiate isomers with difference in CCS as low as 2% (Nichols et al., 2018). Note that a majority of molecules can be lost in the drift tube during the IM mode due to interactions with nitrogen gas (Lu et al., 2018).

For statistical analyses, *t*-test and χ^2 test were conducted using Excel (version 2016) and principal component analysis (PCA) was conducted using R Studio (version 1.1) with package "factoextra." A significant level of 0.05 (i.e., $p < 0.05$ was considered significant) was used throughout this work.

RESULTS

Changes in Hydrological Parameters in High Flow Events

Salinities at sampling sites were <1%, with the exception of NR and LR sites (**Supplementary Table S1**). Salinity at these two sites can reach over 8‰ occasionally due to the presence of a water dam and/or the high evaporation rate in South Texas. Dissolved oxygen (DO) concentrations and saturation percentages were high at all sampling sites at base flow (DO > 5 mg·L^{-1}; DO% > 70%; **Supplementary Table S1**). However, after high-flow events (2017 September, 2018 June and September), both DO concentration and saturation percentage decreased significantly ($p = 0.03$ for DO%; $p = 0.04$ for DO). The averaged DO concentration during base-flow conditions was 6.4 mg·L^{-1} with an averaged saturation of ca. 83.1%, while after high-flow events, DO dropped to 4.4 mg·L^{-1} with an averaged saturation of 55.6%.

Concentrations of DOC and TDAA at Different Flow Conditions

Dissolved organic carbon concentrations in the four rivers ranged from 316 to 1089 μmol C L^{-1}, and 328 to 1008 μmol C L^{-1} at base-flow and high-flow conditions, respectively, with MR varying the most (**Supplementary Table S2**). Taking all four rivers together, the DOC concentration at base flow was ca. 628 μmol C L^{-1}, and ca. 653 μmol C L^{-1} after high-flow events, on average. However, no statistical difference was detected between different sampling times at base-flow and at high-flow (two-sample *t*-test; $p = 0.76$).

Total dissolved amino acids concentrations ranged from 2.23 to 25.5 μmol·L^{-1} and 1.00 to 37.0 μmol·L^{-1} at base-flow and high-flow conditions, respectively (**Supplementary Table S2**). TDAA at high-flow conditions was more variable, and no statistical difference was detected between different flow conditions (two-sample *t*-test; $p = 0.78$). TDAA-C yield (TDAA-C/DOC%) ranged from 1.67 to 18.5% and 0.90 to 24.6% at base-flow and high-flow conditions, respectively (**Supplementary Table S2**). Even though averaged TDAA-C yield at high-flow (9.86%) was higher than that of base-flow (6.71%), the difference again was not significant (*t*-test; $p = 0.78$). Compared with other large rivers such as Mississippi River (0.85–1.40%) and Atchafalaya River (0.94–2.95%) in subtropical regions (Shen et al., 2012), the four South Texas rivers generally had a higher TDAA-C yield, suggesting that DOM in this region may be more bioavailable than that of Mississippi and Atchafalaya Rivers, which have much longer flow paths.

Glycine (Gly) was the most abundant amino acid, on average accounting for 21.3% of TDAA in molecular composition, followed by aspartic acid (Asp; 11.3%), serine (Ser; 9.68%), and alanine (Ala; 9.46%; compositional data not shown). This pattern is consistent with other studies in riverine systems (e.g., Peter et al., 2012). We further applied PCA on amino acid composition (mol %) to explore any difference between base- and high-flow samples (**Supplementary Figure S2**). Principal component 1 (PC1) and principal component 2 (PC2) explained 50.0% and 17.8% of the data variance, respectively. The separation along the PC1 axis can be attributed to mainly ten variables, namely, β-alanine (BALA), γ-aminobutyric acid (GABA) and Gly with the most negative values, while glutamic acid (Glu), Ser, arginine (Arg), valine (Val), leucine (Leu) and isoleucine (Ile) with the most positive PC1 values. Therefore, PC1 provides preliminary separation of DOM samples based on their diagenetic characteristics, as an enrichment of Glu, Arg, Leu, and Ile suggests a fresh DOM source (Li et al., 2018), while a higher percentage of Gly, BALA, and GABA is indicative of a highly altered and degraded sample (Dauwe and Middelburg, 1998; Chen et al., 2004; Davis et al., 2009; Peter et al., 2012). Though no clear separation can be made, compared with base-flow samples, the trend that high-flow samples were positioned toward the positive or right end of PC1 is notable (**Supplementary Figure S2**).

Comparison of DOM Molecular Composition at Different Flow Conditions

Our previous study showed that the spatial difference in riverine DOM composition among these rivers is generally small (Lu et al., 2018), considering these rivers are spatially close (within 200 km), and have similar drainage basins (Mission and Aransas rivers from San Antonio-Nueces Coastal Basin, Nueces river from Nueces-Rio Grande Coastal Basin, and Lavaca river from Lavaca-Guadalupe Coastal Basin[2]). Furthermore, the difference among HPLC chromatographs across different rivers (**Supplementary Figure S3**) is much smaller than those from different sampling times at the same river (**Supplementary Figure S4**). Therefore, results will be more focused on temporal (among flow conditions) rather than spatial difference (among rivers).

High performance liquid chromatography is an important tool in molecular-level analysis of complex samples (Hertkorn et al., 2007), and has been used to isolate and identify biomolecules in many studies (Ogawa et al., 2001; Leenheer and Croué, 2003; Rathgeb et al., 2017). Using DOM samples collected from MR as an example, the HPLC chromatograms (i.e., the shape and the retention time of peaks) at base-flow were comparable (**Supplementary Figure S4**). Even though it is hard to extract a consistent trend from the HPLC chromatograms, it is clear that some peaks disappeared at high-flow conditions (e.g., peaks at ca. 5.8 min and ca. 11.0–12.0 min from ESI+; peaks at ca. 4.6–6.0 min, and peaks at ca. 8.0 min from ESI−; purple shades in **Supplementary Figure S4**), while other peaks emerged (e.g., peaks at ca. 6.0 and 14.0 min from ESI+; blue shades in **Supplementary Figure S4**), indicating changes in the DOM composition.

The averaged peak assignment percentage (Number of peaks assigned with formula/Number of peaks above S/N threshold × 100%) was 58.4% under ESI+, and 64.3% under ESI−, respectively. Element stoichiometry of a sample was calculated by averaging the H/C, O/C and N/C ratios of all assigned formulas. Element stoichiometry of one river at a certain sampling time (e.g., AR at-May 27, 2016) was calculated as the average of the duplicates (**Supplementary Table S3**), and element stoichiometry of a certain sampling time (e.g., May 27, 2016) was calculated as the average of all rivers on that sampling day (**Table 1**). Standard errors between duplicates were generally small (<0.01). Overall, under ESI+ mode, H/C ranged from 1.46 to 1.60 and O/C ranged from 0.21 to 0.27 at base flow condition, while H/C and O/C was in the range of 1.48–1.55 and 0.21–0.26, respectively, at high flow condition (**Table 1**). Under ESI+ mode, H/C decreased from 1.52 to 1.51 at high flow condition, but O/C remained constant (0.24). Statistical analysis showed that base and high flow samples were not different in terms of element stoichiometry under ESI+. However, under ESI− mode, H/C decreased from an average of 1.19 (1.07–1.26) at base flow, to an average of 1.07 (1.03–1.12) at high flow (*t*-test; $p = 0.02$), while O/C increased from 0.31 (0.29–0.33) at base flow, to 0.33 (0.32–0.34) at high flow (*t*-test; $p = 0.03$).

These changes in element ratios can be further visualized by van Krevelen diagrams (ESI+ mode, **Supplementary Figure S5**; ESI−, **Supplementary Figure S6**), in which H/C was plotted against O/C and each dot represents one formula. The van Krevelen diagrams of the four rivers, regardless of the flow condition, resembled published work (e.g., Tfaily et al., 2015), characterized by a large fraction of high H/C and low O/C molecules. Meanwhile, the change after high-flow events was clear, with a fraction of low H/C but high O/C molecules emerging in high-flow samples. This change is more evident when unique features were extracted from different flow conditions (**Figure 2**). Unique features at base flow were dominated by formulas with high H/C but low O/C ratios (**Figure 2A**), while those at high flow were mainly characterized by formulas with low H/C ratios (**Figure 2B**). The appearance of high-flow molecules (**Figure 2B**) and the loss of base-flow unique molecules (**Figure 2A**) shifted the element stoichiometry toward low H/C but high O/C (**Table 1**).

Dissolved organic matter was further categorized into different compound groups based on element stoichiometry. Again, changes in the proportions of these categories were more evident in ESI− mode (**Table 2**, **Figure 3B**, and **Supplementary Figure S6**) than those in ESI+ mode (**Supplementary Table S4**, **Figure 3A**, and **Supplementary Figure S5**). Regardless of the flow conditions, riverine DOM was dominated by lignin-like compounds (34.8%), followed by condensed aromatics (18.9%), and protein-like compounds (9.1%), under ESI−. From high-flow to low-flow, fractions of lignin-like compounds (34.7% to 35.1%; $p = 0.42$), tannin-like compounds (2.11% to 4.16%; $p < 0.01$), and condensed aromatics (16.2% to 23.3%; $p = 0.04$) all increased, while decreases were observed for unsaturated hydrocarbons (9.19% to 6.28%; $p = 0.04$), protein-like (9.92% to 7.71%; $p = 0.06$), lipid-like (3.23% to 1.59%; $p = 0.03$), and carbohydrate-like compounds (6.65% to 6.62%; $p = 0.48$). The distribution of compound classes under ESI− mode can

TABLE 1 | Element stoichiometry of riverine DOM.

Flow condition	Sampling time	ESI+			ESI−		
		H/C	O/C	N/C	H/C	O/C	N/C
Base flow	27-05-2016	1.46 ± 0.01	0.26 ± 0.00	0.09 ± 0.00	1.24 ± 0.01	0.29 ± 0.00	0.07 ± 0.00
	19-07-2016	1.55 ± 0.00	0.22 ± 0.00	0.06 ± 0.00	1.26 ± 0.02	0.29 ± 0.01	0.07 ± 0.00
	07-10-2016	1.60 ± 0.00	0.21 ± 0.00	0.07 ± 0.00	1.18 ± 0.03	0.31 ± 0.01	0.07 ± 0.00
	19-06-2017	1.50 ± 0.02	0.25 ± 0.00	0.07 ± 0.00	1.07 ± 0.03	0.33 ± 0.00	0.08 ± 0.00
	21-03-2018	1.47 ± 0.00	0.27 ± 0.00	0.06 ± 0.00	1.19 ± 0.01	0.32 ± 0.00	0.08 ± 0.00
High flow	28-09-2017	1.51 ± 0.01	0.21 ± 0.00	0.10 ± 0.00	1.12 ± 0.03	0.32 ± 0.00	0.08 ± 0.00
	21-06-2018	1.48 ± 0.03	0.26 ± 0.00	0.06 ± 0.00	1.07 ± 0.01	0.33 ± 0.00	0.08 ± 0.00
	19-09-2018	1.55 ± 0.01	0.25 ± 0.01	0.06 ± 0.00	1.03 ± 0.02	0.34 ± 0.01	0.08 ± 0.00

---

[2] http://www.twdb.texas.gov/

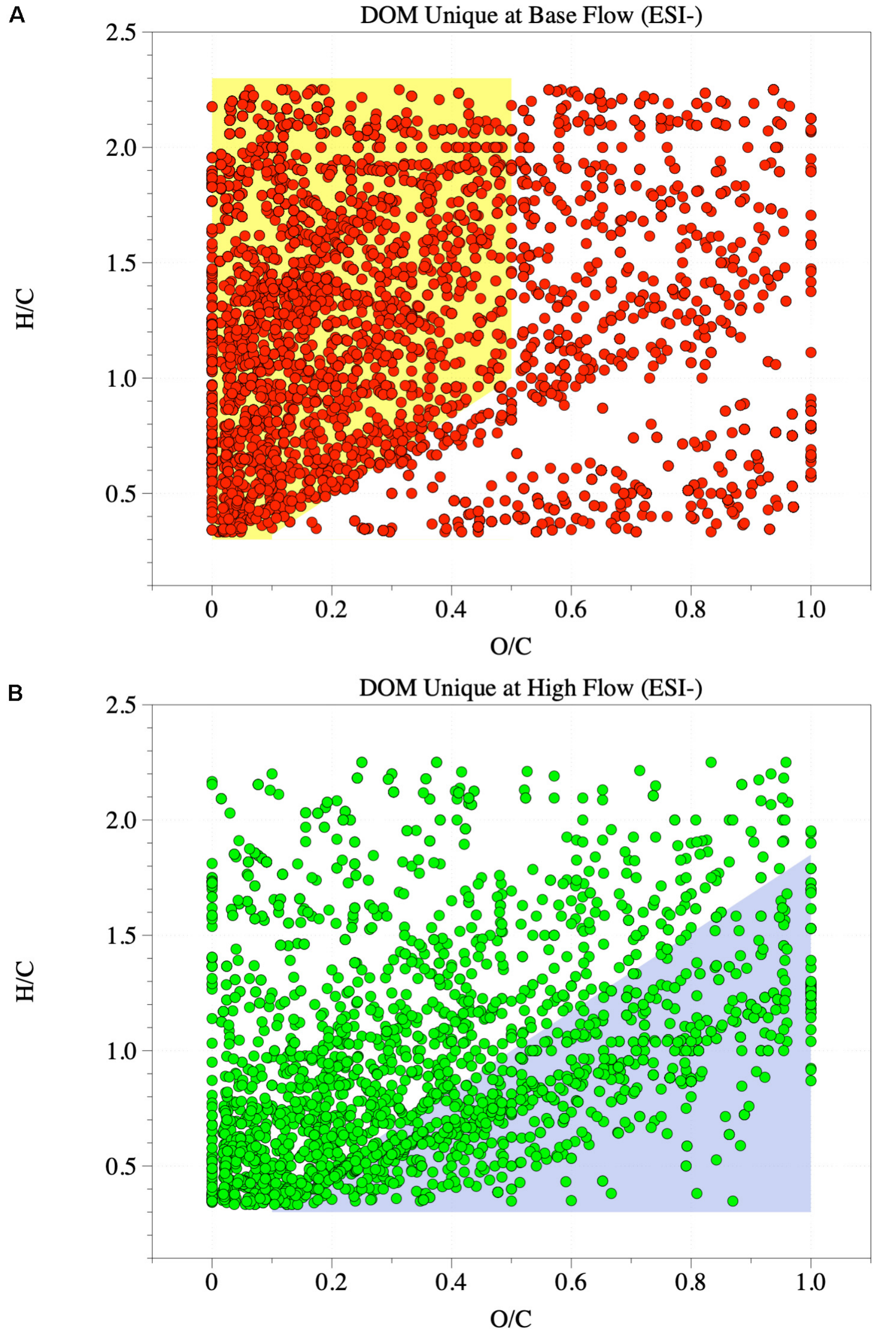

FIGURE 2 | van Krevelen diagrams of riverine DOM under ESI– mode. **(A)** Unique features at base-flow (6725 unique formulas). **(B)** Unique features at high-flow (2622 unique formulas). Yellow shade in **A** indicates high H/C and low O/C formulas. Blue shade in **B** indicates low H/C formulas.

be further visualized by PCA (percentages of each category as the PCA data input, and data were normalized before analysis; **Figure 4**), where base-flow samples were characterized by relative high fractions of protein- and lipid-like structures, while high-flow samples were characterized by elevated levels of carbohydrate-, lignin-, tannin-like compounds, and condensed aromatics. A similar pattern was observed under ESI+ mode, yet none of those trends was statistically significant (**Figure 3A**, **Supplementary Figure S5**, and **Supplementary Table S4**). Also noted were the much higher percentages (24–36%) of protein-like compounds under ESI+ mode, a pattern that was caused by preferential ionization of nitrogen containing molecules (Lin et al., 2012; Ohno et al., 2016).

The aromaticity of riverine DOM was calculated by AI (Koch and Dittmar, 2006, 2016). Based on AI, riverine DOM was dominated by non-aromatics under both ESI modes regardless

TABLE 2 | Compound categories (%) at base-flow and high-flow (ESI−).

Flow condition	Sampling time	Lipids	Unsaturated hydrocarbons	Condensed aromatic structures	Proteins	Lignin	Tannins	Carbohydrates	Others
Base flow	27-05-2016	3.02	12.1	12.2	10.6	35.3	1.88	6.57	18.3
	19-07-2016	4.66	10.2	13.9	13.0	31.2	1.54	5.57	19.9
	07-10-2016	3.96	7.65	18.1	10.1	33.1	2.49	6.28	18.3
	19-06-2017	1.65	6.28	23.1	7.16	37.7	3.08	7.89	13.3
	21-03-2018	2.86	9.69	13.6	8.84	36.0	1.54	6.98	20.5
	Average	3.23	9.19	16.2	9.92	34.7	2.11	6.65	18.1
High flow	28-09-2017	0.70	7.59	19.6	9.12	37.7	3.86	8.13	13.2
	21-06-2018	2.12	6.83	22.6	7.41	33.7	3.92	5.74	17.6
	19-09-2018	1.95	4.40	27.8	6.59	33.7	4.69	6.00	14.9
	Average	1.59	6.28	23.3	7.71	35.1	4.16	6.62	15.3

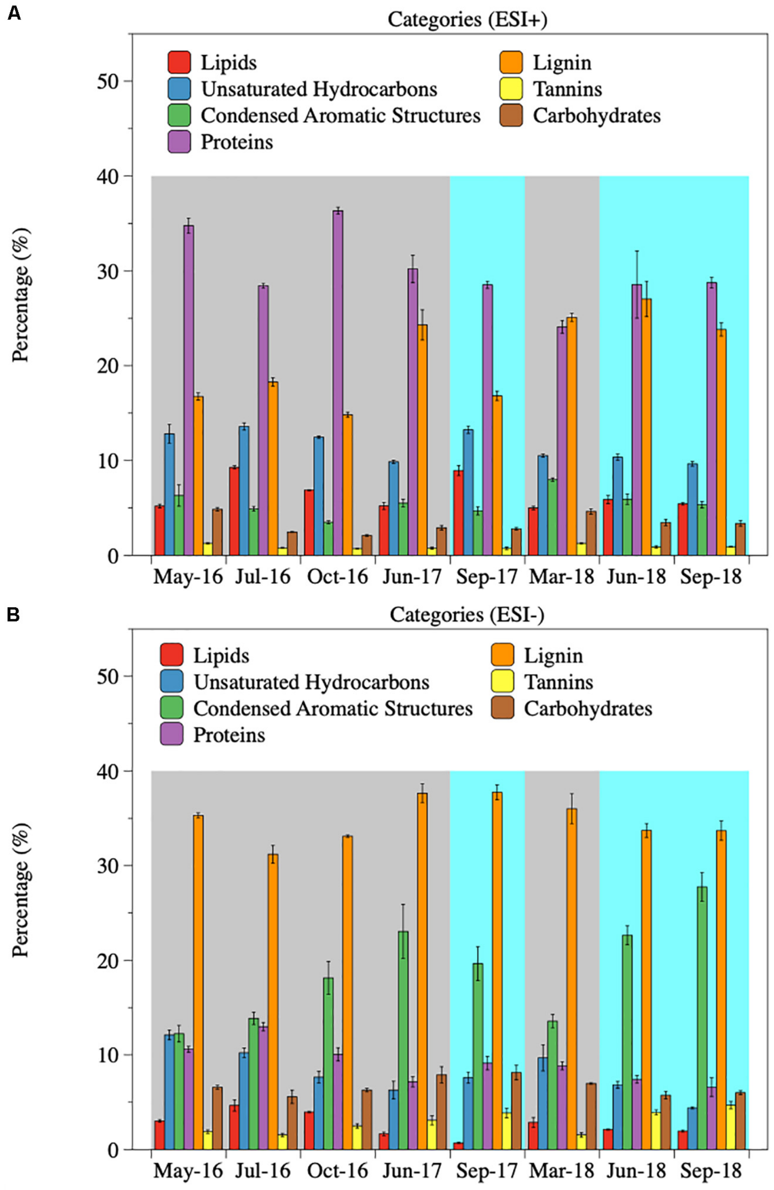

FIGURE 3 | Percentages of different compound classes under ESI+ **(A)** and ESI− **(B)** modes. DOM was categorized into different compound classes based on the assigned formula and element stoichiometry. Gray shades indicate base-flow condition. Cyan shades indicate high-flow condition.

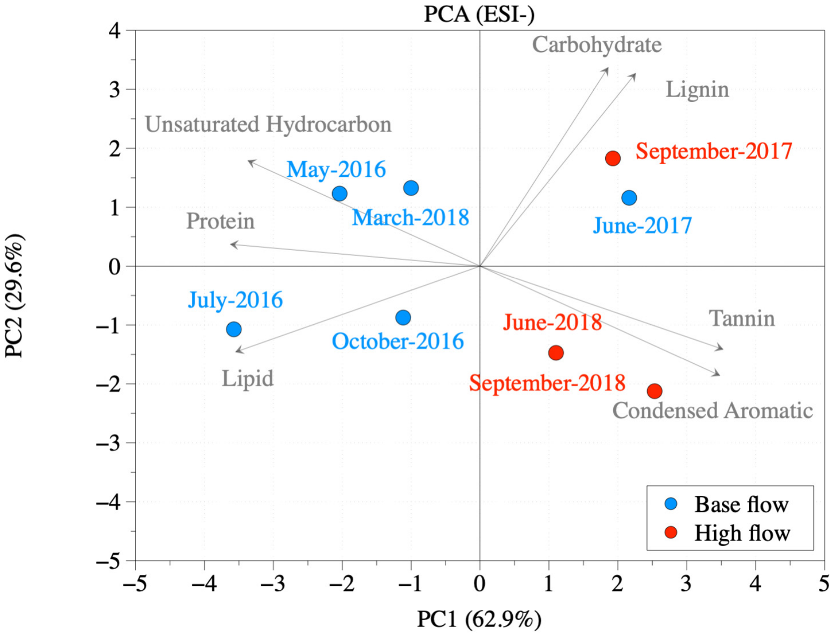

FIGURE 4 | PCA based on the percentage of different compound classes under ESI– mode. Blue indicates samples at base-flow condition (May 2016, July 2016, October 2016, June 2017, and March 2018). Red indicates samples at high-flow condition (September 2017, June 2018, and September 2018).

TABLE 3 | Compound aromatic classes (%) at base-flow and high-flow (ESI−).

Flow condition	Sampling time	Aromatic	Condensed aromatic	Non-aromatic
Base flow	27-05-2016	16.1	12.1	71.9
	19-07-2016	15.7	15.0	69.3
	07-10-2016	16.5	18.5	65.0
	19-06-2017	17.5	23.7	58.8
	21-03-2018	16.6	16.2	67.2
	Average	16.5	17.1	66.4
High flow	28-09-2017	18.7	19.3	62.0
	21-06-2018	16.8	23.1	60.1
	19-09-2018	17.8	26.2	56.1
	Average	17.7	22.8	59.4

of flow conditions (**Table 3**, **Supplementary Table S5**, and **Figure 5**). However, a significant increase in aromaticity was observed at high flow, as the proportion of aromatic and condensed aromatic formulas increased from 16.5 and 17.1% ($p = 0.06$) at base flow to 17.7 and 22.8% ($p = 0.04$) at high flow under ESI− mode, respectively (**Table 3** and **Figure 5B**), consistent with the observed increase in condensed aromatics based on element stoichiometry (**Table 1**, **Figure 3B**, and **Supplementary Figure S6**). Under ESI+ mode, the changes in aromatic and condensed aromatic compounds were not significant ($p = 0.18$ and 0.23, respectively; **Supplementary Table S5** and **Figure 5A**).

Since changes in DOM composition were more evident in ESI− based on MS, the MS/MS analysis was focused on ESI−. On average, ca. 500 MS/MS features were obtained for each sample, and the non-targeted MS/MS assigned a total of 829 compounds based on the precursor and product ion spectra (ESI− mode), while the majority cannot be assigned due to the limitation of the database. Even though this assignment cannot guarantee an exact structure of the DOM compound, it provides insights into the possible structural moieties of DOM, and how these moieties changed during a high-flow event. When focused on the unique formulas found only at high-flow conditions, a total number of 73 compounds were found. These 73 compounds contained various metabolites from Loquatoside ($C_{20}H_{22}O_{11}$), with a possible source from the fruit of loquat (*Eriobotrya japonica*; common in South Texas[3]), to Egonol ($C_{19}H_{18}O_5$) from mushrooms *Laetiporus sulphureus var. miniatu* (also present in South Texas), with an average H/C of 1.22 and O/C of 0.40 (a list of compounds can be found in the **Supplementary Data Sheet S1**). The matches with metabolites in the database do not necessarily confirm the exact structures, which would

---

[3] https://aggie-horticulture.tamu.edu/citrus/loquat.htm

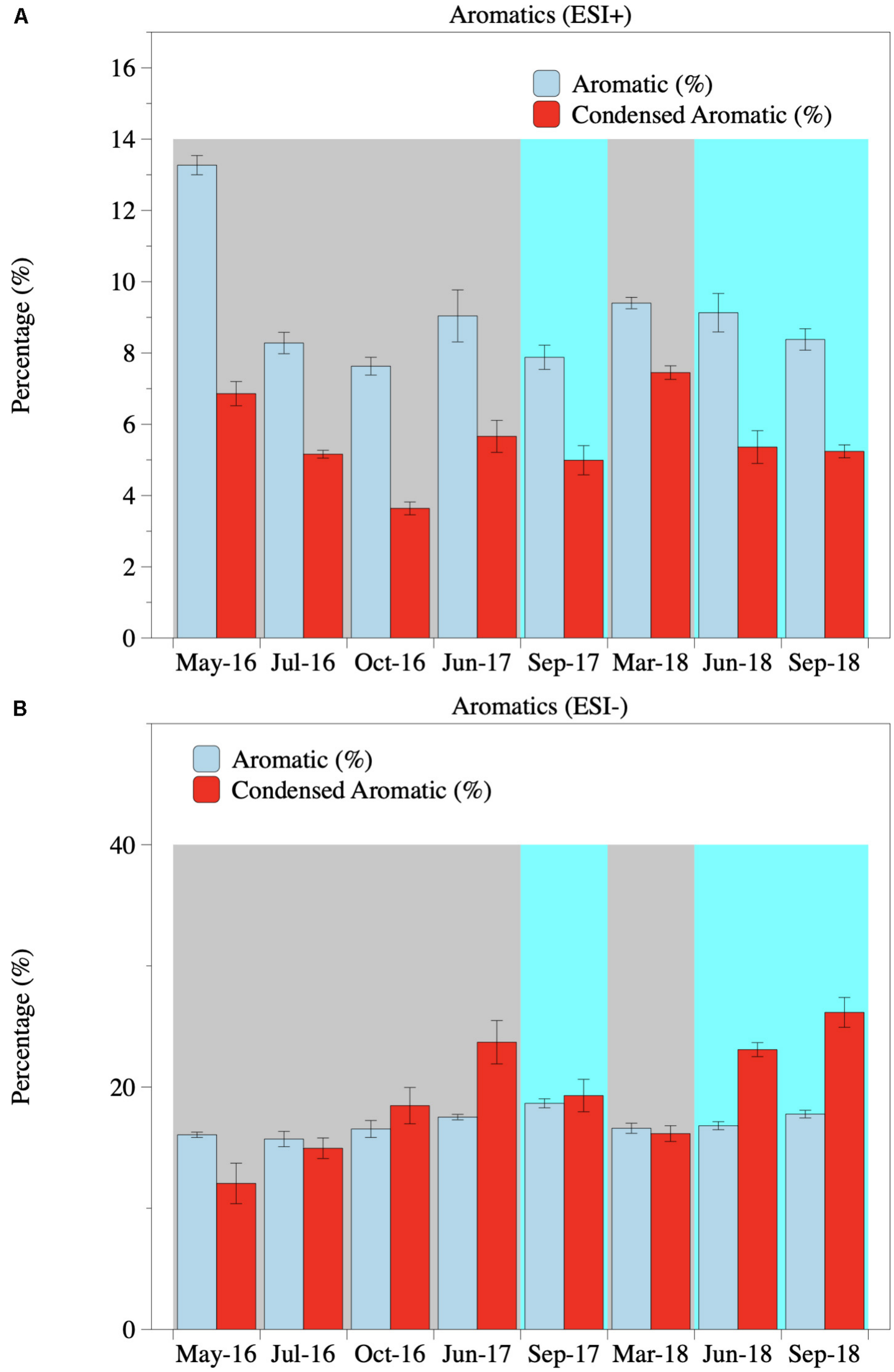

FIGURE 5 | Percentages of different compound classes under ESI+ **(A)** and ESI– **(B)** modes. DOM was categorized into different aromatic classes based on the assigned formula and the calculated AI. Gray shades indicate base-flow condition. Cyan shades indicate high-flow condition.

need further work, such as running with known standards, but these results show the power of non-targeted MS/MS in seeking molecules of interest from an extremely complex DOM pool. The MS/MS fragments of precursor molecules can be assigned to exact structures with confidence due to their smaller *m/z* and the distribution of these fragments further facilitates the assignment of precursor ions with the database. Most of these assigned compounds have multiple aromatic rings and multiple O atoms in their structure, which can be further confirmed by their product ion spectra (e.g., the presence of C_6H_5 fragments). For instance, precursor ion (*m/z* of 473.0747) MS spectrum (**Figure 6B**) was first extracted from the HPLC chromatogram

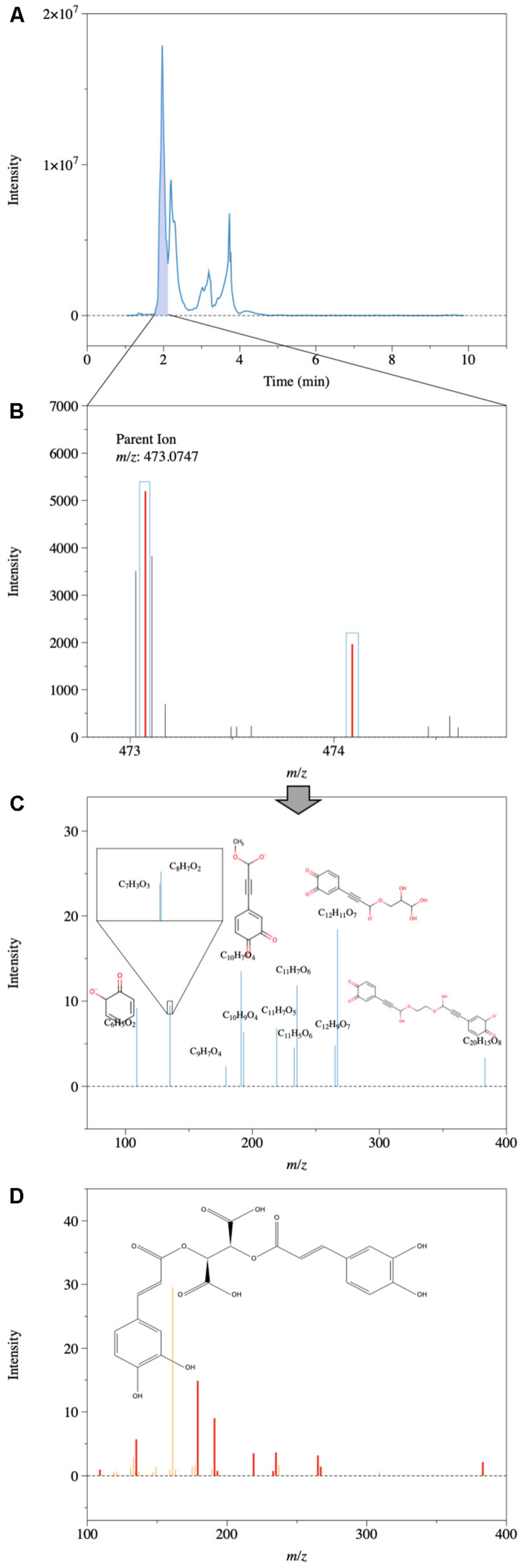

FIGURE 6 | Continued

FIGURE 6 | One example of assigned structures based on MS/MS spectra and a METLIN metabolites database. Note that the exact structures may not be right, but the product ions after collision proved the presence of aromatic ring structures and O atoms. **(A)** HPLC chromatogram; **(B)** Precursor ion (*m/z* of 473.0747) extracted from the HPLC chromatogram. **(C)** Detected product ion spectra after application of a collision energy of 40 V. **(D)** Predicted product ion spectrum of compound $C_{22}H_{18}O_{12}$ based on database (METLIN and Human Metabolome Database at: http://www.hmdb.ca/) at the same collision energy of 40 V, matches between detected spectra and predicted spectra are shown in bold red.

(**Figure 6A**). The precursor ion was selected by quadrupole mass filter and was further fragmented by collision to produce product ion spectra (**Figure 6C**). The product ion spectra were further compared with the database (**Figure 6D**), and the presence of several aromatic-ring structures after collision in the product ion spectra confirmed an oxygenated, aromatic-rich structure for the compound $C_{22}H_{18}O_{12}$. Another example can be found in **Supplementary Figure S7**.

Comparison of Geometric Configurations and Isomeric Percentage During Different Flow Conditions

In ion mobility, separation of different molecules is achieved by low-energy interactions between molecules and the inert buffer gas. The time (drift time) for each molecule to traverse the mobility tube is a function of its 3D structure, i.e., molecules with more stretched structures are slowed down more easily by the inert gas, and thus possess longer drift times. Therefore, the geometric configuration of DOM molecules, in the form of collision section area (collision cross section, CCS) values, can be quantified by calibrating with known standards (Tune Mix, G2421A, Agilent Technologies, Santa Clara, CA, United States). CCS values of the DOM molecules generally increased with increasing *m/z* (**Figure 7** and **Supplementary Figure S8**). Compared with biomolecule standards (May et al., 2014), natural DOM molecules had more compacted geometric configurations, which was consistent with our previous findings (Lu et al., 2018). However, a group of DOM compounds possessed CCS values even higher than those of tetraalkylammonium standards. These compounds were generally in the m/z range of 100–400, and were mainly from high-flow DOM. Assigned molecular formula based on MS data indicate that these compounds had much higher O/C ratios (average of 0.51; **Supplementary Table S6**) compared with bulk O/C under ESI+. However, MS/MS analysis did not find any match in the metabolite database, suggesting that these compounds are likely natural and/or processed organic matter. Nevertheless, the similar CCS values between high- and base-flow DOM (**Figure 7** and **Supplementary Figure S8**), suggest that the overall geometric configuration of DOM was not affected by flow conditions.

Isomeric information on DOM was obtained via IM-MS (Lu et al., 2018). Structural isomers, though possessing a same molecular formula, have different three-dimensional structures. With a resolving power of ca. 60, drift time IM-MS can separate isomers with a 2% difference in their CCS values

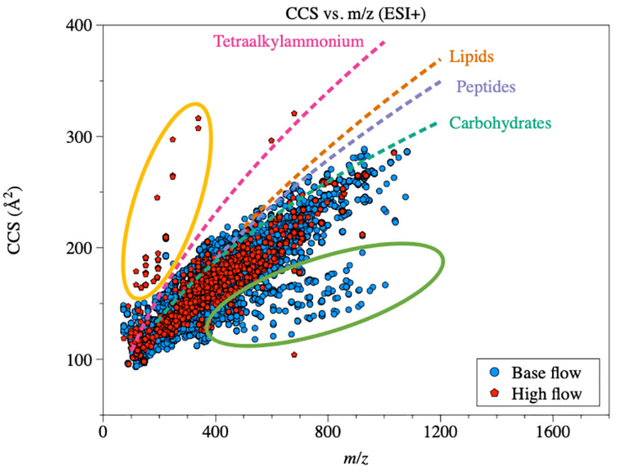

FIGURE 7 | CCS vs. *m/z* under ESI+ mode. Trend lines of CCS vs. *m/z* for biomolecules were calculated based on May et al. (2014). CCS of riverine DOM was generally lower than biomolecules. The majority from different flow conditions cannot be clearly separated. Green oval indicates more compacted compounds (more diagenetically altered) from base-flow samples. Yellow oval indicates more extended compounds (less diagenetically altered) from high-flow samples.

(Nichols et al., 2018). Therefore, isomer percentage was further defined as:

$$\text{Isomer Percentage} = \frac{\text{Number of different formulas possessing isomer}}{\text{Total number of different formulas}} \times 100\% \quad (1)$$

At base-flow condition, isomer percentages of riverine DOM molecules ranges from 5.71 to 17.3% across different rivers, with the highest isomer number of 8 in ESI+ mode, and 3.76 to 21.8%, with the highest isomer number of 10 in ESI− mode (**Table 4**), consistent with a previous study (Lu et al., 2018). At high-flow, isomer percentage under ESI+ mode ranges from 8.48 to 15.2%, while from 3.44 to 14.0% under ESI− mode (**Table 4**). The change in isomer percentage under ESI+ mode was not significant ($p = 0.17$). However, under ESI− mode, isomer percentage decreased significantly from 11.3% at base-flow to 7.72% at high-flow ($p = 0.02$). Further information on the change in isomeric percentage at different flow conditions can be found in the **Supporting Information**.

DISCUSSION

Impact of Storm Events on Riverine DOM

Besides quantity, a high-flow event can affect the composition of DOM (Gremm and Kaplan, 1998; Hood et al., 2006; Zhang et al., 2007; Spencer et al., 2008), which is a result of mobilization of different terrestrial DOM pools that are not available under base flow conditions (Vidon et al., 2008; Fellman et al., 2009; Osburn et al., 2019). The appearance of a group of new compounds under high flow is consistent with this idea (**Figure 2B**). In terms of compound classes, high-flow DOM was more aromatic (**Tables 2, 3** and **Figure 5**), and had elevated proportions of lignin- and tannin-like compounds (**Table 2** and **Figures 3, 4**). During periods of high flow, elevated water level and faster flow can mobilize the DOM on the higher part of the riverbank and watershed. In these watersheds, DOM is mainly sourced from higher plants (Mooney and McClelland, 2012). This speculation is supported by the PCA (**Figure 4**), in which the high-flow DOM has positive PC1 loading, showing a strong terrestrial signal, and an elevated contribution from higher plants. Furthermore, the non-targeted MS/MS confirmed the terrestrial source, as the assigned structures from MS/MS are highly oxygenated (O/C of 0.40) and contain multiple aromatic structures.

However, the bioavailability of high flow DOM is controversial. Since no bioassay experiment was conducted to quantify the bioavailability of DOM from different flow conditions, we have to mainly rely on the chemical composition information obtained through MS and MS/MS. It has been suggested that hydrogen-deficient molecules with low H/C ratios are not easily metabolized by microbes (Kim et al., 2006), and molecules with a H/C $\leq$ 1.5 are considered to be

TABLE 4 | Isomer percentages (%) of riverine DOM at base-flow and high-flow conditions.

Flow condition	Sampling time	ESI+				ESI−			
		AR	LR	MR	NR	AR	LR	MR	NR
Base flow	27-05-2016	9.99	9.65	13.7	13.2	13.9	9.27	9.49	9.98
	19-07-2016	7.24	7.78	6.13	5.71	3.76	7.6	17.3	12.9
	07-10-2016	12.1	11.8	9.95	12.1	8.93	9.34	4.00	13.1
	19-06-2017	8.67	9.48	10.4	10.6	10.9	10.1	17.1	17.0
	21-03-2018	11.6	10.3	17.3	9.72	10.8	21.8	10	9.31
	Average	9.92	9.80	11.5	10.3	9.66	11.6	11.6	12.4
High flow	28-09-2017	11.7	13.0	10.2	8.48	4.05	6.11	3.44	3.46
	21-06-2018	15.2	11.1	11.5	8.89	10.4	10.6	5.78	9.82
	19-09-2018	N.D.	10.8	14.7	12.0	N.D.	14.0	10.5	7.20
	Average	13.5	11.6	12.2	9.80	7.25	10.2	6.58	6.83

recalcitrant (D'Andrilli et al., 2015). Therefore, a decrease in H/C at high-flow in both ESI modes (**Table 1**, **Supplementary Table S3**, and **Figure 2**) may suggest an increase in recalcitrance in DOM at high-flow. However, other studies have demonstrated that terrestrial DOM with high O/C and enriched aromatic structures are selectively degraded in fresh water systems (e.g., Kellerman et al., 2014, 2015). Furthermore, the amino acids analysis showed that the majority of base-flow DOM (except for May-2016 and October-2016 samples) had high mol% of Gly, BALA, and GABA, clearly suggesting a more diagenetically altered nature (**Supplementary Figure S2**). As a comparison, DOM at high-flow tended to be at the positive end of PC1, characterized by high mol% of Glu, Arg, Leu, and Ile, indicating that these DOM were less altered. This, again, suggests a decrease in recalcitrance of DOM at high flow.

The "apparent" conflicting results may be reconciled by the fact that high-flow DOM may contain both recalcitrant and highly labile fractions of DOM. In addition, at base-flow conditions, due to the low flow rate, high temperature, and strong irradiation in South Texas, riverine DOM may have been heavily processed due to strong microbial activities and photochemical reactions. This explains the fact that the base-flow DOM appears to be more diagenetically altered based on amino acids analysis. At high-flow conditions, the chemical composition of river DOM is mainly shaped by terrestrial DOM, as the most degraded base-flow DOM is carried away by elevated flow with less time for processing during the transit. The mobilized DOM, often enriched in O but depleted in H due to the presence of aromatic structures (e.g., Vidon et al., 2008; Majidzadeh et al., 2017; Osburn et al., 2019; Wagner et al., 2019), tends to resist biodegradation (Spencer et al., 2016), but can be selectively degraded with the presence of sunlight (Stubbins et al., 2010). However, photochemical degradation may be inhibited at high flow due to several reasons. First, the residence time of river water, as well as mobilized terrestrial DOM, is highly reduced during a high-flow event due to the increased flow rate (**Supplementary Figure S1B**). Hence, the exposure time of DOM to sunlight is reduced. Second, an increase in turbidity due to the resuspension of sediment at high flow would reduce the amount of light absorbed by DOM. Finally, the remaining aromatic DOM might be protected by the self-shading effect when the colored DOM (CDOM) concentration is high (Del Castillo et al., 1999; Köhler et al., 2002; Larson et al., 2007; Granskog, 2012; Wagner et al., 2019).

Overall, DOM at high-flow appears to contain relatively higher percentages of aromatic structures, which may represent a recalcitrant nature under certain conditions, but can be very reactive when conditions change. Therefore, the high-flow events can relocate a large amount of terrestrial photo-active DOM to coastal region, where it could be rapidly utilized by microbes and further fuel primary production in brackish water (e.g., Liu et al., 2011; Mooney and McClelland, 2012; Bruesewitz et al., 2013; Reyna et al., 2017). High flow DOM also seems to contain a fraction of highly bioavailable DOM in the form of hydrolyzable amino acids, which can further supply labile substrates to estuaries and bays. At the same time, the refractory components of the relocated terrestrial DOM may persist for a prolonged period of time (e.g., from weeks to months), and can cause lingering impact on estuarine C cycling (Osburn et al., 2019).

Changes in the Geometric Configuration and Isomeric Composition of Riverine DOM

The correlations between CCS and *m/z* in base-flow and high-flow conditions can be described adequately by a power-law relationship (base-flow ESI+: $y = 18.7\ x^{0.37}$, $R^2 = 0.72$; high-flow ESI+: $y = 16.0\ x^{0.40}$, $R^2 = 0.80$; base-flow ESI−: $y = 23.1\ x^{0.35}$, $R^2 = 0.20$; high-flow ESI−: $y = 38.9\ x^{0.25}$, $R^2 = 0.12$). χ^2 tests were performed and no statistical difference was detected in CCS-*m/z* distribution between base-flow and high-flow samples (**Figure 7** and **Supplementary Figure S8**; p-value > 0.05 for both ESI modes), suggesting that the flow condition did not affect the geometric configuration of riverine DOM. This pattern implies that DOM from different sources and processes (i.e., highly altered at base flow vs. terrestrial at high flow) has similar geometric structures. As natural DOM is originated from biopolymers, the fact that the majority of riverine DOM molecules possessed lower CCS values (i.e., more compacted geometric structures) compared with standard biomolecules suggests that environmental degradation tends to make natural DOM more compacted (Lu et al., 2018). Even though no statistical difference was detected, CCS values of some DOM at base flow were lower than the others (green oval in **Figure 7**), while high-CCS molecules appeared in high-flow samples (yellow oval in **Figure 7**). Based on the formula assigned, these high-CCS compounds generally have a relative high O/C ratio (average 0.51; 0.33–0.71), indicating a strong terrestrial signal. The presence of these two groups of features in IM-MS diagram supports the speculation that CCS can reflect the diagenetic status of DOM to an extent, as more diagenetically altered compounds (from base-flow, green oval) tend to have even more compacted structures, while less altered compounds (from high-flow, yellow oval) may have extended geometric structure as biomolecules. However, this is only the case for a small group of compounds in IM-MS diagram, as base-flow and high-flow samples were statistically similar. Also, IM-MS analysis can only represent a small fraction of molecules detected in MS (Lu et al., 2018). Therefore, more studies are needed to reveal the relationship between the CCS of DOM and its reactivity.

Although no direct measurement was conducted, a recent study suggested that riverine DOM after storm events could potentially have high structural diversity (Wagner et al., 2019), based on modeling results (Zark et al., 2017; Hawkes et al., 2018; Zark and Dittmar, 2018). Based on the central limit theorem, these modeling studies assumed a random combination of atoms in DOM molecules and suggested that each formula assigned in ultrahigh-resolution mass spectrometry potentially represents 10–100 different isomers (Zark et al., 2017; Hawkes et al., 2018). Our results, however, suggested an opposite pattern. The percentages of molecules that have isomers, across different sampling sites, sampling time and ESI modes, were highly constrained, ranging from ca. 3% to ca. 22%. Also highly constrained was the number of isomers for each formula,

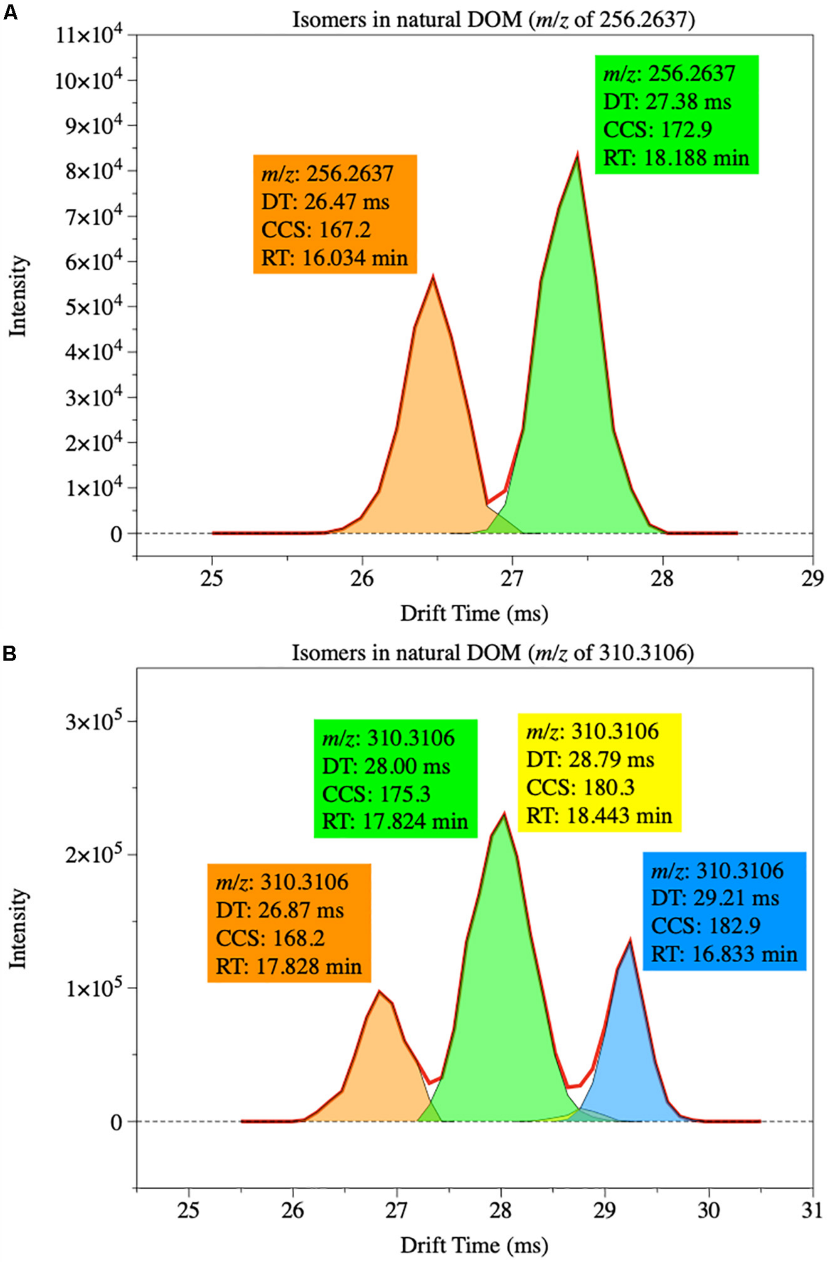

FIGURE 8 | Examples of isomer distribution of two sets of compounds in riverine DOM. **(A)** Compound with a *m/z* of 256.2637 has two isomers. **(B)** Compound with a *m/z* of 310.3106 has four isomers.

with most formula having only 2 isomers (one formula, two different molecules) and the largest of 10 (one formula, ten different molecules). This distribution pattern can be further visualized by overlying all isomers together, with isomers in DOM having separated, non-even peaks (**Figure 8**). The lower isomer percentages indicate that DOM formation may have gone through certain biochemical pathways, and that there are additional constraints on the bonds breaking and formation processes of natural DOM. This is in sharp contrast with crude oil, in which the isomers of a given hydrocarbon are more evenly distributed (Benigni et al., 2017). The formation of crude oil involves random chemical reactions under high pressure and heat (e.g., Tissot et al., 1974; Vandenbroucke and Largeau, 2007), while the biogeochemical pathways, key to DOM formation, may not be random. For example, odd- and even-numbered *n*-alkanes are evenly distributed in crude oil, while the odd-numbered dominates even-numbered *n*-alkanes in samples derived from high plants.

While more work is needed to reconcile the discrepancy between our data and modeling results, this dataset provides one of the first few quantitative studies about DOM isomers based on actual measurements (Benigni et al., 2017; Lu et al., 2018; Leyva et al., 2019), and it opens a new direction in molecular-level DOM analysis for the future.

CONCLUSION

A multi-dimension molecular level analysis of riverine DOM via IM Q-TOF LCMS revealed molecular level changes in DOM at different flow conditions in the South Texas region. Our results showed that high-flow events driven by storm or hurricane, as well as the subsequent biotic and abiotic process, changed the chemical composition of riverine DOM. Even though the bulk concentrations of DOM were similar across the sampling period, DOM pool experienced an increase in the proportions of lignin-, tannin-, carbohydrate-like, and condensed aromatic formulas, showing a stronger terrestrial signal as expected. With LC and IM, we obtained a direct measurement of isomers in riverine DOM. With an isomer percentage ranging from 3 to 22%, our data indicated that the number of isomers in riverine DOM was highly constrained. This finding in the isomeric information on riverine DOM not only showed the impacts of high-flow events on DOM, but also provided crucial insights into molecular and structural details of riverine DOM under extreme weather events.

DATA AVAILABILITY STATEMENT

All datasets generated for this study are available upon request and most of them can be found in the article/**Supplementary Material**.

AUTHOR CONTRIBUTIONS

KL and ZL designed the experiments and wrote the manuscript. KL conducted the experiments.

FUNDING

This study was supported by the NOAA (NA15NOS4780185), an Institutional Grant (NA14OAR4170102) to the Texas Sea Grant College Program from the National Sea Grant Office, NOAA, and the NSF Chemical Oceanography program (OCE 1763167).

ACKNOWLEDGMENTS

We thank Dr. Ryan Hladyniuk from the UTMSI Core Facility Lab for helping assemble and maintain the equipment, and Drs. Carol Haney Ball, Dawn Stickle, Caroline S. Chu, and Daniel Cuthbertson from the Agilent Technologies for invaluable technical support. Special thanks to Drs. Robert Dickey and Ed Buskey for making the instrumentation available at UTMSI. We also thank Dr. Xianbiao Lin, Dr. Kai Wu, Jason Jenkins, John O'Connor, and Cory Staryk for their help in sampling trips.

SUPPLEMENTARY MATERIAL

The Supplementary Material for this article can be found online at: https://www.frontiersin.org/articles/10.3389/fmars.2019.00673/full#supplementary-material

REFERENCES

Bender, M. A., Knutson, T. R., Tuleya, R. E., Sirutis, J. J., Vecchi, G. A., Garner, S. T., et al. (2010). Modeled impact of anthropogenic warming on the frequency of intense Atlantic Hurricanes. *Science* 327, 454–458. doi: 10.1126/science.1180568

Benigni, P., Sandoval, K., Thompson, C. J., Ridgeway, M. E., Park, M. A., Gardinali, P., et al. (2017). Analysis of photoirradiated water accommodated fractions of crude oils using tandem TIMS and FT-ICR MS. *Environ. Sci. Technol.* 51, 5978–5988. doi: 10.1021/acs.est.7b00508

Bomar, G. W. (1983). *Texas Weather*, 1st Edn. Austin, TX: University of Texas Press.

Bomar, G. W. (2017). *Weather in Texas: The Essential Handbook*, Third Edn. Austin, TX: University of Texas Press.

Bruesewitz, D. A., Gardner, W. S., Mooney, R. F., Pollard, L., and Buskey, E. J. (2013). Estuarine ecosystem function response to flood and drought in a shallow, semiarid estuary: nitrogen cycling and ecosystem metabolism. *Limnol. Oceanogr.* 58, 2293–2309. doi: 10.4319/lo.2013.58.6.2293

Buffam, I., Galloway, J. N., Blum, L. K., and McGlathery, K. J. (2001). A stormflow/baseflow comparison of dissolved organic matter concentrations and bioavailability in an Appalachian stream. *Biogeochemistry* 53, 269–306. doi: 10.1023/A:1010643432253

Cai, Y., Guo, L., Wang, X., Lohrenz, S. E., and Mojzis, A. K. (2013). Effects of tropical cyclones on river chemistry: a case study of the lower Pearl River during Hurricanes Gustav and Ike. *Estuar. Coast. Shelf Sci.* 129, 180–188. doi: 10.1016/j.ecss.2013.05.019

Carlson, C. A., and Hansell, D. A. (2015). "DOM Sources, Sinks, Reactivity, and Budgets," in *Biogeochemistry of Marine Dissolved Organic Matter*, Second Edn, eds D. A. Hansell, and C. A. Carlson, (Boston, MA: Academic Press), 65–126. doi: 10.1016/b978-0-12-405940-5.00003-0

Cauwet, G. (2002). "DOM in the coastal zone," in *Biogeochemistry of Marine Dissolved Organic Matter*, First Edn, eds D. A. Hansell, and C. A. Carlson, (Boston, MA: Academic Press), 579–609. doi: 10.1016/b978-012323841-2/50014-2

Chen, J., Li, Y., Yin, K., and Jin, H. (2004). Amino acids in the Pearl River Estuary and adjacent waters: origins, transformation and degradation. *Cont. Shelf Res.* 24, 1877–1894. doi: 10.1016/j.csr.2004.06.013

Dai, M., Yin, Z., Meng, F., Liu, Q., and Cai, W.-J. (2012). Spatial distribution of riverine DOC inputs to the ocean: an updated global synthesis. *Curr. Opin. Environ. Sustain.* 4, 170–178. doi: 10.1016/j.cosust.2012.03.003

Dalzell, B. J., Filley, T. R., and Harbor, J. M. (2007). The role of hydrology in annual organic carbon loads and terrestrial organic matter export from a midwestern agricultural watershed. *Geochim. Cosmochim. Acta* 71, 1448–1462. doi: 10.1016/j.gca.2006.12.009

D'Andrilli, J., Cooper, W. T., Foreman, C. M., and Marshall, A. G. (2015). An ultrahigh-resolution mass spectrometry index to estimate natural organic matter lability. *Rapid Commun. Mass Spectrom.* 29, 2385–2401. doi: 10.1002/rcm.7400

Dauwe, B., and Middelburg, J. J. (1998). Amino acids and hexosamines as indicators of organic matter degradation state in North Sea sediments. *Limnol. Oceanogr.* 43, 782–798. doi: 10.4319/lo.1998.43.5.0782

Davis, J., Kaiser, K., and Benner, R. (2009). Amino acid and amino sugar yields and compositions as indicators of dissolved organic matter diagenesis. *Org. Geochem.* 40, 343–352. doi: 10.1016/j.orggeochem.2008.12.003

Del Castillo, C. E., Coble, P. G., Morell, J. M., López, J. M., and Corredor, J. E. (1999). Analysis of the optical properties of the Orinoco River plume by absorption and fluorescence spectroscopy. *Mar. Chem.* 66, 35–51. doi: 10.1016/S0304-4203(99)00023-7

Dittmar, T., Koch, B., Hertkorn, N., and Kattner, G. (2008). A simple and efficient method for the solid-phase extraction of dissolved organic matter (SPE-DOM) from seawater. *Limnol. Oceanogr. Methods* 6, 230–235. doi: 10.4319/lom.2008.6.230

Evans, C. D., Freeman, C., Cork, L. G., Thomas, D. N., Reynolds, B., Billett, M. F., et al. (2007). Evidence against recent climate-induced destabilisation of soil carbon from 14C analysis of riverine dissolved organic matter. *Geophys. Res. Lett.* 34:L07407. doi: 10.1029/2007GL029431

Fellman, J. B., Hood, E., Edwards, R. T., and D'Amore, D. V. (2009). Changes in the concentration, biodegradability, and fluorescent properties of dissolved organic matter during stormflows in coastal temperate watersheds. *J. Geophys. Res. Biogeosci.* 114:G01021. doi: 10.1029/2008JG000790

Granskog, M. A. (2012). Changes in spectral slopes of colored dissolved organic matter absorption with mixing and removal in a terrestrially dominated marine system (Hudson Bay, Canada). *Mar. Chem.* 134, 10–17. doi: 10.1016/j.marchem.2012.02.008

Gremm, T. J., and Kaplan, L. A. (1998). Dissolved carbohydrate concentration, composition, and bioavailability to microbial heterotrophs in stream water. *Acta Hydrochim. Hydrobiol.* 26, 167–171.

Han, X., Feng, L., Hu, C., and Kramer, P. (2018). Hurricane-induced changes in the everglades national park mangrove forest: landsat observations between 1985 and 2017. *J. Geophys. Res. Biogeosci.* 123, 3470–3488. doi: 10.1029/2018JG004501

Hawkes, J. A., Patriarca, C., Sjöberg, P. J. R., Tranvik, L. J., and Bergquist, J. (2018). Extreme isomeric complexity of dissolved organic matter found across aquatic environments. *Limnol. Oceanogr. Lett.* 3, 21–30. doi: 10.1002/lol2.10064

Hedges, J. I. (2002). "Why Dissolved Organics Matter," in *Biogeochemistry of Marine Dissolved Organic Matter*, First Edn, eds D. A. Hansell, and C. A. Carlson, (Boston: Academic Press), 1–33. doi: 10.1016/b978-012323841-2/50003-8

Hedges, J. I., Keil, R. G., and Benner, R. (1997). What happens to terrestrial organic matter in the ocean? *Org. Geochem.* 27, 195–212. doi: 10.1016/S0146-6380(97)00066-1

Hertkorn, N., Harir, M., Koch, B. P., Michalke, B., and Schmitt-Kopplin, P. (2013). High-field NMR spectroscopy and FTICR mass spectrometry: powerful discovery tools for the molecular level characterization of marine dissolved organic matter. *Biogeosciences* 10, 1583–1624. doi: 10.5194/bg-10-1583-2013

Hertkorn, N., Ruecker, C., Meringer, M., Gugisch, R., Frommberger, M., Perdue, E. M., et al. (2007). High-precision frequency measurements: indispensable tools at the core of the molecular-level analysis of complex systems. *Anal. Bioanal. Chem.* 389, 1311–1327. doi: 10.1007/s00216-007-1577-4

Hinton, M. J., Schiff, S. L., and English, M. C. (1997). The significance of storms for the concentration and export of dissolved organic carbon from two Precambrian Shield catchments. *Biogeochemistry* 36, 67–88. doi: 10.1023/A:1005779711821

Hood, E., Gooseff, M. N., and Johnson, S. L. (2006). Changes in the character of stream water dissolved organic carbon during flushing in three small watersheds, Oregon. *J. Geophys. Res. Biogeosci.* 111:G01007. doi: 10.1029/2005JG000082

Inamdar, S. P., Christopher, S. F., and Mitchell, M. J. (2004). Export mechanisms for dissolved organic carbon and nitrate during summer storm events in a glaciated forested catchment in New York, USA. *Hydrol. Process.* 18, 2651–2661. doi: 10.1002/hyp.5572

Jiao, N., Herndl, G. J., Hansell, D. A., Benner, R., Kattner, G., Wilhelm, S. W., et al. (2011). The microbial carbon pump and the oceanic recalcitrant dissolved organic matter pool. *Nat. Rev. Micro* 9:555. doi: 10.1038/nrmicro2386-c5

Kellerman, A. M., Dittmar, T., Kothawala, D. N., and Tranvik, L. J. (2014). Chemodiversity of dissolved organic matter in lakes driven by climate and hydrology. *Nat. Commun.* 5:3804. doi: 10.1038/ncomms4804

Kellerman, A. M., Kothawala, D. N., Dittmar, T., and Tranvik, L. J. (2015). Persistence of dissolved organic matter in lakes related to its molecular characteristics. *Nat. Geosci.* 8, 454–457. doi: 10.1038/ngeo2440

Kim, S., Kaplan, L. A., and Hatcher, P. G. (2006). Biodegradable dissolved organic matter in a temperate and a tropical stream determined from ultra-high resolution mass spectrometry. *Limnol. Oceanogr.* 51, 1054–1063. doi: 10.4319/lo.2006.51.2.1054

Kim, S., Kramer, R. W., and Hatcher, P. G. (2003). Graphical method for analysis of ultrahigh-resolution broadband mass spectra of natural organic matter, the Van Krevelen Diagram. *Anal. Chem.* 75, 5336–5344. doi: 10.1021/ac034415p

Knutson, T. R., McBride, J. L., Chan, J., Emanuel, K., Holland, G., Landsea, C., et al. (2010). Tropical cyclones and climate change. *Nat. Geosci.* 3, 157–163. doi: 10.1038/ngeo779

Knutson, T. R., Sirutis, J. J., Garner, S. T., Vecchi, G. A., and Held, I. M. (2008). Simulated reduction in Atlantic hurricane frequency under twenty-first-century warming conditions. *Nat. Geosci.* 1, 359–364. doi: 10.1038/ngeo202

Koch, B. P., and Dittmar, T. (2006). From mass to structure: an aromaticity index for high-resolution mass data of natural organic matter. *Rapid Commun. Mass Spectrom.* 20, 926–932. doi: 10.1002/rcm.2386

Koch, B. P., and Dittmar, T. (2016). From mass to structure: an aromaticity index for high-resolution mass data of natural organic matter. *Rapid Commun. Mass Spectrom.* 30, 250–250. doi: 10.1002/rcm.7433

Köhler, S., Buffam, I., Jonsson, A., and Bishop, K. (2002). Photochemical and microbial processing of stream and soil water dissolved organic matter in a boreal forested catchment in northern Sweden. *Aquat. Sci.* 64, 269–281. doi: 10.1007/s00027-002-8071-z

Kramer, M. G., Sanderman, J., Chadwick, O. A., Chorover, J., and Vitousek, P. M. (2012). Long-term carbon storage through retention of dissolved aromatic acids by reactive particles in soil. *Glob. Change Biol.* 18, 2594–2605. doi: 10.1111/j.1365-2486.2012.02681.x

Kujawinski, E. B. (2002). Electrospray ionization fourier transform ion cyclotron resonance mass spectrometry (ESI FT-ICR MS): characterization of complex environmental mixtures. *Environ. Forensics* 3, 207–216. doi: 10.1006/enfo.2002.0109

Kujawinski, E. B., and Behn, M. D. (2006). Automated analysis of electrospray ionization fourier transform ion cyclotron resonance mass spectra of natural organic matter. *Anal. Chem.* 78, 4363–4373. doi: 10.1021/ac0600306

Kuznetsova, M., and Lee, C. (2002). Dissolved free and combined amino acids in nearshore seawater, sea surface microlayers and foams: influence of extracellular hydrolysis. *Aquat. Sci.* 64, 252–268. doi: 10.1007/s00027-002-8070-0

Larson, J. H., Frost, P. C., Lodge, D. M., and Lamberti, G. A. (2007). Photodegradation of dissolved organic matter in forested streams of the northern Great Lakes region. *J. N. Am. Benthol. Soc.* 26, 416–425. doi: 10.1899/06-097.1

Lee, C., Wakeham, S. G., and Hedges, J. I. (2000). Composition and flux of particulate amino acids and chloropigments in equatorial pacific seawater and sediments. *Deep Sea Res. Part 1 Oceanogr. Res. Papers* 47, 1535–1568. doi: 10.1016/S0967-0637(99)00116-8

Leenheer, J. A., and Croué, J.-P. (2003). Peer reviewed: characterizing aquatic dissolved organic matter. *Environ. Sci. Technol.* 37, 18A–26A. doi: 10.1021/es032333c

Leyva, D., Valadares, L., Porter, J., Wolff, J., Jaffè, R., and Fernandez-Lima, F. (2019). Understanding the structural complexity of dissolved organic matter: isomeric diversity. *Faraday Discuss.* 218, 431–440. doi: 10.1039/C8FD00221E

Li, X., Liu, Z., Chen, W., Wang, L., He, B., Wu, K., et al. (2018). Production and transformation of dissolved and particulate organic matter as indicated by amino acids in the Pearl River Estuary, China. *J. Geophys. Res. Biogeosci.* 123, 3523–3537. doi: 10.1029/2018JG004690

Lin, P., Rincon, A. G., Kalberber, M., and Yu, J. (2012). Elemental composition of HULIS in the Pearl River Delta region, China: results inferred from positive and negative electrospray high resolution mass spectrometric data. *Environ. Sci. Technol.* 46, 7454–7462. doi: 10.1021/es300285d

Liu, Z., Liu, S., Liu, J., and Gardner, W. S. (2013). Differences in peptide decomposition rates and pathways between hypoxic and oxic coastal environments. *Mar. Chem.* 157, 67–77. doi: 10.1016/j.marchem.2013.08.003

Liu, Z., Sleighter, R. L., Zhong, J., and Hatcher, P. G. (2011). The chemical changes of DOM from black waters to coastal marine waters by HPLC combined with ultrahigh resolution mass spectrometry. *Estuar. Coast. Shelf Sci.* 92, 205–216. doi: 10.1016/j.ecss.2010.12.030

Lu, K., Gardner, W. S., and Liu, Z. (2018). Molecular structure characterization of riverine and coastal dissolved organic matter with ion mobility quadrupole time-of-flight LCMS (IM Q-TOF LCMS). *Environ. Sci. Technol.* 52, 7182–7191. doi: 10.1021/acs.est.8b00999

Ludwig, W., Probst, J.-L., and Kempe, S. (1996). Predicting the oceanic input of organic carbon by continental erosion. *Glob. Biogeochem. Cycles* 10, 23–41. doi: 10.1029/95GB02925

Majidzadeh, H., Uzun, H., Ruecker, A., Miller, D., Vernon, J., Zhang, H., et al. (2017). Extreme flooding mobilized dissolved organic matter from coastal forested wetlands. *Biogeochemistry* 136, 293–309. doi: 10.1007/s10533-017-0394-x

Mangal, V., Shi, Y. X., and Guéguen, C. (2017). Compositional changes and molecular transformations of dissolved organic matter during the arctic spring floods in the lower Churchill watershed (Northern Manitoba, Canada). *Biogeochemistry* 136, 151–165. doi: 10.1007/s10533-017-0388-8

Mangal, V., Stock, N. L., and Guéguen, C. (2016). Molecular characterization of phytoplankton dissolved organic matter (DOM) and sulfur components using high resolution Orbitrap mass spectrometry. *Anal. Bioanal. Chem.* 408, 1891–1900. doi: 10.1007/s00216-015-9295-9

May, J. C., Goodwin, C. R., Lareau, N. M., Leaptrot, K. L., Morris, C. B., Kurulugama, R. T., et al. (2014). Conformational ordering of biomolecules in the gas phase: nitrogen collision cross sections measured on a prototype high resolution drift tube ion mobility-mass spectrometer. *Anal. Chem.* 86, 2107–2116. doi: 10.1021/ac4038448

McGlynn, B. L., and McDonnell, J. J. (2003). Role of discrete landscape units in controlling catchment dissolved organic carbon dynamics. *Water Resour. Res.* 39:1090. doi: 10.1029/2002WR001525

Meybeck, M. (1993). Riverine transport of atmospheric carbon: sources, global typology and budget. *Water Air Soil Pollut.* 70, 443–463. doi: 10.1007/BF01105015

Mooney, R. F., and McClelland, J. W. (2012). Watershed export events and ecosystem responses in the mission–aransas national estuarine research reserve, South Texas. *Estuar. Coasts* 35, 1468–1485. doi: 10.1007/s12237-012-9537-4

Nesbit, T. A., and Mitsch, W. J. (2018). Hurricane and seasonal effects on hydrology and water quality of a subtropical urban stormwater wetland. *Ecol. Eng.* 120, 134–145. doi: 10.1016/j.ecoleng.2018.05.041

Nichols, C. M., Dodds, J. N., Rose, B. S., Picache, J. A., Morris, C. B., Codreanu, S. G., et al. (2018). Untargeted molecular discovery in primary metabolism: collision cross section as a molecular descriptor in ion mobility-mass spectrometry. *Anal. Chem.* 90, 14484–14492. doi: 10.1021/acs.analchem.8b04322

Ogawa, H., Amagai, Y., Koike, I., Kaiser, K., and Benner, R. (2001). Production of refractory dissolved organic matter by bacteria. *Science* 292, 917–920. doi: 10.1126/science.1057627

Ohno, T., and Ohno, P. E. (2013). Influence of heteroatom pre-selection on the molecular formula assignment of soil organic matter components determined by ultrahigh resolution mass spectrometry. *Anal. Bioanal. Chem.* 405, 3299–3306. doi: 10.1007/s00216-013-6734-3

Ohno, T., Sleighter, R. L., and Hatcher, P. G. (2016). Comparative study of organic matter chemical characterization using negative and positive mode electrospray ionization ultrahigh-resolution mass spectrometry. *Anal. Bioanal. Chem.* 408, 2497–2504. doi: 10.1007/s00216-016-9346-x

Osburn, C. L., Rudolph, J. C., Paerl, H. W., Hounshell, A. G., and Dam, B. R. V. (2019). Lingering carbon cycle effects of Hurricane Matthew in North Carolina's coastal waters. *Geophys. Res. Lett.* 46, 2654–2661. doi: 10.1029/2019GL082014

Oss, M., Kruve, A., Herodes, K., and Leito, I. (2010). Electrospray ionization efficiency scale of organic compounds. *Anal. Chem.* 82, 2865–2872. doi: 10.1021/ac902856t

Peter, S., Shen, Y., Kaiser, K., Benner, R., and Durisch-Kaiser, E. (2012). Bioavailability and diagenetic state of dissolved organic matter in riparian groundwater. *J. Geophys. Res. Biogeosci.* 117:G04006. doi: 10.1029/2012JG002072

Rathgeb, A., Causon, T., Krachler, R., and Hann, S. (2017). From the peat bog to the estuarine mixing zone: common features and variances in riverine dissolved organic matter determined by non-targeted analysis. *Mar. Chem.* 194, 158–167. doi: 10.1016/j.marchem.2017.06.012

Raymond, P. A., and Bauer, J. E. (2001). Riverine export of aged terrestrial organic matter to the North Atlantic Ocean. *Nature* 409, 497–500. doi: 10.1038/35054034

Raymond, P. A., and Saiers, J. E. (2010). Event controlled DOC export from forested watersheds. *Biogeochemistry* 100, 197–209. doi: 10.1007/s10533-010-9416-7

Raymond, P. A., and Spencer, R. G. M. (2015). "Riverine DOM," in *Biogeochemistry of Marine Dissolved Organic Matter*, Second Edn, eds D. A. Hansell, and C. A. Carlson, (Boston, MA: Academic Press), 509–533. doi: 10.1016/b978-0-12-405940-5.00011-x

Reyna, N. E., Hardison, A., and Liu, Z. (2017). Influence of major storm events on the quantity and composition of particulate organic matter and the phytoplankton community in a subtropical estuary, Texas. *Front. Mar. Sci.* 4:43.

Ridgwell, A., and Arndt, S. (2015). "Why Dissolved Organics Matter: DOC in Ancient Oceans and Past Climate Change," in *Biogeochemistry of Marine Dissolved Organic Matter*, Second Edn, ed. D. A. H. A. Carlson, (Boston, MA: Academic Press), 1–20.

Seitzinger, S. P., Harrison, J. A., Dumont, E., Beusen, A. H. W., and Bouwman, A. F. (2005). Sources and delivery of carbon, nitrogen, and phosphorus to the coastal zone: an overview of Global Nutrient Export from Watersheds (NEWS) models and their application. *Glob. Biogeochem. Cycles* 19:GB4S01. doi: 10.1029/2005GB002606

Shen, Y., Fichot, C. G., and Benner, R. (2012). Floodplain influence on dissolved organic matter composition and export from the Mississippi—Atchafalaya River system to the Gulf of Mexico. *Limnol. Oceanogr.* 57, 1149–1160. doi: 10.4319/lo.2012.57.4.1149

Smith, C. A., Maille, G. O., Want, E. J., Qin, C., Trauger, S. A., Brandon, T. R., et al. (2005). METLIN: a metabolite mass spectral database. *Ther. Drug Monit.* 27, 747–751.

Spencer, R. G. M., Aiken, G. R., Wickland, K. P., Striegl, R. G., and Hernes, P. J. (2008). Seasonal and spatial variability in dissolved organic matter quantity and composition from the Yukon River basin, Alaska. *Glob. Biogeochem. Cycles* 22:GB4002. doi: 10.1029/2008GB003231

Spencer, R. G. M., Mann, P. J., Dittmar, T., Eglinton, T. I., McIntyre, C., Holmes, R. M., et al. (2016). Detecting the signature of permafrost thaw in Arctic rivers. *J. Geophys. Res. Oceans* 42, 2830–2835. doi: 10.1002/2015GL063498

Stubbins, A., Spencer, R. G. M., Chen, H., Hatcher, P. G., Mopper, K., Hernes, P. J., et al. (2010). Illuminated darkness: molecular signatures of Congo River dissolved organic matter and its photochemical alteration as revealed by ultrahigh precision mass spectrometry. *Limnol. Oceanogr.* 55, 1467–1477. doi: 10.4319/lo.2010.55.4.1467

Tfaily, M. M., Chu, R. K., Toliæ, N., Roscioli, K. M., Anderton, C. R., Paša-Toliæ, L., et al. (2015). Advanced solvent based methods for molecular characterization of soil organic matter by high-resolution mass spectrometry. *Anal. Chem.* 87, 5206–5215. doi: 10.1021/acs.analchem.5b00116

Tissot, B., Durand, B., Espitalie, J., and Combaz, A. (1974). Influence of nature and diagenesis of organic matter in formation of petroleum. *AAPG Bull.* 58, 499–506.

Vandenbroucke, M., and Largeau, C. (2007). Kerogen origin, evolution and structure. *Org. Geochem.* 38, 719–833. doi: 10.1016/j.orggeochem.2007.01.001

Vidon, P., Wagner, L. E., and Soyeux, E. (2008). Changes in the character of DOC in streams during storms in two Midwestern watersheds with contrasting land uses. *Biogeochemistry* 88, 257–270. doi: 10.1007/s10533-008-9207-6

Wagner, S., Fair, J. H., Matt, S., Hosen, J. D., Raymond, P., Saiers, J., et al. (2019). Molecular hysteresis: hydrologically driven changes in riverine dissolved organic matter chemistry during a storm event. *J. Geophys. Res. Biogeosci.* 124, 759–774. doi: 10.1029/2018JG004817

Ward, N. D., Richey, J. E., and Keil, R. G. (2012). Temporal variation in river nutrient and dissolved lignin phenol concentrations and the impact of storm events on nutrient loading to Hood Canal, Washington, USA. *Biogeochemistry* 111, 629–645. doi: 10.1007/s10533-012-9700-9

Zark, M., Christoffers, J., and Dittmar, T. (2017). Molecular properties of deep-sea dissolved organic matter are predictable by the central limit theorem: evidence from tandem FT-ICR-MS. *Mar. Chem.* 191, 9–15. doi: 10.1016/j.marchem.2017.02.005

Zark, M., and Dittmar, T. (2018). Universal molecular structures in natural dissolved organic matter. *Nat. Commun.* 9:3178. doi: 10.1038/s41467-018-05665-9

Zhang, Z., Fukushima, T., Onda, Y., Gomi, T., Fukuyama, T., Sidle, R., et al. (2007). Nutrient runoff from forested watersheds in central Japan during typhoon storms: implications for understanding runoff mechanisms during storm events. *Hydrol. Process.* 21, 1167–1178. doi: 10.1002/hyp.6677

Conflict of Interest: The authors declare that the research was conducted in the absence of any commercial or financial relationships that could be construed as a potential conflict of interest.

frontiers in Marine Science

ORIGINAL RESEARCH
published: 31 January 2020
doi: 10.3389/fmars.2020.00026

Disparate Responses of Carbonate System in Two Adjacent Subtropical Estuaries to the Influence of Hurricane Harvey – A Case Study

Xinping Hu[1]*, Hongming Yao[1], Cory J. Staryk[1], Melissa R. McCutcheon[1], Michael S. Wetz[2] and Lily Walker[2]

[1] Department of Physical and Environmental Sciences, Texas A&M University – Corpus Christi, Corpus Christi, TX, United States, [2] Harte Research Institute for Gulf of Mexico Studies, Texas A&M University – Corpus Christi, Corpus Christi, TX, United States

Edited by:
Hans Paerl,
The University of North Carolina at Chapel Hill, United States

Reviewed by:
Joseph Crosswell,
CSIRO Oceans and Atmosphere (O&A), Australia
Liang Xue,
The First Institute of Oceanography, State Oceanic Administration, China

***Correspondence:**
Xinping Hu
xinping.hu@tamucc.edu

Specialty section:
This article was submitted to Marine Biogeochemistry, a section of the journal Frontiers in Marine Science

Received: 05 August 2019
Accepted: 15 January 2020
Published: 31 January 2020

Citation:
Hu X, Yao H, Staryk CJ, McCutcheon MR, Wetz MS and Walker L (2020) Disparate Responses of Carbonate System in Two Adjacent Subtropical Estuaries to the Influence of Hurricane Harvey – A Case Study. Front. Mar. Sci. 7:26. doi: 10.3389/fmars.2020.00026

Two adjacent estuaries in the northwestern Gulf of Mexico (GOM) (Mission–Aransas or MAE and Guadalupe–San Antonio or GE), despite their close proximity and similar extents of freshening caused by Hurricane Harvey, exhibited different behaviors in their post-hurricane carbonate chemistry and CO_2 fluxes. The oligotrophic MAE had little change in post-Harvey CO_2 partial pressure (pCO_2) and CO_2 flux even though the center of Harvey passed right through, while GE showed a large post-Harvey increases in both pCO_2 and CO_2 flux, which were accompanied by a brief period of low dissolved oxygen (DO) conditions likely due to the large input of organic matter mobilized by the hurricane. The differences in the carbonate chemistry and CO_2 fluxes were attributed to the differences in the watersheds from which these estuaries receive freshwater. The GE watershed is larger and covers urbanized areas, and, as a result, GE is considered relatively eutrophic. On the other hand, the MAE watershed is smaller, much less populous, and MAE is oligotrophic when river discharge is low. Despite that Harvey passed through MAE, the induced changes in carbonate chemistry and CO_2 flux there were less conspicuous than those in GE. This study suggested that disturbances by strong storms to estuarine carbon cycle may not be uniform even on such a small spatial scale. Therefore, disparate responses to these disturbances need to be studied on a case-by-case basis.

Keywords: estuary, carbon cycle, CO_2 flux, Hurricane Harvey, Gulf of Mexico

INTRODUCTION

Estuaries are considered efficient "filters" that trap a large fraction of terrestrial organic carbon (OC) delivered by rivers. As estuaries receive terrestrial OC, remineralization often outweighs primary production from the accompanying nutrients, leading to negative net ecosystem production (NEP) (Smith and Hollibaugh, 1997; Gazeau et al., 2005; Borges et al., 2008). Consistent with this heterotrophy, along with the input of high CO_2 river water (Borges et al., 2006), estuaries generally act as a CO_2 source to the atmosphere (Frankignoulle et al., 1998). However, exceptions do occur in eutrophic systems where nutrient input has increased significantly due to human activities; hence, autochthonous production in some estuaries can be the dominant OC source in sediment (e.g., Paerl et al., 2018). Nevertheless, estuaries play a disproportionately important role in global carbon cycle, representing an important reservoir for terrestrial OC deposition (Hedges and Keil, 1995; Bauer et al., 2013) and at the same time, generating 0.10–0.25 Pg-C yr^{-1} in the form of CO_2 efflux (Bauer et al., 2013; Chen et al., 2013) to the atmosphere, a budgetary term that probably carries an uncertainty of at least 100%. This uncertainty is due to large spatial and temporal heterogeneity across all types of estuaries worldwide, most of which have been poorly studied hence CO_2 flux sometimes had to be estimated using other biogeochemical processes, for example, the net ecosystem metabolism (e.g., Maher and Eyre, 2012; Laruelle et al., 2013).

Because estuaries act as a continuum between the terrestrial environment and the coastal ocean (Dürr et al., 2011), the amount of freshwater discharge from rivers controls both the freshwater residence time (Solis and Powell, 1999) and mechanisms of carbon processing. Under high freshwater discharge conditions, excess CO_2 from river water degases to the atmosphere during estuarine mixing and accounts for most of the CO_2 flux (Abril et al., 2000; Borges et al., 2006), and this excess CO_2 is typically a result of water column and soil respiration in rivers before reaching the estuaries (Butman and Raymond, 2011). On the other hand, under low river discharge conditions, organic matter remineralization dominates dissolved inorganic carbon (DIC) buildup in the estuarine water column hence is responsible for the subsequent CO_2 emission (Borges et al., 2006). In addition to riverine input, subterranean groundwater discharge represents a possibly important yet poorly quantified source for various solutes that may be important for estuarine biogeochemical processes, including carbon (Church, 2016). However, due to the relative extent of weathering and microbial processes, groundwater discharge has been suggested to either increase estuarine and coastal CO_2 flux (e.g., Ruiz-Halpern et al., 2015; Jeffrey et al., 2016; Liu et al., 2017; Pain et al., 2020) or decrease such flux by providing extra buffer through disproportionally higher alkalinity input than that of DIC (e.g., Murgulet et al., 2018; Crosswell et al., 2019).

CO_2 flux in estuaries is not only affected by riverine and groundwater input, disturbances caused by strong storms can also significantly alter the estuarine carbon cycle. The storms affect air–water CO_2 exchange through enhanced physical activities (e.g., increased gas transport and sediment resuspension that release high CO_2 pore water, the latter is due to sedimentary respiration and slow pore-bottom water exchange) and hydrologic changes, as more freshwater discharge brings in additional terrestrial OC and nutrients through river runoff. In addition, physical disturbances also lead to sediment resuspension that releases sediment-bound OC available for remineralization (Crosswell et al., 2014; Paerl et al., 2018; Van Dam et al., 2018). During the storms, high gas transfer velocity because of high wind also contributes to large CO_2 effluxes (Crosswell et al., 2014). Through examining North Carolina's estuaries on the U.S. east coast over a two-decade period, Paerl et al. (2018) suggested that CO_2 flux can be enhanced by both storm-generated floodwater ("wet" storm) and mobilization of previously accumulated terrigenous OC in the watershed ("dry storm"). Nevertheless, given the dearth of studies focusing on the influence of strong storms on estuarine carbon cycle and the forecasts for possibly more/stronger hurricane activities in the future (Emanuel, 2005, 2013; Webster et al., 2005), understanding the influence of storms on estuarine environments is important in the context of carbon cycle and to interpret its climatic feedback.

Compared to the U.S. east coast where a multidecadal observational effort has been in place to evaluate the effect of tropical storms on estuarine biogeochemistry and carbon cycle (Paerl et al., 2018), there has not been a study that examines this problem in the Gulf of Mexico (GOM), where the world's largest lagoonal systems are located (Dürr et al., 2011) and where the majority of hurricanes made landfall in the contiguous United States since 1851 (Landsea, 2019).

Hurricane Harvey made landfall at the uninhabited San José Island, north of Port Aransas, Texas on August 25, 2017 with a Category 4 wind force (**Figure 1**). The center of the storm kept category 4 wind speed (>200 km h^{-1}) when it crossed Aransas Bay of the Mission–Aransas Estuary (MAE), and it then moved north-northwest toward Victoria, Texas. After moving inland, the movement of the storm center slowed to near 8 km h^{-1} (5 mph). During the 1.5-day period, significant rain had fallen down before the center of the storm moved out into the GOM from across the Matagorda Bay on the afternoon of August 28, 2017.

Harvey caused extensive destruction to coastal and inland communities and an economic loss of ~$100 billion (Benfield, 2018). At the same time, it also offered an unprecedented opportunity for us to examine the effect of storm events on estuarine carbonate chemistry and CO_2 flux in the semiarid northwestern GOM coastal estuaries. This manuscript presents the temporal changes in the estuarine carbonate system and CO_2 flux as disparate post-Harvey influences were exemplified in the estuaries in the northwestern GOM, have similar geomorphic structure and physiography but receive freshwater from significantly different watersheds.

MATERIALS AND METHODS

Study Area

Mission–Aransas Estuary and Guadalupe–San Antonio Estuary (GE) are both shallow lagoonal estuaries (1.5–2 m) in the south Texas coast (Montagna et al., 2013; **Figure 1**) with a diurnal tidal range of 12–15 cm (Evans et al., 2012; Ward, 2013). MAE includes three interconnected water bodies – Aransas Bay (primary bay) is connected to the GOM through the Aransas Ship Channel, Copano and Mesquite Bays are both secondary bays that are more directly affected by riverine input (Kim and Montagna, 2012). Mission and Aransas rivers discharge into Copano Bay, and Mesquite Bay receives water from the adjacent San Antonio Bay under flooding conditions. GE is adjacent to MAE to the north and includes Mission Lake, Hynes Bay, and San Antonio Bay, with the latter being the primary bay. The total area of San Antonio and Guadalupe watershed is 26,244 km^2 (GE) (Texas Water Development Board), much greater than that (4,821 km^2)

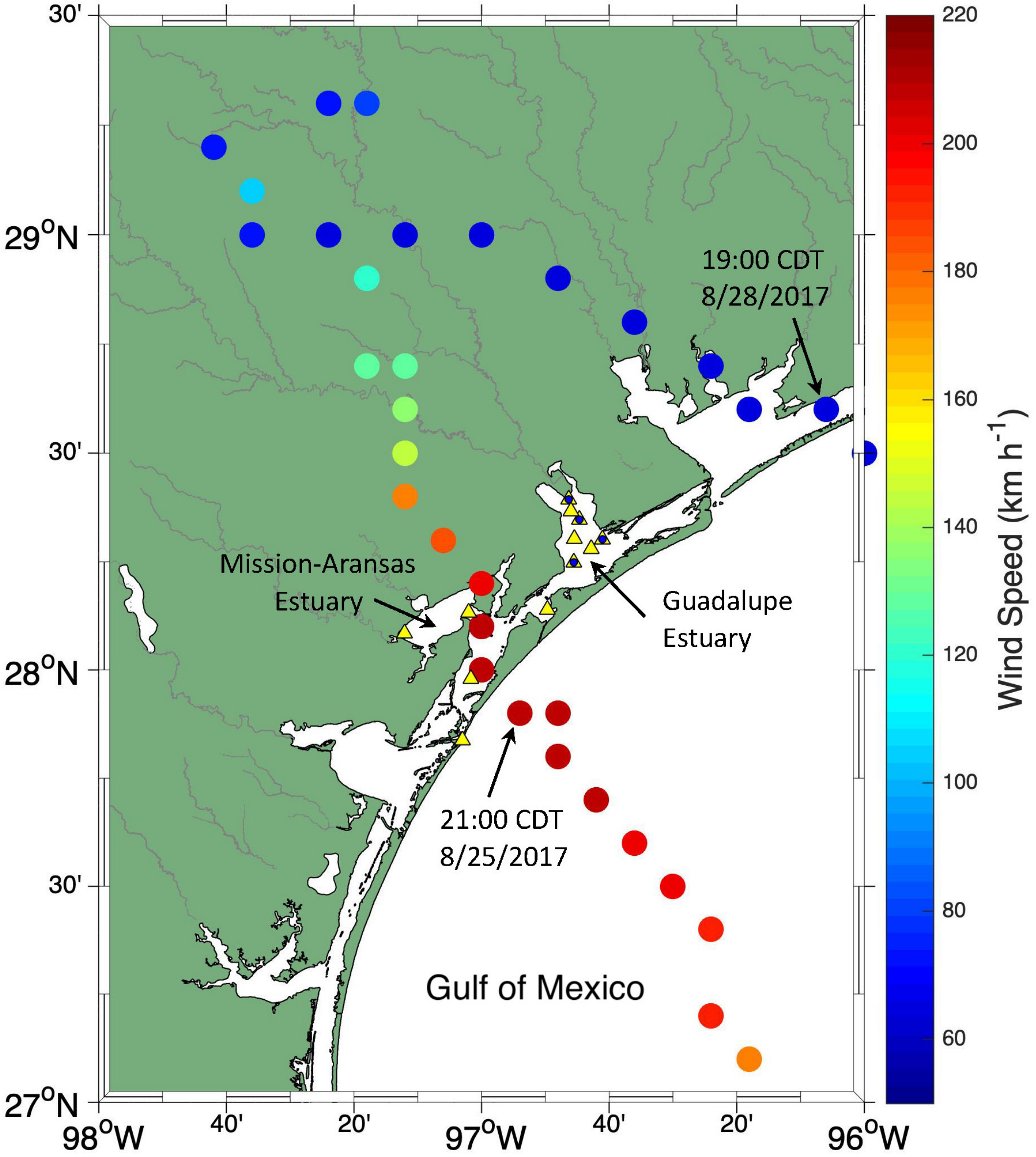

FIGURE 1 | The track of Hurricane Harvey and wind speed (colorbar). The sampling stations in Mission-Aransas Estuary (MAE) and Guadalupe Estuary (GE) are shown in yellow triangles. The blue circles superimposed on the triangles in GE represent quarterly sampling stations (see text for details).

of Aransas and Mission rivers (MAE) (Mooney and McClelland, 2012). The GE watershed includes extensive urbanized areas and is considered eutrophic (Arismendez et al., 2009; Turner et al., 2014). In comparison, the MAE watershed has a small population and is mostly composed of agricultural/grass/shrub land, and MAE can be oligotrophic under low river discharge conditions (Evans et al., 2012).

Five long-term System Wide Monitoring Program (SWMP) stations in MAE were sampled from May 2014 on a bimonthly or monthly basis since May 2014 (Yao and Hu, 2017). Four stations have been sampled in GE from January 2014 on a quarterly basis (Montagna et al., 2018). However, starting from May 2017, bimonthly trips were carried out in GE until early December 2017 with an additional three stations (**Figure 1**). We focused on the observations made in 2017 but these results were also compared and contrasted with data from prior to 2017 (Yao et al., 2020).

Sample Collection

We followed the sample collection and analytical approaches outlined in McCutcheon et al. (2019) and Montagna et al. (2018) for sampling in GE. Briefly, a calibrated YSI 6920 multisonde was used to obtain *in situ* temperature, salinity, and dissolved oxygen (DO) concentration at both the surface (~0.5 m) and the bottom (within 0.5 m from the sediment–water interface) of the water column, and a Van Dorn water sampler was used to take water samples from the surface and bottom. Following the standard OA sample collection and preservation protocol (Dickson et al., 2007), unfiltered water samples were collected into 250 mL borosilicate glass bottles for the lab analyses of total alkalinity (TA), total DIC, and pH. 100 μL saturated mercuric chloride ($HgCl_2$) was added into the sampling bottles and the bottle stoppers were sealed using Apiezon® L grease, rubber band, and a hose clamp. Chlorophyll *a* and dissolved OC (DOC) samples from GE were preserved on ice until return to our shore-based lab for processing and analysis (Montagna et al., 2018). Field condition observations and carbonate chemistry sampling in MAE followed protocols in Yao and Hu (2017), and chlorophyll samples were collected using the same approach as that in the literature (Mooney and McClelland, 2012; Bruesewitz et al., 2013). No DOC samples were collected in MAE.

Chemical Analysis and Carbonate System Speciation Calculations

Total alkalinity was analyzed at 22 ± 0.1°C using Gran titration. DIC was analyzed using infrared detection. Both DIC and TA analyses had a precision of ±0.1%, and Certified Reference Material (CRM) was used throughout the sample analyses to ensure data quality (Dickson et al., 2003). Two approaches were taken to measure pH (Yao and Hu, 2017). Prior to mid September, 2017, pH for salinity <20 was measured using a calibrated high precision glass Orion^{TM} pH electrode, and the electrode was calibrated using three pH standards (4.01, 7.00, and 10.01); for samples with salinity ≥20, pH was measured using purified m-cresol purple with the method in Carter et al. (2013). The equation in Liu et al. (2011) was used in calculating pH values. After mid September 2017, a new equation (Douglas and Byrne, 2017) for wider salinity range (0–40, vs. 20–40 in the Liu et al.'s study) was used for the low salinity samples (<20) to replace the potentiometric measurement. All pH measurements were done at 25°C. Calcium concentration ($[Ca^{2+}]$) was measured (from non-preserved water samples) using automatic titration on a Metrohm Titrando and ethylene glycol tetraacetic acid (EGTA) titrant, with a precision of ± 0.02 mmol kg^{-1}.

Carbonate speciation calculations were conducted using the MatLab® version CO2SYS program. Carbonic acid dissociation constants (K_1 and K_2) from Millero (2010) were used to account for the wide salinity range of the samples. Bisulfate dissociation constant was from Dickson (1990), and borate concentration was from Uppström (1974). Input variables for the speciation calculation were measured DIC and pH at 25°C. For this study we did not perform underway measurements due to logistical constraints. However, a 10-month time-series study conducted at the nearby Aransas Ship Channel revealed that the calculated CO_2 partial pressure (pCO_2) using discrete samples and those obtained by a calibrated SAMICO2 sensor (Sunburst®) agreed within 15 μatm and an uncertainty of ∼30 μatm (McCutcheon et al., unpublished).

Chlorophyll and DOC analyses followed the protocols in Montagna et al. (2018) for the GE samples, and chlorophyll samples from MAE were analyzed using the method in Mooney and McClelland (2012). Data from MAE can be accessed through the Centralized Data Management Office of the National Estuarine Research Reserve Program[1].

CO_2 Flux Calculation

The air–water flux of CO_2 was calculated using Eq. 1:

$$F = kK_0(pCO_{2,water} - pCO_{2,air}) \quad (1)$$

here k (m d^{-1}) is the gas transfer velocity calculated from wind speed (Jiang et al., 2008), K_0 (mol m^{-3} atm^{-1}) is the gas solubility constant at *in situ* temperature and salinity (Weiss, 1974), $pCO_{2,water}$ and $pCO_{2,air}$ are partial pressure of CO_2 in surface water and the atmosphere, respectively. Wind speed data were downloaded from monitoring sites close to these estuaries https://tidesandcurrents.noaa.gov/map/index.shtml?type=MeteorologicalObservations&region=Texas and corrected to 10 m using the equation in Hsu et al. (1994). Positive *F*-value means CO_2 degassing to the atmosphere. $pCO_{2,air}$ were calculated from:

$$pCO_{2,air} = xCO_{2,air} \times (P_b - P_w) \quad (2)$$

In Eq. 2, P_b (atm) is the barometric pressure from the weather stations in these two estuaries, P_w (atm) is the water vapor pressure calculated using salinity and temperature (Weiss and Price, 1980), and $xCO_{2,air}$ (ppm) is the mole fraction atmospheric CO_2 in dry air. We did not measure air xCO_2 directly but chose to download monthly averaged xCO_2 data from http://www.esrl.noaa.gov/gmd/ccgg/trends. The area-weighted CO_2 flux in each estuary was calculated using the approach in Yao and Hu (2017) by separately calculating the fluxes in both the primary and secondary bays and then integrating them together.

RESULTS

River Discharge Into MAE and GE

Daily mean river discharge data were obtained from the United States Geological Survey[2] (**Figure 2A**) from the beginning of our sampling period till April 2018. Three gauges (Aransas River – 08189700 and Mission River – 08189500 for MAE and Guadalupe River – 08188810 for GE) were used here. Note the Guadalupe gauge measures combined input of both San Antonio and Guadalupe rivers as the former merges with the latter before reaching this gauge.

Compared to Guadalupe River that had continuous freshwater discharge, both Aransas and Mission rivers had low discharge during most of the study period (**Figure 2A**). One month prior to Harvey, Aransas, Mission, and Guadalupe (from south to north) rivers had the average hourly discharge rates of 0.2 ± 0.1, 0.1 ± 0.6, and $120.6 \pm 50.5 \times 10^3$ m^3 h^{-1}, respectively. Hurricane precipitation-induced increase in river discharge started to be observed on August 26 in Aransas River (2.2×10^3 m^3 h^{-1}), in which the discharge peaked on August 27 (9.7×10^3 m^3 h^{-1}) and quickly returned to the baseline rate in 15 days. Mission

---

[1] http://cdmo.baruch.sc.edu/

[2] https://waterdata.usgs.gov/nwis

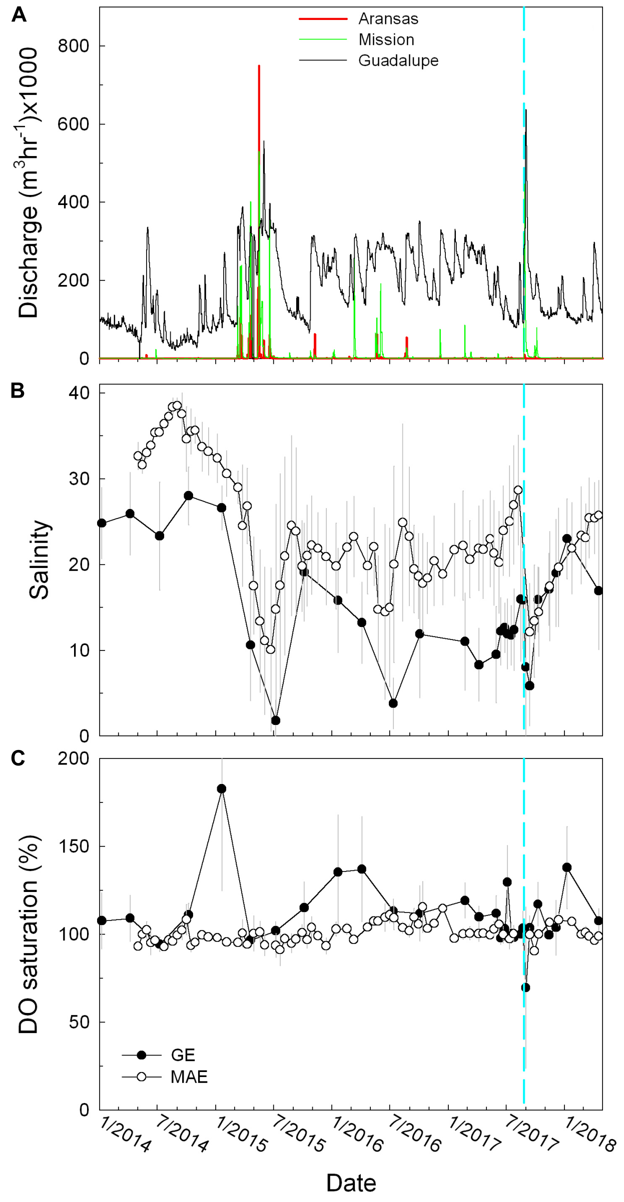

FIGURE 2 | (A) Discharge of Aransas (red), Mission (green), and Guadalupe (black) rivers. **(B)** Average salinity in MAE (open circles) and GE (closed circles). **(C)** Percent saturation of dissolved oxygen. The gray vertical lines represent standard deviation of the mean. The cyan dashed lines (and in figures hereafter) represent the date (August 25, 2017) on which Hurricane Harvey made landfall.

River had near zero freshwater discharge prior to the hurricane although the value rapidly increased to 217.1 × 10^3 m^3 h^{-1} on August 26 and peaked on August 28 (446.5 × 10^3 m^3 h^{-1}). After half a month, its discharge was still 5.7 × 10^3 m^3 h^{-1}, significantly greater than the baseline level prior to Harvey. In comparison, Guadalupe River saw an increase in discharge from August 26 although the peak (637.1 × 10^3 m^3 h^{-1}) appeared several days later on September 1. Notably, each of the rivers had a secondary peak discharge at the end of September to early October (**Figure 2A**). For example, Aransas River had 5.0 × 10^3 m^3 h^{-1} (September 28), Mission River had 32.8 × 10^3 m^3 h^{-1} (September 29), and Guadalupe River had 217.1 × 10^3 m^3 h^{-1} (October 4), possibly due to intermittent rainfall through the month of September, in addition to the direct Harvey influence.

If accounting for the secondary discharge peaks till the middle of October (i.e., October 15), when all river discharges returned to their respective low levels prior to the hurricane, the three rivers had exported 1.2 × 10^6 (Aransas), 5.3 × 10^7 (Mission), and 3.0 × 10^8 (Guadalupe) m^3 freshwater since Harvey made landfall.

Changes in Estuarine Hydrography

Because of the shallow depths in these two estuaries, both GE and MAE usually had little stratification except under flooding conditions. For example, salinity difference between bottom and surface (ΔS) in GE was 2.2 ± 3.4 and 0.7 ± 1.7 in MAE across all sampling stations in our multiyear surveys (2014–2018). Prior to Harvey (August 23), surface salinity in GE ranged from 5.7 at close to the Guadalupe River mouth to 20.0 in lower GE with ΔS as much as 6.9 in the latter (2 m depth). A few days after Harvey made landfall (September 1), salinity at the station close to the river mouth decreased to near zero (0.2) at both surface and bottom, and surface water at all other stations decreased to 0.3–5.5, while bottom water salinity decreases were small (up to 6.0) compared to the values prior to the hurricane, with a range of 9.7–20.9. In mid-September (September 13), continued salinity decrease in bottom water was observed (ranging from 1.2 to 13.9) while surface salinity remained similar to September 1, suggesting continued river input and mixing that was flushing salt out of GE. Afterward (October 9), the entire GE returned to pre-Harvey salinity with little surface-bottom stratification ($\Delta S<2$). In comparison, slight stratification ($\Delta S \sim 2–3$) was observed in the upper MAE (i.e., the two stations in Copano Bay) on August 8 with the surface salinity of 20.8–20.9 and the rest of MAE was vertically well-mixed, with a salinity range of 27.2–36.4 from mid-MAE to Aransas Ship Channel. In mid-September (September 13), the entire MAE had significant decrease in salinity (6.8–22.2) although stratification was still minimal ($\Delta S<1.5$) except at the station located in Aransas Bay ($\Delta S = 6.8$). However, because MAE was in a state of drought several months prior to Harvey, post-Harvey salinity increased but remained relatively low compared to pre-Harvey months (**Figure 2B**).

In addition to the hurricane-induced strong river discharge in 2017, significant precipitation caused high river discharge in all three rivers and led to prior episodes of estuarine freshening (June–July 2015, **Figures 2A,B**). For example, salinity in GE was as low as 1.8 ± 2.4 on July 8, 2015 and that in MAE was 10.1 ± 9.5 on June 23, 2015, both of which were lower than the values observed after Harvey. A smaller decrease in salinity was also observed in both estuaries in mid-2016 (**Figure 2B**). We recognize that the comparison based on the "snapshots" of sampling events could be overly simplified and the observations were tied to the timing of the field trips. However, the overall greater river discharges in the two non-hurricane years did suggest greater estuarine freshening in these earlier years (**Figure 2A**).

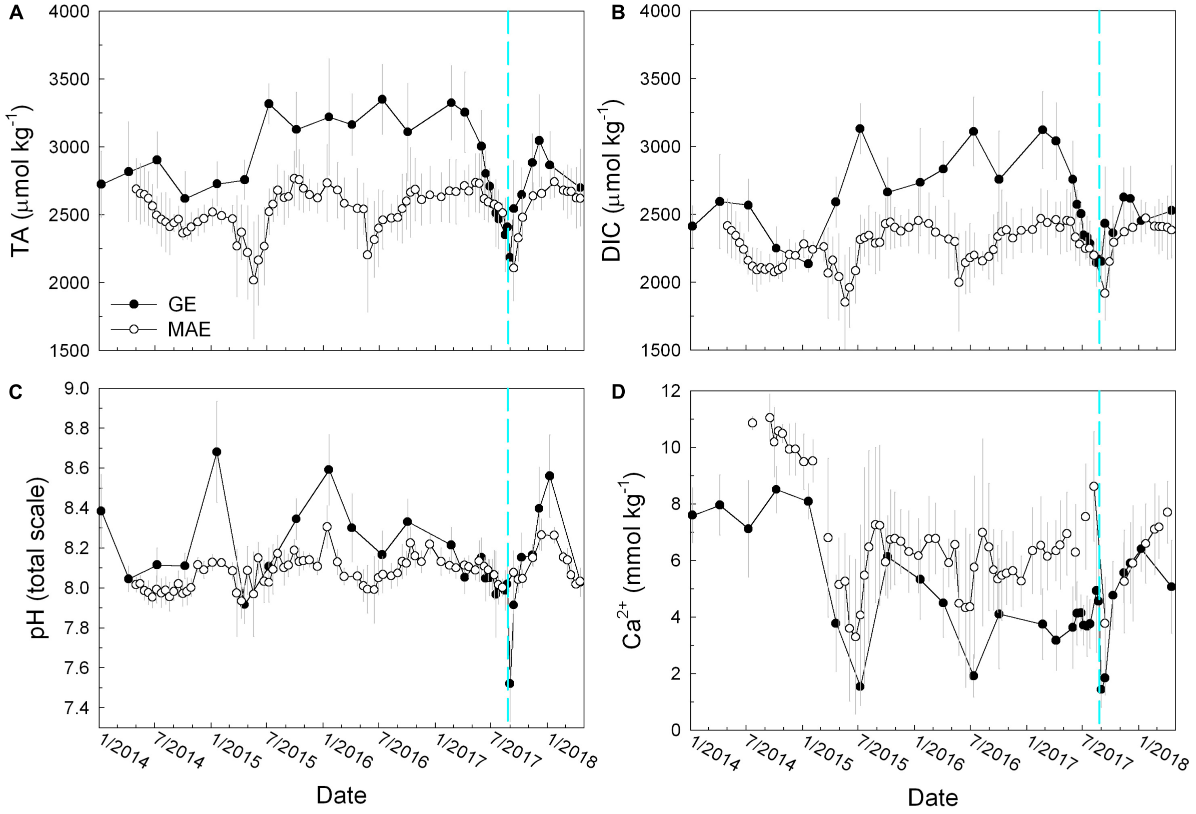

FIGURE 3 | Temporal distributions of **(A)** total alkalinity (TA), **(B)** total dissolved inorganic carbon (DIC), **(C)** *in situ* pH on total scale, and **(D)** calcium ion concentration ([Ca^{2+}]). The open circles represent MAE and the close circles represent GE.

Average DO saturation (%DO) in GE surface water was 108.2 ± 23.7% and bottom water was 93.8 ± 27.1%. In MAE, these values were 100.6 ± 6.7 and 98.8 ± 8.6%, respectively (**Figure 2C**). MAE did not experience substantial DO decrease throughout our sampling period, while discrete sampling suggested that GE had hypoxic conditions in the upper estuary on September 1, 2017, and the hypoxic condition in the station closest to the river mouth persisted for about a week with continued freshwater input that kept salinity low (Walker et al., unpublished).

Carbonate System Parameters

Both GE and MAE had fairly high TA and DIC levels throughout the sampling period (i.e., 2832 ± 315 and 2560 ± 293 μmol kg^{-1} for GE and 2539 ± 161 and 2271 ± 146 μmol kg^{-1} for MAE, respectively), mostly greater than the ocean water values in the northwestern GOM (Hu et al., 2018). At the same time, their pH values were generally higher than (8.151 ± 0.234 in GE) or equivalent (8.078 ± 0.079 in MAE) to the open ocean values.

TA and DIC had already started to decline in both estuaries from early June 2017. Harvey-induced freshwater input further pushed both TA and DIC to their respective minima, i.e., TA = 2186 ± 92 μmol kg^{-1} and DIC = 2154 ± 143 μmol kg^{-1} in GE (September 1), and TA = 2108 ± 240 μmol kg^{-1} and DIC = 1918 ± 199 μmol kg^{-1} in MAE (September 13) (**Figures 3A,B**). pH in MAE did not change much before and after Harvey, i.e., from 8.002 ± 0.043 on August 8 to 8.077 ± 0.108 on September 13. However, a significant pH decline in GE was observed, i.e., pH prior to Harvey was 8.019 ± 0.191 (August 23), several days after Harvey pH dropped significantly (7.521 ± 0.191 on September 1) but then increased again to 7.914 ± 0.212 when both TA and DIC concentrations increased (September 13) (**Figure 3C**). [Ca^{2+}] mostly followed salinity throughout our sampling period (**Figure 3D**) although the regression between [Ca^{2+}] and salinity offered more insights on the river endmember composition changes at different hydrologic conditions (see the section "Discussion" for more details).

Compared to hurricane-induced estuarine carbonate system changes, the period of freshwater discharge increase in mid-2015 caused similar changes to TA and DIC in MAE as those after Harvey, although GE experienced elevated TA and DIC concentrations (**Figures 3A,B**) instead of the large decrease after Harvey.

CO_2 Partial Pressure, Normalized pCO_2, and Air–Water CO_2 Flux

Surface water pCO_2 in GE exhibited much more temporal variability than in MAE (**Figure 4A**), i.e., 666 ± 702 (GE) vs. 477 ± 84 μatm (MAE). Following Harvey, pCO_2 in GE increased significantly compared to the background values and

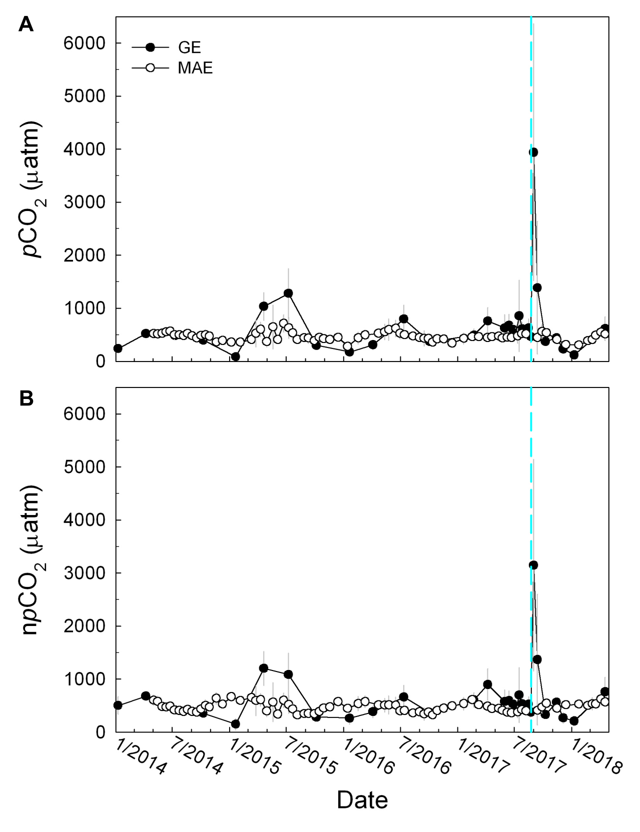

FIGURE 4 | Temporal distributions of **(A)** *in situ* pCO_2 and **(B)** temperature normalized pCO_2 ($npCO_2$) in MAE (open circles) and GE (closed circles), see text for the temperatures that data from these two estuaries were normalized to. The gray vertical lines represent standard deviation of the mean.

reached 3940 ± 2423 µatm (September 1), although the value quickly decreased to near background level 372 ± 40 µatm in slightly greater than a month (October 9). It is worth noting that even though river discharge in mid-2015 (**Figure 2A**) led to more freshening of both estuaries, pCO_2 in GE then was much lower (1278 ± 472 µatm, **Figure 4A**) than the post-Harvey conditions; whereas MAE did not exhibit significant variations in pCO_2 before and after Harvey (pCO_2 was always around 450–550 µatm). In comparison, pCO_2 increased slightly from the drought period in mid-2014 to early 2015 (Yao and Hu, 2017).

To remove the temperature effect on pCO_2 variation, surface water pCO_2 was normalized ($npCO_2$) based on the respective average temperatures of the two estuaries, i.e., 25.9°C in GE and 24.4°C in MAE, following the scheme in Takahashi et al. (2002), also see Yao and Hu (2017). Similar to pCO_2, $npCO_2$ showed the maximum values after Harvey (3147 ± 1365 µatm on September 1, **Figure 4B**), and despite the higher freshwater influence in mid-2015, $npCO_2$ at that time was much lower at the 1100–1200 µatm level.

As defined in Eq. 1, CO_2 flux is a function of wind speed (gas transfer) and air–water pCO_2 gradient. Contrary to the pCO_2 values (**Figure 4A**), the post-Harvey maximum pCO_2 in GE did not translate into the highest CO_2 efflux in our study period (164 ± 122 mmol m^{-2} d^{-1} on September 1, 2017). Instead, the highest calculated CO_2 efflux occurred in mid-2015 (181 ± 100 mmol m^{-2} d^{-1} on July 8, 2015) (**Figure 5A**), and the wind speed 9.3 m s^{-1} on the 2015 observation date was much higher than the post-Harvey date (3.6 m s^{-1}) (**Figure 5B**). In comparison, MAE did not exhibit significant changes in CO_2 flux before and after the hurricane (**Figure 5A**).

Chlorophyll *a* and DOC

Both GE and MAE experienced various extents of changes in chlorophyll concentration throughout our study period although the magnitudes of changes were quite different. Chlorophyll concentration in GE showed significantly greater temporal changes that corresponded to the magnitude of freshwater input than MAE, i.e., higher freshwater discharge in both 2015 and 2016 appeared to coincide with elevated chlorophyll concentration (**Figures 2A, 6**). After Harvey, chlorophyll concentration reached an all-time minimum (4.9 ± 1.3 µg L^{-1}) on September 8 (**Figure 6**) and this value rebounded to 19.8 ± 8.6 on September 13, the same level as that prior to Harvey (August 16). In addition, the chlorophyll minimum coincided with the DOC maximum

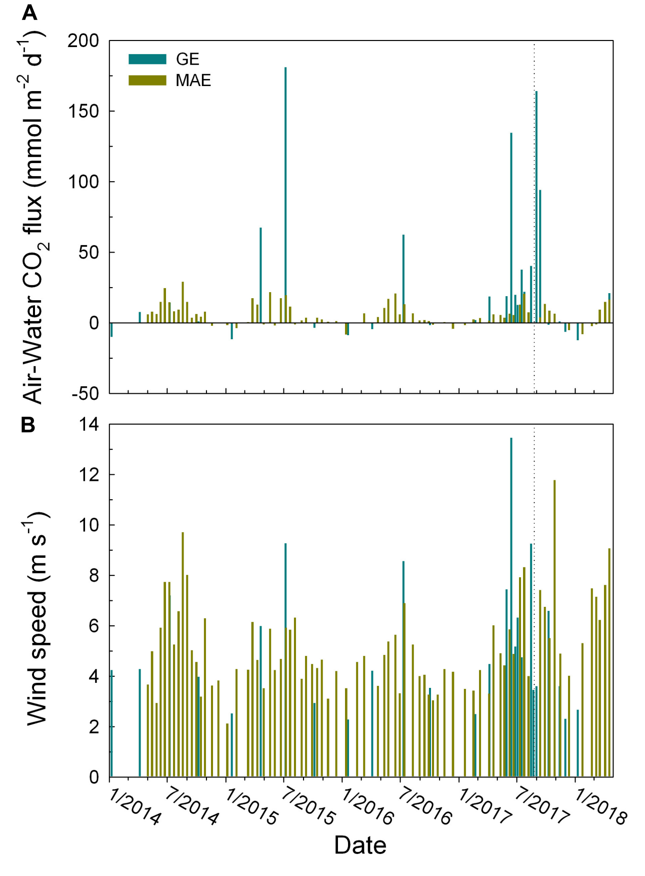

FIGURE 5 | Temporal distributions of **(A)** air–water CO_2 flux (unit mmol m^{-2} d^{-1}) and **(B)** daily wind speed on the sampling days in GE (dark green) and MAE (dark yellow). The dotted lines represent the date (August 25, 2017) on which Hurricane Harvey made landfall.

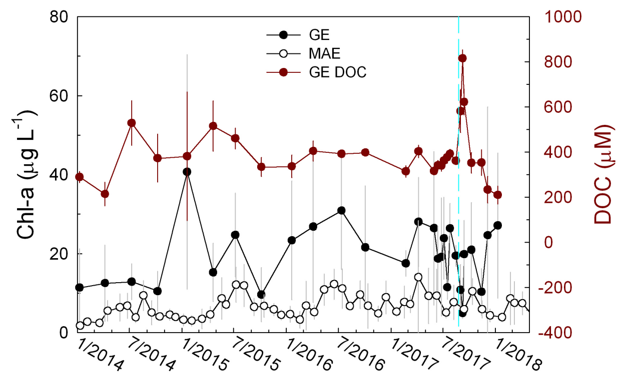

FIGURE 6 | Temporal distributions of chlorophyll *a* concentration in both GE and MAE. DOC from GE is shown in brown circles.

(September 8) and the two parameter exhibited a significant negative correlation ($p = 0.03$).

DISCUSSION

Tropical storms including hurricanes are capable of mobilizing large amounts of terrestrial carbon and nutrients, facilitating their transport across the land–ocean boundary, and at the same time, enhancing sediment resuspension that exposes buried organic matter to oxic conditions for increased microbial respiration; hence, significantly influencing estuarine and coastal carbon cycle (Crosswell et al., 2014; Majidzadeh et al., 2017; Lemay et al., 2018; Paerl et al., 2018; Van Dam et al., 2018; Letourneau and Medeiros, 2019; Osburn et al., 2019). On the other hand, few studies have examined inter-system variabilities and compared the hurricane effect with smaller scale flooding events. Our continuous sampling before and after Harvey provided an opportunity to examine these variabilities.

Spatial Heterogeneity in Estuarine Responses to Hurricane Influence

It is well known that estuaries along the northwestern GOM coast receive decreasing river discharge from northeast to southwest, and at the same time, these estuaries have a gradient of decreasing freshwater balance, i.e., freshwater input minus evaporation (Montagna et al., 2013). GE received much more freshwater than MAE (**Figure 2A**) and the river flow has been continuous despite its temporal changes over time. In comparison, the two rivers that empty into MAE frequently experienced near zero net flow, and conspicuous discharge only appeared intermittently (**Figure 2A**) corresponding to local/regional precipitation. As a result, prior to Harvey, salinity in MAE (28.7 ± 6.4) was substantially higher than in GE (15.8 ± 5.7) (**Figure 2B**). However, both TA and DIC have been showing a decreasing trend since April 2017 (**Figures 3A,B**) leading up to the hurricane as salinity in both estuaries increased (**Figure 2B**). The TA and DIC decreases were mainly caused by the increasing presence of seawater in these estuaries, as seawater has lower levels of TA and DIC but higher [Ca^{2+}] than the freshwater endmembers (**Figure 3D**; Hu et al., 2015).

After Harvey made landfall on August 25, 2017, GE first experienced an ephemeral (hours) storm surge that brought high salinity water to the innermost station where an *in situ* monitoring sonde (for salinity and DO) was in place (Walker et al., unpublished). Half a month after the hurricane, GE and MAE both experienced large decreases in salinity compared with data collected prior to the hurricane (**Figure 2B**). However, TA/DIC ratio in these two estuaries behaved differently before and after the storm, i.e., greater decreases in GE (from 1.11 ± 0.04 and 1.02 ± 0.03) than those in MAE (from 1.14 ± 0.02 to 1.10 ± 0.03), indicating GE became much more enriched in CO_2 (see below for further discussion). This excess CO_2 was then responsible for the much lower pH (**Figure 3C**) and higher pCO_2 in GE (**Figure 4A**). In MAE, however, the similar extent (∼13–16%) of TA and DIC dilution before and after Harvey did not result in large changes in estuarine carbonate speciation in MAE. Hence, neither pH nor pCO_2 varied substantially.

The similarity (i.e., freshwater discharge induced estuarine freshening) and contrast (i.e., difference in carbonate speciation after Harvey) reflected spatial heterogeneity of hurricane influence on coastal estuaries, even though these estuaries are spatially close to each other. Precipitation caused by Harvey was mostly concentrated in the Houston area in the north and decreased to the south (this study area) and east along the coast (van Oldenborgh et al., 2017). Therefore, even though the center of the hurricane passed right through MAE (**Figure 1**), precipitation and the resulted river discharge there was lower than in GE. For example, integrated freshwater input into GE from August 26 to September 13, when the minimum salinity was observed, was 3.6 times of that into MAE (1.59×10^8 vs. 0.45×10^8 m^3). The greater amount of freshwater input into GE also should stem from its much larger watershed area. Considering that the two estuaries have similar total volume (Montagna et al., 2013), freshwater thus caused more extensive flushing in GE than in MAE (also see Solis and Powell, 1999). The faster salinity change (i.e., first decrease and then increase) in GE than in MAE, which tends to remained freshened for prolonged period (Orlando et al., 1993), also indicated relatively more efficient water exchange with the coastal ocean in GE (**Figure 2B**).

In addition to the difference in the amount of freshwater input, apparently the characteristics of the freshwater coming into these estuaries were different between the two estuaries. While MAE did not exhibit significant changes in chlorophyll level after the storm (**Figure 6**), GE had large increase in DOC concentration (**Figure 6**) along with freshening of the entire estuary (**Figure 2B**) and decrease in overall DO (**Figure 2C**) chlorophyll levels (**Figure 6**), the latter was probably caused by increases in water turbidity that inhibited estuarine primary production. In fact, the *in situ* sonde at the innermost station in GE revealed a week-long hypoxic condition after the hurricane till 3–4 days before our post-Harvey field sampling on September 13 (Walker et al., unpublished). The high OC input as a result of hurricane activity might have prompted extensive suboxic to anoxic conditions in GE due to high rates of metabolic reactions.

High post-Harvey DOC levels have been observed in other storm-perturbed estuarine systems in which CO_2 production is enhanced (Van Dam et al., 2018; Osburn et al., 2019). Similarly, the excess OC input into GE was consistent with the observed high pCO_2 levels (**Figures 3D**, **4A**).

Temporal Heterogeneity in Estuarine Carbonate System in Response to Storm-Induced Freshwater Input

Not only did the estuaries respond to hurricane-induced freshwater discharge differently, even though they are closely located in a narrow geographic range, within each estuary the responses were also different at different times. There were two occasions of large pulses of freshwater input into both estuaries, i.e., June–July 2015 and the similar period in 2016, with the 2015 flooding event having higher amount of freshwater discharge and lower salinity in these estuaries compared to the post-Harvey conditions (**Figures 2A,B**). Nevertheless, the patterns for MAE have been rather consistent between "normal" flooding conditions and that after Harvey, i.e., both TA and DIC appeared being "diluted" at each of the salinity minima (**Figures 3A,B**) with modest increase in pCO_2 (by <100 μatm on average, **Figure 4A**) but virtually unchanged pH (**Figure 3C**, also see Yao and Hu, 2017). However, water chemistry in GE exhibited different behaviors when encountering significant increase in river discharge. For example, following a drought in south Texas prior to mid-2015, the large increase in river discharge elevated both TA and DIC concentrations in GE, and the highest concentrations corresponded to the lowest salinity (**Figures 2B**, **3A,B**). Then again in mid-2016, another lesser extent of river input also increased both TA and DIC. The increase in river influence following river flooding can also be viewed using the time-series of the intercept of Ca^{2+} vs. salinity linear regression ($[Ca^{2+}]_0$, **Figure 7**) as Ca^{2+} concentration often exhibited excellent linear relationship with salinity hence $[Ca^{2+}]_0$ can be used to infer river water Ca^{2+} concentration. During the 2015 and 2016 flooding periods, $[Ca^{2+}]_0$ values for GE were 1.25 and 1.18 mmol kg^{-1}, respectively (**Figure 7A**). Because of relatively narrow range of calcium ion to TA ratios in Guadalupe and San Antonio Rivers (Ca^{2+}:TA = 0.42 ± 0.05, Texas Commission on Environmental Quality), river alkalinity

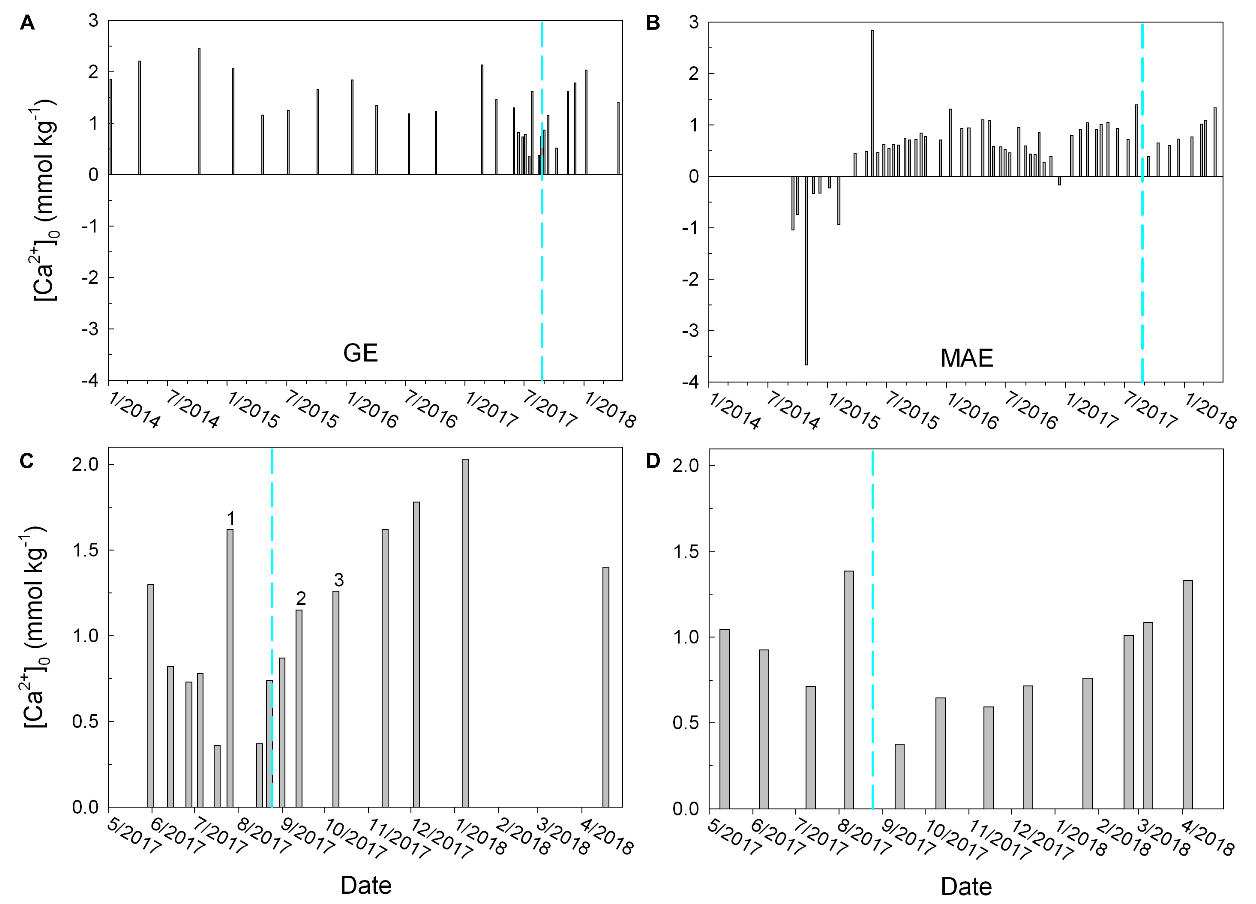

FIGURE 7 | Temporal changes in the intercept of $[Ca^{2+}]$ and salinity regression (i.e., $[Ca^{2+}]_0$) in both GE **(A)** and MAE **(B)**. Panels **(C)** and **(D)** show the data during the period of May 2017 to April 2018 for these estuaries, respectively. Other than the marked $[Ca^{2+}]_0$ bars that have regressed r^2 values of 0.75 (#1, July 26), 0.80 (#2, September 13), and 0.95 (#3, October 9), all other r^2 values in **(C)** and **(D)** are better than 0.98. The lower r^2 values were all due to one data point that did not fall on each regression line possibly due to the significantly varying river endmember on the time scale of estuarine mixing (Cifuentes et al., 1990).

was estimated to be in the range of 2800–3000 μmol kg^{-1}. This high riverine TA thus can explain the high TA values in 2015 and 2016 (**Figure 3A**). In comparison, $[Ca^{2+}]_0$ was 0.74 mmol kg^{-1} on August 23 (prior to Harvey) and 0.87 mmol kg^{-1} on September 1 (**Figure 7C**), despite the fact that salinity has decreased from 15.8 to 8.1 on the latter date (**Figure 2B**). The nearly invariant $[Ca^{2+}]_0$ suggested that initial Harvey-induced freshwater input into GE was low in weathering products, likely a result of local precipitation and runoff from adjacent area around GE. Similarly, the post-Harvey samples in MAE suggested the estuarine water was mostly diluted by precipitation because $[Ca^{2+}]_0$ decreased from 1.39 mmol kg^{-1} on August 8 (prior to Harvey) to 0.37 mmol kg^{-1} on September 13 (**Figure 7D**). After the initial dilution period, GE started receiving river waters with substantially higher levels of weathering products as indicated by the large increase in the $[Ca^{2+}]_0$ value (**Figure 7C**), although that for MAE remained relatively low (0.6–0.7 mmol kg^{-1}) through December 2017, suggesting that watershed that contributed to GE continued moving high levels of weathering products downstream while MAE watershed did not have high levels of these solutes thus precipitation-led dilution dominated the post-Harvey months. It is worth noting that the Ca^{2+} vs. salinity regression is not reliable for predicting river endmember under drought conditions, as MAE in much of 2014 (**Figure 7B**) exhibited a reverse estuary pattern with the upper estuary having greater salinity due to net evaporation (see Yao and Hu, 2017); hence, the regressed intercept became negative, a physically impossible freshwater endmember.

The immediate post-Harvey increase in pCO_2 was much larger than those from the two prior flooding periods (**Figure 4A**) and it was also higher when the values were normalized to the same temperature (npCO_2, **Figure 4B**). Based on the comparison between the prior flooding event and post-Harvey, it appeared that the hurricane and its associated freshwater input were able to mobilize OC from the lower reaches of Guadalupe/San Antonio rivers, which then fueled strong microbial respiration through physical disturbance to the watershed (Paerl et al., 2018), compared to regular river flooding caused by large scale precipitation (**Figure 8**), even though the latter could lead to higher amount of freshwater input into GE. On the other hand, such elevated high CO_2 condition was rather short-lived (~1 month). The high levels of weathering product coming off the upper reaches of the rivers (**Figure 7C**) that contributed to GE, along with rebounding estuarine primary production as indicated by the increase in chlorophyll levels (**Figure 6**), should have provided much buffer.

Air–Water CO_2 Flux

Despite the rarity of studies that investigate hurricane influence on estuarine CO_2 fluxes, hurricanes and strong storms are known to significantly increase this flux. For example, Crosswell et al. (2014) observed that CO_2 fluxes in the eutrophic Neuse River Estuary and Pamlico Sound were both −2.4 mmol m^{-2} d^{-1} prior to Hurricane Irene (2011). These two water bodies experienced significant CO_2 efflux during the storm period (i.e., 4080 and 384 mmol m^{-2} d^{-1}, respectively), then the fluxes decreased to 154 and 7 mmol m^{-2} d^{-1} 17 days after Irene, respectively. While directly enhanced CO_2 flux was mainly due to strong wind forcing that facilitates OC remineralization caused by physical mixing and sediment resuspension when a hurricane directly passes over (Crosswell et al., 2014), the 2015 Hurricane Joaquin did not make landfall but induced continental flooding in the same region, and this storm event also elevated estuarine CO_2 flux (Van Dam et al., 2018). CO_2 fluxes during the flooding period (62 and 265 mmol m^{-2} d^{-1}) were found to be 3.6 and 15.6 times of those prior to the flood in Neuse River and New River estuaries, respectively.

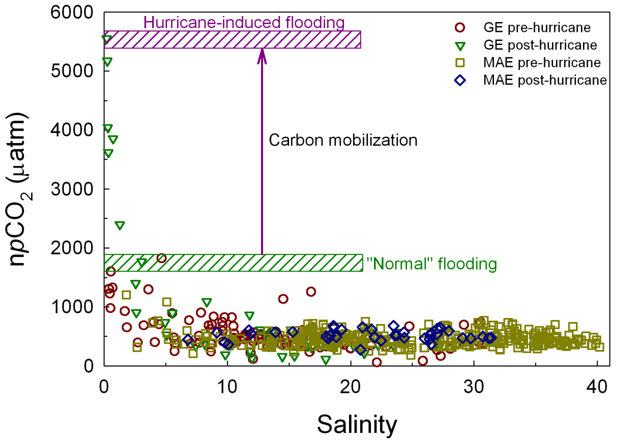

FIGURE 8 | A comparison of temperature normalized pCO_2 (npCO_2) from before and after Hurricane Harvey. The difference between the maximum npCO_2 values from pre-Harvey flooding periods and that from post-Harvey is considered to be CO_2 signal generated from hurricane mobilized carbon.

Compared to these east coast studies, we did not have data during Harvey except the single bottom water monitoring station (Walker et al., unpublished). However, the post-Harvey CO_2 flux in GE increased from the pre-hurricane near neutral levels (−0.2 ± 5.0 mmol m^{-2} h^{-1}) to 164 ± 122 mmol m^{-2} h^{-1} on September 1 and then 94 ± 161 mmol m^{-2} h^{-1} on September 13, both were greater than post-storm CO_2 flux observed in the east coast estuaries (Crosswell et al., 2014; Van Dam et al., 2018). In comparison, post-Harvey CO_2 flux in MAE (4 ± 3 mmol m^{-2} d^{-1}) was much lower but on par with those values obtained from those east coast estuaries. The reason for such distinct difference in CO_2 flux may be explained by the different extents of nutrient pollution that these estuaries experienced (see below).

In fact, despite that observed pCO_2 (hence water–air pCO_2 gradient) was the largest in GE after Harvey, water-to-air CO_2 flux was not the highest at that time (**Figure 5A**). The difference mainly stemmed from the higher gas transfer velocity in 7.8 m d^{-1} (at wind speed 9.3 m s^{-1}) on the sampling day in mid-2015 vs. 1.9 m d^{-1} (at wind speed 3.6 m s^{-1}) after Harvey.

Overall, water-to-air CO_2 flux during the 1-month period after Harvey (August 27–September 26, 2017) was estimated to be 1.6×10^9 mol. Integrating the 2017 flux values to the whole year the CO_2 efflux in GE in 2017 was 4.7×10^9 mol. Therefore, this 1-month period accounted for ~35% annual CO_2 emission in that year, and this estimate should represent a lower limit because CO_2 flux could have been higher during the storm due to much higher gas transfer velocity and potential sediment resuspension in this shallow estuary. In comparison, much sparser measurements in 2015 and 2016 suggested that the flood-induced CO_2 emission accounted for 78 and 132% of annual values, respectively. Note all calculated CO_2 flux values were negative in 2016 except that from the flooding period that year. Considering the limited observations in these 2 years and that both river discharge and wind speed both played an important role in controlling CO_2 flux, these two estimates thus probably had high uncertainties.

CO_2 flux in MAE during the 2015 and 2016 flooding periods reached as much as 21–22 mmol m^{-2} d^{-1}, much greater than that from the post-Harvey value. Furthermore, the latter flux from August 26 to September 25 (6.6×10^7 mol) was not only much smaller than the GE values, but also appeared not extraordinary in the integrated annual CO_2 flux (close to monthly mean of 5.0×10^7 mol), although again the CO_2 flux during the storm is unknown so this value can only be considered as a conservative estimate.

Post-Harvey freshwater input into MAE was less than that from the 2015, and that sedimentary total OC (TOC) content in MAE is <0.2% (Souza et al., 2012), which is much lower than that in the eutrophic system in the east coast (1.3–7.5%, see Cooper et al., 2004) where enhanced OC remineralization following sediment resuspension was attributed to large CO_2 fluxes during the storms (Crosswell et al., 2012). It is therefore unlikely that CO_2 flux in MAE during Harvey was much larger than the values from the flooding period in 2015 and 2016 because of low sedimentary carbon content and the extent that resuspended OC can stimulate respiration. Similarly, TOC concentration in GE sediment is ~0.65% (Trefry and Presley, 1976), also suggesting the sediment resuspension and subsequent remineralization probably was not as large a CO_2 source hence flux as in the east coast estuaries, despite that fact that GE was more eutrophic than MAE (for example, the higher overall chlorophyll levels, **Figure 6**). Nevertheless, to obtain accurate quantification of CO_2 flux in these dynamic estuaries, especially those that are affected by irregular freshwater input such as these in the semiarid environments, higher frequency and sustained measurements than what is presented here are needed.

CONCLUSION

This is the first study that examined carbonate chemistry and CO_2 flux as a result of a major hurricane in the semiarid northwestern GOM coast. The two studied estuaries are next to each other and have similar geomorphic structure and physiography, yet the watershed areas of major contributing rivers differ by five times. In addition, MAE in the south mostly experienced wind forcing with smaller freshwater input, while GE in the north received much larger freshwater input from a much greater expanse of watershed. Therefore, both water column carbonate chemistry and air–water CO_2 flux exhibited different behaviors. MAE mostly reflected a dilution effect (for TA and DIC) with limited changes in pH and CO_2 flux after Harvey, while GE first showed dilution accompanied by enhanced respiration and short-lived low oxygen conditions, which was followed by large input of river water enriched in TA and DIC and elevated primary production that helped to buffer the acidified conditions (low pH and high pCO_2) after Harvey.

Because of the different behaviors in pCO_2 and wind conditions, GE experienced significant increase in CO_2 efflux that was disproportionally larger than average monthly CO_2 flux in this estuary, yet MAE did not exhibit significant change in CO_2 flux as a result of the hurricane. However, when the post-Harvey CO_2 flux was compared with prior flooding events in these estuaries, the CO_2 efflux cause by hurricane influences may not be necessarily larger. Instead, flooding in the past that was not associated with strong storms such as Harvey may have caused more CO_2 emission in these estuaries, as respiration based on sediment resuspension liberated OC may not be as significant as in the eutrophic estuaries in the U.S. east coast, given the much lower sedimentary OC contents in our studied estuaries.

Nevertheless, we recognize that the relatively small hurricane influence on estuarine CO_2 flux was dependent on the assumption that this flux during the hurricane did not differ significantly from the observations after the storm, mainly based on the lower sediment OC contents than the much more eutrophic U.S. east coast estuaries. However, to better constrain this flux term, which is exceedingly dynamic in the semiarid environment, sustained observations in conjunction with high resolution monitoring are needed.

DATA AVAILABILITY STATEMENT

Data used in this manuscript can be accessed through BCO-DMO repository (https://www.bco-dmo.org/dataset/784673).

AUTHOR CONTRIBUTIONS

CS, HY, MM, and LW conducted the field sampling and laboratory analyses. XH designed this study, performed the data analysis, and worked with HY on CO_2 flux calculations and with MW on interpreting dissolved organic carbon and chlorophyll *a* data. XH wrote the manuscript and other authors participated in the discussions and finalized the manuscript.

FUNDING

This study was funded by the National Science Foundation (NSF) Chemical Oceanography Program (OCE-1760006 and OCE-1654232). Earlier sampling has been supported by NOAA's NOS National Center for Coastal Ocean Science (Contract No. NA15NOS4780185) and the Texas Research Development Fund from the Research and Commercialization Office of Texas A&M University – Corpus Christi, respectively.

ACKNOWLEDGMENTS

We are grateful for the fieldwork assistance provided by the staff and students at both the Mission Aransas National Estuarine Research Reserve (NERR) and the University of Texas Marine Science Institute. We also thank R. Kalk, L. Hyde, and E. Morgan in P. Montagna's Lab as well as K. Hayes in MW's Lab for their help with field sampling and logistics in Guadalupe Estuary. The MAE research was supported in part by operations grants to the Mission–Aransas National Estuarine Research Reserve from the Office of Coastal Management, National Oceanic and Atmospheric Administration. System-Wide Monitoring Program data were collected by the research staff of the Mission–Aransas NERR and hosted by the Central Data Management Office of the National Estuarine Research Reserve System. The two reviewers provided constructive comments, which helped to improve the quality of this work.

REFERENCES

Abril, G., Etcheber, H., Borges, A. V., and Frankignoulle, M. (2000). Excess atmospheric carbon dioxide transported by rivers into the Scheldt estuary. *Comptes Rendus de l'Académie des Sci. - Series IIA - Earth Planet. Sci.* 330, 761–768. doi: 10.1016/s1251-8050(00)00231-7

Arismendez, S. S., Kim, H.-C., Brenner, J., and Montagna, P. A. (2009). Application of watershed analyses and ecosystem modeling to investigate land–water nutrient coupling processes in the Guadalupe Estuary Texas. *Ecol. Inform.* 4, 243–253. doi: 10.1016/j.ecoinf.2009.07.002

Bauer, J. E., Cai, W.-J., Raymond, P. A., Bianchi, T. S., Hopkinson, C. S., and Regnier, P. G. (2013). The changing carbon cycle of the coastal ocean. *Nature* 504, 61–70. doi: 10.1038/nature12857

Benfield, A. (2018). *Weather, Climate and Catastrophe Insight: 2017 Annual Report*. (Aon Rep. GDM05083). London: AON.

Borges, A. V., Ruddick, K., Schiettecatte, L. S., and Delille, B. (2008). Net ecosystem production and carbon dioxide fluxes in the Scheldt estuarine plume. *BMC Ecol.* 8:15. doi: 10.1186/1472-6785-8-15

Borges, A. V., Schiettecatte, L. S., Abril, G., Delille, B., and Gazeau, F. (2006). Carbon dioxide in European coastal waters. *Estuar. Coast. Shelf Sci.* 70, 375–387. doi: 10.1016/j.ecss.2006.05.046

Bruesewitz, D. A., Gardner, W. S., Mooney, R. F., Pollard, L., and Buskey, E. J. (2013). Estuarine ecosystem function response to flood and drought in a shallow, semiarid estuary: nitrogen cycling and ecosystem metabolism. *Limnol. Oceanogr.* 58, 2293–2309. doi: 10.4319/lo.2013.58.6.2293

Butman, D., and Raymond, P. A. (2011). Significant efflux of carbon dioxide from streams and rivers in the United States. *Nat. Geosci.* 4, 839–842. doi: 10.1038/ngeo1294

Carter, B. R., Radich, J. A., Doyle, H. L., and Dickson, A. G. (2013). An automatic system for spectrophotometric seawater pH measurements. *Limnol. Oceanogr.* 11, 16–27. doi: 10.4319/lom.2013.11.16

Chen, C. T. A., Huang, T. H., Chen, Y. C., Bai, Y., He, X., and Kang, Y. (2013). Air-sea exchanges of CO_2 in the world's coastal seas. *Biogeosciences* 10, 6509–6544. doi: 10.5194/bg-10-6509-2013

Church, T. M. (2016). Marine chemistry in the coastal environment: principles, perspective and prospectus. *Aquatic Geochem.* 22, 375–389. doi: 10.1007/s10498-016-9296-0

Cifuentes, L. A., Schemel, L. E., and Sharp, J. H. (1990). Qualitative and numerical analyses of the effects of river inflow variations on mixing diagrams in estuaries. *Estuar. Coast. Shelf Sci.* 30, 411–427. doi: 10.1016/0272-7714(90)90006-d

Cooper, S. R., Mcglothlin, S. K., Madritch, M., and Jones, D. L. (2004). Paleoecological evidence of human impacts on the Neuse and Pamlico estuaries of North Carolina USA. *Estuaries* 27, 617–633. doi: 10.1007/bf02907649

Crosswell, J. R., Carlin, G., and Steven, A. (2019). Controls on carbon, nutrient and sediment cycling in a large, semi-arid estuarine system; Princess Charlotte Bay, Australia. *J. Geophys. Res.* 125:e2019JG005049.

Crosswell, J. R., Wetz, M. S., Hales, B., and Paerl, H. W. (2012). Air-water CO_2 fluxes in the microtidal Neuse River Estuary. North Carolina. *J. Geophys. Res. Oceans* 117:C08017.

Crosswell, J. R., Wetz, M. S., Hales, B., and Paerl, H. W. (2014). Extensive CO_2 emissions from shallow coastal waters during passage of Hurricane Irene (August 2011) over the Mid-Atlantic Coast of the U.S.A. *Limnol. Oceanogr.* 59, 1651–1665. doi: 10.4319/lo.2014.59.5.1651

Dickson, A. G. (1990). Standard potential of the reaction: AgCl(s) + $12H_2$(g) = Ag(s) + HCl(aq), and and the standard acidity constant of the ion HSO4- in synthetic sea water from 273.15 to 318.15 K. *J. Chem. Thermodyn.* 22, 113–127. doi: 10.1016/0021-9614(90)90074-z

Dickson, A. G., Afghan, J. D., and Anderson, G. C. (2003). Reference materials for oceanic CO_2 analysis: a method for the certification of total alkalinity. *Mar. Chem.* 80, 185–197. doi: 10.1016/s0304-4203(02)00133-0

Dickson, A. G., Sabine, C. L., and Christian, J. R. (2007). *Guide to Best Practices for Ocean CO_2 Measurements*. Sidney: North Pacific Marine Science Organization.

Douglas, N. K., and Byrne, R. H. (2017). Spectrophotometric pH measurements from river to sea: calibration of mCP for 0=S=40 and 278.15=T=308.15K. *Mar. Chem.* 197, 64–69. doi: 10.1016/j.marchem.2017.10.001

Dürr, H. H., Laruelle, G. G., Van Kempen, C. M., Slomp, C. P., Meybeck, M., and Middelkoop, H. (2011). Worldwide typology of nearshore coastal systems: defining the estuarine filter of river inputs to the oceans. *Estuar. Coast.* 34, 441–458. doi: 10.1007/s12237-011-9381-y

Emanuel, K. (2005). Increasing destructiveness of tropical cyclones over the past 30?years. *Nature* 436, 686–688. doi: 10.1038/nature03906

Emanuel, K. A. (2013). Downscaling CMIP5 climate models shows increased tropical cyclone activity over the 21st century. *Proc. Natl. Acad. Sci. U.S.A.* 110, 12219–12224. doi: 10.1073/pnas.1301293110

Evans, A., Madden, K., and Palmer, S. M. (eds) (2012). *The Ecology and Sociology of the Mission-Aransas Estuary - An Estuarine and Watershed Profile*. Port Aransas: University of Texas Marine Science Institute.

Frankignoulle, M., Abril, G., Borges, A., Bourge, I., Canon, C., Delille, B., et al. (1998). Carbon dioxide emission from European estuaries. *Science* 282, 434–436. doi: 10.1126/science.282.5388.434

Gazeau, F., Gattuso, J.-P., Middelburg, J. J., Brion, N., Schiettecatte, L.-S., Frankignoulle, M., et al. (2005). Planktonic and whole system metabolism in a nutrient-rich estuary (the Scheldt estuary). *Estuaries* 28, 868–883. doi: 10.1007/bf02696016

Hedges, J. I., and Keil, R. G. (1995). Sedimentary organic matter preservation: an assessment and speculative synthesis. *Mar. Chem.* 49, 81–115. doi: 10.1016/0304-4203(95)00008-f

Hsu, S. A., Meindl, E. A., and Gilhousen, D. B. (1994). Determining the power-law wind-profile exponent under near-neutral stability conditions at sea. *J. Appl. Meteorol.* 33, 757–765. doi: 10.1175/1520-0450(1994)033<0757:dtplwp>2.0.co;2

Hu, X., Nuttall, M. F., Wang, H., Yao, H., Staryk, C. J., Mccutcheon, M. R., et al. (2018). Seasonal variability of carbonate chemistry and decadal changes in waters of a marine sanctuary in the Northwestern Gulf of Mexico. *Mar. Chem.* 205, 16–28. doi: 10.1016/j.marchem.2018.07.006

Hu, X., Pollack, J. B., McCutcheon, M. R., Montagna, P. A., and Ouyang, Z. (2015). Long-term alkalinity decrease and acidification of estuaries in Northwestern Gulf of Mexico. *Environ. Sci. Technol.* 49, 3401–3409. doi: 10.1021/es505945p

Jeffrey, L. C., Maher, D. T., Santos, I. R., Mcmahon, A., and Tait, D. R. (2016). Groundwater, acid and carbon dioxide dynamics along a coastal wetland, lake and estuary continuum. *Estuar. Coasts* 39, 1–20.

Jiang, L.-Q., Cai, W.-J., and Wang, Y. (2008). A comparative study of carbon dioxide degassing in river- and marine-dominated estuaries. *Limnol. Oceanogr.* 53, 2603–2615. doi: 10.4319/lo.2008.53.6.2603

Kim, H.-C., and Montagna, P. A. (2012). Effects of climate-driven freshwater inflow variability on macrobenthic secondary production in Texas lagoonal estuaries: a modeling study. *Ecol. Model.* 23, 67–80. doi: 10.1016/j.ecolmodel.2012.03.022

Landsea, C. (2019). *Atlantic Oceanic and Meteorological Laboratory*. Silver Spring, MA: National Oceanic and Atmospheric Administration.

Laruelle, G. G., Dürr, H. H., Lauerwald, R., Hartmann, J., Slomp, C. P., Goossens, N., et al. (2013). Global multi-scale segmentation of continental and coastal waters from the watersheds to the continental margins. *Hydrol. Earth Syst. Sci.* 17, 2029–2051. doi: 10.5194/hess-17-2029-2013

Lemay, J., Thomas, H., Craig, S. E., Burt, W. J., Fennel, K., and Greenan, B. J. W. (2018). Hurricane Arthur and its effect on the short-term variability of pCO$_2$ on the Scotian Shelf, NW Atlantic. *Biogeosciences* 15, 2111–2123. doi: 10.5194/bg-15-2111-2018

Letourneau, M. L., and Medeiros, P. M. (2019). Dissolved organic matter composition in a marsh-dominated estuary: response to seasonal forcing and to the passage of a hurricane. *J. Geophys. Res.* 124, 1545–1559. doi: 10.1029/2018jg004982

Liu, Q., Charette, M. A., Breier, C. F., Henderson, P. B., Mccorkle, D. C., Martin, W., et al. (2017). Carbonate system biogeochemistry in a subterranean estuary – Waquoit Bay. USA. *Geochim. Cosmochim. Acta* 203, 422–439. doi: 10.1016/j.gca.2017.01.041

Liu, X., Patsavas, M. C., and Byrne, R. H. (2011). Purification and characterization of meta-cresol purple for spectrophotometric seawater pH measurements. *Environ. Sci. Technol.* 45, 4862–4868. doi: 10.1021/es200665d

Maher, D. T., and Eyre, B. D. (2012). Carbon budgets for three autotrophic Australian estuaries: implications for global estimates of the coastal air-water CO_2 flux. *Glob. Biogeochem. Cycles* 26:GB1032.

Majidzadeh, H., Uzun, H., Ruecker, A., Miller, D., Vernon, J., Zhang, H., et al. (2017). Extreme flooding mobilized dissolved organic matter from coastal forested wetlands. *Biogeochemistry* 136, 293–309. doi: 10.1007/s10533-017-0394-x

McCutcheon, M. R., Staryk, C. J., and Hu, X. (2019). Characteristics of the carbonate system in a semiarid estuary that experiences summertime Hypoxia. *Estuar. Coasts* 42, 1509–1523. doi: 10.1007/s12237-019-00588-0

Millero, F. J. (2010). Carbonate constants for estuarine waters. *Mar. Freshw. Res.* 61, 139–142.

Montagna, P., Palmer, T. A., and Beseres Pollack, J. (2013). *Hydrological Changes and Estuarine Dynamics*. New York: Springer.

Montagna, P. A., Hu, X., Palmer, T. A., and Wetz, M. S. (2018). Effect of hydrological variability on the biogeochemistry of estuaries across a regional climatic gradient. *Limnol. Oceanogr.* 63, 2465–2478. doi: 10.1002/lno.10953

Mooney, R. F., and McClelland, J. W. (2012). Watershed export events and ecosystem responses in the Mission–Aransas National Estuarine Research Reserve. South Texas. *Estuar. Coasts* 35, 1468–1485. doi: 10.1007/s12237-012-9537-4

Murgulet, D., Trevino, M., Douglas, A., Spalt, N., Hu, X., and Murgulet, V. (2018). Temporal and spatial fluctuations of groundwater-derived alkalinity fluxes to a semiarid coastal embayment. *Sci. Total Environ.* 630, 1343–1359. doi: 10.1016/j.scitotenv.2018.02.333

Orlando, S. P. J., Rozas, L. P., Ward, G. H., and Klein, C. J. (1993). *Characteristics of Gulf of Mexico estuaries*. Silver Spring, MD: Office of Ocean Resources Conservation and Assessment, National Oceanic and Atmospheric Administration.

Osburn, C. L., Rudolph, J. C., Paerl, H. W., Hounshell, A. G., and Van Dam, B. R. (2019). Lingering carbon cycle effects of Hurricane Matthew in North Carolina's coastal waters. *Geophys. Res. Lett.* 46, 2654–2661. doi: 10.1029/2019gl082014

Paerl, H. W., Crosswell, J. R., Van Dam, B., Hall, N. S., Rossignol, K. L., Osburn, C. L., et al. (2018). Two decades of tropical cyclone impacts on North Carolina's estuarine carbon, nutrient and phytoplankton dynamics: implications for biogeochemical cycling and water quality in a stormier world. *Biogeochemistry* 141, 307–332. doi: 10.1007/s10533-018-0438-x

Pain, A. J., Martin, J. B., Young, C. R., Valle-Levinson, A., and Mariño-Tapia, I. (2020). Carbon and phosphorus processing in a carbonate karst aquifer and delivery to the coastal ocean. *Geochim. Cosmochim. Acta* 269, 484–495. doi: 10.1016/j.gca.2019.10.040

Ruiz-Halpern, S., Maher, D. T., Santos, I. R., and Eyre, B. D. (2015). High CO_2 evasion during floods in an Australian subtropical estuary downstream from a modified acidic floodplain wetland. *Limnol. Oceanogr.* 60, 42–56. doi: 10.1002/lno.10004

Smith, S. V., and Hollibaugh, J. T. (1997). Annual cycle and interannual variability of ecosystem metabolism in a temperate climate embayment. *Ecol. Monogr.* 67, 509–533. doi: 10.1890/0012-9615(1997)067%5B0509:acaivo%5D2.0.co;2

Solis, R. S., and Powell, G. L. (1999). "Hydrography, mixing characteristics, and residence times of Gulf of Mexico Estuaries," in *Biogeochemistry of Gulf of Mexico Estuaries*, eds T. S. Bianchi, J. R. Pennock, and R. R. Twilley (Hoboken, NJ: John Willey & Sons, Inc), 29–61.

Souza, A., Pease, T., and Gardner, W. (2012). Vertical profiles of major organic geochemical constituents and extracellular enzymatic activities in sandy sediments of Aransas and Copano Bays. TX. *Estuar. Coasts* 35, 308–323. doi: 10.1007/s12237-011-9438-y

Takahashi, T., Sutherland, S. C., Sweeney, C., Poisson, A., Metzl, N., Tilbrook, B., et al. (2002). Global sea–air CO_2 flux based on climatological surface ocean pCO$_2$, and seasonal biological and temperature effects. *Deep Sea Res. Part II* 49, 1601–1622. doi: 10.1016/s0967-0645(02)00003-6

Trefry, J. H., and Presley, B. J. (1976). Heavy metals in sediments from San Antonio Bay and the northwest Gulf of Mexico. *Environ. Geol.* 1, 283–294. doi: 10.1007/bf02676717

Turner, E. L., Bruesewitz, D. A., Mooney, R. F., Montagna, P. A., Mcclelland, J. W., Sadovski, A., et al. (2014). Comparing performance of five nutrient phytoplankton zooplankton (NPZ) models in coastal lagoons. *Ecol. Model.* 277, 13–26. doi: 10.1016/j.ecolmodel.2014.01.007

Uppström, L. R. (1974). The boron/chlorinity ratio of deep-sea water from the Pacific Ocean. *Deep Sea Res. Oceanogr. Abstr.* 21, 161–162. doi: 10.1016/0011-7471(74)90074-6

Van Dam, B. R., Crosswell, J. R., and Paerl, H. W. (2018). Flood-driven CO_2 emissions from adjacent North Carolina estuaries during Hurricane Joaquin (2015). *Mar. Chem.* 207, 1–12. doi: 10.1016/j.marchem.2018.10.001

van Oldenborgh, G. J., Van Der Wiel, K., Sebastian, A., Singh, R., Arrighi, J., Otto, F., et al. (2017). Attribution of extreme rainfall from Hurricane Harvey. August 2017. *Environ. Res. Lett.* 12:124009. doi: 10.1088/1748-9326/aa9ef2

Ward, G. H. (2013). *Salinity and Salinity Response in San Antonio Bay, TWDB – UTA Interagency Contract No. 1300011546*. Austin, TX: The Unviersity of Texas at Austin.

Webster, P. J., Holland, G. J., Curry, J. A., and Chang, H.-R. (2005). Changes in tropical cyclone number, duration, and intensity in a warming environment. *Science* 309, 1844–1846. doi: 10.1126/science.1116448

Weiss, R. F. (1974). Carbon dioxide in water and seawater: the solubility of a non-ideal gas. *Mar. Chem.* 2, 203–215. doi: 10.1016/0304-4203(74)90015-2

Weiss, R. F., and Price, B. A. (1980). Nitrous oxide solubility in water and seawater. *Mar. Chem.* 8, 347–359. doi: 10.1016/0304-4203(80)90024-9

Yao, H., and Hu, X. (2017). Responses of carbonate system and CO_2 flux to extended drought and intense flooding in a semiarid subtropical estuary. *Limnol. Oceanogr.* 62, S112–S130.

Yao, H., Mccutcheon, M. R., Staryk, C. J., and Hu, X. (2020). Hydrologic controls on CO_2 chemistry and flux in subtropical lagoonal estuaries of the northwestern Gulf of Mexico. *Limnol. Oceanogr.* (in press). doi: 10.1002/lno.11394

Conflict of Interest: The authors declare that the research was conducted in the absence of any commercial or financial relationships that could be construed as a potential conflict of interest.

frontiers in Marine Science

CORRECTION
published: 25 January 2021
doi: 10.3389/fmars.2021.647961

Corrigendum: Disparate Responses of Carbonate System in Two Adjacent Subtropical Estuaries to the Influence of Hurricane Harvey – A Case Study

Xinping Hu[1]*, *Hongming Yao*[1], *Cory J. Staryk*[1], *Melissa R. McCutcheon*[1], *Michael S. Wetz*[2] *and Lily Walker*[2]

[1] *Department of Physical and Environmental Sciences, Texas A&M University – Corpus Christi, Corpus Christi, TX, United States,* [2] *Harte Research Institute for Gulf of Mexico Studies, Texas A&M University – Corpus Christi, Corpus Christi, TX, United States*

Keywords: estuary, carbon cycle, CO_2 flux, Hurricane Harvey, Gulf of Mexico

OPEN ACCESS

Approved by:
Hans Paerl,
The University of North Carolina at Chapel Hill, United States

****Correspondence:***
Xinping Hu
xinping.hu@tamucc.edu

Specialty section:
This article was submitted to Marine Biogeochemistry, a section of the journal Frontiers in Marine Science

Received: *30 December 2020*
Accepted: *11 January 2021*
Published: *25 January 2021*

Citation:
Hu X, Yao H, Staryk CJ, McCutcheon MR, Wetz MS and Walker L (2021) Corrigendum: Disparate Responses of Carbonate System in Two Adjacent Subtropical Estuaries to the Influence of Hurricane Harvey – A Case Study. Front. Mar. Sci. 8:647961. doi: 10.3389/fmars.2021.647961

A Corrigendum on

Disparate Responses of Carbonate System in Two Adjacent Subtropical Estuaries to the Influence of Hurricane Harvey – A Case Study
by Hu, X., Yao, H., Staryk, C. J., McCutcheon, M. R., Wetz, M. S., and Walker, L. (2020). Front. Mar. Sci. 7:26. doi: 10.3389/fmars.2020.00026

In the original article, there was a mistake in **Figure 5** as published. This is due to an incorrect formulation of gas transfer velocity in the flux calculations. The corrected **Figure 5** appears below.

In the original article, there were errors. The errors were caused by an incorrect formulation of gas transfer velocity in the flux calculations; hence all the flux values need to be corrected.

A correction has been made to ***Results, CO_2 partial pressure, Normalized pCO_2, and Air-Water CO_2 flux, paragraph 3***:

As defined in Eq. (1), CO_2 flux is a function of wind speed (gas transfer) and air-water pCO_2 gradient. Contrary to the pCO_2 values (**Figure 4A**), the post-Harvey maximum pCO_2 in GE did not translate into the highest CO_2 efflux in our study period (164 ± 122 mmol m^{-2} d^{-1} on Sept 1, 2017). Instead, the highest calculated CO_2 efflux occurred in mid-2015 (181 ± 100 mmol m^{-2} d^{-1} on July 8, 2015) (**Figure 5A**), and the wind speed 9.3 m s^{-1} on the 2015 observation date was much higher than the post-Harvey date (3.6 m s^{-1}) (**Figure 5B**). In comparison, MAE did not exhibit significant changes in CO_2 flux before and after the hurricane (**Figure 5A**).

A correction has been made to ***Discussion, Air-water CO_2 flux, paragraph 2-5***:

Compared to these east coast studies, we did not have data during Harvey except the single bottom water monitoring station (Walker et al. ms in prep.). However, the post-Harvey CO_2 flux in GE increased from the pre-hurricane near neutral levels (−0.2 ± 5.0 mmol m^{-2} d^{-1}) to 164 ± 122 mmol m^{-2} d^{-1} on September 1 and then 94 ± 161 mmol m^{-2} d^{-1} on September 13, both were greater than or similar to post-storm CO_2 flux observed in the east coast estuaries (Crosswell et al., 2014; Van Dam et al., 2018). In comparison, post-Harvey CO_2 flux in MAE (4 ± 3 mmol m^{-2} d^{-1}) was much lower but on par with those values obtained from those east coast estuaries. The reason for such distinct difference in CO_2 flux may be explained by the different extents of nutrient pollution that these estuaries experience (see below).

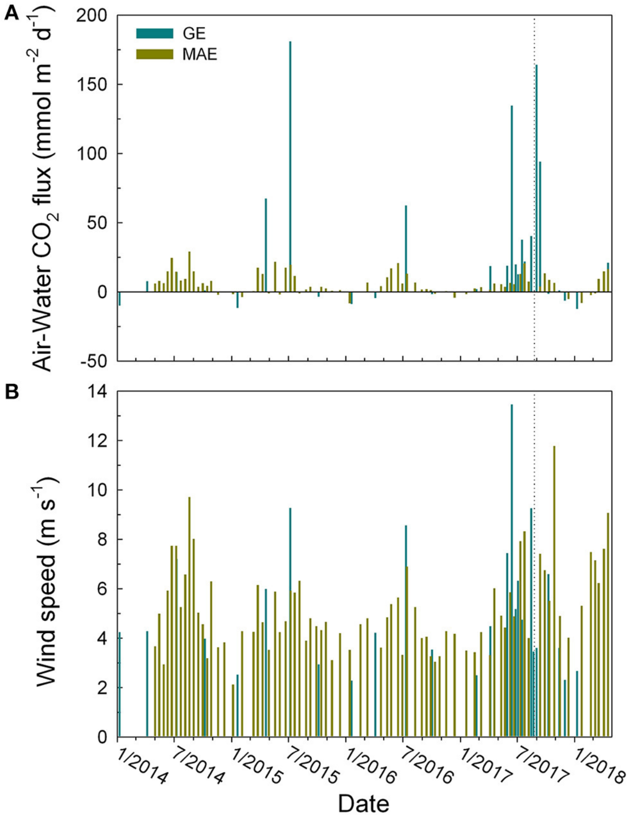

FIGURE 5 | Temporal distributions of **(A)** air–water CO_2 flux (unit mmol m^{-2} d^{-1}) and **(B)** daily wind speed on the sampling days in GE (dark green) and MAE (dark yellow). The dotted lines represent the date (August 25, 2017) on which Hurricane Harvey made landfall.

In fact, despite that observed pCO_2 (hence water-air pCO_2 gradient) was the largest in GE after Harvey, water-to-air CO_2 flux was not the highest at that time (**Figure 5A**). The difference mainly stemmed from the higher gas transfer velocity in 7.8 m d^{-1} (at wind speed 9.3 m s^{-1}) on the sampling day in mid-2015 vs. 1.9 m d^{-1} (at wind speed 3.6 m s^{-1}) after Harvey.

Overall, water-to-air CO_2 flux during the 1-month period after Harvey (August 27-Septemebr 26, 2017) was estimated to be 1.6 × 10^9 mol. Integrating the 2017 flux values to the whole year the CO_2 efflux in GE in 2017 was 4.7 × 10^9 mol. Therefore, this 1-month period accounted for ~35% annual CO_2 emission in that year, and this estimate should represent a lower limit because CO_2 flux could have been higher during the storm due to much higher gas transfer velocity and potential sediment resuspension in this shallow estuary. In comparison, much sparser measurements in 2015 and 2016 suggested that the flood-induced CO_2 emission accounted for 78 and 132% of annual values, respectively. Note all calculated CO_2 efflux values were negative in 2016 except that from the flooding period that year. Considering the limited observations in these 2 years and that both river discharge and wind speed both played an important role in controlling CO_2 flux, these two estimates thus probably had high uncertainties.

CO_2 flux in MAE during the 2015 and 2016 flooding periods reached as much as 21–22 mmol m^{-2} d^{-1}, much greater than that from the post-Harvey value. Furthermore, the latter flux from August 26 to September 25 (6.6 × 10^7 mol) was not only much smaller than the GE values, but also appeared not extraordinary in the integrated annual CO_2 flux (close to monthly mean of 5.0 × 10^7 mol), although again the CO_2 flux during the storm is unknown so this value can only be considered as a conservative estimate.

The authors apologize for this error and state that this does not change the scientific conclusions of the article in any way. The original article has been updated.

REFERENCES

Crosswell, J. R., Wetz, M. S., Hales, B., and Paerl, H. W. (2014). Extensive CO_2 emissions from shallow coastal waters during passage of Hurricane Irene (August 2011) over the Mid-Atlantic Coast of the U.S.A. *Limnol. Oceanogr.* 59, 1651–1665. doi: 10.4319/lo.2014.59.5.1651

Van Dam, B. R., Crosswell, J. R., and Paerl, H. W. (2018). Flood-driven CO_2 emissions from adjacent North Carolina estuaries during Hurricane Joaquin (2015). *Mar. Chem.* 207, 1–12. doi: 10.1016/j.marchem.2018.10.001

frontiers
in Marine Science

ORIGINAL RESEARCH
published: 07 February 2020
doi: 10.3389/fmars.2020.00018

Use of Geospatial, Hydrologic, and Geochemical Modeling to Determine the Influence of Wetland-Derived Organic Matter in Coastal Waters in Response to Extreme Weather Events

Jacob C. Rudolph[1]*, Carli A. Arendt[1], Alexandria G. Hounshell[2,3], Hans W. Paerl[2] and Christopher L. Osburn[1,4]

[1] Department of Marine, Earth, and Atmospheric Sciences, North Carolina State University, Raleigh, NC, United States,
[2] Institute of Marine Sciences, The University of North Carolina at Chapel Hill, Morehead City, NC, United States,
[3] Department of Biological Sciences, Virginia Polytechnic Institute and State University, Blacksburg, VA, United States,
[4] Center for Geospatial Analytics, North Carolina State University, Raleigh, NC, United States

Edited by:
Christian Lønborg,
Australian Institute of Marine Science
(AIMS), Australia

Reviewed by:
Philippe Massicotte,
Laval University, Canada
Kaelin M. Cawley,
National Ecological Observatory
Network, United States

****Correspondence:***
Jacob C. Rudolph
jcrudolp@ncsu.edu

Specialty section:
This article was submitted to
Marine Biogeochemistry,
a section of the journal
Frontiers in Marine Science

Received: *09 September 2019*
Accepted: *10 January 2020*
Published: *07 February 2020*

Citation:
Rudolph JC, Arendt CA, Hounshell AG, Paerl HW and Osburn CL (2020) Use of Geospatial, Hydrologic, and Geochemical Modeling to Determine the Influence of Wetland-Derived Organic Matter in Coastal Waters in Response to Extreme Weather Events. Front. Mar. Sci. 7:18. doi: 10.3389/fmars.2020.00018

Flooding from extreme weather events (EWE), such as hurricanes, exports large amounts of dissolved organic matter (DOM) to both estuaries and coastal waters globally. Hydrologic connectivity of wetlands to adjacent river channels during flood events can potentially have a major control on the DOM exported to coastal waters after EWEs. In this study, a geographic information system based flood model was used to: (1) determine the volume of flooded wetlands in a river corridor following Hurricane Matthew in 2016; (2) compute the resulting volume fluxes of DOM to the Neuse River Estuary-Pamlico Sound (NRE-PS), in eastern North Carolina and (3) use the flood model to quantify the wetland contribution to DOM export. The flood model-derived contributions were validated with a Bayesian Monte Carlo mixing model combining measurements of DOM quality: specific UV Absorbance at 254 nm ($SUVA_{254}$), spectral slope ratio (S_R), and stable isotope ratios of dissolved organic carbon (δ^{13}C-DOC). Results indicated that (1) hydrologic connectivity of the freshwater riparian wetlands caused the wetlands to become the primary source of organic matter (OM) that was exported into the NRE-PS after Matthew and (2) this source lingered in these coastal waters in the months after the storm. Thus, in consideration of the pulse-shunt concept, EWE such as Hurricane Matthew cause pulses of DOM from wetlands, which were the primary source of the OM shunted from the terrestrial environment to the estuary and sound. Wetlands constituted ca. 48% of the annual loading of DOC into the NRE and 16% of DOC loading into the PS over a period of 30 days after Hurricane Matthew. Results were consistent with prior studies in this system, and other coastal ecosystems, that attributed a high reactivity of DOM as the underlying reason for large CO_2 releases following EWE. Adapting the pulse-shunt concept to estuaries requires the addition of a "processing" step to account for the DOM to CO_2 dynamics, thus a new pulse-shunt process is proposed to incorporate coastal waters. Our results suggest that with increasing frequency and intensity of EWE, strengthening of the lateral transfer of DOM from land to ocean will occur and has the potential to greatly impact coastal carbon cycling.

Keywords: hydrologic connectivity, dissolved organic matter, extreme weather events, stable carbon isotopes, wetlands

INTRODUCTION

The frequency of extreme weather events (EWE), such as tropical cyclones, has increased in the southeastern United States (US) in recent decades (Paerl et al., 2018) and since the mid-1990s the coast of North Carolina has experienced many such events. Paerl et al. (2018) classified EWEs occurring over the past 20 years in eastern NC into three categories (dry and windy, wet and calm, and wet and windy) and compared each category to non-storm conditions to show how different types of storms would affect the Neuse River Estuary (NRE), the main tributary to Pamlico Sound (PS), 2nd largest estuarine complex in the United States. Hurricane Matthew, which occurred in October 2016, struck eastern North Carolina and its coastal waters as a Category 1 storm causing ca. $1.6 billion in damage and 28 deaths in North Carolina alone (Stewart, 2017). In their analysis, Paerl et al. (2018) found that “wet and windy” storms, such as Matthew, showed statistical differences in carbon (C) and inorganic nitrogen concentrations, partial pressure of carbon dioxide (pCO_2), and pH in the NRE, indicating such EWEs have major impacts on estuarine and coastal water biogeochemistry in the weeks to months after the storms.

Precipitation from EWE is projected to rise by ca. 7% with each degree Celsius of warming in the future (Prein et al., 2017). Flooding from heavy precipitation associated with EWE can result in a flushing of terrestrial dissolved organic matter (DOM) from land to coastal waters where substantial biogeochemical processing can occur returning CO_2 to the atmosphere (Bianchi et al., 2013). Depending on the residence time of floodwater in receiving waters such as estuaries and large river plumes, DOM degradation can persist for weeks to months following these events (Osburn et al., 2019a). Thus, these episodic large storm events can be significant, yet poorly constrained, influences on coastal C budgets, via terrestrial DOM’s transport to coastal waters (Raymond et al., 2016).

For DOM, changes to its sources following EWEs can influence its biogeochemical processing in coastal waters (Osburn et al., 2012; Bianchi et al., 2013). In part, DOM’s importance in the coastal C cycle arises from its central role in providing a basal resource to the “microbial loop”. Results from Hurricane Floyd in 1999 indicated increased microbial respiration following floodwaters from the Cape Fear River in eastern NC exported into Onslow Bay (Avery et al., 2004). Bianchi et al. (2013) found a consistent post-flood result in shelf waters of the northern Gulf of Mexico, and suggested that soil-sourced DOM was rapidly lost to the atmosphere as CO_2 via photochemical and microbial processing. As a result of high rates of carbon sequestration and sediment trapping, wetlands are major C sinks that store between 350–535 Gt C (Gorham, 1995; IPCC, 2001; Mitra et al., 2005). Wetlands likely play major role in the passive pipe scenario used to describe rivers in the pulse-shunt concept (PSC; Raymond et al., 2016), which builds on earlier concepts of how floods can influence biogeochemistry (Vannote et al., 1980; Junk et al., 1989). While the pulse-shunt concept was initially only applied to upland streams and did not account for wetlands, estuaries or coastal waters, recent work suggests that estuaries may act in similar fashion (Hounshell et al., 2019). Delineating between wetland and upland DOM will be important to evaluate the reactivity and cycling of DOM transported to coastal waters following EWEs. Here we posit that flooding from EWEs mobilizes DOM stored in wetlands into coastal waters where it can be processed back into CO_2.

The complexity of doing so requires a means to assess when hydrologic-connectivity occurs between water from a river and water from wetlands, via either surface waters, groundwater, or both (Pringle, 2003). During floods, an isolated wetland’s hydrological-connection to a river’s main channel allows the flushing of its accumulated recalcitrant OM and nutrients (Tockner et al., 1999; Wolf et al., 2013). However, recalcitrant OM in one system may become labile in another system (Boyd and Osburn, 2004); microorganisms in coastal waters are poised to break down the recalcitrant wetland OM to CO_2, returning stores of terrestrial carbon to the atmosphere (Bauer et al., 2013).

Because wetlands are important reservoirs of OM in coastal watersheds that can become OM sources following EWEs, their contribution to the terrestrial DOM flux must therefore be determined. Osburn et al. (2019a) used geochemical proxies for organic matter (light absorption and stable C isotopes) to posit that wetlands constituted a significant fraction of the terrestrial DOM exported into Pamlico Sound via the Neuse River Estuary following Hurricane Matthew. The main objective of this study was to validate their supposition with a quantitative

---

Abbreviations: δ^{13}C-DOC, stable isotope ratio of dissolved organic carbon (‰); [DOC], concentration of dissolved organic carbon (mg L^{-1}); A_T, total flooded area; A_W, area of flooded wetlands; BMC, bayesian monte carlo; C_{FB}, DOC concentration from river (mg L^{-1}); C_W, DOC concentration from wetland (mg L^{-1}); DEM, digital elevation model; EWE, extreme weather events; f_o, fractional contribution of marine sourced organic matter to BMC mixing model; f_r, fractional contribution of river sourced organic matter to BMC mixing model; f_w, fractional contribution of wetland sourced organic matter to BMC mixing model; L_{DOCR}, dissolved organic carbon mass loading from riverine sources (Gg C); L_{DOCT}, total dissolved organic carbon mass loading from wetland and riverine sources combined (Gg C); L_{DOCW}, dissolved organic carbon mass loading from wetland sources (Gg C); NR, neuse river; NRE, neuse river estuary; PS, pamlico sound; PSC, pulse-shunt concept; REM, relative elevation model; S_R, spectral slope ratio; $SUVA_{254}$, specific UV absorbance at 254 nm (L mg C^{-1} m^{-1}); V_{nW}, volume of flooded non-wetland area; V_T, total flooded volume; V_W, volume of flooded wetlands.

model. We hypothesized that the hydrologic-connectivity of the lower Neuse River to its adjacent riparian wetlands resulted in wetlands as a dominant source of DOM transported in floodwaters from extreme precipitation events, such as Hurricane Matthew. Here, the hydrologic-connectivity of riparian wetlands to a major coastal river in eastern NC was determined by a relative elevation flood model used to determine the extent of flooding that occurred in response to Hurricane Matthew in 2016. Fluxes of DOM to the NRE from its watershed were determined using concentrations of DOC from the river and wetlands and volumetric estimates of each of these two sources. This geospatial approach to compute DOM sources was validated by comparison to a Bayesian Monte Carlo mixing model (Arendt et al., 2015). Sources of OM in this system were determined with bulk carbon stable isotopes of DOC (δ^{13}C-DOC), specific UV absorbance at 254 nm ($SUVA_{254}$), and spectral slope ratio (S_R), analyses that characterize different fractions of OM and have varying rates of source specificity (Bianchi and Canuel, 2011). By implementing the coupled geospatial-geochemical model and these analyses, the change in quality and quantity of OM from the wetlands to the NRE-PS resulting from Matthew's floodwaters was quantified. Previous studies of biogeochemical cycling and past extreme events in the NRE-PS provided important context for this study (e.g., Paerl et al., 2018; Osburn et al., 2019a).

MATERIALS AND METHODS

Study Site and Sample Collection

This study was conducted in the main-stem of the Neuse River in the Coastal Plain of North Carolina, United States (**Figure 1**; Osburn et al., 2019a). Along the lower reach of the river above the head of tides, abundant freshwater riparian wetlands fringe the main channel of the river, before it flows southeast into the NRE-PS (NC-DEQ, 2018). The Neuse River Estuary is the largest tributary to the Pamlico Sound (Paerl et al., 2018). The Pamlico Sound is the larger portion of the Albemarle-Pamlico Estuarine System (APES), which is the second largest estuarine complex in the continental United States (NC-DEQ, 2018). Characteristics of each system are summarized in **Supplementary Table S1**. Both the NRE and PS are relatively shallow (average depths are ca. 3 and 5 m, respectively). There is little tidal effect (0.3–0.6 m; Giese et al., 1985) in this microtidal estuarine complex due to embayment by the barrier islands off the coast of NC (NC-DEQ, 2018). Mixing in the system is strongly affected by winds (Dixon et al., 2014). Moreover, the Neuse River's discharge can vary greatly over the course of a year (ca. 17 to 1400 m^3 s^{-1} for 2016). The embayment of this lagoonal system under low to modest river flow causes the NRE-PS to generally have long water residence times; however, during high flow events like Hurricane Matthew, the residence time can decrease greatly (**Supplementary Table S1**).

Access to a long-term geochemical dataset from routine monitoring of the NRE-PS (the Neuse River Estuary Modeling and Monitoring Project, "ModMon") provided a long-term record against which we compare the system's response to the storm. Surface water samples were collected at sites along the main axis of the Neuse River and NRE-PS over a period of 3 months, between October and December 2016, following the passage of Hurricane Matthew on October 9, 2016 (**Figures 1A,B**). Sampling was conducted ca. weekly across the NR, NRE, and PS sites (**Supplementary Table S2**). Using a bucket riverine samples were collected in 1 L brown HDPE bottles, from bridge overpasses along the main-stem of the NR at United States Geological Survey (USGS) gauged locations (Clayton, Smithfield, Goldsboro, Kinston, and Fort Barnwell; **Figure 1B**).

Estuarine and sound samples were collected during ModMon surveys of the NRE-PS by pumping water using a peristaltic pump from the surface, stored in 1 L opaque HDPE bottles and frozen for shipment to North Carolina State University (**Figure 1B**). Collection bottles were cleaned in a detergent bath, rinsed profusely with Milli-Q ultrapure water, and left to air dry before sampling. Additional surface water sampling was completed in an area of freshwater riparian wetlands between the last riverine site on the NR near Fort Barnwell, NC, United States and head-of-tide for the estuary at the Street's Ferry Bridge crossing near Vanceboro, NC, United States in March and October 2017 (**Figure 1C**).

Sample Processing and Optical Analyses

Surface water samples were thawed at room temperature, and a measured volume of water was filtered through pre-combusted (at 450°C for 5 h) 0.7 μm Whatman glass fiber filters (GF/F) via vacuum. Prior to sample filtration, 150 mL of Milli-Q water was used to rinse each filter. The filtrate was collected into 60 mL polycarbonate bottles (detergent-washed and rinsed thoroughly with Milli-Q water) for optical analyses and 40 mL amber-tinted borosilicate glass vials (detergent-washed, rinsed thoroughly with Milli-Q water, and combusted at 450°C for 5 h) for DOC concentration [(DOC)] and stable carbon isotope (δ^{13}C-DOC, see below) analyses. Filtrate was stored at 4°C until optical measurements were made, generally within 48 h of thaw. Filtrate for DOC analysis was acidified to a pH of 2 with 85% phosphoric acid (H_3PO_4), then stored at 4°C until measurements were completed.

Absorbance measurements were made with a Varian Cary 300UV spectrophotometer in 1 cm quartz cuvettes, over a range of wavelengths (200–800 nm), and then blank corrected using Milli-Q ultrapure water. The Napierian absorption coefficient (*a*) was determined using the formula:

$$a\left(\lambda_{sample}\right) = \frac{A\left(\lambda_{sample} - \lambda_{blank}\right)}{L} \times 2.303 \qquad (1)$$

where *a* is absorption coefficient (m^{-1}), λ is the wavelength (nm), *A* is the absorbance measured on the spectrophotometer, and *L* is pathlength of the quartz cuvette (m) (Kirk, 1994; Osburn and Morris, 2003). Helms et al. (2008) suggested that an absorption coefficient at 254 nm (a_{254}) could be used as a proxy for DOC concentration, due to high correlation of DOC concentration and a_{254}. The spectral slope ratio (S_R) was calculated by dividing the natural log of the slope of the absorbance spectra between 275 and 295 nm by the natural log

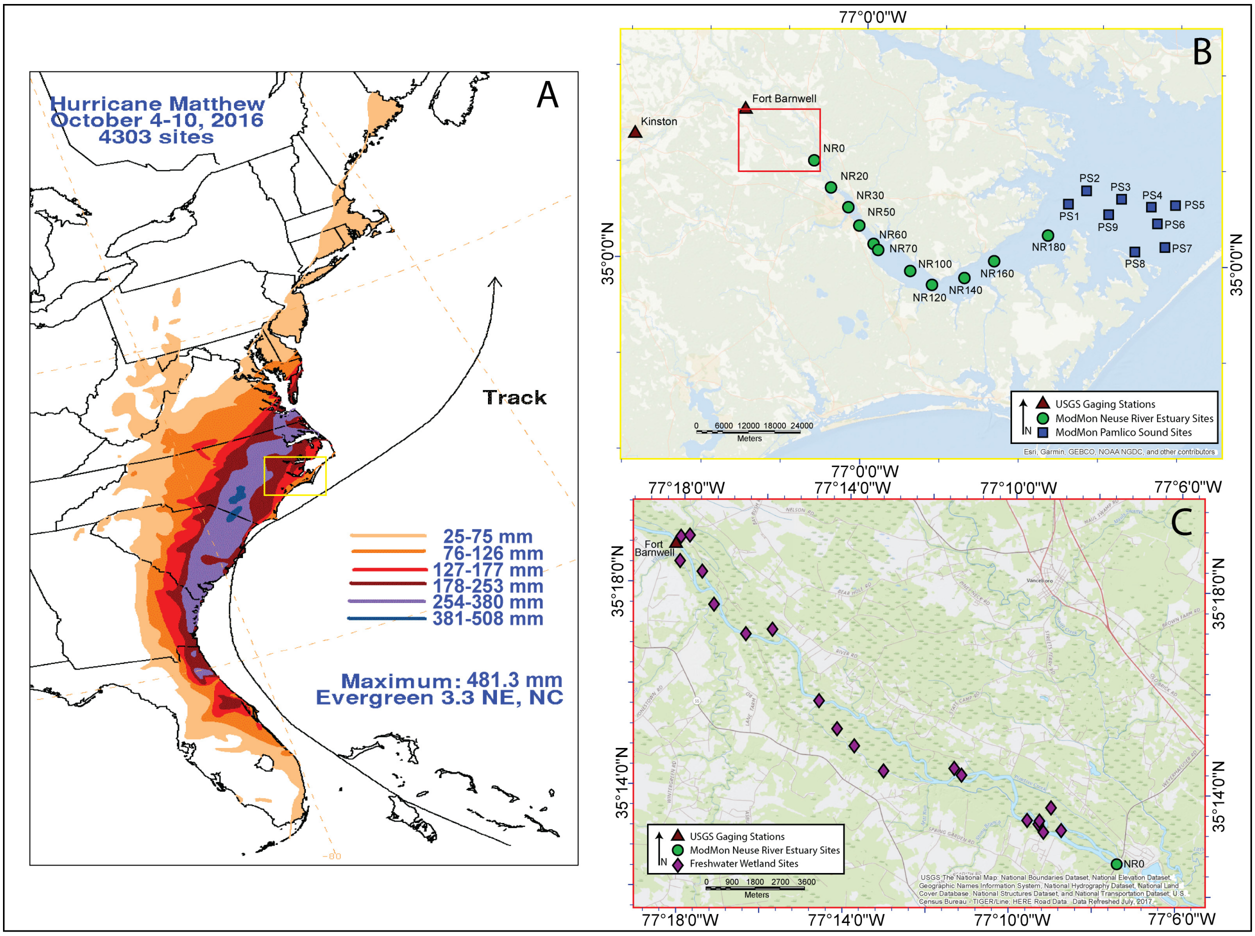

FIGURE 1 | (A) Map from Stewart (2017) showing the rainfall totals and path of Hurricane Matthew during the period of 4–10 October 2016; **(B)** Map of sampling locations in the Neuse River watershed and Pamlico Sound, NC; **(C)** Map of freshwater riparian wetlands along the lower Neuse River, NC. (Modified from Osburn et al., 2019a with permission from John Wiley and Sons, Inc.).

of the slope of the absorbance spectra between 350 and 400 nm. S_R is a qualitative indicator of molecular weight of a sample, with larger values indicating lower molecular weight and smaller values having higher molecular weights (Helms et al., 2008). The specific UV absorbance at 254 nm ($SUVA_{254}$), which is the ratio of the decadic UV absorption at 254 nm divided by the DOC concentration, has been found to be useful in estimating DOM quality parameters such as: the aromaticity of DOM (Weishaar et al., 2003), the molecular weight (Chowdhury, 2013), and the source of DOM and type of environmental degradation (Hansen et al., 2016).

Dissolved Organic Carbon and Stable Carbon Isotope Analyses

For measurement of (DOC), samples were first sparged with ultrapure Argon gas for 20 min to remove dissolved inorganic carbon (DIC). Sparged samples were analyzed on an OI Analytical 1030D Aurora total organic carbon analyzer, using wet chemical oxidation, coupled to a Thermo Delta V Plus isotope ratio mass spectrometer (IRMS) to determine stable isotope values, expressed as the standard delta notation, δ^{13}C-DOC, using Equation 2:

$$\delta^{13}C(‰) = \left[\left(\frac{R_{sample}}{R_{standard}} - 1\right) \times 1000\right] \quad (2)$$

where $\delta^{13}C$ is the stable isotope ratio of carbon in parts per thousand, R_{sample} is the ratio of ^{13}C to ^{12}C for the unknown sample, and $R_{standard}$ is the ratio of ^{13}C to ^{12}C for the known standard (Osburn and St-Jean, 2007).

(DOC) measurements were blank-corrected for ultra-pure Milli-Q water, then calculated using a linear regression curve of known caffeine standards with concentrations from 1 to 20 mg C L^{-1}. δ^{13}C-DOC values were blank corrected and referenced to the Vienna Pee Dee Belemnite (VPDB) scale via a linear regression of six caffeine (IAEA-600, $-27.7 \pm 0.04‰$) and two sucrose (IAEA-C6, $-10.8 \pm 0.03‰$) International Atomic Energy Agency (IAEA) standards. Precision for (DOC) and δ^{13}C-DOC values were ± 0.4‰ based on reproducibility and calibration to sucrose standard. Milli-Q blanks were run every 10 samples for quality control. DOC stable isotope values for different sources of natural OM from previous studies were tabulated for reference (**Supplementary Table S3**).

Geospatial Wetland Flood Model

The area and type of freshwater wetlands that were flooded in response to Hurricane Matthew were determined using Esri's ArcMap 10.5.1. Input variables included: (1) a high-resolution Light Detection and Ranging (LiDAR) digital elevation model (DEM) raster dataset with 6.3 cm vertical accuracy and 1 m horizontal accuracy downloaded from the NOAA Digital Coast data viewer (OCM Partners, 2017), (2) USGS gauge height and discharge rates, and (3) a coastal wetland GIS polygon vector dataset (Sutter, 1999). The relative elevation model (REM) tool within the Riparian Topography Toolbox (Wall, pers. comm.; Dilts et al., 2010) was used for removal of the slope trend of the floodplain from the DEM. Removal of slope trend of the floodplain from the REM was required because the slight slope of the ground to coastal water surface (1:1.8 m over the area of our survey) would cause the lower wetlands to become more flooded than the upper wetlands. Once removed, the water surface at base flow in the river and upper estuary was set to 0 m (REM) to flood an otherwise linear surface.

The study area (**Figure 1C**) was extracted from the DEM using the Spatial Analyst toolbox (ESRI, 2011). The extracted wetland DEM was also processed by the REM toolbox to remove the slope trend from the surface water using kernel density with a search radius set to 3000 meters; this search radius was tested and found to be dependent on the size of the floodplain. The 3D Analyst toolbox (ESRI, 2011) was used to determine six surfaces of the flooded area and volume of the detrended freshwater riparian zone during Hurricane Matthew: relative 0 m, National Weather Service (NWS) flood stage, moderate flood stage, major flood stage, and maximum gauge height. A surface was also determined for mean gauge height over the period of October-December 2016, after the storm. Gauge height and discharge rates were obtained from the USGS gauging station on the Neuse River near Fort Barnwell, NC, United States (#02091814) (**Supplementary Table S4**). The value from the DEM at Ft. Barnwell (1.770 m) was removed from the gauge height values to account for removal of slope trend in the REM. In ArcMap, a constant planer raster layer was created (Spatial Analyst toolbox; ESRI, 2011) using the gauge height value, then the *Cut Fill* tool (3D Analyst toolbox; ESRI, 2011) was used to subtract the constant layer from the DEM. The *Cut Fill* raster layer was then extracted by attributes (Spatial Analyst toolbox; ESRI, 2011) where the volume was negative, to obtain the volume (V_T) and area (A_T) of the total flooded surface. An ArcMap model builder workflow plot indicates the processes that were used to determine the flood model (**Supplementary Figure S1**).

Next, North Carolina's Department of Coastal Management spatial wetland mapping layer (Sutter, 1999) was overlain on the flooded surface and extracted by mask (Spatial Analyst toolbox; ESRI, 2011) to determine the area (A_W) and volume (V_W) of wetlands present during various flood stages. The cell size of the DEM was 1.5 × 1.5 m. A_W was calculated by multiplying the cell area (2.25 m^2) by the cell count of the total wetland flooded area from the attribute table in ArcMap.

DOC mass loading (L) to the NRE from the Neuse River Watershed was calculated from the volumes determined in the ArcGIS flood model (**Supplementary Figure S1**) by first subtracting the V_W from the V_T (Eq. 3) to obtain the volume of the non-wetland area (V_{nW}), then the DOC mass loading from the wetlands (L_{DOCW}) was determined by multiplying the flooded volume of the wetlands by the DOC concentration from the wetlands (C_W) and dividing by 1000 to get units of kg C (Eq. 4). Next, riverine DOC mass loading (L_{DOCR}) was calculated by multiplying the DOC concentration from Fort Barnwell, NC, United States (riverine site; C_{FB}) by the non-wetland flooded volume and dividing by 1000 to value in units of kg C (Eq. 5). Finally, total DOC mass loading (L_{DOCT}) was determined by adding the DOC mass loads of the wetlands and the river and then converting to Gg C (eq. 6).

$$V_{nW} = V_T - V_W \tag{3}$$

$$L_{DOCW} = \frac{V_W C_W}{1000} \tag{4}$$

$$L_{DOCR} = \frac{V_{nW} C_{FB}}{1000} \tag{5}$$

$$L_{DOCT} = \frac{(L_{DOCW} + L_{DOCR})}{1 \times 10^6} \tag{6}$$

Bayesian Monte Carlo Mixing Model

A Bayesian Monte Carlo (BMC) three end-member mixing model was used to validate the geospatial model created during this study (Arendt et al., 2015). BMC has been shown to be useful in determining fractional contributions of unique end-members to bulk samples in many different Earth surface systems, including glacial meltwaters (Bhatia et al., 2011; Arendt et al., 2015), soil nutrients (Chadwick et al., 1999), and stable and radiogenic isotopes in seawater (Pichler, 2005; Rickli et al., 2010). Within our estuarine and sound system, we identified the possible contributing end-member sources as wetland, river, and ocean water. We assumed that there were no other major end-members for this study. Therefore, the sum of the fractional contribution (f) of wetland (w), river (r), and ocean (o) for our estuary and sound samples is given in Eq. 7.

$$f_w + f_r + f_o = 1 \tag{7}$$

To determine the relative contribution of our unique end members (*w*, *r*, or *o*) to the bulk water (NRE or PS), we initially identified both SUVA$_{254}$ and δ^{13}C-DOC as geochemical parameters with ranges specific to our end-members. However, due to linearity between SUVA$_{254}$ and δ^{13}C-DOC values (Osburn et al., 2019a), a third component (S_R) was used to properly constrain the model. Thus, the combination of SUVA$_{254}$, δ^{13}C-DOC, and S_R geochemical components allow us to define unique end-member geochemical compositions based on measurements from wetland (n = 22), river (n = 4), and ocean (n = 2; values from Atar, 2017) samples. End-member compositions are defined as mean SUVA$_{254}$, δ^{13}C-DOC, and S_R values ± the standard deviation for each end member: where the wetland end-member composition is −29.41 ± 0.73‰, 4.94 ± 0.50 L mg C^{-1}m^{-1}, and 0.83 ± 0.06; the river end-member composition is

−25.77 ± 0.10‰, 3.64 ± 0.61 L mg $C^{-1}m^{-1}$, and 0.88 ± 0.06; and the ocean end-member composition is −23. 01 ± 0.50‰, 1.40 ± 0.50 L mg $C^{-1}m^{-1}$, and 1.82 ± 0.50, respectively. The incorporation of standard deviations within each end-member composition allows the model to account for natural variability and uncertainty associated with these end-member compositions.

Once the end members were geochemically defined, the BMC model was fit to our raw sample $SUVA_{254}$, δ^{13}C-DOC, and S_R data from Neuse River Estuary (NRE; n = 70) and Pamlico Sound (PS; n = 52) samples were input to our BMC model to ascertain the f_w, f_r, and f_o for each sample. Intuitively, the NRE and PS samples differ in $SUVA_{254}$, δ^{13}C-DOC, and S_R compositions, with mean values ± standard deviations of −28.56 ± 1.13‰, 4.12 ± 0.53 L mg $C^{-1}m^{-1}$, and 0.84 ± 0.06 for all NRE samples, and −27.46 ± 0.89‰, 3.62 ± 0.32 L mg $C^{-1}m^{-1}$, and 0.99 ± 0.08 for all PS samples. The BMC model is able to provide further insight to these differences and calculate the most likely relative fractional contribution of each end member (f_w, f_r, f_o) to the NRE and PS samples based on the unique 3-component end-member geochemical compositions and associated uncertainties we defined. The BMC model uses prior and posterior probability density functions based on the known (end-member compositions and bulk NRE and PS compositions) and the unknown (relative contributions from each end member to the bulk samples) to determine the likelihood of any fractional contribution outcome. Each outcome is accompanied by a known uncertainty that places constraints on how likely each outcome is. The likelihood of a model prediction was calculated by Eq. 8.

$$L \propto exp\left[\frac{(\delta^{13}C_p - \delta^{13}C_o)^2}{\sigma^2_{\delta^{13}C}}\right] \times \exp\left[\frac{(SUVA_{254\,p} - SUVA_{254\,o})^2}{\sigma^2_{SUVA_{254}}}\right] \times \exp\left[\frac{(S_{R\,p} - S_{R\,o})^2}{\sigma^2_{S_R}}\right] \quad (8)$$

Where subscripts p and o are the predicted and observed measurements of each variable, while σ is the measurement of uncertainty. One hundred million prior and posterior samples were tested for each bulk water sample and three standard deviations of the data for the bulk samples were used. The model was run separately for the NRE and the PS using the same defined end-member ranges. Models were run separately due to spatial and source differences between the NRE and PS, with NRE generally being more terrestrial sourced and PS more marine sourced. Average acceptance rates of the mixing model were determined via the ratio of prior samples to accepted posterior samples (see Eq. 8) and these rates were used to ascertain our confidence in the model fit.

RESULTS

Summary of DOM Quality

δ^{13}C-DOC

Mean δ^{13}C-DOC values in the Neuse River Estuary initially were more enriched during October sampling dates, shortly after the storm (17 October: −27.8 ± 0.8‰; 24 October: −27.8 ± 0.4‰; **Supplementary Figure S2A**) when compared to early November NRE values (01 November: −29.4 ± 0.5‰; 08 November: −29.5 ± 1.1‰; 15 November: −29.2 ± 0.4‰), although more depleted than the Neuse River sites over the entire study period (−25.9 ± 0.4‰). When compared to the range of river values from November (−25.9 ± 0.1 to −25.5 ± 0.4‰), mean δ^{13}C-DOC values in the estuary in October were depleted by ca. 4‰. In late November there was an increase in mean δ^{13}C-DOC values to −27.3 ± 0.9‰, but then in the December, the estuary experienced another decrease in mean δ^{13}C-DOC values to −29.4 ± 1.0‰ (**Supplementary Figure S2A**). These δ^{13}C-DOC values for the NRE oscillated between the mean values for riparian wetlands (−29.4 ± 0.7‰). Similar to the NRE, mean δ^{13}C-DOC values in Pamlico Sound were bounded between the Neuse River and riparian wetland values. Mean δ^{13}C-DOC values for the sound were depleted relative to those for the river, while PS values were enriched relative to mean values for the wetlands. Also, ranges of mean δ^{13}C-DOC values in PS (−28.0 ± 0.2 to −26.7 ± 0.3‰) were slightly enriched compared to the NRE values (−29.5 ± 1.1 to −27.3 ± 0.9‰; **Supplementary Figure S2A**). Attenuation of the flood pulse appeared to create less variability (about 1‰) in the δ^{13}C-DOC values of the sound over the sampling period, with exception of the 09 November and 08 December when ranges in the sound were 2–3‰.

$SUVA_{254}$

Mean $SUVA_{254}$ values in the Neuse River Estuary decreased from a high value of 4.9 ± 0.3 L mg C^{-1} m^{-1} (17 October) in late October and throughout November before increasing slightly on 13 December (4.1 ± 0.3 L mg C^{-1} m^{-1}; **Supplementary Figure S2B**); NRE values were larger than all of the river samples throughout the period following the hurricane. The range of wetland $SUVA_{254}$ values (3.8–5.4 L mg C^{-1} m^{-1}) spanned the full range of estuarine values (3.2–5.3 L mg C^{-1} m^{-1}), while the range of wetlands was larger than all river and sound sampling dates. Mean $SUVA_{254}$ values for PS, like δ^{13}C-DOC values, were less than riparian wetland values but greater than all river sample values (**Supplementary Figure S2B**).

S_R

Mean daily S_R values in the NRE increased from a low value of 0.77 ± 0.02 (17 October) to a maximum mean daily value of 0.90 ± 0.05 on 28 November, before decreasing slightly to 0.86 ± 0.09 on 13 December (**Supplementary Figure S2C**). NRE mean daily S_R values were initially smaller than the mean river and wetland values (0.88 ± 0.06 and 0.83 ± 0.06, respectively), however, as the discharge began to decrease and wetland connectivity decreased the S_R values became larger than the river and wetland values (**Supplementary Figure S2C**). Mean S_R values for the PS were lowest on 02 November (0.94 ± 0.05) before increasing to ca. 1 on 09 November and stayed at 1 for the rest of the sampling dates. The PS mean S_R values were almost half of the coastal ocean S_R values throughout the study [1.82 ± 0.50; Atar (2017)].

Flooding of Wetlands in the Lower Neuse River Watershed in Response to Hurricane Matthew

Hurricane Matthew's rainfall was localized well upstream of the NRE-PS, yet caused major flooding in the river's lower watershed above head-of-tide, its estuary, and the Pamlico Sound. Heavy precipitation from Hurricane Matthew in the Neuse River watershed occurred over a 2-day period from 08 October to 10 October (e.g., maximum of 419 mm at Kinston, NC, United States) (**Figure 1A**; Stewart, 2017). The precipitation associated with the storm caused extensive flooding throughout the watershed (Musser et al., 2017; Stewart, 2017). Flooding was most prevalent in the mid to lower Neuse River watershed, with flood recurrence intervals ranging from ca. 100 to 500 years (Musser et al., 2017).

The USGS gauging station on the Neuse River at Fort Barnwell recorded gauge heights above the US National Weather Service (NWS) flood stage from October 9 through October 22, 2016 (**Figure 2**). NWS major flood stage was recorded from October 12 through October 18, 2016 (**Figure 2**). Flood stage coincided with extremely high discharge at Fort Barnwell (1399 m^3 s^{-1}, Matthew; U.S. Geological Survey [USGS], 2018). After Matthew's floodwaters moved downstream, there was a release of water from the Falls Lake Reservoir into the NR, indicated by the flat area on the mean gauge height curve, from October 30 to November 7, 2016 (**Figure 2**). This secondary flood pulse was followed by a return to base flow, due to a lack of measurable precipitation in the months after Hurricane Matthew (National Weather Service [NWS], 2016; U.S. Geological Survey [USGS], 2018).

Flooding of semi-disconnected to disconnected freshwater wetlands adjacent to the Neuse River's main channel between Fort Barnwell and ModMon sampling station NR0 at Streets Ferry Bridge was evident in satellite imagery comparing May and October 2016 (**Figure 3**). At low gauge height and low discharge, the wetlands were inundated with water; however, they were not connected via surface water to the Neuse River (**Figure 3A**). Groundwater connectivity was assumed, but not known, and is not considered in this study. During the high gauge height and discharge associated with Matthew's rainfall, these wetlands became hydrologically connected to the Neuse River, which allowed for flushing of the water and OM present in these wetlands downstream into the NRE-PS (**Figure 3B**). This connectivity was apparent when examining results of the REM flood model (**Figures 4**, **5**). During base flow and low gauge height conditions (0 m, REM) some wetlands were inundated (brown areas); however, the river was not connected via surface flow to these areas. The total area and volume that was flooded during base flow was 1.88×10^7 m^2 and 2.11×10^6 m^3, respectively, while the flooded wetland area and volume were 1.55×10^7 m^2 and 1.76×10^6 m^3. As the gauge height at Fort Barnwell, NC, United States increased, the areal and volumetric extent of wetlands that were inundated also increased. NWS flood stage (3.598 and 1.828 m; actual and relative gauge height, respectively) is the gauge height at which hydrologic connectivity of the wetlands to the Neuse River occurred (**Supplementary Figure S3**). A_T and V_T were 2.7 and 33.8 times larger during NWS flood stage than at base flow (5.03×10^7 m^2 and 7.12×10^7 m^3, respectively). Similarly, increases in the A_W and V_W were present during NWS flood stage (2.6 and 35.3 times larger than base flow, respectively). A_T, V_T, A_W, and V_W all increased similarly in the moderate and major flood stage models as they did in the flood stage model (**Table 1**). The V_T and V_W for the major flood stage were two orders of magnitude higher than at relative base flow (**Table 1**). Moderate and major flood stage models also had more areas of inundated ground surface that was not classified as wetlands (**Supplementary Figures S4, S5**).

Following the passage of Hurricane Matthew over eastern NC, the peak of the flood pulse on 16 October 2016 caused the most flooding of the wetlands. The A_T was 4.4 times greater than base flow, while the V_T was two orders of magnitude higher than base flow (**Table 1** and **Figures 4**, **5**). Likewise, the A_W (4.65×10^7 m^2) was ca. 3 times larger than base flow, and the V_W (1.57×10^8 m^3) was two orders of magnitude greater than base flow (1.55×10^7 m^2 and 1.76×10^6 m^3, respectively). Also, the area of flooded land that was not considered wetlands was greatest at this gauge height (**Figure 5**). Comparatively, the A_T, V_T, A_w, and V_W at the mean gauge height from 01 October to 31 December (1.930 m, actual; 0.160 m, REM; **Supplementary Figure S6**) was more similar to base flow than during the flood pulse (**Table 1**).

Model Estimates of DOC Fluxes Due to Hurricane Matthew

Flooding following the passage of Hurricane Matthew caused hydrologic connectivity of the riparian wetlands in the Neuse River's floodplain with the main channel, and substantial export of DOC from the riparian wetlands into the lower Neuse River downstream and into the NRE and PS.

Once volumes were determined for the A_T and the A_W, the estimated DOC fluxes from the riparian wetlands and from the river into the NRE and PS were calculated using Eq. 3–6 (**Table 2**). Carbon mass loading from the wetlands was assumed to occur from the start of wetland connectivity until the wetlands became disconnected after the flood pulse had passed. This period was ca. 31 days (08 October through 08 November 2016). Connectivity was determined to occur at a gauge height above 0.7 m on the REM (actual gauge height 2.47 m). The gauge height at each day was matched with the model from different flood stages (2-days, maximum flood stage; 5-days, major flood stage; 3-days, moderate flood stage; 3-days, flood stage; 18-days, 0.7 m REM). These values were summed to determine the total DOC loading to the NRE.

The L_{DOCR} was determined to be 3.76 Gg C, while the L_{DOCW} was 12.65 Gg C, thus the total L_{DOCT} was 16.41 Gg C (**Table 3**). Osburn et al. (2019a) determined the DOC stock change from the storm in the estuary using only concentrations and volume estimates was 4.74 Gg C. Therefore, the modeled L_{DOCT} was ca. 12 Gg greater than the previously calculated DOC stock change. However, this discrepancy in DOC mass loading can be explained by the calculations for the DOC stock change from Osburn et al. (2019a) only covering 1 week of the sample period, while the L_{DOCT} computed here using the flood model was done over

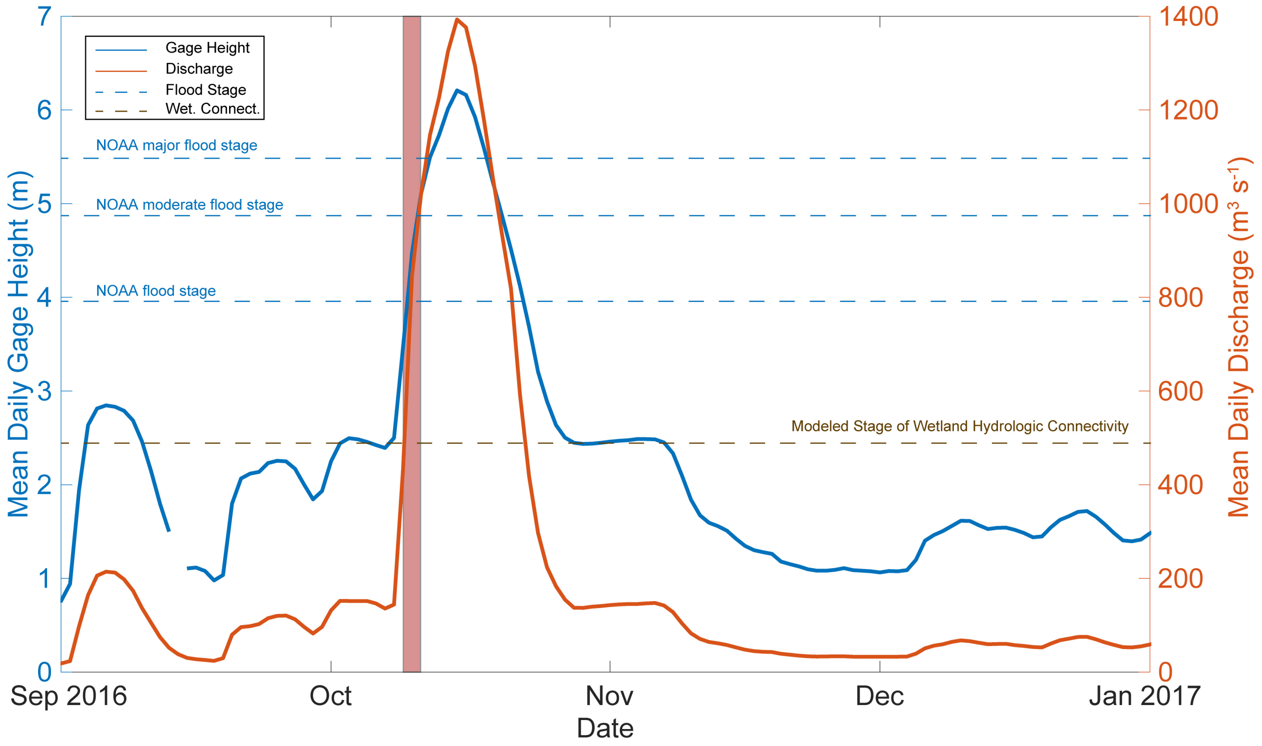

FIGURE 2 | Hydrograph. Mean daily gauge height and mean daily discharge from USGS gauging station 02021814 near Fort Barnwell, NC prior to and after Hurricane Matthew (September 2016-January 2017). NWS flood stage, moderate flood stage, and major flood stage are plotted in blue dotted lines. Limit of wetland hydrologic connectivity from geospatial model plotted in brown dotted line. Red shaded box indicates period of Hurricane Matthew in North Carolina (08–10 October, 2016).

the entire connectivity period (31-days), once that duration was known. Multiplying the DOC stock change in the NRE by 4 gives a value comparable to our modeled number (18.96 vs. 16.41 Gg C, respectively). For context with annual loads in this system, the hydrologic load estimator model, LOADEST (Runkel et al., 2004) was used to determine the estimated annual DOC load from the Neuse River during 2016 (51.32 Gg C) by using discharge data from Fort Barnwell combined with DOC concentrations throughout the year. Combined, L_{DOCR} and L_{DOCW} were a large proportion (ca. 32%) of the annual estimated load (7.3 and 24.6%, respectively; **Table 3**). It was clear from these model calculations that wetlands supplied the bulk of the DOC exported to the NRE-PS as a result of Hurricane Matthew.

Bayesian Monte Carlo Mixing Model of DOM Sources

The NRE was assessed both spatially and temporally using the BMC mixing model. The acceptance rates for our three end-member BMC mixing models ranged from 0.15 to 0.48 for the NRE and 0.31 to 0.49 for the PS. The average acceptance rates of each model were 0.30 and 0.41 (NRE and PS, respectively), which indicated that the PS model performed better than the NRE model (**Table 4**). Rosenthal (2011) suggested that BMC mixing models would provide accurate results if the average acceptance rates were between 0.1 and 0.6, while Lunn et al. (2009) indicated that average acceptance rates should be between 0.2 and 0.4, with 0.4 being optimal.

Similar to results from our geospatial model, the BMC geochemical mixing model showed that the wetlands were the largest contributor of DOC to the NRE and PS following Hurricane Matthew. Spatially across the entire NRE, the mixing model indicated the f_w of DOC was the dominant contributor at ca. 40–90%, followed by the f_r (10–50%), with the ocean end-member generally contributing the least (**Figure 6A**). Temporally, throughout the period of wetland hydrologic connectivity (08 October through 08 November), the source of DOC to the NRE was wetland dominated (**Figures 2**, **6**). Once the river returned to baseflow in late November, there was a transition to a more mixed water source with the river source dominating the DOC (**Figures 2**, **6**).

Examining the source fraction contributions to the estuary spatially showed how the wetland source decreased downstream (**Figure 6**). The estuary sites were spatially divided into upper, middle and lower sections. The upper section included sites NR0-NR50, while the middle section included sites NR60-120 just before the bend in the estuary (**Figure 1B**). The lower section included the remaining sites downstream of the bend in the estuary into southern Pamlico Sound (NR140-NR180). The f_w was predominant in each section of the estuary with few exceptions. In the upper section, there were two sample dates where the river and wetland contribution indicated mixing

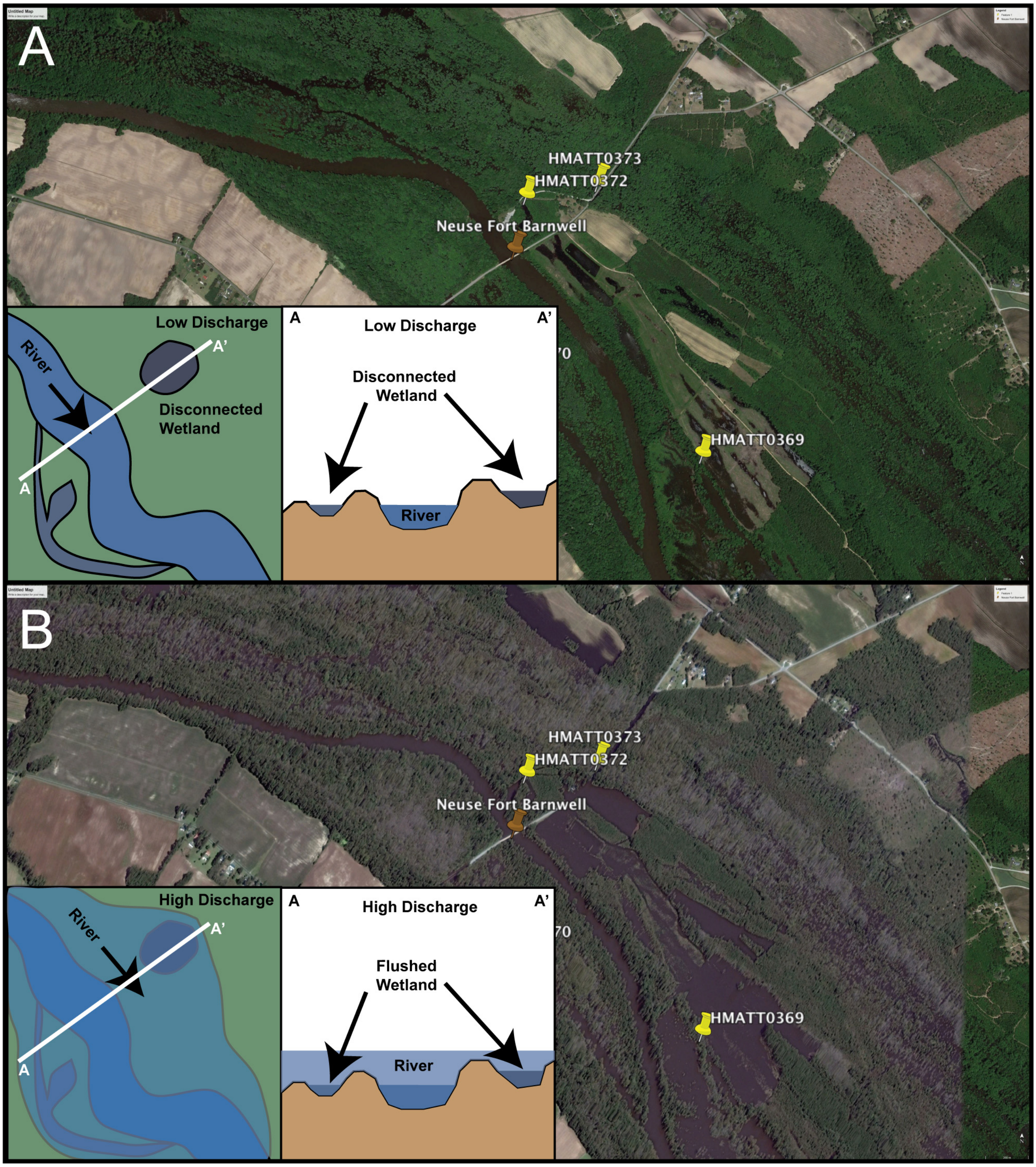

FIGURE 3 | Conceptual diagram and Google Earth Imagery of flow conditions along the Neuse River riparian wetlands during **(A)** low discharge (base flow) and **(B)** high discharge (flood stage). Insets show conceptual model of **(A)** disconnected and **(B)** hydrologically connected wetlands. Map view is depicted in the left inset, while the right inset shows the cross-section line **(A–A')**. Image Data Source: 2019 Google, Maxar Technologies.

(28 November and 13 December), after hydrologic connectivity occurred (**Figure 6B**). For all spatial sections of the estuary, the f_r *and* f_w overlapped on 28 November during the lowest flow of the sampling period (**Figures 2, 6B–D**).

The fractional contribution of wetlands, river, and ocean for PS sites were only examined temporally, due to the spatial proximity of the PS sampling sites (**Figure 1B**). Within the PS, the f_w ranged from ca. 35–65%, which was lower than fractions

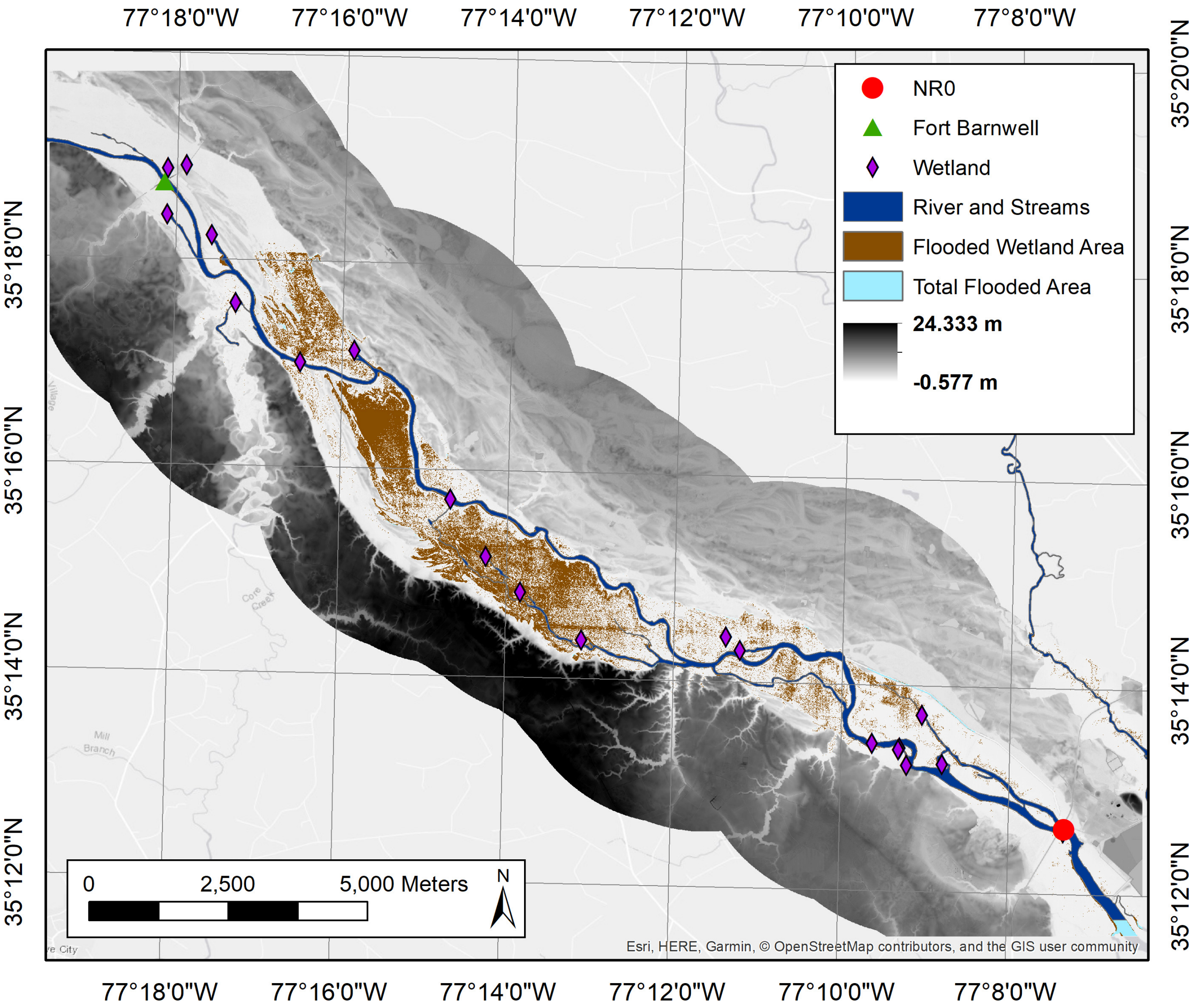

FIGURE 4 | Map showing base flow gauge height at USGS gaging station 02021814 near Fort Barnwell, NC of freshwater wetlands with DEM (Black and White), flooded area (light blue), and wetland flooded area (brown).

in the estuary, due to continued dilution of this source from the upstream wetlands. During the initial sample day (27 October) ca. 3 weeks after the storm, the f_r was the largest contributor to the PS (**Figure 7**). However, once the initial flood pulse reached the PS (02 November) the wetland became the larger contributor. On 09 November mixing of these three sources was apparent due to overlap between the $f_r, f_w, and\ f_o$. The remaining sampling period indicated that wetland DOM was dominant in the PS (**Figure 7**).

Because the BMC mixing model accounts for natural variance in end-member compositions, measurement uncertainty, and factors in the variance and covariance of geochemical indicators, it produces uncertainties associated with each most likely fraction contribution of each end member. The uncertainties associated with the estimated fractional contributions are represented as error bars in **Figures 6**, **7** and decrease with the degree to which the end-member geochemical compositions are distinguishable from one another. For NRE and PS samples with overlapping end-member fraction contribution estimations, **Figures 6**, **7** still show the most-likely fraction contribution but overlapping error bars indicate there is a much less-likely possibility that the fractions exist within the overlapping space. However, the observed fraction contribution trends for our NRE and PS samples and findings from our geospatial model strongly indicate the BMC most likely contributions are likely valid.

DISCUSSION

The main hypothesis of this study was that flooding of freshwater riparian wetlands surrounding the Neuse River, would become a major component of DOM in the NRE-PS due to hydrological connectivity. This hypothesis was confirmed in two ways. First, by expanding on an existing flood model to quantify the areal

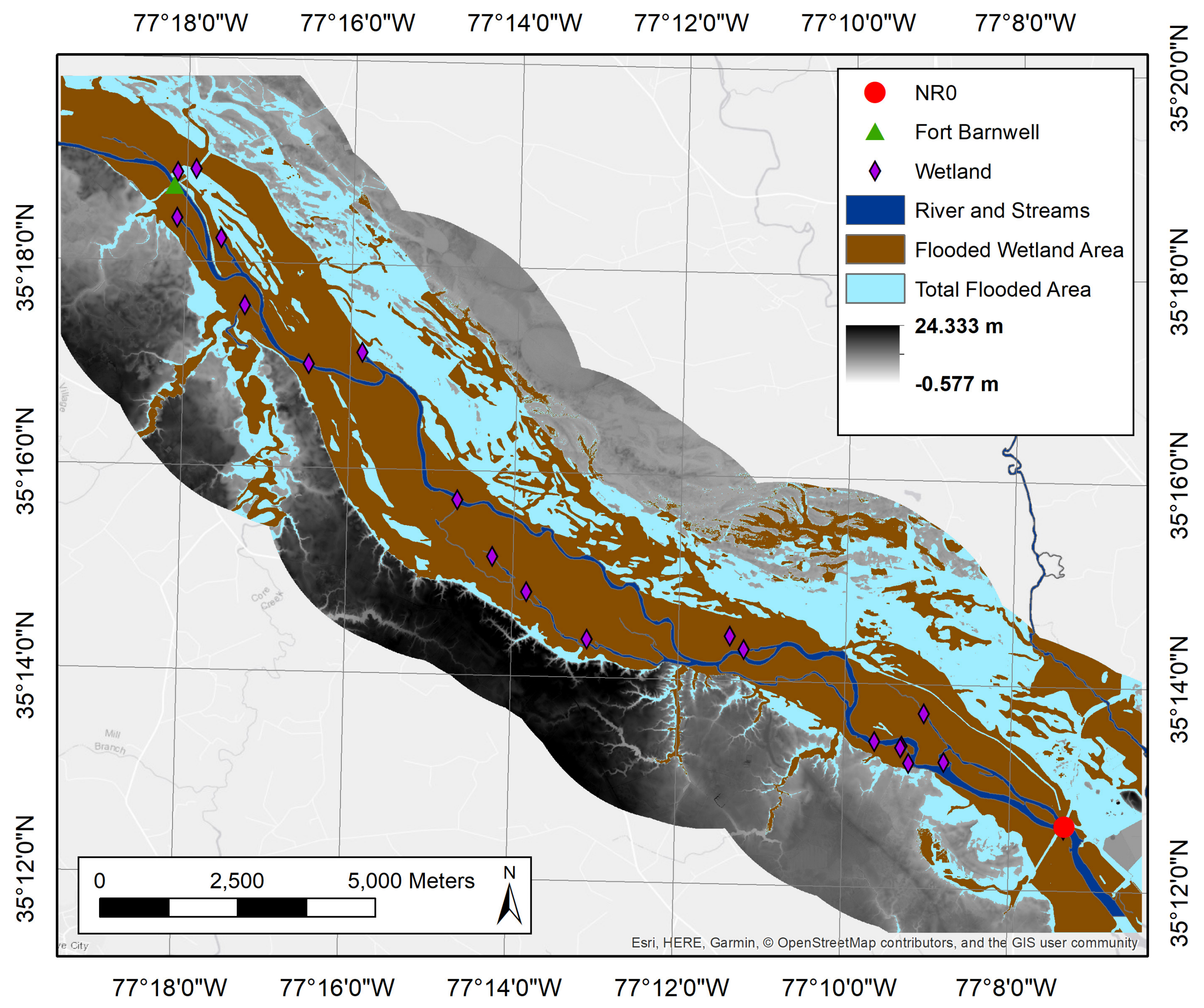

FIGURE 5 | Map showing maximum gauge height (5.844 m) from 16 October 2016 at USGS gaging station 02021814 near Fort Barnwell, NC of freshwater wetlands with DEM (Black and White), flooded area (light blue), and wetland flooded area (brown).

TABLE 1 | Total flooded area, volume, and average depth for the total area and wetland area from geospatial flood model.

Modeled gauge height (m)	Total area (m^2)	Total volume (m^3)	Average depth (m)	Total wetland area (m^2)	Total wetland volume (m^3)	Average wetland depth (m)
0.000[a]	1.88×10^7	2.11×10^6	0.11	1.55×10^7	1.76×10^6	0.11
4.074[a,b]	7.96×10^7	2.16×10^8	2.71	4.65×10^7	1.57×10^8	3.37
1.828[a,c]	5.03×10^7	7.12×10^7	1.42	3.98×10^7	6.03×10^7	1.52
2.742[a,d]	6.11×10^7	1.22×10^8	2.00	4.24×10^7	9.80×10^7	2.31
3.352[a,e]	6.93×10^7	1.62×10^8	2.34	4.40×10^7	1.24×10^8	2.83
0.160[a,f]	2.35×10^7	3.39×10^6	0.14	2.02×10^7	2.83×10^6	0.14

Gauge height values are detrended REM values and are vertically referenced to NAVD88. [a]Relative Elevation Model (REM) value. [b]Hurricane Matthew maximum value (6.27 m) (16 October 2016). [c]NOAA Flood Stage (3.96 m). [d]NOAA Moderate Flood Stage (4.88 m). [e]NOAA Major Flood Stage (5.49 m). [f]Mean value (01 October 2016 to 31 December 2016).

extent and volume of flooded wetlands via their hydrological connectivity to the main stem of the river, we determined the volume of water (and then using concentrations, DOC) exported from the wetlands to the NRE-PS (**Table 4** and **Figures 4**, **5**, **Supplementary Figures S3–S6**). Second, this study combined stable C isotope, SUVA$_{254}$, and S_R values in a Bayesian Monte

Carlo mixing model to determine estimates of the wetlands' contribution to DOM in both the NRE and PS (**Figures 6**, **7**).

This study revealed the substantial contribution of riparian wetlands to the DOC flux from a coastal watershed into receiving waters following a major hurricane. Within the context of the Pulse-Shunt concept, we discuss how our new combination of geospatial and geochemical modeling provides solid estimates on not only the magnitude of DOC fluxes from extreme events but also insight into where the DOC originates. Combined, these modeling approaches offer a key means to track source and fate of DOC delivered to coastal waters after an extreme event. Implications of the exported DOC in coastal waters are discussed.

TABLE 2 | DOC mass loading from Neuse River and freshwater wetlands into the NRE-PS, during hydrologic connectivity, in response to Hurricane Matthew.

Location		Total DOC mass (Gg C)	NRE DOC (%)	PS DOC (%)
Fort Barnwell, NC	1 d[a]	0.436	9.2	3.1
	7 d[a]	3.042	64.1	22.0
Wetlands	Max[b]	2.260	47.7	16.3
	Mean[c]	0.965	20.4	7.0
NRE	Max[d]	4.741	–	34.2
PS	Max[e]	13.849	–	–

[a] Mean (DOC) value from high discharge (7.429 mg C L^{-1}). [b] Maximum (DOC) from freshwater wetlands in autumn (14.4 mg C L^{-1}). [c] Mean (DOC) from freshwater wetlands in autumn (6.15 mg C L^{-1}). [d] Maximum (DOC) stock change from NRE. [e] Maximum (DOC) stock change from PS.

TABLE 3 | Calculated load of DOC exported by Hurricane Matthew's floodwaters for the Neuse River, wetlands, and the NRE.

Parameter	DOC load (Gg C)	% of Estimated annual load DOC	DOC mass flux (Gg d^{-1})
L$_{DOCR}$	3.76 ± 0.30	7.3 ± 0.6%	0.12 ± 0.1
L$_{DOCW}$	12.65 ± 0.77	24.6 ± 1.5%	0.41 ± 0.2
L$_{DOCT}$	16.41 ± 1.07	32.0 ± 2.1%	0.53 ± 0.3
Estimated Annual Load	51.32	n.a.	n.a.

Annual load of DOC was estimated using Load Estimator (LOADEST) software (Runkel et al., 2004). Percent of annual load was calculated by dividing the estimated annual load by the calculated load. DOC mass flux from the terrestrial environment was determined by dividing the DOC load by the number of days the wetlands were hydrologically connected. n.a.-not applicable.

TABLE 4 | Results of the best model output of fractional contributions from the BMC mixing model in the NRE and PS.

Location	End-member	Range of fraction	Mean fraction ± SD
NRE	f_w	0.08–0.97	0.70 ± 0.20
	f_r	0.008–0.73	0.23 ± 0.19
	f_o	0.002–0.28	0.07 ± 0.06
	Average model acceptance rate	**0.30**	
PS	f_w	0.07–0.86	0.52 ± 0.20
	f_r	0.003–0.72	0.31 ± 0.21
	f_o	0.005–0.49	0.17 ± 0.11
	Average model acceptance rate	**0.41**	

Pulse: Wetlands as a Primary Source of DOC to Coastal Waters Following an Extreme Weather Event

Applying the PSC to our results, the change in DOM quality in the estuary and sound was attributable to the pulse of wetland DOM caused by their flooding and hydrological-connectivity to the Neuse River. Using the flood model, it was determined that initial connectivity of the wetlands to the main channel of the Neuse River occurs between a gauge height of 2.274–2.774 m (0.5–1.0 m, REM), though the exact level is variable between the upper and lower wetlands. For context, mean annual gauge height at Fort Barnwell has ranged from 1.32 to 1.98 m over the past 17 years, while mean annual discharge at Fort Barnwell has ranged from 50 m^3 s^{-1} to 181 m^3 s^{-1} over the past 21 years (U.S. Geological Survey [USGS], 2018). Therefore, the increase in downstream export of wetland OM could occur prior to NWS flood stage at Fort Barnwell (3.598 m). This metric is important to establish for coastal rivers with respect to wetland pulses in terrestrial DOC export. Spencer et al. (2013) showed very strong correlation (R^2 = 0.81) between export of CDOM as a marker for terrestrial DOC, and the percent of wetland in a watershed. Hanley et al. (2013) found high positive correlation (R^2 = 0.91) of watershed %wetland cover with SUVA$_{254}$ values in coastal rivers. The watershed% wetland in the Neuse River watershed is 13% (Osburn et al., 2016), which is comparable to the wetland-rich eastern North American rivers (e.g., the Edisto and the Androscoggin) which export substantial amounts of CDOM to the ocean (Spencer et al., 2013).

Geochemical results from this study further indicated a substantial impact on DOM quality in the estuary and sound from wetlands. Ranges of wetland DOM δ^{13}C and SUVA$_{254}$ values after Matthew (−29.4 ± 0.7‰ and 4.94 ± 0.5 L mg C^{-1} m^{-1}, respectively; **Supplementary Figure S8**) overlapped with NRE and PS values after the storm (Osburn et al., 2019a). By contrast, mean (± SD) δ^{13}C-DOC values for the NRE during a low flow period in 2010–2011 was −25.4 ± 2‰, while mean SUVA$_{254}$ values were 2.9 ± 0.7 L mg C^{-1} m^{-1} (Osburn et al., 2016). Marine-sourced DOM generally has enriched δ^{13}C-DOC values, ca. −20 to −23‰ (**Supplementary Table S3**; Raymond and Bauer, 2001), and SUVA$_{254}$ values <2.0 L mg C^{-1} m^{-1} (Helms et al., 2008) when compared to terrestrial organic matter. Coastal plain wetland DOM is −27 to −29‰ (Opsahl, 2005; Vähätalo and Wetzel, 2008) while SUVA$_{254}$ values typically are greater than 3.0 L mg C^{-1} m^{-1} (e.g., Hall et al., 2008). Mean δ^{13}C-DOC and SUVA$_{254}$ values of the NRE after Hurricane Matthew (−28.5 ± 1.1‰, 4.1 ± 0.6 L mg C^{-1} m^{-1}; **Supplementary Figure S8**) were strikingly similar to those of the freshwater reach of the nearby Newport River Estuary which drains a Cypress swamp (−28.5 ± 1.0‰ and 5.3 ± 0.4 L mg C^{-1} m^{-1}; Osburn et al., 2019b; **Supplementary Figure S8**). This means that an increasing wetland influence on DOM results in its characteristics having high SUVA$_{254}$ and depleted δ^{13}C-DOC values.

Hence our results strongly suggest the influence of wetlands in the DOM characteristics of the Neuse River, its estuary, and Pamlico Sound. While the range of our riverine δ^{13}C-DOC

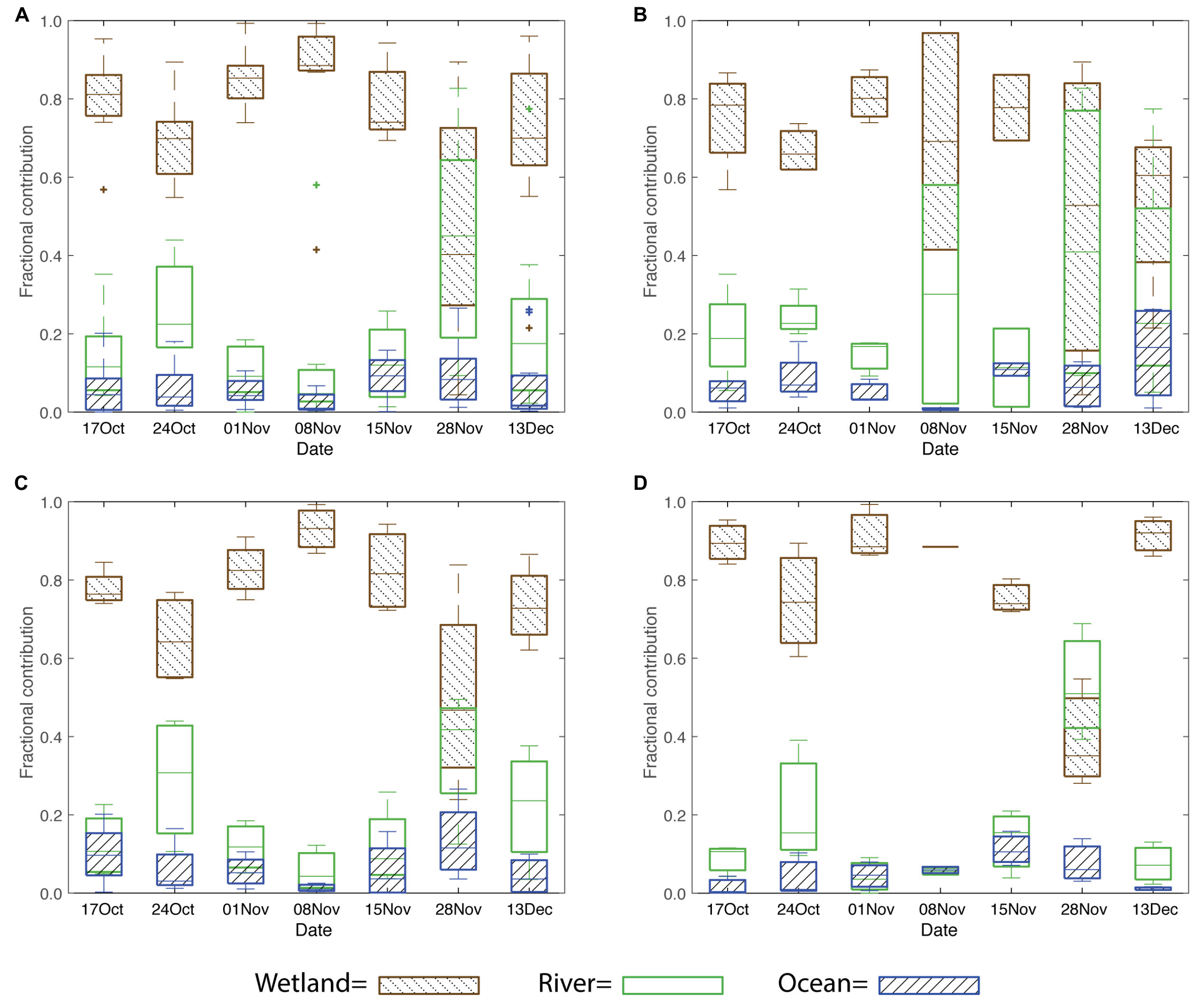

FIGURE 6 | Best fit calculated f_w, f_r and f_s for **(A)** the entire NRE, **(B)** upper NRE, **(C)** middle NRE and **(D)** lower NRE in October through December 2016. On each boxplot: colored line is median, lower and upper extent of box refers to 25th and 75th percentiles, respectively, the whiskers on ends of box are range of samples, not considered outliers, and colored (+) are outliers.

values (−25.9 ± 0.6‰) were similar to results reported from other rivers in the literature including the Tar (NC) and Santa Clara (CA) Rivers (**Supplementary Table S3**), the relatively depleted estuarine δ^{13}C-DOC values and high SUVA$_{254}$ values were consistent with observations of the riparian wetlands. This shift to depleted isotope values is consistent with flooding: in the lower Mississippi River, where for example, δ^{13}C-DOC values decreased from −25.5 to −27‰ as discharge increased (Cai et al., 2015).

Finally, comparing the flood and geochemical modeling approaches revealed similar estimates of wetland contributions to DOC in the estuary and sound, therefore providing independent measures of the pulse. The flood model estimated that 77% of the DOC load from Matthew was due to wetlands (**Table 3**). This model was purely physical in the sense that DOC concentration and water volumes were the two parameters used to compute relative fractions of wetland and river in the DOC load. The BMC mixing model estimated that 70 ± 20% of NRE DOM and 52 ± 20% of Pamlico Sound DOM exhibited a wetland character, considering only mixing of river, wetland, and oceanic sources in both systems (**Table 4**). Segmentation of the NRE into upper, middle, and lower regions further attested to the strong influence exerted on DOM properties by wetlands (**Figures 6B–D**). Segmentation also provided a view of the time-lag of the wetland influence on DOM in the estuary. For example, wetland contribution in the middle estuary peaked at ca. 85% on 08 November, falling to roughly 50% 2 weeks later (**Figure 6C**). In the Pamlico Sound the% wetland contribution was consistent at ca. 60% from 02 November through 14 December (**Figure 6D**). The segmentation and time-series results

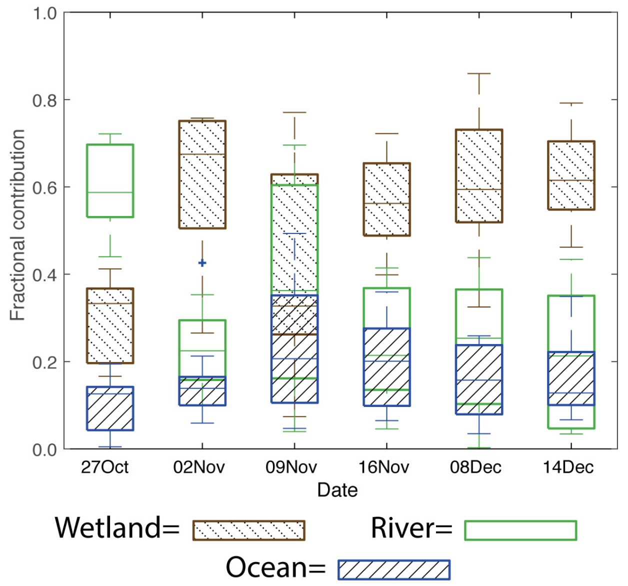

FIGURE 7 | Best fit calculated f_w, f_r and f_s for the entire PS in October through December 2016. Colored line is median, lower and upper extent of box refers to 25th and 75th percentiles, respectively, the whiskers on ends of box are range of samples, not considered outliers, and colored (+) are outliers.

indicated that the wetland characteristics remained a prominent feature of the NRE and PS for nearly 3 months following Matthew (Osburn et al., 2019a).

Shunt: Rapid Delivery of a Majority of DOC Coastal Waters in Response to an EWE

Inland precipitation related to Matthew resulted in a "shunting" of the wetland "pulse" of OM into the NRE-PS which dramatically increased its stock of DOC. Use of long-term monitoring data sets such as ModMon in the NRE-PS allowed for comparisons to be made between extreme events and long-term averages in these systems. We combined analyses from this study with long-term trends in DOC to determine what effect Hurricane Matthew's floodwaters had the shunt of DOM to the NRE-PS.

Osburn et al. (2019a) indicated there was ca. 65% increase in DOC stock in the NRE-PS in response to Hurricane Matthew. When comparing our results from the geospatial and geochemical models, we observed that both produced similar fractional estimates for the river (23%) and wetland end-members in the NRE (70 and 77% for the geochemical and flood models, respectively). The similarity in these estimates is encouraging and demonstrates the need to incorporate lateral flooding of wetlands in coastal watersheds to provide best estimates of C export from land to coastal waters.

About 30–70% of annual DOC export from watersheds occurs following storms (Raymond and Saiers, 2010). Hurricane Matthew's floodwaters caused a total terrestrial DOC load of 16.41 Gg C between 08 October and 08 November, during the period that the riparian wetlands were hydrologically connected to the Neuse River. This episodic load of DOC accounted for ca. 32% of the estimated annual load of DOC for the NRE (**Table 4**) which is similar to what other studies have shown in larger systems. For example, flooding from storm events in the Lower Mississippi River Basin in 2011 caused the DOC export from the Atchafalaya River to coastal waters to increase from ca. 5 to ca. 22 Gg C d^{-1}. This increase accounted for ca. 50% of the annual carbon load (Bianchi et al., 2013). Our results indicate that due to the hydrologic connectivity of the wetlands upstream of the estuary, around 70–77% of the 32% annual load increase in the NRE can be attributed to the wetlands. Similarly, Majidzadeh et al. (2017) indicated that in the Yadkin-Pee Dee Hurricane Matthew exported a large amount of wetland DOC.

Our flood model estimates of DOC flux were conducted using a different approach than prior work, which strongly suggests a convergence on accurately estimating the DOC load caused by storms. For example, Paerl et al. (2018) estimated ca. 19 Gg of DOC loading from storm events in the estuary during 2016 using the Weighted Regressions on Time Discharge and Season (WRTDS; Hirsch et al., 2010; Hirsch and De Cicco, 2015) model. When compared to other storm events in the NRE the present DOC mass loading results were higher than estimated DOC loads from Hurricanes Fran (1996) and Irene (2011) although much lower than estimates from the combination of sequential Hurricanes Dennis, Floyd, and Irene in 1999 (7.4–8.4, 14 (TOC), and ca. 60 Gg C, respectively; Brown et al., 2014; Crosswell et al., 2014; Paerl et al., 1998; Paerl et al., 2018).

The Pulse-Shunt concept proposed by Raymond et al. (2016), was based on headwater fluvial systems but describes the dynamic we have modeled for coastal rivers and estuaries. First, during high discharge, from a low-frequency, large storm event, regional flooding inundates wetlands, with the hydrologic-connectivity of wetlands to the main channel of the river facilitating a flushing of DOM into the river and downstream to receiving waters. Second, as for lower order streams and rivers, estuaries could be turned into passive pipes. Evidence for the NRE existing in a passive pipe mode comes from characteristic where up to ca. 40% of the river's annual load of terrestrial DOM was shunted downstream into Pamlico Sound. Moreover, this last point is important; this study demonstrated the lingering effect of these episodic and infrequent storms and suggest that coastal ecosystems such as the NRE attenuate the floodwater pulse over long periods of time.

Process: Significance of Extreme Weather Events on Coastal Carbon Cycles

Our findings demonstrated that EWE such as Hurricane Matthew, the second 500-year storm to occur in NC within the past 20 years (Paerl et al., 2019), transfer substantial amounts of terrestrial C to coastal waters in just a few weeks. Osburn et al. (2019a) provided evidence suggesting that much of this material can be processed and sustain Pamlico Sound as a weak CO_2 source to the atmosphere. Increases in stock of relatively "fresh", sunlight-absorbing DOC into coastal waters increases the potential for it to be converted to atmospheric CO_2 via microbial respiration and photooxidation during a long residence time (Spencer et al., 2009; Bauer et al., 2013; Ward et al., 2017). Conversion of allochthonous DOM that would normally be stored in the terrestrial environment in soils or wetland sediments to CO_2 in coastal waters creates a feedback loop to the atmosphere, which potentially could influence coastal C cycling (Bauer and Bianchi, 2011).

The geomorphological properties at the land-ocean continuum will modulate the transport and fate of DOM in coastal waters (Bianchi et al., 2007). For example, the NRE-PS is an embayed estuarine system which allows for some export of OM to the coastal Atlantic Ocean through three small inlets. However, the Mississippi and Amazon rivers are open deltas that permit OM to be transferred out into the open ocean (Hedges et al., 1997; Bianchi et al., 2013). Residence time in large river plumes may approximate the long residence time (ca. 1 year) within Pamlico Sound (**Supplementary Table S1**). These differences suggest that in similar embayed lagoons and semi-enclosed estuaries the fate of a large portion of the OM that would normally be stored in the estuaries or exported to the coastal ocean (e.g., DOM in large river plumes) due to flooding caused by extreme precipitation events, is alternatively processed *in situ*. Long residence time lagoonal estuaries constitute about 25% of estuaries globally and are a predominant feature of the SE Atlantic and Gulf coasts of the United States (Dürr et al., 2011).

Extreme weather events are increasing in intensity due to a positive feedback loop created by global warming that will undoubtedly cause a redistribution of water across the planet (Trenberth, 2011). Increased heating leads to longer periods of drought (Trenberth, 2011); extensive dry periods also allows terrestrial OM to accumulate in hydrologically isolated wetlands. However, warming also increases atmospheric water vapor, which leads to a larger moisture supply to fuel more intense precipitation events (Trenberth, 2011) and thus more flooding events (Paerl et al., 2019). Large pulses of reactive terrestrial OM to coastal waters have the potential to contribute to the increase in atmospheric CO_2 through photooxidation and microbial respiration of DOC in estuaries (Bauer et al., 2013). Saturated soils from heavy rainfall in the Neuse River Watershed prior to Hurricanes Fran and Matthew caused similar exports of total organic carbon to coastal waters (ca. 14 and 21 Gg C, respectively), indicating the importance of extreme precipitation events and flooding on the transference of terrestrial OM to the coastal ocean. We suggest that these weather extremes (dry periods punctuated by intense precipitation events) will amplify pulses of C stored in wetlands which then are shunted into receiving coastal waters where this organic C is returned to the atmosphere as CO_2. A predicted rise in the frequency of EWE, including major hurricanes in the Atlantic, where many lagoonal estuaries exist, will continue to exacerbate these conditions (Bender et al., 2010; Trenberth, 2011; Lehmann et al., 2015; Walsh et al., 2016).

CONCLUSION

A Bayesian Monte Carlo (BMC) mixing model combining stable carbon isotope analysis, $SUVA_{254}$ values and S_R values, revealed new insights into the effects of extreme events on this system, improving upon prior work in which OM sources from events such as hurricanes had not been clearly identified (Peierls et al., 2003; Osburn et al., 2012; Brown et al., 2014; Paerl et al., 2018). The BMC method provided estimates of the fractional source contributions from wetlands to the NRE following Hurricane Matthew in 2016, which we then compared to estimates made with a hydrological-connectivity flood model. Through this comparative modeling approach, we determined that the riparian wetlands exported ca. 50–70% of the DOM to the NRE-PS during Hurricane Matthew's floodwaters, confirming predictions from earlier work (Osburn et al., 2019a).

Our modeling approach further provided insight into estuarine responses to low-frequency large storm events in a manner similar to rivers under the PSC (Raymond et al., 2016). For the NRE-PS, this coastal system responds similarly: the estuary essentially became a passive pipe, resulting in $\sim$40% of the annual load of DOM to be shunted through the estuary into Pamlico Sound. An important insight we gained from this approach was that the pulse of DOM from the hydrologically connected wetlands following Hurricane Matthew accounted for ca. 25% of the estimated annual load to the Neuse River Estuary. PSC could be amended for coastal environments such as Pamlico Sound to include processing (P) of DOM into CO_2 by photooxidation or microbial respiration. Our results suggest that EWE, such as tropical cyclones, have a significant effect on coastal carbon cycles, by inducing large pulses of terrestrial DOM from floodwaters associated with them and translocating OM accumulating over time in wetlands into biogeochemically dynamic ecosystems where substantial processing can occur (Crosswell et al., 2014; Osburn et al., 2019a).

Estuarine and coastal waters are home to more than half of the world's population and are important economic, recreational, and environmental ecosystems (Paerl et al., 2014). However, a lack of high-resolution observational data hinders our comprehension of the effects of EWE on coastal biogeochemistry (Brown et al., 2014). Therefore, the development of new interdisciplinary methods such as what we have done for this study is crucial to understanding the coinciding and subsequent processes occurring in coastal waters in response to EWE.

DATA AVAILABILITY STATEMENT

The data used in this project can be found at the NSF Biological and Chemical Oceanographic Data Management Office (BCO-DMO; https://www.bco-dmo.org/project/734599).

AUTHOR CONTRIBUTIONS

JR participated in the experiment design, performed the field samplings of the river and wetlands, conducted laboratory analyses, performed the data analyses, and was responsible for the manuscript preparation. CA contributed to the analysis of the geochemical mixing model and participated in the manuscript preparation. AH participated in field samplings in the estuary and sound, conducted laboratory analyses, and participated in the manuscript preparation. HP provided the estuary and sound samples and participated in the manuscript preparation. CO participated in the experiment design, data analysis, and manuscript preparation.

FUNDING

This work was funded by the National Science Foundation grants OCE 1705972 and OCE 1706009, the North Carolina Sea Grant program, the UNC Water Resources Research Institute, and the National Fish and Wildlife Foundation Project 8020.16.053916.

ACKNOWLEDGMENTS

We would like to thank Roxane Bowden, Stephen Richardson, Nicole Koerth, John Wall, Del Bohnenstiehl, Bill Showers, Mackenzie Fiss, Betsy Abare, Jeremy Braddy, Karen Rossignol, and Randy Sloup for their technical assistance. We would also like to thank the UNC-Chapel Hill/North Carolina Department of Environmental Quality ModMon Project for sampling and logistical support.

SUPPLEMENTARY MATERIAL

The Supplementary Material for this article can be found online at: https://www.frontiersin.org/articles/10.3389/fmars.2020.00018/full#supplementary-material

REFERENCES

Arendt, C. A., Aciego, S. M., and Hetland, E. A. (2015). An open source bayesian monte carlo isotope mixing model with applications in earth surface processes. *Geochem.Geophys., Geosyst.* 16, 1274–1292. doi: 10.1002/2014gc005683

Atar, J. N. (2017). *Contrasting Estuarine and Coastal Organic Matter Dynamics From Varying Climatic Regions*. Master's Thesis,North Carolina State University, Raleigh.

Avery, G. B. Jr., Kieber, R. J., Willey, J. D., Shank, G. C., and Whitehead, R. F. (2004). Impact of hurricanes on the flux of rainwater and cape fear river water dissolved organic carbon to long bay, southeastern United States. *Global Biogeoch. Cycles* 18:GB3015.

Bauer, J. E., and Bianchi, T. S. (2011). *5.02 Dissolved Organic Carbon Cycling and Transformation. Treatise on Estuarine and Coastal Science*. Waltham: Academic Press.

Bauer, J. E., Cai, W. J., Raymond, P. A., Bianchi, T. S., Hopkinson, C. S., and Regnier, P. A. (2013). The changing carbon cycle of the coastal ocean. *Nature* 504, 61–70. doi: 10.1038/nature12857

Bauer, J. E., Druffel, E. R., Wolgast, D. M., and Griffin, S. (2001). Sources and cycling of dissolved and particulate organic radiocarbon in the northwest Atlantic continental margin. *Global Biogeochem. Cycles* 15, 615–636. doi: 10.1029/2000gb001314

Bender, M. A., Knutson, T. R., Tuleya, R. E., Sirutis, J. J., Vecchi, G. A., Garner, S. T., et al. (2010). Modeled impact of anthropogenic warming on the frequency of intense Atlantic hurricanes. *Science* 327, 454–458. doi: 10.1126/science.1180568

Bhatia, M. P., Das, S. B., Kujawinski, E. B., Henderson, P., Burke, A., and Charette, M. A. (2011). Seasonal evolution of water contributions to discharge from a Greenland outlet glacier: insight from a new isotope-mixing model. *J. Glaciol.* 57, 929–941. doi: 10.3189/002214311798043861

Bianchi, T. S., and Canuel, E. A. (2011). *Chemical Biomarkers in Aquatic Ecosystems*. Princeton, NJ: Princeton University Press.

Bianchi, T. S., Galler, J. J., and Allison, M. A. (2007). Hydrodynamic sorting and transport of terrestrially derived organic carbon in sediments of the Mississippi and Atchafalaya Rivers. *Estuar.Coast. Shelf Sci.* 73, 211–222. doi: 10.1016/j.ecss.2007.01.004

Bianchi, T. S., Garcia-Tigreros, F., and Yvon-Lewis, S. A. (2013). Enhanced transfer of terrestrially derived carbon to the atmosphere in a flooding event. *Geophys. Res. Lett.* 40, 116–122. doi: 10.1029/2012GL054145

Boyd, T. J., and Osburn, C. L. (2004). Changes in CDOM fluorescence from allochthonous and autochthonous sources during tidal mixing and bacterial degradation in two coastal estuaries. *Mar. Chem.* 89, 189–210. doi: 10.1016/j.marchem.2004.02.012

Brown, M. M., Mulligan, R. P., and Miller, R. L. (2014). Modeling the transport of freshwater and dissolved organic carbon in the Neuse River Estuary, NC, USA following Hurricane Irene (2011). *Estuar.Coast. Shelf Sci.* 139, 148–158. doi: 10.1016/j.ecss.2014.01.005

Cai, Y., Guo, L., Wang, X., and Aiken, G. (2015).). Abundance, stable isotopic composition, and export fluxes of DOC, POC, and DIC from the lower mississippi river during 2006–2008. *J. Geophys. Res.: Biogeosci.* 120, 2273–2288. doi: 10.1002/2015jg003139

Chadwick, O. A., Derry, L. A., Vitousek, P. M., Huebert, B. J., and Hedin, L. O. (1999). Changing sources of nutrients during four million years of ecosystem development. *Nature* 397, 491–497. doi: 10.1038/17276

Chowdhury, S. (2013). Trihalomethanes in drinking water: effect of natural organic matter distribution. *Water SA* 39, 1–8.

Cloern, J. E., Canuel, E. A., and Harris, D. (2002). Stable carbon and nitrogen isotope composition of aquatic and terrestrial plants of the San Francisco Bay estuarine system. *Limnol. Oceanogr.* 47, 713–729. doi: 10.4319/lo.2002.47.3.0713

Crosswell, J. R., Wetz, M. S., Hales, B., and Paerl, H. W. (2012). Air-water CO2 fluxes in the microtidal neuse river estuary, North Carolina. *J. Geophys. Res.*117, C08017.

Crosswell, J. R., Wetz, M. S., Hales, B., and Paerl, H. W. (2014). Extensive CO2 emissions from shallow coastal waters during passage of Hurricane Irene (August 2011) over the Mid-Atlantic Coast of the USA. *Limnol. Oceanogr.* 59, 1651–1665. doi: 10.4319/lo.2014.59.5.1651

Currin, C. A., Newell, S. Y., and Paerl, H. W. (1995). The role of standing dead Spartina alterniflora and benthic microalgae in salt marsh food webs: considerations based on multiple stable isotope analysis. *Mar. Ecol. Progr. Ser.* 121, 99–116. doi: 10.3354/meps121099

Deegan, L. A., and Garritt, R. H. (1997). Evidence for spatial variability in estuarine food webs. *Mar. Ecol. Progr. Ser.* 147, 31–47. doi: 10.3354/meps147031

Dilts, E., Yang, J., and Weisberg, P. J. (2010). Mapping riparian vegetation with lidar data. *ArcUser Mag.* 13, 18–21. doi: 10.1371/journal.pone.0054776

Dixon, J. L., Osburn, C. L., Paerl, H. W., and Peierls, B. L. (2014). Seasonal changes in estuarine dissolved organic matter due to variable flushing time and wind-driven mixing events. *Estuar. Coast. Shelf Sci.* 151, 210–220. doi: 10.1016/j.ecss.2014.10.013

Dürr, H. H., Laruelle, G. G., van Kempen, C. M., Slomp, C. P., Meybeck, M., and Middelkoop, H. (2011). Worldwide typology of nearshore coastal systems: defining the estuarine filter of river inputs to the oceans. *Estuar. Coas.* 34, 441–458. doi: 10.1007/s12237-011-9381-y

ESRI (2011). *ArcGIS Desktop: Release 10*. Redlands CA: Environmental Systems Research Institute.

Fry, B., and Sherr, E. B. (1989). "δ13C measurements as Indicators of carbon flow in marine and freshwater ecosystems," in In *Stable Isotopes in Ecological Research*, (New York. NY: Springer), 196–229. doi: 10.1007/978-1-4612-3498-2_12

Giese, G. L., Wilder, H. B., and Parker, G. G. Jr. (1985). *Hydrology of major estuaries and sounds of North Carolina(No. 2221)*. Washington, DC: USGPO.

Gorham, E. (1995). "The biogeochemistry of northern peatlands and its possible responses to global warming," in *Biotic Feedbacks in the Global Climatic System*, eds G. M. Woodwell, and F. T. MacKenzie, (New York, NY: Oxford University Press), 169–187.

Hall, B. D., Aiken, G. R., Krabbenhoft, D. P., Marvin-DiPasquale, M., and Swarzenski, C. M. (2008). Wetlands as principal zones of methylmercury production in southern Louisiana and the Gulf of Mexico region. *Environ. Pollut.* 154, 124–134. doi: 10.1016/j.envpol.2007.12.017

Hanley, K. W., Wollheim, W. M., Salisbury, J., Huntington, T., and Aiken, G. (2013). Controls on dissolved organic carbon quantity and chemical character in temperate rivers of North America. *Global Biogeochem. Cycles* 27, 492–504. doi: 10.1002/gbc.20044

Hansen, A. M., Kraus, T. E., Pellerin, B. A., Fleck, J. A., Downing, B. D., and Bergamaschi, B. A. (2016). Optical properties of dissolved organic matter (DOM): Effects of biological and photolytic degradation. *Limnol. Oceanogr.* 61, 1015–1032. doi: 10.1002/lno.10270

Hedges, J. I., Keil, R. G., and Benner, R. (1997). What happens to terrestrial organic matter in the ocean? *Organic Geochem.* 27, 195–212. doi: 10.1016/s0146-6380(97)00066-1

Helms, J. R., Stubbins, A., Ritchie, J. D., Minor, E. C., Kieber, D. J., and Mopper, K. (2008). Absorption spectral slopes and slope ratios as indicators of molecular weight, source, and photobleaching of chromophoric dissolved organic matter. *Limnol. Oceanogr.* 53, 955–969. doi: 10.4319/lo.2008.53.3.0955

Hirsch, R. M., and De Cicco, L. A. (2015). *User guide to Exploration and Graphics for RivEr Trends (EGRET) and dataRetrieval: R packages for hydrologic data (No. 4-A10)*. Reston, VA: US Geological Survey.

Hirsch, R. M., Moyer, D. L., and Archfield, S. A. (2010). Weighted regressions on time, discharge, and season (WRTDS), with an application to Chesapeake Bay river inputs 1. *J. Am. Water Resou. Assoc.* 46, 857–880. doi: 10.1111/j.1752-1688.2010.00482.x

Hounshell, A. G., Rudolph, J. C., Van Dam, B. R., Hall, N. S., Osburn, C. L., and Paerl, H. W. (2019). Extreme weather events modulate processing and export of dissolved organic carbon in the Neuse River Estuary.*Estuar., Coast. Shelf Sci.* 219, 189–200. doi: 10.1016/j.ecss.2019.01.020

IPCC (2001). "A special report of IPCC working group III," in *Summary for Policymakers, Emission Scenarios*, ed. N. Nakiaeenoviae, (Cambridge: Cambridge University Press), 2001.

Junk, W. J., Bayley, P. B., and Sparks, R. E. (1989). The flood pulse concept in river-floodplain systems. *Can. Special Public. Fish. Aquat. Sci.* 106, 110–127.

Kirk, J. T. (1994). *Light and Photosynthesis in Aquatic Ecosystems*. Cambridge: Cambridge university press.

Lehmann, J., Coumou, D., and Frieler, K. (2015). Increased record-breaking precipitation events under global warming. *Clim. Change* 132, 501–515. doi: 10.1007/s10584-015-1434-y

Luettich, R. A., Reynolds-Fleming, J. V., McNinch, J. E., and Buzzelli, C. P. (2000). Circulation characteristics of the neuse river estuary, North Carolina. *Estuaries* 23, 392–399.

Lunn, D., Spiegelhalter, D., Thomas, A., and Best, N. (2009). The BUGS project: Evolution, critique and future directions. *Statist. Med.* 28, 3049–3067. doi: 10.1002/sim.3680

Majidzadeh, H., Uzun, H., Ruecker, A., Miller, D., Vernon, J., Zhang, H., et al. (2017). Extreme flooding mobilized dissolved organic matter from coastal forested wetlands. *Biogeochemistry* 136, 293–309. doi: 10.1007/s10533-017-0394-x

Masiello, C. A., and Druffel, E. R. (2001). Carbon isotope geochemistry of the Santa Clara River. *Global Biogeochem. Cycles* 15, 407–416. doi: 10.1029/2000gb001290

Matson, E. A., and Brinson, M. M. (1990). Stable carbon isotopes and the C: N ratio In the estuaries of the pamlico and neuse rivers. North Carolina. *Limnol. Oceanogr.* 35, 1290–1300. doi: 10.4319/lo.1990.35.6.1290

Mitra, S., Wassmann, R., and Vlek, P. L. (2005). An appraisal of global wetland area and its organic carbon stock. *Curr. Sci.* 88, 25–35.

Mladenov, N., McKnight, D. M., Macko, S. A., Norris, M., Cory, R. M., and Ramberg, L. (2007). Chemical characterization of DOM in channels of a seasonal wetland. *Aquat. Sci.* 69, 456–471. doi: 10.1007/s00027-007-0905-2

Mladenov, N., McKnight, D. M., Wolski, P., and Ramberg, L. (2005). Effects of annual flooding on dissolved organic carbon dynamics within a pristine wetland, the Okavango Delta, Botswana. *Wetland* 25, 622–638. doi: 10.1672/0277-5212(2005)025[0622:EOAFOD]2.0.CO;2

Musser, J. W., Watson, K. M., and Gotvald, A. J. (2017). "Characterization of Peak Streamflows and Flood Inundation at Selected Areas in North Carolina Following Hurricane Matthew, October 2016," in *U.S. Geological Survey Open-File Report* 2017-1047, (Reston, VA: US Geological Survey), 23.

National Weather Service [NWS] (2016). *Advanced Hydrologic Prediction Service*. Available at: https://water.weather.gov/ahps2/hydrograph.php?wfo=mhx&gage=ftbn7. (accessed Dec 30, 2016).

NC-DEQ (2018). *North Carolina Department of Environmental Quality Neuse River Data Sheet*. Avaliable at: https://files.nc.gov/deqee/documents/files/neuse.pdf.(accessed Jan 1, 2018).

Opsahl, S. P. (2005). Organic carbon composition and oxygen metabolism across a gradient of seasonally inundated limesink and riparian wetlands in the southeast Coastal Plain. USA. *Biogeochemistry* 76, 47–68. doi: 10.1007/s10533-005-2074-5

Osburn, C. L., Atar, J. N., Boyd, T. J., and Montgomery, M. T. (2019b). Antecedent precipitation influences the bacterial processing of terrestrial dissolved organic matter in a North Carolina estuary. *Estuar.Coast. Shelf Sci.* 221, 119–131.

Osburn, C. L., Handsel, L. T., Mikan, M. P., Paerl, H. W., and Montgomery, M. T. (2012). Fluorescence tracking of dissolved and particulate organic matter quality in a river-dominated estuary. *Environ. Sci. Technol.* 46, 8628–8636. doi: 10.1021/es3007723

Osburn, C. L., Handsel, L. T., Peierls, B. L., and Paerl, H. W. (2016). Predicting sources of dissolved organic nitrogen to an estuary from an agro-urban coastal watershed. *Environ. Sci.Technol.* 50, 8473–8484. doi: 10.1021/acs.est.6b00053

Osburn, C. L., and Morris, D. P. (2003). Photochemistry of chromophoric dissolved organic matter in natural waters. *Effects Aquat. Org. Ecosyst.* 1, 185–217.

Osburn, C. L., Rudolph, J. C., Paerl, H. W., Hounshell, A. G., and Van Dam, B. R. (2019a). Lingering carbon cycle effects of hurricane matthew in North Carolina's coastal waters. *Geophys. Res. Lett.*. 46, 2654–2661. doi: 10.1029/2019gl082014

Osburn, C. L., and St-Jean, G. (2007). The use of wet chemical oxidation with high-amplification isotope ratio mass spectrometry (WCO-IRMS) to measure stable isotope values of dissolved organic carbon in seawater. *Limnol. Oceanogr.: Methods* 5, 296–308. doi: 10.4319/lom.2007.5.296

Paerl, H. W., Crosswell, J. R., Van Dam, B., Hall, N. S., Rossignol, K. L., Osburn, C. L., et al. (2018). Two decades of tropical cyclone impacts on North Carolina's estuarine carbon, nutrient and phytoplankton dynamics: implications for biogeochemical cycling and water quality in a stormier world. *Biogeochemistry* 141, 1–26.

Paerl, H. W., Hall, N. S., Hounshell, A. G., Luettich, R. A. Jr., Rossignol, K. L., Osburn, C. L., et al. (2019). Recent increase in catastrophic tropical cyclone flooding in coastal North Carolina, USA: long-term observations suggest a regime shift. *Nat. Sci. Rep.* 9:10620. doi: 10.1038/s41598-019-46928-9

Paerl, H. W., Hall, N. S., Peierls, B. L., and Rossignol, K. L. (2014). Evolving paradigms and challenges in estuarine and coastal eutrophication dynamics in a culturally and climatically stressed world. *Estuar. Coast.* 37, 243–258. doi: 10.1007/s12237-014-9773-x

Paerl, H. W., Pinckney, J. L., Fear, J. M., and Peierls, B. L. (1998). Ecosystem responses to internal and watershed organic matter loading: consequences for hypoxia in the eutrophying Neuse River Estuary, North Carolina, USA. *Mar. Ecol. Progr. Ser. es* 166:17. doi: 10.3354/meps166017

Partners, O. C. M. (2017). *North Carolina Statewide Lidar DEM 2014 Phase 1*. Avaliable at: https://inport.nmfs.noaa.gov/inport/item/49411.(accessed Jan 31, 2017).

Peierls, B. L., Christian, R. R., and Paerl, H. W. (2003). Water Quality and phytoplankton as indicators of hurricane impacts on a large estuarine ecosystem. *Estuaries* 26, 1329–1343. doi: 10.1007/bf02803635

Pichler, T. (2005). Stable and radiogenic isotopes as tracers for the origin, mixing and subsurface history of fluids in submarine shallow-water hydrothermal systems. *J. Volcanol. Geother. Res.* 139, 211–226. doi: 10.1016/j.jvolgeores.2004.08.007

Prein, A. F., Rasmussen, R. M., Ikeda, K., Liu, C., Clark, M. P., and Holland, G. J. (2017). The future intensification of hourly precipitation extremes. *Nat. Clim. Change* 7:48. doi: 10.1038/nclimate3168

Pringle, C. (2003). What is hydrologic connectivity and why is it ecologically important? *Hydrol. Process.* 17, 2685–2689. doi: 10.1002/hyp.5145

Raymond, P. A., and Bauer, J. E. (2001). Use of 14C and 13C natural abundances for evaluating riverine, estuarine, and coastal DOC and POC sources and cycling: a review and synthesis. *Org. Geochem.* 32, 469–485. doi: 10.1016/s0146-6380(00)00190-x

Raymond, P. A., and Saiers, J. E. (2010). Event controlled DOC export from forested watersheds. *Biogeochemistry* 100, 197–209. doi: 10.1007/s10533-010-9416-7

Raymond, P. A., Saiers, J. E., and Sobczak, W. V. (2016). Hydrological and biogeochemical controls on watershed dissolved organic matter transport: Pulse-shunt concept. *Ecology* 97, 5–16. doi: 10.1890/14-1684.1

Reynolds-Fleming, J. V., and Luettich, R. A. Jr. (2004). Wind-driven lateral variability in a partially mixed estuary. *Estuar.Coast. Shelf Sci.* 60, 395–407. doi: 10.1016/j.ecss.2004.02.003

Richter, D. D., Markewitz, D., Trumbore, S. E., and Wells, C. G. (1999). Rapid accumulation and turnover of soil carbon in a re-establishing forest. *Nature* 400:56. doi: 10.1038/21867

Rickli, J., Frank, M., Baker, A. R., Aciego, S., De Souza, G., Georg, R. B., et al. (2010). Hafnium and neodymium isotopes in surface waters of the eastern Atlantic Ocean: Implications for sources and inputs of trace metals to the ocean. *Geochim. Cosmochim. Acta* 74, 540–557. doi: 10.1016/j.gca.2009.10.006

Rosenthal, J. S. (2011). Optimal proposal distributions and adaptive MCMC. *Handb. Mark. Chain Monte Carlo* 4, 119–138.

Runkel, R. L., Crawford, C. G., and Cohn, T. A. (2004). *Load Estimator (LOADEST): A FORTRAN program for estimating constituent loads in streams and rivers* (No. 4-A5). Reston, VA: US Geological Survey.

Spencer, R. G., Aiken, G. R., Dornblaser, M. M., Butler, K. D., Holmes, R. M., Fiske, G., et al. (2013). Chromophoric dissolved organic matter export from US rivers. *Geophys. Res. Lett.* 40, 1575–1579. doi: 10.1002/grl.50357

Spencer, R. G., Stubbins, A., Hernes, P. J., Baker, A., Mopper, K., Aufdenkampe, A. K., et al. (2009). Photochemical degradation of dissolved organic matter and dissolved lignin phenols from the Congo River. *J. Geophys. Res.: Biogeosci.* 114:3010.

Stewart, S. R. (2017). *National Hurricane Center Tropical Cyclone Report: Hurricane Matthew*. Miami, FA: National Hurricane Center.

Sullivan, M. J., and Moncreiff, C. A. (1990). Edaphic algae are an important component of salt marsh food-webs: evidence from multiple stable isotope analyses. *Mar. Ecol. Progr. Series. Oldendorf* 62, 149–159. doi: 10.3354/meps062149

Sutter, L. (1999). *DCM wetland mapping in coastal North Carolina*. Quezon City: Department of Environmental and Natural Resources.

Tockner, K., Pennetzdorfer, D., Reiner, N., Schiemer, F., and Ward, J. V. (1999). Hydrological connectivity, and the exchange of organic matter and nutrients in a dynamic river–floodplain system (Danube. Austria). *Fresh. Biol.* 41, 521–535. doi: 10.1046/j.1365-2427.1999.00399.x

Trenberth, K. E. (2011). Changes in precipitation with climate change. *Clim. Res.* 47, 123–138. doi: 10.3354/cr00953

U.S. Geological Survey [USGS] (2018). *National Water Information System data available on the World Wide Web (USGS Water Data for the Nation)*. Avaliable at [http://waterdata.usgs.gov/nwis/ (accessed June 21, 2018)

Vähätalo, A. V., and Wetzel, R. G. (2008). Long-term photochemical and microbial decomposition of wetland-derived dissolved organic matter with alteration of 13C: 12C mass ratio. *Limnol. Oceanogr.* 53, 1387–1392. doi: 10.4319/lo.2008.53.4.1387

Vannote, R. L., Minshall, G. W., Cummins, K. W., Sedell, J. R., and Cushing, C. E. (1980). The river continuum concept. *Can. J. Fish. Aquat. Scie.* 37, 130–137.

Walsh, K. J. E., McBride, J. L., Klotzbach, P. J., Balachandran, S., Camargo, S. J., Holland, G., et al. (2016). Tropical cyclones and climate change. *Wiley Interdiscip. Rev.*7, 65–89. doi: 10.1002/wcc.371

Ward, N. D., Bianchi, T. S., Medeiros, P. M., Seidel, M., Richey, J. E., Keil, R. G., et al. (2017). Where carbon goes when water flows: carbon cycling across the aquatic continuum. *Front. Mar. Sci.* 4:7. doi: 10.3389/fmars.2017.00007

Weishaar, J. L., Aiken, G. R., Bergamaschi, B. A., Fram, M. S., Fujii, R., and Mopper, K. (2003). Evaluation of specific ultraviolet absorbance as an indicator of the chemical composition and reactivity of dissolved organic carbon. *Environ. Sci. Technol.* 37, 4702–4708. doi: 10.1021/es030360x

Wolf, K. L., Noe, G. B., and Ahn, C. (2013). Hydrologic connectivity to streams increases nitrogen and phosphorus inputs and cycling in soils of created and natural floodplain wetlands. *J. Environ. Q.* 42, 1245–1255. doi: 10.2134/jeq2012.0466

Conflict of Interest: The authors declare that the research was conducted in the absence of any commercial or financial relationships that could be construed as a potential conflict of interest.

frontiers
in Marine Science

ORIGINAL RESEARCH
published: 28 February 2020
doi: 10.3389/fmars.2020.00080

Response of Coastal Phytoplankton to High Inflows of Terrestrial Matter

Joanna Paczkowska[1,2†], *Sonia Brugel*[1,2], *Owen Rowe*[1,2,3†], *Robert Lefébure*[1,2†], *Andreas Brutemark*[4,5] *and Agneta Andersson*[1,2*]

[1] Department of Ecology and Environmental Science, Umeå University, Umeå, Sweden, [2] Umeå Marine Sciences Centre, Hörnefors, Sweden, [3] Department of Food and Environmental Sciences, Division of Microbiology and Biotechnology, University of Helsinki, Helsinki, Finland, [4] Novia University of Applied Sciences, Ekenäs, Finland, [5] Tvärminne Zoological Station, University of Helsinki, Hangö, Finland

Edited by:
Hans Paerl,
University of North Carolina at Chapel Hill, United States

Reviewed by:
Patricia M. Glibert,
University of Maryland Center for Environmental Science (UMCES), United States
Sibel Bargu,
Louisiana State University System, United States

***Correspondence:**
Agneta Andersson
agneta.andersson@umu.se

†Present address:
Joanna Paczkowska,
Laboratorio de Oceanografía Biológica (LOBio), Centro para el Estudio de Sistemas Marinos (CESIMAR), Consejo Nacional de Investigaciones Científicas y Técnicas (CONICET), Puerto Madryn, Argentina
Owen Rowe,
Baltic Marine Environment Protection Commission, Helsinki Commission (HELCOM), Helsinki, Finland
Robert Lefébure,
ISEAL Alliance, London, United Kingdom

Specialty section:
This article was submitted to Marine Biogeochemistry, a section of the journal Frontiers in Marine Science

Received: *04 August 2019*
Accepted: *31 January 2020*
Published: *28 February 2020*

Citation:
Paczkowska J, Brugel S, Rowe O, Lefébure R, Brutemark A and Andersson A (2020) Response of Coastal Phytoplankton to High Inflows of Terrestrial Matter. Front. Mar. Sci. 7:80. doi: 10.3389/fmars.2020.00080

Climate change scenarios project that precipitation will increase in northern Europe, causing amplified inflows of terrestrial matter (tM) and inorganic nutrients to coastal areas. How this will affect the plankton community is poorly understood. A mesocosm experiment was carried out to investigate the influence of two levels of tM inputs on the composition, size-structure and productivity of a natural coastal phytoplankton community from the northern Baltic Sea. The tM addition caused browning of the water and decreased underwater light levels, while the concentrations of dissolved organic carbon (DOC) and inorganic nutrients increased. Microphytoplankton were promoted by tM addition, while in the controls picophytoplankton dominated the phytoplankton community. Inorganic nutrient availability was instrumental in defining the phytoplankton community composition and size-structure. As a response to tM addition, the phytoplankton increased their chlorophyll *a* content. This physiological adaptation helped to maintain high primary production rates at the low tM enrichment, but at the high tM load the primary production decreased as did the biomass of mesozooplankton. The ciliate biomass was high when the mesozooplankton biomass was low, indicating that a trophic cascade occurred in the system. Structural equation modeling showed that tM borne DOC promoted ciliates, while primary and bacterial production were disfavored. Thus, DOC originating from soils had an indirect negative effect on the mesozooplankton by reducing their food availability. Although, a positive correlation between heterotrophic bacteria and phytoplankton suggested coupling between phytoplankton produced carbon and heterotrophs growth. The results from our study indicate that river-borne DOC and inorganic nutrients have a large impact on the phytoplankton community, driving the system to the dominance of large diatoms. However, since river-borne humic substances cause browning of the water, phytoplankton increase their light harvesting pigments. At moderate inflow this helps to support the primary production, but at high inflows of terrestrial material the primary production will decrease. As high river inflows have been projected to be a consequence of climate change, we foresee that primary production will decrease in coastal areas in the future, and the impacts of such changes on the food web could be significant.

Keywords: coastal phytoplankton, terrestrial organic matter, climate change, primary production, chlorophyll *a*

INTRODUCTION

Phytoplankton are the major primary producers in aquatic ecosystems (Field et al., 1998; Falkowski et al., 2004). They commonly constitute the base of pelagic food webs, thus changes in their taxonomic composition, size-structure and production due to anthropogenic activity and climate change can have complex and significant knock-on effects on the production at higher trophic levels (Chust et al., 2014; Rasconi et al., 2015). For example, periodically heavy rainfall will increase the transport of river-bond inorganic nutrients from the terrestrial system to the coast. The inorganic nutrient concentrations in the recipient waters will rise, which can promote phytoplankton growth (Dagg et al., 2004; Masotti et al., 2018). River flooding may therefore cause phytoplankton blooms and eutrophication in the recipient coastal ecosystems (Wasmund, 2002; Penna et al., 2004). However, if the river-water also holds high concentrations of colored humic rich matter, the eutrophication process could be counteracted (Andersson et al., 2013). The brownish color of the water causes increased light attenuation, and thus decreased water transparency. In such a scenario, phytoplankton growth would be light limited and their carbon production lowered. This may in turn lead to decreased fish production thus affecting human food resources.

Effects of river flooding on the coastal carbon cycle, induced by changes in the phytoplankton community, can vary (Roelke et al., 2013; Dorado et al., 2015). Increased inorganic nutrient levels would promote large microphytoplankton, such as diatoms (Shangguan et al., 2017a), since they have a competitive advantage when nutrient inputs are high (Legendre and Rassoulzadegan, 1995; Duarte et al., 2000). Furthermore, changes in the inorganic nutrient composition and their stoichiometry can drive the phytoplankton community to change the taxonomic composition and size-structure (Shangguan et al., 2017a,b; Swarbrick et al., 2019). On the other hand, low light levels would promote small phytoplankton, pico- and nanophytoplankton, because of their large surface to volume ratio and distribution of pigments along the outer cell wall (Raven, 1998; Marañón, 2015). This enables more efficient light harvesting in small cells compared to larger cells, where the light harvesting pigments are enclosed in inner cell organelles, i.e., in the chloroplasts (Raven, 1998; Kirk, 2011). However, since river water contains both inorganic nutrients and dissolved organic matter, freshwater inflows or flooding could either promote large or small phytoplankton cells. Moreover, where natural bacterial communities also make a significant part of the food web then the conversion of organic matter and the changes in bioavailability of it may also be critical factors (Asmala et al., 2013; Traving et al., 2017; Asmala et al., 2018). Thus overall, the phytoplankton response may be governed by the magnitude of the inflow and the inorganic nutrient and organic matter concentration in the river water.

Large and small phytoplankton cells can enter the food web, though this takes place at different trophic levels, implying that different shares of the organic carbon produced by phytoplankton reach higher trophic levels. At each trophic level, ∼70% of the energy (organic carbon) is lost due to respiration, sloppy feeding and excretion (Straile, 1997; Berglund et al., 2007). A simplified view is that the food web is size-structured and that the smallest picophytoplankton enter the food web at the flagellate level, while nanophytoplankton enter at the ciliate level and microphytoplankton at the mesozooplankton level (Legendre and Rassoulzadegan, 1995). This means that much less of the primary produced energy reaches higher trophic levels if the phytoplankton community is dominated by picophytoplankton than if the community is dominated by micro-sized phytoplankton (Sommer et al., 2002). In addition to that, there are quality differences between cyanobacteria and other phytoplankton groups (Peltomaa et al., 2017; Jónasdóttir, 2019). Cyanobacteria do not contain storage lipids, while many eukaryotic phytoplankton contain energy rich triacylglycerols (Nordbäck et al., 1998). All this emphasizes the need to understand how changing environmental conditions influence the composition, size-structure and productivity of the phytoplankton community.

To enable photosynthesis and growth at low light conditions phytoplankton often increase their content of light harvesting pigments, i.e., chlorophyll *a* (Markager, 1993; Dubinsky and Stambler, 2009). By this process phytoplankton may be able to maintain high primary production even though light levels and photosynthetic efficiency decrease (Halsey and Jones, 2015). However, with high terrestrial matter (tM) loading, the light may become too low to support primary production. Extreme inflows of tM may cause such a significant decrease in the under-water light conditions that a tipping point could be reached. Presently it is unknown how phytoplankton physiologically react to different loads of terrestrial matter. This is important to find out, since it gives a possibility to make ecological predictions of future climate change scenarios.

Changes in the phytoplankton community composition or size-structure can also be caused by zooplankton grazing under elevated tM loading conditions. Both increases and decreases of the zooplankton biomass have been found in tM-enrichment experiments, as well as alterations in the species composition (Carlsson et al., 1995; Berggren et al., 2010). Due to increased concentrations of nitrogen and phosphorus, intrinsic components of tM, primary production can be heightened, which can stimulate the zooplankton biomass (Klug, 2002; Kissman et al., 2013). Additionally, inorganic nutrients can regulate heterotrophic bacterial growth directly or indirectly via stimulation of autochthonous organic carbon production (Schweitzer and Simon, 1995; Vrede, 1999). On the other hand, if the light availability decreases due to the brown color of the tM, the primary production as well as the zooplankton biomass may decrease. Supply of tM however, also influences other food web components and can nurture the heterotrophic microbial food web, as the terrestrial organic carbon can be used as food source for heterotrophic bacteria (Kaartokallio et al., 2016). This in turn may promote growth of protozoa, which are used as food by mesozooplankton (Berggren et al., 2010; Faithfull et al., 2012). The bottom-up effects are major processes regulating the pelagic food web in oligotrophic ecosystems, while the top-down effects are more often observed in eutrophic ecosystems, where a positive correlation between mesozooplankton and picophytoplankton and heterotrophic bacteria occur due to decreased predation pressure on small cells (a trophic cascade) (Sanders et al., 1992). Furthermore, phytoplankton are not always the most important food source for coastal zooplankton. For example, Carlsson et al. (1995) showed that zooplankton did not significantly influence the phytoplankton community in a coastal area, since the dominant omnivorous zooplankton rather grazed on microzooplankton than on phytoplankton. Additionally, tM may selectively alter the zooplankton species composition, and thus the food web channeling and stoichiometry (Berggren et al., 2010; Faithfull et al., 2012). Cladocerans have relatively low N:P ratio and execute unselective grazing (Hambright et al., 2007). They consume different organisms within the microbial food web, for example bacteria, flagellates and ciliates, and preferentially P-rich phytoplankton (Riemann, 1985; Schatz and McCauley, 2007). In contrast, copepods have a relatively high N:P ratio and are selective grazers (Meunier et al., 2016). They prefer feeding on nano- and microplankton, such as ciliates and N-rich phytoplankton species (Cowles et al., 1988; Walve and Larsson, 1999). The interaction between the food web-base and the mesozooplankton community is thus highly complex and adjustable depending on external forcing, for example varying inorganic nutrient and tM load.

Increasing inflows of tM to coastal areas in northern Europe, such as the Baltic Sea, is one of the projected consequences of future climate change (Meier et al., 2012; Andersson et al., 2015). Regional climate projections estimate an increase in riverine inflow of 15–20% in the northern Baltic Sea area, which will be accompanied by an increase in colored tM loads and inputs enriched with both organic and inorganic nutrients (Meier et al., 2012). We performed an experimental study to elucidate how projected increases in tM inflows will affect the coastal phytoplankton composition, size-structure, production and physiological adaptation. The experiment was performed using natural seawater from a coastal area in the northern Baltic Sea, which included a complete food web from microorganisms to mesozooplankton, with planktivorous fish subsequently added. We hypothesized that: (1) increased inorganic nutrient concentrations via tM inputs would cause an increase in the phytoplankton cell-size, even though the light decreases, (2) photosynthetic efficiency would decrease with increasing tM load and that the phytoplankton would adapt to lower light by increasing their chlorophyll *a* content, (3) at low tM load this adaptation would help maintaining high primary production rates but at high tM load high primary production cannot be sustained, and (4) mesozooplankton would benefit from high primary production, and their functional feeding composition would follow the size-spectrum of the phytoplankton community.

MATERIALS AND METHODS

Mesocosm Experiment

The experiment was carried out from 21st of May to 25th of June 2012, using 12 indoor mesocosms located at the Umeå Marine Sciences Center (UMSC), Sweden (as described in Traving et al., 2017). The mecososm are 5 m high tanks with a volume of 2000 l (see Grubisic et al., 2012; Lefébure et al., 2013 for more details). On May 21st and 22nd, seawater was gently collected at a depth of 4 m from the Bothnian Sea (63°33′N, 19°56′E; salinity ~4 and temperature ~6°C) using a peristaltic pump, and transported in 1 m^3 polythene containers to UMSC. Mesocosms were gently filled and enriched with inorganic nutrients (0.7 μmol l^{-1} nitrogen and 0.09 μmol l^{-1} phosphorus) to prevent nutrient limitation during a 7-day equilibration period prior to imposition of the treatments. The water contained a natural pelagic food web from bacteria to mesozooplankton, while larger organisms (e.g. fish) were excluded by using 1.5 mm mesh during collection. The final mesocosm temperature after a 7-day equilibration period reached 15°C and light was set to a cycle of 12 h light and 12 h dark. Illumination was supplied by 150 W metal halogen lamps (MASTERColour CDM-T 150W/942 G12 1CT) situated above each mesocosm, which provided photosynthetically active radiation (PAR) of 400 μmol photon m^{-2} s^{-1} at the surface. To ensure that the water column was replete with oxygen and well mixed, air was continuously bubbled into the mesocosms (20 ml s^{-1}) in conjunction with thermal cycling that resulted in convective stirring of the water (full mixing of each mesocosm in circa 2–4 h period, unpublished testing data).

Temperature and thermal water cycling within tanks was controlled by an automated heating/cooling system (±0.5°C). One of four treatments was assigned randomly to each mesocosm. Water exchange (40 l, inclusive of sampling water collection) was carried out every second day and replacement water consisted of 0.2 μm filtered natural Bothnian Sea water.

The experiment started on 28th of May (Day 0) and lasted for 28 days. To disentangle the effect of tM borne organic and inorganic nutrients, triplicate mesocosm replication was established. Four treatments were applied. In the tM_L and tM_H treatments, natural tM extracted from soils was added to mimic river inflow. The tM contained both organic matter and inorganic nutrients. Soils were collected at the beginning of May from the banks of the Reda River for tM_H (Southern Baltic Proper, Poland) and Öre River for tM_L (Northern Bothnian Sea, Sweden). The sites were selected to be representative of catchment regions dominated by agriculture and forestry, respectively. The tM extracts were produced following the procedure outlined in Lefébure et al. (2013). To release organic, inorganic nutrients and heavy metals bound to soils, extracts were dispersed in filtered MQ water and mixed with an ion exchange resin (Amberlite IRC 748I) before being stored in the dark at 4°C for 48 h. Extracts were then filtered through a 90 μm mesh and the liquid phase was retained in acid washed tanks in the dark at 4°C for the duration of the experiment. Nutrient (inorganic and total) measurements of these extracts were made on filtered samples from the bulk extracts, and this information was used to create the treatments described below. Dissolved organic carbon (DOC), dissolved inorganic nitrogen and phosphorus (DIN, DIP), total nitrogen and phosphorus (Tot N, Tot P) concentrations were analyzed using a Shimadzu TOC-5000 carbon analyzer and a Braan and Luebbe TRAACS 800 autoanalyzer. The experiment was designed to mimic a future climate change scenario of increased river runoff in the Baltic Sea. The final concentration of DOC targeted was 6 mg l^{-1} in the tM_L treatment and 8 mg l^{-1}

in the tM_H treatment (overall additions), which is equivalent to an increased C concentration of 50 and 100% respectively, based on future scenario from Hägg et al. (2010). The two control treatments $Ctrl_L$ and $Ctrl_H$ were supplemented only with inorganic N and P to match inorganic nutrients concentrations of the respective tM treatments. Three days before the first sampling day, all mesocosms were supplied with a 22% boost of their respective overall additions, followed by daily equal additions to reach future C scenarios (**Table 1**). During the first day of the experiment (Day 0), seven young of the year (YOY), similarly sized, perch (*Perca fluviatilis*) were added per mesocosm to mimic natural predation. The fish survival during the experiment was high, with an average survival rate of 80%.

Sampling

All water samples were collected twice a week in the early morning (06.00 h) using a syphoning hose at 2 m depth, except those for microscopic identification of phytoplankton and zooplankton. These samples were taken at the beginning, middle and end of the experiment (Days 0, 17, and 28) using the same sampling device. Primary production incubation was performed immediately after sample collection and once the automatic light cycle had been initiated (07.00 h).

Physicochemical Factors

Vertical Photosynthetically Active Radiation (PAR) irradiance profiles were taken with a LICOR-193SA light sensor. Light measurements were carried out every 0.2 m from the surface to 0.6 m, and then at 0.5 m intervals down to 4.5 m. The light attenuation coefficient (K_d) was calculated from the slope of the linear regression of the natural logarithm of down-welling irradiance versus depth. Samples for inorganic nutrients Dissolved Inorganic Phosphorus (DIP: phosphate), Dissolved Inorganic Nitrogen (DIN: nitrate + nitrite and ammonium) and silicate were filtered through 0.2 μm cellulose-acetate filters and stored at −20°C, while unfiltered samples for total phosphorus (Tot P) and total nitrogen (Tot N) were directly stored at −20°C. All nutrients were analyzed using a Braan and Luebbe TRAACS 800 autoanalyzer, according to standard analytical methods (Grasshoff et al., 1983). The concentration of humic substances (HS) was measured from unfiltered water samples using a Perkin Elmer LS 30 fluorometer at 350/450 nm excitation/emission wavelengths, calibrated with a serial dilution of quinine sulfate solution (Hoge et al., 1993). DOC concentrations were analyzed on 0.22 μm filtered (Supor Membrane Syringe Filter, non-pyrogenic; Acrodisc®) and acidified samples (18 mM HCl, final concentration) using a Shimadzu TOC-5000 analyzer.

TABLE 1 | Daily addition of C, N and P concentrations in the mesocosms (subsequent to initial addition of tM extracts).

Treatment	C (μmol l^{-1})	N (μmol l^{-1})	P (μmol l^{-1})
tM_L*	10	1.1	0.03
tM_H*	20	2.3	0.13
$Ctrl_L$**	–	0.001	0.0008
$Ctrl_H$**	–	0.009	0.005

**Soil extracts contained both organic and inorganic nutrients as well as dissolved organic carbon. **$Ctrl_L$ and $Ctrl_H$ treatments were supplemented with nitrate ($NaNO_3$), ammonia (NH_4Cl) and phosphate (NaH_2PO_4) in the stoichiometry and concentration equivalent to tM addition treatments, respectively [from Traving et al. (2017)].*

Colored dissolved organic matter (CDOM) absorbance was measured in water samples filtered through a 0.22 μm polycarbonate membrane and stored in amber glass bottles in the dark at 4°C until analysis. Absorbance values were recorded from 250 to 800 nm using a Shimadzu UVPC-2501 scanning spectrophotometer, with Milli-Q water as the blank. The absorption coefficient at 440 nm (g_{440}) was calculated by multiplying the absorbance at specific wavelength with 2.303 and dividing by the length of the cuvette (Kirk, 2011).

Chlorophyll *a* and Primary Production

Samples for chlorophyll *a* (Chl *a*) (100 ml) were filtered onto 25 mm GF/F filters, extracted in 95% ethanol overnight and measured with a Perkin Elmer LS 30 fluorometer (433/674 nm excitation/emission wavelengths). Primary production (PP) rates were measured using the ^{14}C method (Gargas, 1975). Samples were incubated with $NaH^{14}CO_3$ at a final concentration of 0.1 μCi ml^{-1} (^{14}C Centralen Denmark, DHI, activity 100 μCi ml^{-1}) at seven depths: surface, 0.1, 0.2, 0.4, 0.6, 1, and 2 meters, within each mesocosm. Additionally, one dark sample per tank was incubated. After ∼3 h of incubation, 5 ml of each sample were transferred to a scintillation vial, and gently bubbled with 150 μl of 6 M HCl for 30 min. Subsequently, 15 ml of scintillation fluid were added, and samples were measured using a Beckman 6500 scintillation counter. Average daily primary production was calculated in each mesocosm, using the light factor method (Gargas, 1975). PP:Chl *a* was calculated as an indicator of photosynthetic efficiency.

Bacterial Production

The ^3H-thymidine incorporation method was used to measure bacterial production (BP) (Fuhrman and Azam, 1982). Four 1 ml seawater samples (one control and three samples) were incubated with 2 μl of ^3H-thymidine (84 Ci $mmol^{-1}$; PerkinElmer, MA, United States) (final concentration 24 nM) for 1 h at *in situ* temperature. This thymidine addition corresponded to the saturation level. The control sample was pre-killed by adding 100 μl of ice-cold 50% TCA and incubation at −20°C for 5 min. Cell production was calculated using a conversion factor of 1.4×10^{18} cells mol^{-1} of incorporated thymidine (Wikner and Hagström, 1999). Daily net production rates were calculated assuming stable uptake rates over the day and a bacterial carbon content of 20 fgC $cell^{-1}$ (Lee and Fuhrman, 1987).

Plankton Identification and Enumeration

Samples for phytoplankton (>2 μm) identification and counting were preserved with 2% alkaline Lugol's solution in 50 ml volumes. Samples were settled for 24–48 h and counted using the inverted microscope method (Utermöhl, 1958). Microphytoplankton (>20 μm) and nanophytoplankton (2–20 μm) samples were counted at 100× and 400× magnification, respectively. Zooplankton samples were preserved with 2%

alkaline Lugol's solution, counted on a stereomicroscope (Leica), and transformed into carbon biomass (Hernroth, 1985).

Samples for picophytoplankton and heterotrophic bacteria were preserved in 0.1% glutaraldehyde (final concentration) and frozen at −80°C (Marie et al., 2005) for later counts using a BD FACSVerse^{TM} flow cytometer (BD Biosciences) equipped with a 488 nm laser (20 mW output) and a 640 mn laser (output 40 mW). Frozen samples were quickly thawed in a 30°C water bath and pre-filtered through a 50 μm mesh. Picophytoplankton samples were run with 3 μm microspheres (Fluoresbrite® plain YG, Polysciences) as internal standard. Picophytoplankton abundance was converted to biomass using carbon conversion factors: 120 fgC cell^{-1} for picocyanobacteria and 829 fgC cell^{-1} for picoeukaryotic phytoplankton, based on microscopic measurements of cell sizes and use of conversion factors (see below). Heterotrophic bacteria samples were diluted with 0.2 μm filtered seawater, stained with SYBR Green I (Invitrogen) (1:10000, final concentration) and kept in the dark at room temperature for 10 min. 1 μm microspheres (Fluoresbrite® plain YG, Polysciences) were added to each sample as internal standard and analyses were run at a low flow rate of 30 μL min^{-1} with an acquisition time of 2 min. Heterotrophic bacteria abundance was converted to biomass using carbon conversion factor: 20 fgC cell^{-1} (Lee and Fuhrman, 1987).

The phytoplankton cells were divided into different size-classes: pico- ($<$2 μm), nano- (2–20 μm), and micro- ($>$20 μm) phytoplankton based on measurements of the longest cell axis. Functional groups: AU (autotrophs), HT (heterotrophs), and MX (mixotrophs) were assigned according to Olenina et al. (2006). Filamentous cyanobacteria were assigned to the microphytoplankton category based on the size of single cells, as well as tightly clustered amalgamations of cells. Nutritional characteristics of plankton were identified based on cell morphology, size and described trophy (Tikkanen and Willen, 1992; Hällfors, 2004; Olenina et al., 2006). Further, the coloration of the smallest cells was used to support the trophy classification as Lugol's solution stains Chl *a* brown. Phytoplankton biomass was calculated from the geometric shape of cells following Olenina et al. (2006) and cell carbon content was calculated according to Menden-Deuer and Lessard (2000). Total phytoplankton biomass (TB) was defined as the sum of the carbon biomass of autotrophs (including *Mesodinium rubrum*) and mixotrophs. The relative contribution to biomass of size classes and functional groups were calculated. Additionally, Chl *a*:C was estimated as an indicator of acclimation to changing light and nutrient conditions. This indicator was obtained by dividing the Chl *a* concentration by total phytoplankton carbon biomass.

Statistical Analyses

Generalized linear mixed models (GLMM), followed by Tukey's *post hoc* tests, were used to test the effect of treatments, days and their interactions on physicochemical variables and biological variables. Mesocosm tank was included as a random effect. The assumptions of normality were tested using the Shapiro-Wilk test. The fit of the model was estimated by interpreting the diagnostic plots (correlation between model residuals and the fitted values, normality of residuals, homoscedasticity of the residuals and possible data outliers). GLMM models were also performed to evaluate the effects of physicochemical and biological variables (PAR, PO_4, NH_4, $NO_3 + NO_2$, and zooplankton biomass) on phytoplankton related parameters, bacterial biomass and production and ciliate biomass. The remaining physicochemical variables measured during the experiment were not included in analysis due to high multicollinearity indicated by the variance inflation factor (VIP $>$ 10). Physicochemical and biological variables were selected for the final model with a backward stepwise selection process based on based on Akaike's Information Criterion (AIC). Changes in the total phytoplankton biomass composition were visualized by non-metric multidimensional scaling (NMDS), based on Bray-Curtis similarity. Redundancy analysis (RDA) was performed to identify factors influencing the size-structure of the phytoplankton community during the middle and end of the experiment. The relative biomass of pico- ($<$2 μm), nano- (2–20 μm) and micro- ($>$20 μm) phytoplankton were analyzed in relation to zooplankton biomass (Zooplankton), phosphate (PO_4), ammonium (NH_4), nitrate + nitrite ($NO_3 + NO_2$), and Photosynthetically Active Radiation (PAR). Additionally, the relationships between primary production (PP), bacterial production (BP), zooplankton biomass (ZP), and ciliate biomass (Ci) as endogenous variables and phosphate (PO_4) and dissolved organic carbon (DOC) as exogenous variables were examined by structural equation modeling (SEM). Standardized path coefficients and R^2 were calculated, while the goodness of fit of the model was tested by the Chi-square test. Non-parametric correlation (Spearman) analyses were used to test relationships between the relative biomass of major zooplankton groups and bacterial, ciliate biomass and the relative contribution of the size-structure of the phytoplankton. Day 0 was excluded from statistical analyses in order to examine physicochemical and biological variations after the treatments had taken effect. Data analyses were performed in Primer 6, Canoco 5, and R softwares.

RESULTS

Variation of Physicochemical Factors

Photosynthetically Active Radiation (PAR) decreased gradually over time in the mesocosms with tM load (33–4 μmol photon m^{-2} s^{-1}), while in the controls ($Ctrl_L$ and $Ctrl_H$) the PAR values were higher and generally more constant (on average 50 μmol photon m^{-2} s^{-1}) (Tukey's, $p < 0.001$) (**Figure 1A**). Humic substances, K_d, Tot N, DOC and g_{440} increased throughout the experiment in the tM mesocosms (HS: 26–47 μg l^{-1}, K_d: 1.4–4.1 m^{-1}, Tot N: 22–40 μmol^{-1}, DOC: 6-9 mg l^{-1}, g_{440}: 2.6-9.7 m^{-1}), while in the controls the values were relatively unchanged (on average HS: 22 μg l^{-1}, Kd: 1 m^{-1}, Tot N: 17 μmol^{-1}, DOC: 5 mg l^{-1}, g440: 1.7 m^{-1}) (**Figures 1B, 2A,C–E**). The values of these variables were significantly higher in the tM supplemented mesocosms compared to the controls (Tukey's, $p < 0.001$).

In general, nitrate + nitrite decreased steadily over time in all treatments and reached the lowest values on day 24 (**Figure 1C**).

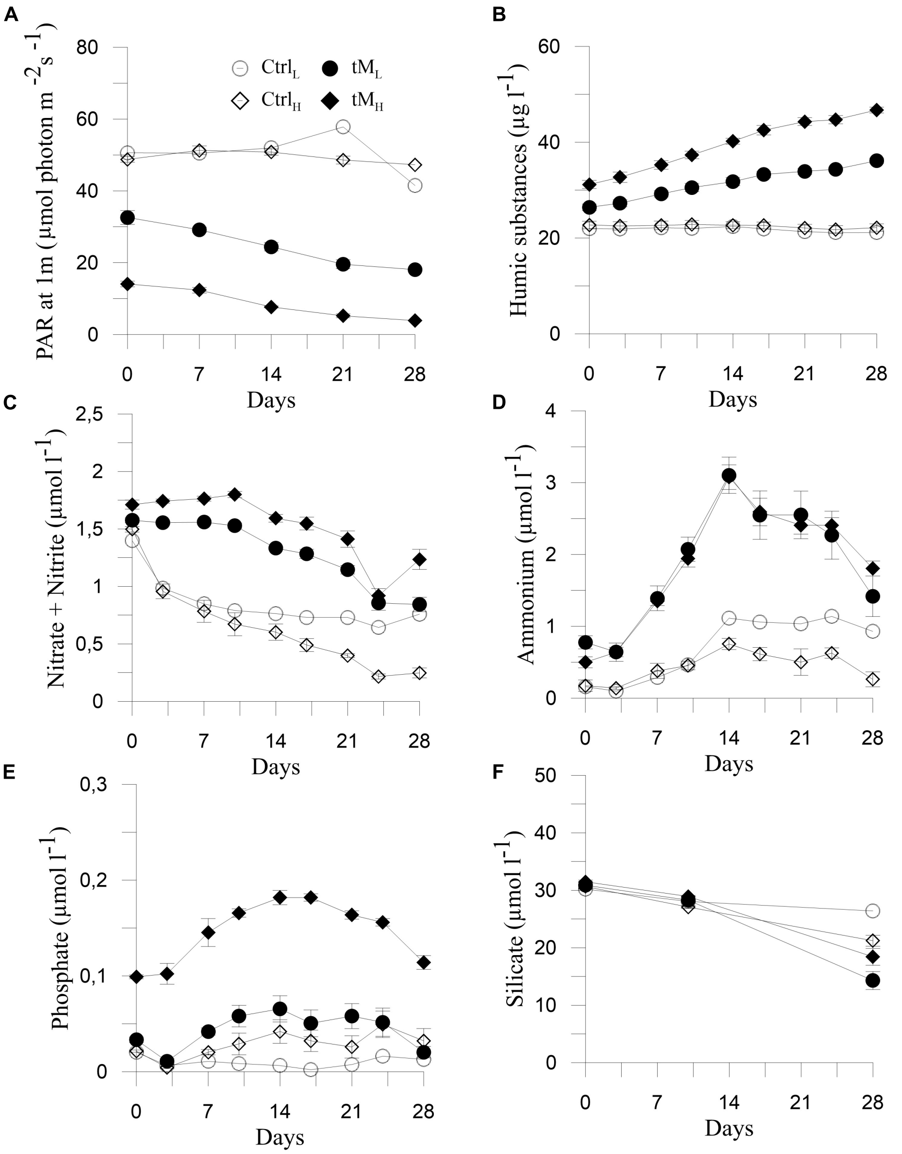

FIGURE 1 | Temporal variation of physicochemical factors during the experiment: Photosynthetic Active Radiation (PAR) at 1 m **(A)** modified after Traving et al. (2017), humic substances **(B)**, nitrate + nitrite **(C)**, ammonium **(D)**, phosphate **(E)**, and silicate **(F)**. Means ± standard error, $n = 3$.

Higher nitrate + nitrite concentration was observed in tM treatments than in controls (1.4 ± 0.1 vs. 0.8 ± 0.1 μmol l^{-1}). Ammonium, phosphate and Tot P peaked at the middle of the experiment, reaching maximum values in tM treatment (3.1 μmol^{-1} for ammonium, 0.18 μmol^{-1} for phosphate and 0.83 μmol^{-1} for Tot P, respectively) (**Figures 1D,E**, **2B**). Inorganic nitrogen (nitrate + nitrite and ammonium), phosphate and Tot P concentrations were significantly higher in the tM mesocosms than in the controls (Tukey's, $p < 0.001$). The higher concentrations of inorganic N and P in the tM treatments than in the controls were likely due to bacterial reduction of organic N and P to inorganic forms. Silicate showed a decreasing trend in all mesocosms, and at the end of the experiment, the silicate concentration was 1.5-fold lower in the tM mesocosms than in the controls (16.4 ± 2.1 vs. 23.8 ± 2.6 μmol^{-1}) (**Figure 1F**). There was no significant difference in silicate concentration between treatments. Highest DIN:DIP ratio was observed in the control (Ctrl_L). In these mesocosms the ratio was 2-fold and 8-fold higher than in the remaining treatments, suggesting strong phosphorus limitation in Ctrl_L (**Figure 2F**).

Effect of tM Load on Phytoplankton Community Composition, Size-Structure and Nutritional Strategy

The taxonomic composition was similar in all mesocosms at the beginning of the experiment (**Figures 3A**, **4**). Bacillariophyceae and Chlorophyceae were the dominant groups (**Figures 3Aa-d**).

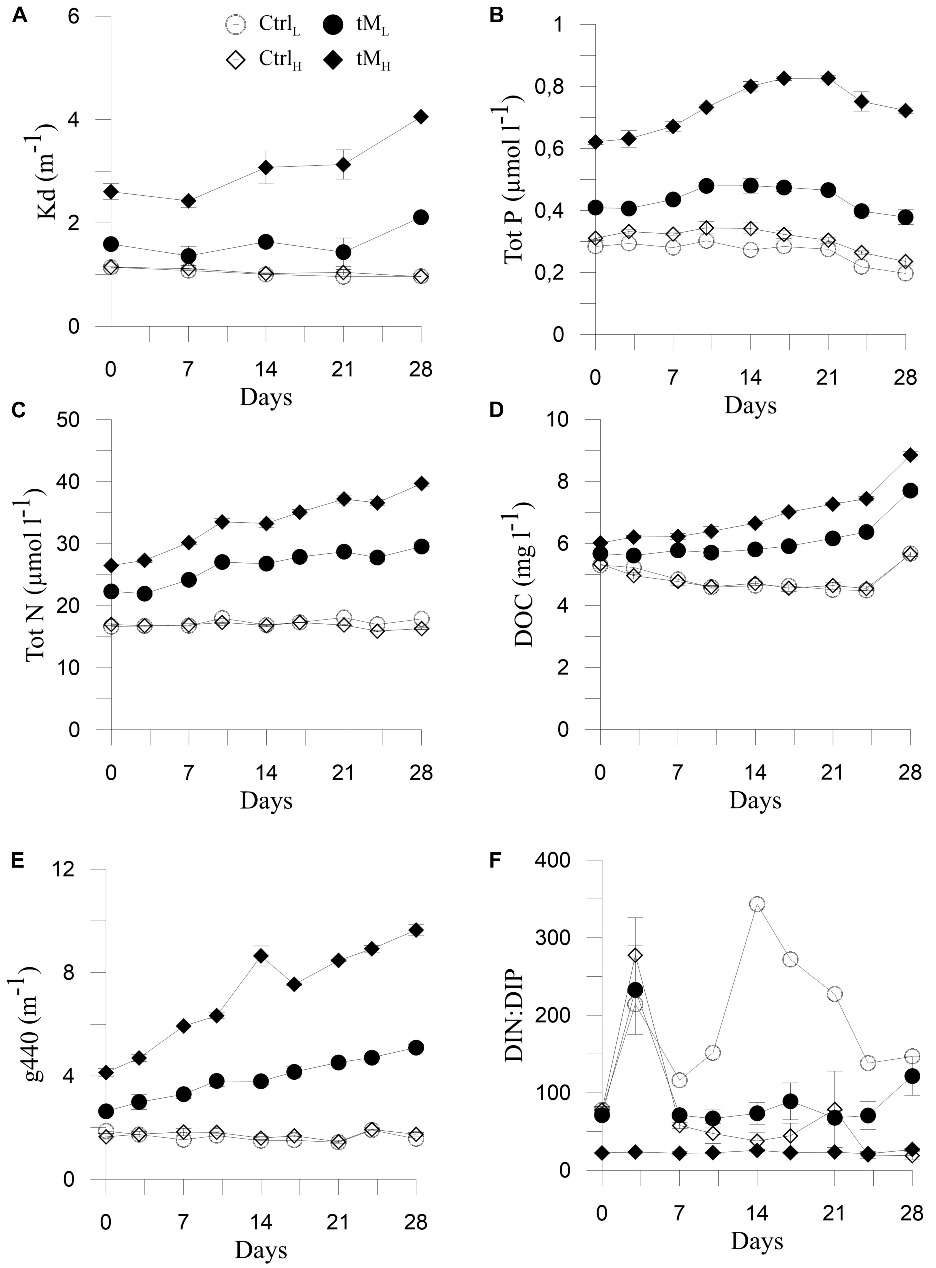

FIGURE 2 | Temporal variation of physiochemical factors: Kd **(A)**, Tot P **(B)**, Tot N **(C)**, DOC **(D)** modified after Traving et al. (2017), g440 **(E)**, and DIN:DIP **(F)**. Mean ± standard error, *n* = 3.

Noticeable taxa were *Skeletonema marinoi* (Cleve), *Thalassiosira baltica, Chaetoceros wighamii* (Brightwell) and *Monoraphidium contortum* (Komárková-Legnerová). The photosynthetic ciliate *Mesodinium rubrum* (Leegaard) also occurred abundantly at the initial phase of the experiment, constituting on average ∼10% of the total biomass in controls and ∼25% in tM treatments (**Figures 3Aa-d**). However, as the experiment progressed the phytoplankton composition showed differences between the controls and tM supplemented mesocosms (**Figures 3A**, **4**). In the controls, unidentified picoeukaryotes dominated the phytoplankton community (**Table 2** and **Figures 3Aa-b**), while in the tM supplemented mesocosms they constituted a smaller share (**Figures 3Ac-d**). Bacillariophyceae (diatoms) were promoted by tM load, and at the end of the experiment this group constituted on average ∼50% of the biomass in these mesocosms (**Figures 3Ac-d**). *Diatoma tenuis* (C. Agardh) and *Synedra acus* var. *acus* (Kützing) were the most abundantly occurring species.

At the start of the experiment, microphytoplankton was the dominant size group in all mesocosms, forming ∼80%

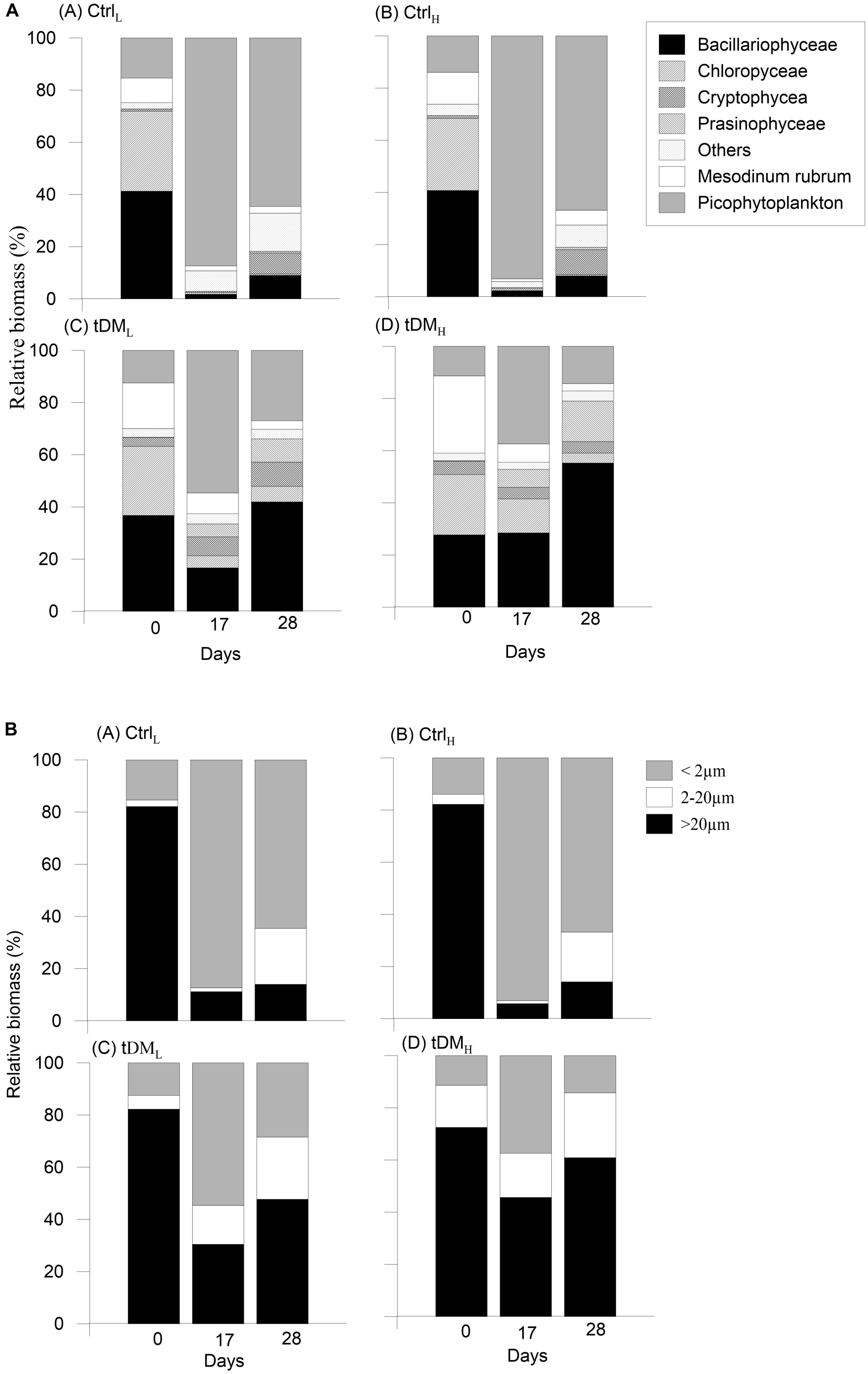

FIGURE 3 | Phytoplankton taxonomic composition and size-structure at the start, middle and end of the experiment: biomass distribution of major phytoplankton taxa: Bacillariophyceae, Chlorophyceae, Cryptophyceae, Prasinophyceae, Others, Mesodinum rubrum and picophytoplankton **(A)**, and biomass distribution of size-classes: pico- (<2 µm), nano- (2–20 µm), and microphytoplankton (>20 µm) **(B)**.

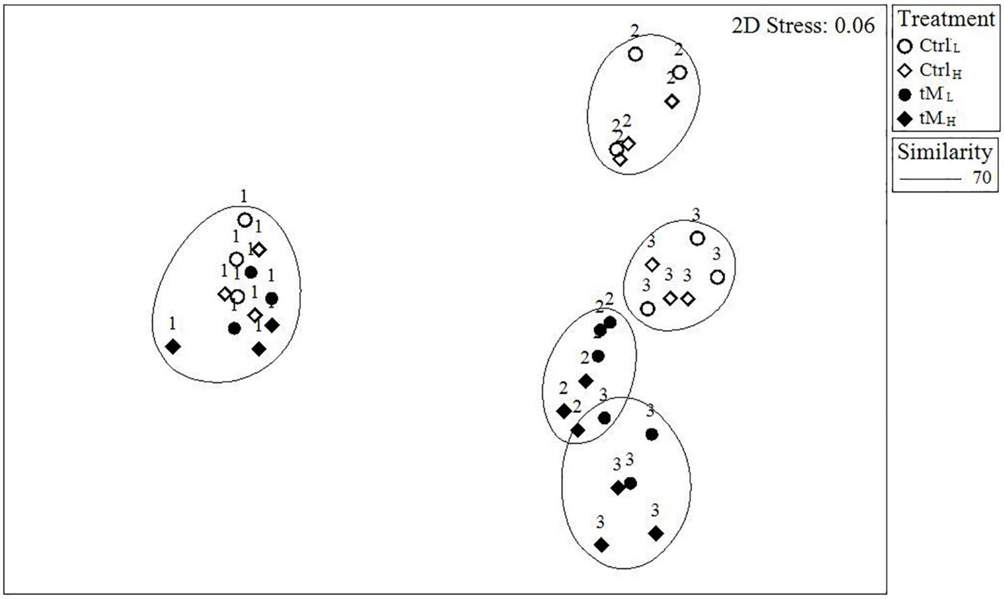

FIGURE 4 | Non-metric multidimensional scaling (NMDS) plot of the phytoplankton community composition. Numbers display the sampling day (1 = Day 0, 2 = Day 17, and 3 = Day 28).

of the biomass (**Figures 3Ba-d**). Their relative contribution decreased most strongly in the controls, falling to less than 10% in the middle of the experiment before increasing slightly by the end of the experiment, reaching ∼14%. In the tM supplemented mesocosms, the microphytoplankton contribution remained high throughout the experiment and ranging between 31 and 46% in the middle of the experiment and 48 and 61% at the end of the experiment. *D. tenuis*, *M. rubrum*, *S. acus* var. *acus* and *M. contortum* dominated this phytoplankton size group over the experiment (**Table 2**). Nanophytoplankton constituted a smaller part of the phytoplankton community, on average ∼1% of the total phytoplankton biomass in the controls and ∼15% in tM treatments in the middle of the experiment, while the highest share, ∼25%, was observed at the end of the experiment in all treatments (**Figures 3Ba-d**). Within the nanophytoplankton, Cryptophyceae and Prasinophyceae were the most abundant taxa, e.g., *Plagioselmis prolonga* (Butcher), *Teleaulax* spp. and *Pyramimonas* spp. (**Table 2**). Picophytoplankton showed maximum contribution in the middle of the experiment in all mesocosms, where they constituted 38–93% of the phytoplankton biomass (**Figures 3Ba-d**). The picophytoplankton share remained high in the controls all through the experiment, while in the tM mesocosms picophytoplankton decreased toward the end, constituting ∼20% of the phytoplankton biomass (**Figures 3Ba-d**).

The proportion of autotroph biomass was high in all treatments, constituting over 96% of the total phytoplankton biomass throughout the experiment. The contribution of heterotrophs and mixotrophs was minimal, contributing a maximum of ∼4% in the tM mesocosms in the middle of the experiment, and 2% in controls at the end of the experiment.

Relation Between Phytoplankton Size-Structure and Potentially Explanatory Factors

The influence of environmental conditions on the size-structure of the phytoplankton community was explored using Redundancy analyses (RDA). The first two RDA axes explained 83.6% of the phytoplankton size-structure (**Table 3**). RDA1 was mainly influenced by PAR and zooplankton biomass, and RDA2 had high scores of zooplankton biomass and inorganic nitrogen forms (nitrate + nitrite) (**Figure 5**). The environmental conditions within the controls contributed to higher relative contributions of picophytoplankton and zooplankton biomass, while microphytoplankton dominated in the tM enriched mesocosms, where PAR was low and inorganic nutrients high.

Chlorophyll *a*, Total Phytoplankton Biomass and Chlorophyll *a* Content

In the controls the Chl *a* and total phytoplankton biomass showed an overall decreasing trend over time, with values that were 2–4 times lower at the end of the experiment than at the start (**Figures 6A,B**). In the tM enriched mesocosms, Chl *a* and total phytoplankton biomass decreased until the middle of the experiment and then slightly increased toward the end of the experiment (**Figures 6A,B**). The Chl *a* concentrations and total phytoplankton biomass were significantly lower in the tM$_H$ mesocosms compared to the other treatments (Tukey's, $p < 0.05$). During the second part of the experiment the average Chl *a* and total phytoplankton biomass were the lowest in the tM$_H$ mesocosms (∼1.1 μg l^{-1} and ∼15 μg C l^{-1}, respectively) (**Figures 7A,B**). Chl *a* concentration was positively

TABLE 2 | Dominating phytoplankton taxa, constituting >25% of the biomass in different size classes, at day 17 and 28 of the mesocosm experiment.

Size fraction	$Ctrl_L$		$Ctrl_H$		tM_L		tM_H	
	Day 17	**Day 28**	**Day 17**	**Day 28**	**Day 17**	**Day 28**	**Day 17**	**Day 28**
<2 µm	Picoeukaryotes	Picoeukaryotes	Picoeukaryotes	Picoeukaryotes	Picoeukaryotes	Picoeukaryotes	Picoeukaryotes	Picoeukaryotes
2–20 µm	Centrales unidentified *Plagioselmis prolonga*	*Pseudopedinella tricostata*	*Plagioselmis prolonga*	*Teleaulax* spp.	*Plagioselmis prolonga* *Pyramimonas* spp.	*Pyramimonas* spp. *Teleaulax* spp.	*Pyramimonas* spp.	*Pyramimonas* spp.
>20 µm	*Merismopedia warmingiana*	*Diatoma tenuis*	*Diatoma tenuis* *Merismopedia warmingiana*	*Mesodinium rubrum*	*Diatoma tenuis* *Mesodinium rubrum*	*Diatoma tenuis* *Synedra acus* var. *acus*	*Diatoma tenuis* *Monoraphidium contortum*	*Diatoma tenuis* *Synedra acus* var. *acus*

TABLE 3 | Variable loadings for the first and second axis of the RDA performed on biological and physicochemical data.

	Axis	
	1	**2**
Eigenvalues	0.811	0.025
Pseudo-canonical correlations	0.941	0.550
Cumulative percentage variance		
of response data	81.1	83.6
of fitted response data	96.9	99.9
Variables:		
Photosynthetically Active Radiation (PAR)	−0.862	0.132
Zooplankton	−0.761	−0.284
Nitrate + nitrite ($NO_3 + NO_2$)	0.545	−0.278
Phosphate (PO_4)	0.498	−0.110
Ammonium (NH_4)	0.486	−0.233

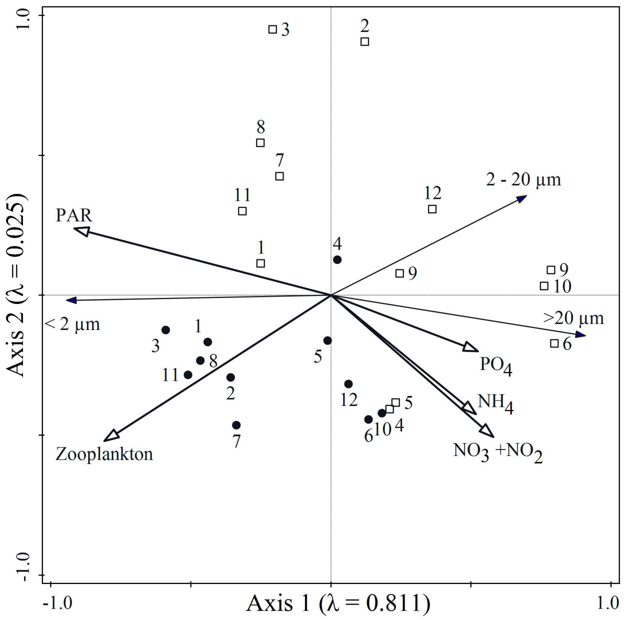

FIGURE 5 | Redundancy analysis (RDA) of factors influencing the size-structure of the phytoplankton community during the middle and end of the experiment. The distribution of pico- (<2 µm), nano- (2–20 µm) and micro- (>20 µm) phytoplankton were analyzed in relation to zooplankton biomass (Zooplankton), phosphate (PO_4), ammonium (NH_4), nitrate + nitrite ($NO_3 + NO_2$) and Photosynthetically Active Radiation (PAR). Numbers display mesocosm numbers (Ctr_L (1,2,7), Ctr_H (3,8,11), tM_L (4,5,12), tM_H (6,9,10), ●- Day 17; ☐ – Day 28).

correlated with ammonium while total phytoplankton biomass was negatively correlated with phosphorus (**Supplementary Table S1**). The Chl *a* content of the phytoplankton cells, measured as the Chl *a*:C ratio, was on average about 50% higher in the tM supplemented mesocosms than in the controls, largely due to increase phosphorus concentrations (**Figure 7C** and **Supplementary Table S1**).

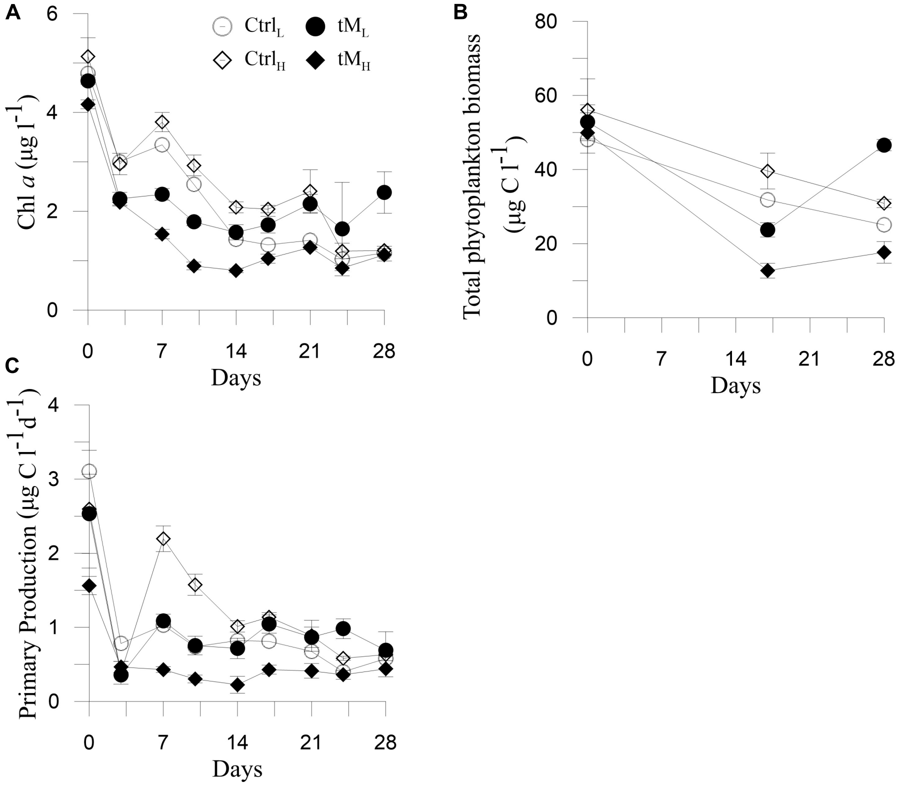

FIGURE 6 | Temporal variation of Chl *a* **(A)** modified from Traving et al. (2017), total phytoplankton biomass **(B)** and primary production **(C)**. Means ± standard error, *n* = 3.

Variation of Phytoplankton Primary Production and Photosynthetic Efficiency

Primary production ranged from 0.2 to 3.1 μg C l^{-1} d^{-1} during the experiment (**Figure 6C**). In the tM enriched mesocosms, primary production was significantly lower than in the controls (**Figures 6C**, **7D**) (Tukey's, $p < 0.01$). When the different treatments had taken effect, i.e., during the second half of the experiment, the low tM enrichment (tM_L) showed a positive effect on primary production compared to the control ($Ctrl_L$) (**Figure 7D**). In fact, the primary production was similar in the control ($Ctrl_H$) and tM enriched mesocosms (tM_L), while in the tM_H mesocosms the primary production was approximately half of that in the other treatments (**Figure 7D**). The photosynthetic efficiency, i.e., the PP:Chl *a* ratio was higher in the controls than in the tM supplemented mesocosms (0.57 ± 0.03 vs. 0.43 ± 0.02) (**Figure 7E**). PP and PP:Chl *a* ratio were negatively correlated with phosphate and positively with zooplankton biomass and ammonium (**Supplementary Table S1**).

Bacterial Biomass and Productivity

Bacterial biomass generally increased until the middle of the experiment in all treatments after which it sharply declined (**Figure 8A**). A significantly higher bacterial biomass was observed in tM_L than tM_H mesocosms (77.5 ± 7.0 vs. 64.8 ± 3.8 μg l^{-1}) (Tukey's, $p < 0.001$). Bacterial production ranged between 0.44 and 2.78 μg C l^{-1} d^{-1} and was on average 1.5 times lower in the $Ctrl_H$ treatment compared to the remaining treatments, with relatively stable values throughout the experiment (**Figure 8B**). In both tM treatments, bacterial production followed a similar trend as bacterial biomass (**Figure 8B**). Bacterial production in tM_H was significantly higher than in $Ctrl_H$ (Tukey's, $p < 0.01$). During the second part of the experiment, higher bacterial production was observed in tM addition treatments than in controls (**Figure 7F**). Bacterial biomass was positively correlated with zooplankton biomass and nitrate + nitrite concentration while bacterial production with ammonium (**Supplementary Table S1**).

Ciliates and Mesozooplankton Biomass

The ciliate biomass, which initially was 0.08 and 0.14 μg C l^{-1} in controls and tM mesocosms, slightly decreased in the middle of the experiment and then decreased to 0.04 and increased to 0.35 μg C l^{-1} by the end of the experiment, respectively (**Figure 8C**). A significant difference between tM treatments and their controls was observed (Tukey's, $p < 0.01$). Ciliate biomass was negatively correlated with phosphate, PAR and ammonium (**Supplementary Table S1**). Mesozooplankton biomass increased from the start to the middle of the experiment and then decreased toward the end of the experiment. Higher mesozooplankton

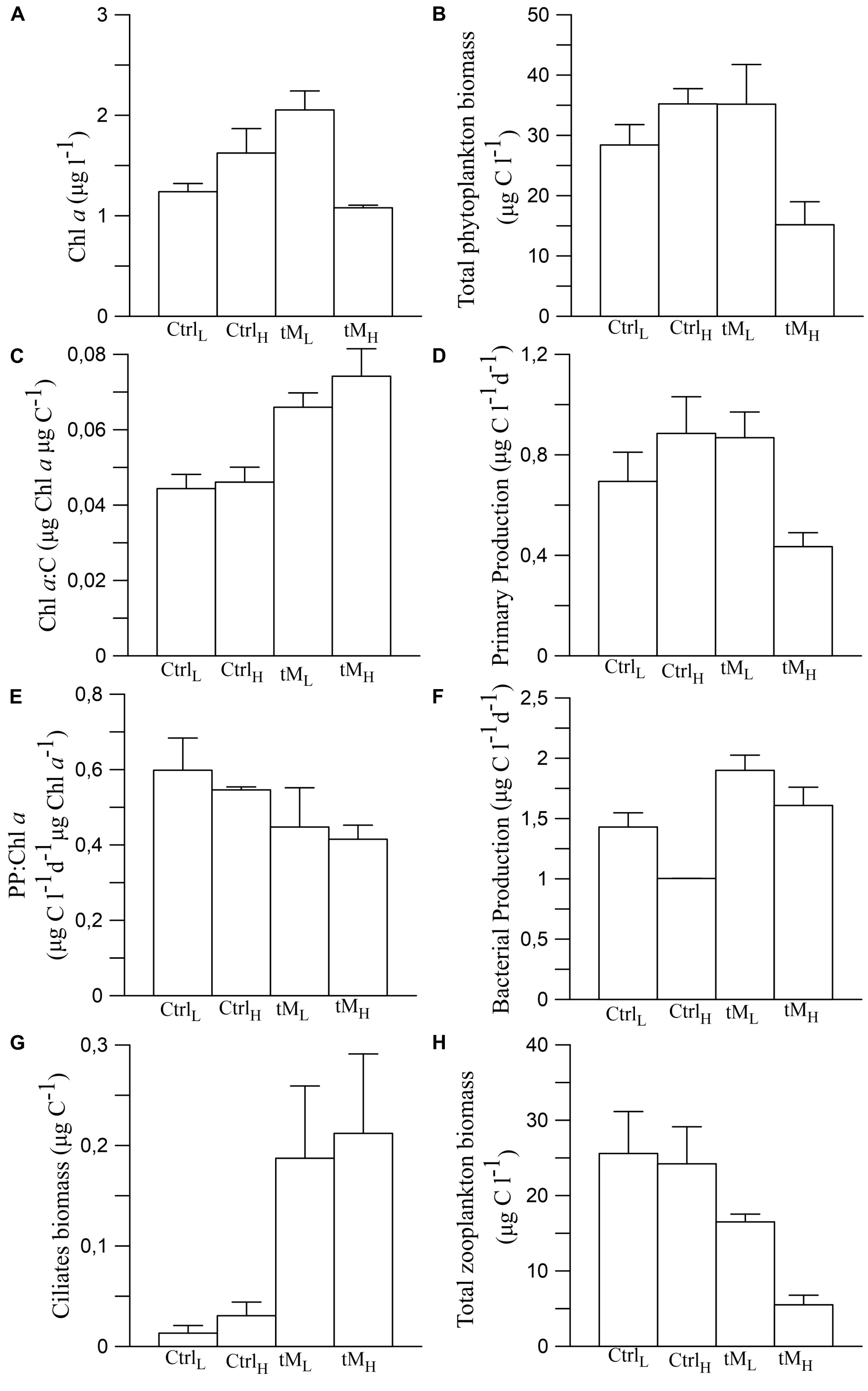

FIGURE 7 | Average Chl *a* **(A)**, total phytoplankton biomass **(B)**, Chl *a*:C **(C)**, primary production **(D)**, PP:Chl *a* **(E)**, bacterial production **(F)**, ciliate biomass **(G)**, and the zooplankton biomass **(H)** during the second part of the experiment (Day 17 and Day 28). Means ± standard error, $n = 2$.

biomass was observed in the controls than in tM treatments (19.7 ± 2.6 vs. 11.7 ± 1.6 μg C l^{-1}) (**Figure 8D**) (Tukey's, $p < 0.01$). During the second part of the experiment, ciliate biomass was higher in tM addition mesocosms, while the opposite trend was observed in relation to the zooplankton biomass (**Figures 7G,H**). Structural equation modeling (SEM) showed that DOC promoted the ciliate biomass (standardized path coefficient 0.74, $p < 0.05$), and was negatively correlated with primary production and zooplankton biomass (standardized path coefficient −0.41 and −0.75, $p < 0.05$, respectively) (**Figure 9**). The model indicated that DOC hampered the bacterial production, and that bacterial and primary production were positively correlated. Overall, the

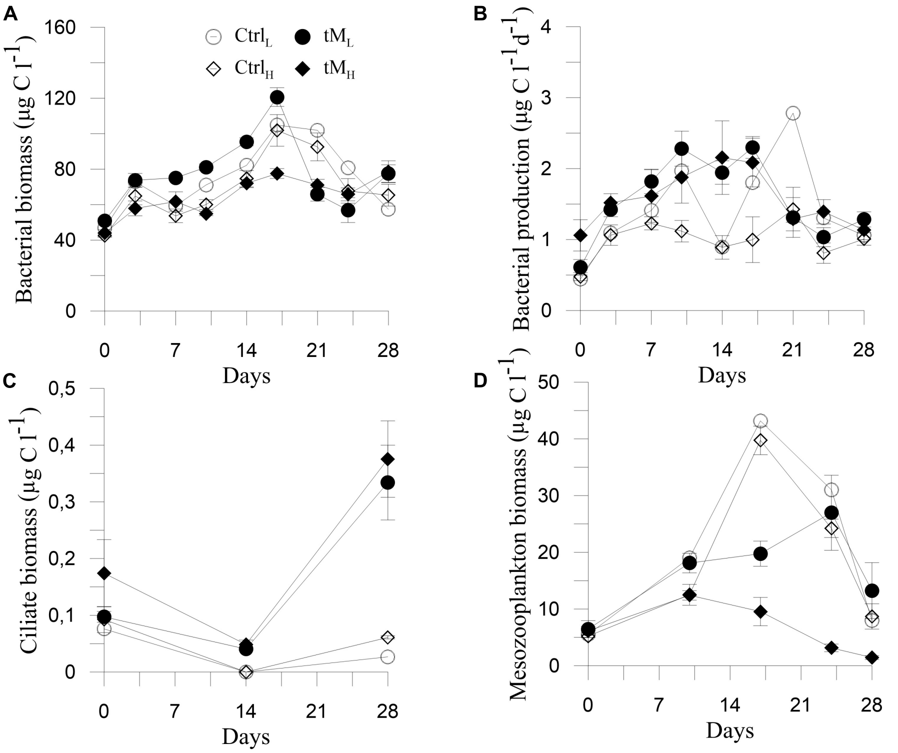

FIGURE 8 | Temporal variation of bacterial biomass **(A)**, bacterial production **(B)**, ciliate biomass **(C),** and mesozooplankton biomass **(D)**. Means ± standard error, *n* = 3.

SEM model showed a similar goodness of fit to the data (χ^2 = 0.40, *df* = 2, *p* = 0.82).

Mesozooplankton Community Composition

At the beginning of the experiment the zooplankton community was dominated by *Limnocalanus macrurus, Eurytemora affinis* and *Synchaeta* spp. in all treatments (**Figure 10**). On day 17, *L. macrurus* and *Bosmina coregoni maritima* made up on average ∼ 70 and ∼ 20% of the zooplankton biomass in the controls and ∼ 30 and ∼ 50% in the tM enriched treatments, respectively. At the end of the experiment, *B. coregoni maritima* dominated in the controls and tM$_L$ treatment, while *B. coregoni maritima* and *L. macrurus* contributed equally ∼ 30% of the zooplankton biomass in tM$_H$.

During the second part of the experiment, the relative contribution of *L. macrurus* was positively correlated with bacterial biomass (Spearman's ϱ = 0.60, $p < 0.01$) and the relative contribution of picophytoplankton (Spearman's ϱ = 0.49, $p < 0.05$), as well as negatively correlated with ciliate biomass (Spearman's ϱ = −0.54, $p < 0.01$) and the relative contribution of nanophytoplankton (Spearman's ϱ = −0.68, $p < 0.01$). The relative contribution of *E. affinis* was positively correlated with the relative contribution of microphytoplankton (Spearman's ϱ = 0.47, $p < 0.05$), while the relative contribution of *B. coregoni maritima* increased with the higher relative contribution of nanophytoplankton (Spearman's ϱ = 0.54, $p < 0.01$) and decreased with higher bacterial biomass (Spearman's ϱ = −0.46, $p < 0.05$).

DISCUSSION

In natural aquatic ecosystems, the phytoplankton communities are controlled both by bottom-up and top-down factors (Andersson et al., 1996; Gruner et al., 2008; Hulot et al., 2014). In our study, the inorganic nutrient availability and light level played large roles in shaping the phytoplankton community. Among these two factors, the inorganic nutrient levels were found to be more important for the phytoplankton species composition and size-structure than the light levels. In the tM enriched mesocosms the nitrogen and phosphorus concentrations were 2-6-fold higher than in the controls, and in these mesocosms the phytoplankton community was dominated by microphytoplankton. On the contrary, picophytoplankton dominated the phytoplankton community in the controls. The results are in accordance with the theory that small cells have a competitive advantage at low inorganic nutrient concentrations (Raven, 1998), and that large phytoplankton cells have lower affinity for nutrients but higher maximum uptake capacity per cell under nutrient-rich conditions. Thus, in our experiment, inorganic nutrients were likely more important than light attenuation in shaping the size-structure of the phytoplankton community. Additionally, Bacillariophyceae and

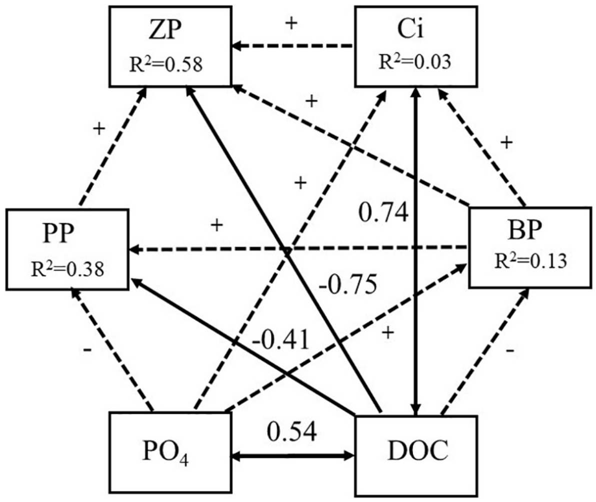

FIGURE 9 | Path diagram for structural equation model relating phosphate (PO_4) and dissolved organic carbon (DOC) to primary production (PP), bacterial production (BA), ciliate biomass (Ci) and zooplankton biomass (ZP) during the second part of the experiment (Day 17 and Day 28). Squared multiple correlation (R^2) in boxes indicate the percent of variance explained through the model. The numbers next to arrow are standardized regression coefficients of the SEM model. Solid black arrows represent significant path ($p < 0.05$) while dash arrows non-significant paths ($p > 0.05$). Plus or minus indicate relationship between variables.

picophytoplankton, prefer different inorganic nitrogen forms (Glibert and Berg, 2009; Glibert et al., 2016). Studies performed in river influenced estuaries or mesocosm experiments showed a positive correlation between the relative contribution of Bacillariophyceae and the proportion of NO_3 uptake while an increase in the picophytoplankton was related with NH_4 uptake (Glibert and Berg, 2009; Glibert et al., 2016).

The PAR levels were 2-12-fold higher in the controls than in the tM mesocosms (across the experiment), which in principle could have promoted small cells in the tM mesocosms. Picophytoplankton are more efficient in catching light at low light levels than large cells, due to their distribution of pigments along the outer cell membrane. The PAR levels were 4–33 μmol photon m^{-2} s^{-1} in the tM mesocosms, which would be below or near the photosynthetic saturation levels. A previous study performed in the same coastal area showed that pico- and nanophytoplankton photosynthesis saturates at ~20 μmol photon m^{-2} s^{-1}, while microphytoplankton require 100–150 μmol photon m^{-2} s^{-1} for photosynthesis saturation (Andersson et al., 1994). These light level thresholds may vary due to physiological adaptations of the phytoplankton, but it still indicates that photosynthesis was saturated in the controls (PAR ~50 μmol photon m^{-2} s^{-1}), on the edge of saturation in the tM$_L$ treatment, and light limited in tM$_H$. However, we can conclude that light levels are of lower priority for governing the phytoplankton cell sizes than the nutrient levels, as microphytoplankton dominated in the inorganic nutrient-rich low-light tM-mesocosms and picophytoplankton dominated in the low-inorganic nutrient and high-light control-mesocosms.

We hypothesized that the photosynthetic efficiency, measured as the primary production to Chl *a* ratio, would decrease in the tM enriched mesocosms due to "overproduction" of chlorophyll

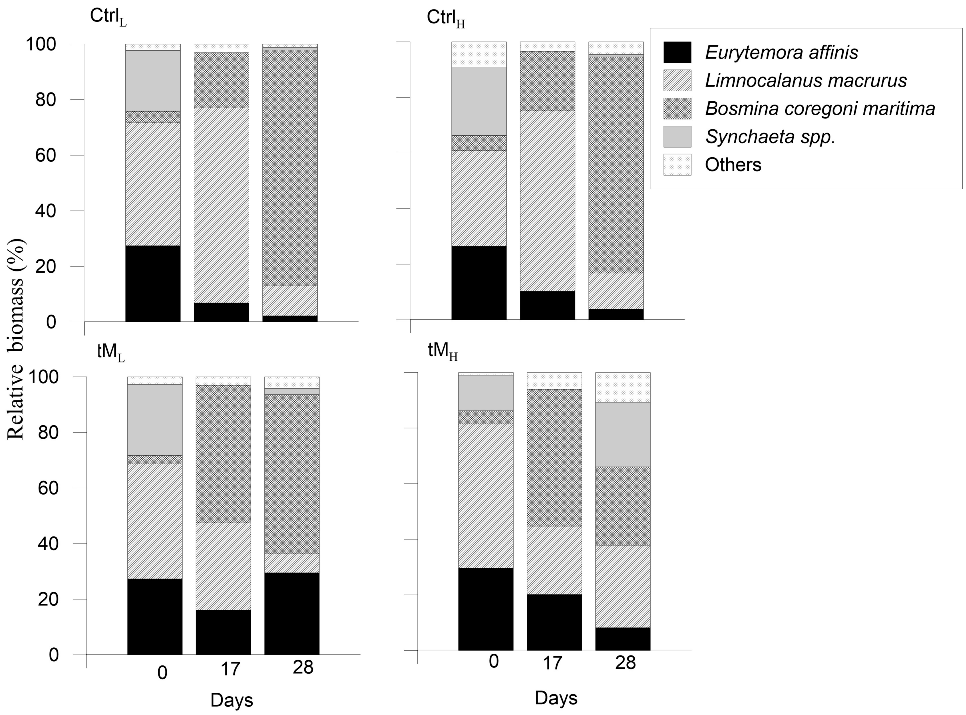

FIGURE 10 | Mesozooplankton taxonomic composition at the start, middle and end of the experiment (Day 0, Day 17, and Day 28) in all treatments.

to increase the light capture. This was indeed seen, even though there was a consecutive decrease of the photosynthetic efficiency from the low nutrient control to the high nutrient tM mesocosms (**Figure 7E**). Adjustment of the cell Chl *a* content is not only due to variations in the light level but also to other factors, such as alterations of the inorganic nutrient concentration (Geider et al., 1998; Staehr et al., 2002; Kirk, 2011). In fact, this is also what we observed in our experiment (**Figure 7E**). The Chl *a*:C ratios as well as the inorganic nutrient concentrations were lowest in the $\mathrm{Ctrl_L}$ treatment and highest in $\mathrm{tM_H}$. Additionally, the size-structure and taxonomic composition of the phytoplankton community have been shown to affect the cell Chl *a* content (Staehr et al., 2002). Smaller cells have higher Chl *a*:C ratios, due to larger surface-to-volume ratio and thus lower "self-shading" (Raven, 1998; Kirk, 2011). In our experiment a higher relative contribution of picophytoplankton was not followed by higher Chl *a*:C, suggesting that the higher chlorophyll content of the phytoplankton in the $\mathrm{tM_H}$ treatment was due to acclimation of larger cells rather than to changes in the phytoplankton size-structure.

The light levels were similar in the controls, while both the inorganic nutrient levels and Chl *a*:C ratio were slightly higher in the $\mathrm{Ctrl_H}$ than in the $\mathrm{Ctrl_L}$. This argues for a slightly higher role of inorganic nutrients than light, at least for the control mesocosms. High inorganic nutrient availability would allow the phytoplankton to allocate resources to build up their biomass and cell constituents including Chl *a*:C. Thus, in the tM-amended mesocosms light reduction in combination with high inorganic nutrient availability would drive the cells to produce higher amounts of chlorophyll.

Increased Chl *a* content of phytoplankton to maintain primary production at decreasing light levels was also a hypothesis of this experiment. This seems to be true in the low tM enriched mesocosms. In this treatment, the primary production was approximately as high as in the high nutrient control. However, the lowest primary production occurred in the high tM treatment. Under the higher level of tM addition the "overproduction" of Chl *a* did not help maintaining high primary production rates. If our experimental results also hold true in nature, then tM inflows causing DOC concentrations of $\sim$7–9 mg $\mathrm{l^{-1}}$ and humic substances concentrations exceeding 40 μg $\mathrm{l^{-1}}$, may be disadvantageous for coastal primary production. Of course, the effect would depend on the depth of the water column, but in coastal areas with a water depth of a couple of meters, tM inflows of such magnitudes would have a negative effect on primary production. However, our results also indicate that tM inflows can have a positive effect on coastal primary production if the tM carries nutrients to the recipient system and DOC and humic substances loads are not exceeded. In general, our experimental results are in agreement with an earlier field study, where Andersson et al. (2018) found that in the upper part of an estuary in the northern Baltic Sea river-borne tM had a hindering effect on primary production when the DOC concentration exceeded 6 mg $\mathrm{l^{-1}}$. Our results also match the proposed hump-shaped relationship between tM inflows to lake ecosystems and productivity (Seekell et al., 2015).

The SEM model provided a broad overview of the interactions taking place between major components of the food web and the major physicochemical drivers (phosphate and DOC). BP was identified as a positive pathway in relation to primary production, though likely the underlying interactions are more complex within these broad patterns reflecting the intricate balance between these biological components and common inorganic nutrient pools, and between the biological components themselves. In our study, both phytoplankton and heterotrophic bacterial growth depended on the same inorganic nutrient pool and phytoplankton were the major source of carbon for heterotrophs. Moreover, bacterial communities are also capable of releasing inorganic nutrients via the breakdown of organic matter, as was documented in this experiment (Traving et al., 2017), making the inorganic nutrient pool an even more critical factor, particularly in the tM treatments. DOC was identified as a major significant positive direct pathway for ciliate biomass, although a direct pathway via the microbial food web could not be confirmed. The SEM model showed also non-significant and negative pathway from DOC to BP, as well as significant and negative pathways from DOC to primary production and to zooplankton biomass. Thus, it is likely that the identified direct pathway from DOC to ciliate biomass overrode the measurable contribution of the microbial food web pathway since the tM additions were filtered through 90 μm mesh, likely providing a valuable source of particulate matter for ciliate biomass production. Though particulate matter was not measured in the experiment directly it was noted that the mesocosms receiving tM additions contained visible sedimentation by the end of the experiment and the particulate matter in question would have likely mirrored the DOC trends since the measured DOC values reflect the additions of tM (soil extract) that took place over the duration of the experiment.

In our experiment, picophytoplankton were positively correlated with mesozooplankton and negatively with ciliates, indicating that grazing exerted by higher trophic levels decreased predation pressure on the small cells (bacteria and picophytoplankton). Further, the proportion of nano- and microphytoplankton showed negative relationships with mesozooplankton, which were positively correlated with ciliates, as a consequence of the trophic cascade. This dynamic was observed mostly at the middle of the experiment, and did not differ markedly between the treatments, indicating that it was likely a general experimental effect, and not due to the addition of tM. In the Baltic Sea, field studies as well as mesocosm experiments have shown that the phytoplankton community is more driven by bottom-up than by top-down factors (Lagus et al., 2004; Legrand et al., 2015). Though mesozooplankton influenced the temporal phytoplankton dynamics, inorganic nutrients were the most important variables shaping phytoplankton composition and size-structure.

The mesozooplankton community seemed to be tightly linked to the taxonomic composition and size-structure of the phytoplankton community. Toward the end of the experiment, the cladoceran *Bosmina coregoni maritima* dominated the mesozooplankton community in the controls and the $\mathrm{tM_L}$ treatment. This zooplankton species is a filter-feeder known to feed on small prey, pico- and nanophytoplankton (Bleiwas and Stokes, 1985; Korosi et al., 2013) and in our experiment *B. coregoni maritima* was observed to increase with the higher relative contribution of nanophytoplankton and decreased with higher bacterial biomass. The zooplankton community likely adapted to the phytoplankton size-structure, as in the controls and the tM_L treatment the pico- and nanophytoplankton constituted 50–95% of the total phytoplankton biomass. By the end of the experiment the zooplankton community in the tM_H treatment was equally distributed between *Synchaeta* spp., *B. coregoni maritima* and *Limnocalanus macrurus*. *L. macrurus* was the largest zooplankton taxa ($>1000\ \mu m$) in the system, and it feeds on smaller zooplankton such as copepodites, nauplii and on larger phytoplankton (Warren, 1985). *L. macrurus* was positively correlated with bacterial biomass, the relative contribution of picophytoplankton and negatively with ciliate biomass and the relative contribution of nanophytoplankton. It is thus possible that *L. macrurus* fed on copepodites of *Eurytemora affinis*, which decreased toward the end of the experiment, as well as on *B. coregoni maritima* and other zooplankters. This could have been driven by high abundances of large diatoms that nurtured *Synchaeta* spp. and other zooplankton groups, which may have benefited from the dominance of large microphytoplankton. Taken together, it seems as if the composition of the mesozooplankton community was driven by phytoplankton size-structure, which in turn was governed by the inorganic nutrient availability. Furthermore, filter feeders may also have been supported by increased bacterial production and biomass in the tM treatments.

CONCLUSION

In conclusion, our study shows that phytoplankton size-structure and primary production were governed foremost by inorganic nutrients, including those associated with tM inputs, with light availability or grazing being secondary drivers. Higher tM promoted microphytoplankton, while the importance of picophytoplankton increased under nutrient limitation. Heterotrophic bacterial growth was tightly coupled with phytoplankton produced carbon. Furthermore, phytoplankton cells acclimated to lower light availability (e.g., moderate addition of tM) by increasing their cell chlorophyll content, allowing them to maintain photosynthetic efficiency at a similar level to the control conditions. This study demonstrates how variable the phytoplankton Chl *a*:C in coastal areas can be due to varying river inputs of freshwater, causing changes in the light and nutrient availability.

This study strongly indicates that an increase in river runoff, as predicted in future climate change scenarios for the region, would affect size-structure and production of phytoplankton depending on the amount of organic and inorganic nutrients associated with tM delivered to the ecosystem. Our study demonstrates that organic nutrients brought by the tM can be transformed to inorganic forms and utilized as growth substrate by coastal phytoplankton. The potential for climate related changes to have differing routes toward impacting higher trophic levels and ecosystem function are highlighted, and the potential for tipping points in the system due to reaching a critical load or light inhibition warrant further research.

DATA AVAILABILITY STATEMENT

The datasets generated for this study can be found in the Data Matrix.

ETHICS STATEMENT

Experiments, methods of sacrifices and design of fish sampling strategies in this study comply with the current laws of Sweden and were approved by the Regional Ethics Committee of the Swedish National Board for Laboratory Animals in Umeå (CFN, license no. A24-11).

AUTHOR CONTRIBUTIONS

All authors designed and performed the experiment. JP and AA took the lead writing the manuscript, and all authors contributed.

FUNDING

Access to the facility and project support was provided by the European Union Seventh Framework Program (FP7/2007-2013) under grant agreement 228224, MESOAQUA. Additionally, this study was supported by the Marine Strategic Research Environment EcoChange (the Swedish Research Council Formas) and the research program WATERS (the Swedish Agency for Marine and Water Management and the Swedish Environmental Protection Agency).

ACKNOWLEDGMENTS

We are grateful to the staff at the Umeå Marine Sciences Centre for their expert assistance, in particular Henrik Larsson for chemical analyses and mesocosm maintenance. We also appreciate the assistance given by Rickard Degerman, Ruaridh Hägglund, Fernanda Helena Bosco de Miranda Vasconcelos, Fidel Chiriboga, and Sachia J. Traving during the project, and thank Dr. Iveta Jurgensone for phytoplankton analysis and Dr. Liudmyla Guleikova for zooplankton analysis.

SUPPLEMENTARY MATERIAL

The Supplementary Material for this article can be found online at: https://www.frontiersin.org/articles/10.3389/fmars.2020.00080/full#supplementary-material

REFERENCES

Andersson, A., Brugel, S., Paczkowska, J., Figueroa, D., Rowe, O., Kratzer, S., et al. (2018). Influence of allochthonous dissolved organic matter on pelagic basal production in a northerly estuary. *Estuar. Coast. Shelf Sci.* 204, 225–235. doi: 10.1016/j.ecss.2018.02.032

Andersson, A., Haecky, P., and Hagström, A. (1994). Effect of temperature and light on the growth of micro- nano- and picoplankton: impact on algal succession. *Mar. Biol.* 120, 511–520. doi: 10.1007/bf00350071

Andersson, A., Hajdu, S., Haecky, P., Kuparinen, J., and Wikner, J. (1996). Succession and growth limitation of phytoplankton in the Gulf of Bothnia (Baltic Sea). *Mar. Biol.* 126, 791–801. doi: 10.1007/bf00351346

Andersson, A., Jurgensone, I., Rowe, O. F., Simonelli, P., Bignert, A., Lundberg, E., et al. (2013). Can humic water discharge counteract eutrophication in coastal waters? *PLoS One* 8:61293. doi: 10.1371/journal.pone.00061293

Andersson, A., Meier, H. E. M., Ripszam, M., Rowe, O., Wikner, J., Haglund, P., et al. (2015). Projected future climate change and Baltic Sea ecosystem management. *Ambio* 44(Suppl. 3), 345–356. doi: 10.1007/s13280-015-0654-8

Asmala, E., Autio, R., Kaartokallio, H., Pitkanen, L., Stedmon, C. A., and Thomas, D. N. (2013). Bioavailability of riverine dissolved organic matter in three Baltic Sea estuaries and the effect of catchment land use. *Biogeosciences* 10, 6969–6986. doi: 10.5194/bg-10-6969-2013

Asmala, E., Haraguchi, L., Jakobsen, H. H., Massicotte, P., and Carstensen, J. (2018). Nutrient availability as major driver of phytoplankton-derived dissolved organic matter transformation in coastal environment. *Biogeochemistry* 137, 93–104. doi: 10.1007/s10533-017-0403-0

Berggren, M., Ström, L., Laudon, H., Karlsson, J., Jonsson, A., Giesler, R., et al. (2010). Lake secondary production fueled by rapid transfer of low molecular weight organic carbon from terrestrial sources to aquatic consumers. *Ecol. Lett.* 13, 870–880. doi: 10.1111/j.1461-0248.2010.01483.x

Berglund, J., Müren, U., Båmstedt, U., and Andersson, A. (2007). Efficiency of a phytoplankton-based and a bacteria-based food web in a pelagic marine system. *Limnol. Oceanogr.* 52, 121–131. doi: 10.4319/lo.2007.52.1.0121

Bleiwas, A. H., and Stokes, P. M. (1985). Collection of large and small food particles by Bosmina. *Limnol. Oceanogr.* 30, 1090–1092. doi: 10.4319/lo.1985.30.5.1090

Carlsson, P., Graneli, E., Tester, P., and Boni, L. (1995). Influences of riverine humic substances on bacteria, protozoa, phytoplankton, and copepods in a coastal plankton community. *Mar. Ecol. Prog Ser.* 127, 213–221. doi: 10.3354/meps127213

Chust, G., Allen, J. I., Bopp, L., Schrum, C., Holt, J., Tsiaras, K., et al. (2014). Biomass changes and trophic amplification of plankton in a warmer ocean. *Glob. Chang. Biol.* 20, 2124–2139. doi: 10.1111/gcb.12562

Cowles, T. J., Olson, R. J., and Chisholm, S. W. (1988). Food selection by copepods: discrimination on the basis of food quality. *Mar. Biol.* 100, 41–49. doi: 10.1007/bf00392953

Dagg, M., Benner, R., Lohrenz, S., and Lawrence, D. (2004). Transformation of dissolved and particulate materials on continental shelves influenced by large rivers: plume processes. *Continent. Shelf Res.* 24, 833–858. doi: 10.1016/j.csr.2004.02.003

Dorado, S., Booe, T., Steichen, J., McInnes, A. S., Windham, R., Shepard, A., et al. (2015). Towards an understanding of the interactions between freshwater inflows and phytoplankton communities in a subtropical estuary in the Gulf of Mexico. *PLoS One* 10:e0130931. doi: 10.1371/journal.pone.0130931

Duarte, C. M., Agusti, S., and Agawin, N. S. R. (2000). Response of a mediterranean phytoplankton community to increased nutrient inputs: a mesocosm experiment. *Mar. Ecol. Prog. Ser.* 195, 61–70. doi: 10.3354/meps195061

Dubinsky, Z., and Stambler, N. (2009). Photoacclimation processes in phytoplankton: mechanisms, consequences, and applications. *Aquat. Microb. Ecol.* 56:2009.

Faithfull, C., Huss, M., Vrede, T., Karlsson, J., and Bergstrom, A. K. (2012). Transfer of bacterial production based on labile carbon to higher trophic levels in an oligotrophic pelagic system. *Can. J. Fish. Aquat. Sci.* 69, 85–93. doi: 10.1139/f2011-142

Falkowski, P. G., Katz, M. E., Knoll, A. H., Quigg, A., Raven, J. A., Schofield, O., et al. (2004). The evolutionary history of eukaryotic phytoplankton. *Science* 305, 354–360.

Field, C. B., Behrenfeld, M. J., Randerson, J. T., and Falkowski, P. (1998). Primary production of the biosphere: integrating terrestrial and oceanic components. *Science* 281, 237–240. doi: 10.1126/science.281.5374.237

Fuhrman, J. A., and Azam, F. (1982). Thymidine incorporation as a measure of heterotrophic bacterioplankton production in marine surface waters: evaluation and field results. *Mar. Biol.* 66, 109–120. doi: 10.1007/bf00397184

Gargas, E. (1975). *A Manual for Phytoplankton Primary Production Studies in the Baltic. The Baltic Marine Biologists, Publication No. 2*. Hørsholm: Water Quality Institute.

Geider, R. J., Macintyre, H. L., and Kana, T. M. (1998). A dynamic regulatory model of phytoplanktonic acclimation to light, nutrients, and temperature. *Limnol. Oceanogr.* 43, 679–694. doi: 10.4319/lo.1998.43.4.0679

Glibert, P. M., and Berg, G. M. (2009). "Nitrogen form, fate and phytoplankton composition," in *Experimental Ecosystems and Scale: Tools for Understanding and Managing Coastal Ecosystems*, eds V. S. Kennedy, W. M. Kemp, J. E. Peterson, and W. C. Dennison, (Cham: Springer), 183–189.

Glibert, P. M., Wilkerson, F. P., Dugdale, R. C., Raven, J. A., Dupont, C. L., Leavitt, P. R., et al. (2016). Pluses and minuses of ammonium and nitrate uptake and assimilation by phytoplankton and implications for productivity and community composition, with emphasis on nitrogen-enriched conditions. *Limnol. Oceanogr.* 61, 165–197. doi: 10.1002/lno.10203

Grasshoff, K., Ehrhardt, M., and Kremling, K. (1983). *Methods of Seawater Analysis, 2nd Revised and Extended Version*. Weinheim: Verlag Chemie.

Grubisic, L. M., Brutemark, A., Weyhenmeyer, G. A., Wikner, J., Båmstedt, U., and Bertilsson, S. (2012). Effects of stratification depth and dissolved organic matter on brackish bacterioplankton communities. *Mar. Ecol. Prog. Ser.* 453, 37–48. doi: 10.3354/meps09634

Gruner, D. S., Smith, J. E., Seabloom, E. W., Sandin, S. A., Ngai, J. T., Hillebrand, H., et al. (2008). A cross-system synthesis of consumer and nutrient resource control on producer biomass. *Ecol. Lett.* 11, 740–755. doi: 10.1111/j.1461-0248.2008.01192.x

Hägg, H. E., Humborg, C., Morth, C. M., Medina, M. R., and Wulff, F. (2010). Scenario analysis on protein consumption and climate change effects on riverine N export to the Baltic Sea. *Environ. Sci. Technol.* 44, 2379–2385. doi: 10.1021/es902632p

Hällfors, G. (2004). *Checklist of Baltic Sea phytoplankton Species*. Nairobi: United Nations Environment Programme.

Halsey, K. H., and Jones, B. M. (2015). Phytoplankton strategies for photosynthetic energy allocation. *Annu. Rev. Mar. Sci.* 7, 265–297. doi: 10.1146/annurev-marine-010814-015813

Hambright, K. D., Hairston, N. G. Jr., Schaffner, W. R., and Howarth, R. W. (2007). Grazer control of nitrogen fixation: synergisms in the feeding ecology of two freshwater crustaceans. *Fundam. Appl. Limnol.* 170, 89–101. doi: 10.1127/1863-9135/2007/0170-0089

Hernroth, L. (1985). Recommendations on methods for marine biological studies in the Baltic. Mesozooplankton biomass assessment. *Balt. Mar. Biol.* 10, 1–32.

Hoge, F. E., Vodacek, A., and Blough, N. V. (1993). Inherent optical properties of the ocean: retrieval of the absorption coefficient of chromophoric dissolved organic matter from airborne laser spectral fluorescence measurements. *Limnol. Oceanogr.* 38, 1394–1402. doi: 10.1364/AO.34.007032

Hulot, F. D., Lacroix, G., and Loreau, M. (2014). Differential responses of size-based functional groups to bottom-up and top-down perturbations in pelagic food webs: a meta-analysis. *Oikos* 123, 1291–1300. doi: 10.1111/oik.01116

Jónasdóttir, S. H. (2019). Fatty acid profiles and production in marine phytoplankton. *Mar. Drugs* 17:151. doi: 10.3390/md17030151

Kaartokallio, H., Asmala, E., Autio, R., and Thomas, D. N. (2016). Bacterial production, abundance and cell properties in boreal estuaries: relation to dissolved organic matter quantity and quality. *Aquat. Sci.* 78, 525–540. doi: 10.1007/s00027-015-0449-9

Kirk, J. T. O. (2011). *Light and Photosynthesis in Aquatic Ecosystems*. Cambridge: Cambridge University Press.

Kissman, C. E. H., Williamson, C. E., Rose, K. C., and Saros, J. E. (2013). Response of phytoplankton in an alpine lake to inputs of dissolved organic matter through nutrient enrichment and trophic forcing. *Limnol. Oceanogr.* 58, 867–880. doi: 10.4319/lo.2013.58.3.0867

Klug, J. L. (2002). Positive and negative effects of allochthonous dissolved organic matter and inorganic nutrients on phytoplankton growth. *Can. J. Fish. Aquat. Sci.* 59, 85–95. doi: 10.1139/f01-194

Korosi, J. B., Kurek, J., and Smol, J. P. (2013). A review on utilizing bosmina size structure archived in lake sediments to infer historic shifts in predation regimes. *J. Plankton Res.* 35, 444–460. doi: 10.1093/plankt/fbt007

Lagus, A., Suomela, J., Weithoff, G., Heikkila, K., Helminen, H., and Sipura, J. (2004). Species-specific differences in phytoplankton responses to N and P enrichments and the N: P ratio in the Archipelago Sea, northern Baltic Sea. *J. Plankton Res.* 26, 779–798. doi: 10.1093/plankt/fbh070

Lee, S., and Fuhrman, J. (1987). Relationship between biovolume and biomass of naturally derived bacterioplankton. *Appl. Environ. Microbiol.* 53, 1298–1303. doi: 10.1128/aem.53.6.1298-1303.1987

Lefébure, R., Degerman, R., Andersson, A., Larsson, S., Eriksson, L. O., Båmstedt, U., et al. (2013). Impacts of elevated terrestrial nutrient loads and temperature on pelagic food-web efficiency and fish production. *Glob. Chang. Biol.* 19, 1358–1372. doi: 10.1111/gcb.12134

Legendre, L., and Rassoulzadegan, F. (1995). Plankton and nutrient dynamics in marine waters. *Ophelia* 41, 153–172. doi: 10.1080/00785236.1995.10422042

Legrand, C., Fridolfsson, E., Bertos-Fortis, M., Lindehoff, E., Larsson, P., Pinhassi, J., et al. (2015). Microbial production in coastal and offshore food webs of the changing Baltic Sea. *Ambio* 44(Suppl. 3), 427–438.

Marañón, E. (2015). Cell size as a key determinant of phytoplankton metabolism and community structure. *Ann. Rev. Mar. Sci.* 7, 241–264. doi: 10.1146/annurev-marine-010814-015955

Marie, D., Simon, N., and Vaulot, D. (2005). "Phytoplankton cell counting by flow cytometry," in *Algal Culturing Techniques*, ed. R. A. Andersen, (San Diego: Academic Press), 253–267. doi: 10.1016/b978-012088426-1/50018-4

Markager, S. (1993). Light absorption and quantum yield for growth in 5 species of marine macroalgae. *J. Phycol.* 29, 54–63. doi: 10.1111/j.1529-8817.1993.tb00279.x

Masotti, I., Aparicio-Rizzo, P., Yevenes, M., Garreaud, R., Belmar, L., and Farías, L. (2018). The influence of river discharge on nutrient export and phytoplankton biomass off the Central Chile coast (33°-37°S). Seasonal cycle and interannual variability. In special issue marine microbiome and biogeochemical cycles in marine productive areas. *Front. Mar. Sci.* 5:423. doi: 10.3389/fmars.2018.00423

Meier, H. E. M., Muller-Karulis, B., Andersson, H. C., Dieterich, C., Eilola, K., Gustafsson, B. G., et al. (2012). Impact of climate change on ecological quality indicators and biogeochemical fluxes in the Baltic Sea: a multi-model ensemble study. *Ambio* 41, 558–573. doi: 10.1007/s13280-012-0320-3

Menden-Deuer, S., and Lessard, E. J. (2000). Carbon to volume relationships for dinoflagellates, diatoms, and other protist plankton. *Limnol. Oceanogr.* 45, 569–579. doi: 10.4319/lo.2000.45.3.0569

Meunier, C. L., Boersma, M., Wiltshire, K. H., and Malzahn, A. M. (2016). Zooplankton eat what they need: copepod selective feeding and potential consequences for marine systems. *Oikos* 125, 50–58. doi: 10.1111/oik.02072

Nordbäck, J., Lundberg, E., and Christie, W. W. (1998). Separation of lipid classes from marine particulate material by HPLC on a polyvinyl alcohol-bonded stationary phase using dual-channel evaporative light-scattering detection. *Mar. Chem.* 60, 165–175. doi: 10.1016/s0304-4203(97)00109-6

Olenina, I., Hajdu, S., Edler, L., Andersson, A., Wasmund, N., Busch, S., et al. (2006). Biovolumes and size-classes of phytoplankton in the Baltic Sea. *HELCOM Balt. Sea Environ. Proc.* 106:144.

Peltomaa, E. L., Aalto, S. L., Vuorio, K. M., and Taipale, S. J. (2017). The importance of phytoplankton biomolecule availability for secondary production. *Front. Ecol. Evol* 5:128. doi: 10.3389/fevo.2017.00128

Penna, N., Capellacci, S., and Ricci, F. (2004). The influence of the Po River discharge on phytoplankton bloom dynamics along the coastline of Pesaro (Italy) in the Adriatic Sea. *Mar. Pollut. Bull.* 48, 321–326. doi: 10.1016/j.marpolbul.2003.08.007

Rasconi, S., Gall, A., Winter, K., and Kainz, M. J. (2015). Increasing water temperature triggers dominance of small freshwater plankton. *PLoS One* 10:e0140449. doi: 10.1371/journal.pone.0140449

Raven, J. A. (1998). The twelfth tansley lecture. small is beautiful: the picophytoplankton. *Funct. Ecol.* 12, 503–513. doi: 10.1046/j.1365-2435.1998.00233.x

Riemann, B. (1985). Potential importance of fish predation and zooplankton grazing on natural populations of freshwater bacteria. *Appl. Environ. Microbiol.* 50, 187–193. doi: 10.1128/aem.50.2.187-193.1985

Roelke, D. L., Li, H. P., Hayden, N. J., Miller, C. J., Davis, S. E., Quigg, A., et al. (2013). Co-occurring and opposing freshwater inflow effects on phytoplankton biomass, productivity and community composition of Galveston Bay, USA. *Mar. Ecol. Prog. Ser.* 477, 61–76. doi: 10.3354/meps10182

Sanders, R. W., Caron, D. A., and Berninger, U. G. (1992). Relationships between bacteria and heterotrophic nanoplankton in marine and fresh waters: an inter-ecosystem comparison. *Mar. Ecol. Prog. Ser.* 86, 1–14. doi: 10.3354/meps086001

Schatz, G. S., and McCauley, E. (2007). Foraging behavior by Daphnia in stoichiometric gradients of food quality. *Oecologia* 153, 1021–1030. doi: 10.1007/s00442-007-0793-0

Schweitzer, B., and Simon, M. (1995). Growth limitation of planktonic bacteria in a large mesotrophic lake. *Microb. Ecol.* 30, 89–104. doi: 10.1007/BF00184516

Seekell, D. A., Lapierre, J. F., Ask, J., Bergstrom, A. K., Deininger, A., Rodriguez, P., et al. (2015). The influence of dissolved organic carbon on primary production in northern lakes. *Limnol. Oceanogr.* 60, 1276–1285. doi: 10.1002/lno.10096

Shangguan, Y., Glibert, P. M., Alexander, J. A., Madden, C. J., and Mursako, S. (2017a). Nutrients and phytoplankton in semienclosed lagoon systems in Florida Bay and their responses to changes in flow from Everglades restoration. *Limnol. Oceanogr.* 62, 327–347.

Shangguan, Y., Glibert, P. M., Alexander, J. A., Madden, C. J., and Murasko, S. (2017b). Phytoplankton assemblage response to changing nutrients in Florida Bay: results of mesocosm studies. *J. Exp. Mar. Biol. Ecol.* 494, 38–53. doi: 10.1016/j.jembe.2017.05.006

Sommer, U., Stibor, H., Katechakis, A., Sommer, F., and Hansen, T. (2002). Pelagic food web configurations at different levels of nutrient richness and their implications for the ratio fish production: primary production. *Hydrobiologia* 484, 11–20. doi: 10.1007/978-94-017-3190-4_2

Staehr, P. A., Henriksen, P., and Markager, S. (2002). Photoacclimation of four marine phytoplankton species to irradiance and nutrient availability. *Mar. Ecol. Prog. Ser.* 238, 47–59. doi: 10.3354/meps238047

Straile, D. (1997). Gross growth efficiencies of protozoan and metazoan zooplankton and their dependence on food concentration, predator-prey weight ratio, and taxonomic group. *Limnol. Oceanogr.* 42, 1375–1385. doi: 10.4319/lo.1997.42.6.1375

Swarbrick, V. J., Simpson, G. L., Glibert, P. M., and Leavitt, P. R. (2019). Differential stimulation and suppression of phytoplankton growth by ammonium enrichment in eutrophic hardwater lakes over 16 years. *Limnol. Oceanogr.* 64, 130–149.

Tikkanen, T., and Willen, T. (1992). *Phytoplankton Flora*. Solna: The Swedish Environmental Protection Agency.

Traving, S. J., Jakobsen, N. M., Sorensen, H., Dinasquet, J., Stedmon, C. A., Andersson, A., et al. (2017). The effect of increased of increase loads of dissolved organic matter on estuarine microbial community composition and function. *Front. Microbiol.* 8:351. doi: 10.3389/fmicb.2017.00351

Utermöhl, H. (1958). Zur vervollkommnung der quantitativen phytoplankton-methodik. *Verh. Int. Ver. Theor. Angew. Limnol.* 9, 1–38. doi: 10.1080/05384680.1958.11904091

Vrede, K. (1999). Effects of inorganic nutrients and zooplankton on the growth of heterotrophic bacterioplankton – enclosure experiments in an oligotrophic clearwater lake. *Aquat. Microb. Ecol.* 18, 133–144. doi: 10.3354/ame018133

Walve, J., and Larsson, U. (1999). Carbon, nitrogen and phosphorus stoichiometry of crustacean zooplankton in the Baltic Sea: implications for nutrient recycling. *J. Plankton Res.* 21, 2309–2321. doi: 10.1093/plankt/21.12.2309

Warren, G. J. (1985). Predaceous feeding habits of *Limnocalanus macrurus*. *J. Plankton Res.* 7, 537–552. doi: 10.1093/plankt/7.4.537

Wasmund, N. (2002). "Harmful algal blooms in coastal waters of the south-eastern Baltic Sea," in *Baltic Coastal Ecosystems*, eds G. Schernewski, and U. Schiewer, (Berlin: Springer), 93–116. doi: 10.1007/978-3-662-04769-9_8

Wikner, J., and Hagström, A. (1999). Bacterioplankton intra-annual variability: importance of hydrography and competition. *Aquat. Microb. Ecol.* 20, 245–260. doi: 10.3354/ame020245

Conflict of Interest: The authors declare that the research was conducted in the absence of any commercial or financial relationships that could be construed as a potential conflict of interest.

frontiers
in Marine Science

ORIGINAL RESEARCH
published: 22 April 2020
doi: 10.3389/fmars.2020.00248

Hurricanes Accelerate Dissolved Organic Carbon Cycling in Coastal Ecosystems

Ge Yan[1,2]*, Jessica M. Labonté[3], Antonietta Quigg[3,4] and Karl Kaiser[1,4]*

[1] Department of Marine and Coastal Environmental Science, Texas A&M University at Galveston, Galveston, TX, United States, [2] Institute of Deep-Sea Science and Engineering, Chinese Academy of Sciences, Sanya, China, [3] Department of Marine Biology, Texas A&M University at Galveston, Galveston, TX, United States, [4] Department of Oceanography, Texas A&M University, College Station, TX, United States

Extreme weather events such as tropical storms and hurricanes deliver large amounts of freshwater (stormwater and river discharge) and associated dissolved organic carbon (DOC) to estuaries and the coastal ocean, affecting water quality, and carbon budgets. Hurricane Harvey produced an unprecedented 1000-year flood event in 2017 that inundated the heavily urbanized and industrialized Houston/Galveston region (TX, United States). Within a week, storm-associated floodwater delivered 87 ± 18 Gg of terrigenous dissolved organic carbon (tDOC) to Galveston Bay and the Gulf of Mexico continental shelves. In situ decay constants of 8.75–28.33 year^{-1} resulted in the biomineralization of ~70% of tDOC within 1 month of discharge from the flood plain. The high removal efficiency of tDOC was linked to a diverse microbial community capable of degrading a wide repertoire of dissolved organic matter (DOM), and suggested hurricane-induced flood events affect net CO_2 exchange and nutrient budgets in estuarine watersheds and coastal seas.

Keywords: terrigenous dissolved organic carbon, Hurricane Harvey, Galveston Bay, lignin phenols, mineralization, coastal carbon cycle, estuary

Edited by:
Christopher Osburn,
North Carolina State University,
United States

Reviewed by:
Wei-dong Zhai,
Shandong University, China
Yihua Cai,
Xiamen University, China

****Correspondence:***
Ge Yan
yange00544@gmail.com
Karl Kaiser
kaiserk@tamu.edu;
kaiserk@tamug.edu

Specialty section:
This article was submitted to
Marine Biogeochemistry,
a section of the journal
Frontiers in Marine Science

Received: *05 August 2019*
Accepted: *30 March 2020*
Published: *22 April 2020*

Citation:
Yan G, Labonté JM, Quigg A and Kaiser K (2020) Hurricanes Accelerate Dissolved Organic Carbon Cycling in Coastal Ecosystems.
Front. Mar. Sci. 7:248.
doi: 10.3389/fmars.2020.00248

INTRODUCTION

Coastal zones connect land and ocean ecosystems and play an important role in the global carbon cycle (Bauer et al., 2013; Regnier et al., 2013). Shelf and shallow water regions together with tidal wetlands are responsible for ~1/3 of the ocean's entire carbon burial (Duarte et al., 2005). Coastal zones are also prodigious CO_2 outgassing regions (0.1–0.4 Pg year^{-1}), as rivers deliver vast stores of terrigenous organic matter to estuaries and the ocean that are efficiently mineralized (Bianchi et al., 2013; Najjar et al., 2018). Further, sun-lit shallow surface waters contribute 10–30% of ocean primary production, and feed productive biological habitats and fisheries (Najjar et al., 2018).

At the same time, these ecologically sensitive ecosystems have undergone profound changes experiencing heavy urbanization and industrialization over the last century (McGrane et al., 2016; Freeman et al., 2019). By 2100, more than 50% of the world's population will live within proximity of the coast accelerating pressure on biogeochemical processes, water quality, and ecosystem services (Neumann et al., 2015). These future changes and emerging issues in urban coastal systems are amplified by sea-level rise and enhanced storm activity. In some regions, including the Gulf of Mexico, subsidence and erosion will exacerbate the negative consequences along coast zones.

Extreme weather events, such as tropical storms and hurricanes, induce extensive precipitation, and massive flooding. Flood waters mobilize large amounts of organic carbon stored in coastal watersheds affecting biogeochemical pathways and carbon storage (Bauer et al., 2013; Bianchi et al., 2013; Hounshell et al., 2019). Previous studies suggested that extreme weather events can account for an important fraction (20–50%) of the annual riverine dissolved organic carbon (DOC) flux in coastal regions (Avery et al., 2004; Yoon and Raymond, 2012; Bianchi et al., 2013; Osburn et al., 2019; Paerl et al., 2019). The substantial input of terrigenous organic matter is known to change DOC composition and bioreactivity in coastal waters (Osburn et al., 2012; Bianchi et al., 2013). Furthermore, Balmonte et al. (2016) and Steichen et al. (2020) have demonstrated that post-hurricane hydrological and geochemical perturbations reshape the bacterial community structure in coastal rivers with the potential to disrupt biological networks.

During flood conditions, estuaries act mainly as flow-through systems for precipitation, and stormwater to the ocean (Bauer et al., 2013; Hounshell et al., 2019). Following extreme weather events, mobilized terrigenous DOC (tDOC) is mineralized by microbial and photochemical processes resulting in outgassing of CO_2 (Bianchi et al., 2013; Osburn et al., 2019). Mineralization of tDOC can explain most of the CO_2 flux in temperate and high-latitude estuarine and coastal ecosystems (Crosswell et al., 2014; Kaiser et al., 2017a; Hounshell et al., 2019; Osburn et al., 2019). Extreme weather events shift the carbon balance in coastal ecosystems from net uptake to a net source of CO_2 to the atmosphere for a period up to several months (Crosswell et al., 2014; Osburn et al., 2019; Paerl et al., 2019).

The frequency and intensity of extreme weather events are predicted to increase in future climate scenarios (Bender et al., 2010; Lehmann et al., 2015; Emanuel, 2017), yet critical knowledge on coastal carbon biogeochemical cycling is still limited (Paerl et al., 2019). Hurricane Harvey struck the southwest coast of Texas as a Category 4 storm on 26 August, 2017. After stalling for 2 day over South Texas, the hurricane returned to the Gulf of Mexico and made a second landfall just east of Houston on 30 August. Over a five-day period, the hurricane produced unprecedented precipitation (>500 mm with return period exceeding 2000 year) within the Houston-Galveston watershed, and entered the annals of history as the wettest and the second most expensive hurricane in the history of the United States. This study examines dissolved organic matter (DOM) fluxes and carbon budgets in Galveston Bay (TX, United States) after Hurricane Harvey over a four-week period through chemical analysis of common biochemicals (lignin, enantiomeric amino acids). In addition, the mineralization of tDOC is explored relative to the microbial community structure. Results from this study revealed fundamental mechanisms that drive organic carbon processing during extreme storm events in coastal ecosystems.

MATERIALS AND METHODS

Estuary and Watershed Characteristics

Galveston Bay sits on the northeastern Texas Coast of the Gulf of Mexico, and is the seventh largest estuary in the continental United States. The bay surface area is 1.6×10^9 m^2, and the average depth is 2.1 m (**Figure 1**). Water exchange between the bay and Gulf of Mexico is limited by narrow outlets, and the average water residence time is 30–60 day (Rayson et al., 2016). Bolivar Roads is the main outlet of Galveston Bay, accounting for around 80% of the outflow (Galveston Bay National Estuary Program, 1994). The dredged Houston Ship Channel runs north from Bolivar Roads through the bay to the man-made Port of Houston at an average depth of 40 feet and 300–400 feet in width.

Fresh water inflows to the bay are dominated by the Trinity River, the San Jacinto River, and Buffalo Bayou. The Trinity River and San Jacinto River host natural ecosystems and heavily urbanized areas, and water flow is controlled by a series of lakes and reservoirs. Buffalo Bayou bisects the Houston metropolitan area and joins the San Jacinto River at the mouth of the bay. Water flow through the main stream channel of Buffalo Bayou is regulated through large man-made flow control structures west of Houston. The confluence of Buffalo Bayou and San Jacinto River forms the entrance to the Port of Houston with numerous industrial and petrochemical facilities in low-lying, flood-prone areas.

Field Sampling and Chemical Analyses

Surface water samples were collected on five consecutive one-day trips aboard R/V Trident along a transect from the Port of Houston to the Galveston Bay entrance following Hurricane Harvey from Sep 4 to Sep 28, 2017 (**Figure 1**). **S**amples were filtered on board through 0.2 μm Whatman -Nucleopore Q-TEC filters (Filtration Solutions) for DOC, optical, and chemical analysis.

Concentrations of DOC were measured by high temperature catalytic oxidation using a Shimadzu TOC-V total organic carbon analyzer. Deep seawater reference standards (Consensus Reference Program, University of Miami) were used to assure the accuracy of DOC measurements. Absorbance was measured in a 1 cm quartz cuvette from 200 to 800 nm using a dual-beam spectrophotometer (UV-1800, Shimadzu) with Milli-Q water as the reference blank. Specific UV absorbance ($SUVA_{254}$) was determined by dividing the UV absorbance at 254 nm by the DOC concentration. The spectral slope ($S_{275-295}$) was calculated using the linear regression of natural log-transformed absorption spectra (Helms et al., 2008).

Samples for dissolved lignin (900 mL) were acidified to pH 2.5 using 6 mol L^{-1} sulfuric acid and extracted through Agilent PPL cartridges (1 g) at 10 mL min^{-1}. After extraction cartridges were rinsed with 10 mL of deionized water acidified to pH 2.5 and dried for 30 s to remove residual water. The cartridges were eluted with 20 mL of methanol at 2 mL min^{-1}, and the eluate was stored in glass vials at -20°C until analysis. Concentrations of lignin phenols were determined using ultra-high performance liquid chromatography-electrospray ionization-tandem mass spectrometry after $CuSO_4$ oxidation following the methods described in Yan and Kaiser (2018a,b). Aliquots of methanol extracts (~30 μg sample OC content) were dried in reaction vials and re-suspended in 200 μL of 1.1 mol L^{-1} argon-sparged NaOH, followed by addition of

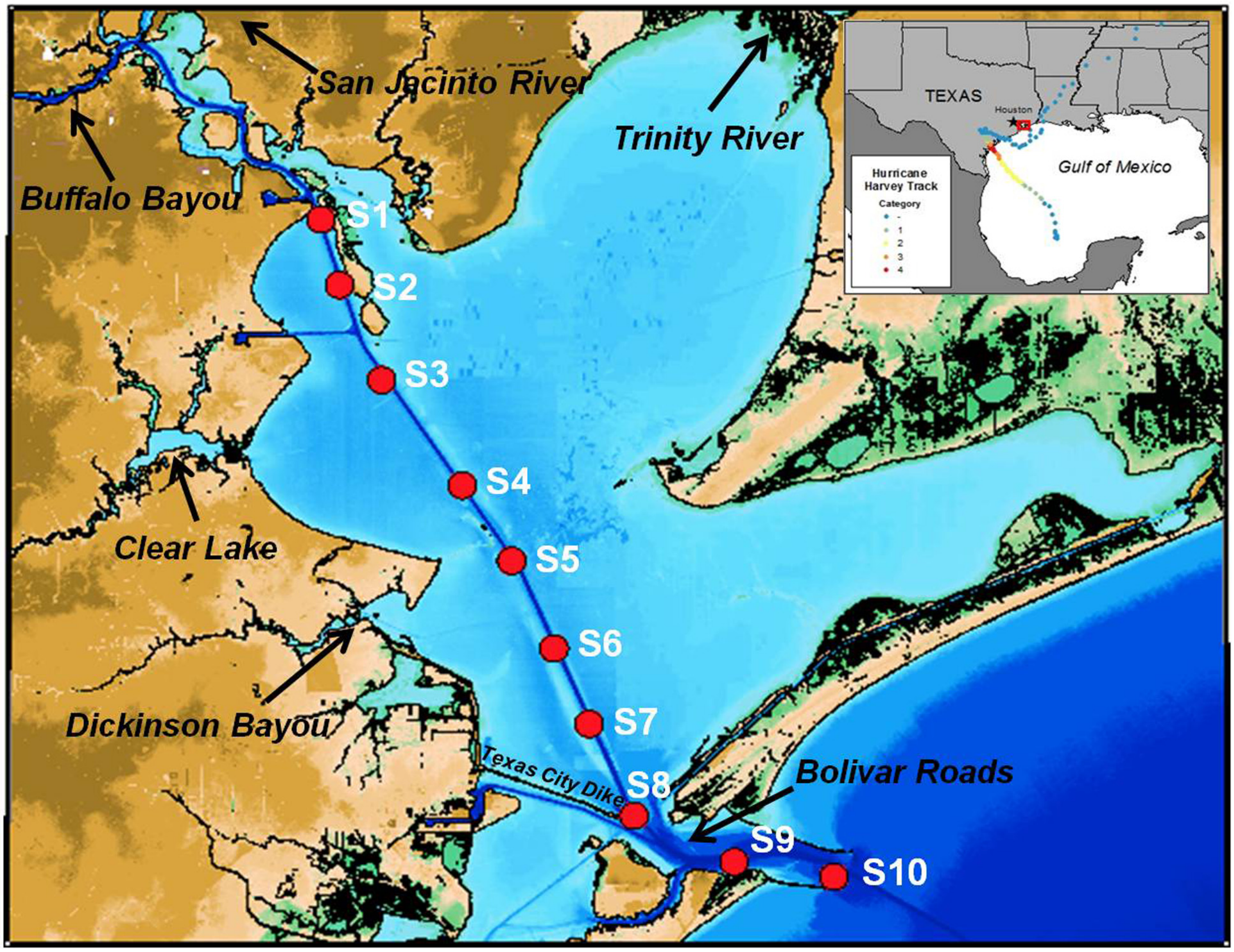

FIGURE 1 | Map of Galveston Bay showing locations of sampling stations (red dots). The inset shows the track of Hurricane Harvey.

10 μL of 10 mmol L^{-1} $CuSO_4$ and 10 μL of 0.2 mol L^{-1} ascorbic acid. Reaction vials were vigorously mixed and placed into 60-mL pressure-tight teflon vessels filled with 5 mL of 1 mol L^{-1} NaOH. The oxidation was conducted at 150°C a for 120 min. Sample solutions were spiked with ^{13}C labeled surrogate standards and purified with Waters HLB cartridges (30 mg, 1 mL). Separation and detection of lignin phenols was performed on an Agilent Infinity 1260 series UHPLC system coupled to an Agilent 6420 QqQ detector operating in alternating positive and negative modes with dynamic multiple reaction monitoring. Eleven lignin phenols were determined in all samples, including vanillyl phenols (V; vanillin, acetovanillone, and vanillic acid), syringyl phenols (S; syringaldehyde, acetosyringone, and syringic acid), p-hydroxyl phenols (P; p-hydroxybenzaldehyde, p-hydroxyacetophenone, and p-hydroxybenzoic acid), and cinnamyl phenols (C; p-coumaric acid and ferulic acid). The sum of nine V, S and P phenols ($TDLP_9$) was used as a tracer of tDOC and was not affected by any nonlignin sources (Fichot and Benner, 2012). Cinnamyl phenols were only used for source identification because of significant different reactivities to $TDLP_9$ (Hernes et al., 2007).

Total hydrolyzable enantiomeric dissolved amino acids (free and combined) including L-and D- forms of aspartic acid, glutamic acid, serine, histidine, threonine, glycine, arginine, alanine, tyrosine, valine, isoleucine, phenylalanine, leucine, and lysine were analyzed using high performance liquid chromatography and fluorescence detection. After microwave assisted vapor phase hydrolysis (Kaiser and Benner, 2005), amino acid monomers were derivatized with a mixture of N-isobutyryl-L-cysteine and o-phthaldialdehyde and separated on an Agilent Poroshell 120 EC-C18 column (4.6 mm × 100 mm, 2.7 μm). A binary solvent system was employed: mobile phase A was 48 mmol L^{-1} KH_2PO_4 with pH adjusted to 6.25, and mobile phase B was methanol/acetonitrile (13/1, v/v). The linear gradient program was: 0% B at 0 min, 39% B at 13.3 min, 54% B at 19.2 min, 60% B at 21.3 min, 80% B at 22 min, and hold at 80% B for 1 min. The flow rate was 1.5 mL min^{-1} and column temperature was maintained at 35°C. Excitation and emission wavelength of the detector was set to 330 nm and 450 nm, respectively. Racemization of amino acid enantiomers occurring during acidic hydrolysis was corrected using the average rates determined on free and protein amino acids (Kaiser and Benner, 2005). Total D-amino acids (D-AA) was defined as the sum of the four D-enantiomers of aspartic acid (D-Asx), glutamic acid (D-Glx), serine (D-Ser), and alanine (D-Ala), which were ubiquitously present in all samples.

The amino acid degradation index was calculated based on the relative abundance of amino acids following the method described by Dauwe et al. (1999). All measured amino acids were included in the calculation. Relative abundances of combined D/L forms of amino acids were normalized by subtracting the average and divided by the standard deviation before principle component analysis.

16S Ribosomal RNA Gene Community Analysis and Metagenomics

For the 16S ribosomal RNA (rRNA) gene analysis, the water samples were filtered on 0.2 μm polyethylsulfone (PES) membrane filters immediately after returning to shore. Filters were stored in -80°C freezer until total nucleic acid was extracted, using the MO Bio PowerSoil DNA Isolation Kit (cat. no. 128888-50). PCR amplification, using Promega GoTaq Flexi DNA Polymerase was performed following the 16S rRNA gene Illumina amplicon protocol from the Earth Microbiome project[1]. Each sample was amplified in triplicate 25 μL reactions with the following cycling parameters: 95°C for 3 min, 30 cycles of 95°C for 45 s, 50°C for 60 s, and 72°C for 90 s, and a final elongation step at 72°C for 10 min. V4 region amplifications were performed using the 515F-806R primer pair (10 μM each) modified to include recently published revisions that reduce bias against the Crenarchaeota and Thaumarchaeota lineages as well as the SAR11 bacterial clade (Parada et al., 2016). The primer pair was additionally modified to include Golay barcodes and adapters for Illumina MiSeq sequencing. Final primer sequences are detailed in Walters et al. (2016). After PCR amplification, samples were run on a 1.5% agarose gel and quantified using Tecan Genios Spark 10 M microplate reader and QuantiFluor DNA dye. Following amplification, the triplicate products were combined together and run on a 1.5% agarose gel to assess amplification success and relative band intensity. Amplicons were then quantified with the QuantiFluor dsDNA System (Promega), pooled at equimolar concentrations, and purified with an UltraClean PCR Clean-Up Kit (MoBio Laboratories; Carlsbad, United States). The purified library, along with aliquots of the three sequencing primers, were sent to the Georgia Genomics Facility (Athens, GA, United States) for MiSeq sequencing (v2 chemistry, 2 × 250 bp). Sequence reads were processed using mothur v.1.39.5 following the MiSeq SOP protocol (Schloss et al., 2009; Kozich et al., 2013). DNA sequences generated can be found in the GenBank Sequence Read Archive under the accession number PRJNA558756.

For the metagenomic analysis, samples (between 4 and 20 L) were pre-filtered immediately after sampling with a nitex filter (30 μm) to remove small grazers and large particles, then filtered through a glass fiber filter (GF/F with a 0.7 μm pore-size or GF/D with a 2.7 μm pore-size), followed by a 0.22 μm pore-size polyvinylidene fluoride (PVDF) filter. Filters were stored at -20°C until further use. DNA was extracted from the GF and PVDF filters (cut to represent ∼3 L of initial samples) via a phenol chloroform method. Filters were aseptically cut to represent a volume of ∼3 L of initial sample water, i.e., if 4 L of water was filtered then 3/4 of the filtered would be used for extraction. Briefly, samples were incubated in 10 mL of lysis buffer (120 mM NaCl, 225 mM sucrose, 6 mM EDTA, and 15 mM Tris HCl, pH = 9) and lysozyme (100 mg mL^{-1}) at 37°C at 350 rpm for 30 min, then with proteinase K (20 mg mL^{-1}) and 10% SDS at 50°C at 350 rpm overnight. DNA was extracted using saturated phenol (pH of 8) followed by two rounds of chloroform:isoamyl alcohol 24:1 before ethanol precipitation (Green and Sambrook, 2017). Residual phenol and chloroform was removed with the QIAamp® DNA mini and Blood mini kit. DNA samples were stored at −20°C until further use. DNA samples were sequenced using Illumina HiSeq chemistry (2 × 150 bp) at the Texas A&M Genomics & Bioinformatics facility in College Station, TX. BBTools were used to remove adapter sequences, sequence artifacts, and merge sequences[2] before de novo assembly with MEGAHIT (Li et al., 2015). Gene prediction was performed using Prodigal (Hyatt et al., 2010) and the translated amino acid sequences were compared to the GenBank nr database using DIAMOND (Buchfink et al., 2015). The results were used to visualized the abundance of characteristic SEED metabolic pathways using MEGAN (Huson et al., 2011). Data are available through the BCO-DMO portal[3].

Calculation of Bacterially-Derived DOC

Bacterial contributions to DOC were estimated following the methods of Kaiser and Benner (2008) according to:

$$\mathrm{Bacterial_{DOC}} = \frac{\mathrm{Biomarker_{DOM}}}{\mathrm{Biomarker_{bacterialDOM}}}$$

where $Biomarker_{DOM}$ and $Biomarker_{bacterialDOM}$ were the C-normalized yields of D-Asx, D-Glx, and D-Ala in sample DOM and freshly-produced bacterial DOM. C-normalized yields of D-Asx, D-Glx, and D-Ala in bacterial DOM were 24.3 nmol mg C^{-1}, 16.5 nmol mg C^{-1}, and 35.0 nmol mg C^{-1}, respectively, and were representative of coastal and marine bacterial assemblages.

Calculation of DOC Export

Two methods were used to estimate DOC export to the bay for the storm event. One method used the measured river DOC concentrations during the first sampling cruise and freshwater export flux. Estimated freshwater volumes for the event was 14–17 × 10^9 m^3 (Du et al., 2019a,b). The second method followed the approach of Officer, 1979 and used in other studies (Cai et al., 2004; He et al., 2010). The calculation of the DOC concentration for freshwater input is graphically shown

---

[1] http://www.earthmicrobiome.org/emp-standard-protocols

[2] https://earthmicrobiome.org/protocols-and-standards/16s/

[3] https://www.bco-dmo.org/project/750430

TABLE 1 | Transect data from five cruises in Galveston Bay after Hurricane Harvey.

Station	Salinity	DOC (μmol L^{-1})	TDLP$_9$ (nmol L^{-1})	THAA (nmol L^{-1})	D-AA (nmol L^{-1})	TDLP$_9$ (%OC)	THAA (%OC)	P/V	S/V	C/V	(Ad/Al)$_V$	DI	SUVA$_{254}$ (L mgC^{-1} m^{-1})	S$_{275-295}$ (nm^{-1})
9/4/2017														
S1	0	566	832	1926	131	1.21	1.24	0.24	0.32	0.06	0.76	0.69	4.30	0.0134
S3	0.63	482	739	1589	113	1.26	1.20	0.25	0.34	0.08	0.88	0.67	4.16	0.0134
S4	0.84	429	514	1257	90	0.99	1.06	0.25	0.37	0.08	0.81	0.44	4.00	0.0139
S6	0.73	457	590	1332	93	1.07	1.06	0.28	0.39	0.08	0.77	0.72	3.79	0.0142
S8	1.07	457	699	1586	116	1.26	1.27	0.24	0.35	0.08	0.87	0.63	4.21	0.0138
S9	5.84	311	341	1313	96	0.90	1.54	0.40	0.48	0.13	0.78	0.65	3.73	0.0143
S10	6.57	308	357	1130	96	0.95	1.33	0.33	0.42	0.11	0.86	0.38	3.70	0.0143
9/9/2017														
S1	4.35	359	398	1410	103	0.92	1.44	0.30	0.38	0.10	0.83	0.71	3.82	0.0141
S2	5.65	377	394	1306	102	0.86	1.26	0.27	0.38	0.08	0.75	0.49	3.75	0.0142
S6	3.76	417	375	1549	118	0.74	1.39	0.28	0.35	0.08	0.82	0.95	3.75	0.0145
S8	8.14	302	186	1143	95	0.50	1.40	0.57	0.43	0.13	0.74	0.80	3.65	0.0145
S9	7.98	316	230	1268	86	0.59	1.51	0.49	0.43	0.12	0.71	0.95	3.62	0.0144
S10	10.38	314	221	1433	82	0.57	1.76	0.49	0.42	0.12	0.70	1.52	3.52	0.0144
9/16/2017														
S1	5.40	335	231	1873	95	0.56	2.23	0.39	0.38	0.10	0.75	2.31	3.87	0.0145
S4	4.16	401	289	3605	140	0.59	3.74	0.37	0.38	0.10	0.80	2.93	3.99	0.0146
S5	6.85	396	260	2944	129	0.54	3.07	0.37	0.38	0.08	0.67	2.77	3.69	0.0152
S7	12.18	334	188	2228	117	0.46	2.75	0.40	0.37	0.09	0.79	2.71	3.22	0.0162
S9	22.55	240	109	1792	127	0.37	3.10	0.51	0.43	0.11	0.69	2.61	2.78	0.0174
S10	19.38	257	130	1995	123	0.41	3.18	0.50	0.42	0.11	0.71	2.61	2.84	0.0172
9/21/2017														
S1	6.84	339	268	619	41	0.65	0.65	0.39	0.41	0.12	0.76	0.17	3.60	0.0158
S4	9.86	331	186	1238	99	0.46	1.35	0.38	0.38	0.09	0.69	0.39	3.37	0.0163
S5	12.07	320	184	1136	88	0.47	1.27	0.41	0.36	0.09	0.72	0.37	3.28	0.0167
S7	15.52	300	147	1211	93	0.40	1.47	0.44	0.39	0.10	0.73	0.47	3.05	0.0174
S9	20.06	257	118	1178	95	0.37	1.71	0.50	0.43	0.11	0.70	0.84	2.75	0.0183
S10	ND	255	117	922	94	0.37	1.32	0.51	0.43	0.11	0.74	0.43	2.77	0.0182
9/28/2017														
S1	7.84	346	210	1394	100	0.50	1.49	0.44	0.42	0.11	0.66	1.02	3.41	0.0163
S4	8.31	358	167	1248	104	0.38	1.30	0.44	0.39	0.09	0.68	0.87	3.27	0.0174
S6	11.24	325	146	1467	107	0.37	1.71	0.50	0.42	0.11	0.66	1.21	2.95	0.0175
S8	12.60	323	133	1292	99	0.34	1.51	0.48	0.42	0.10	0.64	1.01	3.10	0.0178
S9	19.88	267	118	1017	106	0.36	1.44	0.47	0.37	0.09	0.71	0.82	2.84	0.0186
S10	20.08	269	123	1285	124	0.37	1.89	0.48	0.36	0.09	0.67	1.80	2.74	0.0187

Locations are shown in ***Figure 1****. DOC = dissolved organic carbon; TDLP$_9$ = sum of vanillyl, syringyl, and p-hydroxyl phenols; THAA = dissolved total hydrolyzable amino acids; D-AA = sum of dissolved D-amino acids; P/V = p-hydroxyl phenols divided by vanillyl phenols; S/V = syringly phenols divided by vanillyl phenols; C/V = cinnamyl phenols divided by vanillyl phenols; (Ad/Al)$_V$ = vanillic acid divided by vanillin; DI = degradation index calculated based on amino acid relative composition; SUVA$_{254}$ = specific ultraviolet absorbance at 254 nm; S$_{275-295}$ = absorbance spectral slope over 275 to 295 nm; ND = not determined.*

in **Supplementary Figure S1**, applying at tangent to a fitted DOC/salinity relationship at a salinity of 7. This yielded a DOC concentration of 409 μmol L^{-1} for a salinity of 0.

Removal of Terrigenous Dissolved Organic Carbon

The removal of tDOC was calculated from correlations of carbon-normalized concentrations of p-hydroxy phenols, vanillyl phenols, and syringyl phenols ($TDLP_9$-C) with river water fractions. Carbon-normalized concentrations of $TDLP_9$ were calculated by dividing the sum of $TDLP_9$ by the DOC concentration and reported in units of nmol mg C^{-1}. Conservative mixing of $TDLP_9$-C concentrations in bay waters is described by a rational model, i.e., a ratio of simple polynomials with a 0 intercept according to:

$$\mathrm{TDLP_9 - C}\left[\mathrm{nmol\ mg\,C^{-1}}\right] = \frac{\alpha \times f_R}{f_R + \beta}$$

where f_R is the fraction of river water and α,β are model parameters. Model parameter β was estimated from a theoretical mixing model of river and ocean water from $f_R = 0$ to $f_R = 1$. Model parameter α was fitted with a rational model. The conservative mixing model used DOC and $TDLP_9$ concentrations measured in San Jacinto river water discharged to the head of the bay during the first week of sampling. A graphical approach is presented in **Figure 7** and a detailed description is provided in Kaiser et al. (2017a). Fitted $TDLP_9$-C concentrations at $f_R = 1$ were compared to the river endmember, and first-order decay constants were calculated as follows:

$$k_{\mathrm{tDOC}}[\mathrm{year}^{-1}] = -\frac{\ln \frac{\mathrm{TDLP_9 - C_{sample}}}{\mathrm{TDLP_9 - C_{river}}}}{t}$$

where $TDLP_9$-C_{sample} is the fitted concentration at $f_R = 1$, $TDLP_9$-C_{river} is the concentration of the river endmember, and t is the water residence time in years. The fraction of river water was calculated assuming a salinity of 0 for river water and a salinity of 35.4 for the oceanic endmember. The unit years was used to allow comparison of decay constants published by Kaiser et al. (2017a). Error for calculations of decay constants was evaluated by considering the variability of $TDLP_9$-C concentrations and fitting. Random noise limited by uncertainties of input variables was added to input variables and repeated >1000 times. Uncertainties are reported with decay constants and shown in **Figure 8**.

RESULTS

Freshwater Load to Galveston Bay

During the storm period, the San Jacinto River contributed 73% of the total freshwater discharge. The Trinity River, surface runoff and groundwater contributed the remaining freshwater input. Freshwater release during the entire storm period was 14–17 × 10^9 m^3 (∼4 times of the bay volume) and export peaked at over 2 × 10^4 m^3 s^{-1} immediately following the heaviest precipitation period of August 26–30th (Du et al., 2019a,b).

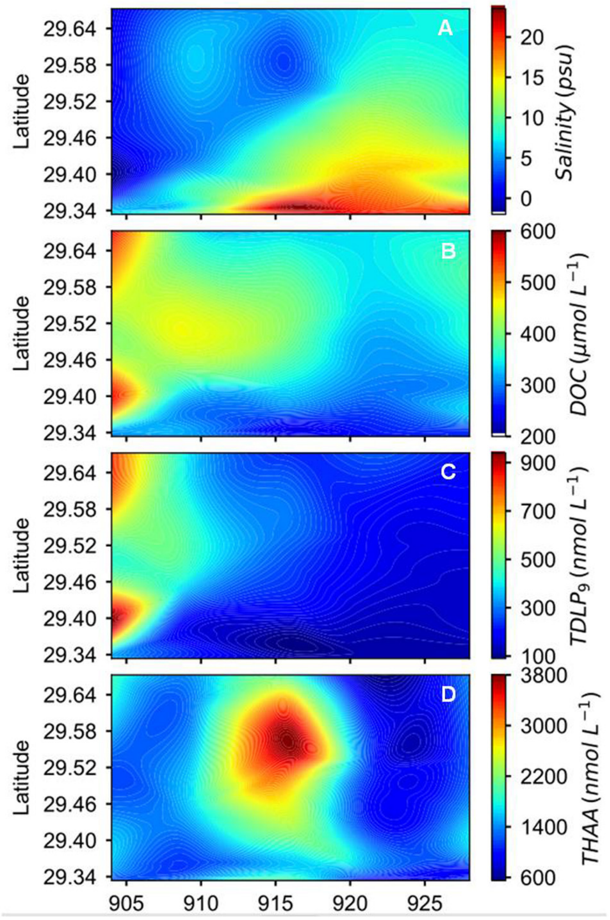

FIGURE 2 | Spatial and temporal variations of **(A)** salinity, **(B)** DOC, **(C)** sum of nine dissolved p-hydroxyl, vanillyl, and syringyl phenols ($TDLP_9$), and **(D)** total hydrolyzable amino acids (THAA) concentrations during the sampling period after Hurricane Harvey.

The salinity range across the bay was 0–7 immediately following the main precipitation event and as sampling was initiated on September 4th (**Table 1** and **Figure 2A**). Water transit times in the bay were on the order of 1–2 day on August 27th, adjusting to 60–90 day after September 3rd (Du et al., 2019c). The salinity in the bay eventually recovered to 8–20 after 4 weeks (**Table 1** and **Figure 2A**). Complete recovery of salinity after the storm took ∼2 month (Du et al., 2019a,b).

Concentrations and Distributions of DOC and Biochemicals

Temporal and spatial distribution patterns of DOC concentrations showed an inverse relationship to salinity (**Figure 2B**, **Supplementary Figure S1**, and **Table 1**). Concentrations of DOC were highest (566 μmol L^{-1}) in freshwater entering the bay and gradually decreased toward the mouth of the estuary and over the four-week sampling period (**Figure 2B**). Changes in DOC concentrations were most pronounced in the first 2 weeks of sampling. Locally elevated

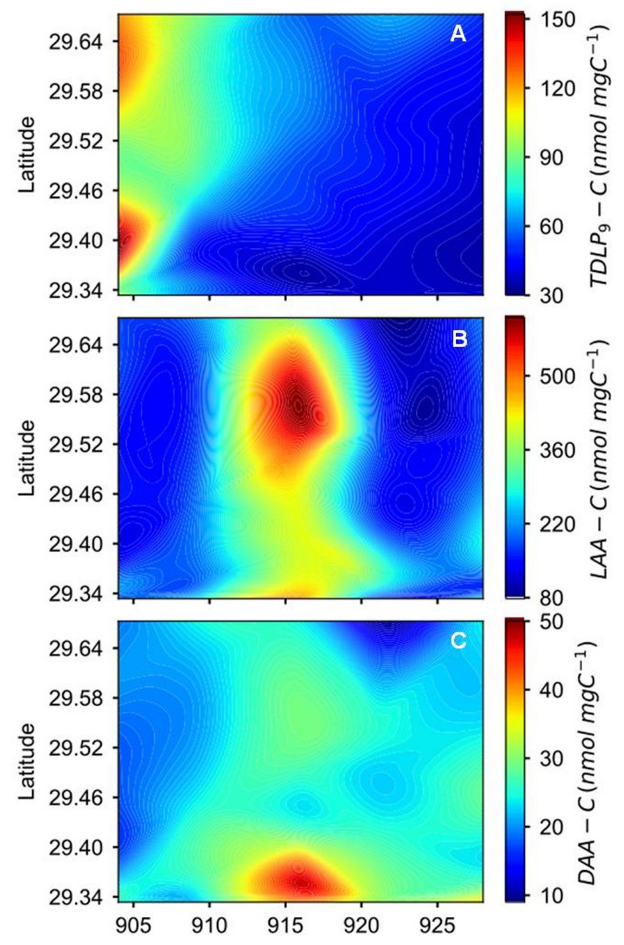

FIGURE 3 | Spatial and temporal variations of **(A)** carbon-normalized concentrations of p-hydroxyl, vanillyl, and syringyl phenols ($TDLP_9$-C), **(B)** carbon-normalized concentrations of dissolved L-amino acids (LAA-C), and **(C)** carbon-normalized concentrations of dissolved D-amino acids (DAA-C) during the sampling period after Hurricane Harvey.

concentrations were found at mid-bay stations 6 to 8 during the first sampling cruise, and stations 4 and 6 during the second and third cruises.

Concentrations of $TDLP_9$ ranged from 109 to 832 nmol L^{-1} (**Figure 2C**, **Supplementary Figure S1**, and **Table 1**). Highest $TDLP_9$ concentrations were observed during lowest salinity and highest discharge demonstrating the input of terrigenous DOM to the bay. Like concentrations, $SUVA_{254}$, which is representative of aromatic moieties in DOM molecules, and carbon-normalized yields of $TDLP_9$ were highest at the mouth of the bay at the start of the sampling program and declined profoundly over the following month (**Table 1**, **Figure 3**, and **Supplementary Figure S1**).

Amino acid concentrations varied from 619 to 3605 nmol L^{-1} and increased as water clarity improved after 2 weeks (**Table 1**, **Figure 2D**, and **Supplementary Figure S1**). Both, D-amino acid concentrations (DAA) and carbon-normalized yields of amino acids followed the same trend as observed for concentration.

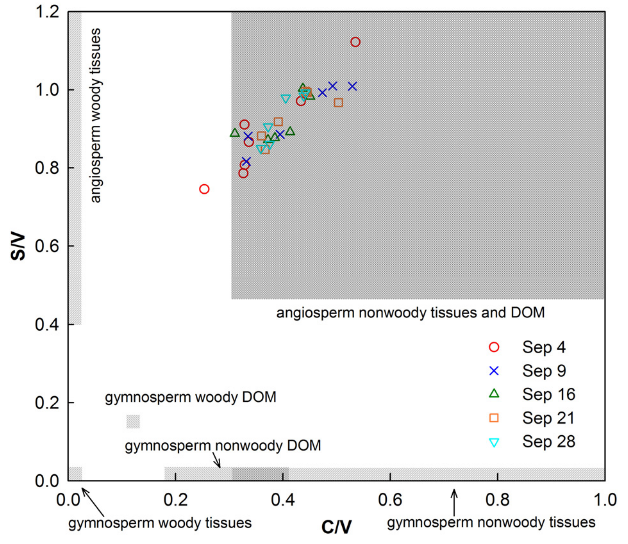

FIGURE 4 | Ratios of syringyl/vanillyl (S/V) and cinnamyl/vanillyl (C/V) phenols in water samples collected in Galveston Bay after Hurricane Harvey. The shaded boxes denote ranges of phenol ratios in representative source vegetation materials and their leachates (see **Supplementary Table S1**). Phenols were analyzed with a new method, and phenol ratios were corrected for comparison with literature values (Yan and Kaiser, 2018b).

Amino acid degradation index values calculated from amino acid compositions (Dauwe et al., 1999; Kaiser and Benner, 2009) showed relatively large variations (from 0.17 to 2.93), with distinctly higher values during the third sampling trip. High carbon-normalized yields of amino acids and degradation index values during the third cruise were indicative of bioreactive DOC.

The compositional lignin phenol parameters S/V, and C/V ranged from 0.32 to 0.48, and 0.06 to 0.13, respectively, and did not exhibit substantial changes with locations and time (**Table 1** and **Figure 4**). S/V and C/V are generally employed to explore sources of tDOC (i.e., angiosperm versus gymnosperm and woody versus nonwoody) (Hedges and Mann, 1979; Goñi and Hedges, 1995; Godin et al., 2017). Representative tissues and their leachates were integrated in **Figure 4** to aid with identification of tDOC sources (**Supplementary Table S1**). Leaching and sorptive processes can skew diagnostic ratios (Hernes et al., 2007; Spencer et al., 2008), but the dominance of DOC leached from nonwoody angiosperm tissues was clearly evident.

P/V ratios significantly increased (t-test, $p < 0.001$) temporally and spatially exhibiting consistently lower values in the upper bay compared to the lower bay. The increase in P/V was negatively correlated ($R^2 = 0.73$, $p < 0.001$) to carbon-normalized $TDLP_9$ ($TDLP_9$-C) concentrations (**Figure 5**). Average $(Ad/Al)_V$ gradually decreased from 0.88–0.64 (**Table 1** and **Figure 6**) over the sampling period, whereas the average spectral slope ($S_{275-295}$) increased. Both parameters were significantly lower than values observed for the coastal Gulf of Mexico (Fichot et al., 2014).

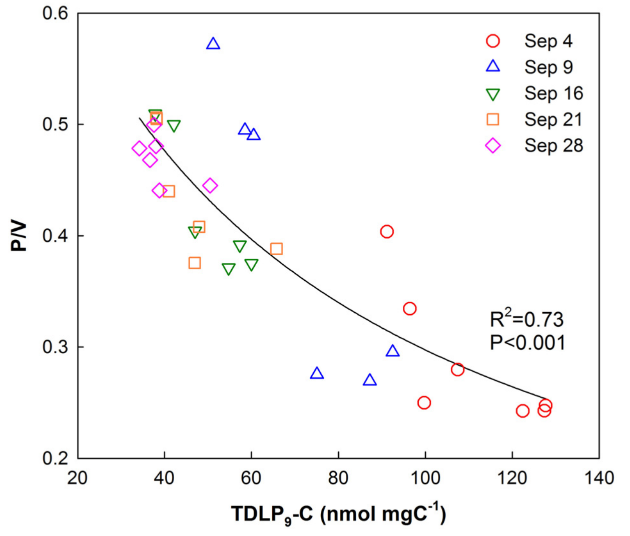

FIGURE 5 | Relationship of p-hydroxyl phenol/vanillyl phenol (P/V) ratios with TDLP$_9$-C (nmol mg C^{-1}) for all water samples collected in Galveston Bay after Hurricane Harvey.

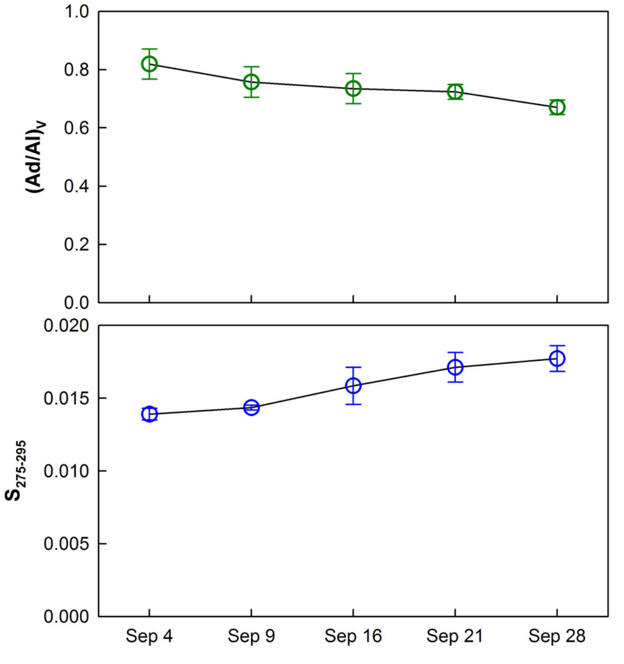

FIGURE 6 | Temporal trends of average vanillic acid/vanillin (Ad/Al)$_V$ ratios and the spectral slope (S$_{275\text{-}295}$) for water samples collected during each cruise. Error bars show standard deviations.

Degradation and Mineralization of Flood-Derived Dissolved Organic Carbon

The approach to calculate tDOC removal is shown in **Figure 7**. It was assumed the loss of dissolved lignin phenols reflected the loss of bulk tDOC (Hernes and Benner, 2003). TDLP$_9$-C for river water was 124.8 nmol/mg C^{-1} and likely presented a conservative endmember for river input. The exponential decay constant for mineralization of tDOC was 25.99 ± 4.31 year^{-1} for the first 2 weeks, and decreased to 9.80 ± 4.96 year^{-1} for the remainder of the sampling period. The decay constant for tDOC observed during the first 2 weeks was about 3 times higher than decay constants observed among tDOC from high and low latitudes (**Figure 8**, Kaiser et al., 2017a). The compilation of decay constants represented in-situ observation and experimental assays, and included tDOC from Arctic rivers, from rivers within the Gulf of Mexico watershed, and from rivers along the Southeastern seaboard. Decay constants were compared in consideration of the time dependence of decay kinetics that recognized compositional changes during decomposition (Kaiser et al., 2017a). After the second week, the tDOC decay constant conformed to globally observed tDOC decay constants.

Removal of tDOC was calculated according to:

$$\mathrm{tDOC}_{\mathrm{removed}} = 1 - \exp(-k \times t_{\mathrm{residence\ time}})$$

Of tDOC 57 ± 10% was lost in the bay within 2 weeks of discharge, and additional 11 ± 5% was lost over the remaining sampling period.

Bacterial Community Composition and Metabolic Pathway Components

The major bacterial classes identified in Galveston Bay included Betaproteobacteria, Alphaproteobacteria, Gammaproteobacteria, Actinobacteria, Flavobacteriia, Sphingobacteriia, Cyanobacteria, Deltaproteobacteria, Acidimicrobiia, Planctomycetacia, Opitutae, and OPB35_soil_group, and Chloroflexia (**Figure 9**). Floodwaters strongly modified water characteristics in the bay (e.g., salinity and temperature) and introduced soil (e.g., Opitutae and OPB35_soil_group), freshwater (e.g., Betaproteobacteria), and sedimentary (e.g., Actinobacteria) microorganisms, replacing the previously dominant marine species.

During the high discharge stage the microbial community composition was similar between the upper and lower bay. Over the following month, the microbial community composition slowly changed from bacteria inhabiting terrestrial environment (e.g., Betaproteobacteria) to those in marine environment (e.g., Cyanobacteria; **Figure 9**) and reverted to pre-hurricane conditions, where freshwater microbes were dominant in upper bay region and marine species prevalent in the lower bay. In particular, Cyanobacteria exhibited the most prominent transition pattern, as they accounted for less than 5% of the total bacterial community initially and then increased over time to reach 20–30% at the end of sampling campaign. The recovery time for the microbial community to pre-storm conditions was ~5 weeks.

Changes in microbial community composition were also reflected in the distribution of D-amino acids (D-Ala, D-Glx, and D-Asx) (**Figures 10B,C**). D-amino acids were characteristic of specific bacterial biopolymers including peptidoglycan, teichoic acids, siderophores, and other cell membrane-derived sources (Kaiser and Benner, 2008). A diversity measure of the microbial community expressed through the Simpson index showed that species richness and evenness declined as the bay adjusted to a

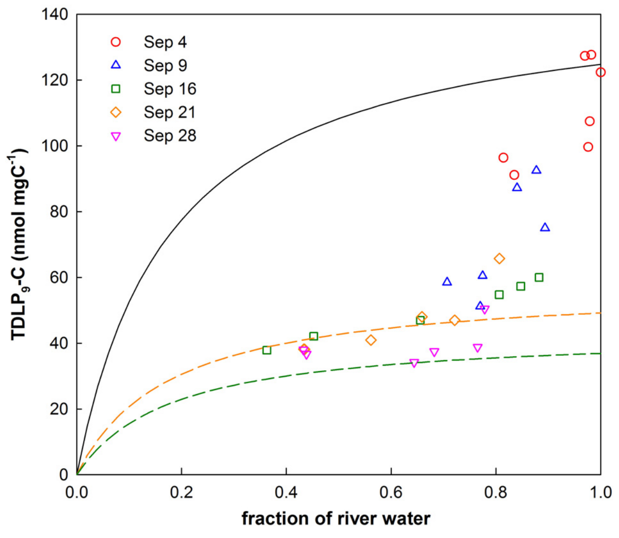

FIGURE 7 | Relationship of river water fractions with carbon-normalized concentrations of dissolved lignin phenols (TDLP$_9$-C). Conservative mixing of bay waters with shelf water follows a rational model. The solid black line represents the conservative mixing curve for river water with shelf water. The dashed colored lines show mixing curves for samples collected during the third (9/16) and fifth (9/28) cruise according to the rational model.

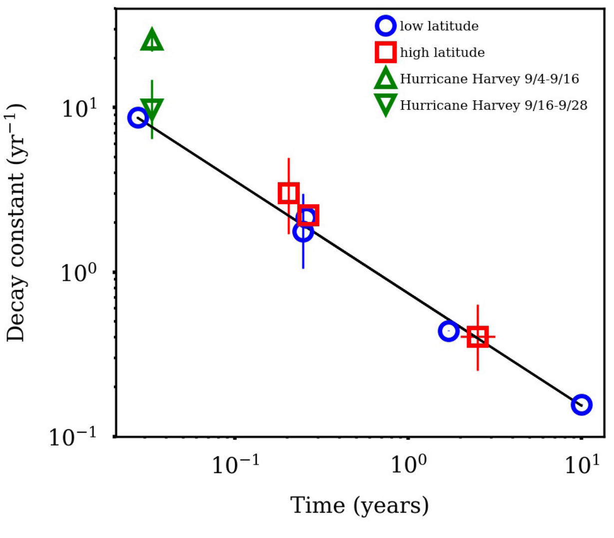

FIGURE 8 | Comparison of terrigenous dissolved organic carbon (tDOC) decay constants in this study with those from high and low latitude watersheds Kaiser et al. (2017a). Decay constants are plotted relative to decomposition time. The abnormally high decay constant for hurricane tDOC was observed during the first 2 weeks of sampling.

normal salinity regime (**Figures 10A,D**). It is known that the Simpson index is more sensitive to species evenness than richness (DeJong, 1975).

Sampling of the microbial community identified gene content and prevalent metabolic pathway components by comparison against the SEED subsystem (**Figure 11**). Specific identified genes and metabolic traits showed large differences between the first 2 weeks compared to the last 2 weeks. During the first 2 weeks, enrichment in heterotrophic metabolisms such as degradation of aromatic, nitrogen and sulfur compounds were prevalent. In the last 2 weeks, metabolic traits were associated with photosynthesis and paralleled the high abundance of cyanobacteria.

DISCUSSION

Tropical cyclones are regular events that threaten coastal ecosystems and inland environments. Such environmental disturbances harm or benefit natural systems and biological life by profoundly altering biogeochemical processes, sediment distributions, and biological diversity (Sousa, 1984; Du et al., 2019b; Osburn et al., 2019; Steichen et al., 2020). As affected regions are home to almost ~40% of the global population, cyclone activity, and impact are invariably linked to financial losses, loss of ecosystem services, dispersal of harmful chemicals from industries, or human fatalities and require proper preparation and analysis.

There is much debate on how climate change and human perturbations affect future storm activity and impact (Sobel et al., 2016). Physical considerations and model simulations predict an increase in storm severity and wetness as more heat and moisture is available (Trenberth et al., 2005, 2018). Observational records indicate hurricane-related flooding events have increased in severity and magnitude (Freeman et al., 2019; Paerl et al., 2019). Historic geological storm records linked increased hurricane intensity in the western North Atlantic to climate variability or the strength of the North Atlantic Meridional Overturning Circulation (Toomey et al., 2017). Fingerprints of a weakening circulation have been reported (Caesar et al., 2018), serving as a bellwether for these changes.

Hurricane Harvey described a realistic scenario of storm evolution in a warmer climate affecting an extremely urbanized and industrialized coastal environment. Hurricane Harvey's path was erratic, reversing its course and making landfall twice, and producing record rain fall in less than a week. Major flooding was the main issue for the Houston/Galveston coastal region where the hurricane made the second landfall inundating low-lying urban and industrialized areas and briefly converting Galveston Bay into a freshwater system (see also Steichen et al., 2020). The following discussion sheds light on carbon cycling issues during such a unique hurricane event that may be representative of storms in the near future.

DOM Sources in Galveston Bay After Hurricane Harvey

The input of tDOC to Galveston Bay for the entire storm event was 87 ± 18 Gg of DOC derived from terrigenous sources, of which the large majority (95%) was delivered within the first week. Error in the estimated DOC input resulted from the assumed DOC concentration of run-off (see methods) and variability in freshwater load estimates (Du et al., 2019a,b). The amount of tDOC input during the storm period represented the average annual tDOC load to Galveston Bay

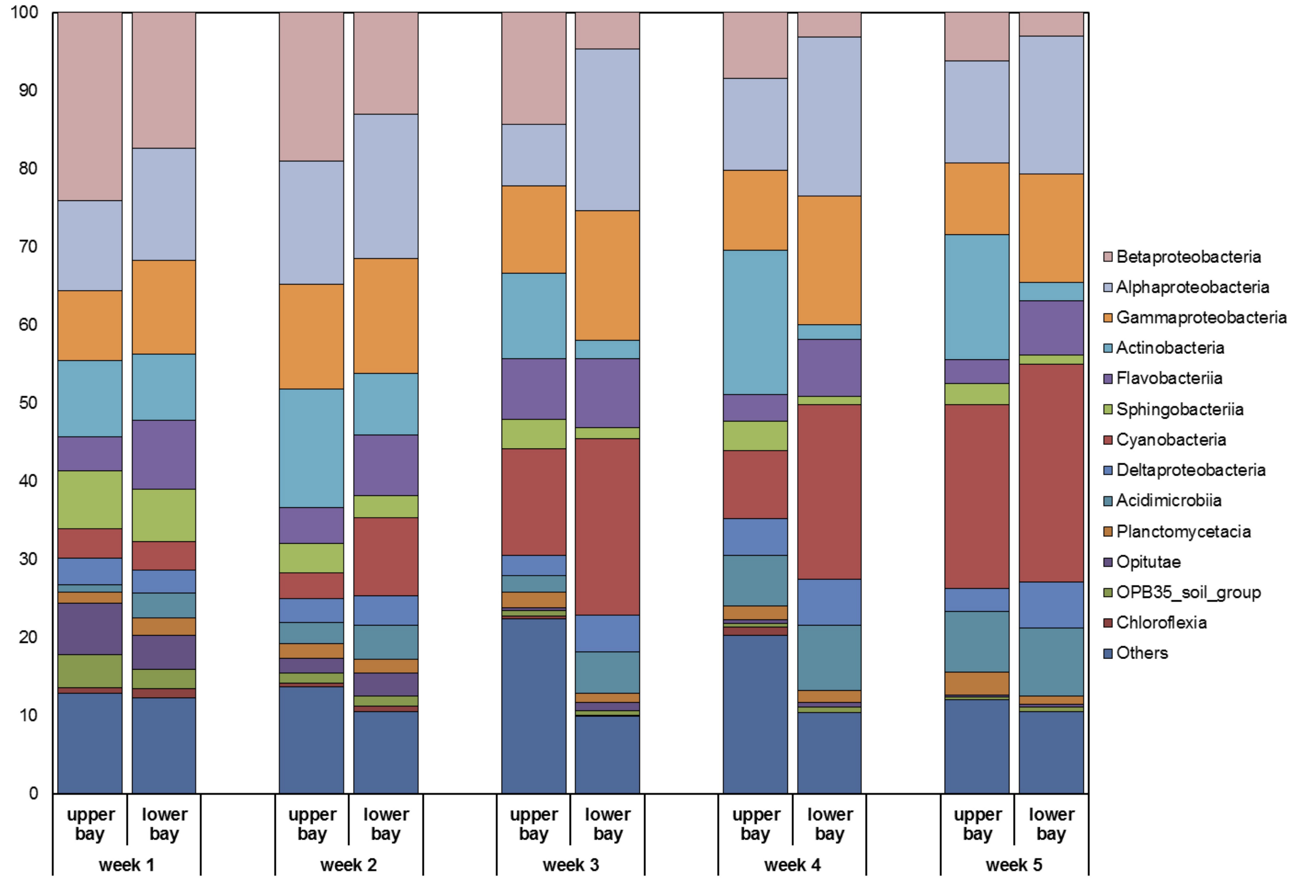

FIGURE 9 | Relative compositions of major bacterial classes identified in water samples collected in Galveston Bay after Hurricane Harvey.

(Warnken and Santschi, 2004) and exceeded estimates of tDOC fluxes during previous hurricanes hitting the East Coast by up to 6 times (Avery et al., 2004; Osburn et al., 2019). For comparison, the tDOC flux for the storm event was equivalent to ∼3% of average annual tDOC export from the Mississippi-Atchafalaya River System (Shen et al., 2012), which supplies more than 80% of freshwater input to the northern Gulf of Mexico (Dunn, 1996).

Source ratios of syringyl (S), vanillyl (V), and cinnamyl (C) phenols in flood-derived tDOC were typical of leached organic matter from non-woody tissues (e.g., leaves and grasses) of angiosperm vegetation. Remarkably, source composition of tDOC did not change substantially post-flood as indicated by relatively invariant S/V and C/V ratios. The remaining variability among lignin phenol source ratios could be attributed to diagenetic alterations of terrestrial macromolecules that was supported by increasing P/V ratios (Hernes et al., 2007). For comparison, similar S/V ratios were measured in adjacent rivers such as the Brazos River and Mississippi River (0.78–0.90), but C/V ratios were elevated compared to both of these rivers emphasizing the dominance of non-woody tissues in flood-derived tDOC (Shen et al., 2012; Yan and Kaiser, 2018b).

Polluted storm runoff from urbanized and industrialized areas contributes an additional source of DOM to estuaries (McGrane et al., 2016; Freeman et al., 2019; Steichen et al., 2020). Floodwaters quickly overwhelmed wastewater infrastructure and released an estimated 30 million gallons of untreated sewage (Environment Texas Research and Policy Center, 2017). In addition, spills of gasoline and crude oil among other industrial chemicals occurred from numerous chemical and tank facilities that were swept along with flood waters. The quantity of these inputs was poorly resolved as only few measurements were performed. Microbial community analysis showed elevated levels of *Escherichia coli*, a fecal indicator, in Houston bayou waters and flooded residential areas immediately after the storm (Yu et al., 2018). Bay floodwaters sampled at the head of the bay during the first cruise had higher contributions of Sphingobacteria, which are common in activated sludge, but gut-associated bacteria (i.e., Enterobacteria and Firmicutes) were not elevated (**Figure 9**). At the same time, only low levels of common pharmaceuticals and polycyclic aromatic hydrocarbons (PAHs) were detected (Steichen et al., 2020). Sampling was initiated 4 day after overflowing wastewater treatment plants were reported by local news outlets suggesting the peak of untreated sewage release was not captured with this sample set.

While tDOC dominated the DOC pool during the first 2 weeks of sampling, a bloom event of diatoms, chlorophytes,

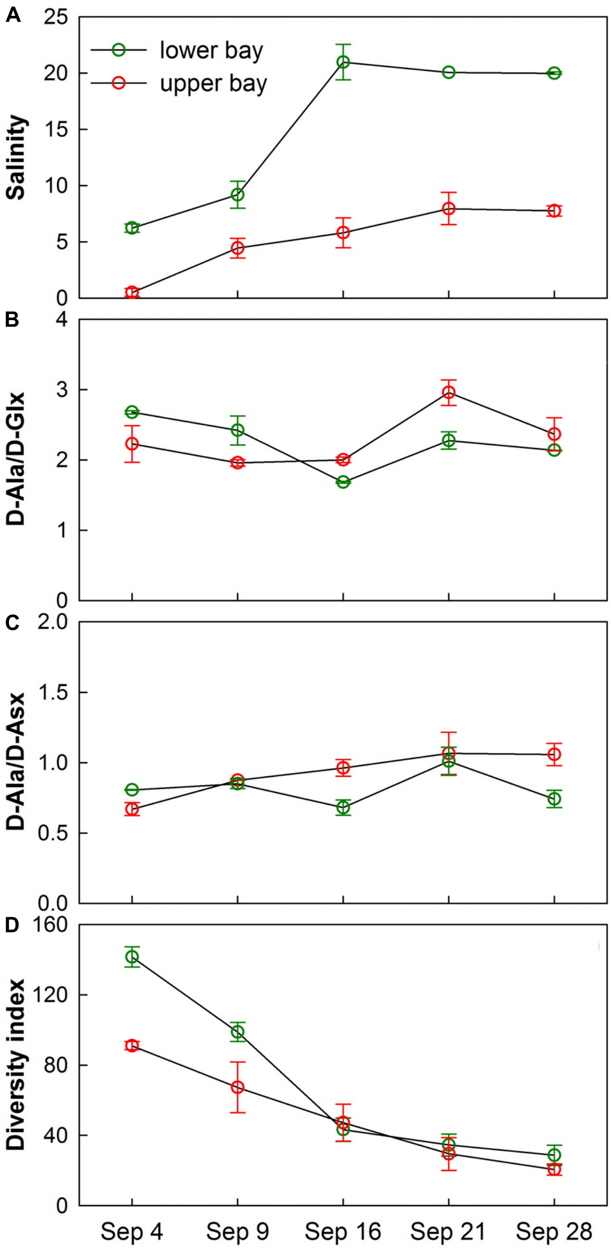

FIGURE 10 | Temporal trends of average **(A)** salinity, **(B)** D-Ala/D-Glx, **(C)** D-Ala/D-Asx, and **(D)** Simpson's Diversity Index for water samples collected in upper bay and lower bay during each cruise. Error bars show standard deviations.

and dinoflagellates fed by ample supply of nutrients and clearer surface waters during the third cruise (Steichen et al., 2020) lead to input of biolabile planktonic DOM and marked a transition to a DOM pool with variable contributions from terrestrial and in-situ derived DOM sources. The transition to a mixed DOM pool in the bay was indicated by higher amino acid yields and degradation index values, both robust indicators of biolabile DOM from phytoplankton exudation (Davis et al., 2009; Kaiser and Benner, 2009).

Yields of D-amino acids quickly increased as tDOC loss and input of DOC from a planktonic source was observed, demonstrating the enrichment of bacterial macromolecules and a close link between removal processes and microbial mineralization. Bacterially-derived DOC contributed 26 ± 4% of DOC within the first 2 weeks, and 37 ± 9% of DOC over remaining 2 weeks of sampling in the bay. The biological reactivity of this newly produced bacterial DOC included labile and refractory biomolecules (Kaiser and Benner, 2008). Although the majority of DOC from flooding and planktonic sources was presumably mineralized to CO_2, the production of refractory DOC suggested that storm events can also contribute to the long-term storage of carbon and associated bioelements in the ocean.

Mineralization of Terrigenous DOC and Linkage to Microbial Community Structure

Estimated decay constants indicated the rapid removal of storm-derived tDOC in the bay. In particular, the decay constant estimated for tDOC immediately after the storm was ~3 times higher than decay constants observed for tDOC across high and low latitude environments (**Figure 8**; Kaiser et al., 2017a). Following the initial high loss of tDOC, the decay constant for tDOC over the latter 2 weeks quickly adjusted to the range of global tDOC decay constants. The rapid and presumed extensive mineralization of tDOC was likely linked to its high biolability, efficient removal processes, or both. The presence of some sewage-derived DOM may have contributed to the high removal efficiency of storm-derived DOC, although fresh plant leachates, and flood-derived DOM also exhibit high biolability (Holmes et al., 2008; Wickland et al., 2012; Harfmann et al., 2019).

Mechanisms of tDOC removal in ocean margins include sorption or flocculation, and mineralization by microbial and photochemical processes. Relatively low spectral slope values ($S_{275-295}$, 0.0134–0.0187 nm^{-1}) indicated minor exposure to solar radiation (Helms et al., 2008; Fichot and Benner, 2012). Likewise, $(Ad/Al)_V$ ratios were low (0.71–0.86) confirming microbial oxidation was the dominant mode of mineralization of tDOC. In the Northern Gulf of Mexico, where photochemical processes play an important role in the mineralization of DOM, $(Ad/Al)_V$ ratios were typically >2 (Hernes and Benner, 2003). Sorption was found to be of minor significance in the Mississippi River plume, but flocculation could have led to some loss of hydrophobic macromolecules (Benner and Opsahl, 2001; Hernes and Benner, 2003; Fichot and Benner, 2014).

As the microbial community played a dominant role in the mineralization of storm-derived DOC, the diversity of microbial taxa and their metabolic capabilities were investigated to gain insights on controls of mineralization efficiency. River and estuarine systems show distinct shifts in bacterial communities driven by flow regime and the composition of organic matter to benefit from pulses of biolabile DOM (Crump et al., 2009; Kaiser et al., 2017b). Driven by floodwaters, the microbial community completely changed after the hurricane and resembled communities typical for rivers and soil environments (**Figure 9**; Steichen et al., 2020). Synchronous to the shift

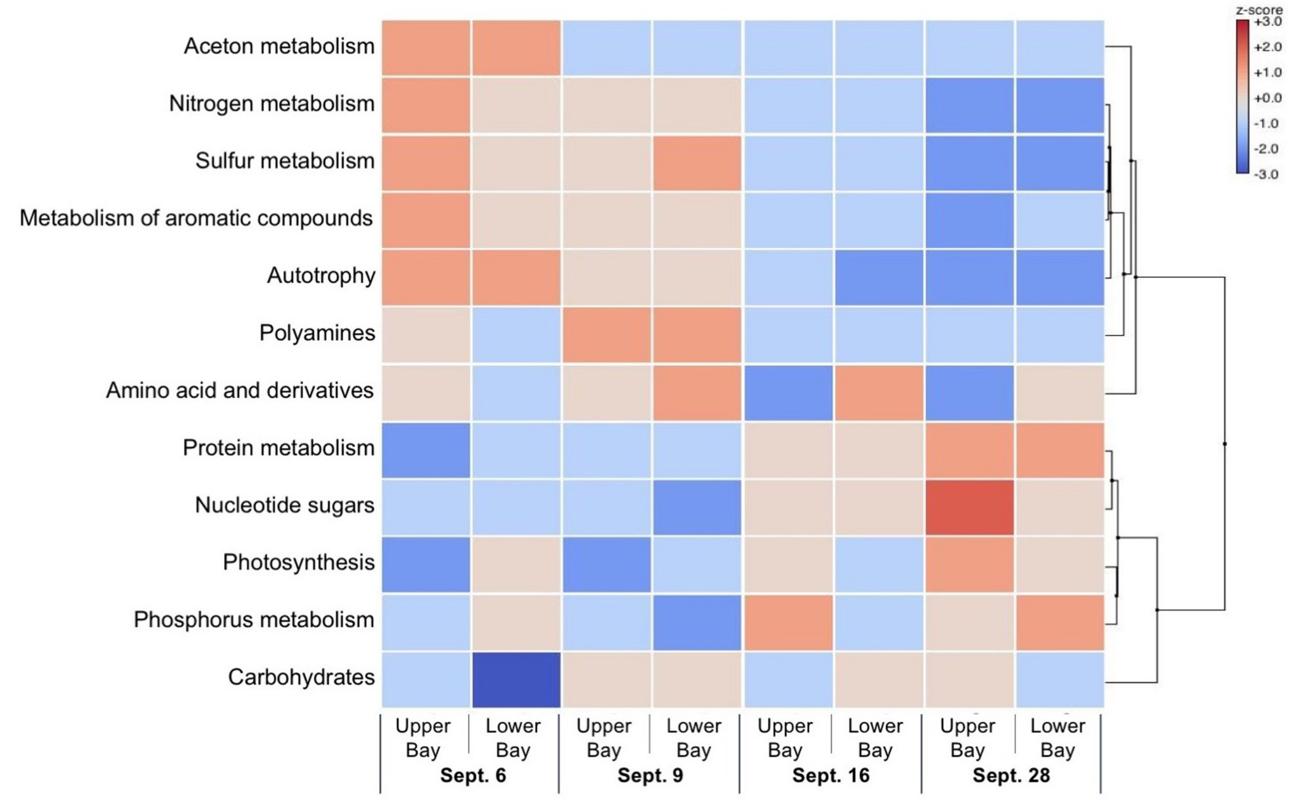

FIGURE 11 | Heat map showing scores of gene expressions of the bacterial community in Galveston Bay after Hurricane Harvey.

in microbial communities and the massive tDOC input, heterotrophic metabolisms dominated during the first 2 weeks of sampling. In particular, the enrichment of genes for the decomposition of aromatic compounds was evident immediately after the storm when mineralization was highest. This suggested the enzymatic capabilities of the microbial community were well tuned to the chemical composition of the existing DOM pool that was dominated by aromatic moieties in lignin and tannin-type structures. At the same time, high microbial diversity potentially promoted metabolic efficiency and energy harvesting through microbial cooperation (Coyte et al., 2015).

With the transition of the DOM pool to a mixture of tDOC and planktonic DOM, enrichment in protein, nucleotide and nucleoside, RNA, DNA, and carbohydrate metabolisms demonstrated a domain shift in the functional gene repertoire and metabolic potential. In addition, gene sequences for aromatic compound metabolism were vastly reduced or absent as microbial communities adjusted to changing chemical composition of the DOM pool and took advantage of biolabile planktonic DOM sources. Remaining terrigenous macromolecules were diagenetically altered as indicated by elevated P/V ratios. Together with the absence of genes for aromatic compound metabolism, this may explain the lower removal efficiency of tDOC as time progressed.

Given the large export of tDOC during the storm event, the presumed mineralization of tDOC potentially resulted in a large flux of CO_2 from Galveston Bay and adjacent coastal shelf. High freshwater discharge during the flood event quickly delivered tDOC to the bay and shelf areas. For calculation of total CO_2 from the presumed mineralization of tDOC it was assumed mineralization efficiencies were similar in the bay and on the coastal shelf. In the bay microbial processes dominated the mineralization of tDOC. Higher light availability in the shelf mixed layer could have could have led to enhanced biomineralization from photochemical processes (Fichot and Benner, 2014).

Within 1 month, 68 ± 15% of tDOC or 65 ± 15 Gg was mineralized, of which 57 ± 10% occurred within the first 2 weeks, and 11 ± 5% over the remaining 2 weeks. The extent of tDOC removal substantially exceeded removal efficiencies of tDOC observed in ocean margins (∼50% per year) (Fichot et al., 2014; Kaiser et al., 2017a) or spring flood-derived DOC of Arctic rivers (17–53% over 1–3 month) (Holmes et al., 2008; Wickland et al., 2012). This suggested hurricanes impose unique conditions on biogeochemical cycles in the coastal zones and affect the connectivity between terrestrial and aquatic ecosystems.

CONCLUSION

Recent hurricanes have carried a climatic fingerprint and had a profound impact on human infrastructure and coastal ecosystems. Observations made during heavy flooding by Hurricane Harvey in the Houston/Galveston watershed showed the majority (68 ± 15%) of flood plain-derived DOC was removed in bay and shelf waters within 1 month. The high biolability of this mobilized DOC was mainly linked to freshly-leached plant-derived organic matter and an active microbial community with functional gene repertoires. Intense microbial processing of flood-derived DOC contributed to both mineralization and production of biorefractory DOM, affecting feedback mechanisms within the coastal and ocean carbon cycle. The efficient mineralization of flood-derived DOC suggests hurricane-induced flood events alter net CO_2 exchange and nutrient budgets in estuarine watersheds and coastal seas.

DATA AVAILABILITY STATEMENT

rRNA sequences can be found in the GenBank Sequence Read Archive under the accession number PRJNA558756. Metagenomic data are available through the BCO-DMO portal at https://www.bco-dmo.org/project/750430. Data are publicly available through the Gulf of Mexico Research Initiative Information and Data Cooperative (GRIIDC) at http://data.gulfresearchinitative.org (doi: 10.7266/PGC99C7D).

AUTHOR CONTRIBUTIONS

GY, KK, and JL collected the samples onboard RV Trident. GY conducted DOC, lignin, amino acids, and UV-Vis absorbance analysis. JL performed rRNA gene and metagenomic sequencing analysis. KK and GY wrote the manuscript with comments and inputs from AQ and JL.

FUNDING

This work was supported by NSF grant 1333633 to KK, a NSF grant 1801367 to JL, and by a grant from The Gulf of Mexico Research Initiative to support consortium research entitled ADDOMEx (Aggregation and Degradation of Dispersants and Oil by Microbial Exopolymers), SA15-22 to AQ. Funds from the Hundred Talent Program of the Chinese Academy of Sciences (Y990030101, GY) supported part of the publication charges.

ACKNOWLEDGMENTS

We thank Amanda Sterne, Laura Leonard, Jamie Steichen, and Rachel Windham and the captain and crew of the R/V Trident for assistance with sample collection.

SUPPLEMENTARY MATERIAL

The Supplementary Material for this article can be found online at: https://www.frontiersin.org/articles/10.3389/fmars.2020.00248/full#supplementary-material

REFERENCES

Avery, G. B., Kieber, R. J., Willey, J. D., Shank, G. C., and Whitehead, R. F. (2004). Impact of hurricanes on the flux of rainwater and Cape Fear river water dissolved organic carbon to Long Bay, southeastern United States. *Glob. Biogeochem. Cycles* 18:GB3085. doi: 10.1029/2004GB002229

Balmonte, J. P., Arnosti, C., Underwood, S., McKee, B. A., and Teske, A. (2016). Riverine bacterial communities reveal environmental disturbance signatures within the Betaproteobacteria and Verrucomicrobia. *Front. Microbiol.* 7:1441. doi: 10.3389/fmicb.2016.01441

Bauer, J. E., Cai, W., Raymond, P. A., Bianchi, T. S., Hopkinson, C. S., and Regnier, P. A. G. (2013). The changing carbon cycle of the coastal ocean. *Nature* 504, 61–70. doi: 10.1038/nature12857

Bender, M. A., Knutson, T. R., Tuleya, R. E., Sirutis, J. J., Vecchi, G. A., Garner, S. T., et al. (2010). Modeled impact of anthropogenic warming on the frequency of intense Atlantic hurricanes. *Science* 327, 454–458. doi: 10.1126/science.1180568

Benner, R., and Opsahl, S. (2001). Molecular indicators of the sources and transformations of dissolved organic matter in the Mississippi River plume. *Org. Geochem.* 32, 597–611. doi: 10.1016/s0146-6380(00)00197-2

Bianchi, T. S., Garcia-Tigreros, F., Yvon-Lewis, S. A., Shields, M., Mills, H. J., Butman, D., et al. (2013). Enhanced transfer of terrestrially derived carbon to the atmosphere in a flooding event. *Geophys. Res. Lett.* 40, 116–122. doi: 10.1029/2012GL054145

Buchfink, B., Xie, C., and Huson, D. H. (2015). Fast and sensitive protein alignment using DIAMOND. *Nat. Methods* 12, 59–60. doi: 10.1038/nmeth.3176

Caesar, L., Rahmstorf, S., Robinson, A., Feulner, G., and Saba, V. (2018). Observed fingerprint of a weakening Atlantic ocean overturning circulation. *Nature* 556:191. doi: 10.1038/s41586-018-0006-5

Cai, W.-J., Dai, M., Wang, Y., Zhai, W., Huang, T., Chen, S., et al. (2004). The biogeochemistry of inorganic carbon and nutrients in the Pearl river estuary and the adjacent Northern South China sea. *Cont. Shelf Res.* 24, 1301–1319. doi: 10.1016/j.csr.2004.04.005

Coyte, K. Z., Schluter, J., and Foster, K. R. (2015). The ecology of the microbiome: networks, competition, and stability. *Science* 350, 663–666. doi: 10.1126/science.aad2602

Crosswell, J. R., Wetz, M. S., Hales, B., and Paerl, H. W. (2014). Extensive CO_2 emissions from shallow coastal waters during passage of Hurricane Irene (August 2011) over the mid-Atlantic Coast of the U.S.A. *Limnol. Oceanogr.* 59, 1651–1665. doi: 10.4319/lo.2014.59.5.1651

Crump, B. C., Peterson, B. J., Raymond, P. A., Amon, R. M. W., Rinehart, A., McClelland, J. W., et al. (2009). Circumpolar synchrony in big river bacterioplankton. *Proc. Natl. Acad. Sci. U.S.A.* 106, 21208–21212. doi: 10.1073/pnas.0906149106

Dauwe, B., Middelburg, J. J., Herman, P. M. J., and Heip, C. H. R. (1999). Linking diagenetic alteration of amino acids and bulk organic matter reactivity. *Limnol. Oceanogr.* 44, 1809–1814. doi: 10.4319/lo.1999.44.7.1809

Davis, J., Kaiser, K., and Benner, R. (2009). Amino acid and amino sugar yields and compositions as indicators of dissolved organic matter diagenesis. *Org. Geochem* 40, 343–352. doi: 10.1016/j.orggeochem.2008.12.003

DeJong, T. M. (1975). A comparison of three diversity indices based on their components of richness and evenness. *Oikos* 26, 222–227. doi: 10.2307/3543712

Du, J., Park, K., Dellapenna, T. M., and Clay, J. M. (2019a). Corrigendum to "dramatic hydrodynamic and sedimentary responses in Galveston Bay and adjacent inner shelf to hurricane Harvey" [Sci. Total Environ. 653, 554–564]. *Sci. Total Environ.* 697:134219. doi: 10.1016/j.scitotenv.2019.134219

Du, J., Park, K., Dellapenna, T. M., and Clay, J. M. (2019b). Dramatic hydrodynamic and sedimentary responses in Galveston Bay and adjacent inner shelf to Hurricane Harvey. *Sci. Total Environ.* 653, 554–564. doi: 10.1016/j.scitotenv.2018.10.403

Du, J., Park, K., Yu, X., Zhang, Y. J., and Ye, F. (2019c). Massive pollutants released to Galveston Bay during Hurricane Harvey: understanding their retention and pathway using Lagrangian numerical simulations. *Sci. Total Environ.* 704:135364. doi: 10.1016/j.scitotenv.2019.135364

Duarte, C., Middleburg, J., and Caraco, N. (2005). Major role of marine vegetation on the ocean carbon cycle. *Biogeosciences* 2, 1–8. doi: 10.5194/bg-2-1-2005

Dunn, D. D. (1996). *Trends in Nutrient Inflows to the Gulf of Mexico from Streams Draining the Conterminous United States, 1972–1993.* Water-Resources Investigations Report 96-4113. Austin, TX: USGS.

Emanuel, K. (2017). Assessing the present and future probability of Hurricane Harvey's rainfall. *Proc. Natl. Acad. Sci. U.S.A.* 114, 12681–12684. doi: 10.1073/pnas.1716222114

Environment Texas Research and Policy Center (2017). *Raw SewageReleased by Hurricane Harvey*. Available online at: https://environmenttexascenter.org/ (accessed May, 2019).

Fichot, C. G., and Benner, R. (2012). The spectral slope coefficient of chromophoric dissolved organic matter ($S_{275-295}$) as a tracer of terrigenous dissolved organic carbon in river-influenced ocean margins. *Limnol. Oceanogr.* 57, 1453–1466. doi: 10.4319/lo.2012.57.5.1453

Fichot, C. G., and Benner, R. (2014). The fate of terrigenous dissolved organic carbon in a river-influenced ocean margin. *Global Biogeochem. Cycles* 28, 300–318. doi: 10.1002/2013GB004670

Fichot, C. G., Lohrenz, S. E., and Benner, R. (2014). Pulsed, cross-shelf export of terrigenous dissolved organic carbon to the Gulf of Mexico. *J. Geophys. Res. Ocean.* 119, 1176–1194. doi: 10.1002/2013JC009424

Freeman, L. A., Corbett, D. R., Fitzgerald, A., Lemley, D. A., Quigg, A., and Steppe, C. (2019). Impacts of urbanization on estuarine ecosystems and water quality. *Estuaries Coast.* 42, 1821–1838. doi: 10.1007/s12237-019-00597-z

Galveston Bay National Estuary Program (1994). "The state of the Bay: a characterization of the Galveston Bay ecosystem," in *Proceedings of the Galveston Bay National Estuary Program GBNEP-44*, (Austin, TX: University of Texas).

Godin, P., Macdonald, R. W., Kuzyk, Z. Z. A., Goñi, M. A., and Stern, G. A. (2017). Organic matter compositions of rivers draining into Hudson Bay: present-day trends and potential as recorders of future climate change. *J. Geophys. Res. Biogeosci.* 122, 1848–1869. doi: 10.1002/2016JG003569

Goñi, M. A., and Hedges, J. I. (1995). Sources and reactivities of marine-derived organic matter in coastal sediments as determined by alkaline CuO oxidation. *Geochim. Cosmochim. Acta* 59, 2965–2981. doi: 10.1016/0016-7037(95)00188-3

Green, M. R., and Sambrook, J. (2017). Isolation of high-molecular-weight DNA using organic solvents. *Cold Spring Harb. Protoc.* 2017, 356–359. doi: 10.1101/pdb.prot093450

Harfmann, J. L., Guillemette, F., Kaiser, K., Spencer, R., Chuang, C.-Y., and Hernes, P. (2019). Convergence of terrestrial dissolved organic matter composition and the role of microbial buffering in aquatic ecosystems. *J. Geophys. Res. Biogeosci.* 124, 3125–3142. doi: 10.1029/2018jg004997

He, B., Dai, M., Zhai, W., Wang, L., Wang, K., Chen, J., et al. (2010). Distribution, degradation and dynamics of dissolved organic carbon and its major compound classes in the Pearl River estuary, China. *Mar. Chem.* 119, 52–64. doi: 10.1016/j.marchem.2009.12.006

Hedges, J. I., and Mann, D. C. (1979). The characterization of plant tissues by their lignin oxidation products. *Geochim. Cosmochim. Acta* 43, 1803–1807. doi: 10.1016/0016-7037(79)90028-0

Helms, J. R., Stubbins, A., Ritchie, J. D., Minor, E. C., Kieber, D. J., and Mopper, K. (2008). Absorption spectral slopes and slope ratios as indicators of molecular weight, source, and photobleaching of chromophoric dissolved organic matter. *Limnol. Oceanogr.* 53, 955–969. doi: 10.4319/lo.2008.53.3.0955

Hernes, P., and Benner, R. (2003). Photochemical and microbial degradation of dissolved lignin phenols: implications for the fate of terrigenous dissolved organic matter in marine environments. *J. Geophys. Res.* 108:3291. doi: 10.1029/2002JC001421

Hernes, P. J., Robinson, A. C., and Aufdenkampe, A. K. (2007). Fractionation of lignin during leaching and sorption and implications for organic matter "freshness". *Geophys. Res. Lett.* 34:L17401. doi: 10.1029/2007GL031017

Holmes, R. M., McClelland, J. W., Raymond, P. A., Frazer, B. B., Peterson, B. J., and Stieglitz, M. (2008). Lability of DOC transported by Alaskan rivers to the Arctic Ocean. *Geophys. Res. Lett.* 35:L03402. doi: 10.1029/2007GL032837

Hounshell, A. G., Rudolph, J. C., Van Dam, B. R., Hall, N. S., Osburn, C. L., and Paerl, H. W. (2019). Extreme weather events modulate processing and export of dissolved organic carbon in the Neuse River Estuary, NC. *Estuar. Coast. Shelf Sci.* 219, 189–200. doi: 10.1016/j.ecss.2019.01.020

Huson, D., Mitra, S., and Ruscheweyh, H. (2011). Integrative analysis of environmental sequences using MEGAN4. *Genome Res.* 21, 1552–1560. doi: 10.1101/gr.120618.111.Freely

Hyatt, D., Chen, G. L., Locascio, P. F., Land, M. L., Larimer, F. W., and Hauser, L. J. (2010). Prodigal: prokaryotic gene recognition and translation initiation site identification. *BMC Bioinform.* 11:119. doi: 10.1186/1471-2105-11-119

Kaiser, K., and Benner, R. (2005). Hydrolysis-induced racemization of amino acids. *Limnol. Oceanogr.* 3, 318–325. doi: 10.4319/lom.2005.3.318

Kaiser, K., and Benner, R. (2008). Major bacterial contribution to the ocean reservoir of detrital organic carbon and nitrogen. *Limnol. Oceanogr.* 53, 99–112. doi: 10.4319/lo.2008.53.1.0099

Kaiser, K., and Benner, R. (2009). Biochemical composition and size distribution of organic matter at the Pacific and Atlantic time-series stations. *Mar. Chem.* 113, 63–77. doi: 10.1016/j.marchem.2008.12.004

Kaiser, K., Benner, R., and Amon, R. M. W. (2017a). The fate of terrigenous dissolved organic carbon on the Eurasian shelves and export to the North Atlantic. *J. Geophys. Res. Oceans* 122, 4–22. doi: 10.1002/2016JC012380

Kaiser, K., Canedo-Oropeza, M., McMahon, R., and Amon, R. M. W. (2017b). Origins and transformations of dissolved organic matter in large Arctic rivers. *Sci. Rep.* 7:13064. doi: 10.1038/s41598-017-12729-1

Kozich, J. J., Westcott, S. L., Baxter, N. T., Highlander, S. K., and Schloss, P. D. (2013). Development of a dual-index sequencing strategy and curation pipeline for analyzing amplicon sequence data on the MiSeq illumina sequencing platform. *Appl. Environ. Microbiol.* 79, 5112–5120. doi: 10.1128/AEM.01043-13

Lehmann, J., Coumou, D., and Frieler, K. (2015). Increased record-breaking precipitation events under global warming. *Clim. Chang.* 132, 501–515. doi: 10.1007/s10584-015-1434-y

Li, D., Liu, C. M., Luo, R., Sadakane, K., and Lam, T. W. (2015). MEGAHIT: an ultra-fast single-node solution for large and complex metagenomics assembly via succinct de Bruijn Graph. *Bioinformatics* 31, 1674–1676. doi: 10.1093/bioinformatics/btv033

McGrane, S. J., Hutchins, M. G., Miller, J. D., Bussi, G., Kjeldsen, T. R., and Loewenthal, M. (2016). During a winter of storms in a small UK catchment, hydrology and water quality responses follow a clear rural-urban gradient. *J. Hydr.* 545, 463–477. doi: 10.1016/j.jhydrol.2016.12.037

Najjar, R. G., Herrmann, M., Alexander, R., Boyer, E. W., Burdige, D. J., Butman, D., et al. (2018). Carbon budget of tidal wetlands, estuaries, and shelf waters of eastern North America. *Glob. Biogeochem. Cycles* 32, 389–416. doi: 10.1002/2017GB005790

Neumann, B., Vafeidis, A. T., Zimmermann, J., and Nicholls, R. J. (2015). Future coastal population growth and exposure to sea-level rise and coastal flooding – a global assessment. *PLoS One* 10:e0118571. doi: 10.1371/journal.pone.0118571

Officer, C. B. (1979). Discussion of the behaviour of nonconservative dissolved constituents in estuaries. *Estuar. Coast. Mar. Sci.* 9, 91–94. doi: 10.1016/0302-3524(79)90009-4

Osburn, C. L., Handsel, L. T., Mikan, M. P., Paerl, H. W., and Montgomery, M. T. (2012). Fluorescence tracking of dissolved and particulate organic matter quality in a river-dominated estuary. *Environ. Sci. Technol.* 46, 8628–8636. doi: 10.1021/es3007723

Osburn, C. L., Rudolph, J. C., Paerl, H. W., Hounshell, A. G., and Van Dam, B. R. (2019). Lingering carbon cycle effects of Hurricane Matthew in North Carolina's coastal waters. *Geophys. Res. Lett.* 46, 2654–2661. doi: 10.1029/2019GL082014

Paerl, H. W., Hall, N. S., Hounshell, A. G., Luettich, R. A., Roddignol, K. L., Osburn, C. L., et al. (2019). Recent increase in catastrophic tropical cyclone flooding in coastal North Carolina, USA: long-term observations suggest a regime shift. *Sci. Rep.* 9:10620. doi: 10.1038/s41598-019-46928-9

Parada, A. E., Needham, D. M., and Fuhrman, J. A. (2016). Every base matters: assessing small subunit RRNA primers for marine microbiomes with mock communities, time series and global field samples. *Environ. Microbiol.* 18, 1403–1414. doi: 10.1111/1462-2920.13023

Rayson, M. D., Gross, E. S., Hetland, R. D., and Fringer, O. B. (2016). Time scales in Galveston Bay: an unsteady estuary. *J. Geophys. Res. Oceans* 121, 2268–2285. doi: 10.1002/2015JC011181

Regnier, P., Friedlingstein, P., Clais, P., Mackenzie, F. T., Gruber, N., Janssens, A. I., et al. (2013). Anthropogenic perturbation of the carbon fluxes from land to ocean. *Nat. Geosci.* 6, 597–607. doi: 10.1038/ngeo1830

Schloss, P. D., Westcott, S. L., Ryabin, T., Hall, J. R., Hartmann, M., Hollister, E. B., et al. (2009). Introducing Mothur: open-source, platform-independent, community-supported software for describing and comparing microbial communities. *Appl. Environ. Microbiol.* 75, 7537–7541. doi: 10.1128/AEM.01541-09

Shen, Y., Fichot, C. G., and Benner, R. (2012). Floodplain influence on dissolved organic matter export from the low Mississippi-Atchafalaya river system to the Gulf of Mexico. *Limnol. Oceanogr.* 57, 1149–1160. doi: 10.4319/lo.2012.57.4.1149

Sobel, A. H., Camargo, S. J., Hall, T. M., Lee, C.-Y., Tippett, M. K., and Wing, A. A. (2016). Human influence on tropical cyclone intensity. *Science* 353, 242–246. doi: 10.1126/science.aaf6574

Sousa, W. P. (1984). The role of disturbance in natural communities. *Ann. Rev. Ecol. Syst.* 15, 353–391. doi: 10.1146/annurev.es.15.110184.002033

Spencer, R. G. M., Aiken, G. R., Wickland, K. P., Striegl, R. G., and Hernes, P. J. (2008). Seasonal and spatial variability in dissolved organic matter quantity and composition from the Yukon river basin, Alaska. *Glob. Biogeochem. Cycles* 22:GB4002. doi: 10.1029/2008GB003231

Steichen, J. L., Labonté, J. M., Windham, R., Hala, D., Kaiser, K., Setta, S., et al. (2020). Microbial, physical, and chemical changes in Galveston Bay following an extreme flooding event, Hurricane Harvey. *Front. Mar. Sci.* 7:186. doi: 10.3389/fmars.2020.00186

Toomey, M. R., Korty, R. L., Donnelly, J. P., van Hengstum, P. J., and Curry, W. B. (2017). Increased hurricane frequency near Florida during Younger Dryas Atlantic meridional overturning circulation slowdown. *Geology* 45, 1047–1050. doi: 10.1130/G39270.1

Trenberth, K. E., Fasullo, J., and Smith, L. (2005). Trends and variability in column-integrated atmospheric water vapor. *Clim. Dyn.* 24, 741–758. doi: 10.1007/s00382-005-0017-4

Trenberth, K. E., Cheng, L., Jacobs, P., Zhang, Y., and Fasullo, J. (2018). Hurricane Harvey links to ocean heat content and climate change adaptation. *Earths Future* 6, 730–744. doi: 10.1029/2018EF000825

Walters, W., Hyde, E. R., Berg-Lyons, D., Ackermann, G., Humphrey, G., Parada, A., et al. (2016). Improved bacterial 16S rRNA gene (V4 and V4-5) and fungal internal transcribed spacer marker gene primers for microbial community surveys. *Msystems* 1:e00009–15. doi: 10.1128/mSystems.00009-15

Warnken, K. W., and Santschi, P. H. (2004). Biogeochemical behavior of organic carbon in the Trinity river downstream of a large reservoir lake in Texas, USA. *Sci. Total Environ.* 329, 131–144. doi: 10.1016/j.scitotenv.2004.02.017

Wickland, K. P., Aiken, G. R., Butler, K., Dornblaser, M. M., Spencer, R. G. M., and Striegl, R. G. (2012). Biodegradability of dissolved organic carbon in the Yukon River and its tributaries: Seasonality and importance of inorganic nitrogen. *Glob. Biogeochem. Cycles* 26:GB0E03. doi: 10.1029/2012GB004342

Yan, G., and Kaiser, K. (2018a). A rapid and sensitive method for the analysis of lignin phenols in environmental samples using ultra-high performance liquid chromatography-electrospray ionization-tandem mass spectrometry with multiple reaction monitoring. *Anal. Chim. Acta* 1023, 74–80. doi: 10.1016/j.aca.2018.03.054

Yan, G., and Kaiser, K. (2018b). Ultra-low sample volume cupric sulfate oxidation method for the analysis of dissolved lignin. *Anal. Chem.* 90, 9289–9295. doi: 10.1021/acs.analchem.8b01867

Yoon, B., and Raymond, P. A. (2012). Dissolved organic matter export from a forested watershed during Hurricane Irene. *Geophys. Res. Lett.* 39, 1–6. doi: 10.1029/2012GL052785

Yu, P., Zaleski, A., Li, Q., He, Y., Mapili, K., Pruden, A., et al. (2018). Elevated levels of pathogenic indicator bacteria and antibiotic resistance genes after Hurricane Harvey's flooding in Houston. *Environ. Res. Lett.* 5, 481–486. doi: 10.1021/acs.estlett.8b00329

Conflict of Interest: The authors declare that the research was conducted in the absence of any commercial or financial relationships that could be construed as a potential conflict of interest.

frontiers
in Marine Science

ORIGINAL RESEARCH
published: 22 April 2020
doi: 10.3389/fmars.2020.00186

Microbial, Physical, and Chemical Changes in Galveston Bay Following an Extreme Flooding Event, Hurricane Harvey

Jamie L. Steichen[1]*, Jessica M. Labonté[1], Rachel Windham[1], David Hala[1], Karl Kaiser[2,3], Samantha Setta[1], Patricia C. Faulkner[1], Hernando Bacosa[1], Ge Yan[2], Manoj Kamalanathan[1] and Antonietta Quigg[1,3]

[1] Department of Marine Biology, Texas A&M University at Galveston, Galveston, TX, United States, [2] Department of Marine Science, Texas A&M University at Galveston, Galveston, TX, United States, [3] Department of Oceanography, Texas A&M University, College Station, TX, United States

Edited by:
Hans Paerl,
The University of North Carolina at Chapel Hill, United States

Reviewed by:
Siddhartha Mitra,
East Carolina University, United States
Nathan Samuel Hall,
The University of North Carolina at Chapel Hill, United States

***Correspondence:**
Jamie L. Steichen
jamie.steichen@tamu.edu

Specialty section:
This article was submitted to Marine Biogeochemistry, a section of the journal Frontiers in Marine Science

Received: *05 August 2019*
Accepted: *10 March 2020*
Published: *22 April 2020*

Citation:
Steichen JL, Labonté JM, Windham R, Hala D, Kaiser K, Setta S, Faulkner PC, Bacosa H, Yan G, Kamalanathan M and Quigg A (2020) Microbial, Physical, and Chemical Changes in Galveston Bay Following an Extreme Flooding Event, Hurricane Harvey. Front. Mar. Sci. 7:186. doi: 10.3389/fmars.2020.00186

Hurricane Harvey (category four storm) made landfall along the coast of Texas (United States) and then stalled out over Texas and Louisiana, releasing 1.29 × 10^{11} m^3 of precipitation over 5 days. This caused extensive flooding that elevated freshwater river discharge and land runoff into Galveston Bay and eventually into the Gulf of Mexico. The floodwaters delivered a significant influx of dissolved organic carbon (DOC), organic pollutants and nutrients along with terrestrial and freshwater associated microbes. Over the 24 days following the flooding event, samples were collected on five cruises across Galveston Bay from the mouth of the San Jacinto River (Houston, TX, United States) to the Gulf of Mexico. Parameters measured for this study include: water quality (temperature, salinity, pH, and dissolved oxygen), nutrients (NO_3^-, NO_2^-, NH_4^+, P_i, and $HSiO_3^-$), polycyclic aromatic hydrocarbons (PAHs), pharmaceuticals (cotinine, carbamazepine, carbamazepine-epoxide, and prednisone), biocide (imidacloprid), DOC, bacteria, and the eukaryotic community composition (16S and 18S rRNA genes). In the week after the flood event, bay-wide salinities decreased to 0–5 compared to the higher pre-Harvey salinities of 20–30 (recorded 5 days before the flood). Water treatment facilities and petrochemical plants were compromised due to the heavy flooding in the region. Increased concentrations of DOC, nutrients, PAHs, pharmaceuticals, and biocides were observed across Galveston Bay immediately following the storm. During the 4 weeks after Harvey, concentrations of DOC, nutrients, and organic pollutants began to decrease coinciding with rising salinities as the freshwater was flushed into the Gulf of Mexico and seawater began moving back into the Bay. Successive blooms of Chlorophyta, diatoms (Bacillariophyta), and dinoflagellates (Dinophyta) occurred similar to post-storm communities from past hurricanes that have impacted estuarine systems along the Gulf of Mexico. The bacterial community showed an increase in the abundance of bacteria associated with terrestrial soils and freshwater at the initial time point and then decreased over time and were replaced by their estuarine and marine relatives within the month following the hurricane. The eukaryotic community changed substantially following Harvey and did not recover to pre-Harvey conditions during our study period, suggesting a longer recovery time compared to the prokaryotes. Although the water quality parameters and prokaryotic community showed signs of returning to pre-Harvey conditions within the month following the flood event, long-term impacts need to be measured in the years following the flood.

Keywords: hurricane, microbes, 16S rRNA, 18S rRNA, organic pollutants, freshwater inflows, estuary, carbon

INTRODUCTION

Houston, Texas (United States) is located within the watershed of Galveston Bay, which is the second largest estuary system in the northern Gulf of Mexico. The volume of freshwater delivered to Galveston Bay during Hurricane Harvey (1.40–1.70 $\times$ 10^{10} m^3) was similar in magnitude to the volume of freshwater inflow that is typically delivered to the Bay over the course of a year (1.86 $\times$ 10^{10} m^3) [Du et al., 2019; Texas Water Development Board, 2019; Thyng et al., 2020 (*in review*)]. During the passing of Hurricane Harvey from 25–30 August 2017, more than 1.29 $\times$ 10^{11} m^3 of rain fell across Texas and Louisiana (United States). It is estimated that during the flooding event, locations in Houston, TX, sank into the Earth ~2 cm where rainfall totals reached up to 1.54 m (van Oldenborgh et al., 2017; Blake and Zelinsky, 2018; Milliner et al., 2018).

The Trinity and San Jacinto Rivers deliver >70% of the freshwater inflow into Galveston Bay (Guthrie et al., 2012). Highly contaminated Superfund sites which were compromised from the deluge that Hurricane Harvey produced (Chapin, 2017) are located within the lower watershed of the San Jacinto River. Spills from compromised wastewater treatment systems, industrial facilities, oil refineries, and chemical plants released $> 1.17 \times 10^5$ m^3 of raw sewage and toxic chemicals as well as 4.53 $\times$ 10^5 kg of deadly air pollutants (Environment Texas Research and Policy Center, 2017; van Oldenborgh et al., 2017; Wolf, 2017; Kiaghadi and Rifai, 2019). Pollutants released by Texas facilities include benzene, 1,3-butadiene, hexane, hydrogen sulfide, toluene, and xylene (all known carcinogens except hexane) and >300,000 kg of sulfur dioxide, which can lead to the formation of dangerous contaminants (Wolf, 2017). Non-point sources of polycyclic aromatic hydrocarbons (PAHs) could have also included those previously found in the sealant of parking lots (Van Metre et al., 2006) and in sediments disturbed by floodwaters (Horney et al., 2018). Due to the increased industrial pollution in the region, Galveston Bay sediments and biota are traditionally key focus areas for environmental monitoring of petrogenic PAHs, and legacy pollutants such as polychlorinated biphenyls (PCBs), dioxins, and metals (Roach et al., 1993; Willett et al., 1997; Qian et al., 2001; Suarez et al., 2006; Howell et al., 2008; Lakshmanan et al., 2010; Yin et al., 2015). While attention is typically focused on monitoring such pollutants, recent concerns have grown for the environmental presence of new or "emerging" pollutants (Ankley et al., 2007; Boxall et al., 2012), such as pharmaceuticals and/or biocides (PBs). Although the occurrence and bioaccumulation potential of select PBs has been reported in surface waters and fish inhabiting river systems (Du et al., 2016), to our knowledge studies focused on the presence of PBs in the Galveston Bay watershed have not been conducted previously.

Previous studies on the water quality within Galveston Bay have been conducted which have provided a baseline of the pre-Harvey conditions (Guo et al., 1999; Örnólfsdóttir et al., 2004; Roelke et al., 2013; Dorado et al., 2015). Freshwater inflow pulses which deliver nutrients and organic matter to Galveston Bay vary seasonally, producing a dynamic and complex system (Roelke et al., 2013; Dorado et al., 2015; Pinckney et al., 2017). The microbial community responds to variations in the water quality by displaying seasonal changes in the community structure within this highly productive estuary (Lester and Gonzalez, 2011; Roelke et al., 2013; Dorado et al., 2015). Depending on the volume of freshwater delivered to Galveston Bay, phytoplankton biomass has actually been shown to decrease following these pulses due to hydraulic displacement (Roelke et al., 2013). The response of the phytoplankton community has also been shown to be dependent on the level of nutrient limitation present before the freshwater pulse occurs (Roelke et al., 2013; Dorado et al., 2015). Guo et al. (1999) observed that dissolved organic carbon (DOC) in Galveston Bay decreased non-conservatively with increasing salinity indicating a removal of the DOC with increased mixing between freshwater and seawater. At low to intermediate salinities input of DOC was observed that was attributed to primary productivity and resuspension of DOC from bottom sediments.

Hurricane Harvey caused extensive flooding of rivers and produced land runoff to the point that freshwater draining into Galveston Bay via the Houston Ship Channel pushed the leading edge of the saltwater wedge out toward the Gulf of Mexico [Du et al., 2019; Thyng et al., 2020 (*in review*)]. Flooding of this volume has not been recorded previously in Galveston Bay leading to questions regarding the response of the biological community. This paper summarizes the water quality parameters, PBs, DOC, PAHs, and changes in the microbial community (16S rRNA and 18S rRNA analyses) in Galveston Bay immediately following Hurricane Harvey. Collectively, these findings show a transition from an estuarine microbial community preceding the hurricane to a primarily freshwater microbial community after the flooding event, which then began the shift back to an estuarine/marine biotic community. Within the month after the passing of the hurricane, the prokaryotes showed signs of returning to a pre-flooding community while the eukaryotic community still appeared to be in transition. The impacts of the increased contaminants and the extensive period of low salinity should be monitored in years to come to determine the long-term effects on the biological community including the fisheries. This collaborative effort will allow for improved understanding of the physicochemical and biological changes following a large storm event within subtropical estuaries.

MATERIALS AND METHODS

Study Area and Sampling Design

The San Jacinto and Trinity Rivers are the two major sources of freshwater inflows to Galveston Bay (**Figure 1**), delivering 16 and 55% of the annual riverine discharge to the northwest and northeastern reaches of the Bay, respectively (Guthrie et al., 2012). Buffalo Bayou, adjacent to the San Jacinto River, brings in an additional 12% while smaller tributaries around the Bay account for the rest of the inputs (Guthrie et al., 2012; **Figure 1**). Five sampling cruises T1 (09/04/2017), T2 (09/09/2017), T3 (09/16/2017), T4 (09/21/2017), and T5 (09/28/2017) were conducted during the month following Hurricane Harvey onboard the R/V Trident. Ten stations (1–10) were sampled to capture the conditions immediately following Hurricane Harvey on a transect from the San Jacinto River mouth (station 1) near the Port of Houston to the mouth of Galveston Bay near the Gulf of Mexico (station 10) (**Figure 1**).

Water Quality Sampling

While the average water depth in the bay is ∼2.4 m, sampling close to the ship channel allowed us to evaluate a deeper profile. A calibrated Hydrolab MS5 datasonde was used to collect water quality parameters from surface down to 4 m at each station including temperature (°C), salinity, dissolved oxygen (mg L^{-1} and %), and pH. Secchi depth (m) was collected simultaneously. Unfiltered surface water samples ($\geq$100 mL) were collected for total nitrogen (TN) and total phosphorus (TP). Surface water ($\geq$100 mL) was also vacuum-filtered through a pre-rinsed, 47 mm glass fiber filter (GF/F), and the filtrate was used to measure the dissolved nutrients including: nitrate (NO_3^-), nitrite (NO_2^-), ammonium (NH_4^+), phosphate (P_i), and silicate ($HSiO_3^-$). Filtrate was placed in acid-washed (10% HCl) 250-mL polyethylene Nalgene bottles rinsed three times with filtrate from the sample and then frozen until analysis. All water samples collected for total and dissolved nutrient analysis were shipped to the Geochemical and Environmental Research Group at Texas A&M University for analysis on the Lachat QuikChem AE autoanalyzer (American Public Health Association [APHA], 1985). The sum of NO_3^-, NO_2^-, and NH_4^+ was used to calculate dissolved inorganic nitrogen (DIN). The resulting DIN value was then divided by P_i to calculate the ratio of inorganic nitrogen to phosphate (DIN:P_i). Samples for DOC were filtered through 0.2 μm Whatman-Nucleopore Q-TEC filters (Filtration Solutions) on board. Concentrations of DOC were determined using a high temperature-combustion method and a Shimadzu TOC-V analyzer (Benner and Strom, 1993). Total suspended sediments (TSS) were collected from the surface water samples during all time points at all stations; 150 mL of surface water was filtered through a pre-weighed and combusted 47 mm GF/F. After filtration the sample was placed in a drying oven at 103–105°C for at least 24 h and then weighed. The difference in weight was used to calculate the TSS (Method 2540 D of Standard Methods; American Public Health Association [APHA], 1998).

16S rRNA and 18S rRNA Gene Community Analyses

For the 16S and 18S ribosomal RNA (rRNA) gene analysis samples were collected at every station during each time point. The water samples were filtered on 0.2 μm polyethylsulfone (PES) membrane filters immediately after returning to shore. Two pre-Harvey samples (named pre-Harvey controls) were collected off the Texas A&M University at Galveston Boat Basin (coordinates) on 07/31/2017 and 08/22/2017. Each sample was filtered through a GF/F (with a 0.7 μm pore-size), followed by a 0.22 μm pore-size polyvinylidene fluoride (PVDF) filter. Filters were stored in −80°C freezer until total nucleic acid was extracted, using the MO Bio PowerSoil DNA Isolation Kit (cat. no. 128888-50). DNA could not be extracted from the pre-Harvey controls GF/F filters, therefore all further PCR amplifications were performed from the PVDF DNA extractions. PCR amplification using Promega GoTaq Flexi DNA Polymerase was performed following the 16S/18S rRNA gene Illumina amplicon protocol from the Earth Microbiome project.[1] Each sample was amplified in triplicate 25 μL reactions with the following cycling parameters: 95°C for 3 min, 30 cycles of 95°C for 45 s, 50°C for 60 s, and 72°C for 90 s, and a final elongation step at 72°C for 10 min. For the prokaryotes, amplifications were performed using the 515F-806R primer pair (10 μM each) modified to include recently published revisions that reduce bias against the *Crenarchaeota* and *Thaumarchaeota* lineages as well as the SAR11 bacterial clade (Apprill et al., 2015; Parada et al., 2016). The primer pair was additionally modified to include Golay barcodes and adapters for Illumina MiSeq sequencing. Final primer sequences are detailed in Walters et al. (2016). The primer pair utilized for the Eukaryote analysis was V8f-1510r (Bradley et al., 2016). For eukaryotes the V8V9 hypervariable region on the 18S rRNA and for prokaryotes the V4 hypervariable region on the 16S rRNA were used for amplification (Caporaso et al., 2011; Bradley et al., 2016). Following amplification, the triplicate products were combined together and run on a 1.5% agarose gel to assess amplification success and relative band intensity. Amplicons were then quantified with the QuantiFluor dsDNA System (Promega), pooled at equimolar concentrations, and purified with an UltraClean PCR Clean-Up Kit (MoBio Laboratories; Carlsbad, CA, United States). The purified library, along with aliquots of the three sequencing primers, were sent to the Georgia Genomics Facility (Athens, GA, United States) for MiSeq sequencing (v2 chemistry, 2 × 250 bp). Sequence reads for both the 16S rRNA and 18S rRNA were processed separately using *mothur* v.1.39.5 following the MiSeq SOP https://www.mothur.org/wiki/MiSeq_SOP (Schloss et al., 2009; Kozich et al., 2013).

---

[1] http://www.earthmicrobiome.org/emp-standard-protocols

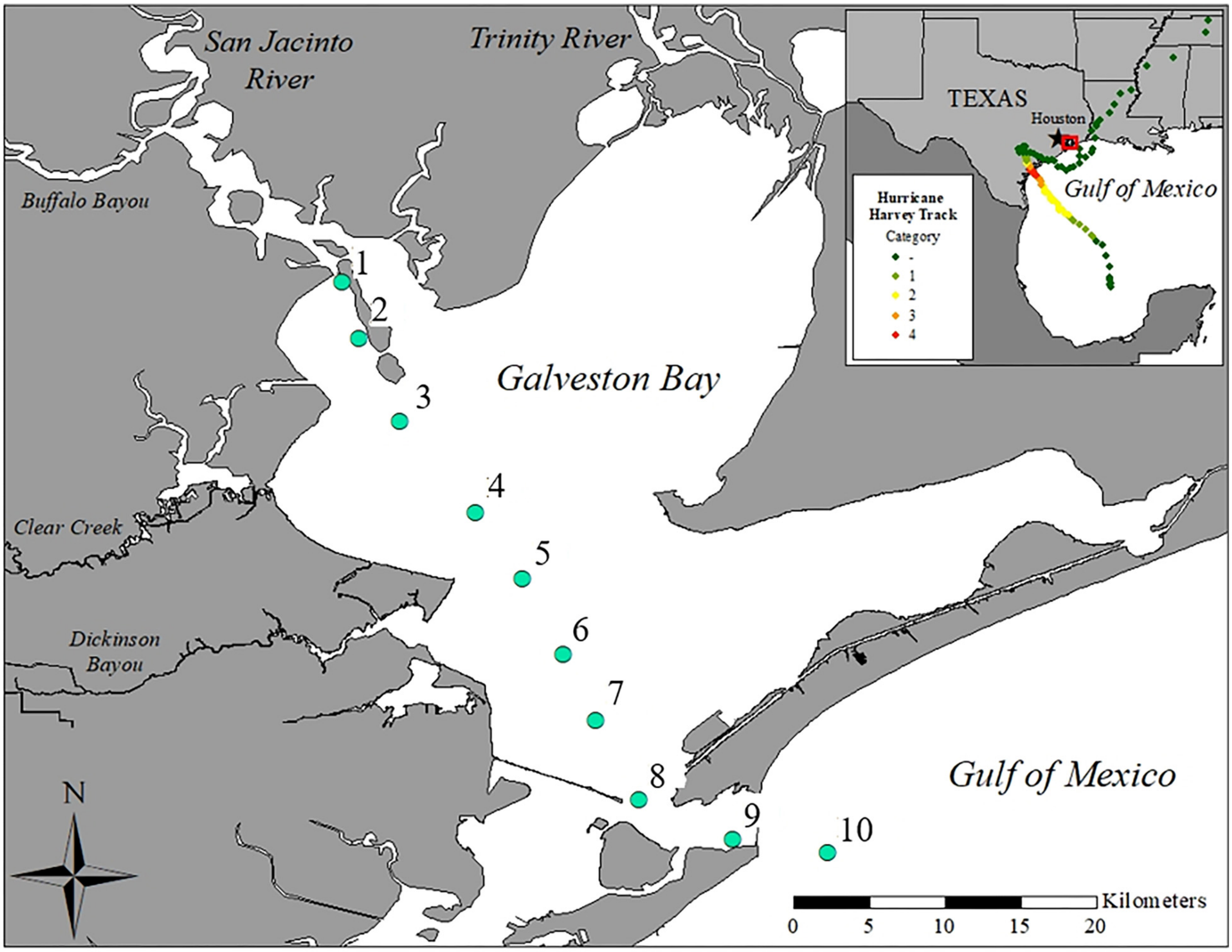

FIGURE 1 | Map of Galveston Bay, TX (United States) showing the ten stations sampled during each cruise labeled as stations 1–10. Inset shows location of Galveston Bay along the upper Texas coastline of the Gulf of Mexico. The color dotted line displays the path and landfalls of Hurricane Harvey.

Organic Pollutants

Pharmaceuticals and Biocides

Twenty-eight pharmaceuticals and biocides (PBs) were monitored in water samples from Galveston Bay. These included: amphetamine, atenolol, carbamazepine, carbamazepine epoxide, chlorfenvinphos, cotinine, dexamethasone, diazepam, dichlofenthion, diclofenac, drospirenone, fluoxetine, gestodene, imazalil, imidacloprid, ketoprofen, levonorgestrel, melengestrol acetate, nicotine, norethindrone, prednisolone, prednisone, prochloraz, progesterone, propranolol, pyriproxyfen, sulfamethoxazole, and trimethoprim (along with representative internal standards). All analytes were assessed in unfiltered water samples from Galveston Bay. Of the 28 monitored compounds, only five analytes presented levels above limits of detection (set to the lowest respective standard yielding an accuracy of *geq*70% and precision *leq* 20%). The pharmaceuticals measured included cotinine (nicotine metabolite), carbamazepine (anti-epileptic and bi-polar disorder medication), carbamazepine-epoxide (carbamazepine metabolite), prednisone (anti-inflammatory synthetic corticoid), and the biocide, imidacloprid (insecticide). Samples (1 L) for PBs analysis were collected at each station during every time-point. Collectively, these can be used as proxies for human activities and in the case of this study, for excess flows, over flows, and other flood impacts on waste water treatment facilities that would release them into the environment. PBs were quantified using an Agilent 1260 UHPLC system with triple-quad 6420 mass detector using an Agilent jet-stream electrospray source. PBs from Galveston Bay water samples (500 mL) were spiked with an internal standard (deuterated carbamazepine or d10-carbamazepine) and extracted using Oasis HLB solid phase cartridges (500 mg, Waters Cat#186000115). The mass spectrometer settings included a capillary voltage of 3.5 kV and nebulizer gas temperature of 350°C and gas flow of 12 L/min. All PBs were quantified using multiple-reaction-monitoring (using previously optimized precursor > product ions) in positive electrospray ionization (ESI +) mode. These included: 177.1 > 80.2 (cotinine), 237.1 > 194 (carbamazepine), 253.1 > 180 (carbamazepine epoxide), 359.2 > 341.1 (prednisone), and 256.1 > 175 (imidacloprid). Deuterated carbamazepine (d10-carbamazepine, 247.2 > 204.1) was used as internal standard and all compounds were chromatographically separated on an Agilent poroshell EC-C18 column (3 × 50 mm, 2.7 μm). The mobile phase comprised of LC-MS grade Milli-Q water and methanol, with each containing 5 mM ammonium formate. The mobile phase gradient transitioned from 30%, increasing linearly to 70% in 3 min, and then to 95% over 6 min. The gradient was subsequently decreased from 95 to 70% over 3 min and from 70 to 30% (initial condition) in 3 min with a constant flow rate of 0.4 mL/min. The total chromatographic runtime was 25 min.

Polycyclic Aromatic Hydrocarbons (PAHs)

The 16 PAHs included in this study are naphthalene, acenaphthylene, acenaphthene, fluorene, phenanthrene, anthracene, fluoranthene, pyrene, benzo(a)anthracene, chrysene, benzo(b)fluoranthene, benzo(k)fluoranthene, benzo(a)pyrene, indeno(1,2,3-cd)pyrene, dibenzo(a,h)anthracene, and benzo(ghi)perylene. Water samples were collected at each station during each time point throughout the sample period. The PAHs from the water samples were extracted using liquid–liquid extraction based on Wade et al. (2011) with few modifications. Briefly, the water sample was placed in a 2-L separatory funnel, acidified by sulfuric acid, and extracted three times with 30 mL of dichloromethane. Prior to extraction, a mixture of deuterated standards containing naphthalene-d_8, phenanthrene-d_{10}, and perylene-d_{12} was added (Kamalanathan et al., 2019). The extract was filtered through a chromatography column containing anhydrous sodium sulfate and concentrated by rotary evaporator. The samples were then analyzed by gas chromatography (HP-6890 Series) interfaced with an Agilent 5973 inert mass selective detector (MSD), and operated in a selective ion-monitoring (SIM) mode (Bacosa et al., 2018). The PAHs were quantified using a calibration curve of PAHs standards. The final concentration was corrected based on the recovery of the standards.

Multivariate Statistical Analysis

Statistical analyses were conducted using PRIMER v6 + PERMANOVA add-on package software (Plymouth Routines in Multivariate Ecological Research; Clarke and Warwick, 1994). Environmental variables including water quality parameters, nutrients, DOC, PAHs, and PBs were square root transformed, normalized to place all parameters on the same unit less scale, and then used to build a similarity matrix based on the calculated Euclidean distances. The 16S rRNA gene and 18S rRNA gene community analyses were conducted on the operational taxonomic unit (OTU) abundance data which were square root transformed and then used to calculate a Bray–Curtis similarity index matrix. This index best represents the similarities (or dissimilarities) within the biotic community due to the fact these data are not normally distributed and have unequal variance distribution characteristics (Clarke and Gorley, 2006).

The relationship between the distributions of the biological and environmental variables was investigated using the distance-based linear model (DISTLM) in the PRIMER v6 software package (Clarke and Warwick, 2001). The DISTLM calculates the correlations between each of the environmental variables and the biological dataset. The DISTLM was run on the Bray–Curtis similarity matrix of the 16S rRNA and 18S rRNA OTU abundances. The DISTLM routine was carried out to provide a method of matching the microbial community from the 16S rRNA and 18S rRNA results with the environmental variables. A permutational analysis of variance (PERMANOVA) was run to determine significant differences between time points and stations for both the environmental and biological data. PERMANOVA was run on the Euclidean distance matrix of the transformed and normalized environmental data and the Bray–Curtis similarity matrix built from the square root transformed biological data. The biological data points were displayed in an nMDS to visualize the distribution of the biotic data in ordination space. The environmental vectors were overlain on the nMDS to show the Pearson correlations in relation to the biotic community changes temporally and spatially.

RESULTS

Water Quality

The elevated precipitation and freshwater inflows entering the Bay from the San Jacinto and Trinity Rivers resulted in decreased salinity and increased sediment load (**Figures 1, 2**, **Supplementary Figures S1**, **S2**, and **Table 1**). During the T1 cruise (1 week after Hurricane Harvey passed over the Houston metro region) salinities across the Bay were low (0.02–6.57 at surface and 0.04–13.90 at 4 m depth). Near the mouth of the San Jacinto River (station 1) salinities were 0.02 at the surface and 0.36 at 4 m depth (**Figure 2**). Four weeks after hurricane passed the salinities began to increase ranging from 7.82 at the surface closest to the San Jacinto River up to 21.14 (4 m depth) at the Gulf of Mexico location (station 10) (**Figure 2**). Temperatures were lowest during the T2 sampling and then increased over time through T5 (**Figure 3A** and **Table 1**). The pH was lowest during the T1 sampling event and then increased during T2 and T3 and began to plateau during T4 and T5 (**Figure 3B** and **Table 1**).

Dissolved organic carbon concentrations were highest (308–566 μM) during the first cruise at stations 1–8 (**Figures 3C**, **4** and **Table 1**). As the salinity began to increase during the last three cruises, DOC concentrations declined and ranged from 267 to 401 μM across the bay (**Figures 2**, **4**). The DOC displays an inverse relationship with Secchi depth with increasing time after the flooding event (**Figures 3C, I** and **Table 1**). Highest TSS concentrations were recorded during T1, T2, and T4 (**Figure 3F** and **Table 1**). The highest TSS concentration was observed during the T4 cruise at 122 mg L^{-1} at station 10 while the lowest value (20 mg L^{-1}) was observed during the T1 cruise (**Figure 3F** and **Table 1**).

$NO_3^- + NO_2^-$ (NO_x) concentrations increased with time at the stations nearest the river mouth with highest concentrations observed during the last time point (**Figure 3G** and **Table 1**). NH_4^+ was observed in the highest concentrations at stations 1–8 during the first cruise (T1) ranging from 4.77 to 14.16 μM (**Figure 3H** and **Table 1**). The concentrations of NH_4^+ remained elevated at the stations 1 and 2 nearest the San Jacinto River mouth during the first three cruises (T1–T3) ranging from 14.17

to 14.97 μM (**Figure 3H** and **Table 1**). Over time and with increasing distance from the mouth of the river, the NH_4^+ concentrations decreased to concentrations < 6 μM (**Figure 3H** and **Table 1**). The TN ranged from 23.26 to 114.98 μM with lowest concentrations occurring near the Gulf of Mexico and higher concentrations present near the river mouth during T3 and T4 (**Figure 3I** and **Table 1**). The orthophosphate (P_i) concentrations were lowest immediately following the flooding event at all stations ranging from 1.11 to 3.74 μM (**Figure 3J** and **Table 1**). The highest concentrations of P_i were observed at the northernmost stations during T2–T4 and also at mid bay stations during the latest time point (**Figure 3J** and **Table 1**). TP exhibited two peaks along the cruise transect at stations 1 and 2 and stations 8 and 9 during the latter time points (T3–T5; **Figure 3K** and **Table 1**). The DIN:P_i was below 16 during the entire cruise period indicative of nitrogen limitation across the bay system (**Table 1**). The highest concentrations of silicate were observed in the samples collected during T2 ranging from 68.01 μM at the northernmost site (station 1) to 49.86 μM at the furthest point from the river mouth (station 10; **Table 1**). At the last time point, the $HSiO_3^-$ remained high at station 1 (63.37 μM) but decreased to 30.69 μM at station 10 nearest the Gulf of Mexico (**Figure 3L** and **Table 1**).

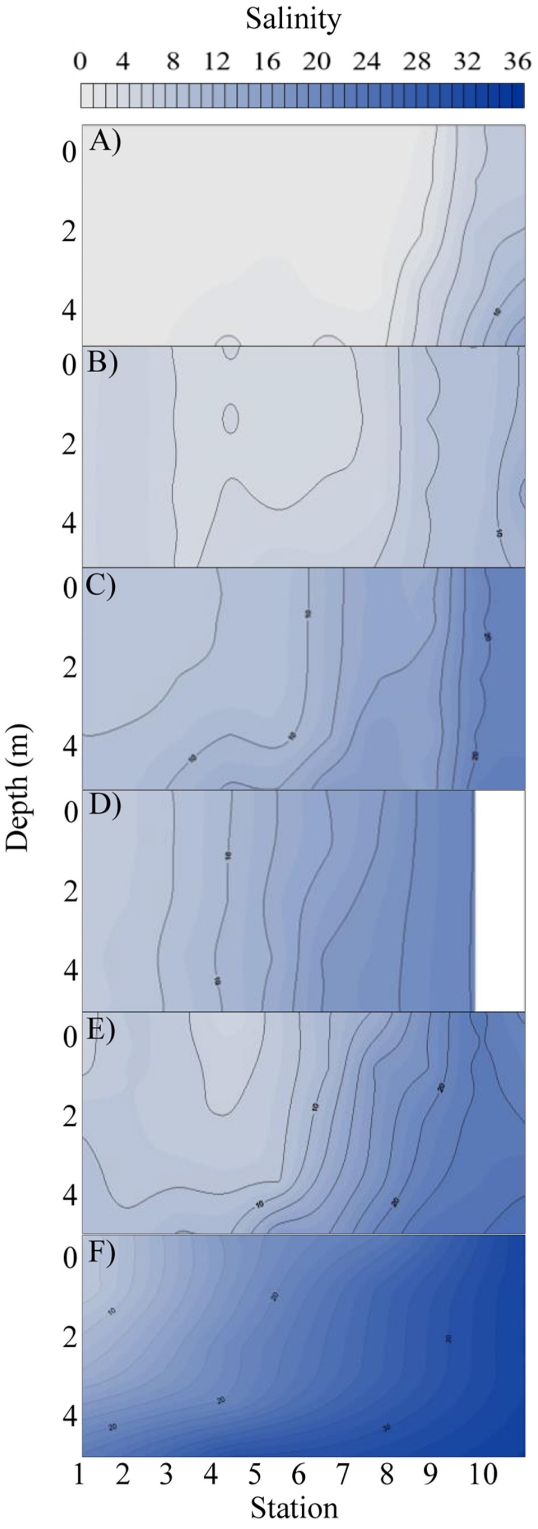

FIGURE 2 | Salinity profile with depth (*y*-axis) at each station (*x*-axis) along the cruise transect for each time point: **(A)** T1, **(B)** T2, **(C)** T3, **(D)** T4, **(E)** T5, and **(F)** pre-Harvey. The pre-Harvey salinity was measured in the same month (August) during the previous year (2016) along the same sample transect used for this study. Salinities are shown from zero to thirty six along a color gradient from light gray to dark blue, respectively.

16S and 18S rRNA Gene Community Analysis

Prokaryotic community analysis (16S rRNA) revealed the generally dominant members of the marine bacteria coastal community pre-Harvey (07/31/2017 and 08/22/2017) including Acidimicrobiia, Cyanobacteria, Betaproteobacteria, SAR11, Gammaproteobacteria, and Oceanospirillales (**Figures 5**, **6**). These estuarine/marine bacteria were replaced by microorganisms of terrestrial origin including bacteria within the phyla Actinobacteria and Verrucomicrobia (class Opitutae), sedimentary classes with the phylum Actinobacteria, and freshwater origin phyla Betaproteobacteria, Burkholderiales, and Sphingobacteria (associated with treated wastewater) following Harvey (**Figures 5**, **6** and **Supplementary Figure S4**). Spartobacteria began to increase in relative abundance during time points T3 and T5 (**Figure 5**). Marine Cyanobacteria, dominated by *Synechococcus* sp., normally represent ∼20–30% of the total abundance of all OTUs on average in Galveston Bay. After Hurricane Harvey, <5% of all OTUs were Cyanobacteria and then increased back to normal levels within 6 weeks following Harvey. Betaproteobacteria followed an opposite trend and decreased in abundance from early to late time-points over time (**Figures 5**, **6** and **Supplementary Figure S4**). Although the relative abundance of the phyla Proteobacteria did not change greatly over the sample period, the classes within this group of bacteria did fluctuate with the variability in salinity and other environmental parameters (**Figure 6**). The Alphaproteobacteria, Deltaproteobacteria, and Gammaproteobaceteria increased in OTU relative abundance with increasing salinities post-Harvey (**Figure 6**). The Betaproteobacteria groups made up a majority of the relative abundance immediately following the flooding event

TABLE 1 | Water quality parameters that were measured at each stations during each time point.

Time point	Station	Water Quality							Nutrients							DOC (μM)
		Temp (°C)	Sal	DO (mg L^{-1})	DO (%)	pH	TSS (g mL^{-1})	Secchi (m)	NO$_x$ (μM)	NH$_4$$^+$ (μM)	P$_i$ (μM)	DIN:P$_i$	TN (μM)	TP (μM)	HSiO$_3$$^-$ (μM)	
T1	1	27.23	0.02	7.63	96.20	6.32	20.00	0.25	10.61	14.16	2.47	10.04	73.39	4.68	56.08	566.00
	2	27.16	0.53	6.41	80.80	7.43	32.00	0.25	8.16	11.42	2.41	8.13	59.40	5.54	65.72	–
	3	27.69	0.63	6.02	79.20	7.32	60.00	0.25	7.30	7.58	1.90	7.84	49.05	4.66	58.15	482.07
	4	27.66	0.84	6.28	80.90	7.42	82.00	0.25	7.82	6.63	1.63	8.89	77.84	5.09	58.55	429.48
	5	27.54	0.64	5.88	75.70	7.35	74.00	0.25	8.20	7.79	1.62	9.87	55.65	5.08	59.05	–
	6	27.60	0.73	5.79	75.40	7.36	82.00	0.25	8.21	6.77	1.47	10.16	45.43	5.30	52.33	457.00
	7	27.79	0.81	6.12	80.10	7.37	88.00	0.25	7.75	4.77	1.38	9.10	47.89	5.16	54.16	–
	8	28.11	1.07	6.28	82.40	7.41	44.00	0.25	9.50	7.52	1.68	10.16	55.22	5.27	57.49	457.28
	9	28.66	5.84	6.48	88.00	7.77	22.00	0.50	7.68	3.79	1.15	9.95	39.67	3.11	49.56	311.45
	10	28.92	6.57	6.56	90.90	7.83	30.00	0.50	8.35	5.52	1.30	10.63	52.15	3.14	50.74	308.46
T2	1	25.93	4.35	5.24	67.40	7.42	96.00	0.25	20.27	14.93	3.42	10.28	57.73	5.44	68.01	358.84
	2	26.03	5.65	5.40	71.20	7.50	80.00	0.30	18.01	15.61	3.26	10.30	64.79	4.95	59.42	376.79
	3	25.81	3.62	6.63	85.10	7.68	46.00	0.25	14.00	8.95	2.41	9.52	57.33	5.59	68.20	–
	4	25.78	4.09	6.88	88.90	7.71	112.00	0.25	15.05	8.16	2.41	9.64	60.83	5.12	61.08	–
	5	25.54	3.58	7.17	91.90	7.83	90.00	0.50	14.76	4.75	2.11	9.25	58.16	4.76	65.41	–
	6	26.09	3.76	7.46	96.60	7.85	100.00	0.50	12.92	3.43	1.62	10.12	53.40	4.20	62.76	416.74
	7	25.00	4.52	7.52	97.70	7.88	70.00	0.50	8.35	2.49	1.28	8.44	40.59	3.59	59.90	345.68
	8	26.61	8.14	7.05	94.60	7.91	36.00	0.60	5.96	3.40	1.20	7.78	39.04	2.98	51.36	302.04
	9	26.60	7.98	7.44	99.80	7.99	62.00	0.50	6.68	4.28	1.18	9.27	36.96	2.80	52.98	316.20
	10	26.73	10.38	7.55	103.00	8.03	20.00	0.75	5.03	2.59	1.11	6.87	39.37	2.98	49.86	314.20
T3	1	26.97	5.40	6.4	85.10	7.73	59.33	0.40	30.72	14.71	3.12	14.58	89.21	6.15	65.42	335.34
	2	26.92	7.26	6.85	92.10	7.97	72.67	0.50	19.04	9.79	2.39	12.04	66.35	4.43	49.20	–
	3	27.13	6.40	8.92	119.80	8.40	16.67	0.55	1.86	2.32	1.36	3.06	51.68	3.84	45.83	–
	4	27.34	4.16	8.79	116.50	8.36	24.67	0.50	1.12	2.39	1.45	2.43	50.75	4.58	45.29	401.23
	5	27.36	6.85	8.64	116.70	8.32	21.33	0.50	1.40	2.88	1.31	3.27	44.97	3.92	53.51	396.45
	6	27.69	9.88	8.94	123.10	8.32	18.67	0.75	0.45	1.83	1.18	1.94	50.01	3.32	60.46	–
	7	28.48	12.18	8.78	124.30	8.33	23.33	0.75	0.40	1.93	1.20	1.95	33.20	2.93	48.53	334.21
	8	29.89	17.54	7.35	109.80	8.16	34.67	0.90	0.88	4.62	3.76	1.46	24.76	4.98	52.01	272.70
	9	27.64	22.55	6.99	103.50	8.14	43.33	0.90	0.53	3.71	2.46	1.72	114.98	3.72	28.96	239.88
	10	28.32	19.38	7.76	114.90	8.22	26.00	2.50	0.50	4.41	2.96	1.66	25.17	4.41	35.07	257.29
T4	1	27.86	6.84	5.93	80.80	7.83	71.33	0.25	33.94	5.33	3.74	10.49	71.26	6.57	45.68	339.06
	2	28.19	6.86	5.28	70.30	7.76	61.33	0.50	33.23	5.34	3.77	10.22	72.48	6.32	45.08	–
	3	28.39	8.23	5.94	81.60	7.97	68.67	0.50	12.25	4.42	2.22	7.49	51.41	5.24	47.89	–
	4	28.70	9.86	6.04	84.60	8.05	76.00	0.50	6.55	4.83	1.70	6.70	48.72	4.21	40.98	330.82
	5	28.81	12.07	6.46	91.90	8.08	86.67	0.50	4.80	2.66	1.44	5.16	45.71	3.83	41.51	319.52
	6	29.56	14.07	7.04	102.80	8.20	116.00	0.50	0.56	2.21	1.49	1.85	24.94	6.38	39.55	–
	7	29.34	15.52	6.9	101.10	8.17	90.00	0.75	0.50	5.33	1.89	3.09	29.63	5.68	44.05	299.80
	8	29.33	18.56	6.53	97.50	8.13	96.00	1.00	0.81	5.40	3.17	1.96	23.26	4.98	37.40	–
	9	29.23	20.06	6.17	92.30	8.20	113.33	1.50	0.96	6.28	2.97	2.44	42.34	4.53	34.54	257.16
	10	29.00	21.00	6.28	92.00	8.20	122.00	1.50	1.16	5.35	2.71	2.40	27.14	4.09	33.40	255.13
T5	1	28.92	7.84	5.94	82.80	7.92	18.67	0.50	40.47	2.82	4.46	9.71	92.88	7.08	63.37	346.00
	2	28.74	7.57	6.87	95.30	7.97	6.67	0.75	37.28	2.78	3.90	10.26	88.26	6.13	58.74	–
	3	28.93	7.23	8.14	113.20	8.28	4.00	0.75	2.45	2.66	1.79	2.86	62.26	4.23	65.62	377.99
	4	29.03	8.31	7.75	104.00	8.26	10.67	1.00	0.60	2.07	1.64	1.63	53.11	3.91	51.25	357.56
	5	29.39	8.32	7.16	100.90	8.24	8.67	0.75	0.62	1.89	1.62	1.55	54.51	4.09	47.50	356.86
	6	29.10	11.24	7.12	99.80	8.15	2.67	0.75	0.69	1.88	1.49	1.73	44.24	3.49	58.05	325.00
	7	29.19	13.60	7.14	103.40	8.14	6.67	0.90	0.57	5.52	4.09	1.49	36.44	6.43	56.67	312.85
	8	29.46	12.60	7.18	104.10	8.17	na	0.75	0.56	5.70	4.03	1.55	46.72	6.75	52.57	323.32
	9	29.20	19.88	6.26	93.90	8.07	na	1.00	0.84	4.95	2.96	1.96	38.51	4.66	38.46	267.23
	10	29.55	20.08	6.99	105.40	8.13	4.00	3.00	0.79	5.06	2.63	2.22	45.47	3.69	30.69	268.86

Abbreviations are defined as: temperature (Temp), salinity (Sal), dissolved oxygen (DO), total suspended sediments (TSS), nutrients [NO$_x$: nitrate (NO$_3$$^-$) + nitrite (NO$_2$$^-$)], ammonium (NH$_4$$^+$), dissolved inorganic nitrogen (DIN), phosphate (P$_i$) total nitrogen (TN), total phosphorus (TP), and dissolved organic carbon (DOC). Time points when data were not collected are indicated by –.

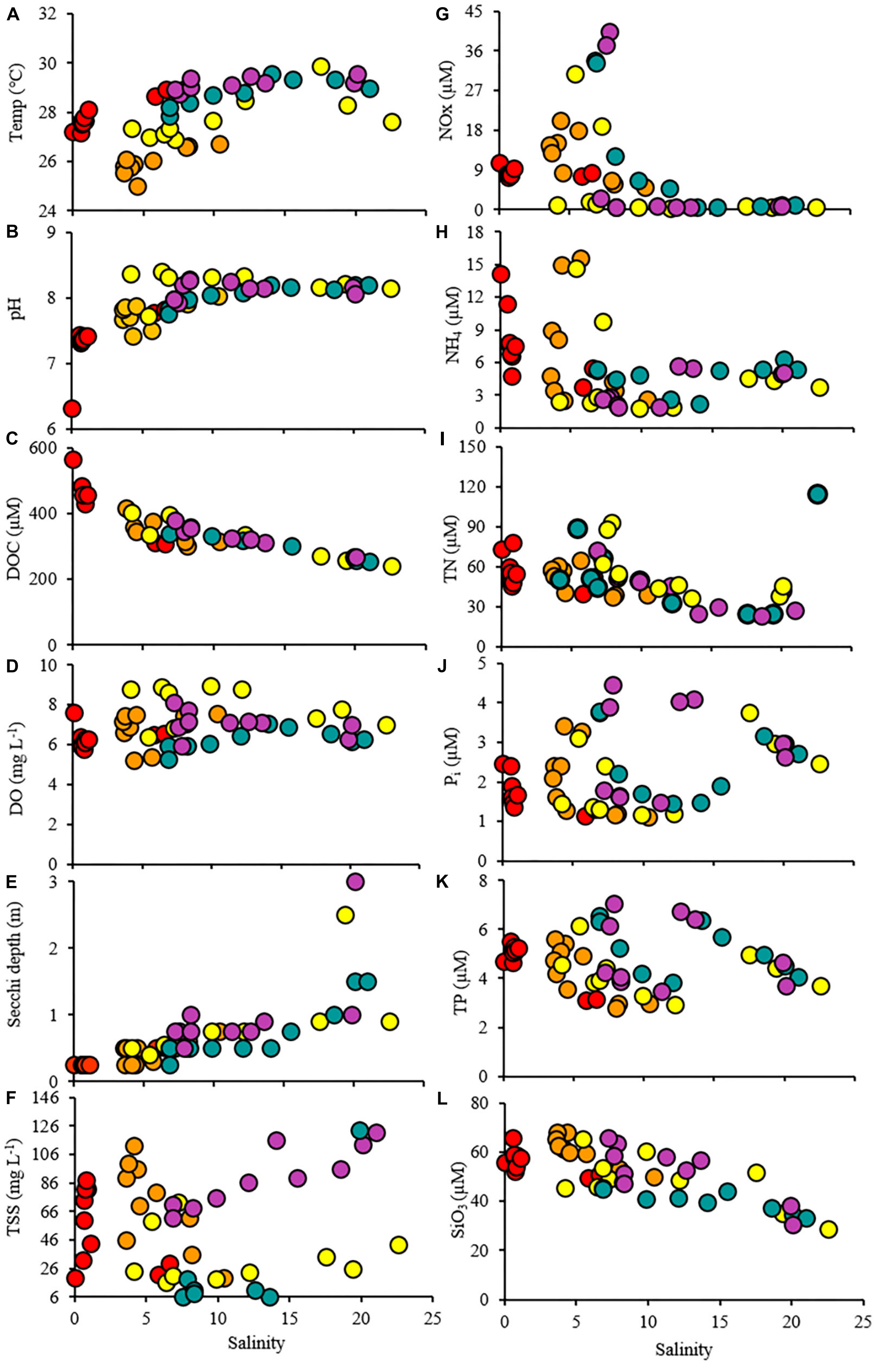

FIGURE 3 | Scatterplots showing the relationship between the salinity and the water quality parameters throughout the study period. Time points are indicated by colors (T1: red, T2: orange, T3: yellow, T4: green, T5: purple).

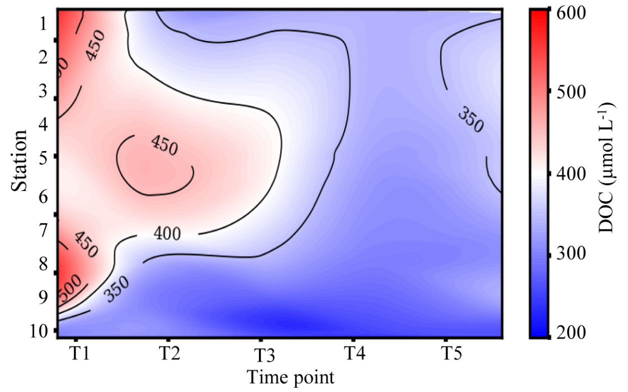

FIGURE 4 | Time series of dissolved organic carbon (DOC) from the mouth of the San Jacinto River to the Gulf of Mexico. Stations are indicated along the *y*-axis and time points are represented along the *x*-axis.

and then decreased with time as the salinities increased across the Bay (**Figure 6**).

The eukaryotic community (18S rRNA gene) analysis shows that the dominant members of the community were Cryptophyta, Oligotrichea (ciliates), and Ochrophyta (mostly comprised of species within Bacillariophyta hereafter referred to as diatoms). Immediately following Hurricane Harvey (T1), the relative abundance of both Cryptophyta, Oligotrichea, and diatoms reflected that of Pre-Harvey conditions (**Figure 7**). At the next time point (T2), the highest relative abundance of freshwater chlorophytes were observed at transect stations closer to the San Jacinto River mouth (**Figure 7**). The relative abundance of diatoms dominated the community at all stations during T2 and even more so during T3 cruise (**Figure 7**). During the T3 cruise, the chlorophytes were replaced by Ochrophyta (predominantly diatoms) and Myzozoa (mostly Dinophyceae). In contrast, the relative abundance of Dinophyceae (dinoflagellates) was lower during these two cruises in and was highest at stations closest to the Gulf of Mexico during T4 and T5 cruises (**Figure 7**).

Water sampling in Galveston Bay during all cruises (T1–T5) showed the presence of PBs in the weeks following Hurricane Harvey varying on both temporal and spatial scales (**Figure 8A**, **Table 2**, and **Supplementary Figure S5**). Temporally the concentrations of cotinine, carbamazepine, carbamazepine-epoxide, and imidacloprid, behaved similarly to each other, while prednisone did not (**Figure 8A** and **Table 2**). Levels for cotinine (0.005–0.013 ng L^{-1}), imidacloprid (0.026–0.074 ng L^{-1}), carbamazepine (0.017–0.036 ng L^{-1}), and carbamazepine-epoxide (0.004–0.011 ng L^{-1}) were all lower immediately following Hurricane Harvey during T1, and then steadily increased over successive weeks (**Figure 8A** and **Table 2**). However, prednisone levels were highest immediately following the storm (21.07 ng L^{-1}) at station 1 and then decreased with increasing distance from the mouth of the San Jacinto River to station 10 (7.29 ng L^{-1}). After T1, prednisone was only detected at station 4 during T2 (0.154 ng L^{-1}) and then during T3 at stations 1, 2, 4, and 6 in low concentrations (0.291–1.23 ng L^{-1}; **Figure 8A** and **Table 2**). PAHs in the water column were relatively higher during T1 at stations 1, 2, and 6 and then declined with increasing distance from the mouth of the San Jacinto River (**Figure 8B**). At stations 1, 2, and 6, the concentration of PAHs was 102, 167, and 103 ng L^{-1}, respectively. The concentrations of PAHs decreased to 24 ng L^{-1} at station 10 closest to the Gulf of Mexico. For the time points T2–T5, the concentrations of PAHs ranged from a minimum of 19 ng L^{-1} at station 7 during the T4 cruise to a maximum of 69 ng L^{-1} at station 2 during the T2 cruise. Overall, PAHs levels declined with increasing time after the hurricane passed.

Multivariate Analysis

The results of the DISTLM analysis showed salinity, pH, DIN:P_i, secchi, temperature, dissolved oxygen, $HSiO_3^-$, and DIN were all strongly significantly correlated ($p < 0.001$) with the changes in the biotic community (**Table 3**). The P_i and TN were also significantly correlated ($p < 0.05$) with the changes in the biotic community (**Table 3**). The nMDS shows the distribution of the biotic community measured at each time point and station with a stress level of 0.10 which corresponds to an acceptable ordination that represents the distribution of data points accurately (**Figure 9**). Increased salinity, pH, dissolved oxygen, and temperature were all strongly correlated ($\rho > 0.70$) with biotic community that was present during the later time points (T4 and T5) and stations that were closest to the Gulf of Mexico (stations 6–10; **Figure 9**). Increased nutrients (DIN:P_i and $HSiO_3^-$) were correlated ($\rho > 0.4$) with the biotic community that was present during the early time points (T1, T2 and select stations during T3) and stations located closer to the mouth of the San Jacinto river stations 1–5; **Figure 9**). The results of the PERMANOVA confirm that there was a significant difference in the biological community when comparing T1 to T2 ($p < 0.05$) and T3–T5 ($p < 0.001$; **Table 4** and **Supplementary Table S1**). The biotic variables during T2 were also significantly different from T3–T4 ($p < 0.01$) and T5 ($p < 0.001$; **Table 4**). T3 biological variability was significantly different from T4–T5 ($p < 0.001$) and T4 was significantly different from T5 ($p < 0.01$; **Table 4**). Regarding the environmental variability across time points, T1 and T2 were significantly different from each other ($p < 0.001$) and were also significantly different from all other time points ($p < 0.001$; **Table 4**). T3, T4, and T5 were also significantly different from each other in terms of environmental variability ($p < 0.01$; **Table 4**). When considering biological community variability between stations looking at all the time points combined stations 2–4 were all significantly different from station 10 ($p < 0.05$) and station 5 was significantly different from stations 8 and 9 ($p < 0.05$; **Table 4**). While the environmental variability between station 1 and station 2 was not different they were both significantly different from stations 3–8 ($p < 0.05$) and from stations 9–10 ($p < 0.01$; **Table 4**).

DISCUSSION

The total volume of freshwater that entered Galveston Bay by rainfall and runoff during Hurricane Harvey was approximately

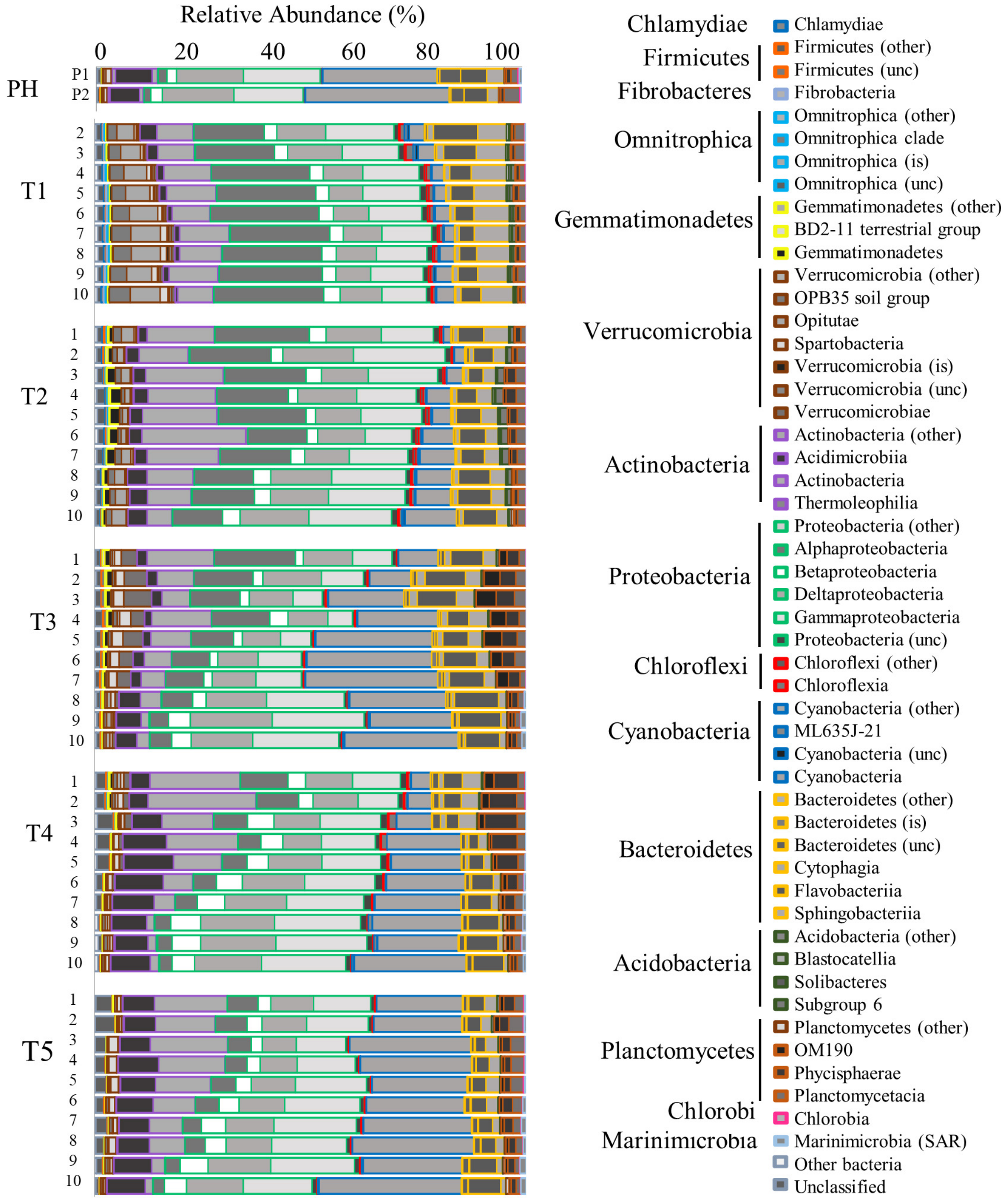

FIGURE 5 | Bar graph showing the relative abundance of OTUs for the Bacteria community identified by 16s rRNA analysis. Time points are separated into blocks (T1–T5). Within each time point block, each bar represents the relative abundance for the members of the Bacteria community at each station (1–10). The phyla are indicated by differing border color on the bar graphs [incertae sedis (is) and unclassified (unc)]. P1 and P2 are pre-Harvey (PH) samples from 07/31/17 and 08/22/17, respectively.

three to six times the bay volume [Du et al., 2019; Thyng et al., 2020 (*in review*)]. Historically salinities at the same locations and time of year would range from 20 to 30 (Roelke et al., 2013; Dorado et al., 2015; Pinckney et al., 2017) which is similar to what was observed in during the pre-Harvey sample collections. This flooding event pushed the saltwater out of the bay via hydraulic flushing creating freshwater conditions for over 2 weeks. Although the salinities

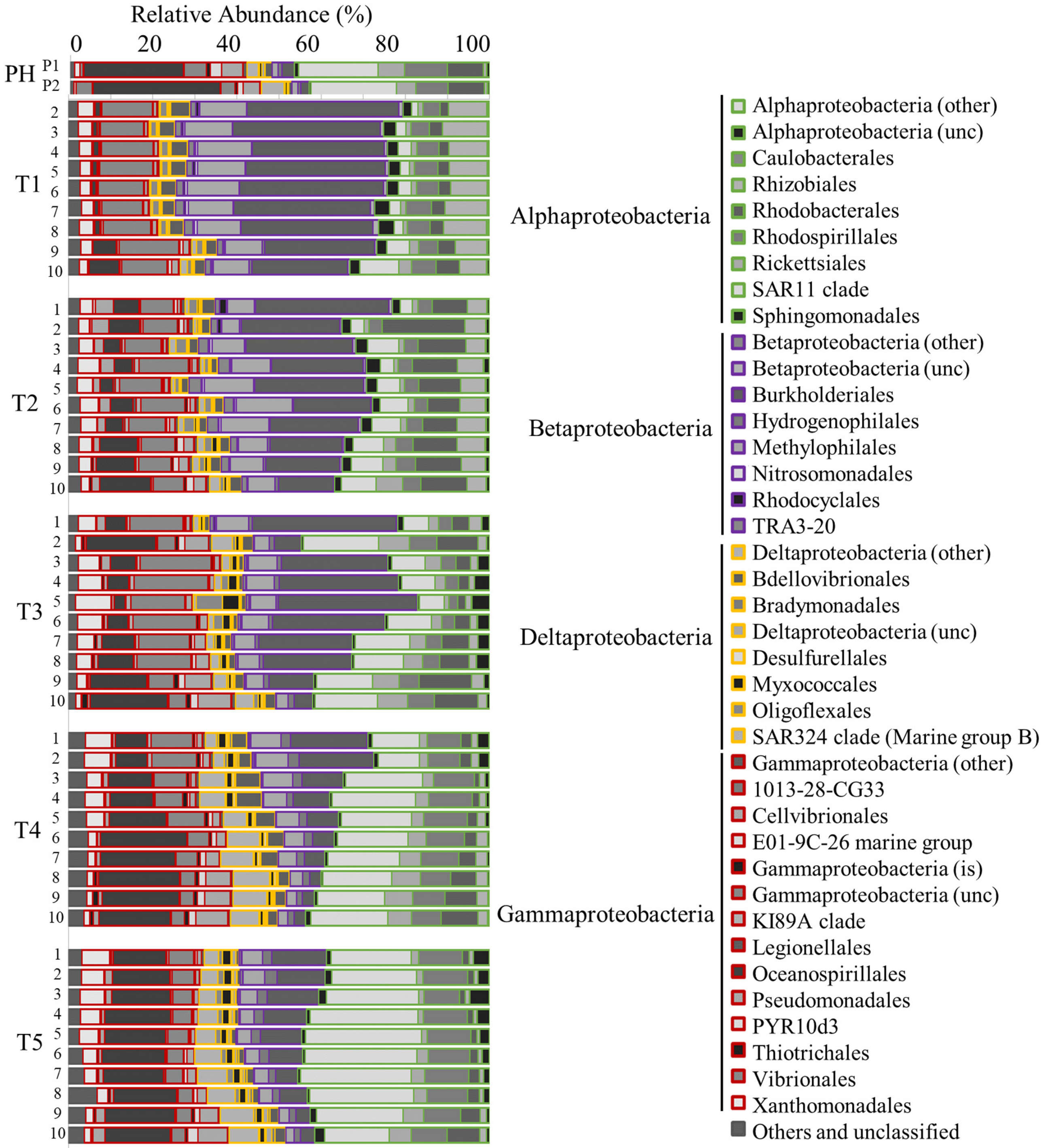

FIGURE 6 | Bar graph showing the relative abundance of OTUs for the Proteobacteria community identified by 16s rRNA analysis. Time points are separated into blocks (T1–T5). Within each time point block, each bar represents the relative abundance for the members of the bacteria community at each station (1–10). The phyla are indicated by differing border color on the bar graphs [incertae sedis (is) and unclassified (unc)]. P1 and P2 are pre-Harvey samples from 07/31/17 and 08/22/17, respectively.

did begin to increase in the weeks following the flood event, pre-flood salinities were not reached during this study period reflective of the large displacement of bay waters associated with this storm (**Figure 2** and **Supplementary Figures S1, S2**). This large pulse of freshwater via river discharge, runoff, and direct precipitation delivered 105 ± 10 Gg

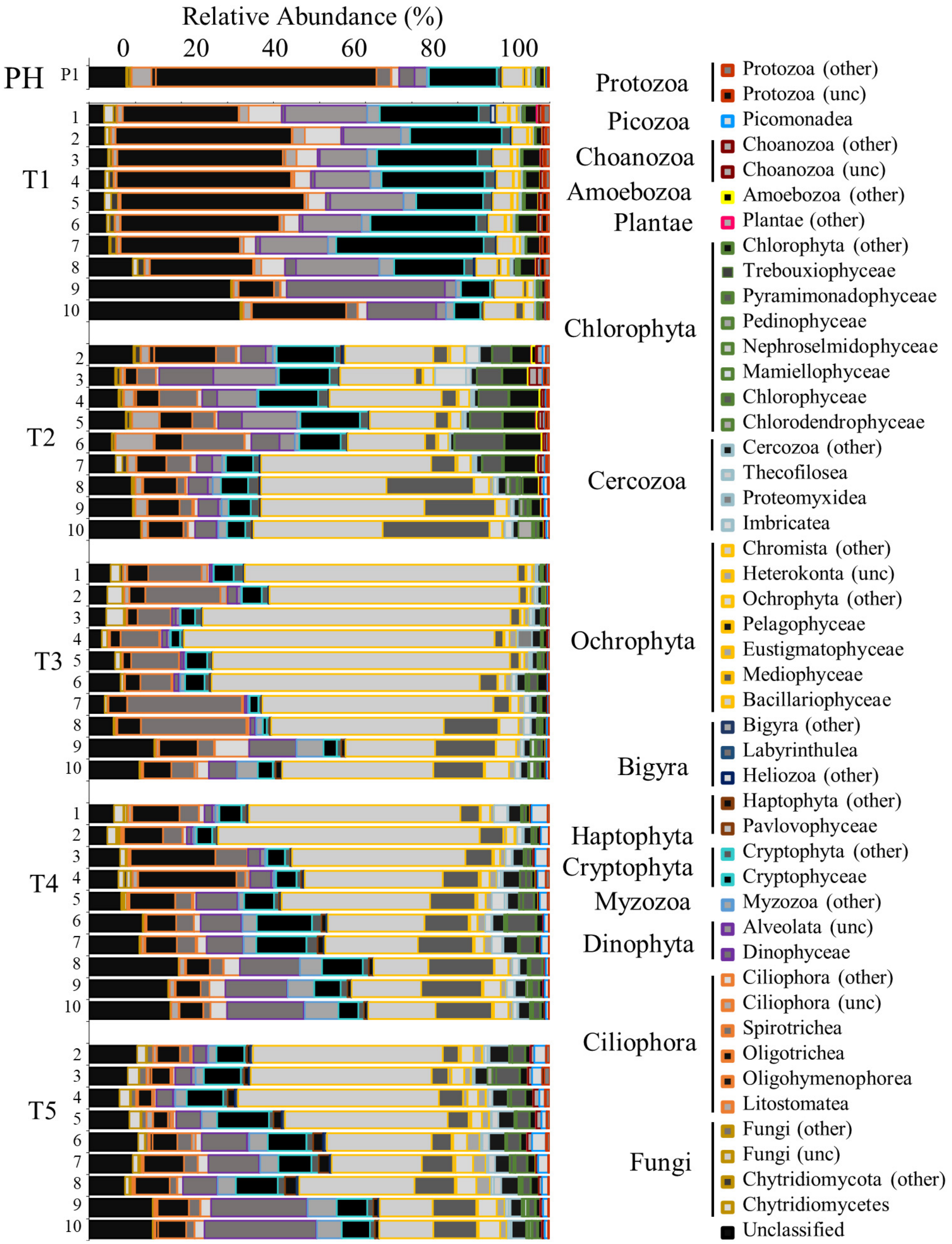

FIGURE 7 | Bar graph showing the relative abundance of OTUs for the eukaryotic community identified by 18s rRNA analysis. Time points are separated into blocks (T1–T5). Within each time point block, each bar represents the relative abundance for the members of the bacteria community at each station (1–10). The phyla are indicated by differing border color on the bar graphs [unclassified (unc)]. P1 is a pre-Harvey sample from 07/31/17.

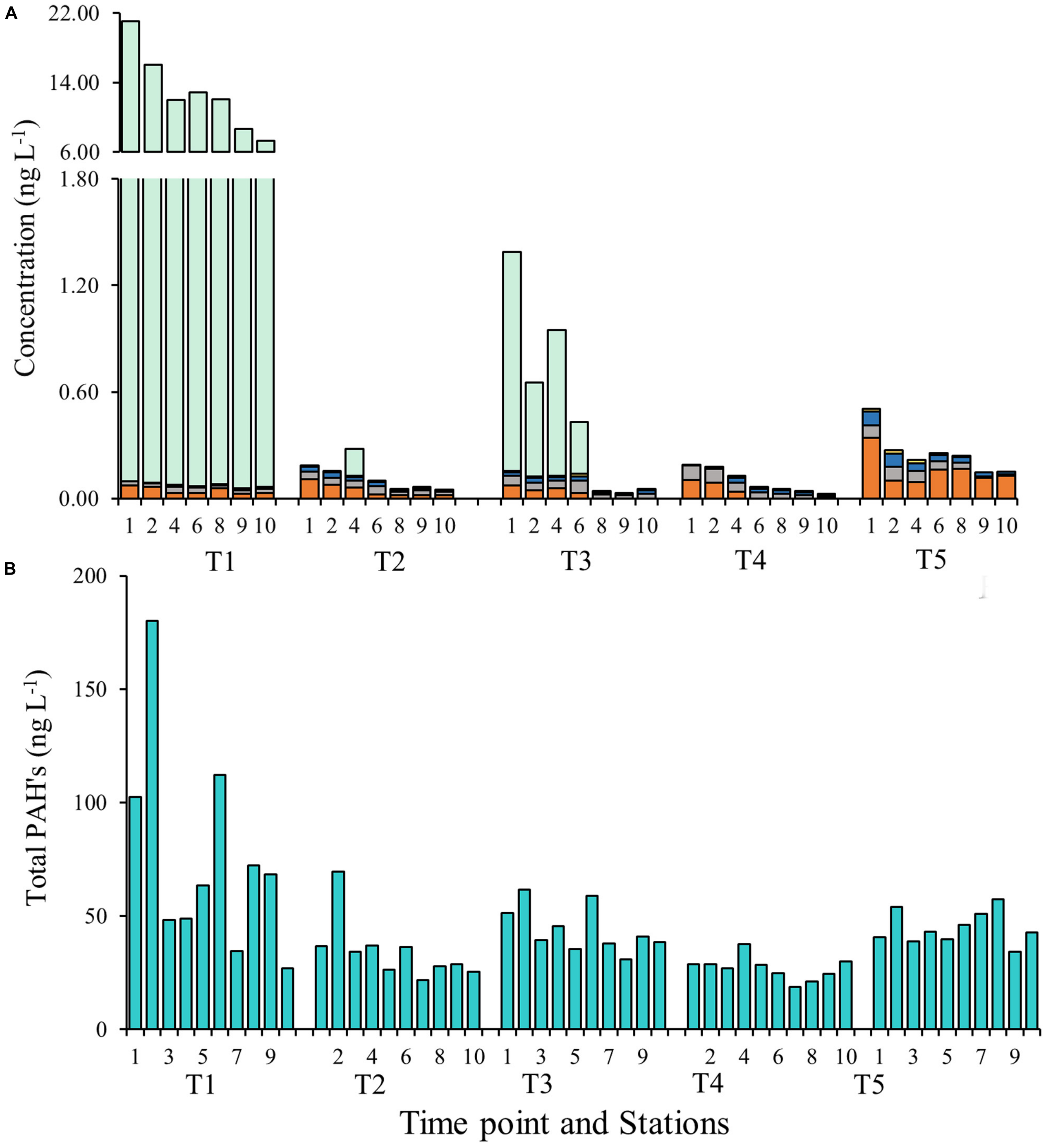

FIGURE 8 | (A) Concentrations of pharmaceuticals and biocides at each time point and station. The *y*-axis on the left corresponds to the imidacloprid (orange), carbamazepine (gray), cotinine (blue), and carbamazepine-epoxide (yellow) and the *y*-axis on the right corresponds to Prednisone (green). **(B)** Concentrations of polycyclic aromatic hydrocarbons (PAHs) at each time point and at each station.

of terrigenous DOC to the bay within one week following the hurricane (Yan et al., this issue). With this initial pulse of freshwater, elevated concentrations of ammonium were measured in the bay from and were believed to be from a variety of sources associated with Harvey including agricultural runoff, waste water, and storm water. The

TABLE 2 | Additional abiotic factors including the pharmaceuticals and biocide data collected at each time point at the respective time point and station.

Time point	Station	Pharmaceauticals & Biocides (ng L^{-1})				
		Cotinine	Carbamazepine	Carbamazepine epoxide	Prednisone	Imidacloprid
T1	1	–	0.021	–	21.071	0.074
	2	–	0.021	0.004	16.063	0.065
	3	–	–	–	–	–
	4	–	0.036	0.011	11.961	0.030
	5	–	–	–	–	–
	6	–	0.032	0.008	12.899	0.030
	7	–	–	–	–	–
	8	0.005	0.017	0.004	12.028	0.056
	9	0.007	0.019	0.004	8.614	0.026
	10	0.013	0.022	–	7.299	0.031
T2	1	0.027	0.045	0.008	–	0.107
	2	0.035	0.036	0.007	–	0.078
	3	–	–	–	–	–
	4	0.020	0.039	0.007	0.154	0.061
	5	–	–	–	–	–
	6	0.020	0.049	0.010	–	0.022
	7	–	–	–	–	–
	8	0.012	0.021	0.004	–	0.017
	9	0.012	0.028	0.005	–	0.019
	10	0.013	0.018	–	–	0.019
T3	1	0.018	0.055	0.009	1.230	0.074
	2	0.029	0.043	0.008	0.530	0.044
	3	–	–	–	–	–
	4	0.020	0.041	0.009	0.820	0.058
	5	–	–	–	–	–
	6	0.026	0.070	0.013	0.291	0.029
	7	–	–	–	–	–
	8	0.014	0.021	0.006	–	–
	9	0.010	0.018	0.004	–	–
	10	0.021	0.025	0.008	–	–
T4	1	0.005	0.082	–	–	0.103
	2	0.008	0.076	0.005	–	0.089
	3	–	–	–	–	–
	4	0.030	0.050	0.011	–	0.037
	5	–	–	–	–	–
	6	0.021	0.034	0.010	–	–
	7	–	–	–	–	–
	8	0.018	0.028	0.007	–	–
	9	0.016	0.020	0.006	–	–
	10	0.013	0.011	0.004	–	–
T5	1	0.078	0.070	0.015	–	0.342
	2	0.075	0.078	0.018	–	0.100
	3	–	–	–	–	–
	4	0.044	0.059	0.018	–	0.094
	5	–	–	–	–	–
	6	0.036	0.046	0.010	–	0.164
	7	–	–	–	–	–
	8	0.030	0.034	0.009	–	0.167
	9	0.024	0.009	–	–	0.116
	10	0.017	0.008	–	–	0.127

Time points when data were not collected are indicated by –.

TABLE 3 | Results of the DISTLM analysis that was run on biological data matrix with the environmental data as the predictor variables.

Variable	SS (trace)	Pseudo-F	*P*	Prop.
Sal	6604.70	32.31	0.0001	0.4179
pH	6379.80	30.46	0.0001	0.4037
DIN:P_i	4473.30	17.77	0.0001	0.2830
Secchi	3995.50	15.23	0.0001	0.2528
Temp	3405.00	12.36	0.0001	0.2155
DO	3331.70	12.02	0.0001	0.2108
$HSiO_{3-}$	3060.40	10.81	0.0001	0.1936
DIN	2085.10	6.84	0.0009	0.1319
P_i	903.68	2.73	0.0383	0.0572
TN	895.71	2.70	0.0402	0.0567
TP	319.32	0.93	0.4134	0.0202

There were 9999 permutations ran to achieve the results. Variable abbreviations and units are defined as follows: Temp: temperature (°C), Sal: salinity, DO: dissolved oxygen (mg L^{-1}), DIN: dissolved inorganic nitrogen (μM), DIN:Pi dissolved inorganic nitrogen to phosphate ratio, TN: total nitrogen (μM), TP: total phosphorus (μM), DOC: dissolved organic carbon (μM).

ammonium concentration was elevated during the first two cruises and then declined as it was potentially taken up by the bacterioplankton and phytoplankton. The TN also increased in concentration during the first cruise and showed a decrease over time potentially indicating that the microbial community was remineralizing this source of organic nitrogen to ammonium and also converting the ammonium to NO_x.

Flooding of the bay impacted microbial communities such that the generally dominant members of the marine coastal bacteria community (Acidomicrobia, Alphaproteobacteria, Cyanobacteria, Betaproteobacteria SAR11, and Gammaproteobacteria Oceanospirillales), were replaced by microorganisms of terrestrial (Actinobacteria, OBP45 Soil Group, Opitutae, OBP35 soil group), sedimentary (Actinobacteria), agricultural (OM190 soil group), and freshwater (Betaproteobacteria: Burkholderiales and Methylophilales) origin (**Figures 5–7**, **9**; Chistoserdova, 2011a,b; Beck et al., 2013). During the first cruise, the bacterial communities at all stations were very homogenous, consistent with the parallel trends observed in the water quality values. Sphingobacteria, more commonly found in activated sludge from wastewater treatment plants (Herlemann et al., 2013), had higher relative abundance during the first two cruises and at the freshwater sites for the later time points. Microbes associated with surface sediments (species within the class Opitutae) were observed in the earlier cruises, which could explain times when terrestrial soils may have been present in the floodwaters. Four weeks after the hurricane, a shift in the members of the phylum Verrucomicrobia occurred from the soil-based Opitutae class to the aquatic Spartobacteria class indicating that the estuarine/marine conditions were returning to the system (Herlemann et al., 2013). There was no increase in the relative abundance of gut-associated bacteria (i.e., Enterobacteria and Firmicutes), suggesting there was minimal human influence on the bacterial community in earlier time points compared (Zhang et al., 2015). van Oldenborgh et al. (2017) calculated that there was a pulse (1.14×10^5 m^3) of untreated wastewater and raw sewage into the bay during the flooding event. For this study, the first cruise took place approximately 1 week after the flooding event, thus the gut-associated signal may have been missed if it was present during and immediately following the storm, or that our detection limit is too high to pick up the least abundant microorganisms. Members of the microbial community typically present in the bay and normally associated with coastal marine environments, such as Oceanospirillales, SAR11, and Marine Group A, were barely detectable after Hurricane Harvey and slowly increase with time after the storm. Marine Cyanobacteria dominated by *Synechococcus* sp. typically represent ∼20–30% of the total abundance of all OTUs within Galveston Bay. After Hurricane Harvey, Cyanobacteria represented <5% of all OTUs and gradually came back to pre-hurricane levels within the 6 weeks following the flood. The observed decrease in marine Cyanobacteria could be due to the lower salinity and lower water temperatures, a seasonal trend that has been observed along the coast of Texas (Suttle and Chan, 1994) and other environments (Xia et al., 2015; Kim et al., 2018).

The response of the microbial community (including bacteria and phytoplankton) after a flooding event can be dependent on the nutrient concentrations present in the estuary before the storm waters were introduced to the system (Roelke et al., 2013; Dorado et al., 2015). Initially DIN:P_i observed in Galveston Bay following Harvey was relatively high (∼10), particularly adjacent to the river mouth, and then returned closer to ∼1 by the end of the month, indicating the phytoplankton populations were nitrogen limited as has been observed previously (Roelke et al., 2013; Dorado et al., 2015). The organic phosphorus continued to increase with time as the flood waters continued to move out of the bay toward the Gulf of Mexico. The P_i also increased with time after the initial flooding event supporting the idea that the bacterial community was remineralizing the organic phosphorus throughout the bay. In previous studies, members of the phytoplankton community (diatoms) have responded by increasing in biomass if nutrients were limiting prior to a flooding event (Paerl et al., 2001; Roelke et al., 2013; Dorado et al., 2015). When pulses of nutrients are introduced into a system that is nutrient replete, the phytoplankton biomass may not increase in response to additional nutrients (Roelke et al., 2013; Dorado et al., 2015). Inversely, the Dinophyceae have shown a negative correlation with freshwater inflows or added nutrients (Roelke et al., 2013; Dorado et al., 2015). Other factors that may contribute to changes in the phytoplankton abundance depend on the volume of floodwater and how the residence time of the system is affected. Phytoplankton biomass has been shown to decrease following large flooding events due to the hydraulic flushing physically pushing the bay waters out of the system (Paerl et al., 2001; Pinckney et al., 2009; Roelke et al., 2013). Immediately following Harvey, a small phytoplankton bloom occurred with a dominance of diatoms, cryptophytes, and chlorophytes, in response to the freshwater inflow and pulse of nutrients from Hurricane Harvey suggesting nutrients may have been limiting prior to this flooding event (Piehler et al., 2004). Blooms of both diatoms and dinoflagellates have previously been seen after

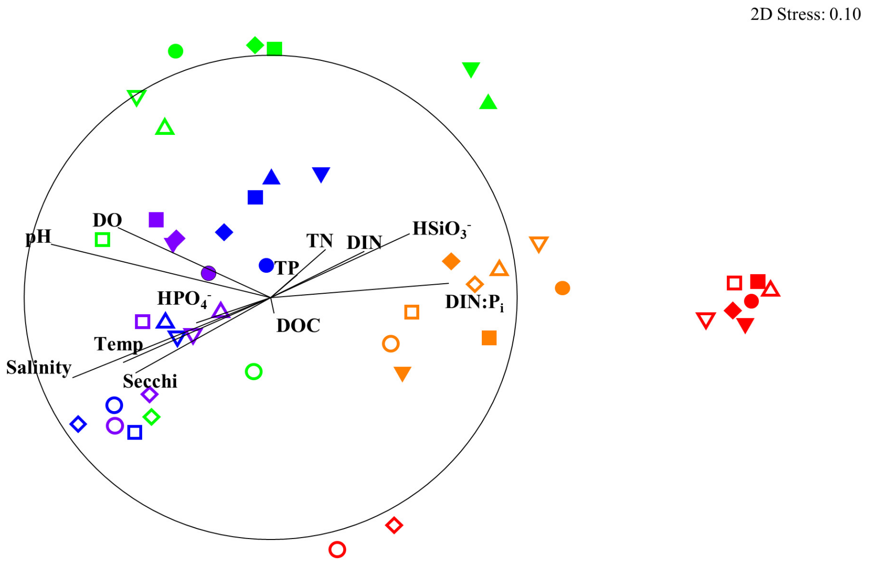

FIGURE 9 | nMDS of biological community showing Pearson correlation of environmental parameters as Temp: temperature (°C), Sal: salinity, DO: dissolved oxygen (mg L^{-1}), DIN: dissolved inorganic nitrogen (μM), DIN:Pi: dissolved inorganic nitrogen to phosphate ratio, TN: total nitrogen (μM^1), TP: total phosphorus (μM), DOC: dissolved organic carbon (μM). Stations are shown as differing symbols: Station 1 (closed upward triangle), 2 (closed downward triangle), 3 (closed square), 4 (closed diamond), 5 (closed circle), 6 (open upward triangle), 7 (open downward triangle), 8 (open square), 9 (open diamond), 10 (open circle). Time points are differentiated by color T1 (red), T2 (orange), T3 (green), T4 (blue), and T5 (purple). nMDS constructed from square root transformed values from the 16S and 18S rRNA OTU abundance data that were used to construct a Bray–Curtis similarity matrix. The circle represents a Pearson correlation of 1.0.

flooding events in an Australian lagoon (Cook et al., 2010; Hallegraeff, 2010) and in North Carolina's Neuse River Estuary after Hurricane Isabel (Wetz and Paerl, 2008) and in Lake Ponchetrain, LA (United States) following Hurricanes Katrina and Rita (Pinckney et al., 2009).

Alongside changes in phytoplankton communities are corresponding changes in eukaryotic grazers. Ciliate grazers, including select freshwater Oligotrichea, preferentially consume cryptophytes (Müller and Schlegel, 1999; Posch et al., 2015). Before Harvey, Oligotrichea (a ciliate grazer) was dominant alongside its prey the cryptophytes. Similar to what Posch et al. (2015) had observed following the hurricane, diatoms were in high in relative abundance along with the ciliate grazers Listomatae. During the third cruise, the ciliate grazer Spirotrichae increased in abundance compared to earlier time points, after which Oligotrichea had the highest abundance of the ciliates which is a pattern that had previously been documented during Hurricanes Katrina and Rita and in freshwater lakes (Amaral-Zettler et al., 2008; Posch et al., 2015). Notably, the ciliate grazer sequences which were discovered in this study were similar to that observed after Hurricanes Katrina and Rita by Posch et al. (2015). After Hurricane Harvey, the eukaryotic community changed drastically, and did not recover to pre-Harvey conditions within the month of sampling, suggesting a longer recovery period compared to the prokaryotes. While much is known about commercial and recreational fisheries (Thronson and Quigg, 2008; Lester and Gonzalez, 2011; Tolan, 2013; Steichen and Quigg, 2018; Oakley and Guillen, 2019) less is known about the lower eukaryotic trophic levels and how they respond to extreme events.

The Galveston Bay watershed is a sink for runoff, major industrial, agricultural, municipal effluent discharges, and also serves as a high-intensity transportation hub for regional oil refineries and industries with intensive shipping traffic visiting its three major ports (Steichen et al., 2012). In addition to these anthropogenic pressures, spills from tankers and barges have released a variety of chemicals (including petroleum products) into Galveston Bay (Williams et al., 2017). As a result of these various contamination sources, Galveston Bay waters, sediments, and biota (microbes, invertebrates, finfish, etc.) are traditionally key focus areas for environmental monitoring studies observing legacy pollutants, such as PAHs, PCBs, dioxins, and metals (Roach et al., 1993; Willett et al., 1997; Qian et al., 2001; Suarez et al., 2006; Howell et al., 2008; Lakshmanan et al., 2010; Yin et al., 2015). Flooding from large storm events has been shown to affect estuarine systems by decreasing residence times, delivering increased concentrations of nutrients, organic matter, and potentially pollutants (Paerl et al., 2001; Peierls et al., 2003; Pinckney et al., 2009).

In general, the low volatility and polar nature of PBs ensure widespread distributions through primarily aqueous transport routes (mainly surface waters) or through food-chain (trophic) transfer (Daughton and Ternes, 1999). Major sources of pharmaceuticals in the environment include effluent outfalls from wastewater treatment plants and runoff from agriculture or from landfill leachates (Boxall et al., 2012; Gaw et al., 2014). In this study, the PBs (cotinine, imidacloprid,

TABLE 4 | Results of the PERMANOVA analysis that was run on biological data matrix with the environmental data as the predictor variables.

	Time points					Station			
	Groups	**t**	***P***	**Perms**		**Groups**	**t**	***P***	**Perms**
BIOT	T1, T2	2.769	0.006	9937	BIOT	2, 10	1.911	0.044	5256
	T1, T3	4.295	0.001	9940		3, 10	1.771	0.035	5342
	T1, T4	5.479	0.000	9936		4, 9	1.872	0.046	5326
	T1, T5	5.870	0.000	9917		4, 10	2.003	0.025	5379
	T2, T3	3.526	0.001	9951		5, 8	1.957	0.044	5307
	T2, T4	3.831	0.001	9948		5, 9	1.835	0.043	5301
	T2, T5	5.315	0.000	9929	ENV	1, 3	2.506	0.040	5365
	T3, T4	3.107	0.001	9937		1, 4	2.641	0.038	5302
	T3, T5	3.622	0.001	9958		1, 5	2.949	0.028	5316
	T4, T5	2.341	0.003	9950		1, 6	3.075	0.023	5278
ENV	T1, T2	3.202	0.001	9932		1, 7	2.931	0.021	5338
	T1, T3	3.712	0.001	9924		1, 8	2.902	0.019	5321
	T1, T4	4.289	0.000	9931		1, 9	3.337	0.008	5302
	T1, T5	4.128	0.000	9926		1, 10	3.789	0.009	5296
	T2, T3	3.288	0.000	9935		2, 3	2.751	0.031	5302
	T2, T4	4.221	0.001	9935		2, 4	2.609	0.037	5323
	T2, T5	3.572	0.000	9930		2, 5	2.834	0.030	5338
	T3, T4	2.748	0.002	9923		2, 6	2.903	0.021	5310
	T3, T5	2.028	0.005	9931		2, 7	2.840	0.018	5302
	T4, T5	2.613	0.002	9918		2, 8	2.565	0.028	5329
						2, 9	2.893	0.007	5270
						2, 10	3.494	0.007	5303
						3, 9	1.799	0.049	5341
						3, 10	2.529	0.013	5323
						4, 10	2.617	0.010	5307
						5, 10	2.495	0.020	5328
						6, 10	2.143	0.042	5324
						7, 10	2.048	0.028	5296
						8, 10	2.403	0.046	5276

There were 9999 permutations run to achieve the results. Only results with significant differences are shown in table (other data available in ***Supplementary Table S1****).*

carbamazepine, and carbamazepine-epoxide) increased in concentration with time indicating a dilution effect by the freshwater pulse following this flooding event. Prednisone, a commonly prescribed steroidal (glucocorticoid) anti-inflammatory drug in North America (Cdc Md STARnet, 2019), had been measured in Galveston Bay previously by Rashid and Duffett (2016). The level of prednisone following Harvey presents an exception to the trends observed for the remainder PBs showing an increase from pre-Harvey conditions, compared to the undetectable levels at the subsequent time points. This result is difficult to explain as it is counter to the expectation of PB dilution following the six orders of magnitude of rainfall relative to sewage overflow. It may be likely that a point-source release of prednisone due to the flooding caused by Harvey is responsible for the observed trends (i.e., high levels immediately following Harvey, with levels decreasing thereafter). Overall, our results indicate that there is likely to be a low level of PB contamination ($\sim$0.01–0.1 ng L^{-1}) in Galveston Bay, with elevated levels more characteristic of the upper reaches of the Bay and around the entrance to the Houston Ship Channel. It is likely that these compounds constitute commonly occurring PBs that represent an "anthropogenic footprint" in the Houston/Galveston Bay watershed but further work is necessary to provide confirmation.

In what is argued to be an extremely rare event, the 1000-year flooding associated with Hurricane Harvey occurred in a region already showing positive trends in terms of intensity and frequency of extreme precipitation events (van Oldenborgh et al., 2017). In a modeling study, Emanuel (2017) estimated that the annual probability of 500 mm of area-integrated rainfall was about 1% in the period 1981–2000 but increased to 18% in the period 2081–2100. Both studies make it clear that extreme rainfall events along the Texas Gulf Coast are on the rise. Recent events along the northern Gulf of Mexico coast, including two 500-year floods in the years immediately prior to Hurricane Harvey (May 2015 and April 2016) as well as several other severe storm events which directly impacted the Houston area this century (Tropical Storm Allison, 2001 and Hurricane Ike, 2008), indicate these models are tracking observations. Extreme rainfall events should be part of the discussion of environmental management and mitigation and future improvements to flood protection systems in major cities around the Gulf and globally. Although the water quality and microbial community showed signs of returning to pre-Harvey conditions within the month following the flood event, long-term impacts need to be measured in the years following the flood. While the nekton community in estuarine systems is resilient to short-term disturbances, there may be more lasting effects with the predicted rise in the frequency and magnitude of these large rain events (Waide, 1991; Paperno et al., 2006; Oakley and Guillen, 2019). With an increase in frequency and intensity of these coastal disturbances and extreme flooding events, there may be a shift in the amount of time needed for a system to recover (Paerl et al., 2001). Rapid declines in the salinity of estuarine systems such as what was observed in Galveston Bay have been shown to impact the resident nekton community by decreasing the availability of suitable habitat for these macrofauna (Lenihan and Peterson, 1998; Eby et al., 2000; Paerl et al., 2001; McFarlin et al., 2015). Future work should be done on the effects this freshening had on the organisms in the bay following a disruption at the base of the food web. The impacts of the increased contaminants and the extensive period of low salinity created due to this flooding event warrant continued monitoring of the water quality conditions and microbial community of this system in years to come to determine the long-term effects on the biological community from the base of the food web upward within Galveston Bay.

Collectively, these findings showed that over the month following the storm, a transition occurred from an estuarine biotic community before the hurricane to a primarily freshwater biotic community after the flooding event and then began the shift back to an estuarine/marine biotic community within about a month after the flood event. There was a large pulse of organic matter that provided substrate for microbial degradation. The bacterial community showed an increase in the abundance of bacteria associated with terrestrial soils and freshwater at the initial time point and then decreased over time and were replaced by their estuarine and marine relatives within the month following the hurricane. The microbial eukaryotic community (phytoplankton and grazers) displayed a rapid transition from an estuarine community to a freshwater community following the storm with a slower recovery compared to the 16S rRNA community. This collaborative effort will allow for improved understanding of the physicochemical and biological changes following a large storm event within subtropical estuaries. While this work captured the immediate impact of a hurricane on an estuarine system, future work is recommended to enhance our understanding pertaining to the long-term effects of a storm of this magnitude on various levels of the food web.

DATA AVAILABILITY STATEMENT

The datasets generated for this study can be found in the BioProject #PRJNA558756. This research was made possible by a grant from The Gulf of Mexico Research Initiative to support consortium research entitled ADDOMEx (Aggregation and Degradation of Dispersants and Oil by Microbial Exopolymers) Consortium. Data are publicly available through the Gulf of Mexico Research Initiative Information and Data Cooperative (GRIIDC) at http://data.gulfresearchinitative.org (doi: 10.7266/PGC99C7D).

AUTHOR CONTRIBUTIONS

The author contribution to this manuscript is as follows: JS 25%, AQ 20%, JL 15%, RW 5%, DH 5%, PF 5%, KK 5%, SS 5%, HB 5%, GY 5%, and MK 5%.

FUNDING

AQ, JS, RW, SS, and MK were either fully or partially supported by the GOMRI (ADDOMEx; project SA15-22) and by the Texas Commission on Environmental Quality: Galveston Bay Estuary Program (US EPA Grant Number: CE-00655006). Work done by JL was funded by the National Science Foundation—RAPID Response (Award #1801367). KK and GY were funded by National Science (Grant #: 1333633).

ACKNOWLEDGMENTS

We would like to thank all members of the Phytoplankton Dynamics lab at Texas A&M University at Galveston (TAMUG) that assisted with cruise plans and organization, sample collection, and processing. Many thanks to the crew of the TAMUG R/V Trident and to everyone from TAMUG that came along (with very short notice) to assist in sample collection, sample processing, and data analysis.

SUPPLEMENTARY MATERIAL

The Supplementary Material for this article can be found online at: https://www.frontiersin.org/articles/10.3389/fmars.2020.00186/full#supplementary-material

FIGURE S1 | MODIS images (http://ge.ssec.wisc.edu/modis-today/) of Galveston Bay before, during, and after the passing of Hurricane Harvey on 22, 29, 31 August and 9, 16, 28 September 2017.

FIGURE S2 | The daily river inflow for the San Jacinto and Trinity Rivers ($\log_{10}$ scale). To account for total San Jacinto River daily discharge multiple gage locations are summed: Cedar (USGS 08067500), Brays (USGS 08075000), Buffalo (USGS 08073600), Chocolate (USGS 08078000), Greens (USGS 08076000), Halls (USGS 08076500), Hunting (USGS 08075770), Lake Houston (USGS 08072000),Vince (USGS 08075730), and White Oak (USGS 08074500). The Trinity River flow was measured at the Liberty gage (USGS 08067000). Arrow indicates the passing of Hurricane Harvey.

FIGURE S3 | PCA of environmental data with base environmental variables shown as vectors: Temp: temperature (°C), Sal: salinity, DO: dissolved oxygen (mg L^{-1}), DIN: dissolved inorganic nitrogen (μM), DIN:Pi: dissolved inorganic nitrogen to phosphate ratio, TN: total nitrogen (μM), TP: total phosphorus (μM), DOC: dissolved organic carbon (μM). Stations are shown as differing symbols: Station 1 (closed upward triangle), 2 (closed downward triangle), 3 (closed square), 4 (closed diamond), 5 (closed circle), 6 (open upward triangle), 7 (open downward triangle), 8 (open square), 9 (open diamond), 10 (open circle). Time points are differentiated by color T1 (red), T2 (orange), T3 (green), T4 (blue), and T5 (purple). Environmental data were square root transformed and normalized then used to calculate the Euclidean matrix and construct the PCA.

FIGURE S4 | nMDS of biological community showing taxa as vectors (Pearson correlation > 0.8). Stations are shown as differing symbols: 1 (closed upward triangle), 2 (closed downward triangle), 3 (closed square), 4 (closed diamond), 5 (closed circle), 6 (open upward triangle), 7 (open downward triangle), 8 (open square), 9 (open diamond), 10 (open circle). Time points are differentiated by color T1 (red), T2 (orange), T3 (green), T4 (blue), and T5 (purple). nMDS constructed from square root transformed values from the 16S and 18S rRNA OTU abundance data that were used to construct a Bray–Curtis similarity matrix.

FIGURE S5 | PCA of the PAHs and PBs with base environmental variables shown as vectors. Stations are shown as differing symbols: Station 1 (closed upward triangle), 2 (closed downward triangle), 3 (closed square), 4 (closed diamond), 5 (closed circle), 6 (open upward triangle), 7 (open downward triangle), 8 (open square), 9 (open diamond), 10 (open circle). Time points are differentiated by color T1 (red), T2 (orange, T3 (green), T4 (blue), and T5 (purple). Environmental data were square root transformed and normalized then used to calculate the Euclidean matrix and construct the PCA.

TABLE S1 | Non-significant results of the PERMANOVA analysis that was run on biological data matrix with the environmental data as the predictor variables. There were 9999 permutations ran to achieve the results.

REFERENCES

Amaral-Zettler, L. A., Rocca, J. D., Lamontagne, M. G., Dennett, M. R., and Gast, R. J. (2008). Changes in microbial community structure in the wake of Hurricanes Katrina and Rita. *Environ. Sci. Technol.* 42, 9072–9078. doi: 10.1021/es801904z

American Public Health Association [APHA] (1985). *Standard Methods for the Examination of Water and Wastewater*, 16th Edn. Washington, D.C.: American Public Health Association.

American Public Health Association [APHA] (1998). *Standard Methods for the Examination of Water and Wastewater*, 20th Edn. Washington, D.C.: APHA, AWWA, and WEF.

Ankley, G. T., Brooks, B. W., Huggett, D. B., and Sumpter, J. P. (2007). Repeating history: pharmaceuticals in the environment. *Environ. Sci. Technol.* 41, 8211–8217. doi: 10.1021/es072658j

Apprill, A., McNally, S., Parsons, R., and Weber, L. (2015). Minor revision to V4 region SSU rRNA 806R gene primer greatly increases detection of SAR11 bacterioplankton. *Aquat. Microb. Ecol.* 75, 129–137. doi: 10.3354/ame01753

Bacosa, H. P., Kamalanathan, M., Chiu, M. H., Tsai, S. M., Sun, L., Labonté, J. M., et al. (2018). Extracellular polymeric substances (EPS) producing and oil degrading bacteria isolated from the northern Gulf of Mexico. *PLoS ONE* 13:e0208406. doi: 10.1371/journal.pone.0208406

Beck, D. A., Kalyuzhnaya, M. G., Malfatti, S., Tringe, S. G., del Rio, T. G., Ivanova, N., et al. (2013). A metagenomic insight into freshwater methane-utilizing communities and evidence for cooperation between the *Methylococcaceae* and the *Methylophilaceae*. *PeerJ* 1:e23. doi: 10.7717/peerj.23

Benner, R., and Strom, M. (1993). A critical evaluation of the analytical blank associated with DOC measurements by high-temperature catalytic oxidation. *Mar. Chem.* 41, 153–160. doi: 10.1016/0304-4203(93)90113-3

Blake, E. S., and Zelinsky, D. A. (2018). *"National Hurricane Center Tropical Cyclone Report Hurricane Harvey": National Oceanic and Atmospheric Administration.* Report No. AL092017. Available online at: https://www.nhc.noaa.gov/data/tcr/AL092017_Harvey.pdf

Boxall, A. B., Rudd, M. A., Brooks, B. W., Caldwell, D. J., Choi, K., and Hickmann, S. (2012). Pharmaceuticals and personal care products in the environment: what are the big questions? *Environ. Health Perspect.* 120, 1221–1229.

Bradley, I. M., Pinto, A. J., and Guest, J. S. (2016). Design and evaluation of Illumina MiSeq-compatible, 18S rRNA gene-specific primers for improved characterization of mixed phototrophic communities. *Appl. Environ. Microbiol.* 82, 5878–5891. doi: 10.1128/aem.01630-16

Caporaso, J. G, Lauber, C. L., Walters, W. A., Berg-Lyons, D., Lozupone, C. A., Turnbaugh, P. J., et al. (2011). Global patterns of 16S rRNA diversity at a depth of millions of sequences per sample. *Proc. Natl. Acad. Sci.* 108, 4516–4522. doi: 10.1073/pnas.1000080107

Cdc Md STARnet (2019). *Data and Statistics Muscular Dystrophy, On-Line (cited 2019 Oct 14)*. Available online at: https://www.cdc.gov/ncbddd/musculardystrophy/data.html

Chapin, J. (2017). *EPA approves plan to clean up San Jacinto waste pits. KHOU (newspaper on the Internet)*. Available online at: http://www.khou.com/news/local/epa-approves-plan-to-clean-up-san-jacinto-waste-pits/482678370

Chistoserdova, L. (2011a). Methylotrophy in a lake: from metagenomics to single-organism physiology. *Appl. Environ. Microbiol.* 77, 4705–4711. doi: 10.1128/aem.00314-11

Chistoserdova, L. (2011b). Modularity of methylotrophy, revisited. *Environ. Microbiol.* 13, 2603–2622. doi: 10.1111/j.1462-2920.2011.02464.x

Clarke, K. R., and Gorley, R. N. (2006). *Primer Manual*. Plymouth: PRIMER-e.

Clarke, K. R., and Warwick, R. M. (1994). Similarity-based testing for community pattern: the two-way layout with no replication. *Mar. Biol.* 118, 167–176. doi: 10.1007/bf00699231

Clarke, K. R., and Warwick, R. M. (2001). *Change in Marine Communities. An Approach to Statistical Analysis and Interpretation*. Plymouth: PRIMER-e.

Cook, P. L., Holland, D. P., and Longmore, A. R. (2010). Effect of a flood event on the dynamics of phytoplankton and biogeochemistry in a large temperate Australian lagoon. *Lim. Ocean.* 55, 1123–1133. doi: 10.4319/lo.2010.55.3.1123

Daughton, C. G., and Ternes, T. A. (1999). Pharmaceuticals and personal care products in the environment: agents of subtle change? *Environ. Health Perspect.* 6, 907–938. doi: 10.1289/ehp.99107s6907

Dorado, S., Booe, T., Steichen, J., McInnes, A. S., Windham, R., and Shepard, A. (2015). Towards an understanding of the interactions between freshwater inflows and phytoplankton communities in a subtropical estuary in the Gulf of Mexico. *PLoS One* 10:e0130931. doi: 10.1371/journal.pone.0130931

Du, B., Haddad, S. P., Luek, A., Scott, W. C., Saari, G. N., Burket, S. R., et al. (2016). Bioaccumulation of human pharmaceuticals in fish across habitats of a tidally influenced urban bayou. *Environ. Tox. Chem.* 35, 966–974. doi: 10.1002/etc.3221

Du, J., Park, K., Dellapenna, T. M., and Clay, J. M. (2019). Dramatic hydrodynamic and sedimentary responses in Galveston Bay and adjacent inner shelf to Hurricane Harvey. *Sci. Tot. Environ.* 653, 554–564. doi: 10.1016/j.scitotenv.2018.10.403

Eby, L. A., Crowder, L. B., and McClellan, C. (2000). *Neuse River Estuary Modeling andMonitoring Project, Stage 1, Effects of Water Quality on Distribution and Composition of the Fish Community, Report 325C*. Raleigh, NC: Univ. of North Carolina Water Resources Res. Inst.

Emanuel, K. (2017). Assessing the present and future probability of Hurricane Harvey's rainfall. *Proc. Nat. Acad. Sci. U.S.A.* 114, 12681–12684. doi: 10.1073/pnas.1716222114

Environment Texas Research and Policy Center (2017). *Raw Sewage Released by Hurricane Harvey*. Available online at: https://environmenttexascenter.org/

Gaw, S., Thomas, K. V., and Hutchinson, T. H. (2014). Sources, impacts and trends of pharmaceuticals in the marine and coastal environment. *Philos. Trans. R. Soc. Lond. B Biol. Sci.* 369, 20130572. doi: 10.1098/rstb.2013.0572

Guo, L., Santschi, P. H., and Bianchi, T. S. (1999). "Dissolved organic matter in estuaries of the Gulf of Mexico," in *Biogeochemistry of Gulf of Mexico Estuaries*, eds T.S. Bianchi, J. Pennock, and R. R. Twilley (New York, NY: Jhon Wiley and Sons). 269–299.

Guthrie, C. G., Matsumoto, J., and Solis, R. S. (2012). "Analysis of the influence of water plan strategies on inflows and salinity in galveston bay," in *Final Report to the United States Army Corps of Engineers, Contract #R0100010015*. (Austin, TX: Texas Water Development Board), 71.

Hallegraeff, G. M. (2010). Ocean climate change, phytoplankton community responses, and harmful algal blooms: a formidable predictive challenge. *J. Phycol.* 46, 220–235. doi: 10.1111/j.1529-8817.2010.00815.x

Herlemann, D. P., Lundin, D., Labrenz, M., Jürgens, K., Zheng, Z., Aspeborg, H., et al. (2013). Metagenomic de novo assembly of an aquatic representative of the verrucomicrobial class Spartobacteria. *Mar. Bio.* 4:e569-12.

Horney, J. A., Casillas, G. A., Baker, E., Stone, K. W., Kirsch, K. R., Camargo, K., et al. (2018). Comparing residential contamination in a houston environmental justice neighborhood before and after Hurricane Harvey. *PLoS ONE* 13:e0192660. doi: 10.1371/journal.pone.0192660

Howell, N. L., Suarez, M. P., Rifai, H. S., and Koenig, L. (2008). Concentrations of polychlorinated biphenyls (PCBs) in water, sediment, and aquatic biota in the Houston Ship Channel, Texas. *Chemosphere* 70, 593–606. doi: 10.1016/j.chemosphere.2007.07.031

Kamalanathan, M., Chiu, M. H., Bacosa, H., Schwehr, K., Tsai, S. M., Doyle, S., et al. (2019). Role of polysaccharides in diatom Thalassiosira pseudonana and its associated bacteria in hydrocarbon presence. *Plant Phys.* 180, 1898–1911. doi: 10.1104/pp.19.00301

Kiaghadi, A., and Rifai, H. S. (2019). Physical, chemical, and microbial quality of floodwaters in houston following hurricane harvey. *Environ. Sci. Technol.* 53, 4832–4840. doi: 10.1021/acs.est.9b00792

Kim, Y., Jeon, J., Kwak, M. S., Kim, G. H., Koh, I., and Rho, M. (2018). Photosynthetic functions of *Synechococcus* in the ocean microbiomes of diverse salinity and seasons. *PLoS One* 13:e0190266. doi: 10.1371/journal.pone.0190266

Kozich, J. J., Westcott, S. L., Baxter, N. T., Highlander, S. K., and Schloss, P. D. (2013). Development of a dual-index sequencing strategy and curation pipeline for analyzing amplicon sequence data on the MiSeq Illumina sequencing platform. *Appl. Environ. Microbiol.* 79, 5112–5120. doi: 10.1128/aem.01043-13

Lakshmanan, D., Howell, N. L., Rifai, H. S., and Koenig, L. (2010). Spatial and temporal variation of polychlorinated biphenyls in the Houston Ship Channel. *Chemosphere* 80, 100–112. doi: 10.1016/j.chemosphere.2010.04.014

Lenihan, H. S., and Peterson, C. H. (1998). How habitat degradation through fishery disturbance enhances impacts of hypoxia on oyster reefs. *Ecol. Appl.* 8, 128–140. doi: 10.1890/1051-0761(1998)008[0128:hhdtfd]2.0.co;2

Lester, L. J., and Gonzalez, L. A. (2011). *State of the Bay: A Characterization of the Galveston bay Ecosystem Texas Commission on Environmental Quality*, third Edn. Houston, TX: Galveston Bay Estuary Program.

McFarlin, C. R., Bishop, T. D., Hester, M. W., and Alber, M. (2015). Context-dependent effects of the loss of Spartina alterniflora on salt marsh invertebrate communities. *Estuar. Coastal Shelf Sci.* 163, 218–230. doi: 10.1016/j.ecss.2015.05.045

Milliner, C., Materna, K., Bürgmann, R., Fu, Y., Moore, A. W., Bekaert, D., et al. (2018). Tracking the weight of Hurricane Harvey's stormwater using GPS data. *Sci. Adv.* 4:eaau2477. doi: 10.1126/sciadv.aau2477

Müller, H., and Schlegel, A. (1999). Responses of three freshwater planktonic ciliates with different feeding modes to cryptophyte and diatom prey. *Aquat. Microb. Ecol.* 17, 49–60. doi: 10.3354/ame017049

Oakley, J. W., and Guillen, G. J. (2019). Impact of hurricane harvey on galveston bay saltmarsh nekton communities. *Estuar. Coasts* 1–9. doi: 10.1007/s12237-019-00581-7

Örnólfsdóttir, E. B., Lumsden, S. E., and Pinckney, J. L. (2004). Nutrient pulsing as a regulator of phytoplankton abundance and community composition in Galveston Bay, Texas. *J. Exp. Mar. Biol. Ecol.* 303, 197–220. doi: 10.1016/j.jembe.2003.11.016

Paerl, H. W., Bales, J. D., Ausley, L. W., Buzzelli, C. P., Crowder, L. B., and Eby, L. A. (2001). Ecosystem impacts of three sequential hurricanes (Dennis, Floyd, and Irene) on the United States' largest lagoonal estuary, Pamlico Sound, NC. *Proc. Natl. Acad. Sci. U.S.A.* 98, 5655–5660. doi: 10.1073/pnas.101097398

Paperno, R., Tremain, D. M., Adams, D. H., Sebastian, A. P., Sauer, J. T., and Dutka-Gianelli, J. (2006). The disruption and recovery of fish communities in the Indian River lagoon, Florida, following two hurricanes in 2004. *Estuar. Coasts* 29, 1004–1010. doi: 10.1007/bf02798662

Parada, A. E., Needham, D. M., and Fuhrman, J. A. (2016). Every base matters: assessing small subunit rRNA primers for marine microbiomes with mock communities, time series and global field samples: primers for marine microbiome studies. *Environ. Microbiol.* 18, 1403–1414. doi: 10.1111/1462-2920.13023

Peierls, B. L., Christian, R. R., and Paerl, H. W. (2003). Water quality and phytoplankton as indicators of hurricane impacts on a large estuarine ecosystem. *Estuaries* 26, 1329–1343. doi: 10.1007/BF02803635

Piehler, M. F., Twomey, L. J., Hall, N. S., and Paerl, H. W. (2004). Impacts of inorganic nutrient enrichment on phytoplankton community structure and function in Pamlico Sound, NC, USA. *Estuar. Coastal Shelf Sci.* 61, 197–209. doi: 10.1016/j.ecss.2004.05.001

Pinckney, J. L., Quigg, A. S., and Roelke, D. L. (2017). Interannual and seasonal patterns of estuarine phytoplankton diversity in Galveston Bay, Texas, USA. *Estuar. Coasts* 40, 310–316. doi: 10.1007/s12237-016-0135-8

Pinckney, J. L., Wee, J. L., Hou, A., and Walker, N. D. (2009). Phytoplankton community structure responses to urban effluent inputs following Hurricanes Katrina and Rita. *Mar. Ecol. Prog. Ser.* 387, 137–146. doi: 10.3354/meps08091

Posch, T., Eugster, B., Pomati, F., Pernthaler, J., Pitsch, G., and Eckert, E. M. (2015). Network of interactions between ciliates and phytoplankton during spring. *Front. Microbiol.* 6:1289.

Qian, Y., Wade, T. L., and Sericano, J. L. (2001). Sources and bioavailability of polynuclear aromatic hydrocarbons in Galveston Bay. *Texas. Estuar.* 24, 817–827.

Rashid, A. R., and Duffett, M. (2016). Medications for children: a survey of community pharmacists. *J. Ped. Pharm. Therap.* 21, 213–223. doi: 10.5863/1551-6776-21.3.213

Roach, R. W., Carr, R. S., Howard, C. L., and Cain, B. W. (1993). "An assessment of produced water impacts at two sites in the Galveston Bay system," in *Proceedings of the Galveston Bay Characterization Workshop;* 1991 Feb 21-23, eds F. S. Shipley and R. W. Kiesling (Webster, TX: Galveston Bay National Estuary Program Publication GBNEP-6).

Roelke, D. L., Li, H. P., Hayden, N. J., Miller, C. J., Davis, S. E., Quigg, A., et al. (2013). Co-occurring and opposing freshwater inflow effects on phytoplankton biomass, productivity and community composition of Galveston Bay, USA. *Mar. Ecol. Prog. Ser.* 477, 61–76. doi: 10.3354/meps10182

Schloss, P. D., Westcott, S. L., Ryabin, T., Hall, J. R., Hartmann, M., and Hollister, E. B. (2009). Introducing mothur: open-source, platform-independent, community-supported software for describing and comparing microbial communities. *Appl. Environ. Microbiol.* 75, 7537–7541. doi: 10.1128/aem.01541-09

Steichen, J. L., and Quigg, A., (2018). Fish species as indicators of freshwater inflow within a subtropical estuary in the Gulf of Mexico. *Ecol. Indicat.* 85, 180–189. doi: 10.1016/j.ecolind.2017.10.018

Steichen, J. L., Windham, R., Brinkmeyer, R., and Quigg, A. (2012). Ecosystem under pressure: ballast water discharge into Galveston Bay, Texas (USA) from 2005 to 2010. *Mar. poll. Bull.* 64, 779–789. doi: 10.1016/j.marpolbul.2012.01.028

Suarez, M. P., Rifai, H. S., Palachek, R., Dean, K., and Koenig, L. (2006). Distribution of polychlorinated dibenzo-p-dioxins and dibenzofurans in suspended sediments, dissolved phase and bottom sediment in the Houston Ship Channel. *Chemosphere* 62, 417–429. doi: 10.1016/j.chemosphere.2005.04.088

Suttle, C. A., and Chan, A. M. (1994). Dynamics and distribution of cyanophages and their effect on marine *Synechococcus* spp. *Appl. Environ. Microbiol.* 60, 3167–3174. doi: 10.1128/aem.60.9.3167-3174.1994

Texas Water Development Board (2019). *Water Data for Coastal Texas Database*. Available online at: https://www.waterdatafortexas.org/coastal/hydrology/galveston

Thronson, A., and Quigg, A., (2008). Fifty-five years of fish kills in coastal Texas. *Estuar. Coasts* 31, 802–813. doi: 10.1007/s12237-008-9056-5

Thyng, K. M., Hetland, R. D., Socolofsky, S. A., Fernando, N., Turner, E. L., and Schoenbaechler, C. (2020). Hurricane Harvey caused unprecedented freshwater inflow to Galveston Bay. *Estuar. Coasts* (in review)

Tolan, J. M. (2013). "Estuarine fisheries community-level response to freshwater inflows," in *Water Resources Planning, Development and Management*, ed. R. Wurbs (London: IntechOpen), doi: 10.5772/52313

Van Metre, P. C., Mahler, B. J., Scoggins, M., and Hamilton, P. A. (2006). *Parking lot Sealcoat: A Major Source of Polycyclic Aromatic Hydrocarbons (PAHs) in Urban and Suburban Environments*. Reston, VA: USGS.

van Oldenborgh, G. J., Van Der Wiel, K., Sebastian, A., Singh, R., Arrighi, J., Otto, F., et al. (2017). Attribution of extreme rainfall from Hurricane Harvey, August 2017. *Environ. Res. Let.* 12:124009. doi: 10.1088/1748-9326/aa9ef2

Wade, T. L., Sweet, S. T., Sericano, J. L., Guinasso, N. L. Jr., Diercks, A. R., and Highsmith, R. C. (2011). "Analyses of water samples from the Deepwater Horizon oil spill: documentation of the subsurface plume," in *Monitoring and Modeling the Deepwater Horizon Oil Spill: A Record-Breaking Enterprise*, eds Y. Liu, A. Macfadyen, Z.-G. Ji, and R. H. Weisberg (Washington, DC: John Wiley & Sons), 77–82. doi: 10.1029/2011gm001103

Waide, R. B. (1991). Summary of the response of animal populations to hurricanes in the Caribbean. *Biotropica* 23, 508–512.

Walters, W., Hyde, E. R., Berg-Lyons, D., Ackermann, G., Humphrey, G., Parada, A., et al. (2016). Improved bacterial 16S rRNA gene (V4 and V4-5) and fungal internal transcribed spacer marker gene primers for microbial community surveys. *Msystems* 1:e00009-15.

Wetz, M. S., and Paerl, H. W. (2008). Estuarine phytoplankton responses to hurricanes and tropical storms with different characteristics (trajectory, rainfall, winds). *Estuar. Coasts* 31, 419–429. doi: 10.1007/s12237-008-9034-y

Willett, K. L., McDonald, S. J., Steinberg, M. A., Beatty, K. B., Kennicutt, M. C., and Safe, S. H. (1997). Biomarker sensitivity for polynuclear aromatic hydrocarbon contamination in two marine fish species collected in Galveston Bay, Texas. *Environ. Toxicol. Chem.* 16, 1472–1479. doi: 10.1002/etc.5620160721

Williams, A. K., Bacosa, H. P., and Quigg, Q. (2017). The impact of dissolved inorganic nitrogen and phosphorous on responses of microbial plankton to the Texas City "Y" Oil Spill in Galveston Bay, Texas (USA). *Mar. Pollut. Bull.* 121, 32–44. doi: 10.1016/j.marpolbul.2017.05.033

Wolf, S. (2017). *Press Release Analysis: Nearly One Million Pounds of Seven Deadly Air Pollutants Released by Texas Refineries during Harvey Floods*. Arizona: Center for Biological Diversity.

Xia, X., Vidyarathna, N. K., Palenik, B., Lee, P., and Liu, H. (2015). Comparison of the seasonal variations of *Synechococcus* assemblage structures in estuarine waters and coastal waters of Hong Kong. *Appl. Environ. Microbiol.* 81, 7644–7655. doi: 10.1128/aem.01895-15

Yan, G., Labonte, J., Quigg, A., and Kaiser, K. (this issue). Hurricanes accelerate carbon cycling in coastal ecosystems.

Yin, F., Hayworth, J. S., and Clement, T. P. (2015). A tale of two recent spills—comparison of 2014 Galveston Bay and 2010 Deepwater Horizon oil spill residues. *PLoS ONE* 10:e0118098. doi: 10.1371/journal.pone.0124645

Zhang, Y. J., Li, S., Gan, R. Y., Zhou, T., Xu, D. P., and Li, H. B. (2015). Impacts of gut bacteria on human health and diseases. *Int. J. Mol. Sci.* 16, 7493–7519. doi: 10.3390/ijms16047493

Conflict of Interest: The authors declare that the research was conducted in the absence of any commercial or financial relationships that could be construed as a potential conflict of interest.

Advantages of publishing in Frontiers

OPEN ACCESS
Articles are free to read
for greatest visibility
and readership

FAST PUBLICATION
Around 90 days
from submission
to decision

HIGH QUALITY PEER-REVIEW
Rigorous, collaborative,
and constructive
peer-review

TRANSPARENT PEER-REVIEW
Editors and reviewers
acknowledged by name
on published articles

Frontiers
Avenue du Tribunal-Fédéral 34
1005 Lausanne | Switzerland

Visit us: www.frontiersin.org
Contact us: frontiersin.org/about/contact

REPRODUCIBILITY OF RESEARCH
Support open data
and methods to enhance
research reproducibility

DIGITAL PUBLISHING
Articles designed
for optimal readership
across devices

FOLLOW US
@frontiersin

IMPACT METRICS
Advanced article metrics
track visibility across
digital media

EXTENSIVE PROMOTION
Marketing
and promotion
of impactful research

LOOP RESEARCH NETWORK
Our network
increases your
article's readership